transactions of the ASME

journal of heat transfer

Published Quarterly by
The American Society of
Mechanical Engineers
Volume 95 • Series C • Number 4
NOVEMBER 1973

EDITED and PUBLISHED quarterly at the offices of The American Society of Mechanical Engineers, United Engineering Center, 345 E. 47th St., New York, N. Y. 10017. Cable address, "Mechaneer," New York. Second-class postage paid at New York, N. Y., and at additional mailing offices.

CHANGES OF ADDRESS must be received at Society headquarters seven weeks before they are to be effective. Please send old label and new address.

PRICES: To members, $15.00, annually; to nonmembers, $30.00. Single copies, $10.00 each. Add $1.50 for postage to countries outside the United States and Canada.

STATEMENT from By-Laws. The Society shall not be responsible for statements or opinions advanced in papers or . . . printed in its publications (B13, Par. 4).

INDEXED by the Engineering Index, Inc.

(Contents continued on page 576)

CONTENTS

(CONTINUED)

D. K. EDWARDS
Professor.
Mem. ASME

A. BALAKRISHNAN
Postgraduate Research Engineer.

Energy and Kinetics Department,
University of California,
Los Angeles, Calif.

Radiative Cooling of a Turbulent Flame Front

Temperature profiles arising from simultaneous radiation and turbulent diffusion in combustion gas products in the vicinity of a turbulent flame front are obtained analytically. Account is taken of the highly nongray nature of the gas absorption and emission by use of band absorption properties and slab band absorptance functions. Radiative cooling is shown to be quite effective, not by acting directly upon the eddies themselves at the flame front, but by acting indirectly to cool greatly the gases in the vicinity of the flame front, which in turn cool the eddies through turbulent mixing. Generalized dimensionless results, as well as particularized examples, are presented. It was found that CO_2, being an intense emitter, reduces flame front temperature to a greater degree than H_2O, a less intense emitter, even though the total emissivity of H_2O exceeds that of CO_2. For this reason flue gas recirculation appears more advantageous than water or steam injection in achieving radiative cooling.

Introduction

In a combustion chamber, two major mechanisms serve to transfer heat from the hot combusting gases to cooler regions, turbulent diffusion and radiation. The first, turbulent diffusion, is effective over short distances when the temperature gradients are large. The second, heat radiation, is effective over long distances, and does not require high temperature gradients within the gaseous medium itself, if the walls are cold and black. These heat transfer mechanisms have an important effect on the combustion process, because the heat release and removal rates fix the combustion temperature, and the temperature strongly influences the thermodynamic and kinetic parameters. For example, formation rates of nitric oxide, a serious atmospheric pollutant in some parts of the United States, are strongly influenced by combustion temperature [1, 2].[1]

In order to examine the role of simultaneous turbulence and radiative transfer, a very simple model is taken as shown in Fig. 1. A thin slab of fuel-bearing gases is imagined to be symmetrically enclosed by oxygen-bearing gases which in turn are enclosed by cooled, parallel black walls. Flame fronts are imagined to be present between the fuel layer and oxidizing layers. The volume of gases between the walls is imagined to be turbulent. Soot is neglected in the present paper, because it is desired to establish to what extent molecular gas radiation acting alone can reduce the temperature of a flame front.

Certainly a flame front in a fixed sense does not exist in a turbulent gas. Eddies of fuel and eddies of air intermix; the eddies themselves may contain smaller eddies. Burning takes place at the eddy boundaries, and to an observer the combustion appears to be occurring here and there, now and again over an appreciable volume. But on a statistically-averaged basis, consistent with turbulence viewed as a steady diffusion process carried out by mixing eddies, the notion of a flame front may have relevance despite the appearance presented to the eye. One must be careful, however, to regard the results obtained from such a viewpoint in their proper perspective. The temperature predicted at the "flame front," for example, is not a peak transient temperature at an eddy boundary, but is a statistically-averaged,

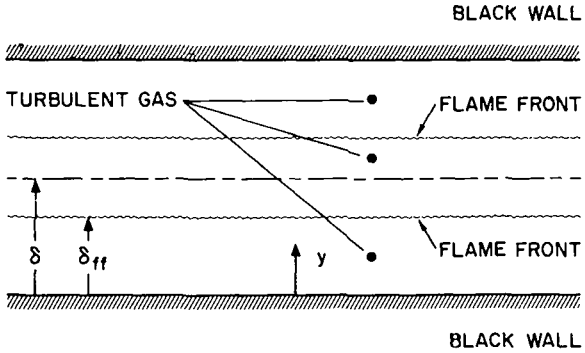

Fig. 1 Flame front model geometry

[1] Numbers in brackets designate References at end of paper.

Contributed by the Heat Transfer Division and presented at the Winter Annual Meeting, New York, N. Y., November 26–30, 1972, of The American Society of Mechanical Engineers. Manuscript received by the Heat Transfer Division August 14, 1972; revised manuscript received February 16, 1973. Paper No. 72-WA/HT-27.

steady temperature prevailing at the statistically-averaged location of the flame front.

Furthermore, in relating the present Couette-flow-like model to actual combustion, it is necessary to allow for the convective flow of heat. The convective flow acts somewhat as a volume heat sink. On the other hand, volume-distributed combustion acts as a volume heat source. The flame-front situation investigated in what follows can be viewed as corresponding approximately to volume combustion counterbalanced by convective heat flow, and additional flame-front heat release; the latter is assumed to flow ultimately to the cold wall.

Literature Survey

Beer and Howarth [3] and Lefebvre [4] have reviewed the level at which conventional radiation analysis for combustion chamber design is carried out. Spalding [5] has argued that a more scientific approach may find application, particularly because of the need to understand the formation of NO, smoke, and malodorous compounds during combustion. However, as Spalding states, "Scientists have to simplify, often to over-simplify, in order to reduce their observations to quantitative order."

One of the complicating factors in radiation transport is luminous radiation [3, 4]. A simplified situation, nonluminous radiation, exists under conditions of steam or water injection or in some cases of natural gas combustion. In the realm of nonluminous radiation coupled with conductive or convective transport, Cess, Mighdoll, and Tiwari [6] have treated nongray molecular gas radiation and laminar conduction in volume-heated carbon monoxide gas between infinite black parallel plates. A substitute kernel was used, and quadratic and quartic colocation was found to fix the temperature profile adequately. Greif and Habib [7] considered turbulent channel flow of an optically thin radiating gas. The assumption of small optical depth allowed a simplified kernel to be used, which facilitated solution. Nichols [8] and Landram, Greif, and Habib [9] studied turbulent flow in cylindrical ducts. Schimmel, Novotny, and Olsofka [10] examined radiation and laminar natural convection in a molecular gas.

Gille and Goody [11] and Wang [12] made use of the fact that plane parallel problems can be formulated in terms of a "modified emissivity." Recently a slab band absorptance [13] was introduced for plane parallel problems involving nongray molecular gas band radiation, and nongrey radiative transfer in a volume heated molecular gas was solved [14]. In this latter work the linearized problem was treated consistent with the "modified emissivity" concept, thus avoiding the complications of variable gas properties considered by Chan and Tien [15], Cess and Wang [16], and Edwards and Morizumi [17].

Analysis

Fig. 1 shows the model situation selected. Two flame fronts are symmetrically located about the mid-plane of a plane parallel duct. The duct walls are distance 2δ apart and are taken to be black and maintained at temperature T_w by internal cooling passages. Heat is released at each flame front at the statistically averaged steady value of q Btu/hr ft^2. This heat diffuses through turbulent mixing into the adjacent volumes of gas, and these volumes radiate to the walls and adjacent layers as well as mixing turbulently with the immediately adjacent layers.

The eddy diffusivity within the duct is modeled by the Van Driest law of the wall [18] corrected by the Mei and Squire channel factor [19]. The ratio of the molecular to the turbulent Prandtl number is taken to be unity.

$$\epsilon^+ = \frac{k_m + \rho c_p \epsilon_H}{k_m} = \frac{0.5 + 0.5[1 + 4V^2 y^{*2}(1 - e^{-y^*/y_0^*})^2]^{1/2}}{1 + 3.4y^*} \quad (1)$$

where

Nomenclature

A = total band absorption, cm^{-1}
A_s^* = slab band absorptance, dimensionless
$A_{i,j}$ = defined in Appendix
B = Planck black body spectral radiosity, Btu/hr ft^2 cm^{-1}
B' = first derivative of B with respect to T
c_f = skin friction coefficient
c_p = specific heat at constant pressure, Btu/lb$_m R$
c = speed of light, cm/sec
C = dz^*/dy^* defined in Appendix
D^* = dimensionless eddy diffusivity grouping defined in Appendix
D_h = hydraulic diameter, ft
E_n = exponential integral function of order n
f = friction factor
$F_{i,j}$ = matrix element defined in Appendix
h = Planck's constant, erg sec
k_m = molecular thermal conductivity, Btu/hr ft R
K = von Karman constant
k = Boltzmann constant, erg/K → erg/R
l = subdivision at the flame front
m = total number of subdivisions
n = total number of spectral bands
Nu = Nusselt number
P = temperature gradient dT/dy
P^* = dimensionless temperature gradient dT^*/dz^*
Pr = Prandtl number
q = heat flux, Btu/hr ft^2
R_{dm} = radiation conductance to molecular conductance parameter defined in Appendix
R_t = turbulent Reynolds number, $(1/4)\sqrt{c_f/2}\ \mathrm{Re}_{D_h}$
Re_{D_h} = Reynolds number based on hydraulic diameter
S^* = zeroth moment of slab band absorptance defined in Appendix
T = temperature, R
T^* = dimensionless temperature defined in Appendix
T_v = volume average temperature, R
V = a constant, defined by equation (3); also velocity, ft/sec, in Reynolds number
W = dimensionless weighting ratio defined in Appendix
y = distance from wall, ft
y^* = dimensionless distance defined by equation (2)
z^* = dimensionless distance defined in Appendix
α = integrated band intensity, cm^{-1}/g m^{-2} or cm^{-1}/lb$_m$ ft^{-2}
δ = half thickness of gas layer, ft
$\delta_{i,j}$ = Kronecker delta
δ_{ff}^* = dimensionless flame front location
ϵ_H = eddy diffusivity of heat, ft^2/hr
ϵ^+ = dimensionless eddy diffusivity
μ = viscosity, lb$_f$ sec/ft^2
ν_k = wavenumber, cm^{-1}
ν = band center or band head of the kth band, cm^{-1}
π = 3.1415927...
ρ = density of gas, lb$_m$/ft^3
τ = optical depth at maximum absorption in band, dimensionless
ω = bandwidth parameter, cm^{-1}

Subscripts

C = convective
ff = flame front
H = half width of channel
i = ith location in channel
j = jth location in channel
k = kth band in spectrum
Q = from spectral quadrature
R = radiative
s = slab
T = total
t = turbulent
v = volume
w = wall
ν = spectral

$$y^* = y/\delta \tag{2}$$

$$V = K\mathrm{R}_t \tag{3}$$

$$y_0^* = 26/\mathrm{R}_t \tag{4}$$

$K = 0.4$ (the von Karman constant)

$$\mathrm{R}_t = \sqrt{\frac{c_f}{2}}\left(\frac{V\delta\rho}{\mu}\right) = \frac{1}{4}\sqrt{\frac{f}{8}}\,\mathrm{Re}_{D_h} \tag{5}$$

and c_f is the skin friction coefficient, f the friction factor, and Re_{D_h} the Reynolds number based upon hydraulic diameter $D_h = 4\delta$. The Mei and Squire correction, the denominator of equation (1), reduces the central value of ϵ^+ to 0.09 R_t instead of giving it the value $V = 0.4\ \mathrm{R}_t$ according to the Van Driest law extrapolated outside its range of validity.

Conservation of energy within the two layers of turbulent gas is given by two equations, each of the form

$$0 = \frac{d}{dy}\left(k_m\epsilon^+\frac{dT}{dy}\right) + \frac{d}{dy}(-q_R) \tag{6}$$

subject to four boundary conditions

$$y = 0, \qquad T = T_w \tag{7}$$

$$y = 0, \qquad -q_R + k_m\epsilon^+\frac{dT}{dy} = q \tag{8}$$

$$y = \delta_{ff}, \qquad T(\delta_{ff}^-) = T(\delta_{ff}^+) \tag{9}$$

$$y = \delta, \qquad k_m\epsilon^+\frac{dT}{dy} = 0 \tag{10}$$

In order to compute q_R, symmetry in T about the center line is invoked. This symmetry makes q_R at the center, $y = \delta$, zero. Equation (6) may be integrated and boundary conditions (8) and (10) satisfied by writing

$$0 \le y < \delta_{ff} \qquad -q_R + k_m\epsilon^+\frac{dT}{dy} = q \tag{11}$$

$$\delta_{ff} < y \le \delta \qquad -q_R + k_m\epsilon^+\frac{dT}{dy} = 0 \tag{12}$$

Equations (11) and (12), since q_R is an integral term, as will be shown in the following, constitute two simultaneous integro-differential equations.

References [13] and [14] have developed an expression for q_R in particularly convenient form for molecular gases such as CO_2, H_2O, CH_4, etc., provided overlapping gas bands are treated as a single band and provided the temperature variations are small and the bands not too wide so that B_k' may be treated as constant. For uniform gas composition

$$-q_R = \sum_{k=1}^{n}\omega_k B_k'\int_0^1 \{A_s^*(\tau_{H,k}(2 - y^* - y'^*)) - A_s^*(\tau_{H,k}|y^* - y'^*|)\}\frac{dT}{dy'^*}\,dy'^* \tag{13}$$

where

$$B_k' = \frac{\partial B(\nu_k, T)}{\partial T}, \qquad B(\nu, T) = \frac{2\pi hc^2\nu^3}{e^{hc\nu/kT} - 1} \tag{14}$$

$$\tau_{H,k} = \frac{\alpha_k\rho_k\delta}{\omega_k} \tag{15}$$

The quantity B is the Planck black body radiosity. The quantity $\tau_{H,k}$ is the maximum optical depth for the kth gas radiation band based upon the half channel width and assuming uniform composition throughout the gas layer. The bands are located at wavenumber ν_k and are modeled by the exponential-winged gas band model with overlapped lines and integrated intensity α_k and band width parameter ω_k. Recently values of α_k and ω_k have been presented for H_2O, CO_2, CO, NO, SO_2, and CH_4 [20].

By virtue of the fact that equation (13) has been put in the form shown, equations (11) and (12) are pure integral equations in dependent variable

$$P = dT/dy \tag{16}$$

and have a symmetric kernel. Note that there is a discontinuity in P at the flame front, and note also that the governing integral equations require no boundary conditions.

Equation (13) may be approximated accurately by a sum of P values at a discrete set of coordinate points y_i, $i = 1, 2, \ldots, m$. At the flame front two values of i are assigned, that is, $y_l = \delta_{ff}^-$ and $y_{l+1} = \delta_{ff}^+$ as shown in the Appendix. Then equations (11) and (12) written at the m locations become m simultaneous algebraic equations in P_i ($i = 1, m$). Once these are solved by matrix inversion or reiteration, the temperatures T_i can be found by forward marching integration, using the boundary conditions $T_{i=1} = T_w$ and $T_l = T_{l+1}$. The Appendix shows details of the solution procedure.

Results

Calculations were carried out for two cases. In one case the gas was taken to have $\tau_{H,k}$ and ω_k invariant with k, and the temperature, composition, and band locations were otherwise unspecified and therefore general. In the other case the gas was taken to be a two-foot-thick layer ($\delta = 0.305$ m) of H_2O or CO_2 having a mean temperature in the neighborhood of 3600 R (2000 K). In the former case two flame front locations were investigated, $\delta_{ff}^* = 1$ and $\delta_{ff}^* = 0.81$.

The results for $\tau_{H,k}$ and ω_k invariant with k are shown in Table 1 based upon a value of dimensionless volume average temperature equal to unity. The flame-to-volume-average-temperature difference ratio is shown, as well as total and radiative wall fluxes made dimensionless by $k_m(T_v - T_w)/\delta$, i.e.,

Table 1 Results for flame front heat release at $y^* = 0.81$. Parameters ω_k and $\tau_{H,k}$ invariant with k.

Effect of turbulent Reynolds number for $\tau_H = 50$, $A_s^*(2\tau_H) = 5.682$, $\delta_{ff}^* = 0.81$

R_{dm}/A_s^*		$\mathrm{R}_t =$ 100	$\mathrm{R}_t =$ 300	$\mathrm{R}_t =$ 1000	$\mathrm{R}_t =$ 3000	$\mathrm{R}_t =$ 5000
0	Nu_T	5.18	14.0	41.7	105.3	140.9
	Nu_R	0.0	0.0	0.0	0.0	0.0
	T_{ff}^*/T_v^*	1.31	1.24	1.20	1.17	1.14
10.0	Nu_T	37.3	47.4	77.1	143.0	181.1
	Nu_R	31.0	35.0	39.6	43.3	45.6
	T_{ff}^*/T_v^*	1.62	1.41	1.28	1.20	1.16
100.0	Nu_T	316.6	330.9	370.5	457.2	515.2
	Nu_R	302.0	314.2	351.8	384.6	411.4
	T_{ff}^*/T_v^*	2.25	1.87	1.58	1.39	1.30

Effect of maximum optical depth for $R_t = 1000$, $\delta_{ff}^* = 0.81$

R_{dm}/A_s^*		$\tau_H =$ 5	$\tau_H =$ 10	$\tau_H =$ 100	$\tau_H =$ 1000
		$A_s^*(2\tau_H) = 3.380$	$A_s^*(2\tau_H) = 4.073$	$A_s^*(2\tau_H) = 6.376$	$A_s^*(2\tau_H) = 8.678$
0	Nu_T	41.7	41.7	41.7	41.7
	Nu_R	0.0	0.0	0.0	0.0
	T_{ff}^*/T_v^*	1.20	1.20	1.20	1.20
10.0	Nu_T	69.3	72.6	78.1	79.2
	Nu_R	29.9	33.8	41.0	42.5
	T_{ff}^*/T_v^*	1.25	1.26	1.28	1.29
100.0	Nu_T	312.9	340.0	375.7	381.0
	Nu_R	281.3	309.4	347.5	353.2
	T_{ff}^*/T_v^*	1.53	1.55	1.59	1.60

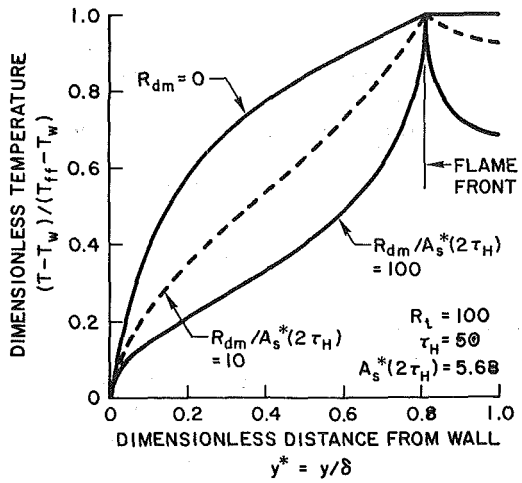

Fig. 2 Temperature profiles for low turbulence (R_t = 100). Flame front at y^* = 0.81.

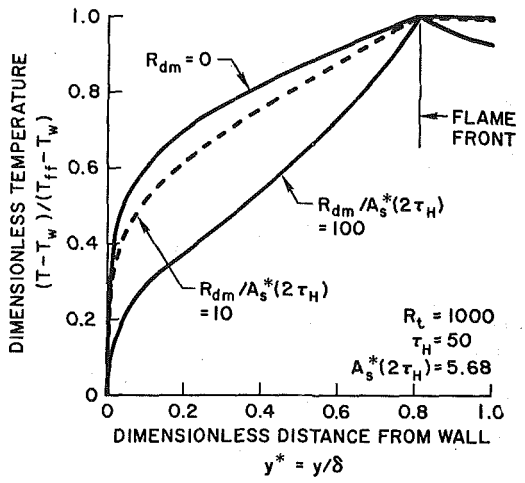

Fig. 3 Temperature profiles for high turbulence (R_t = 1000). Flame front at y^* = 0.81.

$$\mathrm{Nu}_T = \frac{-q(0)\delta}{k_m(T_v - T_w)}$$

$$\mathrm{Nu}_R = \frac{-q_R(0)\delta}{k_m(T_v - T_w)}$$

Parameters are $R_{dm}/A_s^*(2\tau_H)$, R_t and $\tau_{H,k} = \tau_H$, and δ_{ff}^*. If Nusselt numbers based upon flame front temperature are desired, Nu_T may be divided by

$$T_{ff}^*/T_v^* = (T_{ff} - T_w)/(T_v - T_w)$$

which is also tabulated. Note that the Nusselt numbers are based upon channel half width δ. Values based upon hydraulic diameter would be four times as large.

Figs. 2 and 3 show temperature profiles normalized with respect to the flame front temperature.

Results for H_2O and CO_2 at 3600 R and δ = 1 ft (0.305 m) are shown in Table 2.

Discussion

The results can be viewed in a number of ways. For example, one can ask what flame front temperatures are achieved at equal values of heat release per unit area or one can ask what values of heat release per unit area can be achieved at equal flame front temperatures. Viewed in either of these ways radiation is seen to play a dominant role when R_{dm} is large. For equal values of $T_{ff} - T_w$ the relative heat fluxes are measured by $\mathrm{Nu}_T/(T_{ff}^*/T_v^*)$. For nominal values of R_t = 1000 and τ_H = 50, the results may be used to obtain the following values:

	Relative heat flux	
$R_{dm}/A_s^*(2\tau_H)$	δ_{ff}^* = 1	δ^*_{ff} = 0.81
0	1.00	1.07
0.1	1.01	1.08
1.0	1.07	1.16
10.0	1.68	1.88
100.0	5.70	7.28

As the value of R_{dm} increases from 56.8 to 568 ($A_s^*(2\tau_H$ = 100) = 5.68), the acceptable heat release rate for a fixed maximum acceptable flame front temperature is increased more than three fold. When the distance between flame fronts is thickened to about one fifth (0.19) of the channel width, such as might be done by combustion product recirculation or steam injection, an additional 28 percent increase in heat release rate becomes acceptable.

Table 2 Results for a multi-band gas. Flame front at center, T = 3600 R, half thickness δ = 1 ft, P = 1 atm

Water vapor

Mole fraction = 0.18, R_{dm} = 689, k_m = 0.0680 (nitrogen diluent)

Band No.	Wave-number ν_k, cm^{-1}	Maximum optical depth $\tau_{H,k}$	Band decay width ω_k	Slab band absorption $A_s^*(2\tau_{H,k})$	Weighting factor $W_kA_s^*$ $(2\tau_{H,k})$
1	500	4.82	127	3.34	0.020
2	1600	0.98	252	1.77	0.199
3	3760	0.56	268	1.28	0.530
4	5350	0.14	193	0.46	0.163
5	7250	0.12	143	0.40	0.087

For R_t = 300, Nu_T = 796 and T_{ff}^*/T_v^* = 4.56
For R_t = 1000, Nu_T = 817 and T_{ff}^*/T_v^* = 2.81

Carbon dioxide

Mole fraction = 0.333, R_{dm} = 330, k_m = 0.0656 (nitrogen diluent)

Band No.	Wave-number ν_k, cm^{-1}	Maximum optical depth $\tau_{H,k}$	Band decay width ω_k	Slab band absorption $A_s^*(2\tau_{H,k})$	Weighting factor $W_kA_s^*$ $(2\tau_{H,k})$
1	667	9.11	57	3.98	0.027
2	960	0.10	60	0.34	0.005
3	1060	0.13	45	0.43	0.006
4	2410	59.8	50	5.86	0.368
5	3660	1.89	105	2.41	0.541
6	5200	0.04	154	0.13	0.053

For R_t = 300, Nu_T = 801 and T_{ff}^*/T_v^* = 3.48
For R_t = 1000, Nu_T = 837 and T_{ff}^*/T_v^* = 2.52

These effects are even more pronounced at lower values of turbulence parameter R_t.

An increase in turbulence also increases the acceptable heat release rate for a fixed flame front temperature, but not as dramatically as radiation. For example, as R_t increases from 300 to 3000 at R_{dm} = 568, the acceptable heat release rate increases 125 percent.

In one of the sample calculations for a multi-band gas, a 2 ft thick layer (δ = 0.305 m) of a H_2O–N_2 gas mixture with 0.18 mole fraction H_2O in N_2 was assumed. Such a concentration of H_2O could result from stoichiometric combustion of methane. A volume average temperature for the layer of 3600 R was taken. The assumed values give R_{dm} equal to 689 and a heat release rate of 12 Btu/hr ft^2 per deg Rankine (68 w/m^2-deg K) of temperature difference between the flame front and wall when R_t = 300. This value of R_t corresponds to a value of Re_{D_h} of 2.1×10^4 and thus a gas velocity of approximately 20 ft/sec.

In the CO_2 gas calculation, the value of heat release rate per degree of temperature difference between flame front and wall is somewhat higher, even though R_{dm} is smaller, because the CO_2 bands are stronger, and a high mole fraction (corresponding to combustion of CO with air) was assumed. The stronger bands serve to bring radiation into play in a smaller thickness of gas about the flame front with the result that T_{ff}^*/T_v^* is considerably smaller for the gas with stronger bands.

The results suggest that radiation can be an extremely important mechanism in lowering flame front temperatures and that radiation properties may be changed by such factors as steam or water injection and exhaust gas recirculation. However, it can hardly be overstressed that the model employed is quite simplified. While realistic nongray gas properties were employed, the gas composition was taken to be uniform, and the radiation transfer was treated under the additional constraints of small temperature differences and constant properties. Luminous radiation from soot was neglected as was streamwise convective transfer. Soot is not necessarily beneficial, as too large amounts can actually reduce radiative transfer and promote hotter flames. The geometry chosen for investigation was a simple one-dimensional one, and streamwise temperature gradients were neglected. It is thought that the model considered here is a first step in accounting for cooling by nongray molecular gas radiation from combustion products.

Acknowledgment

Computations were carried out at the UCLA Campus Computing Network. Mr. Balakrishnan gratefully acknowledges support received from State of California Air Pollution Grant No. 4-402474.

References

1 Newhall, H. K., and Shahed, S. M., "Kinetics of Nitric Oxide Formation in High Pressure Flames," *Thirteenth Symposium (International) on Combustion*, The Combustion Institute, 1971, pp. 381–388.

2 Breen, B. P., Bell, A. W., Bayard de Volo, N., Bagwell, F. A., and Rosenthal, K., "Combustion Control for Elimination of Nitric Oxide Emissions From Fossil-Fuel Power Plants," op. cit., pp. 391–401.

3 Beer, J. M., and Howarth, C. R., "Radiation From Flames in Furnaces," *Twelfth Symposium (International) on Combustion*, 1968, pp. 1205–1217.

4 Lefebvre, A. H., "Radiation From Flames in Gas Turbines and Rocket Engines," op. cit., pp. 1247–1253.

5 Spalding, D. B., "Combustion as Applied to Engineering," *J. Inst. of Fuel*, Apr. 1971, pp. 196–203.

6 Cess, R. D., Mighdoll, P., and Tiwari, S. N., "Infrared Radiative Heat Transfer in Nongray Gases," *International Journal of Heat and Mass Transfer*, Vol. 10, 1967, pp. 1521–1532.

7 Greif, R., and Habib, I. S., "Heat Transfer in Turbulent Flow With Radiation for Small Optical Depths," *Appl. Sci. Res.*, Vol. 22, 1970, pp. 31–43.

8 Nichols, L. D., "Temperature Profile in the Entrance Region of an Annular Passage Considering the Effects of Turbulent Convection and Radiation," *International Journal of Heat and Mass Transfer*, Vol. 8, 1965, pp. 589–607.

9 Landram, C. S., Greif, R., and Habib, I. S., "Heat Transfer in Turbulent Pipe Flow With Optically Thin Radiation," JOURNAL OF HEAT TRANSFER, Series C, Vol. 91, 1969, pp. 330–336.

10 Schimmel, W. P., Novotny, J. L., and Olsofka, F. A., "Interferometric Study of Radiation-Conduction Interaction," *Heat Transfer 1970*, preprints of papers presented at the Fourth International Heat Transfer Conference, Elsevier Publishing Co., Amsterdam, 1970, Vol. III, paper R2.1.

11 Gille, J., and Goody, R. M., "Convection in a Radiating Gas," *J. Fluid Mechanics*, Vol. 20, 1964, pp. 47–79.

12 Wang, L. S., "The Role of Emissivities in Radiative Transport Calculations," *J. Quant. Spectrosc. Radiat. Transfer*, Vol. 8, 1968, pp. 1233–1240.

13 Edwards, D. K., and Balakrishnan, A., "Slab Band Absorptance for Molecular Gas Radiation," op. cit., Vol. 12, 1972, pp. 1379–1387.

14 Edwards, D. K., and Balakrishnan, A., "Nongray Radiative Transfer in a Turbulent Gas Layer," *International Journal of Heat and Mass Transfer*, Vol. 16, 1973, pp. 1003–1015.

15 Chan, S. H., and Tien, C. L., "Total Band Absorptance of Nonisothermal Infrared Radiating Gases," *J. Quant. Spectrosc. Radiat. Transfer*, Vol. 9, 1969, pp. 1261–1271.

16 Cess, R. D., and Wang, L. S., "A Band Absorptance Formulation for Nonisothermal Gaseous Radiation," *International Journal of Heat and Mass Transfer*, Vol. 13, 1970, pp. 547–556.

17 Edwards, D. K., and Morizumi, S. J., "Scaling of Vibration-Rotation Band Parameters for Nonhomogeneous Gas Radiation," *J. Quant. Spectrosc. Radiat. Transfer*, Vol. 10, 1970, pp. 175–188.

18 Van Driest, E. R., "On Turbulent Flow Near a Wall," *J. Aero. Sci.*, Vol. 23, 1956, pp. 1007–1011.

19 Mei, J., and Squire, W., "A Simple Eddy Viscosity Model for Turbulent Pipe and Channel Flow," *AIAA Journal*, Vol. 10, 1972, pp. 350–352.

20 Edwards, D. K., and Balakrishnan, A., "Thermal Radiation by Combustion Gases," *International Journal of Heat and Mass Transfer*, Vol. 16, 1973, pp. 25–40.

APPENDIX

The governing integral equation is solved in much the same manner as employed in reference [14]. Temperature is made dimensionless by use of the prescribed heat flux q and the maximum value of ϵ^+

$$T^* = \frac{(T - T_w)k_m\epsilon^+(y^* = 1)}{q\delta}$$

Equation (13) is written

$$q_R^* = -\frac{q_R}{q} = \left(\frac{\delta}{k_m}\sum_{k=1}^{n}\omega_k B_k' A_s^*(2\tau_{H,k})\right)\frac{1}{\epsilon^+(1)} \cdot \sum_{k=1}^{n} W_k \int_0^1 \{A_s^*(\tau_{H,k}(2 - y'^* - y^*)) - A_s^*(\tau_{H,k}|y^* - y'^*|)\}\frac{dT^*}{dy'^*}\,dy'^*$$

where W_k is introduced arbitrarily as

$$W_k = \frac{\omega_k B_k'}{\sum_{k=1}^{n}\omega_k B_k' A_s^*(2\tau_{H,k})}$$

The foregoing expression may be written

$$q_R^* = \frac{R_{dm}}{\epsilon^+(1)}\sum_{k=1}^{n} W_k\, q_{R,k}^*$$

where R_{dm} is a ratio of radiation conductance to molecular conductance

$$R_{dm} = \frac{\delta}{k_m}\sum_{k=1}^{n}\omega_k B_k' A_s^*(2\tau_{H,k})$$

and

$$q_{R,k}^* = \int_0^1 \{A_s^*(\tau_{H,k}(2 - y'^* - y^*)) - A_s^*(\tau_{H,k}|y^* - y'^*|)\}\frac{dT^*}{dy'^*}\,dy'^*$$

In order to expand the region near the wall an arbitrary scale transformation is made from y^* to z^* (we deviate from reference [14] in this scale transformation),

$$z^*(y^*) = \frac{1}{2.3}[1 - e^{-2.3y^*}]$$

$$y^*(z^*) = \frac{1}{2.3}\ln\frac{1}{1 - 2.3z^*}$$

The z^* scale is divided into m equally spaced values, except that $z_l^* = z_{l+1}^* = z^*(\delta_{ff}^*)$,

$$z_i^* = (i-1)\Delta z^* \qquad i = 1, l$$
$$z_i^* = i\Delta z^* \qquad i = l+1, m$$
$$z^* = z^*(1)/(m-2)$$

at the ith value of the abscissa

$$q_{R,k}^* = \int_0^1 \{A_s^*(\tau_{H,k}(2 - y'^* - y_i^*)) - A_s^*(\tau_{H,k}|y_i^* - y'^*|)\} \frac{dT^*}{dz'^*} \frac{dz'^*}{dy'^*} dy'^*$$

Denote

$$\left.\frac{dT^*}{dz'^*}\right|_{z'^* = z_j^*} = P_j^*$$

and

$$\left.\frac{dz^*}{dy'^*}\right|_{y'^* = y_j^*} = C_j$$

and let $q_{R,k}^*$ be represented by the sum

$$q_{R,k}^* = \sum_{j=2}^{m} \left\{ \int_{y_{j-1}^*}^{y_j^*} [A_s^*(\tau_{H,k}(2 - y_i^* - y'^*)) - A_s^*(\tau_{H,k}|y_i^* - y'^*|)] dy'^* \cdot \frac{1}{2} (C_{j-1}P_{j-1}^* + C_jP_j^*) \right\}$$

As in reference [14] let $F_{i,j,k}$ represent the integral. As shown previously

$$F_{i,j,k} = \frac{1}{\tau_{H,k}} \{ [S^*(\tau_{H,k}(2 - y_i^* - y_{j-1}^*)) - S^*(\tau_{H,k}(2 - y_i^* - y_j^*))] - |S^*(\tau_{H,k}(y_j^* - y_i^*)) - S^*(\tau_{H,k}|y_{j-1}^* - y_i^*|)| \}$$

where

$$S^*(t) = \int_0^t A_s^*(t')dt' = t\left[\ln t + \gamma - \frac{1}{2}\right] + [1 - E_2(t)] - \left[\frac{1}{3} - E_4(t)\right]$$

Note that at the flame front

$$F_{i,j-l+1,k} = 0$$

The result is that

$$q_R^* = \frac{R_{dm}}{\epsilon^+(1)} \sum_{k=1}^{n} W_k \sum_{j=2}^{m} F_{i,j,k} \frac{1}{2} (C_{j-1}P_{j-1}^* + C_jP_j^*)$$

$$q_R^* = \frac{R_{dm}}{\epsilon^+(1)} \sum_{j=1}^{m} A_{i,j}P_j^*$$

where

$$A_{i,j} = \tfrac{1}{2}(F_{i,j} + F_{i,j+1})C_j, \qquad j = 2, \ldots, m-1$$
$$A_{i,1} = \tfrac{1}{2}F_{i,2}C_1$$
$$A_{i,m} = \tfrac{1}{2}F_{i,m}C_m$$
$$F_{i,j} = \sum_{k=1}^{n} W_kF_{i,j,k}$$

Equations (11) and (12) now can be written in the form

$$\sum_{j=1}^{m} \left(\delta_{i,j}D_i^* + \frac{R_{dm}}{\epsilon^+(1)} A_{i,j} \right) P_j^* = 1, \qquad i = 1, l$$

and

$$\sum_{j=1}^{m} \left(\delta_{ij}D_i^* + \frac{R_{dm}}{\epsilon^+(1)} A_{i,j} \right) P_j^* = 0, \qquad i = l+1, m$$

respectively. The quantity $\delta_{i,j}$ represents the Kronecker delta function, $\delta_{i,j} = 1 (i = j)$ and 0 otherwise. The quantity D_i^* is

$$D_i^* = \frac{\epsilon^+(y_i^*)}{\epsilon^+(1)} C_i$$

An expansion of scale was also employed near the flame front in some of the calculations. In this case a $z^*(y_{ff}^*)$ similar to that near the wall was used with y_{ff}^* measured from the flame front. This z^* scale was patched onto the one which commenced at the wall. However, the numerical results were not greatly affected by this refinement. All calculations were carried out with a value of $m = 51$.

Properties for the H_2O and CO_2 calculations were taken from reference [20]. The A/A_Q correction discussed there was not applied; thus the calculated values of R_{dm} for these gases are somewhat low, and the radiation effect somewhat underestimated here. In the case of the rotation band of H_2O, the portion from 0 to 500 cm^{-1} was neglected, because the contribution is small at the high temperatures considered.

Natural Convection in Horizontal Thin-Walled Honeycomb Panels

K. G. T. HOLLANDS
Assistant Professor,
Department of Mechanical Engineering,
University of Waterloo,
Waterloo, Ontario, Canada

This paper presents an experimental study of the stability of and natural convection heat transfer through a horizontal fluid layer heated from below and constrained internally by a honeycomb. Examination of the types of boundary conditions exacted on the fluid at the cell side-walls has shown that there are three limiting cases: (1) perfectly conducting side-walls; (2) perfectly adiabatic side-walls; and (3) side-walls having zero thickness. Experiments described in this paper approach the latter category. The fluid used is air and the honeycomb used is square-celled. Measured critical Rayleigh numbers are found to be intermediate between those applying to cases (1) and (2), and consistent with an "equivalent wave number" of approximately 0.95 times that for case (1). The measured natural convective heat transfer after instability is found to be significantly less than that predicted by the Malkus-Veronis power integral technique. However, it is found to approach asymptotically the heat transfer which would take place through a similar fluid layer unconstrained by a honeycomb. A general correlation equation for the heat transfer is given.

Introduction

THIS PAPER treats natural convection in a horizontal layer of air constrained internally by a thin-walled honeycomb. The physical processes occurring here are best understood in terms of the Bènard Problem [1],[1] that is, the problem of stability and convection in an infinite horizontal fluid layer heated from below. For a sufficiently small Rayleigh number, such a fluid layer is stagnant and the Nusselt number is unity; however, if the Rayleigh number exceeds a certain critical value, the top-heavy situation becomes unstable, convective cells occur, and the Nusselt number increases; further increases in the Rayleigh number cause additional cells, each of a decreasing scale and each contributing to the heat transfer; finally a completely turbulent situation prevails. If now a thin-walled honeycomb structure is introduced into this layer [2, 3], the first convective cell occurring in the unconstrained layer will generally have a scale larger than the honeycomb cell size, and will therefore be unable to satisfy the boundary conditions demanded by the honeycomb cell-walls.

[1] Numbers in brackets designate References at end of paper.

Contributed by the Heat Transfer Division of THE AMERICAN SOCIETY OF MECHANICAL ENGINEERS and presented at the AIChE-ASME Heat Transfer Conference, Denver, Colo., August 6–9, 1972. Manuscript received by the Heat Transfer Division, May 8, 1972; revised manuscript received June 12, 1973. Paper No. 72-HT-60.

Nomenclature

- a = horizontal wavenumber
- a_1 = least permissible eigenvalue of appropriate differential equation; $= 5\sqrt{\pi}\cdot A$ for a square-celled honeycomb
- A = aspect ratio of square cell; $= \frac{L}{W}$
- C_p = specific heat at constant pressure for air
- D_h = hydraulic diameter of honeycomb cell cross section; $= W$ for a square celled honeycomb
- e = emf from heat flux meter
- g = acceleration of gravity
- G = dimensionless group; $= k_w D_h/kt$
- h = natural convection heat transfer coefficient, lower to upper plate
- H = dimensionless group; $= k_w t/kD_h$
- k = thermal conductivity of fluid
- k_w = thermal conductivity of honeycomb wall material
- L = vertical depth of horizontal fluid layer; also equal to vertical height of horizontal honeycomb panel (see Fig. 3)
- Nu = Nusselt number; $= hL/k$
- p = air pressure
- Pr = Prandtl number; $= C_p\mu/k$
- q = heat flow from heater plate to upper plate in experimental apparatus
- q_E = rate of electrical heating supplied to heater plate
- R = gas constant for gas used as fluid
- Ra = Rayleigh number; $= \frac{g\rho^2\beta\Delta TL^3C_p}{\mu k}$
- Rac = critical Rayleigh number
- t = honeycomb wall thickness
- T = absolute temperature of air
- ΔT = temperature difference from lower to upper plate, or across the honeycomb panel
- W = width of honeycomb cell (see Fig. 3)
- α = calibration constant of heat flux meter
- β = volumetric thermal expansion coefficient
- μ = viscosity of fluid
- ρ = density of fluid

The occurrence of the first convective motion is thereby displaced by the honeycomb to a higher Rayleigh number at which the incipient convective cell can "fit into" the honeycomb cell. As the Rayleigh number is increased past this critical value, additional convective cells of decreasing scale again occur, and again, each contributes to the heat transfer. As the fully turbulent situation is approached, an increasing proportion of the heat transfer is carried by eddies of a scale very much smaller than the honeycomb cell sizes. The rate of heat transfer becomes independent of the presence of the honeycomb, and finally, the heat transfer becomes the same as that in the unconstrained fluid layer at the same Rayleigh number.

The combined effect of the foregoing is that at small Rayleigh numbers and at large Rayleigh numbers a honeycomb has no effect on the heat transfer through the fluid; at intermediate values it may have a profound effect. The engineering significance of this fact need hardly be pointed out. In some instances, as for example in a flat plate solar collector [2], it may be desirable to design the honeycomb to suppress convection currents and thereby restrict heat transfer; in others it may be desirable to promote heat transfer. In either event, it is important that the process be understood and be made predictable. This paper presents an experimental study of these phenomena. The fluid used is air, the honeycomb is square-celled and fabricated from thin polyethylene sheet. The information gained has application to the design on flat-plate solar collectors.

Previous Investigations

Critical Condition. The critical Rayleigh number of a honeycomb depends on the aspect ratio of the honeycomb cell. In addition it depends on two groups which define the thermal boundary conditions demanded on the fluid at the honeycomb cell walls. The first of these, the group $H = k_w t/kD_h$ is associated with the heat conducted along the walls in the vertical and horizontal directions. The second, the group $G = k_w D_h/kt$ is associated with the heat conducted across the walls in the horizontal direction and is related to the coupling of heat transfer between adjacent cells. If one considers only extreme values of the groups there are four possible limiting cases and theses are shown in Table 1. The cases where $H = \infty$, correspond to infinitely conducting side-walls. (Since for a honeycomb, $t/w < 1$, if $H = \infty$, G must also be infinite, and the case $H = \infty$ and $G = 0$ (Case II) cannot in fact arise.) In Case I the wall temperature is maintained linear with respect to height, and the problem of determining the critical Rayleigh number reduces to the same as that for a single isolated cell having perfectly conducting side-walls. This problem has been treated in various approximate ways by a number of workers (references [5 through 9]). Case III: $H = 0$, $G = 0$ corresponds to zero wall conductivity so that there is no heat flux through the wall in either the vertical or horizontal direction. The problem of determining the critical Rayleigh number and Nusselt number can again be reduced to that for a single isolated cell, this time with perfectly adiabatic side-walls. This problem has been treated by fewer workers notably in references [4 and 6]. Catton and Edwards [3] proposed an approximate "adjusted wave number" technique for determining the critical Rayleigh number in Cases I and III. This method "forces" the form of the known solution for the infinite fluid layer to fit the bounded fluid layer (or cell), thereby generating a horizontal wave number a, related to the dimensions of the cell, from which the critical Rayleigh number is determined. By defining different values of the wavenumber for adiabatic and perfectly conducting side-walls, Catton and Edwards forced the method to be in agreement with Yih's theoretical result for an infinite cylinder with adiabatic side-walls, and another solution known to be very nearly correct for an infinite cylinder with perfectly conducting side-walls. On comparing the predictions of this adjusted wave number technique with their own experimental observations on liquid layers using phenolic (Case III) and aluminum (Case I) honeycombs, these authors found generally good agreement.[2]

The remaining case, Case IV: $H = 0$, $G = \infty$ has not previously been treated and is the subject of this paper. In this case there is no significant heat transfer through the cell walls in the vertical direction, but in the horizontal direction there is no resistance to heat transfer between adjacent cells. Obviously this case cannot be reduced to treating a single cell. While there has been no theoretical treatment of this problem per se, Edwards' [10] treatment of a set of parallel vertical walls inserted into an infinite fluid layer is very much to the point. (Implicit in this approximate treatment is the assumption that $G = \infty$, the walls being treated as fins with no temperature difference across them.) Values of the critical Rayleigh number for this geometry are given for values of H ranging from 0.02 to 200.

Heat Transfer. For the infinite fluid layer (unconstrained by a honeycomb) empirical equations for the Nusselt number covering the complete range of Rayleigh number have been given by Schmidt and Silverston [11]. For large Rayleigh numbers the correlation due to Globe and Dropkin [12]: $\mathrm{Nu} = 0.069\ \mathrm{Ra}^{1/3}\ \mathrm{Pr}^{0.074}$ is generally accepted. Several analytical treatments of the heat transfer have been attempted and the power integral technique due to Malkus and Veronis [13] while having a questionable theoretical base, has found some success as has been pointed out by Hollands [14] and by Catton [15], who compared the predictions of the technique with the experiments of Schmidt and Silveston on liquids of high Prandtl number. The technique predicts no dependence of the Nusselt number on Prandtl number and therefore must break down at high Rayleigh number as can be seen by inspecting Globe and Dropkin's correlation. In the case of a fluid layer restricted by a honeycomb, Edwards and Catton [16] have demonstrated that the power integral method gives good agreement with their experiments using water and heavy oils with (presumably) high Prandtl numbers.

Present Investigation. Experiments reported in this paper differ from previous investigations in two main respects: (i) the wall boundary conditions most closely approach Case IV of Table 1; (ii) the fluid used (air) has a low Prandtl number compared with that of previous investigators, (water, oil). Measurements of both the critical Rayleigh number and heat transfer are reported. The values of H used in the experiments are less than 0.06, and of G, greater than 5000. These values were achieved using a square-celled honeycomb having 0.004 in. thick polyethylene walls and cells 1 to 2 in. wide. This set of conditions corresponds approximately to that which may be used in solar collectors for convection suppression.

Experimental Apparatus and Procedure

The measurement of the heat flow through a horizontal layer of fluid heated from below is amply treated in the literature [11, 12, 13, and 7]. The present study uses two techniques of special interest. The first is the method of measuring the heat flux; the second is the method of varying the Rayleigh number by means of varying the pressure of the fluid (in this case air).

Inspection of the expression for the Rayleigh number:

$$\mathrm{Ra} = \frac{g\rho^2\beta\Delta T L^3 C_p}{\mu k}$$

shows why the method of varying the Rayleigh number by vary-

Table 1 Possible combinations of limiting values for groups G and H

Case	I	II	III	IV
H	∞	∞	0	0
G	∞	0	0	∞

[2] The value of G used in their phenolic honeycombs was not in fact small by absolute standards, being of the order of 100. However, their results for this honeycomb were consistent with Yih's theory which is based on an adiabatic wall ($G = 0$). For this reason they are classed here as Case III.

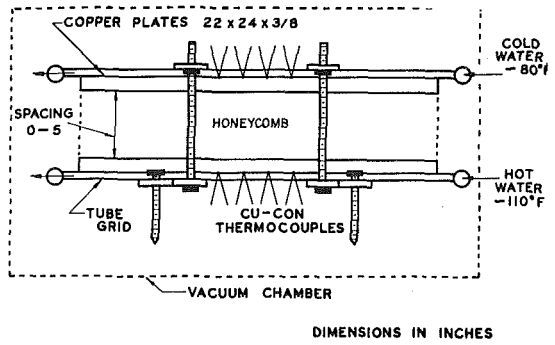

Fig. 1 Sketch of experimental apparatus

ing the gas pressure was adopted. For a given honeycomb, the fluid height L is fixed and therefore aside from fluid properties only the temperature difference, ΔT, can be varied. It is not feasible to vary ΔT over a factor greater than about 10. Assuming air obeys the ideal gas law, the Rayleigh number can be written as:

$$\mathrm{Ra} = \frac{p^2 \Delta T g L^3 C_p}{R^2 T^3 k \mu}$$

Over a sizable pressure range, μ and k are independent of pressure and hence other things being constant, the Rayleigh number varies as the square of the pressure. As an example, using a 5 in. plate spacing and a temperature difference of 30 deg F, the Rayleigh number can be varied from 10 to 10^7 by varying the pressure from 2 mm Hg to 2 atmospheres.

Fig. 1 shows a sketch of the apparatus. Two 3/8 in. by 22 in. by 24 in. copper plates were used as the upper and lower bounds of the air layer. Banks of copper tubes were soldered to the top of the upper plate and bottom of the lower plate and by circulating cold water from a thermostatically controlled bath through the upper bank and hot water (~110 F) from a similar bath through the lower bank, the necessary temperature difference was set up. The spacing between the plates could be adjusted from 0 to 5 in., and maintained constant locally to within ±0.0025 in. Four copper constantan thermocouples connected in thermopile measured this temperature difference. The thermocouples were imbedded into the plates at points four in. from the center. The plates were located in a pressure vessel consisting of a steel box 30 in. by 30 in. by 10 in. high connected to a vacuum pump and a compressed dry air supply allowing a pressure range of from a few mm of Hg or less to 2 atmospheres pressure. Air pressure was measured by a pressure transducer in the low (0–15 psia) range and a mercury manometer in the high (15 to 30 psia) range. Further details on the apparatus may be found in reference [18].

The method of measuring the heat flux is sketched in Fig. 2. A recess 5 in. by 5 in. by 1/4 in. deep machined into the lower

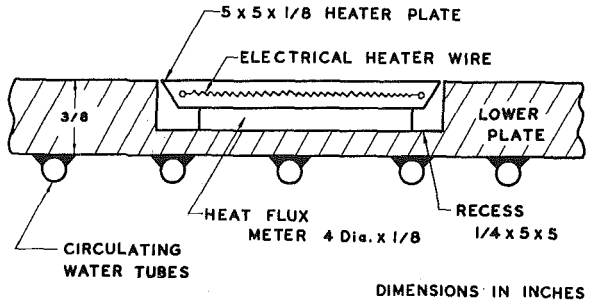

Fig. 2 Sectional view of lower plate showing assembly of heater plate and heat flux meter in the recess. (Note: drawing not to scale.)

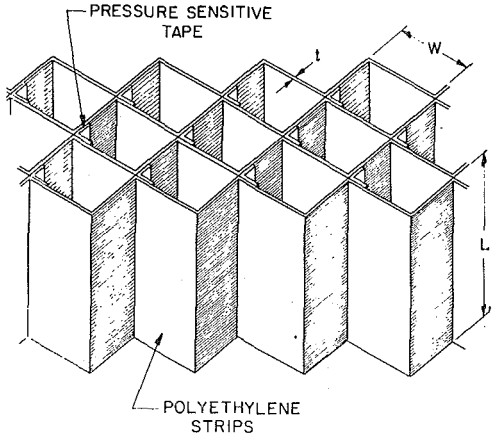

Fig. 3 Sketch of honeycomb showing method of fabrication

plate contained a heat flux meter and a 1/4 in. copper plate (heater plate) in which a nichrome resistance wire of known resistance was imbedded. The heat flux meter consists of a polyvinylchloride disk 1/8 in. thick by 4 in. in diameter with approximately 600 thermocouples connected in thermopile and woven into the disk so as to measure the temperature difference across it. The principle of the method used is the same as the guarded hot plate principle in that when the heater current has been varied until the heater plate is at the same temperature as the lower plate, all of the electrical heating supplied to the heater plate goes into the air layer above, and hence the heat flux through the air layer can be determined directly. The condition for equality of temperature of the heater plate and lower plate is obviously met when the heat flux meter emf is zero. By using the heat flux meter to determine the condition for equality of the two temperatures rather than say, a thermocouple imbedded in each plate, a much higher degree of sensitivity is gained in the heat flux measurement. Further details of this measurement may be found in reference [18].

The honeycombs were fabricated from 0.004 in. thick polyethylene film using 0.002 in. thick pressure sensitive tape (see Fig. 3). Their dimensions and values of H and G are given in Table 2. The radiative transmittance, absorptance, and reflectance of the polyethylene film to a black body at 80 F are estimated to be 0.87, 0.05, and 0.08, respectively, and of the pressure sensitive tape, 0.0, 0.92, and 0.08. The tape occupied roughly 8 percent of total wall area so that the area-weighted absorptance (emittance) of the walls was approximately 0.12. This figure is considered sufficiently small to prevent any interaction between the convective and radiative modes of heat transfer (see "Discussion of Results"). The cells were sized so that to have an integral number of cells over the test area, —i.e., over the heater plate area.

The experimental procedure followed consisted in flushing the pressure vessel with dry air, drawing a vacuum of approximately 1 mm Hg and taking a complete set of measurements. The

Table 2 Descriptions of honeycombs tested and measured critical Rayleigh numbers

Honeycomb designation number	Cell width W in.	Cell height L in.	Aspect ratio $A = L/W$	Group H	Group G	Measured Rac
1	2.50	2.500	1.00	0.03	13,300	5,800
2	2.50	5.035	2.01	0.03	13,300	40,800
3	1.67	5.017	3.00	0.045	8,900	192,900
4	1.27	5.017	3.96	0.059	6,670	529,000
5	2.50	3.010	1.20	0.03	13,300	8,090
6	2.50	1.928	0.771	0.03	13,300	3,610

pressure was then raised to 80 percent of the calculated critical pressure corresponding to the estimated critical Rayleigh number for the honeycomb under test. Although this involved a considerable change in pressure, without exception, no significant change in the heat flux was observed. The pressure was then increased in 2 percent steps, readings being taken at each step until the maximum allowable pressure of 2 atmospheres was reached. At one step in this process, the heat flux, having previously remained constant, independent of the pressure, would increase, corresponding to the critical condition. Subsequent increases in pressure would then result in increased heat transfer.

In processing the data, it was necessary to substract from the measured heat transfer the radiative heat exchange between the plates, and the heat conducted directly through the honeycomb walls. These were determined from the very first reading taken at approximately 1 mm Hg. At this condition, the air layer was known to be stagnant. From the known thermal conductivity of air, the component of this low pressure heat transfer associated with conduction through the air could be calculated and subtracted from the total low pressure heat transfer, leaving only radiation and wall conduction components of the heat transfer. The latter were assumed constant with respect to pressure and subtracted from all subsequent heat transfer measurements in that run.

Property values for air were taken from Glassman and Bonilla [19], the thermal conductivity and viscosity being independent of pressure over the range used. Property values were evaluated at the arithmetic mean of the two plate temperatures.

An error analysis indicated that the maximum expected error in the Nusselt number was 3 percent and in the Rayleigh number, 2 percent. As a check on the apparatus, the thermal conductivity of air was measured by measuring the heat flux at low pressure with no honeycomb for various plate spacings and plotting the measured heat transfer coefficient across the air space for various spacings. The thermal conductivity, as determined from the slope of this graph was within 1 percent of the literature value. As a further check, the critical Rayleigh number was determined with no honeycomb between the plates and compared with the accepted theoretical value for an infinite fluid layer (Rac = 1708). Over four determinations, the measured value did not deviate more than 1.2 percent from the theoretical value.

Experimental Results

Critical Condition. In the immediate vicinity of the critical condition, i.e., near the first appearance of first convective flow when the Rayleigh number is slowly increased, the heat transfer, (at least in the unconstrained fluid layer case) has been demonstrated to be

$$\mathrm{Nu} = 1 \qquad \mathrm{Ra} < \mathrm{Rac}$$

$$\mathrm{Nu} = 1 + K\left(1 - \frac{\mathrm{Rac}}{\mathrm{Ra}}\right) \qquad \mathrm{Ra} > \mathrm{Rac}$$

where K is a constant. The latter equation was first derived by Malkus and Veronis [13] and was shown to be exact in the limit $\mathrm{Ra} \to \mathrm{Rac} + 0$ by Platzman [20]. Therefore if one plots the experimental points in the immediate vicinity of the critical condition in the form Nu − 1 versus 1/Ra the result should be a straight line with intercepts K and 1/Rac. In this manner the measured critical Rayleigh numbers for each honeycomb were determined.

Fig. 4 shows the relevant plot for a honeycomb having an aspect ratio of unity (No. 1 in Table 1). Table 2 summarizes the dimensions and measured critical Rayleigh numbers of the six honeycombs tested.

Heat Transfer. Fig. 5 shows the measured Nusselt number versus Rayleigh number plots for honeycombs 1, 2, 3, and 4 (Table 2). Also shown on this plot for comparison is the Globe and Dropkin correlation using Pr = 0.71; and the predictions of the Malkus-Veronis power integral technique for a cell aspect ratio of 2.

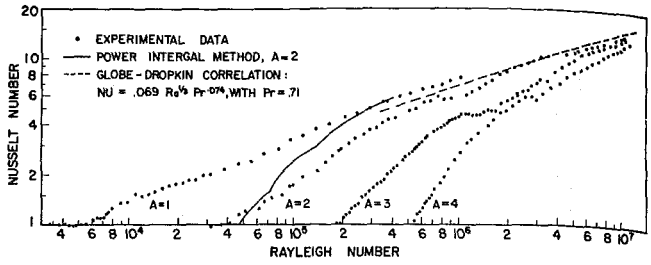

Fig. 5 Plot of measured Nusselt number versus Rayleigh number for honeycombs number 1, 2, 3, and 4. Also shown are predictions of the power integral technique, and the Globe-Dropkin correlation

Discussion of Results

Critical Condition. Fig. 6 shows a plot of the measured critical Rayleigh numbers versus aspect ratio, together with the predictions of other treatments for various extreme values of H and G. Curves (1) and (2) are the predictions of the adjusted wave number technique of Catton and Edwards for a square-celled honeycomb. These curves are determined using the value a_1 for a square-celled honeycomb as $a_1 = 5\sqrt{\pi}\,A$; the adjusted or equiva-

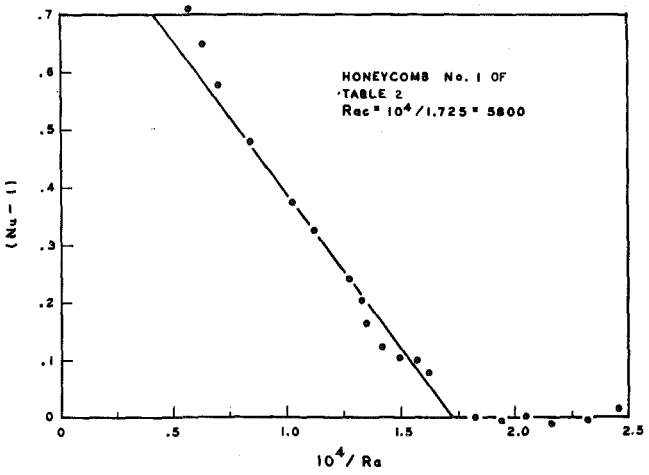

Fig. 4 Plot of experimental data in vicinity of critical condition for honeycomb number 1, Table 2, showing how the critical Rayleigh number was determined

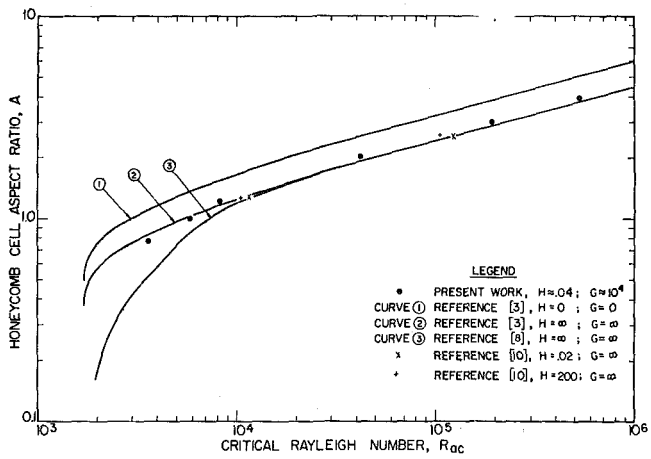

Fig. 6 Comparison of measured critical Rayleigh numbers with those predicted by some approximate solutions

lent wave number of the honeycomb cell is then $a = a_1$ for perfectly conducting side-walls, (curve 2), and $a = 0.75\ a_1$ for adiabatic side-walls, (curve 1); Rac is then determined from the equation:

$$\text{Rac} = \frac{(a^2 + 3.99^2)^3}{a^2} \tag{1}$$

Curve 3, which is a plot of the results of Catton's analysis [8] for perfectly conducting side-walls and square cells shows that the adjusted wave number technique (curve 2) is in significant error for small aspect ratios. From the treatment of Edwards [10] on the effect of a set of parallel vertical thin walls on the stability of a fluid layer, it is possible to cull four theoretical values of the critical Rayleigh number for a square-celled honeycomb. (These are obtained by interpreting the value of the horizontal wave number a in this treatment as 2π: the proper heat transfer boundary conditions will in fact be satisfied by only two of the square-cell walls.) The four values are plotted in Fig. 6.

The present set of results is seen to be intermediate between those for perfectly adiabatic and perfectly conducting side-walls, and much closer to the latter. They also appear to be in quite close agreement with the points taken from Edwards treatise [10]. It is important to note that the adjusted wave number technique, if evaluated purely on the basis of the value of H, would predict the present set of results to fall on curve 1. The group G is therefore of some importance and should not be overlooked. It is of interest to determine experimentally an expression for the adjusted or equivalent wave number for the present set of conditions. The critical Rayleigh numbers for the four largest aspect ratio honeycombs have been found to be well fitted by following the adjusted wave number technique, as outlined previously, if one takes for the value of $a = 0.95\ a_1$. The critical Rayleigh number is then found in the usual way by substituting this a into equation (1). For aspect ratios below unity the technique will yield approximate results only.

An alternate explanation of the departure of the data from curve (1) in Fig. 6, is the effect of a coupling with the radiant mode of transfer in the honeycomb. This radiant interaction has been analyzed by Edwards and Sun [21] for an infinitely long vertical cylinder with opaque grey walls insulated on the exterior. To give a first approximation of the effect, their results have been applied to the present situation, using a wall emissivity of 0.12. The result of this calculation indicates that the effect of radiation may be encompassed by using values of H roughly three times those given in Table 2. Although the direction of the change in Ra_c due to this change in H is correct, in the author's opinion, the high value of G used in the present experiments is a much more likely explanation of the observed result.

Heat Transfer. Catton and Edwards [16] found good agreement between their experimental results and the predictions of the Malkus-Veronis power integral technique; however, such agreement has not been found in the present study, as can be seen from inspecting Fig. 5 which shows the predictions of this technique for an aspect ratio of 2. (In fact the predictions are those for perfectly conducting side-walls; however predictions based on the present boundary conditions would lie further to the left and therefore be in greater disagreement with the data.) The predicted Nusselt number rises much more quickly than the measured after the critical condition. The same occurs at other aspect ratios but the predictions are not shown for clarity of graphical presentation. The discrepancy is very likely a Prandtl number effect. Implicit in the power integral method is the assumption that the Prandtl number is small, although how small it may be is not known. It appears on the basis of this study that a Prandtl number as low as 0.72 can cause significant departures.

The data for all aspect ratios are largely assymptotic to the Globe-Dropkin relation for large Rayleigh numbers. To correlate the present data, a single equation was sought which satisfied conditions: $\text{Nu} = 1$ at $\text{Ra} = \text{Rac}$ and $\text{Nu}/\text{Ra}^{1/3} = \text{constant}$ at large Ra. The fitted equation is

$$\text{Nu} = 1 + 0.0585X\left(1 - \exp\left(\frac{-\gamma(X - X_c)}{X_c}\right)\right) \qquad X > X_c \tag{2}$$

where $X = \text{Ra}^{1/3}$, $X_c = \text{Rac}^{1/3}$, and $\gamma = 1.19$. Of course the equation:

$$\text{Nu} = 1 \qquad X < X_c$$

also applies. These equations correlate very nearly all of the data to within 10 percent. The critical Rayleigh numbers used for calculating the Nusselt numbers in this correlation were the experimentally determined values given in Table 2. Further details of this fit are given in reference [18].

Conclusions

1 In addition to the two cases of perfectly conducting and perfectly adiabatic side walls, a third case of extreme side-wall boundary conditions can apply to a horizontal layer of fluid heated from below and constrained internally by a honeycomb panel. This is the case where the walls are so thin as to carry no significant heat transfer vertically, while offering no significant resistance to heat transfer in the horizontal direction.

2 The critical Rayleigh number for the stability of such a fluid layer has been found experimentally to be intermediate between that for the other two cases. Using the adjusted wave number approximation, the adjusted wave number for this case is 0.95 times that for the perfectly conducting case.

3 Heat transfer through the fluid layer after instability rises to approach assymptotically that through an unconstrained fluid layer, and may be calculated from equation (2) for $\text{Pr} = 0.71$.

4 Heat transfer rates measured in the present study using air ($\text{Pr} = 0.71$) are lower than those predicted by Malkus' power (integral technique).

Acknowledgments

This work was supported in part from a grant from the National Research Council of Canada, and in part from the Brace Bequest to McGill University. The author is indebted to Drs. J. M. Dealy and G. T. Ward for their encouragement.

References

1 Chandrasekhar, S., *Hydrodynamics and Hydromagnetic Stability*, Oxford at the Clarendon Press, England, 1961, pp. 9–73.

2 Hollands, K. G. T., "Honeycomb Devices in Flat Plate Solar Collectors," *Solar Energy*, Vol. IX, No. 3, 1965, pp. 159–164.

3 Catton, I., and Edwards, D. K., "Effect of Side Walls on Natural Convection Between Horizontal Plates Heated From Below," JOURNAL OF HEAT TRANSFER, TRANS. ASME, Series C, Vol. 89, No. 4, Nov. 1967, pp. 295–299.

4 Yih, C. S., "Thermal Stability of Viscous Fluids," *Quarterly of Applied Mathematics*, Vol. 17, 1959, pp. 25–42.

5 Ostroumov, G. A., "Free Convection Under Conditions of the Internal Problem," NACA TM 1407, 1958.

6 Charlson, G. S., and Sani, R. L., "Thermo-Convective Instability in a Bounded Cylindrical Fluid Layer," *International Journal of Heat Transfer*, Vol. 13, 1970, pp. 1479–1496.

7 Davis, S. H., "Convection in a Box: Linear Theory," *Journal of Fluid Mechanics*, Vol. 30, 1967, pp. 465–478.

8 Catton, I., "Convection in a Closed Rectangular Region: The Onset of Motion," JOURNAL OF HEAT TRANSFER, TRANS. ASME, Series C, Vol. 92, No. 1, Feb. 1970, pp. 186–188.

9 Ostrach, S., and Pneuli, D., "The Thermal Instability of Completely Confined Fluids Inside Some Particular Configurations," JOURNAL OF HEAT TRANSFER, TRANS. ASME, Series C, Vol. 85, 1963, pp. 1346–1354.

10 Edwards, D. K., "Suppression of Cellular Convection by, Lateral Walls," JOURNAL OF HEAT TRANSFER, TRANS. ASME, Series C, Vol. 91, No. 1, Feb. 1969, pp. 145–150.

11 Schmidt, E., and Silveston, P. L., "Natural Convection in Horizontal Liquid Layers," Chemical Engineering Progress, Symposium Series, Vol. 29, 1959, pp. 163–169.

12 Globe, S., and Dropkin, D., "Natural Convection Heat Transfer in Liquids Confined by Two Horizontal Plates and Heated From Below," JOURNAL OF HEAT TRANSFER, TRANS. ASME, Series C, Vol. 81, 1959, pp. 24–30.

13 Malkus, W. V. R., and Veronis, G., "Finite Amplitude Cellular Convection," *Journal of Fluid Mechanics*, Vol. 4, 1958, pp. 225–260.

14 Hollands, K. G. T., "Convectional Heat Transport Between Rigid Horizontal Boundaries After Instability," *Physics of Fluids*, Vol. 8, 1965, pp. 389–390.

15 Catton, I., "Natural Convection in Horizontal Liquid Layers," *Physics of Fluids*, Vol. 9, pp. 2521–2522.

16 Edwards, D. K., and Catton, I., "Prediction of Heat Transfer by Natural Convection in Closed Cylinders Heated From Below," *International Journal of Heat and Mass Transfer*, Vol. 12, 1969, pp. 23–30.

17 Thompson, H. A., and Sogin, H. H., "Experiments on the Onset of Thermal Convection in Horizontal Layers of Gases," *Journal of Fluid Mechanics*, Vol. 24, 1966, pp. 451–479.

18 Hollands, K. G. T., "Natural Convection in a Horizontal Layer of Air With Internal Constraints," PhD thesis, McGill University, Montreal, Canada, 1967.

19 Glassman, I., and Bonilla, C. F., "Thermal Conductivity and Prandtl Number of Air at High Temperatures," Chemical Engineering Progress, Symposium Series, Vol. 49, 1953, pp. 153–162.

20 Platzman, G. W., "The Spectral Dynamics of Laminar Convection," *Journal of Fluid Mechanics*, Vol. 23, 1965, pp. 481–510.

21 Edwards, D. K., and Sun, W. M., "Effect of Wall Radiation on Thermal Instability in a Vertical Cylinder," *International Journal of Heat and Mass Transfer*, Vol. 14, 1971, pp. 15–18.

A. D. CARR
Professor,
Department of Chemical Engineering,
University of Cape Town,
Rondebosch, C. P., South Africa

M. A. CONNOR
Senior Lecturer,
University of Stellenbosch,
South Africa

H. O. BUHR
Senior Lecturer,
University of Cape Town,
South Africa

Velocity, Temperature, and Turbulence Measurements in Air for Pipe Flow With Combined Free and Forced Convection

Experimental results are presented for velocity and temperature profiles and for the turbulence quantities v_z', t' and $\overline{v_z t}$, for up-flow of air in a vertical pipe with constant heat flux at Reynolds numbers of 5000 to 14,000. The measurements show that, with increasing heat flux, superimposed free convection effects cause marked distortion of the flow structure at low Reynolds numbers, with the velocity maximum moving from the tube center to a position near the wall. The axial turbulence intensity, v_z', is depressed by increasing heat flux while the temperature intensity, t', first decreases and then rises, with a shift in the position of the peak intensity away from the wall. On the basis of an analysis developed for heated turbulent flow, the turbulent shear stress and heat flux distributions are calculated from the experimental results. As the flow field becomes appreciably distorted on heating, it is found that the turbulent shear stress becomes very small, while the heat flux distribution suggests an increase in the width of the viscous sublayer.

Introduction

When air in turbulent forced convection flow is heated, a free convection effect is superimposed on the main flow. Under certain conditions this effect can become significant and can lead to marked distortion of the flow field. Such distortion has been demonstrated by Horsten [1] who studied the effect of heat flux on velocity and temperature profiles in mercury, and by Steiner [2] who has made some measurements in air. The present investigation is an experimental study of the changes which occur with increasing free convection effects for turbulent flow in a vertical pipe with uniform heat flux. Measurements were made at $L/D = 100$ in the Reynolds number range 5000 to 14,000 and with heat flux varying from 5 to 100 Btu/hr-ft.[2]

Time-averaged equations describing turbulent flow under conditions of mixed free and forced convection have previously been given by Ojalvo and Grosh [3]; their analysis, however, ignores the effects of local fluctuations in density caused by instantaneous temperature variations. The present analysis allows for these fluctuations and shows that their effect is to introduce additional turbulence interaction terms into the basic flow equations.

[1] Numbers in brackets designate References at end of paper.

Contributed by the Heat Transfer Division of The American Society of Mechanical Engineers and presented at the AIChE-ASME Heat Transfer Conference, Denver, Colo., August 6–9, 1972. Manuscript received by the Heat Transfer Division, April 6, 1973; revised manuscript received June 14, 1973. Paper No. 72-HT-19.

Theory

The velocity and temperature distributions in heated flow may be described by the momentum and energy equations together with the equation of continuity. In this instance the case of vertical up-flow in a smooth pipe with constant-flux heating is considered and an analysis is developed for a section of the tube where the temperature profile has reached a fully established condition. An assumption of constant specific heat then requires that the axial temperature gradient, $d\bar{T}/dz$, be constant, and if it is further assumed that the cross-sectional static pressure is constant, it follows that no net radial flow takes place.

The Continuity Equation. In cylindrical coordinates the steady-state continuity equation is [4]

$$\frac{1}{r}\frac{\partial}{\partial r}(r\rho V_r) + \frac{1}{r}\frac{\partial}{\partial \theta}(\rho V_\theta) + \frac{\partial}{\partial z}(\rho V_z) = 0 \qquad (1)$$

The density, ρ, may be expanded as $\rho_m\{1 - \beta_m(T - T_m)\}$, an approximation which introduces an error of less than $1/2$ percent over the temperature range 70–250 deg F used here, and instantaneous values of variables such as velocity may be expressed as the sum of a mean and fluctuating quantity, e.g., $V_z = \bar{V}_z + v_z$. Then, on time averaging, omitting $\partial/\partial\theta$ terms on the grounds of axial symmetry, and setting $\bar{V}_r = 0$, equation (1) becomes

$$\frac{1}{r}\frac{\partial}{\partial r}\, r(-\rho_m\beta_m\overline{v_r t})$$

$$+\frac{\partial}{\partial z}\left\{\rho_m \bar{V}_z - \rho_m \bar{V}_z\beta_m(\bar{T}-\bar{T}_m) - \rho_m\beta_m\overline{v_z t}\right\} = 0 \quad (2)$$

or, recombining density terms,

$$\frac{1}{r}\frac{\partial}{\partial r}\, r\,(-\rho_m\beta_m\overline{v_r t}) + \frac{\partial}{\partial z}\,(\rho\bar{V}_z - \rho_m\overline{v_z t}) = 0 \quad (3)$$

The Momentum Equation. For the z direction the steady-state momentum equation with the usual shear stress relations [4] is

$$\frac{1}{r}\frac{\partial}{\partial r}\,(r\rho V_r V_z) + \frac{1}{r}\frac{\partial}{\partial\theta}\,(\rho V_\theta V_z) + \frac{\partial}{\partial z}\,(\rho V_z V_z) + \frac{dp}{dz} + \rho g$$

$$= \frac{1}{r}\frac{\partial}{\partial r}\left\{r\mu\left(\frac{\partial V_z}{\partial r}+\frac{\partial V_r}{\partial z}\right)\right\} + \frac{1}{r}\frac{\partial}{\partial\theta}\left\{\mu\left(\frac{\partial V_\theta}{\partial z}+\frac{1}{r}\frac{\partial V_z}{\partial\theta}\right)\right\}$$

$$+\frac{\partial}{\partial z}\left[\mu\left\{{}^4/_3\frac{\partial V_z}{\partial z} - {}^2/_3\left(\frac{1}{r}\frac{\partial}{\partial r}\,(rV_r)+\frac{1}{r}\frac{\partial V_\theta}{\partial\theta}\right)\right\}\right] \quad (4)$$

Developing equation (4) by the same procedure as used in the previous section, gives

$$\frac{1}{r}\frac{\partial}{\partial r}\left\{r\,(\overline{\rho v_r v_z} - \rho_m\beta_m\bar{V}_z\overline{v_r t} - \rho_m\beta_m\overline{v_r v_z t})\right\}$$

$$+\frac{\partial}{\partial z}\,(\bar{\rho}\bar{V}_z^2 + \overline{\rho v_z^2} - 2\bar{V}_z\rho_m\beta_m\overline{v_z t} - \rho_m\beta_m\overline{v_z^2 t})$$

$$+\frac{d\bar{p}}{dz} + \rho_m g - \rho_m g\beta_m(\bar{T}-T_m)$$

$$-\frac{1}{r}\frac{\partial}{\partial r}\left(r\mu\frac{\partial\bar{V}_z}{\partial r}\right) - \frac{\partial}{\partial z}\left({}^4/_3\mu\frac{\partial\bar{V}_z}{\partial z}\right) = 0 \quad (5)$$

The following simplifications are now introduced:

(*a*) $\overline{v_z^2}/\bar{V}_z^2$ has a magnitude of about 0.01 and, for a region far from the tube entrance, is assumed to be very nearly constant at a given radial position, so that $\partial/\partial z\,(\bar{\rho}\overline{v_z^2})$ may be neglected in comparison with $\partial/\partial z(\bar{\rho}\bar{V}_z^2)$,

(*b*) triple correlations and the term $\dfrac{\partial}{\partial z}\left({}^4/_3\mu\dfrac{\partial\bar{V}_z}{\partial z}\right)$ are assumed small enough to be neglected,

(*c*) for the purpose of eliminating the axial derivative of $\overline{v_z t}$, the terms $\dfrac{1}{r}\dfrac{\partial}{\partial r}\,(-r\rho_m\beta_m\bar{V}_z\overline{v_r t}) + \dfrac{\partial}{\partial z}\,(\bar{\rho}\bar{V}_z^2 - 2\bar{V}_z\rho_m\beta_m\overline{v_z t})$ can be expanded and rearranged using the continuity equation. The resulting terms may be simplified by making use of the fact that $\beta_m\overline{v_z t} \ll \bar{V}_z$ to drop one of the intermediate terms, giving

$$-\rho_m\beta_m\overline{v_r t}\frac{\partial\bar{V}_z}{\partial r} + \frac{\bar{V}_z}{r}\frac{\partial}{\partial r}\,(r\rho_m\beta_m\overline{v_r t}) - \bar{V}_z^2\frac{\partial\bar{\rho}}{\partial z}.$$

Then equation (5) becomes

$$\frac{1}{r}\frac{\partial}{\partial r}\,(r\overline{\rho v_r v_z}) - \rho_m\beta_m\overline{v_r t}\frac{\partial\bar{V}_z}{\partial r} + \frac{\bar{V}_z}{r}\frac{\partial}{\partial r}\,(r\rho_m\beta_m\overline{v_r t}) - \bar{V}_z^2\frac{\partial\bar{\rho}}{\partial z}$$

$$+\frac{d\bar{p}}{dz} + \rho_m g - \rho_m g\beta_m(\bar{T}-T_m) - \frac{1}{r}\frac{\partial}{\partial r}\left(r\mu\frac{\partial\bar{V}_z}{\partial r}\right) = 0 \quad (6)$$

This version of the equation of motion may be rewritten in the integrated form

$$\overline{\rho v_r v_z} - \frac{2\mu}{D}\frac{\partial\bar{V}_z}{\partial\eta} = \frac{D}{2\eta}\,\rho_m\beta_m g\int_0^\eta(\bar{T}-T_m)\eta d\eta + \frac{1}{\eta}\int_0^\eta$$

$$\times\left(\rho_m\beta_m\overline{v_r t}\frac{\partial\bar{V}_z}{\partial\eta}\right)\eta d\eta - \frac{1}{\eta}\int_0^\eta\left\{\bar{V}_z\frac{\partial}{\partial\eta}\,(\eta\rho_m\beta_m\overline{v_r t})\right\}d\eta$$

$$+\frac{D}{2\eta}\int_0^\eta\left(\bar{V}_z^2\frac{\partial\bar{\rho}}{\partial z}\right)\eta d\eta - \frac{D\eta}{4}\frac{d\bar{p}}{dz} - \frac{D\eta}{4}\rho_m g \quad (7)$$

where $\eta = 2r/D$.

Equation (7) contains the terms $\overline{v_r t}$, which is obtained from the energy equation (following), and $\partial\bar{\rho}/\partial z$, which is easily determined from the axial temperature gradient at constant heat flux. To obviate the need for accurate local pressure drop measurements, it is possible to obtain $d\bar{p}/dz$ evaluating equation (7) at $\eta = 1$. Making use of experimentally measured quantities, the

Nomenclature

A, B = King's law constants
a, a_1 = thermal conductivity coefficients
C_p = specific heat of air
D = tube diameter
d = diameter of hot-wire
e = fluctuating component of hot-wire voltage
f = Fanning friction factor
Gr = Grashof number, $\rho^2\beta_m g D^4(d\bar{T}/dz)/\mu^2$
g = acceleration due to gravity
I = hot-wire current
K = constant, $\bar{R}_w/\bar{R}_g$
k = thermal conductivity of air
L = distance from tube entrance
l = length of hot-wire
P = sensitivity correction factor
p = pressure
$\tilde{p}$ = fluctuating component of pressure
q = heat flux
R = tube radius
R(subscripted) = hot-wire resistance
r = radial distance from tube center
Re = Reynolds number, DV_{av}/ν
s, s_v = sensitivities of hot-wire to velocity fluctuations
s_t = sensitivity of hot-wire to temperature fluctuations
T = temperature
T^* = dimensionless temperature, $q_W/\rho C_p u^*$
T_m = cross-sectional mean temperature, $\int_0^1 2T\eta d\eta$
t = fluctuating component of temperature
t' = intensity of temperature fluctuations, $\sqrt{\bar{t}^2}$
u^* = friction velocity, $V_{av}\sqrt{f/2}$
u^+ = dimensionless velocity, $\bar{V}_z/u^*$
V = velocity
v = fluctuating component of velocity
v' = intensity of turbulence, $\sqrt{\bar{v}^2}$
y = distance from pipe wall
y^+ = dimensionless distance from wall, yu^*/ν
α = thermal diffusivity, $k/\rho C_p$
β = coefficient of volume expansion
γ = temperature coefficient of resistance
η = dimensionless radial distance from center, $2r/D$
μ = viscosity
ν = kinematic viscosity, μ/ρ
ρ = density

Subscripts

av = bulk mean
c = center
f = evaluated at film temperature
g = evaluated at the local gas temperature
m = evaluated at the cross-sectional mean temperature
0 = evaluated at arbitrary reference temperature, T_0
r, z, θ = radial, axial, and circumferential directions
W = wall
w = wire

term $\bar{\rho}\overline{v_r v_z}$ may now be obtained. This term, $\bar{\rho}\overline{v_r v_z}$, is conventionally described as the turbulent shear stress and this definition is retained here, but it should be noted that equation (7) contains additional turbulence interaction terms. Thus $\bar{\rho}\overline{v_r v_z}$ does not express the total effect of turbulence in nonisothermal flow.

The Energy Equation. The steady-state energy equation without dissipation is [4]

$$\frac{1}{r}\frac{\partial}{\partial r}(r\rho C_p T V_r) + \frac{1}{r}\frac{\partial}{\partial \theta}(\rho C_p T V_\theta) + \frac{\partial}{\partial z}(\rho C_p T V_z) = \frac{1}{r}\frac{\partial}{\partial r}\left(rk\frac{\partial T}{\partial r}\right) + \frac{1}{r}\frac{\partial}{\partial \theta}\left(\frac{k}{r}\frac{\partial T}{\partial \theta}\right) + \frac{\partial}{\partial z}\left(k\frac{\partial T}{\partial z}\right) + \frac{V_r}{r}\frac{\partial}{\partial r}(rp) + \frac{V_\theta}{r}\frac{\partial p}{\partial \theta} + V_z\frac{\partial p}{\partial z} \quad (8)$$

By the same procedure as before, equation (8) becomes

$$-\frac{1}{r}\frac{\partial}{\partial r} r\,(\bar{\rho}C_p\overline{v_r t} - \rho_m\beta_m C_p\bar{T}\overline{v_r t} - \rho_m\beta_m C_p\overline{t^2 v_r}) + \frac{\partial}{\partial z}(\bar{\rho}C_p\bar{T}\bar{V}_z + \bar{\rho}C_p\overline{v_z t} - \rho_m\beta_m C_p\bar{T}\overline{v_z t} - \rho_m\beta_m C_p\bar{V}_z\overline{t^2} - \rho_m\beta_m C_p\overline{t^2 v_z}) + \frac{1}{r}\frac{\partial}{\partial r}\left(rk\frac{\partial\bar{T}}{\partial r}\right) + \frac{\partial}{\partial z}\left(k\frac{\partial\bar{T}}{\partial z}\right) + \frac{1}{r}\overline{v_r\frac{\partial}{\partial r}r\tilde{\rho}} + \bar{V}_z\frac{\partial\bar{\rho}}{\partial z} + \overline{v_z\frac{\partial\tilde{\rho}}{\partial z}} = 0 \quad (9)$$

The following simplifications, similar to those for equation (5), are now introduced:

(*a*) $\overline{v_z t}/\bar{V}_z\bar{T}$ is small and is assumed to be constant for any radial position, so that $\partial/\partial z(\bar{\rho}C_p\overline{v_z t})$ can be neglected in comparison with $\partial/\partial z(\bar{\rho}C_p\bar{V}_z\bar{T})$,

(*b*) triple correlations and pressure-velocity correlations are assumed small and are neglected, together with the term $\partial/\partial z(k\partial\bar{T}/\partial z)$.

(*c*) the terms

$$-\frac{\partial}{\partial z}(\bar{\rho}C_p\bar{T}\bar{V}_z) + \frac{\partial}{\partial z}(\rho_m\beta_m C_p\bar{T}\overline{v_z t}) + \frac{1}{r}\frac{\partial}{\partial r}(r\rho_m\beta_m C_p\bar{T}\overline{v_r t})$$

can be expanded, rearranged and simplified as in (*c*) in the foregoing, to give

$$-\bar{\rho}C_p\bar{V}_z\frac{\partial\bar{T}}{\partial z} + \rho_m\beta_m C_p\overline{v_r t}\frac{\partial\bar{T}}{\partial r}.$$

Thus equation (9) becomes

$$-\bar{\rho}C_p\bar{V}_z\frac{\partial\bar{T}}{\partial z} - C_p\frac{1}{r}\frac{\partial}{\partial r}(r\bar{\rho}\overline{v_r t}) + \rho_m\beta_m C_p\overline{v_r t}\frac{\partial\bar{T}}{\partial r} + \frac{1}{r}\frac{\partial}{\partial r}\left(rk\frac{\partial\bar{T}}{\partial r}\right) + \bar{V}_z\frac{\partial\bar{\rho}}{\partial z} = 0 \quad (10)$$

Integration of equation (10) gives, after rearranging,

$$-\bar{\rho}C_p\overline{v_r t} + \frac{1}{\eta}\rho_m\beta_m C_p\int_0^\eta \overline{v_r t}\frac{\partial\bar{T}}{\partial\eta}\eta d\eta + \frac{2k}{D}\frac{\partial\bar{T}}{\partial\eta} + \frac{D}{2\eta}\int_0^\eta \bar{V}_z\frac{d\bar{\rho}}{dz}\eta d\eta = \frac{D}{2\eta}C_p\frac{\partial\bar{T}}{\partial z}\int_0^\eta \bar{\rho}\bar{V}_z\eta d\eta. \quad (11)$$

The second term on the L.H.S. arises from instantaneous fluctuations in density with temperature and is additional to the terms that would be obtained in the usual simplified analysis (4). The term containing $d\bar{p}/dz$ is sufficiently small in relation to the other terms to be neglected and equation (11) can be solved by iteration to give $\overline{v_r t}$.

It is possible also to measure the turbulence quantities $\overline{v_r t}$ and $\overline{v_r v_z}$ experimentally, by inclined hot-wire anemometry. However, experience of the authors with this method indicated that results were subject to considerable error, and that the use of equations (7) and (11), employing normal-wire time-averaged temperature and velocity measurements, enabled much greater accuracy to be obtained.

Equipment

Experimental measurements were made in the flow system shown in Fig. 1. The vertical test section was a 40-ft long aluminum tube of 3.886 in. ID and wall thickness 0.056 in. The first 4.25 ft were unheated and a hot-wire probe was positioned 2.25 ft from the tube outlet, giving unheated and heated length-to-diameter ratios of 113 and 100, respectively, to the point of measurement. A flow straightener was inserted at the entrance to the test section to minimize swirling effects. The test section was heated with 1-in. Nichrome ribbon wrapped around the tube in a close spiral and covered with 2 in. of asbestos and fibre glass insulation. Thermocouples were installed at inlet and outlet and at 16 points along the test section. Temperature readings confirmed that uniform heat flux was achieved. Heat was removed from the system by a water cooler in the return leg.

Velocity and temperature profiles and turbulence intensities were measured using a Transmetrics constant-current hot-wire anemometer unit, with the wire normal to the direction of the mean flow. Probes were prepared by soldering lengths of 0.00015 in. dia tungsten wire to supports 0.08 to 0.09 in. apart, giving a wire l/d ratio of 500–600 as recommended [5] for flows where large temperature fluctuations occur. Probe supports were held at a small angle to the vertical so as to minimize interference effects while still allowing measurements to be made right up to the tube wall.

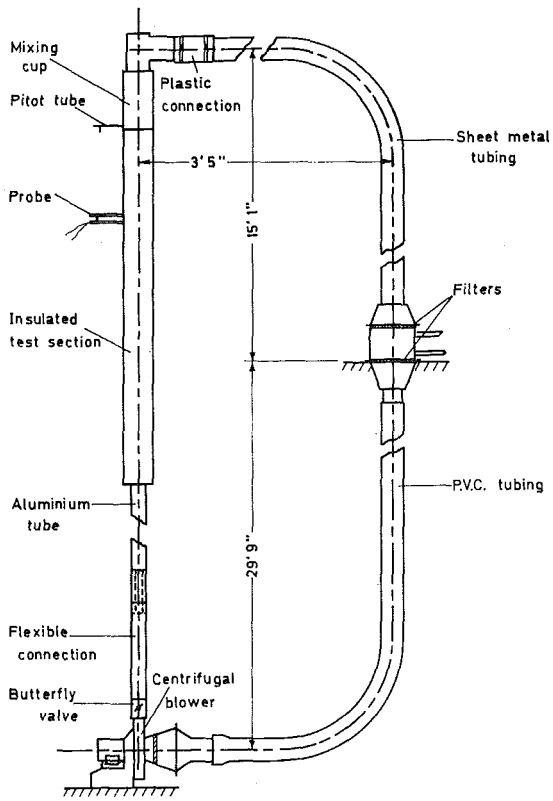

Fig. 1 Diagram of flow system

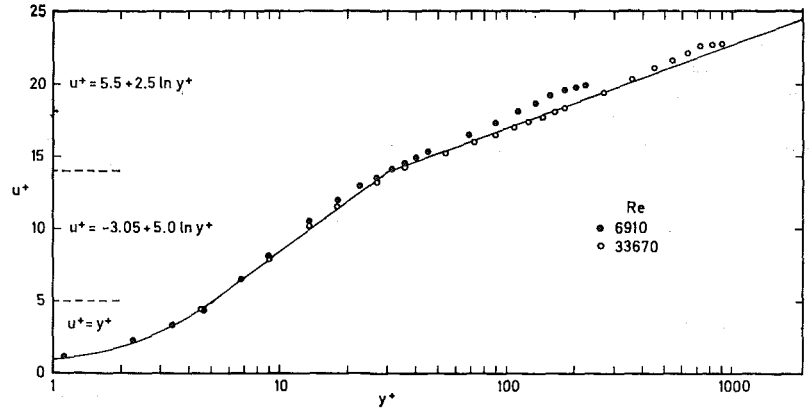

Fig. 2 Isothermal velocity profiles

Calibration and Calculation Procedures

Calibration of Probe for Mean Velocity and Temperature Measurements. In general, hot wires were calibrated in situ against a pitot-tube connected to a micromanometer (accuracy ± 0.0002 in. butanol). The pitot-tube was situated 2 ft downstream from the hot-wire probe; it was found that with both pitot-tube and probe at the center of the pipe, pressure readings were unaffected by the presence of the hot-wire probe. For low velocities, wires were calibrated externally in a specially constructed calibration unit containing a contracting cone and total flow meter [6]. The basic hot-wire equation, King's law,

$$(I^2\bar{R}_w)/(\bar{R}_w - \bar{R}_g) = A + B\bar{V}_z^{0.5} \tag{12}$$

was assumed to apply and the conventional plot of $I^2\bar{R}_w/(\bar{R}_w - \bar{R}_g)$ vs $\bar{V}_z^{0.5}$ was prepared. This calibration curve was straight over most of the range but slightly curved at the low velocity end. It was experimentally established [6] that the equation proposed by Hinze [7]

$$\frac{I^2\bar{R}_w}{\bar{R}_w - \bar{R}_g} = A_g\left\{1 + \frac{a_1(\bar{R}_w - \bar{R}_g)}{2(a + a_1T_g)\gamma R_0}\right\} + B\bar{V}_z^{0.5} \tag{13}$$

satisfactorily allowed for the variation of the calibration curve with temperature.

Temperature measurements were made by operating the hot-wire as a resistance thermometer, the parameters R_0 and γ in the relationship $\bar{R}_g = R_0(1 + \gamma\bar{T})$ being obtained by externally calibrating the hot-wire in a heated air supply.

Calculation of Turbulence Quantities. Under isothermal conditions the turbulence intensity, v_z', may be obtained from the fluctuating component of the hot-wire voltage by using the relationship [7]

$$\sqrt{\overline{e^2}} = sv_z'$$

where

$$s = \frac{(\bar{R}_w - \bar{R}_g)^2}{2I\bar{R}_g}\frac{B\sqrt{\bar{V}_z}}{\bar{V}_z} \tag{14}$$

Under nonisothermal conditions the applicable equation is [7]

$$\overline{e^2} = s_v^2\overline{v_z^2} + s_t^2\overline{t^2} - 2s_vs_t\overline{v_zt} \tag{15}$$

where

$$s_v = s/(1 + PK), \qquad s_t = \frac{1 - P}{1 + PK}\frac{I\gamma\bar{R}_wR_0}{\bar{R}_g},$$

$$P = \frac{A_0a_1}{2(a + a_1T_0)\gamma R_0}\Big/\frac{A_f + B\sqrt{\bar{V}_z}}{\bar{R}_w - \bar{R}_g}$$

and

$$K = \bar{R}_w/\bar{R}_g.$$

Hinze [7] has suggested the use of simplified sensitivities with $P = 0$, but the authors have found this assumption to be in error by up to 20 percent at low velocities.

Values of the temperature intensities were obtained by operating the wire at very low current (typically less than 2 mA), when equation (15) becomes, within limits of experimental accuracy,

$$\overline{e^2} = s_t^2\overline{t^2} \tag{16}$$

To obtain $\overline{v_z^2}$ and $\overline{v_zt}$, equation (15) may be rewritten as

$$\frac{\overline{e^2}}{s_t^2} - \overline{t^2} = \left\{\frac{s_v}{s_t}\right\}^2\overline{v_z^2} - 2\frac{s_v}{s_t}\overline{v_zt} \tag{17}$$

Following the procedure of Arya and Plate [8], the term $(\overline{e^2}/s_t^2 - \overline{t^2})$ was plotted against s_v/s_t for overheating ratios of 0.05, 0.1, 0.3, 0.5, and 0.7. The best-fit parabola through the points gave the required values of $\overline{v_z^2}$ and $\overline{v_zt}$.

Experimental Results

Isothermal Data. As a check on the operation of the experimental equipment, isothermal velocity profiles and axial turbulence intensities were measured over the Reynolds number range of 5000 to 34,000. Two typical velocity profiles are shown in Fig. 2 in comparison with the usual logarithmic velocity distribution.

Axial turbulence intensities at Re ≃ 5000 and 16,000 are plotted in Fig. 3. The intensity data are in generally good agreement with other published results [9, 10], most of the disagreement occurring in the regions of peak intensity. Such variations are attributable [11] to differences in low-frequency response of the equipment used by different workers. The present equipment has a high-pass cut-off of 0.1 Hz, and low-frequency losses are considered to be small.

Nonisothermal Data. A study was made of velocity and temperature profiles, the intensities v_z' and t' and the correlation $\overline{v_zt}$, at Re ≃ 5000 for various heat fluxes, and at Re ≃ 14,000 for one relatively high heat flux. Operating conditions are given in Table 1, where the prefix N denotes runs in which emphasis was placed on accurate profile measurements while the NT runs were directed specifically toward obtaining turbulence data.

Velocity Profiles. The variation of the velocity distribution with heat flux at Re ≃ 5000 is shown in Fig. 4. The effect of increasing heat flux, characterized by the Grashof number, is to raise the relative velocity near the wall, and hence reduce the velocity at the tube center, with the result that the maximum velocity moves from the center to a position close to the wall. At high heat flux little further change in the profile shape is observed. The approach to such a limiting condition, noted also

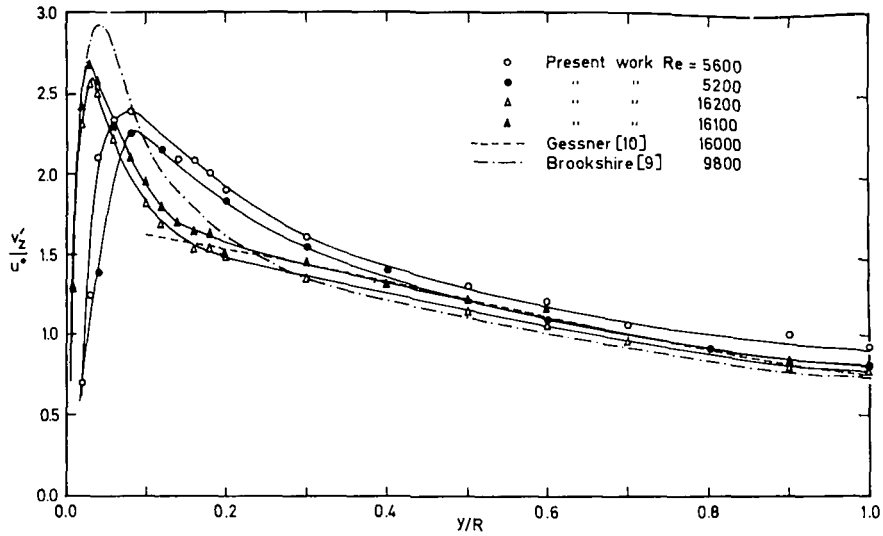

Fig. 3 Isothermal axial turbulence intensities

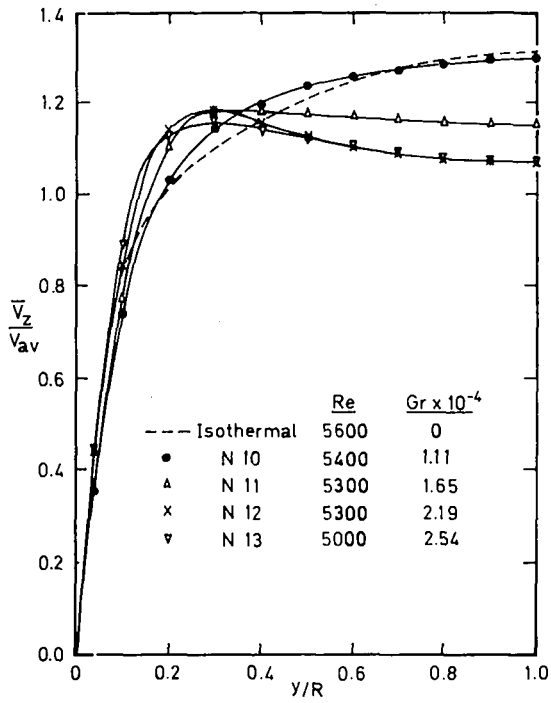

Fig. 4 Nonisothermal velocity profiles at Re $\simeq$ 5000

for profiles measured at Re $\simeq$ 8000 [6] and reported as well by Horsten [1] in mercury, is illustrated by the similarity of runs N 12 and 13 in Fig. 4. Profiles for Re $\simeq$ 14,000, measured under the conditions of Table 1, showed negligible distortion and corresponded in shape to the isothermal profile.

Temperature Profiles. Temperature profiles are plotted in Fig. 5. Good agreement is shown between the profile for Re = 14,000 and that measured by Johnk [12] at Re = 17,600. At Re $\simeq$ 5000 the effect of heating is less marked than in the case of the velocity data. A tendency for temperature profiles also to reach a limiting condition at high heat flux is again shown by runs N 12 and 13.

Turbulence Measurements. Axial velocity intensities are shown in Fig. 6 where they are compared with isothermal data and the results of Bremhorst and Bullock [13]. At Re $\sim$ 5000 the effect

Table 1 Operating conditions for nonisothermal runs

Run	Re	q_w Btu/ hr-ft^2	Gr $\times 10^{-4}$	V_{av} ft/s	f	T_w deg F	T_c deg F
N10	5400	8.4	1.11	2.97	0.00797	111.5	96.4
N11	5300	13.3	1.65	3.02	0.00834	138.2	102.5
N12	5300	20.7	2.19	3.19	0.00971	164.8	114.8
N13	5000	26.9	2.54	3.21	0.01077	192.5	130.8
N14	14000	89.4	2.89	9.04	0.00726	196.7	138.9
NT1	5400	5.0	0.78	2.85	0.00807	89.7	81.4
NT2	5500	10.7	1.58	2.95	0.00811	102.6	83.7
NT3	5400	13.4	1.76	3.02	0.00835	128.5	92.1
NT4	5200	21.1	2.40	3.06	0.00970	161.6	107.4
NT5	14000	103.9	3.08	9.44	0.00716	199.4	136.6

of increasing heat input is, in general, to reduce the axial intensity to a level as low as half the isothermal. For the higher heat fluxes the reduction in the intensity peak near the wall results in very nearly constant values of v_z' across the pipe cross section. At Re $\sim$ 14,000 nonisothermal and isothermal intensities are similar, as would be expected from the similarity of the velocity profiles.

Temperature fluctuation intensities are given as t'/T^* in Fig. 7.

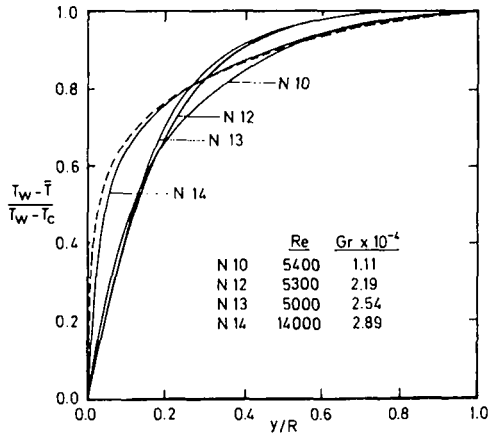

Fig. 5 Temperature profiles
– – – Johnk [12], Re = 17,600
——— This work

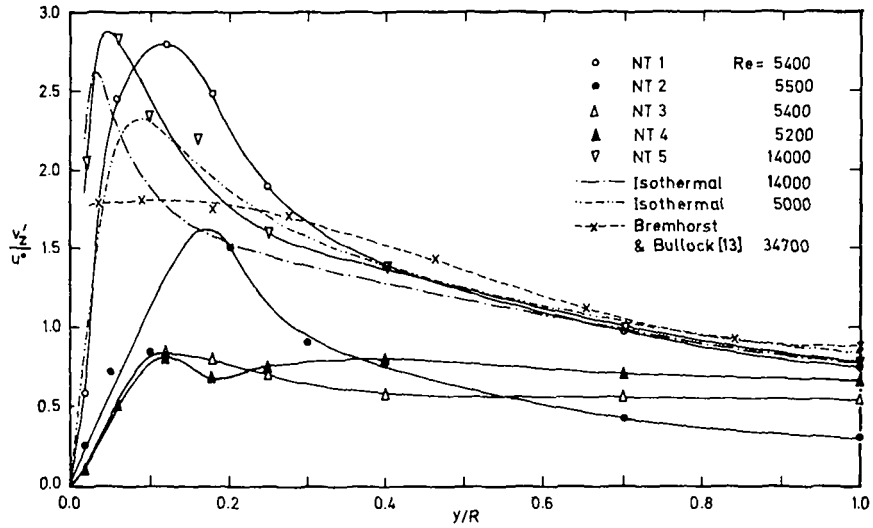

Fig. 6 Nonisothermal axial turbulence intensities

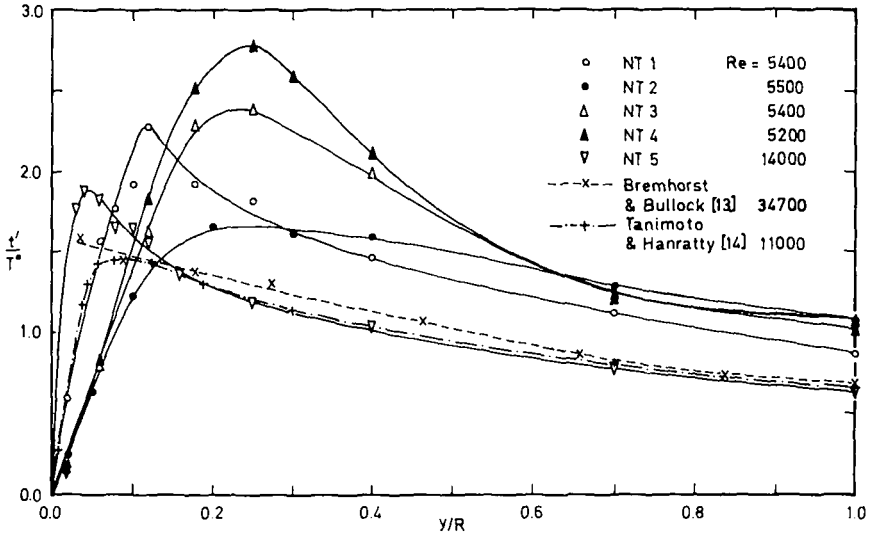

Fig. 7 Temperature intensities

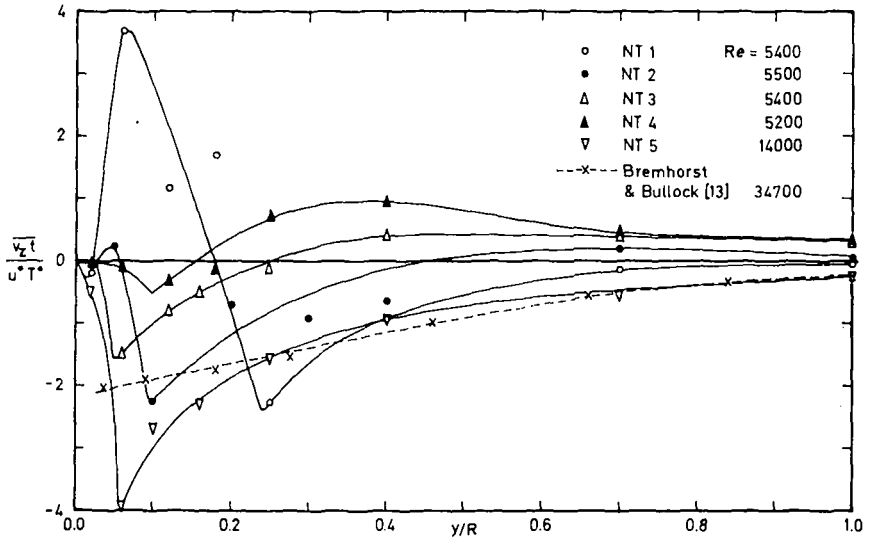

Fig. 8 Velocity—temperature correlations

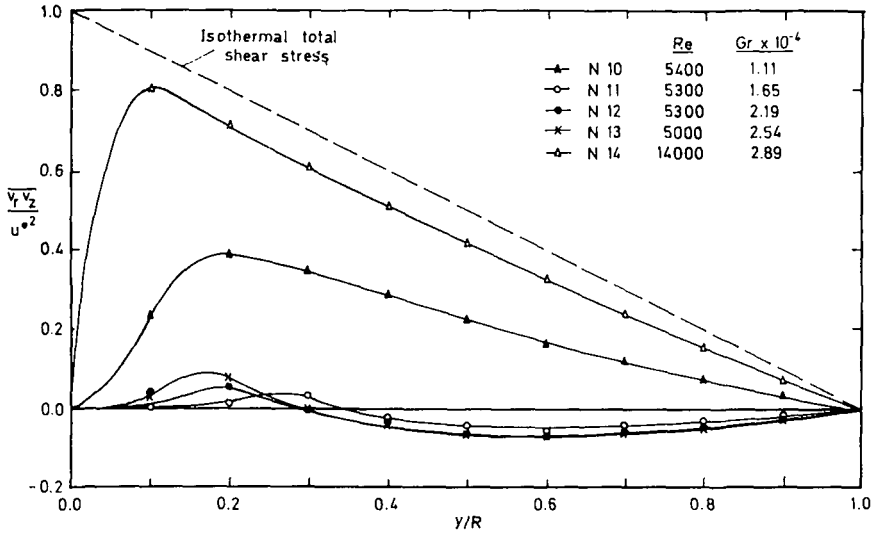

Fig. 9 Nonisothermal shear stress distribution

At Re $\simeq$ 5000 the intensities are approximately the same for $y/R > 0.5$ and higher than the values at Re $\simeq$ 14,000. Nearer the wall the normalized peak intensity first falls and then increases with increasing heat flux—the initial decrease is probably related to the drop in v_z' (see Fig. 6). At Re $\sim$ 14,000, the present results agree well with those of Bremhorst and Bullock [13] and of Tanimoto and Hanratty [14] but show a more pronounced peak near the wall.

Velocity-temperature correlations, $\overline{v_z t}$, are shown in Fig. 8. The $\overline{v_z t}$ data are more scattered than v_z' or t' because $\overline{v_z t}$ is more sensitive to experimental inaccuracies, as pointed out by Verollet [15]. Over most of the tube cross section ($y/R > 0.2$), $\overline{v_z t}$ shows an orderly increase with heat input, and the values at higher heat flux become positive, as compared with the negative values obtained for essentially undistorted conditions. Good agreement is shown between $\overline{v_z t}$ correlations for those profiles showing the least distortion, namely runs *NT* 1 and *NT* 5, and the data of Bremhorst and Bullock for Re = 34,700.

Calculated Results

Turbulent Shear Stress and Heat Flux Distribution. Values of $\overline{v_r v_z}$ and $\overline{v_r t}$ may be calculated from the experimental data by using the momentum and energy equations (7) and (11). In carrying out these computations the following observations were made:

In equation (7) the second, third, and fourth terms on the right-hand side (which are the terms additional to those that are obtained from an isothermal incompressible analysis) were found to have magnitudes of up to +3 percent, −8 percent, and +2 percent, respectively, of the pressure drop terms (the last two terms on the right-hand side.) The net contribution of these terms is thus generally small, but becomes important where the pressure drop terms are counter-balanced by the buoyancy term (first term on right-hand side). This situation arises when the maximum velocity occurs away from the tube center.

In equation (11) computation showed that the contribution of the "additional" term (the second term on the left-hand side) is small over most of the tube cross section but increases to about 5 percent near the wall.

The Nonisothermal Turbulent Shear Stress. Calculated values of the turbulent shear stress are plotted as $\overline{v_r v_z}/u^{*2}$ in Fig. 9. The results show that in general the effect of increasing heat flux is to decrease $\overline{v_r v_z}$. For those runs, such as *N* 11–13, where the velocity profiles exhibit a maximum away from the pipe center, $\overline{v_r v_z}$ has very small values over the whole pipe cross section and passes through zero at, or close to, the point of zero velocity gradient. The low shear stress values, as well as the even intensity distribution, suggest that the turbulent flow field for these conditions is close to isotropic.

The Turbulent Heat Flux Distribution. Fig. 10 shows the variation of $\rho C_p \overline{v_r t}$ with heat input. Also shown in the figure are the curves for the total radial heat flux, as represented by the term on the right-hand side of equation (11), normalized with respect to q_w. Increasing the heat input has relatively little effect on the total radial distribution, while for $\overline{v_r t}$ the effect is to reduce the values and move the $\overline{v_r t}$ peak further from the wall, thus apparently decreasing the relative contribution of the turbulent component to the total heat flux.

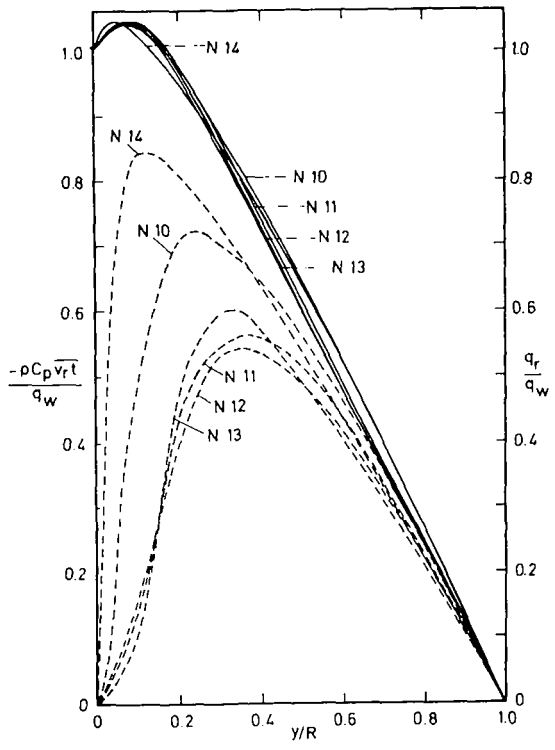

Fig. 10 Heat flux distributions
— — Total radial heat flux, q_r/q_w
– – – Turbulent component, $-\rho C_p \overline{v_r t}/q_w$

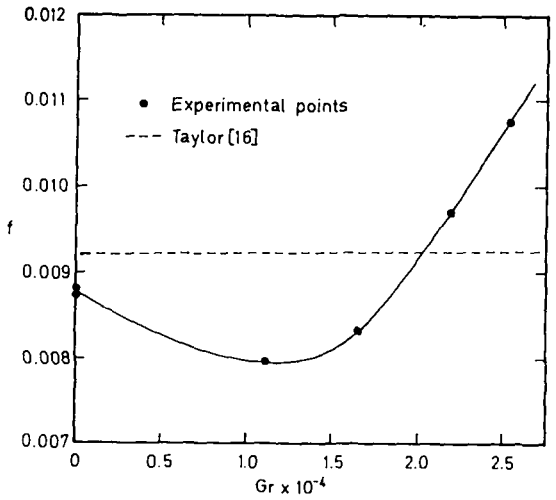

Fig. 11 Effect of heat flux on friction factor

Nonisothermal Friction Factors. When the velocity profile is distorted by heating, the slope at the wall differs from that for an undistorted profile at the same Reynolds number. Consequently the friction factor, f, which may be calculated from this slope, is expected to differ from normally accepted isothermal values. Fig. 11 shows friction factors obtained from velocity measurements close to the wall (Runs N 10–13) and it is clear that f exhibits a considerable variation with increasing heat input. Also shown in the figure is the correlation proposed by Taylor [16] for nonisothermal flow. This correlation, which utilizes the wall-to-bulk temperature ratios, yields an approximately constant value of f, and is clearly not adequate for predicting friction factors under conditions where appreciable profile distortion occurs.

Conclusions

For heated turbulent flow of air it has been found that superimposed buoyancy forces may considerably modify the flow structure. Measurements made at Re $\simeq$ 5000 showed that, with increasing heat flux:

1 The velocity profile becomes distorted in comparison with the profile obtained in isothermal flow to the extent that the velocity maximum moves from the pipe center to a position closer to the tube wall.

2 The axial turbulence intensity decreases and becomes more uniform over the tube cross section. At the same time the turbulent shear stress tends to very low values, indicating a tendency to isotropic turbulence at high heat flux.

3 The turbulent contribution to the total heat flux distribution decreases. The reduction is most significant in the region near the wall and suggests an effective increase in the thickness of the viscous sublayer. Temperature and velocity intensities remain significant, however, and confirm that turbulent flow is maintained.

Acknowledgment

The authors wish to acknowledge financial support received from the S.A. Council for Scientific and Industrial Research and advice from Dr. W. W. Willmarth of the University of Michigan.

References

1 Horsten, E. A., "Combined Free and Forced Convection in Turbulent Flow of Mercury," PhD thesis, University of Cape Town, 1971.

2 Steiner, A., "On the Reverse Transition of a Turbulent Flow Under the Action of Buoyancy Forces," *Journal of Fluid Mechanics*, Vol. 47, Part 3, 1971, pp. 503–512.

3 Ojalvo, M. S., and Grosh, R. J., "Combined Forced and Free Turbulent Convection in a Vertical Tube," Argonne National Laboratory Report ANL-6528, Jan. 1962.

4 Bird, R. B., Stewart, W. E., and Lightfoot, E. N., *Transport Phenomena*, Wiley, New York, 1960.

5 Weinberg, B. C., and Lederman, S., "Constant Current Anemometer Diagnostics of Flow Fields," Polytechnic Institute of Brooklyn, PIBAL Report No. 69-13, 1969.

6 Connor, M. A., "Velocity, Temperature and Turbulence Measurements in Air Under Combined Free and Forced Convection Conditions," PhD thesis, University of Cape Town, 1971.

7 Hinze, J. O., *Turbulence*, McGraw-Hill, New York, 1960.

8 Arya, S. P. S., and Plate, E. J., "Hot-Wire Measurements of Turbulence in a Thermally Stratified Flow," Colorado State University Technical Report CEM67-68SPSA-EJP11, 1968.

9 Brookshire, W. A., "The Structure of Turbulent Shear Flow in Pipes," PhD thesis, Louisiana State University, 1961.

10 Gessner, F. B., "A Method of Measuring Reynolds Stresses With A Constant Current, Hot-Wire Anemometer," ASME Paper No. 64-WA/FE-34, 1964.

11 Coantic, M., "Evolution, en fonction du nombre de Reynolds, de la distribution des vitesses moyennes et turbulentes dans une conduite," *Comptes Rendus de L'Academie des Sciences*, Paris, Series A, Vol. 264, 1967, pp. 849–852.

12 Johnk, R. E., "Development of Temperature Profile for Turbulent Heat Exchange in a Pipe," PhD thesis, University of Illinois, 1961.

13 Bremhorst, K., and Bullock, K. J., "Spectral Measurements of Temperature and Longitudinal Velocity Fluctuations in Fully Developed Pipe Flow," *International Journal of Heat and Mass Transfer*, Vol. 13, 1970, pp. 1313–1329.

14 Tanimoto, S., and Hanratty, T. J., "Fluid Temperature Fluctuations Accompanying Turbulent Heat Transfer in a Pipe," *Chemical Engineering Science*, Vol. 18, 1963, pp. 307–311.

15 Verollet, E., "Contribution aux Methods de Mesures de Turbulence de Vitesse et de Temperature par L'Anemometre a Fil Chaud," Doctoral thesis, Universite D'Aix-Marseille, 1962.

16 Taylor, M. F., "A Method of Correlating Local and Average Friction Coefficients for Both Laminar and Turbulent Flow of Gases Through a Smooth Tube With Surface to Fluid Bulk Temperature Ratios From 0.35 to 7.35," *International Journal of Heat and Mass Transfer*, Vol. 10, 1967, pp. 1123–1128.

J. W. YANG
Associate Professor.

NANSEN LIAO
Research Assistant.

Department of Mechanical Engineering,
State University of New York at Buffalo,
Buffalo, N. Y.

An Experimental Study of Turbulent Heat Transfer in Converging Rectangular Ducts

The turbulent heat transfer rate, wall temperature, and pressure distributions in the hydrodynamically and thermally developing region of rectangular converging ducts of taper angle 0, 2½, 5, and 7½ deg have been determined experimentally. The heating condition is such that the top and bottom walls are uniformly heated while the two side walls are unheated. The fluid is air and the experiments cover the Reynolds number range from 2.4 × 10⁴ to 4.8 × 10⁴. The results show that the heat transfer coefficient is increased by the increasing of either the taper angle or the inlet Reynolds number. An empirical correlation between the local Nusselt number and the local Reynolds number was determined.

Introduction

THE HEAT TRANSFER characteristics of rectangular ducts have been investigated extensively in recent years because of their technical importance in heat exchanger design. The majority of the experimental and theoretical work has been confined to parallel ducts, i.e., ducts with longitudinally unchanging cross-sectional area. It has been shown that for such parallel ducts, the turbulent heat transfer rate can be approximated from the well-known circular-tube relations when the hydraulic diameter of the duct is used as the characteristic length for the Nusselt number and the Reynolds number. The analytical and empirical correlations for turbulent heat transfer in parallel rectangular ducts have been discussed in detail in reference [1].[1] It is known that the Nusselt number strongly depends on the Reynolds number. For a given mass flow rate, the Reynolds number based on the mean flow velocity does not vary longitudinally in parallel ducts. The effects of the longitudinal variation of hydraulic diameter, and hence the local Reynolds number, in nonparallel rectangular ducts have not yet been fully investigated. In fact, only a few studies concerning the laminar flow in converging and diverging plane-walled channels (the limiting case of rectangular ducts) were reported in literature. For example, the Jeffery-Hamel type flow, which represents the fully developed laminar flow in converging and diverging plane-walled channels, has been cited as a classical case for which the exact solutions of the Navier-Stokes equations can be obtained [2]. The analysis of the heat transfer characteristics of the Jeffery-Hamel flow for the two fundamental thermal boundary conditions of prescribed wall heat flux and prescribed wall temperature was given by Sparrow and Starr [3]. The laminar flow development and heat transfer in the entry region of the converging plane-walled channels was studied by Yang and Price [4]. These works indicate that the laminar Nusselt number is increased significantly by the flow acceleration in converging channels. The augmentation of heat transfer rate in converging ducts can, therefore, be utilized for the development of modern heat exchangers. However, there are many engineering systems which are operating in the turbulent flow regime and cannot be represented by the idealization of the two-dimensional laminar flow. At present, it appears that the case of turbulent flow has not yet been studied.

This report presents turbulent heat transfer in converging rectangular ducts. The flow is hydrodynamically and thermally developing in the ducts. The heating condition is such that the top and bottom walls are uniformly heated, while the two side walls are unheated. This experimental model represents closely many engineering systems.

Description of Experimental Apparatus

The main elements of the experimental apparatus included an air blower, a calibrated ASME standard orifice, a large settling chamber, a section of unheated parallel duct and the heated converging ducts. The blower was driven by a variable-speed d-c motor and a d-c generator. The flow rate was controlled by adjusting the output of the generator. The Reynolds number in the parallel section was in the range 2.4 × 10⁴ to 4.8 × 10⁴, which is in the regime of the fully turbulent flow. The concentric orifice plate (Model 951B30, Meriam Instrument Co.) was calibrated by integrating velocity profiles measured at 10 in. downstream of the plate. The orifice meter was followed by the settling chamber to which the parallel duct was connected with an abrupt entry. In order to reduce the effect of entry configuration, three layers of fine screen (mesh size 80) were inserted in the parallel section at a few inches in front of the converging section. (See Fig. 1 and

[1] Numbers in brackets designate References at end of paper.

Contributed by the Heat Transfer Division and presented at the Winter Annual Meeting, Detroit, Mich., November 11–15, 1973, of THE AMERICAN SOCIETY OF MECHANICAL ENGINEERS. Manuscript received by the Heat Transfer Division October 30, 1972. Paper No. 73-WA/HT-27.

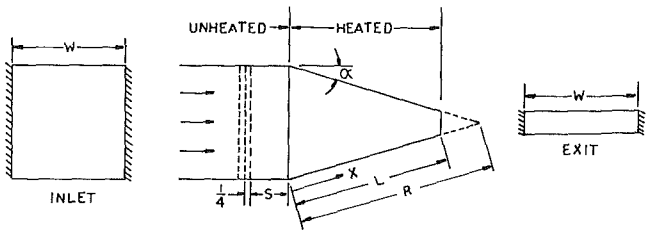

Fig. 1 Schematic of ducts

Table 1 Dimensions of ducts (all length dimensions in inches)

Duct No.	α	A_i	A_e	L	R	S
1	0	2 × 2	2 × 2	16	...	4.25
2	2½	2 × 2	½ × 2	17.20	22.92	3.25
3	5	2 × 2	½ × 2	8.60	11.47	4.25
4	7½	2 × 2	½ × 2	5.74	7.66	2.875

Table 1.) Velocity measurements at two inches away from the screen show that fairly uniform velocity distributions were obtained. The variation of velocity distribution is 3.7 percent at $\mathrm{Re} = 4.8 \times 10^4$ and 5.6 percent at $\mathrm{Re} = 2.4 \times 10^4$.

Three rectangular ducts of taper angle 2½, 5, and 7½ deg and a parallel duct were used in the present investigation. The schematic diagram is shown in Fig. 1. All ducts were of the same construction and materials, differing only in dimensions as given in Table 1. The top and bottom walls were constructed from 0.033-in-thick Inconel (600) sheet and the two side walls were made of 0.75-in-thick Benelex (grade 401) plate. The Inconel sheets were inserted in grooves milled on the Benelex plates to form the rectangular duct with specified taper angle. The Benelex is a thermally and electrically insulating laminate and is used to approach the condition of adiabatic side walls. The entire duct was mounted in a large wooden box which was filled with Zonolite insulation powder. Uniform heat generation in the top and bottom walls was achieved by passing a direct current longitudinally through the duct walls. The electric current was supplied by a regulated d-c generator (Model LB-703-FMOV, Lambda Electronics Corp.). The power dissipation in the duct was determined by measuring the total current through the Inconel sheets and the voltage drop across the duct. Iron-constantan thermocouples were first attached with Thermcoat (a thermocouple cement from Omega Engineering Inc.) to the outer surface of the Inconel sheet and then covered with a layer of epoxy cement. The wall thermocouples, which ranged in number from 24 to 15 depending on the duct size, were distributed longitudinally along the duct and across the span at a few stations.

Experimental Procedure and Data Reduction

The essential quantities which were measured in this study included the mass flow rate, longitudinal static pressure variations, wall temperatures, electric power input to the duct, and the velocity and temperature profiles at the inlet and exit sections. The mass flow rate was calculated from the measured values of pressure differential of the orifice plate, the absolute pressure and temperature of the fluid at about 5 dia downstream of the orifice plate. The inlet Reynolds number is defined in terms of the mean fluid velocity and the hydraulic diameter and is expressed in terms of the mass flow rate:

$$\mathrm{Re}_i = uD_{hi}/\nu = m/\mu w \tag{1}$$

The wall temperatures were measured by thermocouples mounted along the center line of the outer surface of the Inconel sheets. The temperature drop across the thickness of the sheet was neglected. The spanwise temperature variation measured at a few stations was found to be about 6 F at high heating rate and about 2.5 F at low heating rate. The bulk fluid temperature was calculated by using a total energy balance:

$$T_b = T_i + \frac{2wqx}{mC_p} \tag{2}$$

The wall heat flux q is based on the total power input and the total surface area of the two heated walls. The convective heat transfer coefficient is then defined by

$$h = q/(T_w - T_b) \tag{3}$$

where T_w is the wall temperature measured along the center line of the duct. It is noted that the heat which flows by conduction from the heated walls to the unheated side walls and the heat which flows from the wooden box to the ambient air are not included. An error analysis performed for this experiment shows that the uncertainty of the final results is within 10 percent. Further check of the experimental data was done by examining the results obtained from the parallel duct. Representative graphs of wall temperature distribution and Nusselt number are shown in Fig. 2. The longitudinal wall temperature approaches a curve linear and parallel to the corresponding bulk temperature curve. This agrees with the condition for fully developed heat transfer in ducts with longitudinally uniform heat flux. The Nusselt number decreases rapidly along the duct and approaches an asymptotic value. The asymptotic value is the Nusselt number in the fully developed region given by Novotny, et al. [5]. In reference [5] the turbulent heat transfer in the fully developed region of a square duct (0.980 in. × 0.980 in.) was measured under the same heating condition employed in this experiment. At eight hydraulic diameters the Nusselt number is about 30 percent higher than its asymptotic value. This difference is comparable with that reported by Boelter, et al. [6]. In a study of the effect of entry configurations on turbulent heat transfer in the entry region of circular pipe of constant surface temperature, Boelter, et al. [6] have shown that at eight hydraulic diameters the Nusselt number is 5 percent to 35 percent higher than its asymptotic value.

Nomenclature

A = cross-sectional area
C_p = heat capacity at constant pressure
D_h = hydraulic diameter
h = convective heat transfer coefficient
k = thermal conductivity
K = acceleration parameter, equation (8)
L = duct length
m = total mass flow rate
Nu_x = Nusselt number, hx/k
P = static pressure
Pr = Prandtl number
q = wall heat flux
r = radial coordinate
S = distance (Fig. 1)
R = radial distance of duct inlet section (Fig. 1)
Re = Reynolds number
T = temperature
u = fluid mean velocity in axial direction
w = duct width
x = distance measured on the wall from inlet section
α = taper angle
μ = dynamic viscosity
ν = kinematic viscosity
ρ = density

Subscripts

b = bulk property
e = exit section
i = inlet section
w = wall

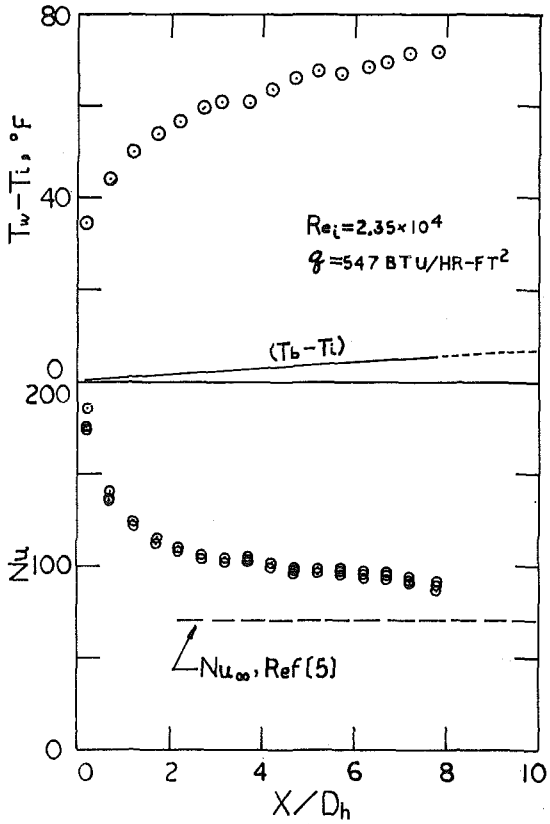

Fig. 2 Longitudinal wall temperature and heat transfer variations in parallel duct

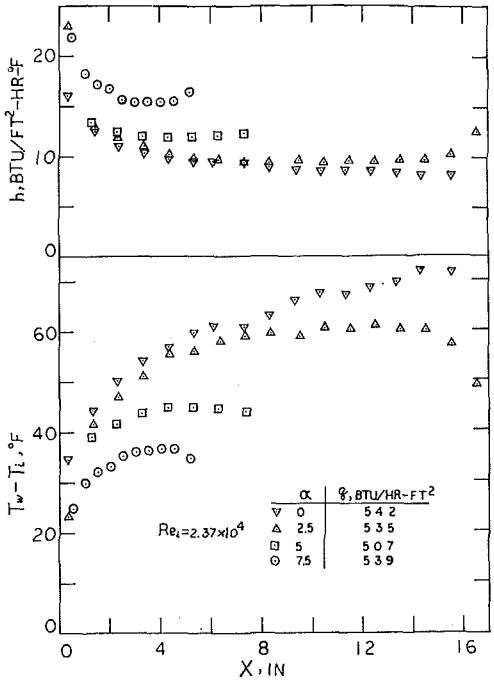

Fig. 3 Comparison of heat transfer and wall temperature in converging and parallel ducts

Discussion of Results

Comparisons of the longitudinal variation of wall temperature and heat transfer coefficient are given in Fig. 3 for the four ducts. Some interesting points are revealed in this figure. It is seen that the wall temperature of the converging ducts increases at first along the duct, reaches a maximum, and then decreases toward the duct exit. Meanwhile, the wall temperature of the parallel duct exhibits a monotonic increasing along the duct. Corresponding to the wall temperature variation, the heat transfer coefficient behaves in a reverse manner. Apparently, there are two opposing effects governing the heat transfer mechanism in the converging duct. Starting with uniform velocity and temperature profiles at the inlet section, boundary layers develop along the duct walls. The boundary layer provides the thermal resistance and results in an increase of wall temperature but a decrease of heat transfer coefficient along the duct, as one expects. On the other hand, the longitudinal increase of local mean velocity yields an increase of local heat transfer rate, if one assumes that the local Nusselt number is directly proportional to the local Reynolds number. This assumption is valid in many heat transfer processes, such as flow over a body of arbitrary shape [1]. One of the characteristics of accelerating flow is that the boundary layer thickness is greately reduced by the flow acceleration. The reduction of heat transfer rate due to the development of boundary layer in converging ducts is not as strong as in the parallel duct. Hence, the effect of increasing local Reynolds number becomes appreciable in ducts with high acceleration. The net effect on heat transfer depends on the relative order of each effect. The minimum point of the h-curve in Fig. 3 represents a balance between the opposing effects due to the increase of boundary layer thickness and mean velocity. Hypothetically, as flow approaches the apex of the converging duct, the mean velocity, and hence the local Reynolds number, $\frac{ux}{\nu}$, become infinite as the cross-sectional area vanishes. Thus, it is expected that, at the apex, the wall temperature approaches the bulk fluid temperature and the heat transfer coefficient approaches infinity. This is clearly shown by the wall temperature and heat transfer distributions in Figs. 4 and 5, in which the dimensionless distance x/R is used.

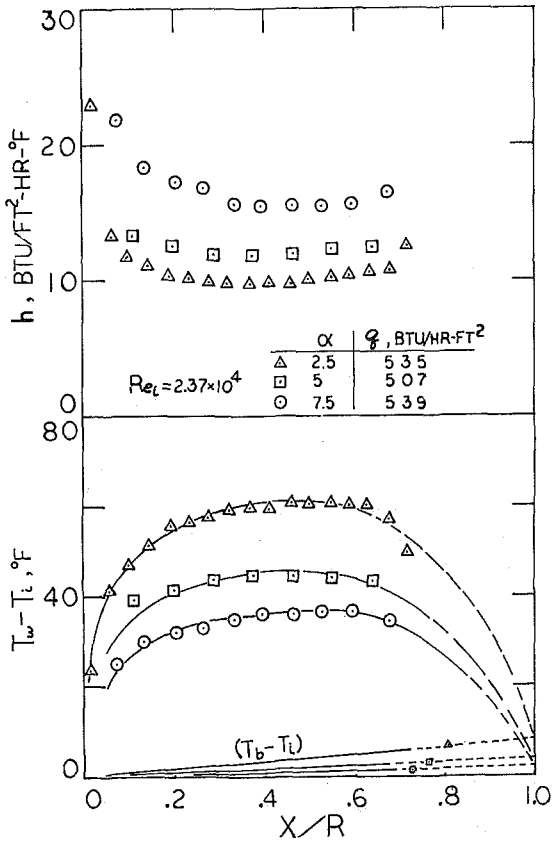

Fig. 4 Effect of inlet Reynolds number on heat transfer and wall temperature variations

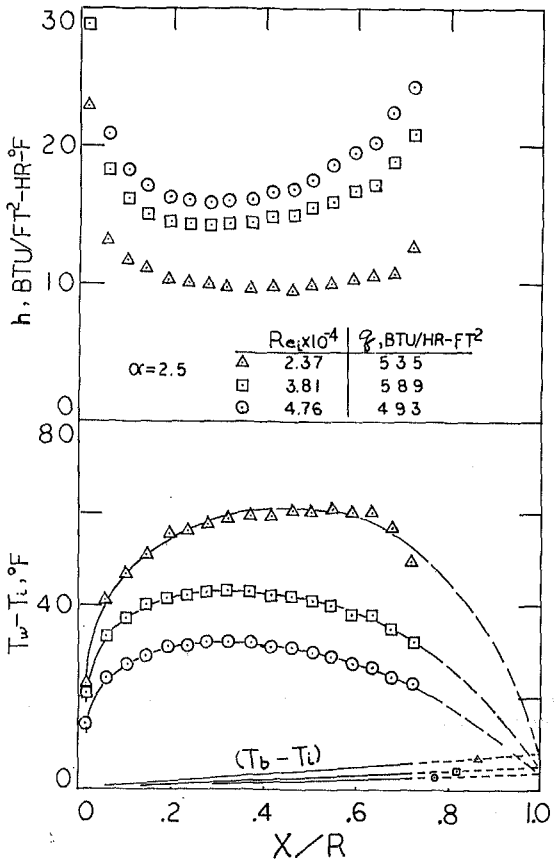

Fig. 5 Effect of taper angle on heat transfer and wall temperature variations

Fig. 4 shows the effect of inlet Reynolds number at $\alpha = 2.5$ deg and Fig. 5 illustrates the effect of taper angle at $\mathrm{Re}_i = 2.37 \times 10^4$. The heat transfer rate increases significantly with the increase of either the taper angle or the inlet Reynolds number as indicated in these two figures. It is noted, in Fig. 4, that the position of the minimum point of the h-curve changes with the inlet Reynolds number. The minimum point is moved upstream when the effect of increasing heat transfer at higher Reynolds number is stronger than the opposing effect of boundary layer development. The effect of taper angle on the position of the minimum point is not so apparent as seen in Fig. 5.

The single correlation of the local Nusselt number and the local Reynolds number is given in Fig. 6. The characteristic length is the longitudinal distance x. The experimental results can be represented by the following empirical equation:

$$\mathrm{Nu}_x = 0.184\,\mathrm{Re}_x^{0.65} \tag{4}$$

where

$$\mathrm{Nu}_x = \frac{hx}{k} \text{ and } \mathrm{Re}_x = \frac{ux}{\nu}$$

The existence of such a correlation, which is independent of the taper angle, inlet Reynolds number, and the local hydraulic diameter, reveals the fact that the internal flow in the entry region of converging ducts possesses the strong character of boundary layer type flow. No single correlation was obtained when the local hydraulic diameter was used as the characteristic length. For turbulent accelerating boundary layer flow, correlation between the local Stanton number and a modified Reynolds number is given by reference [1] as:

$$\frac{h}{\rho C_p U_\infty} = 0.0295\,\mathrm{Pr}^{-0.4}\left(\frac{1}{\nu}\int_0^x U_\infty dx\right)^{-0.2} \tag{5}$$

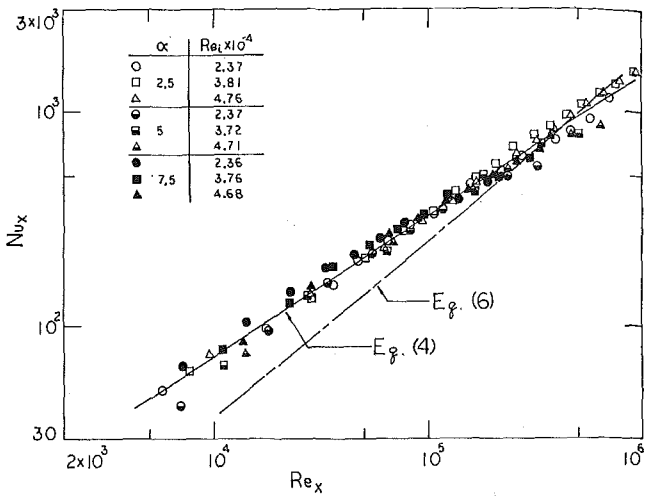

Fig. 6 Local Nusselt number and Reynolds number correlation

where U_∞ is the free stream velocity for the boundary layer flow. Using the local Nusselt number and Reynolds number based on the longitudinal distance x as defined in equation (4), and replacing U_∞ by the mean velocity u, the foregoing equation becomes:

$$\mathrm{Nu}_x = 0.0295\,\mathrm{Pr}^{0.6}\mathrm{Re}_x\left(\frac{1}{\nu}\int_0^x u dx\right)^{-0.2} \tag{6}$$

Equation (6) is shown in Fig. 6 in comparison with the experimental data. It should be pointed out that the thermal boundary conditions of the two cases are different. The correlation of the boundary layer flow, equation (6), corresponds to an isothermal wall while the measured data represent cases of which the wall temperature variations are indicated in Figs. 3 to 5. Nevertheless, quantitive comparison can be made in Fig. 6. It is seen that the Nusselt number of the accelerating internal flow is higher than that of the accelerating boundary layer flow near the inlet section. The high turbulence intensity created by the three layers of screen probably contributes to the high heat transfer rate near the inlet section. The difference between the Nusselt numbers of the two cases becomes smaller as the flow moves downstream and the two curves cross at some point near the exit of the duct. Apparently, the internal flow has a smaller change of Nusselt number with Reynolds number. The comparison of the local Nusselt number of the tapered ducts with that of the parallel duct is illustrated in Fig. 7, in which equation (4) was used to represent the data of tapered ducts for the sake of clarity. The fairly good agreement in the upstream portion of the duct indicates the character of boundary layer flow in both tapered and parallel ducts. In the downstream portion, the convergence of the duct yields a smaller Nusselt number as shown in Fig. 7. The slower variation of local Nusselt number with the local Reynolds number in Figs. 6 and 7 is partially due to the rapid decay of turbulence intensity caused by flow acceleration.

Since the flow is accelerating in the tapered duct, it will be interesting to examine whether laminarization may occur. The possible occurrence of the laminarization may also explain the slower variation of Nusselt number in the downstream portion of the tapered duct. The phenomenon of reverse transition in external boundary layer flow due to acceleration has been investigated by several authors in recent years. It is known that the phenomenon is characterized by an acceleration parameter K defined as

$$K = -\frac{\nu}{U_\infty^2}\frac{dU_\infty}{dx} \tag{7}$$

where U_∞ is the free stream velocity for the external boundary layer flow. The critical value of the acceleration parameter for

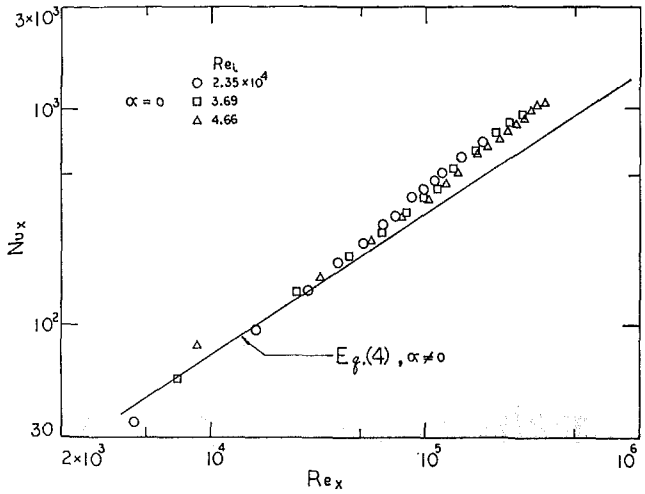

Fig. 7 Comparison with Nusselt number of parallel duct flow

which laminarization occurs is about 3.5×10^{-6} [1]. The laminarization due to high heating rate in channels of constant cross-sectional area has also been studied by several investigators. Some equivalent forms of the same parameter K have been used as the convenient parameter in correlating experimental data. The critical value is reported as 1.5×10^{-6} by Coon and Perkins [7], and between 0.8 and 1.14×10^{-6} by Bankston [8]. For the present case, the acceleration parameter is related to the taper angle and the inlet Reynolds number as shown in the following:

$$K = -\frac{\nu}{u^2}\frac{du}{dr} = \frac{\nu}{ru} = \frac{2\alpha w\mu}{m} = \frac{2\alpha}{\mathrm{Re}_i} \tag{8}$$

In this experiment, the values of the parameter K are in the range 1.86×10^{-6} to 11.1×10^{-6}. If the foregoing values can be used as criteria, then it is possible for the occurrence of laminarization in converging rectangular ducts. It should be pointed out that laminarization is a very complicated process and is associated with the flow very close to the wall. More detailed studies are needed for this phenomenon.

Finally, the longitudinal pressure variation is shown in Fig. 8. It is seen in Fig. 8(a) that, for all the three tapered ducts, the pressure variation is small and is approximately linear in the region near the inlet section. The pressure variation increases rapidly as the flow is accelerated toward the exit of the duct. The variation of pressure is indifferent to the taper angle but is pronounced as the inlet Reynolds number is increased. The dependence of inlet Reynolds number can be eliminated when the pressure variation is normalized by $(\frac{1}{2}\rho u^2)$ as shown in Fig. 8(b). It is interesting to compare the results with that calculated for potential flow. It can be shown that, for potential flow in converging plane-walls, the following relationslip holds [10]:

$$P - P_e = \tfrac{1}{2}\rho u^2\left[\left(\frac{r}{r_e}\right)^2 - 1\right] \tag{9}$$

In terms of the longitudinal distance x, equation (9) becomes

$$\frac{P - P_e}{\frac{1}{2}\rho u^2} = \left(\frac{A_i}{A_e}\right)^2\left(1 - \frac{x}{R}\right)^2 - 1 \tag{10}$$

For the present case, the ratio of the inlet area to the exit area is 16. The foregoing equation is independent of inlet Reynolds number and tapered angle and applies to flow with uniform velocity distribution at any given axial position. Comparison of equation (10) with the measured data reveals again the characteristics of the accelerating flow. The small difference indicates the existence of wall shear stress due to the nonuniformity of the velocity profile in the thin layer near the wall.

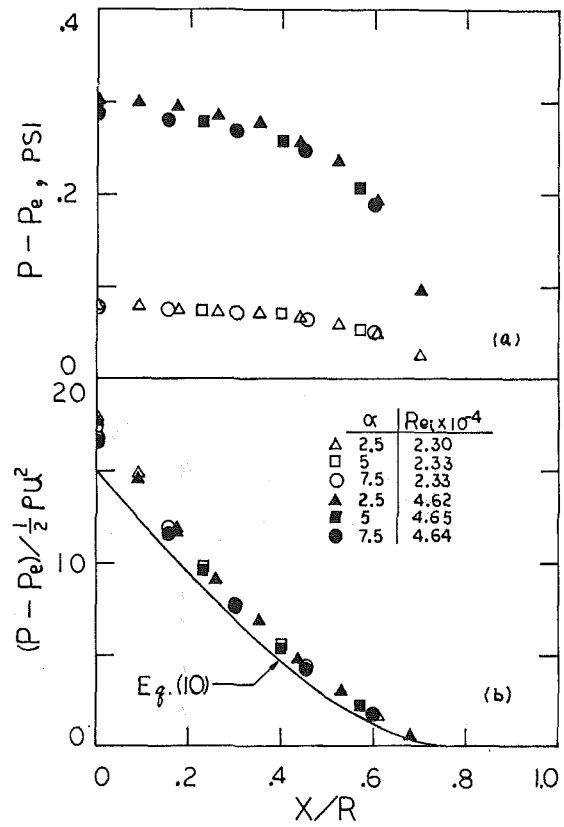

Fig. 8 Longitudinal pressure variation

Acknowledgment

The support of this work by the National Science Foundation under Grant No. GK-6948 is gratefully acknowledged.

References

1 Kays, W. M., *Convective Heat and Mass Transfer*, McGraw-Hill, New York, 1966.

2 Schlichting, H., *Boundary Layer Theory*, McGraw-Hill, New York, 1960.

3 Sparrow, E. M., and Starr, J. B., "Heat Transfer to Laminar Flow in Tapered Passages," *Journal of Applied Mechanics*, Vol. 32, TRANS. ASME, Vol. 87, 1965, p. 684.

4 Yang, J. W., and Price, M., "Laminar Flow Development and Heat Transfer in Converging Plane-Walled Channels," *Applied Scientific Research*, Vol. 25, 1972, p. 361.

5 Novotny, J. L., McComas, S. T., Sparrow, E. M., and Eckert, E. R. G., "Heat Transfer for Turbulent Flow in Rectangular Ducts With Two Heated and Two Unheated Walls," *J. AIChE*, Vol. 10, 1964, p. 466.

6 Boelter, L. M., Young, K. G., and Inverson, H. W., "An Investigation of Aircraft Heaters," NACA TN 1451, 1948.

7 Coon, C. W., and Perkins, H. C., "Transition From the Turbulent to the Laminar Regime for Internal Convective Flow With Large Property Variation," ASME Paper No. 69-HT-9.

8 Bankston, C. A., "The Transition From Turbulent to Laminar Gas Flow in a Heated Pipe," ASME Paper No. 69-HT-54.

9 Yang, J. W., and Mathur, S., "Experiments on Turbulent Flow in Converging Rectangular Ducts," FTSL TR 72-1, Fluid and Thermal Sciences Laboratory, Faculty of Engineering and Applied Sciences, SUNY at Buffalo.

10 Millsaps, K., and Pohlhausen, K., "Thermal Distribution in Jeffery-Hamel Flow Between Nonparallel Plane Walls," *J. Aero. Science*, Vol. 20, 1953, p. 187.

M. BENTWICH
Division of Fluid Mechanics and Transport Phenomena, University of the Negev, Beer-sheva, Israel

Multistream Countercurrent Heat Exchangers

An idealized model multistream countercurrent exchanger is considered. It comprises a number of parallel two-dimensional streams in channels separated by thin conductive partitions. The streams on the two sides of any partition flow in opposite directions. Thus the heat contained in one set of co-directional currents, which enters the exchanger at a high temperature, is transferred through the partitions to the oppositely directed cooling streams. The analysis accounts for the entire temperature distribution in this model when the axial conduction in the streams and in the partitions is neglected. The solution is obtained by expressing the temperature field in terms of the inlet conditions and the flux across the partitions. The latter is represented by as many a priori unknown functions of the axial distance as there are partitions. They are governed by the same number of linear integral equations. Using a finite-difference technique, these are solved for a variety of cases that are of practical interest.

Introduction

Considered is the model multichamber countercurrent parallel-plate heat exchanger shown schematically in Fig. 1. The temperature distribution within it is solved under the following rather idealized, yet widely accepted, assumptions:

(*a*) steady state prevails
(*b*) physical properties of the fluids and the solids are constant
(*c*) flow in every chamber is fully developed and parabolic
(*d*) axial conduction in the stream and in the partition is negligible
(*e*) the entire pattern is two-dimensional
(*f*) the outer partitions 0 and $2n_{max}$ are insulated.

Considerable effort was devoted to the examination of these assumptions. It has been shown that one can indeed neglect axial conduction in the stream [1][1] and in the partitions [2] provided the Peclet numbers are large and the partitions are thin and highly conductive. Note also that various profiles can emerge in a fully developed channel flow, and that as with most of the works cited here, the proposed analysis is applicable, in principle, to any exchanger in which the profile is known. Parabolic rather than uniform distribution (plug flow) was assumed because with this choice it is easier to demonstrate how the difficulties associated with transverse variations are overcome. It is shown here that it is indeed important to account for these. Again, the geometry of multichamber exchangers does not often resemble the one assumed, Fig. 1. However, the extension of this work to the familiar concentric shell-and-tube case in which there is rotational symmetry is immediate. It is also noted that the analyses of one and two-stream systems that are based on assumptions (*a*)–(*f*), which are mentioned below [3–10], appear to have produced acceptable results. It is hoped that this analysis of a multichamber pattern will yield similarly reliable findings.

The two-chamber counterpart of the problem treated here was first posed by Nunge and Gill [3]. In that work and elsewhere [4–6] the Graetz form of solution is adopted and a variety of cases are solved. In [7, 8] the author obtains a general solution of what is essentially the same two-stream problem by adopting

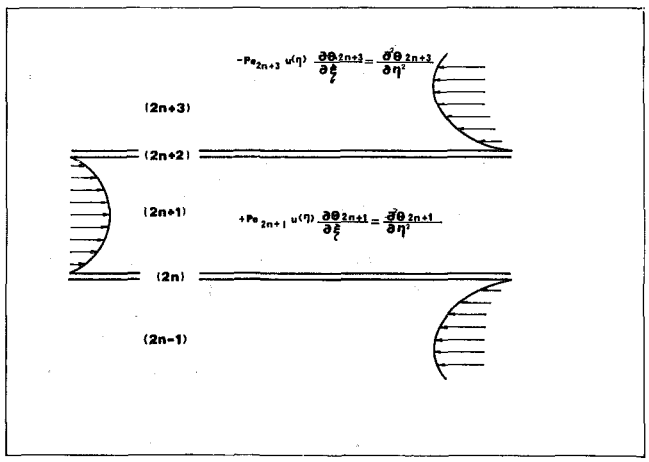

Fig. 1 General scheme of the multistream heat exchanger

[1] Numbers in brackets designate References at end of paper.

Contributed by the Heat Transfer Division for publication (without presentation) in the Journal of Heat Transfer. Manuscript received by the Heat Transfer Division November 23, 1971. Paper No. 73-HT-L.

an altogether different approach. In the latter works, the temperature in each current is defined in terms of the flux across the partition. The solution for the flux is shown to be governed by a Fredholm integral equation of the second kind. The solution proposed here for multichamber exchangers is an extension of the latter. It is thus demonstrated that the fluxes across two or more partitions are governed by as many integral equations. These are linked so that the mutual influences of the fluxes across a pair of partitions bounding one stream is accounted for. It must be pointed out that attempts were also made to extend the method of Nunge and Gill to a multichamber exchanger. Thus Blanco and Gill [9] analyze the case of an (infinitely) many stream exchanger made of identical components. However, in that work, as well as in the numerical solution of Gutfinger, Isenberg, and Zeitlin [10], use is made of the periodic nature of the distribution (when end effects are neglected). Such situations can be analyzed by considering the pseudo two-stream exchanger bounded by the mid-planes of streams $2n + 1$ and $2n + 3$, see Fig. 1. In view of the periodicity of the distribution, these midplanes can be assumed insulative, so that for given inlet conditions the distribution between them can be solved. Unlike these, the present work is not restricted to such periodic solution. Thus results for five-chamber exchanger are presented herewith.

For cases in which more stringent assumptions than (*a*)–(*f*) hold, the equations governing the axial temperature distribution in multistream exchangers were derived by Wolf [11]. Interesting results were obtained by Aulds and Barron [12], as well as by Chato Laverman, and Shah [13] and others who solve these equations. In these analyses, the authors do not account for the transverse variations of the temperature distribution due to nonuniformity in the flow profile as well as to the diffusion across the stream. The refinement proposed is believed to be important from theoretical and practical viewpoints. Indeed, it is shown here that variation of the inlet profile gives rise to a marked change in the overall efficiency of a three-stream exchanger.

The solution of the linked integral equations mentioned yields the flux across every partition. Therefore, by straightforward integration one can calculate the total heat transferred by the exchanger. That quantity, when normalized in a suitable manner, is also the efficiency of the exchanger ν. It is defined here for the cases in which the temperature of the coolant at the inlet is uniform, and the temperature scale is defined so that this temperature is zero. Then, in view of assumption (*d*), the heat flux supplied to the exchanger is the integral across the hot inlets of the local temperature times the mass flux times the specific heat; ν is the ratio between the total heat transferred across the partitions into the coolant and that supplied. When ν is close to unity, optimum performance is approached and the temperature of the originally hot liquid leaves the exchanger at a temperature that is close to zero. In such a case, almost all the heat supplied is dumped into the coolant. As explained in [8], ν cannot approach unity in a cocurrent exchanger. For example, if it has two streams of identical features and dimensions, then in an optimal situation the exit temperature is uniform and ν is one-half. Clearly two- or multistream countercurrent exchangers do not have this limitation, and the results presented show under what circumstances ν approaches unity. Finally, it is remarked that the notion of exchanger efficiency appears elsewhere. For example, it is used in [13], where it is defined differently. Comparison of these results with the results obtained there is impossible, because that work is based on the assumption that there are three distinct inlet temperatures.

Analysis

The model analyzed is shown in Fig. 1. The relatively thin strips designated by even indices represent solid partitions. The strips with the odd indices represent the streams. In the chambers designated by $2n - 3$, $2n + 1$, $2n + 5$, and so on, the flow is from left to right, and in the adjacent currents $2n - 1$ and $2n + 3$ the flow is from right to left. The situation shown repeats itself for both decreasing and increasing n, except that the outer partitions marked by 0 and $2n_{max}$ are assumed to be well insulated. All the internal partitions are designed to be highly conductive.

It can easily be shown that the reduced temperatures in the streams flowing from left to right and right to left are governed by

$$\mathrm{Pe}_{2n+1}(1 - \eta^2)\frac{\partial\theta_{2n+1}}{\partial\xi} = \frac{\partial^2\theta_{2n+1}}{\partial\eta^2} \qquad -1 < \eta < 1 \qquad 0 < \xi < l \quad (1_{2n+1})$$

and

$$-\mathrm{Pe}_{2n-1}(1 - \eta^2)\frac{\partial\theta_{2n-1}}{\partial\xi} = \frac{\partial^2\theta_{2n-1}}{\partial\eta^2} \qquad -1 < \eta < 1, \qquad 0 < \xi < l \quad (1_{2n-1}) \quad (1)$$

respectively. The independent variables η, ξ are obtained for

Nomenclature

A_i^{2n+1}, A_i, B_i = expansion coefficients associated with the inlet conditions

d_r, e_r = expansion coefficients appearing in the kernel of the integral equations

f_{2n}, f, g = functions proportional to the heat flux across the partitions

H = Heaviside's step function

k_{2n}, k_{2n+1} = conductivity of medium $2n$, $2n + 1$

l = ratio of the stream's axial length to half its width

L = effective stream length $l/-\mathrm{Pe}_{2n+1}$

Pe_{2n+1} = Peclet number of stream $(2n + 1)$ defined in terms of the local diffusivity, maximum flow velocity in that stream and half its width

q_{2n} = flux across the partition $2n$

x, y = scaled cartesian coordinates

α_{2n}, α = the ratio between the Peclet numbers for the two streams adjacent to the $2n$th partition

ξ, η = nondimensional cartesian coordinates

ζ = dummy variable

ϕ_r = eigenfunctions of system (3)

λ_r = eigenvalues of system (3)

τ_{2n+}, τ_{2n-} = dimensionless width of partition $2n$

θ_{2n+1} = reduced nondimensional temperature in stream $2n + 1$

$\hat{\theta}_{2n+}, \hat{\theta}_{2n-}$ = influence functions defined by equations (5) and (6)

ρ_{2n}, ρ = ratio between widths of the the two streams adjacent to the partition $2n$

ν = efficiency of the exchanger defined in the Introduction

Indices

$2n$ = indicates solid partition

$2n + 1$ = indicates a stream

$2n+, 2n-$ = reflects influence between partition $2n$ and streams $2n + 1$ and $2n - 1$, respectively

r = subscript in the expansions appearing in the kernel

i = subscript in the expansion associated with the distribution at the inlet

every phase by nondimensionalizing the cartesian coordinates with respect to half the stream width. Thus, although each equation holds for $-1 < \eta < 1$ and $0 < \xi < l$, the values of l and the widths represented by the ranges $-1 < \eta < 1$ are, in general, different for every phase. The Peclet number is defined in terms of the local characteristic length, maximum velocity, and diffusivity.

The solution for the temperature in the $(2n + 1)$th stream can be written as follows

$$\theta_{2n+1} = \sum_{i=0}^{\infty} A_i^{2n+1}\phi_i(\eta) \exp(-\mathrm{Pe}_{2n+1}^{-1}\lambda_i^2\xi) + \int_0^{\xi} f_{2n}'(\zeta)\hat{\theta}_{2n+}(\zeta;\xi,\eta)d\zeta + f_{2n}(0)\hat{\theta}_{2n+}(0;\xi,\eta) + \int_0^{\xi} f_{2n+2}'(\zeta)\hat{\theta}_{2n+2-}(\zeta;\xi,\eta)d\zeta + f_{2n+2}(0)\hat{\theta}_{2n+2-}(0;\xi,\eta) \quad (2_{2n+1})$$

(2)

In this expression, the eigenfunctions ϕ_i and the corresponding eigenvalues λ_i are governed by

$$\phi_i''(\eta) + \lambda_i^2(1-\eta^2)\phi_i = 0 \qquad -1 < \eta < 1$$
$$\phi_i'(-1) = \phi_i'(1) = 0 \quad (3)$$

The coefficients A_i^{2n+1} are obtained by setting $\xi = 0$ and equating the resulting series to the temperature distribution at the inlet to phase $2n + 1$. In other words, the first series on the right-hand side of equation (2_{2n+1}) is the Graetz type of solution that would have prevailed had the partitions been insulated. The other terms express the influence of the flux through these. Here f_{2n} is the temperature difference across the partitions $2n$. The function $\hat{\theta}_{2n+}(\zeta;\xi,\eta)$ is the temperature distribution that prevails in the stream $2n + 1$ when all the constants A_i^{2n+1} are zero, f_{2n+2} vanishes identically, and f_{2n} is given by

$$f_{2n}(\zeta) = H(\xi - \zeta)$$

where H designates Heaviside's step function. Observe that the index of $\hat{\theta}_{2n+}$ commences with $2n$. This indicates that this function is associated with the influence of flux across the partition designated by that number. The index terminates with a plus sign in order to show that this influence is on the stream with an index higher than $2n$. Similarly, $\hat{\theta}_{2n+2-}$ represents the influence of the flux in the partition $2n + 2$ on the stream marked by the lower index $2n + 1$. More specifically, it is the solution for θ_{2n+1} when A_i^{2n+1} and f_{2n} vanish while f_{2n+2} is given by

$$f_{2n+2} = \mathrm{H}(\xi - \zeta)$$

In terms of these notations, the temperature in the $(2n - 1)$th stream can be expressed thus

$$\theta_{2n-1} = \sum_{i=0}^{\infty} A_i^{2n-1}\phi_i(\eta) \exp[-\mathrm{Pe}_{2n-1}^{-1}\lambda_i^2(l-\xi)] f_{2n}(l)\hat{\theta}_{2n-}(l;\xi,\eta) - \int_{\xi}^{l} f_{2n}'(\zeta)\hat{\theta}_{2n-}(\zeta;\xi,\eta)d\zeta$$
$$f_{2n-2}(l)\hat{\theta}_{2n-2+}(l;\xi,\eta) - \int_{\xi}^{l} f_{2n-2}'(\zeta)\hat{\theta}_{2n-2+}(\zeta;\xi,\eta)d\zeta \quad (4_{2n-1})$$

The temperature in all the other streams flowing from right to left can be obtained from the last expression by replacing n with $n + 2r$, where r is an integer. Similarly, equation (2_{2n+1}), with some modifications, expresses the temperature in all the streams flowing from left to right.

As is shown in [8], and can easily be verified, the functions $\hat{\theta}$ are given by

$$\hat{\theta}_{2n+}(\zeta;\xi,\eta) = -\frac{k_{2n}}{k_{2n+1}}\frac{1}{\tau_{2n+}}\left(\frac{3}{8}\right)\left\{\left(\frac{\eta^2}{2} - \frac{\eta^4}{12} - \frac{2}{3}\eta\right) + \mathrm{Pe}_{2n+1}^{-1}(\xi-\zeta) + \sum_{r=0}^{\infty} e_r\phi_r(\eta) \times \exp[-\mathrm{Pe}_{2n+1}^{-1}\lambda_r^2(\xi-\zeta)]\right\} \mathrm{H}(\xi-\zeta) \quad (5)$$

$$\hat{\theta}_{2n+2-}(\zeta;\xi,\eta) = +\frac{k_{2n+2}}{k_{2n+1}}\frac{1}{\tau_{2n+2-}}\left(\frac{3}{8}\right)\left\{\left(\frac{\eta^2}{2} - \frac{\eta^4}{12} + \frac{2}{3}\eta\right) + \mathrm{Pe}_{2n+1}^{-1}(\xi-\zeta) + \sum_{r=0}^{\infty} d_r\phi_r(\eta) \times \exp[-\mathrm{Pe}_{2n+1}^{-1}\lambda_r^2(\xi-\zeta)]\right\} \mathrm{H}(\xi-\zeta) \quad (6)$$

Over the section $1 < \eta < 1$, $\xi = \zeta$, these functions vanish. Therefore the coefficients e_r and d_r satisfy

$$e_r = d_r = -\int_{-1}^{1}\left(\frac{\eta^2}{2} - \frac{\eta^4}{12}\right)(1-\eta^2)\phi_r d\eta \Big/ \int_{-1}^{1}(1-\eta^2)\phi_r^2 d\eta \qquad r \text{ even}$$
$$e_r = -d_r = \int_{-1}^{1}\frac{2}{3}\eta(1-\eta^2)\phi_r d\eta \Big/ \int_{-1}^{1}(1-\eta^2)\phi_r^2 d\eta \qquad r \text{ odd} \quad (7)$$

The constants k are the conductivities of the phases indicated by the indices. The parameters τ_{2n+} and τ_{2n-} designate the ratios between half the width of the partitions $2n$ and the characteristic lengths of the streams $2n + 1$ and $2n - 1$, respectively. The expressions for $\hat{\theta}_{2n-}$ and $\hat{\theta}_{2n-2+}$ are given by the right-hand sides of equations (6) and (5), respectively; when the roles of ξ and ζ are interchanged, k_{2n+1} is replaced by k_{2n-1}, k_{2n+2} is replaced by k_{2n}, and k_{2n} is replaced by k_{2n-2}.

The relationships (2_{2n+1}), (4_{2n-1}), (5), (6), and (7) contain all the ingredients required to construct the solution for the temperature field in an exchanger with any number of streams. The first two of these contain the solutions of the heat equation in each and every stream, when the temperature difference across the partitions $2n$ is f_{2n}. As explained in [8] and elsewhere, if the partition is sufficiently narrow and k_{2n} is sufficiently high, the temperature distribution in these is linear. Under such circumstances the heat flux across the partition is proportional to f_{2n}. The present analysis ensures the continuity of this quantity by letting the function f_{2n} appear in conjunction with both $\hat{\theta}_{2n+}$ and $\hat{\theta}_{2n-}$ in the expressions for θ_{2n+1} and θ_{2n-1}, respectively. The cycle is closed by writing as many equations of the form

$$f_{2n} = \theta_{2n+1}\big|_{\eta=-1} - \theta_{2n-1}\big|_{\eta=+1} \quad (8_{2n})$$

as there are partitions. Care must be exercised in deriving these, because different scaling is used in the definition of ξ, η associated with each stream. This minor difficulty is resolved in the next section.

The following scaling scheme is adopted for variables appearing in the expression for θ_{2n+1}

$$\xi/\mathrm{Pe}_{2n+1} \equiv x \qquad \zeta/\mathrm{Pe}_{2n+1} \equiv y \qquad l/\mathrm{Pe}_{2n+1} \equiv L$$

It follows that the corresponding variables appearing in the expression for θ_{2n-1} are related to x, y, and L by

$$\xi/\mathrm{Pe}_{2n-1} \equiv \alpha\rho x \qquad \zeta/\mathrm{Pe}_{2n-1} \equiv \alpha\rho y \qquad l/\mathrm{Pe}_{2n-1} \equiv \alpha\rho L$$

Here α is given by

$$\alpha \equiv \mathrm{Pe}_{2n+1}/\mathrm{Pe}_{2n-1}$$

and its appearance in the last set of definitions is obvious. ρ is the ratio between the widths of the $(2n+1)$th and $(2n-1)$th streams. It reflects the difference in scaling used so far for the different streams. In terms of these, equation (8_{2n}), when combined with relationships (2_{2n+1}), (4_{2n-1}), (5), (6), and (7), yields

$$f_{2n}(x) = \sum_{i=0}^{\infty} A_i{}^{2n+1}\phi_i(-1)\exp(-\lambda_i{}^2x) - \sum_{i=0}^{\infty} A_i{}^{2n-1}\phi_i(1)\exp[-\lambda_i{}^2\rho\alpha(L-x)]$$
$$- f_{2n}(0)\frac{k_{2n}}{k_{2n+1}}\left(\frac{1}{\tau_{2n+}}\right)\frac{3}{8}\left\{\frac{13}{12}+x+\sum_{r=0}^{\infty} e_r\phi_r(-1)\exp(-\lambda_r{}^2x)\right\}$$
$$- \frac{k_{2n}}{k_{2n+1}}\left(\frac{1}{\tau_{2n+}}\right)\frac{3}{8}\int_0^x\left\{(x-y)+\frac{13}{12}+\sum_{r=0}^{\infty} e_r\phi_r(-1)\exp[-\lambda_r{}^2(x-y)]\right\}f_{2n}'(y)dy$$
$$- f_{2n}(L)\frac{k_{2n}}{k_{2n-1}}\left(\frac{1}{\tau_{2n-}}\right)\frac{3}{8}\left\{\rho\alpha(L-x)+\frac{13}{12}+\sum_{r=0}^{\infty} e_r\phi_r(1)\exp[-\lambda_r{}^2\rho\alpha(L-x)]\right\}$$
$$+ \frac{k_{2n}}{k_{2n-1}}\left(\frac{1}{\tau_{2n-}}\right)\frac{3}{8}\int_x^L\left\{\rho\alpha(y-x)+\frac{13}{12}+\sum_{r=0}^{\infty} e_r\phi_r(1)\exp[-\lambda_r{}^2\rho\alpha(y-x)]\right\}f_{2n}'(y)dy$$
$$+ f_{2n+2}(0)\frac{k_{2n+2}}{k_{2n+1}}\left(\frac{1}{\tau_{2n+2-}}\right)\frac{3}{8}\times\left\{-\frac{1}{4}+x+\sum_{r=0}^{\infty} d_r\phi_r(-1)\exp(-\lambda_r{}^2x)\right\}$$
$$+ \frac{k_{2n+2}}{k_{2n+1}}\left(\frac{1}{\tau_{2n+2-}}\right)\frac{3}{8}\int_0^x\left\{-\frac{1}{4}+(x-y)+\sum_{r=0}^{\infty} d_r\phi_r(-1)\exp[-\lambda_r{}^2(x-y)]\right\}f_{2n+2}'(y)dy$$
$$+ f_{2n-2}(L)\frac{k_{2n-2}}{k_{2n-1}}\left(\frac{1}{\tau_{2n-2+}}\right)\frac{3}{8}\left\{-\frac{1}{4}+\rho\alpha(L-x)+\sum_{r=0}^{\infty} d_r\phi_r(1)\exp[-\lambda_r{}^2\rho\alpha(L-x)]\right\}$$
$$- \frac{k_{2n-2}}{k_{2n-1}}\left(\frac{1}{\tau_{2n-2+}}\right)\frac{3}{8}\int_x^L\left\{-\frac{1}{4}+\rho\alpha(y-x)+\sum_{r=0}^{\infty} d_r\phi_r(1)\exp[-\lambda_r{}^2\rho\alpha(y-x)]\right\}f_{2n-2}'(y)dy \quad (9_{2n})$$

As explained in [8], it is possible to integrate by parts. When this is done, the boundary terms $f(0)$ and $f(L)$ leave no trace, because the functions $\hat{\theta}$ were so constructed that $\hat{\theta}(\zeta;\zeta,\eta)$ vanish. However, the form (9_{2n}) is the one that is actually solved.

Obviously, if $n_{\max}$ is two and, as assumed, the outside partitions are insulated, then f_0 and f_4 vanish identically. Equation (9_2) then reduces to the integral equation treated rather extensively in [8], where f_2 is the only unknown function to be solved. The situation is similar in the case of three streams, $n_{\max} = 3$, provided the dimensions of the exchanger and the inlet temperatures are such that the temperature distribution is symmetric with respect to the central plane of stream three. In such a case the following relationship holds

$$f = -f_4 = +f_2$$

so that again there is only one unknown function. It is convenient in this case to write (9_{2n}) for $n = 1$. Thus α is equal to the ratios Pe_3/Pe_1 and Pe_3/Pe_5, and ρ designates the corresponding ratios of widths. Since in this case the widths of both partitions are equal, the following holds

$$\tau = \tau_{2+} = \tau_{4-} = \tau_{2-}$$

It is similarly clear that the coefficients $A_i{}^5$ and $A_i{}^1$ are identical. Therefore, when use is made of the following definitions

$$A^5{}_i = A^1{}_i = B_i \qquad A^3{}_i = A_i$$

f is found to be governed by

$$f(x) = \sum_{i=0}^{\infty} B_i\phi_i(-1)\exp(-\lambda_r{}^2x) - \sum_{i=0}^{\infty} A_i\phi_i(1)\exp[-\lambda_i{}^2\rho\alpha(L-x)]$$
$$- \frac{3}{4}\frac{1}{\tau}\frac{k}{k_3}f(0)\left\{\frac{5}{12}+x+\sum_{r=0}^{\infty} e_{2r}\phi_{2r}(-1)\exp(-\lambda_{2r}{}^2x)\right\}$$
$$- \frac{3}{4}\frac{1}{\tau}\frac{k}{k_3}\int_0^x\left\{\frac{5}{12}+(x-y)+\sum_{r=0}^{\infty} e_{2r}\phi_{2r}(-1)\exp[-\lambda_{2r}{}^2(x-y)]\right\}f'(y)dy$$
$$- \frac{3}{8}\frac{1}{\tau}\frac{k}{k_3}\cdot\frac{k_3}{k_1}\frac{1}{\rho}f(L)\left\{\frac{13}{12}+\rho\alpha(L-x)+\sum_{r=0}^{\infty} e_r\phi_r(1)\exp[-\lambda_r{}^2\rho\alpha(L-x)]\right\}$$
$$+ \frac{3}{8}\frac{1}{\tau}\frac{k}{k_3}\frac{k_3}{k_1}\frac{1}{\rho}\int_x^L\left\{\frac{13}{12}+\rho\alpha(y-x)+\sum_{r=0}^{\infty} e_r\phi_r(1)\exp[-\lambda_r{}^2\rho\alpha(y-x)]\right\}f'(y)dy \quad (10)$$

Observe that the number $^5/_{12}$ and the summation over the even indices $2r$ were obtained by linearly combining the multipliers of f_2 and f_4. The very same result can be obtained by assuming that the plane of symmetry is insulated and then treating each half of the three-stream exchanger in the manner explained in [8]. Again, in the case considered by Gutfinger, et al., the following holds

$$-f_{2n-2} = f_{2n} = -f_{2n+2} = \ldots = f$$

The unknown function f is then governed by equation (10) in which the kernels and multipliers of $f(0)$ and $f(L)$ contain the number $^5/_{12}$ and the factor $^3/_4$ instead of $^{13}/_{12}$, and $^3/_8$ while the summations are over even indices. There are two unknown functions in the case of five streams, when the following holds

$$f_4 = -f_6 = f \qquad f_2 = -f_8 = g$$

The two coupled integral equations obtained by setting (9_2) and (9_4) will not be spelled out here.

Results and Conclusions

This analysis implicitly contains the solution for the entire temperature distribution in the exchanger. Hopefully, it also provides the tool for predicting the performance of such multistream heat exchangers. Its scope is general in the sense that equations (9_{2n}) set for $n = 1, 2, \ldots, n_{\max}$ govern the heat transfer

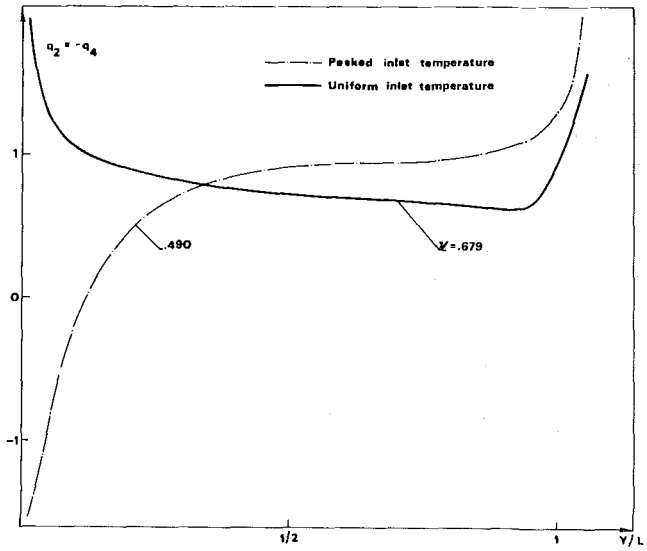

Fig. 2 Heat-flux distribution along the partitions for $n_{max} = 3$, $k_1 = k_3 = k_5 = 1$, $k_{2n+1}\tau_{2n}/k_{2n} = 1/10$, peaked and uniform inlet conditions

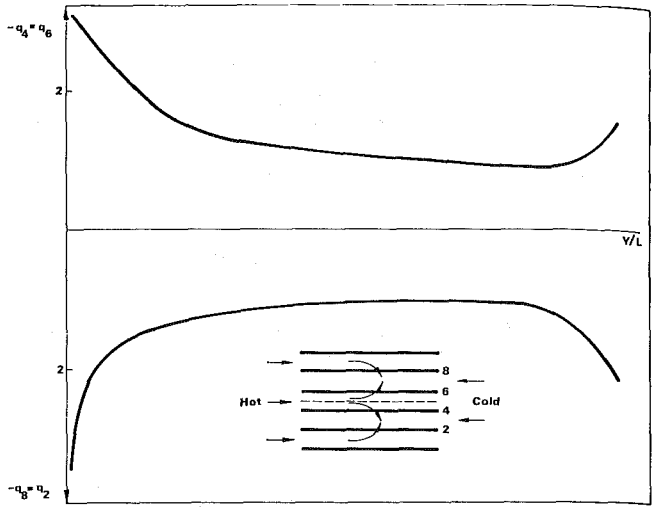

Fig. 3 Heat-flux distributions along the partitions for $n_{max} = 5$, $L = \rho = \alpha = 1$, $k_{2n+1} = 1$, $k_{2n+1}\tau_{2n}/k_{2n} = 1/10$

in an exchanger with any finite number of partitions n_{max}. Moreover, by varying the parameters ρ, α, L, k_{2n}/k_{2n+1}, τ_{2n+}, and so on, one can account for the influence of a variety of properties of fluids and design features. The effectiveness of the tool devised is demonstrated by treating and comparing results for exchangers with three, five, and many streams. The results presented should be treated as illustrative examples. This work is not meant to be a thorough and exhaustive study of heat exchangers with so many streams.

Since it is convenient to present the results in a normalized form, the temperature θ is so defined that at the inlets to one set of co-directional streams, $2n - 1$, $2n + 3$, and so on, it is identically zero. The "mixed-cup" average inlet temperature at every one of the other streams is taken to be unity. The quantity q_{2n} is defined as the heat flux through the partitions $2n$ when the width and conductivity of the phase $2n + 1$ are unity, in terms of a suitable system of physical dimensions. As explained, ν is the ratio between the sum of the integrated value of the flux over the areas of the partitions binding the hot stream(s) and the rate at which heat is convected across the inlet(s) to these.

It has been shown [8, 14, 15] that the heat transfer rate at the inlet to a cocurrent exchanger is very high. There, the partition or interface separates between the hot liquid and the coolant. Therefore, if it is assumed that these are maintained at two given distinct uniform inlet temperatures, the flux is very high. Although the author is unaware of such an attempt, the distribution in such exchangers could probably be represented in terms of a thermal boundary layer developing along the partition and a cold (or hot) core away from it, at the center of the streams. Thus for an interface of zero thickness, the flux has the familiar singular behavior at the leading edge, but if the partition has resistance, then the flux is large but finite.

In the countercurrent exchangers under discussion, the situation is similar, see Figs. 2 and 3. Again, at the end points the partition separates between the coolant (or hot liquid) that enters the exchanger and the somewhat warmer (or cooler) out-flowing liquid. However, in a countercurrent exchanger, only on one side of the partition is the temperature prescribed, while the out-flowing liquid is affected by the environments prevailing inside the exchanger, and therefore the flux profile is less peaked. On the other hand, there is a high transfer rate at both ends of a countercurrent exchanger. This explains why, in general, it is more effective than a cocurrent device of similar dimensions and other features.

The chain dotted curve in Fig. 2 represents the flux in a three-stream exchanger when at the inlet to the central hot stream the temperature is given by $\theta_3(0, \eta) = {}^{16}/_{11}$ $|\eta| < 1/2$; $\theta_3(0, \eta) = 0$ $|\eta| > 1/2$. Note that although its mixed-cup average is unity, the inlet temperature right at the partitions is zero. However, the coolant in streams one and five on the other sides of the partitions has undergone some heating. Hence the flux is locally negative, i.e., heat is transferred from the coolant into the hot stream. Observe also that with such inlet profile and resulting negative flux, the value of ν is 25 percent lower than that obtained for an identical exchanger with uniform hot and cold inlet temperatures. It was possible to detect this, artificially introduced but nevertheless quantitatively significant, disparity because in this analysis transverse variations were accounted for. Judging by the resulting possible variations in ν, it seems that the effort involved in this refinement was worth while.

In studying the influence of various parameters on the performance factor ν, it is convenient to change one parameter at a time. The other parameters are kept at the standard values $\rho = \alpha = L = k_{2n+1}/k_{2n-1} = 1$, $\tau_{2n+1}k_{2n+1}/k_{2n} = 1/10$. The choice of the former reference value is rather obvious. The latter reference value was chosen because when the partition's normalized resistance is $1/10$ or smaller, its effect is essentially insignificant. To be specific, a tenfold reduction in the resistance gives rise to about a 10 percent increase in ν [8].

Although the upper limit of ν is always unity, in order to reach this limit one must increase indefinitely either the length of the exchanger or the conductivity of the coolant or its heat capacity flow rate. The dependence of the effectiveness of exchangers on these design parameters is shown in Figs. 4, 5, and 6. In these, a comparison is drawn between three- and many-stream exchangers. To calculate these results, use was made of the periodicity of the distribution in a multichamber exchanger and the symmetry with respect to the mid-plane of stream three for $n_{max} = 3$. Note that the curves for $n_{max} = 3$ are always higher than those for which $n_{max} = \infty$. This implies that a three-stream exchanger of given length, width ratio, and ratio of conductivities is more efficient than a many-stream exchanger of similar features. This is understandable. A three-stream exchanger has twice as much coolant for a given amount of heat supplied (as defined in the foregoing).

The rise of ν with L and the ratio of conductivities is understandable. Less expected is the relative insensitivity of ν to variation in ρ when $\alpha\rho$ is constant. (The product $\alpha\rho$ can be identified as the ratio between the Graetz numbers for the hot and

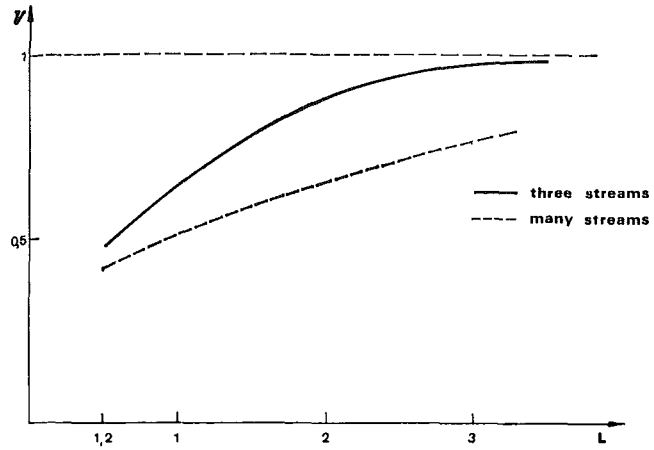

Fig. 4 ν as a function of the slenderness ratio $\rho = \alpha = 1$, $k_{2m+1}r_{2n}/k_{2n} = 1/10$

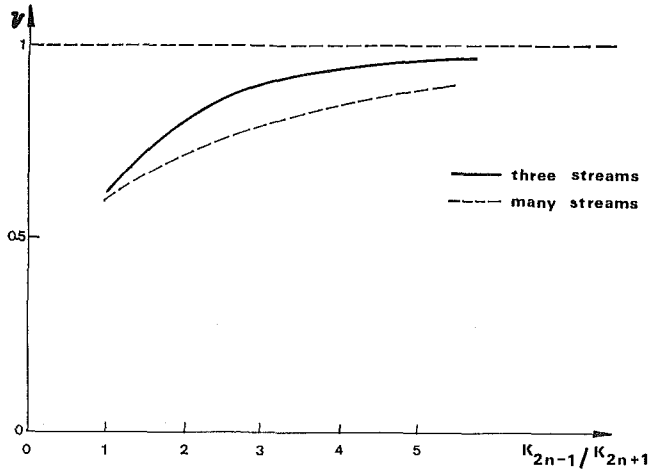

Fig. 5 ν as a function of ratio of conductivities $L = \alpha = \rho = k_{2n+1}r_{2n}/k_{2n} = 1/10$

cold streams.) The curves in Fig. 6 imply that this is a controlling parameter. Indeed, for constant $\alpha\rho$, a change in width ratio from one to two corresponds to a fourfold increase in the ratio between the volumetric flow rates. The resulting changes in ν are much less impressive.

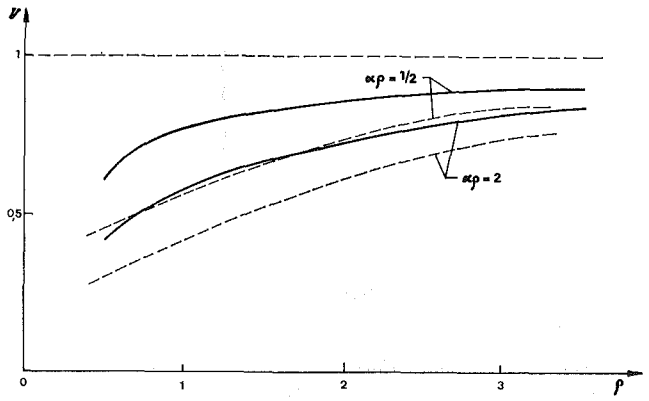

Fig. 6 ν as a function of width ratio $L = 1$, $k_{2n+1}r_{2n}/k_{2n} = 1/10$

Acknowledgment

The results contained in this work were skilfully computed by Shmuel Golda, student at the Technion.

References

1 Taitel, Y., Bentwich, M., and Tamir, A., "Effects of Upstream and Downstream Boundary Conditions on Heat (Mass) Transfer With Axial Diffusion," *International Journal of Heat and Mass Transfer*, Vol. 16, 1973, pp. 359-369.

2 Davies, E. J., and Gill, W. H., "The Effects of Axial Conduction in the Wall on Heat Transfer With Laminar Flow," *International Journal of Heat and Mass Transfer*, Vol. 13, 1970, pp. 459–470.

3 Nunge, R. J., and Gill, W. N., "Analysis of Heat or Mass Transfer in Some Countercurrent Flows," *International Journal of Heat and Mass Transfer*, Vol. 8, 1965, pp. 876–886.

4 Nunge, R. K., and Gill, W. N., "An Analytical Study of Laminar Counterflow Heat Exchangers," *AIChE Journal*, Vol. 12, 1966, pp. 279–289.

5 Stein, R. P., "Computational Procedures for Recent Analyses of Counterflow Heat Exchangers," *AIChE Journal*, Vol. 12, 1966, pp. 127–129.

6 Stein, R. P., in: *Advances in Heat Transfer*, Vol. 3, Irvine, T. F., and Hartnett, J. P., eds., Academic, New York, N. Y., 1966, pp. 101–174.

7 Bentwich, M., "On the Heat Transfer in Two Phase Cocurrent and Countercurrent Flows," *Proceedings of the Second Canadian Congress of Applied Mechanics*, 1969, pp. 231–232.

8 Bentwich, M., "Cocurrent and Countercurrent Parabolic Flow Heat Exchangers," *Israel J. Tech.*, Vol. 8, 1970, pp. 197–207.

9 Blanco, J. A., and Gill, W. N., "Analysis of Multistream Turbulent Forced Convection Systems," *Chem. Eng. Prog. Sym. Series*, Vol. 63, 1967, pp. 66–79.

10 Gutfinger, C., Isenberg, J., and Zeitlin, M. A., "Heat Transfer to Non-Newtonian Fluids in Countercurrent Plate Heat Exchangers," *Israel J. Tech.*, Vol. 8, 1970, pp. 225–237.

11 Wolf, J., "General Solution of the Equations of Parallel-Flow, Multi-Channel Heat Exchangers," *International Journal of Heat and Mass Transfer*, Vol. 7, 1964, pp. 901–919.

12 Aulds, D. D., and Barron, R. F., "Three-Fluid Heat Exchanger Effectiveness," *International Journal of Heat and Mass Transfer*, Vol. 10, 1967, pp. 1457–1462.

13 Chato, J. C., Laverman, R. J., and Shah, J. M., "Analysis of Parallel Flow, Multistream Heat Exchangers," *International Journal of Heat and Mass Transfer*, Vol. 14, 1971, pp. 1691–1703.

14 Bentwich, M., and Sideman, S., "Temperature Distribution and Heat Transfer in an Annular Two-Phase (Liquid–Liquid) Flow," *Can. J. Chem.*, Vol. 42, 1964, pp. 9–14 (correction, Vol. 43, 1965, p. 92).

15 Bentwich, M., and Sideman, S., "Temperature Distribution in Cocurrent Two-Phase (Liquid–Liquid) Laminar Flow on Inclined Surfaces," JOURNAL OF HEAT TRANSFER, TRANS. ASME, Series C, Vol. 86, No. 4, Nov. 1964, pp. 476–480.

B. COX
Nuclear Division,
Union Carbide Corp.,
P. O. Box P,
Oak Ridge, Tenn. Assoc. Mem. ASME

P. A. JALLOUK
Development Engineer,
Oak Ridge Gaseous Plant,[1]
Oak Ridge, Tenn. Assoc. Mem. ASME

Methods for Evaluating the Performances of Compact Heat Transfer Surfaces

Methods are presented for evaluating the performances of compact surfaces based on their simultaneous heat transfer rates and pumping power expenditures. Calculations of approximate total costs and volume requirements for a heat exchanger are simplified with the aid of performance curves based on a unit of heat transfer surface area and a unit of exchanger volume. In certain cases, the minimum cost surface can be determined from a single plot and requires no specific cost information. Basic design data are presented for three plate-fin surfaces, each one having a different degree of heat transfer promotion. The attractiveness of each type of surface is shown to depend on the particular design specifications.

Introduction

THE INCREASING NEED for compact heat exchangers has resulted in greater efforts by industry to manufacture and evaluate new types of heat transfer surfaces. For example, a significant part of the expansion program for the nation's gaseous diffusion plants involves the design of new and more efficient heat exchangers. Because of their high surface area densities and subsequent low volume requirements, compact plate and fin surfaces appeared attractive for these designs. A program was therefore initiated at the Oak Ridge Gaseous Diffusion Plant to test and evaluate several of these surfaces.

For most applications, the optimum heat exchanger is usually the one capable of transferring a specified quantity of heat at the lowest total cost. In process industries, the costs are determined primarily by capital costs for the heat exchanger surface area, plus operating costs to pump the heat transfer fluid. The required amount of surface area for a given heat load and the necessary pumping power are both dependent upon the fluid velocity. This velocity may, in turn, be set by a predetermined heat exchanger frontal area. On the other hand, in aircraft or other mobile applications, the lowest total system cost might correspond to the minimum heat exchanger volume and/or weight. Thus a general design procedure often requires the simultaneous comparison of heat transfer, pumping power, and geometry for many different surfaces. Plots of heat transfer rates and pumping power expenditures versus the exchanger face mass velocity can simplify the comparison procedure in many instances.

Part of the problem in heat exchanger design is that there exist no universal criteria to make even the selection of the best surface an easy task. Many final heat exchanger designs are the result of parametric studies in which total cost is plotted versus different parameters such as exchanger depth or pressure drop. The minimum in each cost curve determines the design value for one parameter. This procedure may be required for many surfaces. Characterizing surface performance with as few parameters as possible could simplify the design procedure.

This paper describes methods for selecting an appropriate surface by plotting only a few parameters. The paper also illustrates the trends that the degree of surface enhancement has on performance, hence on a final design selection. For this latter consideration, basic design data are presented for three types of plate-fin, compact heat exchangers. One of the exchangers had a uniquely enhanced surface with serrated fins. The other two surfaces had straight rectangular fins and offset rectangular fins. The three surfaces were different enough so that the effects of enhancement are well illustrated by comparing their performances.

Experimental Apparatus and Results

The experimental apparatus and procedure are described in detail in reference [1].[2] Fig. 1 shows the major components of the heat exchanger test facility. The system consists of an air loop and a water loop connected to the two sides of the heat exchanger core sample.

Flow was induced through the air loop by a radial compressor. Air flow to the heat exchanger was controlled with butterfly valves located in the main conduit and in the bypass line. Temperatures could be maintained at any desired level between room temperature and 300 F. High temperatures were attained by

[1] Based on work performed at the Oak Ridge Gaseous Diffusion Plant operated by Union Carbide Corporation, Nuclear Division, for the United States Atomic Energy Commission.

Contributed by the Heat Transfer Division and presented at the Winter Annual Meeting, New York, N. Y., November 26–30, 1972, of THE AMERICAN SOCIETY OF MECHANICAL ENGINEERS. Manuscript received by the Heat Transfer Division, August 18, 1972; revised manuscript received June 25, 1973. Paper No. 72-WA/HT-5 6

[2] Numbers in brackets designate References at end of paper.

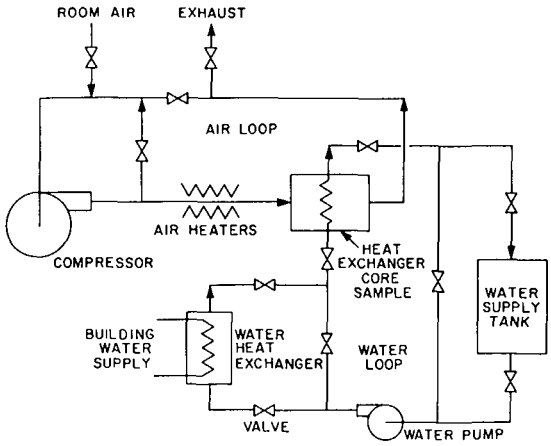

Fig. 1 Diagram of the experimental facility for testing compact heat exchangers

using air heaters located upstream of the core sample. Low temperatures were obtained by adding ambient air to the system. Frontal areas of the core samples averaged 1.5 sq ft. Screens in the upstream duct smoothed out velocity and temperature variations. The air flow rates were measured with a calibrated flow tube.

A centrifugal pump forced water from a storage tank through the core sample. Water traversed the core in one pass, cross-flow to the air stream. Water temperatures were controlled by a water to water heat exchanger. Flow to the core sample was regulated by the gate valves indicated in Fig. 1. An orifice plate and differential pressure cell were used to determine flow rates. Gas-side adiabatic friction factor data were taken with no water flow.

Grids of chromel-alumel thermocouples were placed at the inlets and outlets of the heat exchanger core samples on both the air and water sides. Each thermocouple was connected through an ice reference junction to an integrating digital voltmeter with a paper tape printout. Air static pressure drops were measured with a micromanometer.

Geometrical quantities for the three plate-fin surfaces are given in Appendix Table 1. Surfaces 1 and 2 were brazed aluminum sandwiches. Surface 3 was an aluminum plate with integral, petal fins. The heat transfer and flow friction design data were reduced to the dimensionless form of Colburn j-factors and Fanning friction factors. Accuracy of the results is believed to be 4 percent in f and 6 percent in j. The results are plotted versus Reynolds number in Figs. 2, 3, and 4. A schematic of each surface is included with the appropriate figure. The absence of a j value at a Reynolds number where f is given indicates an adiabatic run. Since the friction factors from adiabatic and heat transfer runs are in good agreement, no significant temperature-dependent property effects are apparent.

Data Reduction Procedure

The following is a summary of equations used to obtain the curves in this study. A more detailed discussion can be found in reference [1].

1 Weighted fin efficiencies were determined using the relation:

$$\epsilon = 1 - (1 - \eta_f)A_f/A \tag{1}$$

2 Air properties were evaluated at the mean temperature. In the experimental system, this temperature could be approximated by

$$T_a = (T_{w,\text{in}} + T_{w,\text{out}})/2 + \overline{\Delta T} \tag{2}$$

Nomenclature

a = constant in equation (7), dimensionless
A = heat transfer area, sq ft
A_f = fin heat transfer area, sq ft
A_{face} = frontal area of exchanger, sq ft
A_{min} = minimum free-flow area, sq ft
b = constant in equation (4), dimensionless
C_p = gas specific heat at constant pressure, Btu/(lb$_m$ deg F)
D = hydraulic diameter, $4A_{\text{min}}L/A$, ft
E = frictional power expenditure, ft lb$_f$/hr, fhp
E'' = standardized power expenditure per unit of area, fhp/sq ft
E''' = standardized power expenditure per unit of volume, fhp/cu ft
f = Fanning friction factor, dimensionless
g_c = conversion factor, 4.17×10^8 lb$_m$ft/(lb$_f$hr^2)
G = mass velocity based on A_{min}, lb$_m$/(hr sq ft)
G_{face} = mass velocity at heat exchanger face, σG, lb$_m$/(hr sq ft)
h = convection heat transfer coefficient, Btu/(hr sq ft deg F)
j = Colburn j factor, dimensionless
k = gas thermal conductivity, Btu/(hr ft deg F)
L = heat exchanger gas flow length, ft
m = constant in equation (7), dimensionless
n = constant in equation (4), dimensionless
p = constant in equation (5), $p = -2/3$ for this study
Pr = Prandtl number, $C_p\mu/k$, dimensionless
Q = heat transfer rate, Btu/hr
Q'' = standardized heat transfer rate per unit area, Btu/(hr sq ft deg F)
Q''' = standardized heat transfer rate per unit volume, Btu/(hr cu ft deg F)
Re = Reynolds number, GD/μ, dimensionless
St = Stanton number, h/C_pG, dimensionless
T = temperature, deg F
V = gas velocity, ft/hr
β = surface area density on one side of heat exchanger, sq ft/cu ft
ΔP_{fric} = pressure drop of gas due to friction plus form drag, lb$_f$/sq ft
ΔT_{film} = temperature difference between wall and bulk gas, deg F
$\overline{\Delta T}$ = log mean temperature difference, deg F
ϵ = weighted fin efficiency, dimensionless
η_f = fin efficiency, dimensionless
η'' = surface area efficiency, dimensionless
η''' = volumetric efficiency, dimensionless
μ = gas viscosity, lb$_m$/(ft hr)
ρ = gas density, lb$_m$/(cu ft)
σ = ratio of free-flow area to frontal area on one side of heat exchanger, $A_{\text{min}}/A_{\text{face}}$, dimensionless

Subscripts

a = air or gas side
0 = reference surface
w = water side
1 = surface 1
2 = surface 2
3 = surface 3

3 Colburn j factors were defined by

$$j = \frac{h}{C_p G} \mathrm{Pr}^{2/3} \tag{3}$$

If experimental j factors are plotted versus Reynolds number, it is found that the data can be approximated by several equations of the form

$$j = b\mathrm{Re}^n, \tag{4}$$

or

$$\mathrm{St} = b\mathrm{Re}^n\mathrm{Pr}^p \tag{5}$$

where b and n are constants and $p = -2/3$ for this study.

4 Fanning friction factors were defined by the expression

$$f = \frac{\Delta P_{\mathrm{fric}}}{4\dfrac{L}{D}\dfrac{G^2}{2\rho g_c}} \tag{6}$$

If experimental f factors are plotted versus Reynolds number, it is found that the data can again be approximated by several equations of the form

$$f = a\mathrm{Re}^m \tag{7}$$

where a and m are constants.

5 Heat transfer rates per unit temperature difference were based on a unit of surface area and on a unit of volume:

$$Q'' = \frac{\epsilon k b \mathrm{Re}^{n+1}\mathrm{Pr}^{p+1}}{D} \tag{8}$$

$$Q''' = \frac{4\sigma\epsilon k b \mathrm{Re}^{n+1}\mathrm{Pr}^{p+1}}{D^2} \tag{9}$$

6 Pumping power required to overcome fluid flow friction was calculated using the following expressions:

$$E = \Delta P_{\mathrm{fric}} A_{\mathrm{min}} V, \tag{10}$$

$$E'' = \frac{\mu^3 a \mathrm{Re}^{m+3}}{2D^3\rho^2 g_c}, \tag{11}$$

$$E''' = \frac{2\sigma\mu^3 a\ \mathrm{Re}^{m+3}}{D^4\rho^2 g_c} \tag{12}$$

Equations (10), (11), and (12) represent total pumping power, pumping power per unit of surface area, and pumping power per unit of volume, respectively.

7 By equating the pumping powers of any surface to those of an arbitrarily chosen reference standard, the Reynolds numbers of the two surfaces can be related using equations (11) or (12). The ratios of their heat transfer rates at equal pumping powers are then expressed by

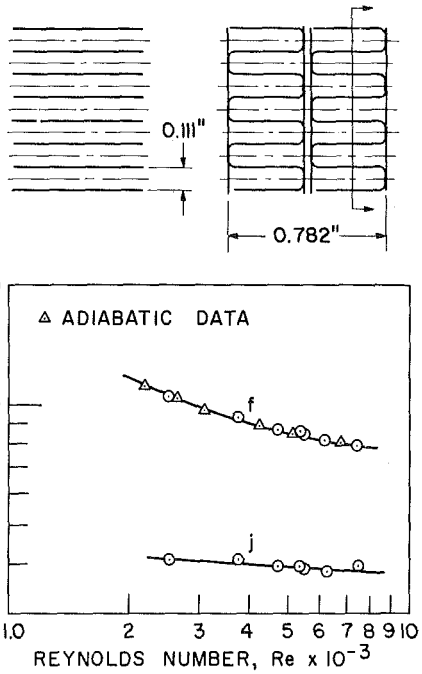

Fig. 3 Surface 2 heat transfer and friction characteristics

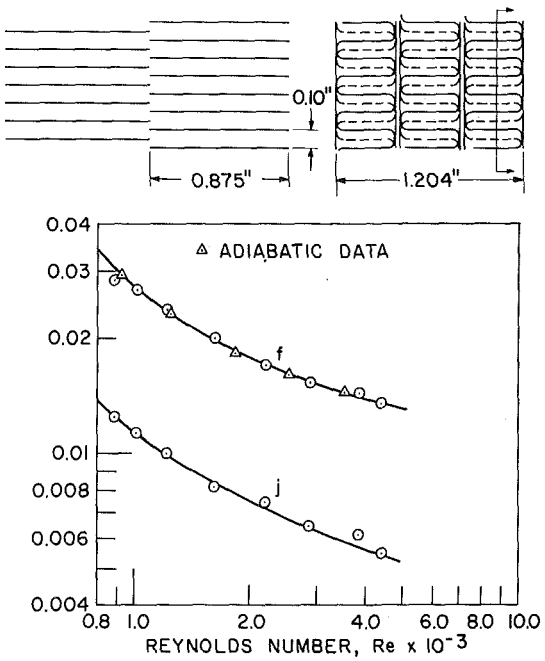

Fig. 2 Surface 1 heat transfer and friction characteristics

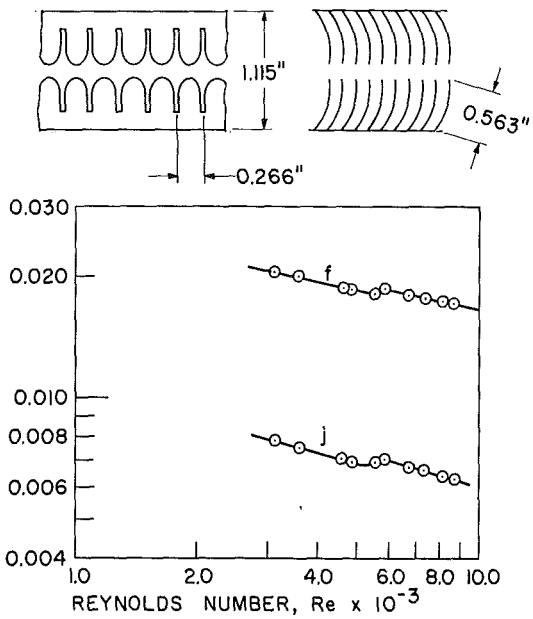

Fig. 4 Surface 3 heat transfer and friction characteristics

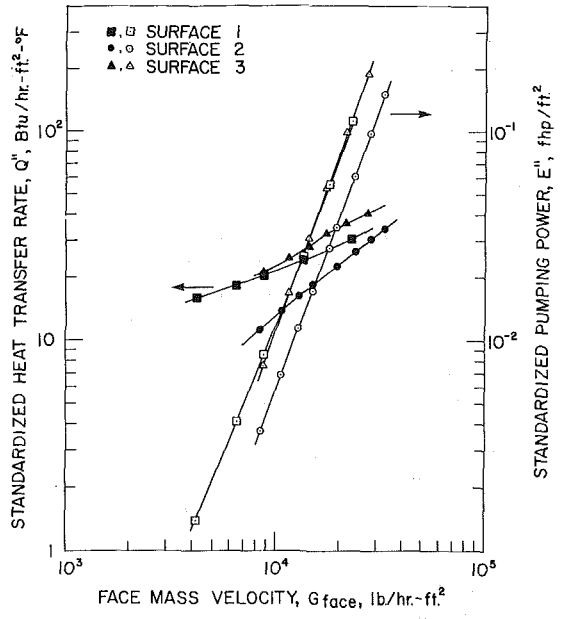

Fig. 5 Standardized heat transfer rates and pumping power versus face mass velocity (surface area basis)

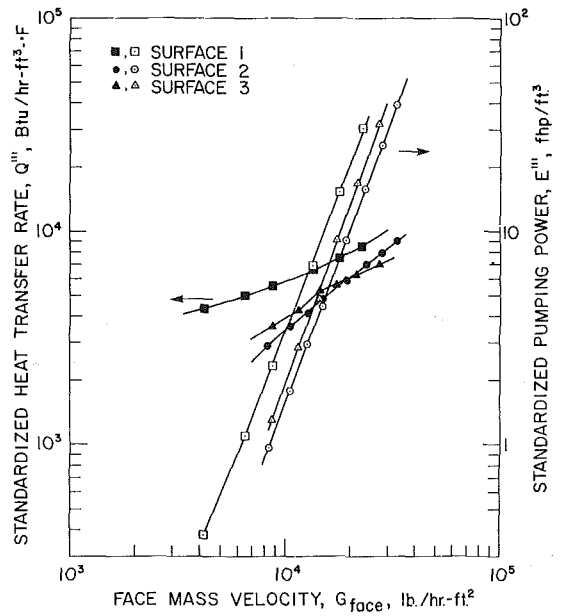

Fig. 6 Standardized heat transfer rates and pumping power versus face mass velocity (volume basis)

$$\eta'' = \frac{Q''}{Q_0''} = \frac{\epsilon}{\epsilon_0}\left(\frac{D}{D_0}\right)^{3\left(\frac{n+1}{m+3}\right)-1}\left(\frac{b}{b_0}\right)\left(\frac{a_0}{a}\right)^{\frac{n+1}{m+3}} \times \mathrm{Re}_0^{\frac{(m_0+3)(n+1)}{m+3}-(n_0+1)} \quad (13)$$

$$\eta''' = \frac{Q'''}{Q_0'''} = \frac{\epsilon}{\epsilon_0}\left(\frac{\sigma_0}{\sigma}\right)^{\left(\frac{n+1}{m+3}\right)-1}\left(\frac{D}{D_0}\right)^{4\left(\frac{n+1}{m+3}\right)-2} \times \left(\frac{b}{b_0}\right)\left(\frac{a_0}{a}\right)^{\frac{n+1}{m+3}} \mathrm{Re}_0^{\frac{(m_0+3((n+1)}{m+3}-(n_0+1)} \quad (14)$$

Equation (13) is the ratio of heat transfer rates for two surfaces with equal heat transfer areas, film temperature drops, and pumping powers. Equation (14) is the ratio of heat transfer rates for two surfaces with equal volumes, film temperature drops, and pumping powers.

It is not necessary that a, b, m, and n be constant over the whole range of Reynolds numbers for the foregoing equations to apply. In the present study, the f and j data could be adequately described by two equations of the form (4) and (7). However, more equations would probably be required if the Reynolds number ranges were extended.

Surface Comparisons

A method of surface comparison commonly employed [2] uses plots of standardized heat transfer coefficients versus standardized power expenditures.[3] This type of comparison can be based on either a unit of heat transfer surface area or a unit of heat exchanger volume [3]. Higher curves on these plots are usually indicative of high performance surfaces which should transfer heat well at relatively moderate power expenditures. A high heat transfer coefficient, however, does not always indicate a high heat transfer rate. The heat transfer rate is proportional to the heat transfer coefficient multiplied by the weighted fin efficiency defined in equation (1). Whereas the additional effects of secondary surfaces are neglected for many turbulence promoter concepts [4], they become very important in compact heat exchangers. In general, a high fin area density is desirable, but the larger the fin or the higher the heat transfer coefficient, the lower the fin efficiency. By multiplying the standardized heat transfer coefficients by the weighted fin efficiencies, a standardized heat transfer rate can be defined. When the thermophysical properties are evaluated at standard conditions, equations (8) and (9) repesent standardized heat transfer rates and equations (11) and (12) standardized pumping powers.

Reynolds number exponents for j and f, defined in equations (4) and (7), are generally slightly negative, as shown in Figs. 2, 3, and 4. Thus equations (8) and (9) suggest that Q'' and Q''' will increase as something less than the first power of the Reynolds number, Re. However, equations (11) and (12) indicate E'' and E''' will increase as about the third power of the Reynolds number. Because of this rapid rise in pumping power as the Reynolds number is increased, economic considerations will usually dictate designs at moderate flows. This corresponds to a moderate face mass velocity and perhaps a large frontal area heat exchanger. However, too large a frontal area might be incompatible with other plant hardware and eliminate many surfaces from consideration.

Figs. 5 and 6 show curves of standardized heat transfer rates and standardized pumping powers versus face mass velocities for surfaces 1, 2, and 3. Fig. 5 is based on a square foot of heat transfer surface area. Fig. 6 is based on a cubic foot of heat exchanger volume. The transformation from area to volume comparisons requires multiplication by the appropriate surface area density, β. Note the steep rise in pumping power and the only mild rise in heat transfer as the mass velocity increases. Also note that the pumping power slopes are all the same while the heat transfer slopes vary appreciably. This reflects the sensitivity of heat transfer to n and the insensitivity of pumping power to m as discussed in the foregoing.

Information necessary to make an approximate design and/or cost calculation is contained in Figs. 5 and 6. The approximations result from the simplified equations which neglect effects due to entrance regions, pump efficiency, fluid compressibility, and temperature variations. Also, the heat transfer rate is assumed to be controlled by the wall to bulk temperature difference only. This neglects the thermal resistances of the wall and of the fluid on the other side of the heat exchanger.

For a given face mass velocity and film temperature drop, the

[3] Standard conditions used in this study are dry air at 1 atm and 500 F.

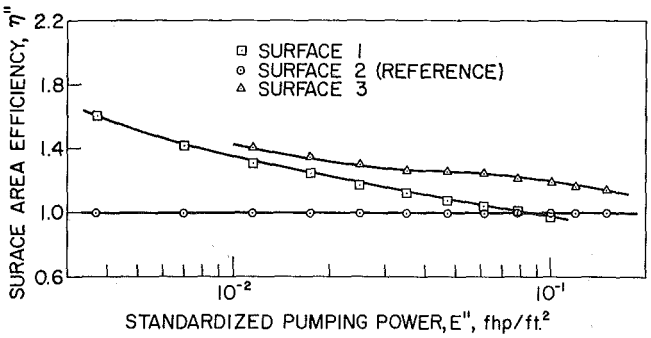

Fig. 7 Surface area eciffiency versus standardized pumping power expenditure

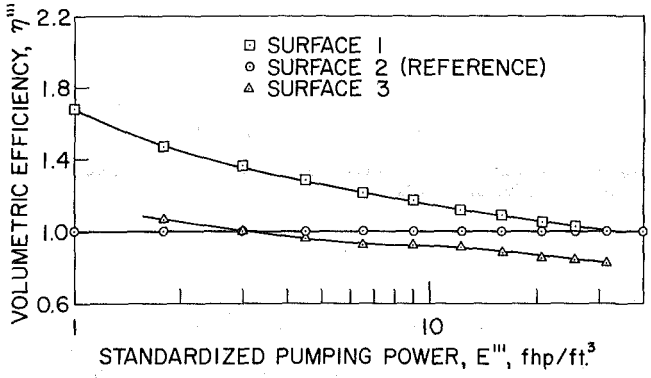

Fig. 8 Volumetric efficiency versus standardized pumping power expenditure

standardized heat transfer rate curves can be used to determine the required amount of surface area and volume needed to handle a specified heat load. Pumping power is then determined by multiplying the appropriate standardized power expenditure by area or volume. If the resulting power expenditure is unacceptable, the same curves could be used to estimate a new value for film temperature drop.

Surface and Volumetric Efficiency. Mitskevich [5] set forth a procedure for estimating the efficiency of heat transfer surfaces. He defined the efficiency of a surface as the ratio of its thermal energy transfer to the thermal energy transfer of a standard surface. Both surfaces were to have the same pumping power expenditure, the same fluid film temperature drop, and the same volume. Using conventional design parameters and the definition of weighted fin efficiency, this idea can be expanded to heat transferred at equal pumping power per unit surface area as well as equal pumping power per unit volume. The resulting efficiencies, defined by equations (13) and (14), are plotted versus pumping power in Figs. 7 and 8. (If the surfaces were to be compared with different working fluids, the resulting equations would contain additional thermophysical property terms [1, 5]. Also, ratios of pumping powers could be determined just as easily and plotted versus heat transfer rates.)

Figs. 7 and 8 represent ratios of the standardized heat transfer rates in Figs. 5 and 6 at equal values of E'' or E'''. Enhanced surfaces have a much higher rate of heat transfer for each unit of surface area, as indicated in Fig. 7. This would be expected since surface interruptions break up boundary layers and increase the heat transfer coefficient. Reference to Fig. 5 shows that equal pumping powers occur at smaller face mass velocities for the enhanced surfaces. Also, the cost of the enhanced surfaces might be higher, negating their heat transfer advantage.

Each curve in Fig. 7 can be considered to be a relative cost comparison between one surface and the reference surface. The higher the efficiency curve, the lower the relative cost of a heat exchanger using that surface. Since

$$\eta'' = \frac{Q''}{Q_0''} = \frac{Q}{Q_0}\frac{A_0}{A}$$

a value of $\eta'' > 1.0$ corresponds to a greater reference surface area requirement at equal heat loads. Since $E = E''A$, the reference would also have a higher pumping power cost. Assuming that both surfaces have the same capital costs per unit area, the total costs of an exchanger using a surface with $\eta'' > 1.0$ would have to be less than the total costs using the reference surface. The reverse would be true for $\eta'' < 1.0$. At $\eta'' = 1.0$, the heat exchanger costs are equal for both surfaces.

A minimum cost heat exchanger should correspond to the highest η'' and the lowest E'' that are available. However, physical limitations such as exchanger frontal area will probably determine the range of η'' using E'' versus G_{face} curves in Fig. 5.

Higher area densities are shown to be most advantageous in Fig. 8 for heat transfer at equal pumping powers per cubic foot of volume. A combination of high area density and surface enhancement makes surface 1 particularly attractive if the associated high frontal area can be tolerated. Note also that the inherent disadvantage of a relatively low surface-area density, surface 3, can be overcome at low enough E''', or high enough frontal area.

Generalized Comparisons. A parameter often of general interest to designers is the ratio of energy expended to energy transferred:

$$\frac{E''}{Q''} = \frac{E'''}{Q'''} = \frac{\mu^3 a \mathrm{Re}^{m-n+2}}{2D^2\rho^2 g_c \epsilon k b \mathrm{Pr}^{p+1}}$$

The standardized heat transfer rates are plotted against this parameter in Fig. 9. A direct comparison can now be made of the area and volume required by different surfaces at a given power expenditure.

Considering an application with no restriction on mass velocity, surface 3 will require the minimum amount of heat transfer area at all but the lowest powers. At low power levels surface 1 appears to become competitive. Similarly, surface 1 will give the smallest volume exchanger except at high levels of power expenditure where surface 2 is competitive.

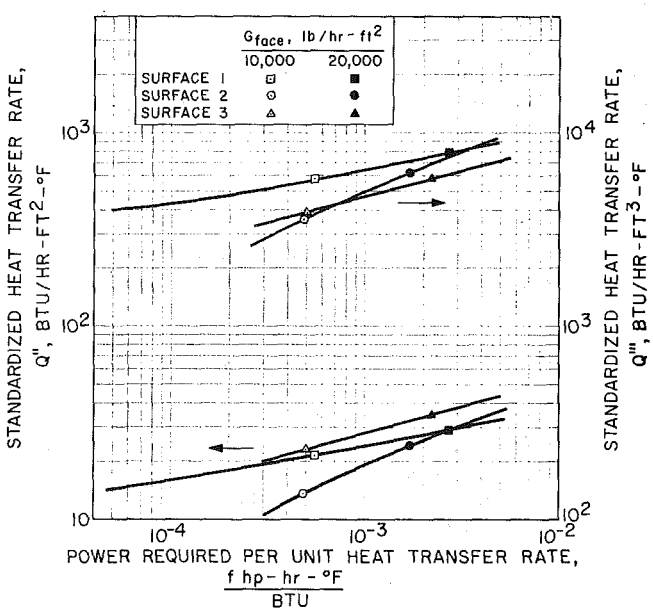

Fig. 9 Standardized heat transfer rates as a function of power expenditure

When the frontal area of the exchanger is restricted, the selection of a surface may be more difficult. Often, a judgment must be made based on the relative cost of power. The curves in Fig. 9 have indicated on them the points that correspond to two values of mass velocity. On an area basis, surface 3 appears to be the optimum surface at 10,000 lb/(hr sq ft). It is superior to surface 1 since it requires less power and less area at equal heat loads. Also, surface 3 requires approximately 50 percent less heat transfer area than surface 2 at the same power. However, at 20,000 lb/(hr sq ft) the choice between surface 2 and surface 3 must be based on the relative benefits of a 30 percent decrease in power versus a 30 percent increase in area.

On a volume basis, surface 1 is most attractive at 10,000 lb/(hr sq ft) because at comparable power levels it requires 50 percent less volume than surfaces 2 or 3. At 20,000 lb/(hr sq ft) the choice between surface 1 and surface 2 is again a judgment based on the merits of a smaller volume exchanger versus possible savings in pumping power. At this same mass velocity surface 2 is clearly superior to surface 3.

Comments on Comparisons. Another possible means of comparison would be on a per unit weight basis. This could be readily achieved from the per unit volume curves and the exchanger weight density. Also, the standardized heat transfer coefficient—power expenditure plots [2] give good general surface comparisons.

Each design problem will probably require an evaluation to determine the best method for comparing surfaces. The advantages of the foregoing methods, as illustrated by the given design data, are: (*a*) they give a quick comparison of performances for specific surfaces under consideration; and (*b*) performance trends as a function of surface enhancement become readily apparent.

Summary and Conclusions

1 Basic heat transfer and flow friction data are presented for three plate-fin, compact surfaces. Surface geometries are given in Table 1. Fanning friction factors and Colburn *j*-factors are plotted versus Reynolds number in Figs. 2, 3, and 4.

2 Surfaces can be compared by plotting their standardized heat transfer rates and pumping power expenditures versus the face mass velocity. The comparisons can be based on: (*a*) a square foot of surface heat transfer area, equations (8) and (11), and Fig. 5; or (*b*) a cubic foot of heat exchanger volume, equations (9) and (12), and Fig. 6.

Several of the advantages and disadvantages of surface enhancement have been illustrated. The results in Figs. 5 and 6 indicate the degree of heat transfer improvement possible along with the corresponding increase in pumping power penalty.

3 Ratios of heat transfer rates between any surface and a reference surface can often be used to determine the lowest cost heat exchanger without the necessity of specific cost information. Total costs are assumed to be the sum of surface area and pumping power costs. The heat transfer ratio expressed by equation (13) is plotted in Fig. 7.

4 A direct comparison of the area and volume required by different surfaces at a given ratio of power expenditure to heat transfer rate is illustrated in Fig. 9. The influence of mass velocity is also indicated in Fig. 9.

References

1 Cox, B., and Jallouk, P. A., "Experimental Determination of the Performance Characteristics of Eight Compact Heat Transfer Surfaces," K-1832, Union Carbide Corporation, Nuclear Division, Oak Ridge Gaseous Diffusion Plant, Oak Ridge, Tennessee, Dec. 1972.

2 Kays, W. M., and London, A. L., *Compact Heat Exchangers*, 2nd ed., McGraw-Hill, New York, 1964.

3 Ackerman, J. W., and Brunswold, A. R., "Heat Transfer and Draft Loss Performances of Extended Surface Tube Banks," JOURNAL OF HEAT TRANSFER, TRANS. ASME, Series C, Vol. 92, May 1970, pp. 215–220.

4 Spalding, D. B., and Lieberam, A., "The Selection of the Most Economical Turbulence Promotion in the Design of Heat Exchangers," *Windscale Trans.*, Vol. 244, 1964.

5 Mitskevich, A. K., "Method for Estimating the Efficiency of Convective Heat Transfer," *Heat Transfer-Soviet Research*, Vol. 1, No. 5, 1969, pp. 1–21.

APPENDIX

Table 1 Geometric quantities for three plate-fin surfaces

	Surface number		
	1	2	3
Fins per inch	10	9	8
Plate spacing, in.	1.204	0.782	1.115
Splitter plate thickness, in.	0.032	0.032	...
Fin length (flow dition), in.	0.875	8.75	0.266
Fin thickness, in.	0.012	0.008	0.017
Ratio fin area to total area	0.937	0.890	0.891
D, ft	0.01184	0.01342	0.02026
β, ft^2/ft^3	272.7	259.7	170.4
σ	0.81	0.87	0.86

J. M. GONZALEZ-SANTALO

R. T. LAHEY, JR.
Mem. ASME

Core Development—APED,
General Electric Co.,
San Jose, Calif.

An Exact Solution for Flow Transients in Two-Phase Systems by the Method of Characteristics

One of the important design considerations in modern water-cooled nuclear reactors is their thermal performance during hypothetical accident situations. However, an accurate analysis of the system thermal-hydraulics is required before the thermal margins can be appraised. In this paper, an analysis based on the method of characteristics has been developed by which the exact solution to flow decay transients in homogeneous two-phase systems can be obtained. The exact solution presented yields the system flow and quality at each point in space and time during an exponential flow decay transient. These parameters can then be combined with an appropriate CHF correlation to predict the occurrence of transient CHF.

Introduction

The occurrence of the critical heat flux (CHF) phenomenon during steady-state conditions has been the objective of extensive experimental investigations. In contrast, the occurrence of CHF during transient operating conditions has not been as thoroughly investigated. If CHF occurs at all in a nuclear reactor, it is most likely to occur during transient accident conditions. In particular, one of the most limiting hypothetical accidents in a boiling water nuclear reactor (BWR) is due to recirculation pump failure, in which the flow to the core is partially or totally interrupted.

Previous investigators [1, 2][1] have shown that the CHF correlations developed from steady-state data can be applied to the prediction of transient CHF, provided that the values of the flow parameters (i.e., flow and quality) are known at each point in space and time.

In this paper, the basic conservation equations for one-component, homogeneous, two-phase flow are presented and, with some simplifying assumptions listed in the next section, an exact solution is obtained for the important case of an exponential flow decay. This type of flow transient can be considered as being representative of the classical BWR "pump trip" type accident.

The partial differential equations that describe the system become ordinary differential equations in a Lagrangian frame of reference and can be integrated exactly for any flow transient of interest. As shown in Appendix A, this is a consequence of the equations forming a hyperbolic system in which one set of characteristics consists of the particle paths of the fluid. For more complicated cases, in which the equations cannot be directly integrated, the technique given in Appendix A is quite useful in setting up numerical solutions [5].

Analysis

The assumptions made in the subsequent analysis are:

1 The flow is homogeneous.
2 The system pressure is constant.
3 The flow conditions at the inlet of the test section (i.e., the mass flux and temperature) are specified as a function of time.
4 The heat flux is constant in both space and time.
5 Both phases are incompressible (i.e., constant thermodynamic properties).
6 The two phases are in thermodynamic equilibrium.

With these assumptions, the basic one-dimensional conservation equations can be written as:

$$\frac{\partial \rho}{\partial t} + V\frac{\partial \rho}{\partial Z} + \rho\frac{\partial V}{\partial Z} = 0 \text{ (continuity equation)} \qquad (1)$$

$$\rho\left[\frac{\partial h}{\partial t} + V\frac{\partial h}{\partial Z}\right] = q''\frac{P_H}{A_{x-s}} \text{ (energy equation)} \qquad (2)$$

The appropriate equation of state needed for solution is,

[1] Numbers in brackets designate References at end of paper.

Contributed by the Heat Transfer Division of The American Society of Mechanical Engineers and presented at the Winter Annual Meeting, New York, N. Y., November 26–30, 1972. Manuscript received by the Heat Transfer Division, August 17, 1972; revised manuscript received February 16, 1972. Paper No. 72-WA/HT-47.

For single phase: $\rho = \rho_f = \text{constant}$ (3)

For homogeneous, two-phase flow:

$$\frac{1}{\rho} = v_f + x v_{fg} \tag{4}$$

$$h = h_f + x h_{fg} \tag{5}$$

Since the equation of state takes two different forms depending on whether it applies to the single-phase liquid or the two-phase mixture, it is convenient to break the solution into two regions.

For the single-phase region the continuity equation (1) with the assumption of constant density reduces to

$$\frac{\partial V}{\partial Z} = 0 \tag{6}$$

The energy equation (2) can be written as

$$\frac{\partial h}{\partial t} + V \frac{\partial h}{\partial Z} = q'' \frac{P_H}{A_{x-s}\rho_f} \tag{7}$$

Equation (6) gives the velocity of the fluid in the single-phase section of the heater as

$$V = V_i(t) \tag{8}$$

The expression for the velocity given by equation (8) can be used to obtain the equation of the particle paths which, as shown in Appendix A, represent one set of characteristic lines in the time-position plane. The equation for the particle paths is

$$\frac{dZ}{dt} = V_i(t) \tag{9}$$

where $V_i(t)$, the inlet velocity to the heated section, is a specified function of time. Equation (9) can be integrated with initial conditions given by

$$Z(t = 0) = Z_0 \tag{10a}$$

$$t(Z = 0) = \tau \tag{10b}$$

Equation (7), when considered along the characteristic direction, can be written as an ordinary differential equation and be integrated as such. This can be shown by using the formal procedure outlined in Appendix A, or by substituting for V from equation (9) and using the definition of a total differential.[2] Hence, equation (7) becomes

$$\frac{Dh}{Dt} = q'' \frac{P_H}{A_{x-s}\rho_f} \tag{11}$$

which has initial conditions that can be given in terms of either Z_0 or τ as

[2] $y = f(t, Z)$; $\frac{dy}{dt} = \frac{\partial f}{\partial t} + \frac{\partial f}{\partial Z}\frac{dZ}{dt}$.

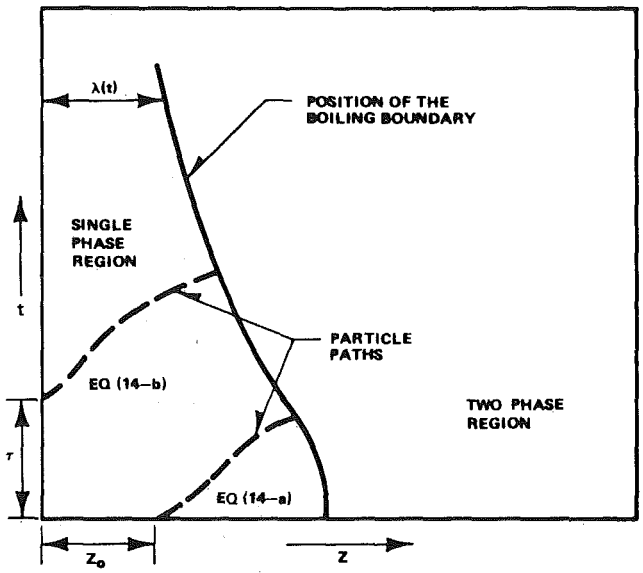

Fig. 1 Basic concepts involved in the transient solution

$$h(Z_0, 0) = h_0(Z) \tag{12a}$$

$$h(0, \tau) = h_i \tag{12b}$$

The solution of equation (11) with equations (12a) or (12b) yields an expression of the form

$$h = h(t, Z_0) \quad \text{(when equation (12}a\text{) is used)} \tag{13a}$$

$$h = h(t, \tau) \quad \text{(when equation (12}b\text{) is used)} \tag{13b}$$

Similarly, equation (9) can be solved to yield

$$Z = Z(t, Z_0) \quad \text{(when equation (10}a\text{) is used)} \tag{14a}$$

$$Z = Z(t, \tau) \quad \text{(when equation (10}b\text{) is used)} \tag{14b}$$

Combining equations (13a) and (14a) to eliminate Z_0, and (13b) and (14b) to eliminate τ, a solution for h in terms of time and position is obtained:

$$h = h(Z, t) \tag{15}$$

Equation (15) is only applicable for the single-phase region. By setting the enthalpy equal to the saturation enthalpy and solving for Z, the boiling boundary, $\lambda(t)$ (i.e., the boundary between the single-phase and two-phase region) is obtained.

Fig. 1 illustrates the concepts that have been introduced up to this point.

Nomenclature

A_{x-s} = flow area (ft²)
D = diameter (ft)
G = mass flux (lb_M/h-ft²)
h = fluid enthalpy (Btu/lb_M)
h_{fg} = latent heat of vaporization (Btu/lb_M)
L_H = heated length (ft)
p = pressure (psi)
P_H = heated perimeter (ft)
q'' = heat flux (Btu/h-ft²)
t = time (sec)
t_0 = the time at which a particle (not in boiling zone at $t = 0$) reaches the boiling boundary (sec)
V = velocity (ft/sec)
V_i = liquid inlet velocity (ft/sec)
v_f = specific volume of the liquid phase [ft³/lb]
v_{gf} = change in specific volume during evaporation [ft³/lb]
x = quality
Z = axial coordinate length (ft)
Δh_{SUB} = $h_f - h_{IN}$, inlet subcooling (Btu/lb_M)
λ = nonboiling length (ft)
$\Omega \triangleq \frac{q'' v_{fg} P_H}{h_{fg} A_{x-s}}$, characteristic reaction frequency (sec^{-1})
$\rho \triangleq (v_f + x v_{fg})^{-1}$, density ($lb_M$/ft³)
ν = the time required for a particle of fluid to lose its subcooling (sec)
τ = time at which a particle enters the test section

Subscripts

i = inlet conditions
o = initial conditions, $t = 0$ (except t_0)

The same general procedure outlined for the single-phase region is now applied to the two-phase region, using the appropriate equation of state. In this case, in order to reduce the number of variables involved, the equations are written in terms of the quality.

Combining equation (2) with the equations of state (4) and (5) to eliminate the variables ρ and h in favor of x,

$$\frac{\partial x}{\partial t} + V\frac{\partial x}{\partial Z} - q''\left[\frac{P_H v_{fg}}{A_{x-s}h_{fg}}\right]x = q''\frac{P_H v_f}{A_{x-s}h_{fg}} \tag{16}$$

Equation (16) can be written more compactly in terms of Zuber's [7] "characteristic reaction frequency, Ω,"

$$\frac{\partial x}{\partial t} + V\frac{\partial x}{\partial Z} - \Omega x = \Omega\frac{v_f}{v_{fg}} \tag{17}$$

where

$$\Omega \triangleq q''\frac{P_H v_{fg}}{A_{x-s}h_{fg}} \tag{18}$$

In accordance with the discussion in Appendix A, equation (17) can be written in a characteristic direction as an ordinary differential equation,

$$\frac{Dx}{Dt} = \Omega\left[x + \frac{v_f}{v_{fg}}\right] \tag{19}$$

and can be integrated with the following initial conditions:

$$x = x_0 \quad \text{at} \quad t = 0 \tag{20}$$

or,

$$x = 0 \quad \text{at} \quad t = t_0 \tag{21}$$

The integration will yield the solution $x = x(x_0, t)$ or $x = x(t_0, t)$, depending on the initial condition used.

The continuity equation (1), combined with the equation of state (4), yields

$$\frac{\partial V}{\partial Z} = \frac{v_{fg}}{(v_f + xv_{fg})}\left[\frac{\partial x}{\partial t} + V\frac{\partial x}{\partial Z}\right] = \frac{v_{fg}}{(v_f + xv_{fg})}\frac{Dx}{Dt} \tag{22}$$

Equation (22) is only applicable in the two-phase region [$Z > \lambda(t)$]. It can be integrated from the position where bulk boiling started, $\lambda(t)$, to any given axial location, Z. Using the boundary condition given in equation (8), equation (22) can be integrated along a constant time characteristic, yielding

$$V(Z, t) = V_i(t) + \int_{\lambda(t)}^{Z}\frac{v_{fg}}{(v_f + xv_{fg})}\left[\frac{Dx}{Dt}\right]dZ' \tag{23}$$

The velocity given in equation (23) can again be used to yield the equation for the particle path characteristics,

$$\frac{dZ}{dt} = \frac{G_i(t)}{\rho_f} + \int_{\lambda(t)}^{Z}\frac{v_{fg}}{(v_f + xv_{fg})}\left[\frac{Dx}{Dt}\right]dZ' \tag{24}$$

Equation (24) is a special case of the more general expression for nonconstant system pressure derived previously by Zuber [7] and Lahey, et al. [5].

Integration of equation (24) yields an expression for $Z = Z(Z_0, t)$ or $Z = Z(t_0, t)$ which, combined with the result of integrating equation (19), gives the desired solution:

$$x = x(Z, t)$$

and

$$V = V(Z, t)$$

In order to achieve an exact solution, equation (19) must be combined with equation (24) to eliminate the quality dependence in the integrand. Rearranging equation (19) one obtains

$$\frac{Dx}{Dt}\Big/(v_f + xv_{fg}) = \Omega/v_{fg} \tag{25}$$

Combining equations (24) and (25) yields

$$\frac{dZ}{dt} = \frac{G_i(t)}{\rho_f} + \int_{\lambda(t)}^{Z}\Omega dZ' \tag{26}$$

Under the present assumptions, for all $G_i(t)$ of practical significance, equations (19) and (26) are always integrable, which means that for *any* constant pressure flow transient it is possible to obtain an exact solution for the quality and velocity as a function of space and time along the heated length.

In the outline for the solution of the flow transients just presented, the momentum equation was not included in the conservation equations. In reference [3] the method of characteristics was applied to the complete set of conservation equations in which compressibility effects were included. It was shown that the characteristic lines in this case are three sets of curves: the particle paths, and two curves representing (in the space-time plane) the trajectories of the acoustic waves propagating in the test section. In this solution, as the propagation velocity of the acoustic waves is increased, the two acoustic characteristics collapse into a single trajectory that is identical to the "constant time" characteristics obtained in Appendix A. Thus assumptions 2 and 5, by which the momentum equation was left out of the system of equations solved, imply that the acoustic waves propagate through the test section instantaneously. This assumption will introduce serious errors only for very rapid flow transients where the duration of the transient is the same order as the time it takes the acoustic waves to propagate through the test section.

Exact Solution for a Constant Pressure, Exponential Flow Decay Transient

In this section the method presented in the foregoing will be applied to a specific case to yield the exact solution for quality and velocity as a function of space and time in the heater. The case to be analyzed is an exponential flow decay, in which the inlet mass flux is specified as:

$$G_i(t) = G_0 e^{-K_2 t} \qquad (\text{for } t > 0) \tag{27}$$

where K_2 is assumed to be real.[3] The complete solution is obtained by integrating the quality propagation equation (19) and the particle paths, equation (26), obtained in the previous section.

For constant Ω, equation (26) becomes

$$\frac{dZ}{dt} - \Omega[Z - \lambda(t)] = \frac{G_i(t)}{\rho_f} \tag{28}$$

Before equation (28) can be integrated, it is necessary to express the position of the boiling boundary as a function of time. This is done by integrating equation (11) to obtain

$$(h - h_i) = \frac{q''P_H}{\rho_f A_{x-s}}\Delta t \tag{29}$$

By definition, the boiling boundary is the position at which the liquid attains saturation enthalpy. Considering a particle that enters the test section at $t = 0$, a characteristic time ν can be defined such that at $t = \nu$ the fluid particle has lost its subcooling. Thus from equation (29),

$$\nu = \frac{\rho_f A_{x-s}}{q''P_H}\Delta h_{\text{SUB}} \tag{30}$$

Since, for a given heat flux and constant inlet and saturation enthalpies, equation (29) indicates a linear relation between the

[3] For a complex K_2 the solution presented here yields the response to a convergent or divergent oscillation. For an imaginary K_2, the solution represents the system response to an oscillating forcing function.

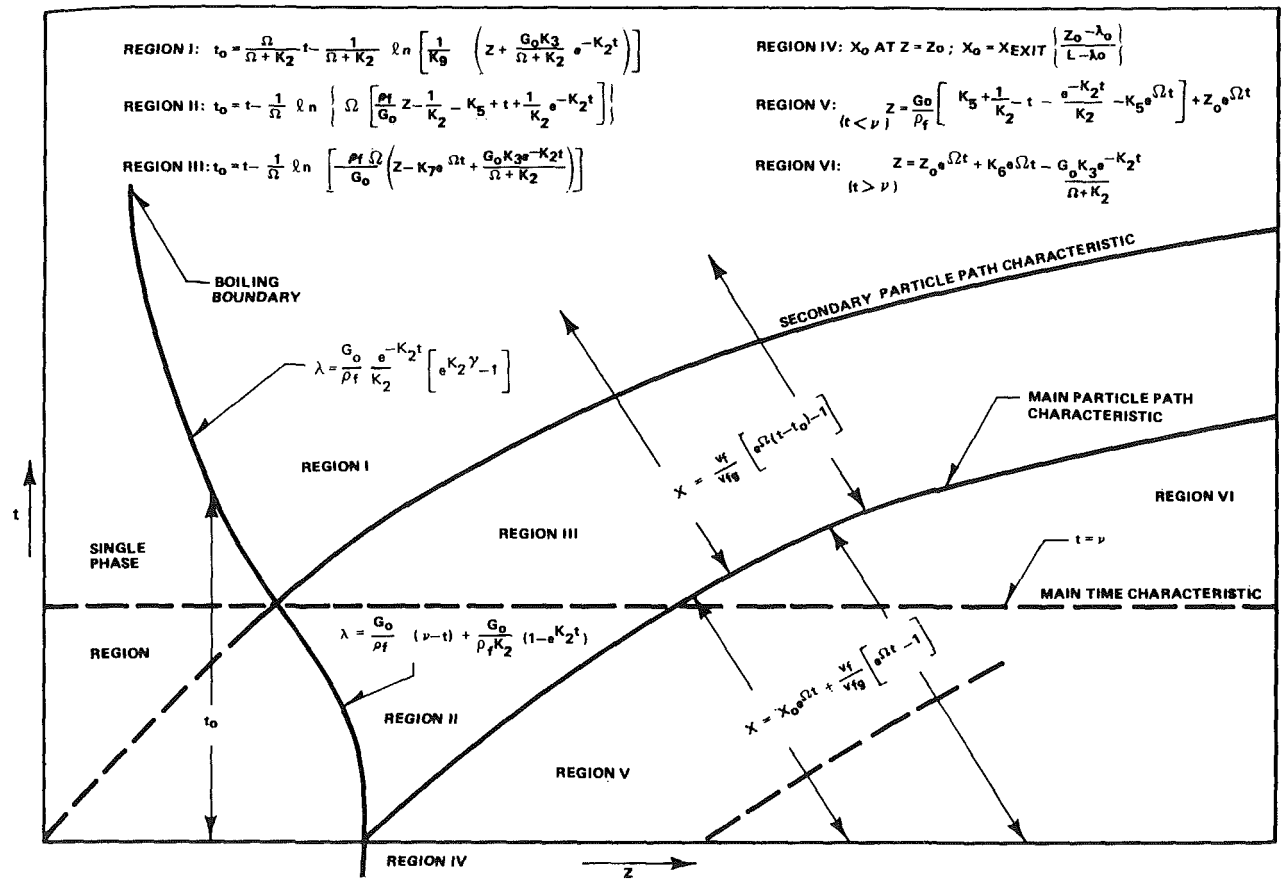

Fig. 2 Map showing the different regions of the exponential flow decay and the corresponding equations

fluid enthalpy and time, any fluid particle will have to remain in the heated section for a period of time equal to ν in order to lose its subcooling. This allows one to express the position of the boiling boundary by integrating the velocity in the single-phase region over a time interval ν. This was originally formulated by Wallis [8] as

$$\lambda(t) = \int_{t-\nu}^{t} \frac{G_i(t')}{\rho_f}\,dt' \tag{31}$$

$G_i(t')$ is given by equation (27) for $t' > 0$. For $t' < 0$, $G_i(t') = G_0$ (i.e., the steady-state mass flux before the beginning of the transient). Introducing the appropriate expression for the inlet mass-flux, one obtains

$$\lambda = \int_{t-\nu}^{0} \frac{G_0}{\rho_f}\,dt' + \int_{0}^{t} \frac{G_0}{\rho_f}\,e^{-K_2t'}dt'$$

$$\lambda = \frac{G_0}{\rho_f}(\nu - t) + \frac{G_0}{\rho_fK_2}(1 - e^{-K_2t}) \qquad (\text{for } t \le \nu) \tag{32}$$

and,

$$\lambda = \int_{t-\nu}^{t} \frac{G_0}{\rho_f}\,e^{-K_2t'}\,dt'$$

$$\lambda = \frac{G_0}{\rho_f}\frac{e^{-K_2t}}{K_2}\left[e^{K_2\nu} - 1\right] \qquad (\text{for } t \ge \nu) \tag{33}$$

Since there are two expressions for the boiling boundary, depending on the value of time considered, it is necessary to divide the integration into two regions. For $t < \nu$, equations (32), (19), and (28) should be used, while for $t > \nu$ applicable equations are (33), (19), and (28) The constants of integration are determined such that at $t = \nu$, the two sets of equations yield the same solution. For clarity of interpretation let us define the line (in the space-time plane) $t = \nu$ as the "main time characteristic." This characteristic is shown in Fig. 2.

Before integrating equations (19) and (28), the initial conditions necessary for determining the constants of integration will be considered. Each fluid particle can be identified by its state at the beginning of the transient.

1 At the beginning of the transient, the fluid particle may be within the two-phase region of the heater. In this case the appropriate initial conditions will be,

$$\text{at} \quad t = 0 \begin{cases} Z = Z_0 \\ x = x_0 \end{cases} \tag{34}$$

where x_0 can be easily determined as a function of Z, by a steady-state heat balance,

$$x_0 = \left[\frac{q''P_HZ_0}{G_0A_{x-s}} - (h_{sat} - h_i)\right]\frac{1}{h_{fg}} \tag{35}$$

2 Another set of fluid particles can be formed by considering all the particles that at the beginning of the transient ($t = 0$) were inside the heater, but still in the single-phase region. For these particles, the appropriate initial condition for the two-phase equations is the time, t_0, at which the particles entered the two-phase region, i.e.,

$$x = 0 \quad \text{at} \quad t = t_0 \tag{36}$$

From the definition of ν, and the fact that these particles were in the heated section, it is evident that for this set $t_0 \le \nu$. Fur-

thermore, the two sets of particles considered until now will be separated by the particle path of the fluid element that was at the boiling boundary at $t = 0$. This particle path, called the "main particle path characteristic," is also shown in Fig. 2.

3 The last set of fluid particles that has to be considered is formed by those that, at $t = 0$, had not yet entered the test section. The appropriate initial condition in this case is again given by equation (36).

As shown in Fig. 2, the particle path that separates the second and third sets of particles is called the "secondary particle path characteristic."

Referring again to Fig. 2, it is seen that the main time characteristic, the main particle path characteristic, and the secondary particle path characteristic, divide the two-phase domain of the Z-t plane into 6 regions. Furthermore, for each region there is a set of boundary conditions and expressions for the boiling boundary that are applicable. The exact solutions for each of these regions will now be obtained.

Region IV. This region corresponds to the steady-state conditions prior to the transient. The mass flux is the equal to the inlet flux, $G = G_0$, and the quality is given by a heat balance in equation (35).

Region V. This region is composed of the particles that at the beginning of the transient were in the two-phase region, and is bounded by the characteristic $t = \nu$. Consequently, the applicable initial conditions are those given by equation (34), where x_0 is obtained from the heat balance (35). The corresponding equation for the boiling boundary is equation (32).

Integrating equation (19) with the initial conditions (34) one obtains

$$x = x_0 e^{\Omega t} + \frac{v_f}{v_{fg}} [e^{\Omega t} - 1] \tag{37}$$

Substituting equation (32) into equation (28), the equation for the particle paths can be integrated. Eliminating the constant of integration with the initial condition, one obtains

$$Z = \frac{G_0}{\rho_f}\left[K_5 + \frac{1}{K_2} - t - \frac{e^{-K_2 t}}{K_2} - K_5 e^{\Omega t}\right] + Z_0 e^{\Omega t} \tag{38}$$

where K_5 was defined as:

$$K_5 \triangleq \left(\nu - \frac{1}{\Omega}\right) \tag{39}$$

For a given Z and t, equation (38) can be solved for Z_0. Using this Z_0 in equation (35), x_0 can be determined. Finally, substituting x_0 in equation (37), the quality is obtained as a function of Z and t. The mass flux can then be obtained by differentiating equation (38) with respect to time and multiplying it by the appropriate density.

Hence equations (37) and (38) represent the complete exact solution for Region V.

Region VI. This region is comprised of the same particles considered in Region V but considers only times greater than ν. The initial conditions for the quality equation are the same as before and consequently the quality is again given by equation (37).

The applicable expression for the boiling boundary is now equation (33), which can be substituted into equation (28). The constant that appears after the integration of equation (33) is evaluated by matching the solution with the result of equation (38) at $t = \nu$, which is the boundary between these two regions. The result of these manipulations is:

$$Z = Z_0 e^{\Omega t} + K_6 e^{\Omega t} - G_0 \frac{K_3}{(\Omega + K_2)} e^{-K_2 t} \tag{40}$$

where K_3 and K_6 have been defined as:

$$K_3 \triangleq \frac{1}{\rho_f}\left[1 - \frac{\Omega}{K_2}(e^{K_2 \nu} - 1)\right] \tag{41}$$

$$K_6 \triangleq e^{-\Omega \nu}\frac{G_0}{\rho_f}\left[\frac{1}{K_2} - \frac{1}{\Omega} - e^{-K_2 \nu}\left(\frac{1}{K_2} - \frac{\rho_f K_3}{(\Omega + K_2)}\right) - K_5 e^{\Omega \nu}\right] \tag{42}$$

The procedure to evaluate x and G as a function of time and position is identical to the one indicated for Region V. Hence, for Region VI, the complete solution consists of equations (40) and (37).

Region II. As can be seen in Fig. 2, this region covers the fluid particles that at $t = 0$ were in the heated section but within the subcooled region. However, it is only for times smaller than ν. The relevant equations for this region are again (19) and (28) with the initial condition (36); and equation (32) for the position of the boiling boundary.

Integrating equation (19) with the initial condition (36):

$$x = \frac{v_f}{v_{fg}} [e^{\Omega(t - t_0)} - 1] \tag{43}$$

Equation (28) can be integrated by substituting λ from equation (32). The constant of integration is evaluated by the setting ($Z = \lambda$ at $t = t_0$). Solving the resulting expression for t_0,

$$t_0 = t - \frac{1}{\Omega} \ln \left\{\Omega\left[\frac{\rho_f}{G_0} Z + t - \frac{1}{K_2} - K_5 + \frac{1}{K_2} e^{-K_2 t}\right]\right\} \tag{44}$$

With equation (44), t_0 can be evaluated for any Z and t and substituted into equation (43) to yield $x(Z, t)$. The velocity can be determined by substituting equation (32) into equation (28).

Region III. This region is comprised of the same fluid particles as Region II but considers times greater than ν. Since the initial conditions are the same as in Region II the equation for the quality is again equation (43).

In this case the applicable expression for the boiling boundary is equation (33). Equation (28) is integrated, by first substituting for λ, and then determining the constant of integration by equating these results and those of equation (44) at $t = \nu$. Solving the final equation for t_0, one obtains:

$$t_0 = t - \frac{1}{\Omega} \ln \left[\frac{\rho_f \Omega}{G_0}\left(Z - K_7 e^{\Omega t} + \frac{G_0 K_3}{(\Omega + K_2)} e^{-K_2 t}\right)\right] \tag{45}$$

where K_7 has been defined as:

$$K_7 \triangleq \frac{G_0}{\rho_f} e^{-\Omega \nu}\left[\frac{1}{K_2} - \frac{1}{\Omega} - \frac{e^{-K_2 \nu}}{K_2} + \frac{\rho_f K_3}{(\Omega + K_2)} e^{-K_2 \nu}\right] \tag{46}$$

Region I. For this region, the applicable initial conditions are again the same as Region III, i.e., equation (36), and the applicable expression for λ is equation (33). The equation for the quality is then again given by equation (43).

The integration of equation (28) is identical to that for Region II. The constant of integration, however, is evaluated by setting $Z = \lambda$ at $t = t_0$. This yields:

$$t_0 = \frac{\Omega}{(\Omega + K_2)} t - \frac{1}{(\Omega + K_2)} \ln \left[\frac{1}{K_9}\left(Z + \frac{G_0 K_3}{\Omega + K_2} e^{-K_2 t}\right)\right] \tag{47}$$

where K_9 has been defined as:

$$K_9 \triangleq \frac{G_0 e^{K_2 \nu}}{\rho_f (K_2 + \Omega)} \tag{48}$$

Region I represents the asymptotic response of the system whereas the other regions represent the startup transient. If K_2 is imaginary, only Region I exists and the present solution reduces to Wallis and Heasley's [8] result.

This completes the set of equations that yields the exact solution for the quality and velocity at any point in space and time during the transient being considered. When evaluating numerically, special care has to be taken in determining the re-

gion of interest. This can be done by either mapping the main characteristics beforehand, or by doing some trial calculations to identify the appropriate initial conditions and the applicable equations.

For purposes of illustration the equations presented in the foregoing were solved for a specific case. The results for quality as a function of time are shown in Fig. 3, for two given axial positions in the heater. The inlet and exit mass fluxes are shown as functions of time in Fig. 4. The most interesting feature of the solution is the time lag that exists between the inlet and exit mass flux. Lags are also noticed in the variation of quality with time, where the exit quality remains fairly constant for a period of time before it starts increasing.

These time lags are of importance in the analysis of accident transients in nuclear reactor cores. Once the local flow conditions are known as a function of time and position, appropriate steady-state CHF correlations can be used to appraise the thermal margins.

For the exponential flow decay case under consideration the location and time of CHF can be predicted quite well [5], though somewhat conservatively, using the exact solution. For the more general case, of combined arbitrary flow, pressure, and power transients, the analysis can be extended numerically [5].

Summary and Conclusions

The basic conservation equations for a homogeneous, two-phase, diabatic system have been arranged in a convenient form that allows their solution. Either numerical techniques available for hyperbolic systems, or, in the case of constant-pressure flow transients, direct integration can be used to yield the solution vectors.

The exact solution for the important case of an exponential flow decay is presented and it can be used to analyze the behavior of a system such as a boiling water nuclear reactor during a hypothetical pump trip accident.

The analysis presented here is considerably simpler to use than the slip flow analysis presented in reference [4], and the equations can be solved for a wider variety of cases. Moreover, for specific cases of commercial interest in which solutions can be obtained by both methods, the results are essentially identical and they agree favorably with experimental transient void fraction measurements [5].

In summary, a simplified analysis has been developed which allows us to readily appraise the transient response of a boiling channel for many situations of interest. An exact solution was obtained for an exponential flow decay and, following exactly the same procedure, a solution for any flow transient at constant system pressure can be obtained. The analysis can also be easily extended [5] to deal with more complicated flow, pressure, and power transients, if an appropriate numerical integration is used.

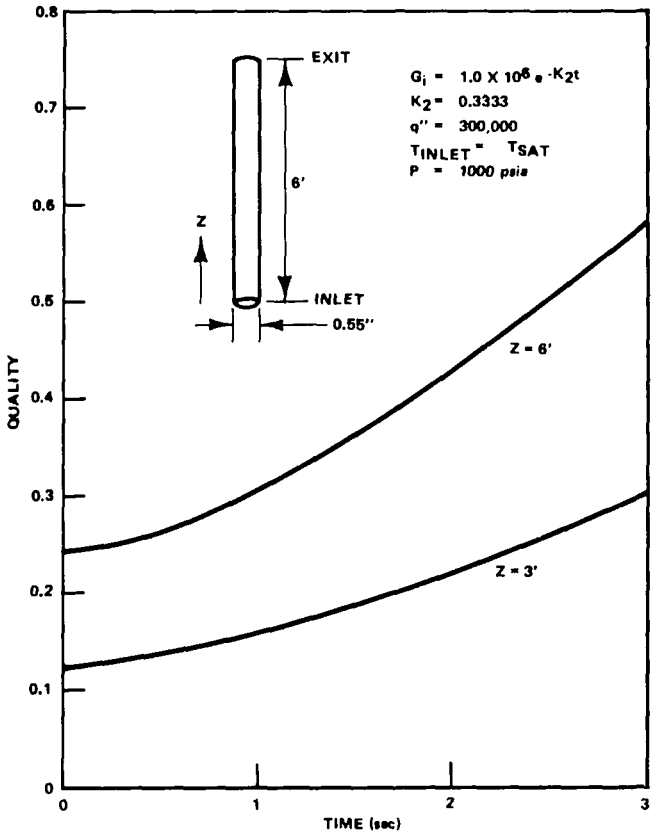

Fig. 3 Change of quality with time at different axial positions in the heater

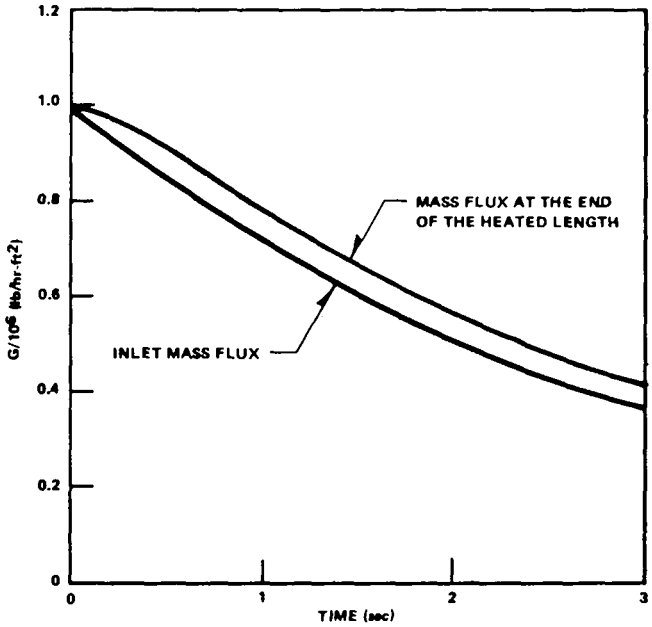

Fig. 4 Change of mass flux with time at different axial positions

Acknowledgments

The authors wish to acknowledge the financial support given this study under U. S. Atomic Energy Commission Contract AT(04-3)-189, Project Agreement No. 55.

References

1 Moxon, D., and Edwards, P. A., "Dry-Out During Flow and Pressure Transients," SEEWR-553, 1967.

2 Cermak, J. O., et al., "Experimental Investigation of the Departure From Nucleate Boiling in Rod Bundles During Pressure Transients," JOURNAL OF HEAT TRANSFER, TRANS. ASME, Series C, Vol. 92, No. 4, Nov. 1970, pp. 621-627.

3 Tong, L. S., and Weisman, J., *Thermal Analysis of Pressurized Water Reactors*, ANS Monograph, 1970.

4 Zuber, N., and Staub, F. W., "The Propagation and the Wave Form of the Vapor Volumetric Concentration in Boiling, Forced Convection System Under Oscillatory Conditions," *International Journal of Heat and Mass Transfer*, Vol. 9, 1966.

5 Lahey, R. T., Shiralkar, B. S., Gonzalez, J. M., and Schnebley, L. E., "The Analysis of Transient Critical Heat Flux," GEAP-13249, 1972.

6 Garabedian, P. R., *Partial Differential Equations*, John Wiley, New York, 1964.

7 Zuber, N., "Flow Excursions and Oscillations in Boiling, Two-Phase-Flow Systems With Heat Addition," Eindhoven Symposium on Two-Phase Flow Dynamics, EUR-4288, 1967.

8 Wallis, G. B., and Heasley, J. H., "Oscillations in Two-Phase Systems," JOURNAL OF HEAT TRANSFER, TRANS. ASME, Series C, Vol. 83, No. 3, Aug. 1961.

APPENDIX A

Classification of the Conservation Equations

In this appendix a general mathematical technique [6] will be employed to classify and transform the conservation equations into canonical form. It will be shown that they form a hyperbolic system, and the equations of the characteristics will be obtained. The system of partial differential equations then reduces to ordinary equations integrable along these characteristics. It is shown that, once the technique of the method of characteristics is used, the equations obtained are those that would result if the problem had been formulated from a Lagrangian point of view. It should be emphasized, however, that the technique presented here is general and can be applied to any hyperbolic system, where the characteristic directions may not be evident or where a Lagrangian formulation may not be applicable.

The energy equation (17) can be expressed as

$$\frac{\partial x}{\partial t} + V\frac{\partial x}{\partial Z} = -b_1(x, Z, t) \tag{A-1}$$

where

$$b_1 \triangleq \Omega x(Z, t) - \Omega v_f/v_{fg}$$

The two-phase continuity equation (22) is given by

$$v_{fg}\left[\frac{\partial x}{\partial t} + V\frac{\partial x}{\partial Z}\right] = (v_f + xv_{fg})\frac{\partial V}{\partial Z} \tag{A-2}$$

Combining equations (A-1) and (A-2) one obtains

$$\frac{\partial V}{\partial Z} = -b_2(x, Z, t) \tag{A-3}$$

where

$$b_2(x, Z, t) \triangleq \{v_{fg}b_1(x, Z, t)\}/(v_f + xv_{fg})$$

Equations (A-1) and (A-2) form the mathematical system under consideration. If equation (A-1) is divided through by the convection velocity V, we can write this system in matrix form as:

$$\begin{bmatrix}1 & 0\\ 0 & 1\end{bmatrix}\begin{pmatrix}\frac{\partial x}{\partial Z}\\ \frac{\partial V}{\partial Z}\end{pmatrix} + \begin{bmatrix}1/V & 0\\ 0 & 1\end{bmatrix}\begin{pmatrix}\frac{\partial x}{\partial t}\\ \frac{\partial V}{\partial t}\end{pmatrix} = -\begin{pmatrix}b_1/V\\ b_2\end{pmatrix}$$

which is in the standard form [6],

$$I\frac{\partial \mathbf{U}}{\partial Z} + F\frac{\partial \mathbf{U}}{\partial t} = -\mathbf{B} \tag{A-4}$$

Let us now rotate from the (Z, t) coordinate system to the characteristic (S, ν) coordinate system, where S is tangent to and ν is normal to the characteristics. One can then write the following identities:

$$\begin{aligned}\mathbf{U}_Z &= \mathbf{U}_\nu\nu_Z + \mathbf{U}_S S_Z\\ \mathbf{U}_t &= \mathbf{U}_\nu\nu_t + \mathbf{U}_S S_t\end{aligned} \tag{A-5}$$

where the subscript notation denotes a partial derivative.

In addition, geometric considerations (i.e., the definition of a cosine function) indicate that

$$S_Z = Z_S, \quad \text{and} \quad S_t = t_S \tag{A-6}$$

Also, since ν and S are orthogonal,

$$\frac{d\nu}{dS} = 0 = \nu_Z Z_S + \nu_t t_S$$

$$\therefore \nu_Z/\nu_t = -t_S/Z_S \tag{A-7}$$

Hence, combining equations (A-4), (A-5), (A-6), and (A-7):

$$\nu_t[-t_S/Z_S I + F]\mathbf{U}_\nu + [Z_S I + t_S F]\mathbf{U}_S = -\mathbf{B} \tag{A-8}$$

On a characteristic the normal derivatives, $\mathbf{U}_\nu$, are indeterminant; thus the matrix of the coefficients must vanish. Hence, finding the eigenvalues,

$$\lambda \triangleq t_S/Z_S = \frac{dt}{dZ},$$

$$|-\lambda I + F| = 0$$

thus,

$$\lambda(1/V - \lambda) = 0$$

hence the two eigenvalues are:

$$\begin{aligned}\lambda_1 &= 0\\ \lambda_2 &= \frac{dt}{dZ} = 1/V\end{aligned} \tag{A-9}$$

Since both the eigenvalues of this second-order system are real and distinct, equations (A-1) and (A-3) form a Hyperbolic System.

It is well known that for each distinct eigenvalue there is an associated eigenvector such that,

$$F^T\mathbf{h}(k) = \lambda_k\mathbf{h}(k) \tag{A-10}$$

or, in terms of inner product notation,

$$\mathbf{h}^{(k)}(-\lambda_k I + F) = 0$$

Thus, once these eigenvectors are obtained, their inner product with equation (A-8) will cause the term multiplying the normal derivative to vanish, yielding the canonical form of the system.

The eigenvectors $\mathbf{h}^{(1)}$ and $\mathbf{h}^{(2)}$ are obtained from equation (A-10) by using the eigenvalues tabulated in equation (A-9). The resulting eigenvectors are:

$$\mathbf{h}^{(1)} \triangleq \begin{pmatrix}0\\1\end{pmatrix} \text{ and, } \quad \mathbf{h}^{(2)} \triangleq \begin{pmatrix}1\\0\end{pmatrix} \tag{A-11}$$

Forming the inner product of $\mathbf{h}^{(1)}$ and equation (A-8) one obtains

$$\frac{dV}{dZ} = -b_2 \tag{A-12}$$

where $\lambda_1 = 0$ implies $dZ = dS$ and $dt = 0$ (i.e., t = constant).

Similarly, forming the inner product of $\mathbf{h}^{(2)}$ and equation (A-8) one obtains

$$\frac{\partial x}{\partial t} + V\frac{\partial x}{\partial Z} = -b_1 \tag{A-13}$$

or,

$$\frac{Dx}{Dt} = -b_1, \text{ along the characteristic } \frac{dZ}{dt} = V$$

where the identities in equation (A-6) have been used.

It can be noted that equations (A-13) and (A-12) are identical to equations (A-1) and (A-3), respectively. Thus it has been shown that the original system was already in canonical form. Moreover, it has been shown that the equation of one of the characteristics,

$$\frac{dZ}{dt} = V,$$

is also the particle path, in which V is the convection velocity of the Lagrangian observer.

J. H. LIENHARD
Professor. Mem. ASME

V. K. DHIR
Research Associate. Assoc. Mem. ASME

D. M. RIHERD
Whirlpool Fellow. Student Mem. ASME

Boiling and Phase Change Laboratory,
Mechanical Engineering Department,
University of Kentucky,
Lexington, Ky.

Peak Pool Boiling Heat-Flux Measurements on Finite Horizontal Flat Plates[1]

Experimental data obtained at both earth-normal and elevated gravity, in a variety of organic liquids and water, are used to verify the hydrodynamic theory for the peak pool boiling heat flux on flat plates. A modification of Zuber's formula, which gives a 14 percent higher peak heat flux, is verified as long as the flat plate is more than three Taylor wavelengths across. For smaller heaters, the hydrodynamic theory requires a wide variation in heat flux owing to discontinuities in the number of escaping jets. Data for smaller plates bear out this predicted variation with heat fluxes that range between 40 percent and 235 percent of Zuber's predicted value. Finally, a method is suggested for augmenting the peak heat flux on large heaters, and shown experimentally to be viable.

Introduction

THE AIM of this study is to provide experimental verification of predictions of the peak heat flux, q_{max}, on horizontal flat plate heaters of *finite* extent.

There has existed for over two decades, a hydrodynamic theory of q_{max} for the *infinite* horizontal flat plate. This theory was given in a fully rationalized form by Zuber [1][2] in 1958 on the basis of a concept and correlation originally suggested by Kutateladze [2] ten years earlier. The now well-known Zuber-Kutateladze expression is[3]

$$q_{max_Z} \equiv \frac{\pi}{24} \rho_g^{1/4} h_{fg} \sqrt[4]{g\sigma(\rho_f - \rho_g)} \tag{1}$$

where, for reasons that will be clear in a moment, we identify this prediction as a particular property of the boiled liquid and designate it as q_{max_Z}.

In a very recent paper [3] we reexamined the derivation of equation (1) in the light of more recent experimental and theoretical findings (notably [4]). We argued that the Helmholtz unstable disturbance, which made the escaping vapor jets collapse and initiated the peak heat flux transition, was not the critical Rayleigh wave in the jet. It is, instead, the Taylor unstable wavelength which is carried into the jet from the horizontal liquid-vapor interface. The resulting expression for the peak heat flux on an infinite flat plate, q_{max_F}, was 14 percent higher than Zuber's. Thus

$$\frac{q_{max_F}}{q_{max_Z}} = 1.14 \tag{2}$$

Equation (2) is a special case of the general sort of correlation that applies to finite heaters (see e.g., [4, 5, 6, and 7])

$$\frac{q_{max}}{q_{max_Z}} = f(L'); \quad L' \equiv L\sqrt{g(\rho_f - \rho_g)/\sigma} \tag{3}$$

where, for infinite heaters, the influence of any characteristic length, L, must disappear.

q_{max_F} for Finite Flat Plates

The problem of verifying equation (2) lies in the fact that data cannot be obtained on infinite flat plate heaters. Whether or not equation (2) has any utility will depend heavily on whether or not, and to what extent, finite plates approximate infinite plates.

Fig. 1 illustrates three kinds of flat plate heaters. Fig. 1(*a*) is the infinite plate thought-model. Fig. 1(*b*) is the logical approximation to the infinite plate. It contains a finite number of jets spaced (in accordance with the hydrodynamic theory) on the most susceptible Taylor wavelength, λ_d. It has vertical side walls located one-half a wavelength from the center line of the outer jets in the grid. We know of no experiments which reflect this configuration exactly. Only two sets of data in the literature approach it. The classical data of Cichelli and Bonilla [8] are for the correct configuration—a 9-1/2-cm-dia disk heater which formed the bottom of the cylindrical container for the boiled liquid. But many of their data must be eliminated because they were obtained on "dirty" heaters. Most of the remainder are for nominal fluids of extremely low purity—actually

[1] This work received support from NASA Grant NGR-18-001-035, under the cognizance of the Lewis Research Center.

[2] Numbers in brackets designate References at end of paper.

[3] Symbols not defined in the text are ones in common use. They are explained in the Nomenclature.

Contributed by the Heat Transfer Division and presented at the Winter Annual Meeting, Detroit, Mich., November 11–15, 1973, of THE AMERICAN SOCIETY OF MECHANICAL ENGINEERS. Manuscript received by the Heat Transfer Division, February 12, 1973. Paper No. 73-WA/HT-30.

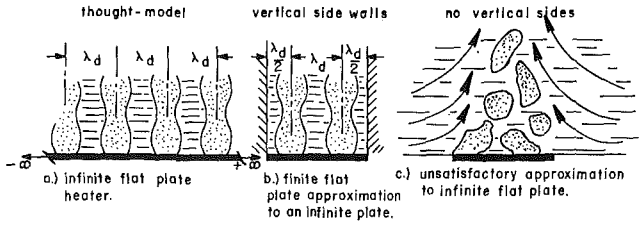

Fig. 1 Horizontal flat plate configurations, idealized and actual

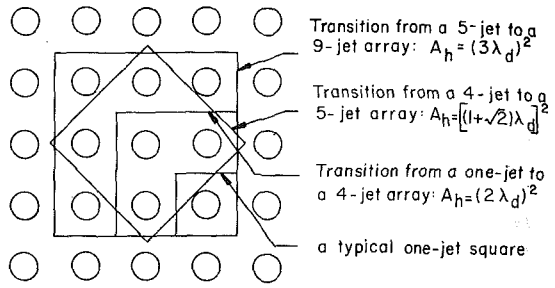

Fig. 2 Jet configurations on square heaters of various sizes

mixtures for which properties are not known and correlations cannot be applied. Only a few of their data for ethanol remain for use. Berenson [9] presented similar data for CCl_4 and n-pentane on 5 cm dia heaters that were subject to very close control of surface condition.

Fig. 1(c) shows another configuration for which there exist plenty of q_{max} data, none of which has much relation to the present "flat plate" configurations. This is the flat heater surrounded by a larger open bath of liquid. The peak heat flux in this configuration was shown in 1970 [10] to be strongly influenced by induced convection effects. These effects in turn required the inclusion of an additional parameter in equation (3), namely, the Borishanski number.

Since λ_d is on the order of two centimeters for most common liquids, a heater must be larger than most laboratory heaters before it includes "many" jets. If the heater area, A_H, does not correspond with an integral or large number of "cells" of area λ_d^2, then the heat flux will be determined by the actual number of jets on the plate, N_j. Thus

$$\frac{q_{max_{finite}}}{q_{max_Z}} = 1.14 \frac{N_j}{A_H/\lambda_d^2} \tag{4}$$

The problem of counting the number of jets on a finite plate is a little tricky. Fig. 2 shows how we would expect jets to be distributed on square plates of various sizes. If we suppose that no jet lies closer than $\lambda_d/4$ to the vertical side walls (except when $A_H < \lambda_d^2$), then transitions from 1 to 4 jets, from 4 to 5 jets, and from 5 to 9 jets will probably occur at $A_H = (2\lambda_d)^2$, $A_H = (1 + \sqrt{2})^2\lambda_d^2$, and $A_H = (3\lambda_d)^2$, respectively.

Proceding in this way and using equation (4), we can construct a sawtooth plot of q_{max} against heater size. This has been done in Fig. 3. Here we use the coordinates, q_{max}/q_{max_Z}, and heater width divided by λ_d (or $L'/2\pi\sqrt{3}$), as suggested by equation (3) where, for a plane interface,

$$\lambda_d = 2\pi\sqrt{3\sigma/g(\rho_f - \rho_g)}. \tag{5}$$

Curves consistent with equation (4) have been drawn in for N_j = 1, 4, 5, 9, ... For $N_j > 1$, only the portion below the line is strictly consistent with the model described in the foregoing. However, it is possible for the jets to locate themselves differently than shown in Fig. 2, particularly as N_j becomes larger. Thus we have arbitrarily extended each curve (for $N_j \geq 5$) to the left until the preceding curve is also above q_{max}/q_{max_Z}.

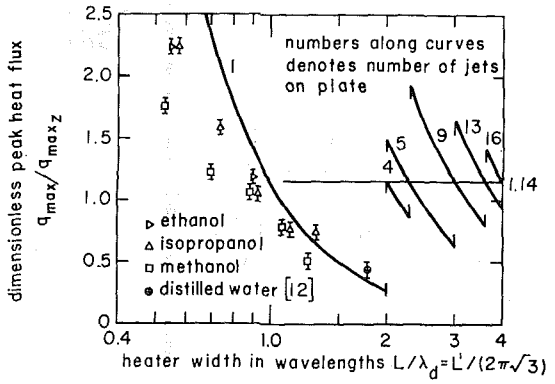

Fig. 3 Peak heat flux on a square finite flat plate with vertical side walls

It should be emphasized that only the curve for $N_j = 1$, and possibly for $N_j = 2$, have real theoretical validity. For the larger N_j's, not only are we unsure of the exact arrangement of jets, but minor variations of the true wavelength about λ_d can actually displace the lines. Thus while equation (4) is valid, the curves drawn on the right-hand side of Fig. 3 (and later in the paper, Fig. 9) should be taken as qualitative indications of behavior. That the curves are double-valued is also no serious objection. This implies simply that data might lie on one curve or the other.

The resulting curves deviate widely from $q_{max}/q_{max_Z} = 1.14$ on the left-hand side, and as L/λ_d is carried to larger and larger values, the deviations will become smaller and smaller. Thus equation (4) will reduce to equation (2) in the limit of large L'. Similar sets of curves can be built for heaters of other shapes. The use of semilogarithmic coordinates in Fig. 3 (and later in Fig. 9) is not implied by the theory, but is simply a convenience in presenting the material.

Experiments

We now need data with which to check equation (2), and its modification for small plates, equation (4). Two experiments

Nomenclature

A_H = area of heater

g, g_e = acceleration of gravity (subscript, e, denotes earth-normal gravity)

h_{fg} = latent heat of vaporization

L = a characteristic length (= width of a square heater or diameter of a circular heater, depending on context)

$L' = L\sqrt{g(\rho_f - \rho_g)/\sigma}$, a dimensionless heater size

N_j = number of escaping vapor jets on a heater of area, A_H

$q_{max}, q_{max_F}, q_{max_Z}$ = peak pool boiling heat flux. Subscript, F, denotes infinite flat plate value. Subscript, Z, denotes Zuber's prediction of q_{max}. q_{max_Z} is viewed as a characteristic of the boiled liquid in this study

λ_d = most susceptible Taylor unstable wavelength in a horizontal liquid-vapor interface

ρ_f, ρ_g = density of saturated liquid and vapor, respectively

σ = surface tension between a liquid and its vapor

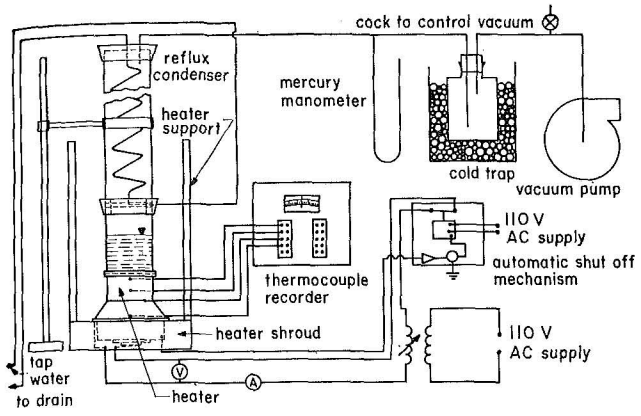

Fig. 4 Schematic diagram of stationary flat plate heater

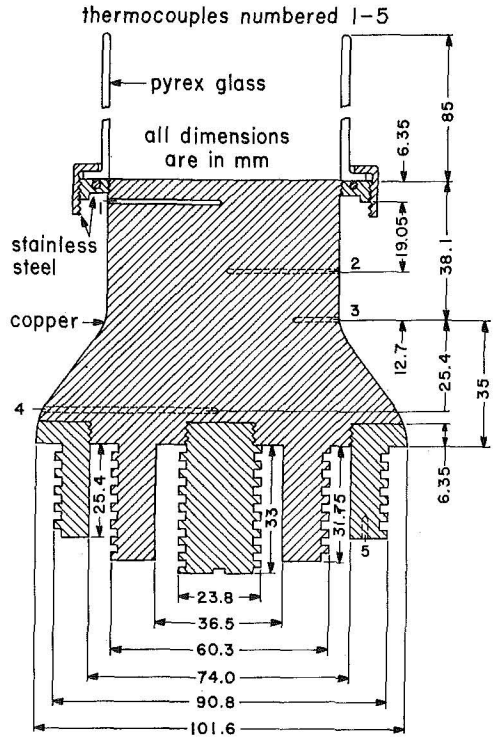

Fig. 5 Sectioned view of the flat plate heater

will be described, one applicable to the range of larger L/λ_d's and one applicable to the smaller L/λ_d's.

Large L/λ_d Experiments. To reach large L/λ_d values we decided not just to make L (in this case the diameter of a circular heater) very large, but also to do experiments in which λ_d was very small. This was done by operating in a centrifuge, since $\lambda_d \sim g^{-1/2}$.

A detailed description of the flat plate apparatus that we developed is given in reference [11], and we shall only describe its major features here. The apparatus consisted of a heater, a heater support, an emergency shut-off mechanism, and a reflux condenser. This entire assembly was designed to operate either at earth-normal gravity or to be installed in Centrifuge Facility of the Boiling and Phase-Change Laboratory at the University of Kentucky.[4] A schematic diagram of the apparatus is shown in Fig. 4.

The heater itself was made of pure copper with a circular bell-shaped configuration. It has a diameter of 6.35 cm at the boiling surface, 10.16 cm at the butt end, and a height of 10.8 cm. A pyrex glass cylinder allowing a liquid head of about 6 cm sits on the heater surface and is held in place by two stainless steel flanges. Stainless steel has a much lower thermal conductivity than copper, hence the flanges have a very small cooling effect on the edges of the boiling surface.

Fig. 5 shows a sectioned view of the heater. Its lower portion consists of three rings wound with 4 m of 1.62-mm-dia nichrome wire, capable of dissipating 6 kw of power. Five iron-constantan thermocouples are positioned as shown in the figure to monitor the temperature in various parts of the heater body. The top two thermocouples were used to determine the heat flux to the boiling surface. A third thermocouple was used for a counter-check on the heat flux calculations and a fourth thermocouple to show whether steady-state conditions are reached.

The thermocouple in the base monitored the temperature for an electronic emergency shut-off system. This system cut off the power supply after the peak heat flux was reached. A cut-off system was necessary because the transition to film boiling effectively insulated the surface and permitted the temperature in the copper heater to run away. The shut-off system is fairly complex and full details are given in reference [11].

The flat plate heater accommodated more than three wavelengths for the alcohols, and about two for water, at earth-normal gravity, while these numbers increased as $g^{1/2}$ at higher gravities. The following reagent grade liquids were used: acetone (CH_3COCH_3), benzene (C_6H_6), isopropanol ($CH_3CHOHCH_3$), methanol (CH_3OH), and distilled water.

Elevated gravity tests were performed with the help of the centrifuge facility. Details of the centrifuge design are given in reference [7], and Fig. 6(*a*) shows the centrifuge facility. When

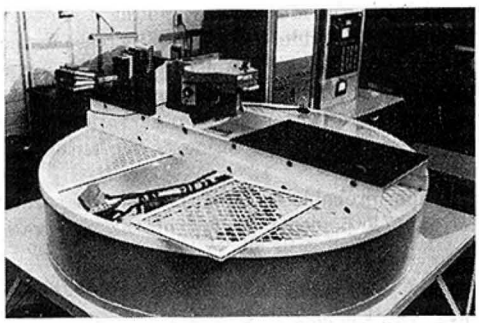

Fig. 6(*a*) Centrifuge facility—general view

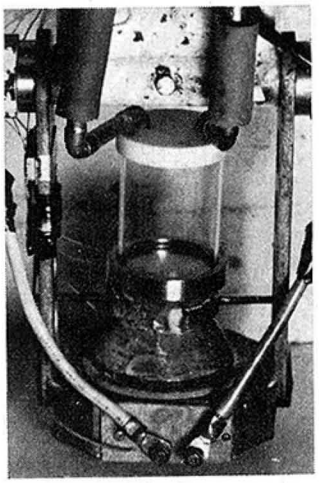

Fig. 6(*b*) Top view of flat-plate heater assembly installed at end of centrifuge arm

Fig. 6 Photographs of flat-plate apparatus and the centrifuge facility

[4] We are grateful to Mr. Eugene Davis for his contributions to the design of this heater.

the flat plate heater is mounted in the centrifuge, its boiling surface is 77.7 cm from the center of rotation.

Electrical connections to the centrifuge are made through slip rings attached to the drive shaft. Those include twelve circuits for power input, voltage measurement, and for thermocouples. The drive shaft also carries a tube which is connected to a vacuum pump through a rotary vacuum seal.

A strobe light is placed on a bracket attached to the stand supporting the centrifuge. It is triggered by a photoelectric pick-off which senses light reflected from a shiny metal piece attached to the centrifuge arm. Thus each revolution of the arm triggers the light and the heater appears to stand still so one can view the boiling process. Fig. 6(*b*) shows the flat plate heater assembly in position on the centrifuge arm.

Before each test, the boiling surface was polished with 220 grit size emery paper to remove any rust or carbon deposit formed during the previous observation. The surface was then cleaned with soap and warm water and rinsed with the test liquid. This was done to insure that there was no uncleanliness on the surface which might affect the wettability and affect the q_{max} data. Berenson's very careful experiments showed that, in this configuration, q_{max} is insensitive to surface conditions and that these precautions are more than ample.

The resistance heating wire was energized and the current was gradually increased in steps. At each step the current and voltage were noted and thermocouple observations were recorded and updated until steady state was reached. It usually took about 5 minutes to reach steady state after the current was increased to the next higher value.

Various regimes of nucleate boiling (e.g., the isolated bubble regime and the transition from single bubbles to slugs and columns) were easily discernible. The transition from nucleate to transitional boiling was identified by noting a slowdown of the boiling process and a sudden continuous increase in the thermocouple reading. The thermocouple reading kept on increasing for a while, even after the power was removed. In most cases, the power was cut off after visual observation of the boiling transition, rather than by triggering of the automatic shut-off mechanism.

The maximum probable error of the peak heat flux was estimated [11] as 7.7 percent. A few of the observations were repeated to check for reproducibility of results. Each time a new observation was made, the aforementioned procedure for cleaning the boiling surface was used and fresh test liquid was employed.

The flat plate test results are tabulated in Table 1 in both raw and reduced form.

Table 1 Peak heat flux data on 6.35-cm-dia circular flat plate heaters

Liquid	g/g_e	Pressure (k Pa)[a]	$\frac{L'}{2\pi\sqrt{\bar{3}}}$	$q_{max} \times 10^{-5}$ $\left(\frac{W}{m^2}\right)$	$\frac{q_{max}}{q_{max_Z}}$
Acetone	1	98.58	3.71	3.94	1.18
	1	98.93	3.71	4.10	1.22
	4.97	23.99	7.69	3.44	1.14
	12.30	25.37	12.07	4.19	1.07
Benzene	4.97	18.06	7.36	2.98	1.21
	8.72	24.88	9.85	3.31	1.05
	17.5	27.09	14.07	4.19	1.07
Isopropanol	1	22.75	3.68	2.08	0.79
		46.53	3.78	3.34	1.00
		73.21	3.85	3.82	0.98
		88.52	3.88	4.54	1.10
		98.72	3.91	4.26	1.00
	4.97	18.06	8.20	5.39	1.51
Methanol	1	44.60	3.56	3.69	0.94
		47.43	3.56	4.13	1.02
		88.04	3.72	5.33	1.04
		96.38	3.75	5.33	1.01
		96.52	3.75	5.33	1.01
		98.10	3.75	5.33	1.00
Distilled water	1	14.48	2.24	3.34	0.70
		25.37	2.27	4.45	0.72
		29.51	2.28	4.26	0.66
		36.54	2.29	4.82	0.67
		39.16	2.29	4.54	0.62
		42.74	2.30	4.54	0.59

[a] 1 kiloPascal equals 101.97 kg/m² or 7.5006 torrs.

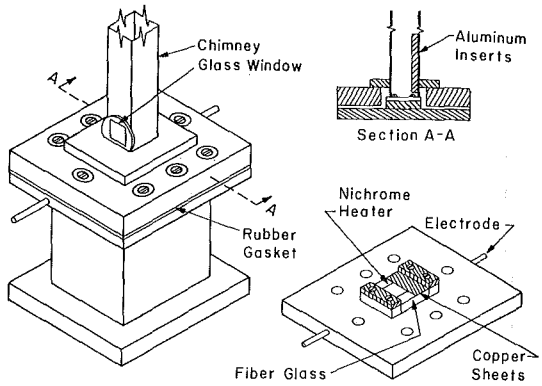

Fig. 7 Small plate heater apparatus

Small L/λ_d Experiments. The small L/λ_d apparatus is shown in Fig. 7. In this case, there was no advantage to working in the centrifuge since its purpose is only to increase L/λ_d by shrinking λ_d. Therefore a simple apparatus was made for stationary use only. It consists of a pair of electrodes positioned to accommodate nichrome resistance heater plates of varying width. Enough of each plate is short-circuited, as shown in the figure, so that the remaining active area is square. A chimney is fitted over the plate to contain the boiled liquid. Within the chimney are included spacers so the inside area of the chimney rises directly upward from the active heater area.

Table 2 Observations of q_{max} for finite horizontal square plates

Liquid	Width (cm)	Power (w)	$\frac{L}{\lambda_d}$	$\frac{q_{max}}{q_{max_Z}}$
Isopropanol	2.16	156	1.32	0.777
		148		0.738
		156		0.777
	1.52	102	0.93	1.021
		105		1.049
Methanol		132	0.89	1.048
		125		0.991
		127		1.010
		130		1.029
Ethanol		130	0.90	1.207
		130		1.207
		130		1.204
		119		1.103
Isopropanol	1.84	110	1.12	0.756
		108		0.743
		111		0.759
Methanol		146	1.07	0.789
		152		0.825
		147		0.800
Isopropanol	0.89	74	0.54	2.183
		80		2.354
		78		2.292
Methanol		74	0.52	1.726
		78		1.817
		74		1.726
Ethanol		80	0.33	2.178
		82		2.238
Methanol	1.21	100	0.70	1.266
		100		1.266
		100		1.266
Isopropanol		101	0.73	1.614
		94		1.506
		101		1.614
Methanol	2.16	118	1.26	0.467
		114		0.451
		110		0.435
		116		0.459

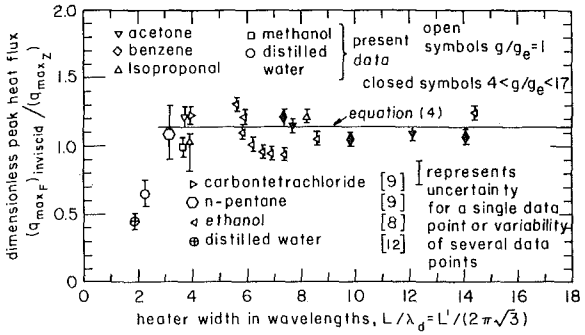

Fig. 8 Peak heat flux on broad flat-plate heaters with vertical side walls

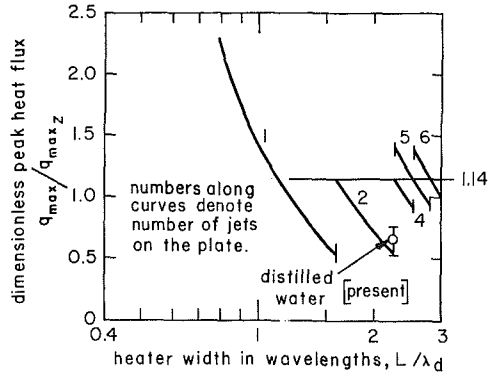

Fig. 9 Peak heat flux on a circular finite flat plate with vertical side walls

Each plate was washed with soap and warm water after it was installed, and then rinsed with the test liquid. This was done before each set of observations was made on the plate. The results of these observations are presented in both raw and reduced form in Table 2. The test liquids included reagent grade isopropanol and methanol, and 95 percent pure ethanol.

Discussion of Experimental Results

The available q_{max} data for $L/\lambda_d \geq 2$, from both this and other investigations, are plotted against L/λ_d (or $L'/2\pi\sqrt{3}$) in Fig. 8. Data for circular heaters (L = diameter) and one point for a square heater (reference [12], L = width) are included in the figure.

With reference to Fig. 8, we see that all the data are very closely represented by our version of Zuber's flat-plate prediction, equation (2), when L/λ_d exceeds about 3. The two data for smaller L/λ_d deviate sharply below the predicted value of $q_{max_F} = 1.14\ q_{max_Z}$, however. One of these data is our own for a circular heater. The other was obtained years ago by Costello [12] with a square heater.

In Fig. 3 we include Costello's data point along with our small L/λ_d data. This figure shows very clearly the effect of finite heater size on q_{max}. The data closely obey equation (4) for $N_j = 1$, between $L/\lambda_d = 1.0$ and 2.0, indicating that only one jet can be accommodated on the plate. This fact was substantiated by the scorch marks on the used plates. Circular marks, $\lambda_d/2$ in diameter, were observed repeatedly.

As the plate is shrunk to $L = \lambda_d/2$ we see that the data fall away from the curve. This is no surprise since the simple inviscid model no longer applies. The liquid return route is being squeezed into a viscous film crowded against the chimney, and considerations not included in the theory dictate q_{max}.

This result provides a dramatic verification of the hydrodynamic theory. It reveals a 5-fold variation of q_{max} which is accurately predicted by the theory until the theory breaks down owing to sidewall effects. It is, perhaps, ironic that Costello used the data point shown in the figure to support his own doubts as to the validity of the hydrodynamic theory.

Fig. 9 is a set of theoretical curves constructed for circular heaters in much the same way as those in Fig. 3 were constructed for square heaters. On this we include our own single data point for L/λ_d = diameter/λ_d = 2.3. This point, which actually represents 6 individual observations, touches the curve which corresponds to two jets on the heater.

A Scheme for Augmenting q_{max} on Large Plates

The fact that we can more than double q_{max} by closing in on the jets with vertical sidewalls suggests that it might be possible to augment q_{max} on large plates by building an "egg-crate" structure of vertical walls above a large plate.

We have built two such aluminum and brass structures to fit inside the glass cylinder shown above the copper heater in Fig. 6(*b*). The layout of these inserts is shown in Fig. 10. There was a clearance of about $^1/_2$ mm between the bottom of the egg crate and the heater surface. This avoided direct thermal contact with the heater surface.

The q_{max} data for stationary runs with the egg-crate structures in place are presented in Table 3. Data were taken with the liquid level both well above, and slightly below, the top of the structure. There was no difference in the resulting values of q_{max}. Since the walls of the egg crates have finite thickness, the heat flow directly under the walls is diverted into the unobstructed area of the heater and q_{max} must be increased to com-

Table 3 Peak heat flux for a large flat plate with an egg-crate structure above it

Egg-crate configuration	Liquid	Pressure kPa	q_{max} 10^5W/m²	q_{max}/q_{max_Z} based on total A_H	q_{max}/q_{max_Z} based on active A_H
L = 1.02 cm center to center, made of 0.81-mm sheet aluminum	Isopropanol	12.62	3.29	1.58	1.86
		12.62	3.29	1.58	1.86
		15.23	3.40	1.52	1.80
		19.90	3.62	1.44	1.70
			3.62	1.44	1.70
			3.51	1.40	1.65
			3.51	1.40	1.65
	Acetone	36.64	4.05	1.70	2.01
L = 0.635 cm center to center, made of 0.51-mm sheet brass	Isopropanol	15.40	3.72	1.65	1.95
		22.60	4.16	1.54	1.82
	Acetone	37.49	4.82	2.00	2.36
		40.61	4.93	2.00	2.36

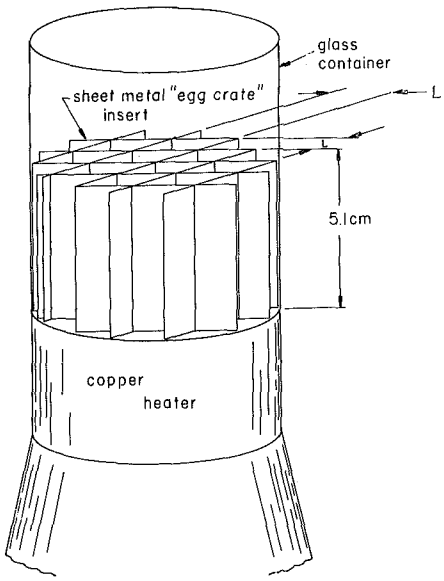

Fig. 10 Insert for augmenting q_{max}

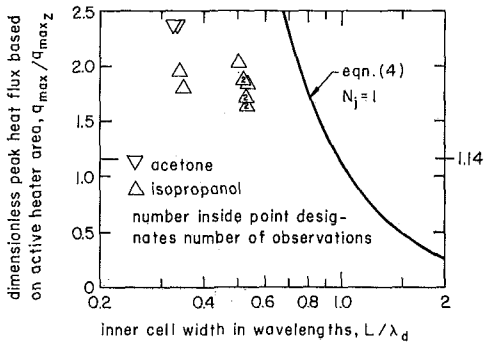

Fig. 11 Peak heat flux for a 6.35-cm-dia heater with an egg-crate structure above it (q_{max} based on active heater area)

pensate. Thus tabled values of q_{max}/q_{maxz} are given for both gross and the corrected surface area.

Fig. 11 shows the resulting corrected data in relation to the hydrodynamic theory. They fall a little low, in much the same way as did the data in Fig. 3. However, the data suggest that it is possible to roughly double the peak heat flux from a flat plate by inserting egg-crate structures. We suspect that these results could be slightly improved using a hexagonal (rather than square) array of walls in the structure since they would provide more nearly circular cells.

Conclusions

1 The peak pool boiling heat flux on an infinite flat plate is given by

$$\frac{q_{maxF}}{q_{maxz}} = 1.14$$

2 If the plate is fewer than 3 wavelengths in width, the variation in q_{max}, as jets are added or removed, becomes very important. In this case:

$$\frac{q_{max}}{q_{maxz}} = 1.14\,\frac{N_j}{A_H/\lambda_d{}^2}$$

3 When N_j is equal to only one or two, the preceding equation can give rise to extremely large variations in q_{max}. This suggests that an egg-crate structure on a flat heater can be used to augment q_{max} significantly.

4 Experiments with appropriately sized egg-crate inserts show that it is possible to roughly double q_{max} over the infinite flat plate value.

References

1 Zuber, N., "Hydrodynamic Aspects of Boiling Heat Transfer," AEC Report No. AECU-4439, *Physics and Mathematics*, 1959.

2 Kutateladze, S. S., "On the Transition to Film Boiling Under Natural Convection," *Kotloturbostroenie*, No. 3, 1948, p. 10.

3 Lienhard, J. H., and Dhir, V. K., "Hydrodynamic Prediction of Peak Pool-Boiling Heat Fluxes From Finite Bodies," JOURNAL OF HEAT TRANSFER, TRANS. ASME, Series C, Vol. 95, No. 2, May 1973, pp. 152–158.

4 Sun, K. H., and Lienhard, J. H., "The Peak Pool Boiling Heat Flux on Horizontal Cylinders," *International Journal of Heat and Mass Transfer*, Vol. 13, 1970, pp. 1425–1439.

5 Bobrovich, G. I., Gogonin, I. I., and Kutateladze, S. S., "Influence of Size of Heater Surface on the Peak Pool Boiling Heat Flux," *Jour. Appl. Mech. and Tech. Phys.*, No. 4, 1964, pp. 137–138.

6 Lienhard, J. H., and Watanabe, K., "On Correlating the Peak and Minimum Boiling Heat Fluxes With Pressure and Heater Configuration," JOURNAL OF HEAT TRANSFER, TRANS. ASME, Series C, Vol. 88, No. 1, Feb. 1966, pp. 94–100.

7 Lienhard, J. H., "Interacting Effects of Gravity and Size Upon the Peak and Minimum Pool Boiling Heat Fluxes," NASA CR-1551, May 1970.

8 Cichelli, M. T., and Bonilla, C. F., "Heat Transfer to Liquids Boiling Under Pressure," *Trans. AIChE*, Vol. 41, 1945, p. 755.

9 Berenson, P. J., "Transition Boiling Heat Transfer From a Horizontal Surface," M.I.T. Heat Transfer Laboratory Technical Report No. 17, 1960.

10 Lienhard, J. H., and Keeling, K. B., Jr., "An Induced-Convection Effect Upon the Peak-Boiling Heat Flux," JOURNAL OF HEAT TRANSFER, TRANS. ASME, Series C, Vol. 92, No. 1, Feb. 1970, pp. 1–5.

11 Dhir, V. K., "Viscous Hydrodynamic Instability Theory of the Peak and Minimum Heat Fluxes," College of Engineering, Bulletin No. UKY-100, University of Kentucky, PhD dissertation, Nov. 1972.

12 Costello, C. P., Bock, C. O., and Nichols, C. C., "A Study of Induced Convective Effects on Pool Boiling Burnout," *CEP Symposium Series*, Vol. 61, 1965, pp. 271–280.

V. K. DHIR
Research Associate. Assoc. Mem. ASME

J. H. LIENHARD
Professor. Mem. ASME

Mechanical Engineering Department,
University of Kentucky,
Lexington, Ky.

Similar Solutions for Film Condensation With Variable Gravity or Body Shape

The configurations of laminar film condensation on two-dimensional isothermal surfaces, for which the complete boundary layer equations admit similarity solutions, are described. These configurations include certain kinds of curved surfaces at earth-normal gravity and/or certain variable-gravity fields. The bodies have forward stagnation points, near which the governing equations break down. A criterion is given for delimiting the region in which the theory does not apply. It is shown how to compute heat transfer results for the similar solutions and some examples are worked. Condensation on a cool plate, synchronously rotating with a vapor, is treated in some detail.

Introduction

Since Sparrow and Gregg's [1][1] full boundary layer treatment of laminar film condensation on an isothermal vertical plate, many authors have done full boundary layer treatments of condensation. They have generally been unable to use similarity transforms, as Sparrow and Gregg originally did, without introducing additional approximations.

Actually reference [1] (and possibly the next one or two boundary layer studies that followed it) might properly have put an end to such studies. They invariably lead to minimal correction of results obtained by the simple Nusselt [2]-Rohsenow [3] method, except in the low Prandtl number range where the boundary layer treatments themselves cease to be valid. We have elaborated this point in references [4 and 5].

Nevertheless boundary layer solutions continue to appear in the literature, and they are usually much more complex than Sparrow and Gregg's original study was. The reason is that none of them has succeeded in using a similar solution. This causes us to ask, as Braun, Ostrach, and Heighway [6] previously did for natural convection configurations: "What other configurations *admit* a similar solution?"

In addressing this question we shall consider that the basic variable characterizing a condenser configuration is the local gravity, $g(x)$. As a condensing surface curves, the component of gravity parallel with the surface will vary with the distance, x, from the leading edge or the stagnation point. We then wish to learn which bodies (i.e., which functions, $g(x)$) will admit similar solutions, and to provide some of those solutions.

Derivation of Similarity Requirements

The conventional equation of motion for condensation as expressed in terms of the stream function, ψ, is

$$\frac{\partial\psi}{\partial y}\frac{\partial^2\psi}{\partial x\partial y} - \frac{\partial\psi}{\partial x}\frac{\partial^2\psi}{\partial y^2} = \frac{g(x)(\rho_f - \rho_g)}{\rho_f} + \frac{\mu}{\rho_f}\frac{\partial^3\psi}{\partial y^3} \tag{1}$$

with the usual boundary conditions

$$\frac{\partial\psi}{\partial y} = \frac{\partial\psi}{\partial x} = 0 \text{ at } y = 0; \qquad \frac{\partial^2\psi}{\partial y^2} = 0 \text{ at } y = \delta \tag{2}$$

The energy equation is

$$\frac{\partial\psi}{\partial y}\frac{\partial T}{\partial x} - \frac{\partial\psi}{\partial x}\frac{\partial T}{\partial y} = \alpha\frac{\partial^2 T}{\partial y^2} \tag{3}$$

with boundary conditions

$$T = T_w \text{ at } y = 0; \qquad T = T_{sat} \text{ at } y = \delta \tag{4}$$

We next seek a similarity transform in terms of an unknown stretching function, $f(x)$, and earth-normal (or a characteristic) gravity, g_e:

$$F(\eta) = \psi g_e/\alpha g(x) f^3(x); \qquad \eta = ly/f(x) \tag{5}$$

where

$$l \equiv [g_e\rho_f(\rho_f - \rho_g)c_p/\mu k]^{1/3} \tag{6}$$

Under these changes of variables, equation (1) becomes

$$F''' + \frac{A}{\Pr}FF'' - \frac{B}{\Pr}F'^2 + 1 = 0 \tag{7}$$

where

$$A \equiv \frac{f}{lg_e}\frac{d}{dx}(f^3 g) \quad \text{and} \quad B \equiv \frac{f^2}{lg_e}\frac{d}{dx}(f^2 g) \tag{8}$$

and the boundary conditions (2) become

[1] Numbers in brackets designate References at end of paper.

Contributed by the Heat Transfer Division for Publication (without presentation) in the Journal of Heat Transfer. Manuscript received by the Heat Transfer Division, March 29, 1973. Paper No. 73-HT-W.

$$F(0) = F'(0) = 0; \qquad F''(\eta_\delta) = 0 \tag{9}$$

We then define $\theta(\eta) \equiv (T - T_{sat})/(T_w - T_{sat})$ and enter equation (3) with it, and the transformations (5). The result is

$$\theta'' + AF\theta'' = 0 \tag{10}$$

where the boundary conditions, (4), become

$$\theta(0) = 1; \qquad \theta(\eta_\delta) = 0 \tag{11}$$

The problem is then that of identifying the values of $g(x)$ for which $f(x)$ can be selected so that A and B are constant. Without loss of generality we can choose

$$A = 3 \tag{12}$$

so the present equations will match Sparrow and Gregg's, for the vertical plate. We must next find what variations of g will lead to constant values of B.

The Gravity Variations Admitting Similar Solutions

Some manipulation of equations (8) and (12) leads to the relation

$$gg'' = [4(B - 3)/3(B - 2)]g'^2 \tag{13}$$

which can be integrated twice to get

$$g = (C_1x + C_2)^n \tag{14}$$

where $n = (3B - 6)/(6 - B)$, and C_1 and C_2 are constants of integration.

From equation (5) we see that the product gf^3 must vanish at $x = 0$ if the stream function is to vanish. Thus C_2 must be zero, unless g is constant in which case equations (8) give $f \sim x^{1/4}$. Accordingly, the family of gravity variations which admit similar solutions is

$$g = C_3x^n; \qquad n \geq 0 \tag{15}$$

These are all stagnation point flows since the liquid is stationary at $x = 0$. For such surfaces equations (8) and (12) lead to $B = 6(n + 1)/(n + 3)$, and we obtain a general expression for f:

$$f(x) = \left[\frac{12g_el}{(n + 3)}\frac{x}{g(x)}\right]^{1/4} \tag{16}$$

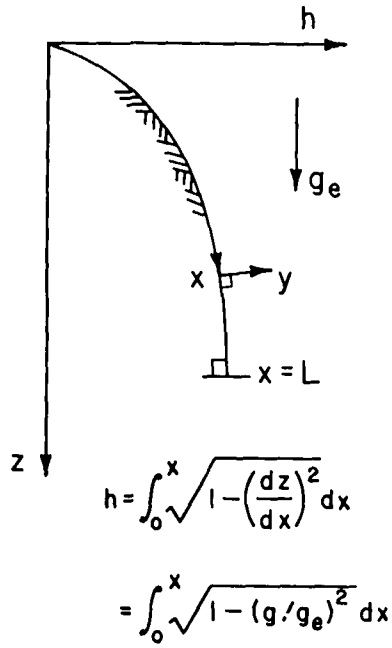

Fig. 1 Coordinates of condensing surfaces

Two-Dimensional Surfaces Admitting Similar Solutions

Next, let us consider curved surfaces at earth-normal gravity as indicated in Fig. 1. In this case $g(x)/g_e = dz/dx$, so

$$h = \int_0^x \sqrt{1 - (g/g_e)^2}\, dx \tag{17}$$

For the forward stagnation point flows that admit similar solutions,

$$\frac{dz}{dx} = \frac{g(x)}{g_e} = \left(\frac{x}{L}\right)^n \tag{18}$$

where L is the value of x at which the surface becomes vertical (cf.

Nomenclature

A, B = constant functions of x in equation (7), defined in equation (8)
C_1, C_2, C_3 = various constants described in context
c_p = specific heat at constant pressure
D = diameter of a cylinder
F = dimensionless stream function
f = stretching-function of x (see equation (5))
$g(x), g_e$ = body force acting along the condensing surface; earth-normal gravity
h = heat transfer coefficient, or position coordinate for the surface
h_{fg}, h_{fg}' = latent heat of vaporization; $h_{fg}' \equiv h_{fg} + 0.68\ c_p\Delta T$
k = thermal conductivity of condensate
L = length of condenser
l = dimensionless inverse length, equation (6)
$\mathrm{Nu}_x, \mathrm{Nu}_L, \mathrm{Nu}_D$ = local Nusselt number, hx/k; Nusselt numbased on h averaged over the condenser, and on L or D
n = exponent of power-law dependence of g on x, $(3B - 6)/(6 - B)$
Pr = Prandtl number, $\rho_f\mu c_p/k$
T, T_w, T_{sat} = temperature (subscripts denote wall and saturation temperatures, respectively; $\Delta T \equiv T_{sat} - T_w$)
x, y = coordinates parallel and normal to heater surface, respectively
z = coordinate parallel with earth-normal gravity or centrifugal force
α = thermal diffusivity of condensate, $k/\rho_f c_p$
δ = condensate film thickness
η, η_δ = dimensionless independent variable, $ly/f(x)$. Subscript δ designates value at outer edge of condensate film.
θ = dimensionless temperature, $(T - T_{sat})/(T_w - T_{sat})$
μ = viscosity of condensate
ρ_f, ρ_g = densities of liquid and vapor phases, respectively
ψ = stream function in the condensate
ω = angular speed of rotation

equation (15) and Fig. 1(*a*)). Integration of this expression yields

$$\frac{z}{L} = \frac{(x/L)^{n+1}}{n+1} \tag{19}$$

The dimensionless expression for h is, for stagnation-point condensation,

$$\frac{h}{L} = \int_0^{x/L} \sqrt{1-(x/L)^{2n}}\, d\left(\frac{x}{L}\right) \tag{17a}$$

Fig. 2 displays the family of earth-normal gravity surfaces corresponding with equation (18) as calculated numerically using equations (19) and (17*a*). Four of these attract particular interest.

The Vertical Plate. This was treated in detail in [1].

The Almost-Cylinder. When $n = 1/\sqrt{2} \simeq 0.70711$, $h(L) = z(L)$ and the body shape is very nearly cylindrical. Its radius deviates less than one percent from that of true cylinder. This is consistent with the fact that Sparrow and Gregg [7] could obtain an approximate similar solution for film condensation from a cylinder. In this case $B = 2.76$ and $f = (3.24\, g_e l x/g)^{1/4}$.

The Synchronously Rotating Plate. When $n = 1$ the gravity varies linearly with the distance from the leading edge, as occurs during condensation on a plate rotating synchronously with a surrounding vapor (i.e., the plate and vapor rotate at the same speed as they would in a closed centrifuge.) While this g would also vary linearly with x on a curved body in an earth-normal gravity field, as shown in Fig. 2, the rotating plate is of far greater practical interest. The axis of the plate is located on the line, $x = 0$; and g and g_e can be replaced by $\omega^2 x$ and $\omega^2 L$, where ω is the angular speed of the plate. In this case $B = 3$ and $f = (3Ll)^{1/4}$. Any static component of the external gravity field is considered to be much less than $\omega^2 x$, in this case.

Stagnation Point Flows in Earth-Normal Gravity Fields With Large *n*. As n becomes large the surfaces flatten out and earth-normal gravity lies virtually perpendicular to much of the surface. The limiting situation was analyzed by Leppert and Nimmo [8] who pointed out that the main driving force would be the pressure gradient generated by the varying film height. Accordingly, they neglected inertia and wrote a momentum equation which takes the following form in the present case:

$$0 = g(x) - g_e \frac{d\delta}{dx}\frac{dh}{dx} + \frac{\mu}{\rho_f}\frac{\partial^2 u}{\partial y^2} \tag{20}$$

This expression must replace our momentum equation unless

$$g(x) \gg g_e \frac{d\delta}{dx}\sqrt{1-\left(\frac{x}{L}\right)^{2n}} \tag{21}$$

Since $\sqrt{1-(x/L)^{2n}}$ is always equal to or less than unity we can ignore the square-root term and obtain

$$\frac{x}{L} \gg \left[(n+1)\frac{\delta}{L}\right]^{\frac{1}{n+1}} \tag{22}$$

But $\eta_\delta = \theta(1) = \delta l/f$ and for the stagnation point flows equation (16) can be rewritten as

$$f = \left[\frac{12xl}{(n+3)}\left(\frac{L}{x}\right)^n\right]^{1/4} \tag{16a}$$

Thus we should distrust the present solutions, for larger values of n, at earth-normal gravity, unless

$$\frac{x}{L} \gg \left[\frac{12(n+1)^4}{(n+3)(lL)^3}\right]^{1/(3n+5)} \tag{23}$$

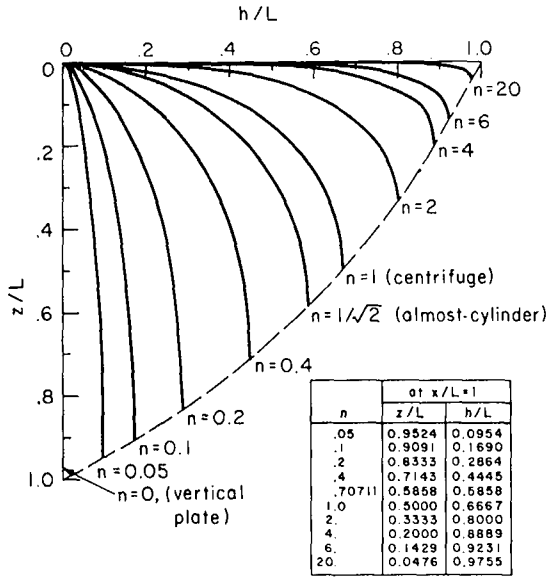

n	at x/L=1 z/L	h/L
.05	0.9524	0.0954
.1	0.9091	0.1690
.2	0.8333	0.2864
.4	0.7143	0.4445
.70711	0.5858	0.5858
1.0	0.5000	0.6667
2.	0.3333	0.8000
4.	0.2000	0.8889
6.	0.1429	0.9231
20.	0.0476	0.9755

Fig. 2 The family of body shapes for two-dimensional stagnation point condensing flows which admit similar solutions

The Solution of Some Heat Transfer Problems

To complete the heat transfer calculation it is necessary to obtain the condensate film thickness from an energy balance. It is easy to show that Sparrow and Gregg's original result:

$$\frac{c_p \Delta T}{h_{fg}} = -3\frac{F(\eta_\delta)}{\theta'(\eta_\delta)}, \tag{24}$$

where $\Delta T \equiv T_{sat} - T_w$, is still applicable in the present cases. The numerical integration of equations (7) and (10) under the use of an assumed η_δ in the boundary condition, $F''(\eta_\delta) = 0$, then gives the value of $c_p\Delta T/h_{fg}$ for which that η_δ is correct.

Then the local Nusselt number, Nu_x, can be computed in terms of the slope of the temperature gradient at the wall:

$$\mathrm{Nu}_x = \frac{hx}{k} = -\theta'(0)\frac{lx}{f(x)} = -\theta'(0)lL\frac{x/L}{f(x/L)} \tag{25}$$

and the Nusselt number based on a value of h averaged over x is

$$\mathrm{Nu}_L = -\theta'(0)lL\int_0^1 \frac{d(x/L)}{f(x/L)} \tag{26}$$

The Upper Half of the Almost-Cylinder. We have performed this exercise for the surface given by $n = 0.70711$, between $x = 0$ and $\pi D/4$. The use of a reasonably small value of $c_p\Delta T/h_{fg}$ ($= 0.015$) and $\mathrm{Pr} = 1.0$, insured that Nu_D would be nearly a constant, independent of either Pr or $c_p\Delta T/h_{fg}$. The resultant overall Nusselt number is

$$\mathrm{Nu}_D = 0.856\sqrt[4]{(lD)^3\frac{h_{fg}}{c_p\Delta T}} \tag{27}$$

The corresponding value of the constant as given by the Nusselt-Rohsenow theory can be computed by the method given in [4]. For the stagnation point cases we get, in general,

$$\mathrm{Nu}_L = 0.707\frac{4}{n+3}\sqrt[4]{\frac{n+3}{3}}\sqrt[4]{(lL)^3\frac{h_{fg}'}{c_p\Delta T}} \tag{28}$$

and for the upper-half of the almost-cylinder ($n = 0.70711$ and $L = \pi D/4$) this gives

$$\mathrm{Nu}_D = 0.852\sqrt[4]{(lD)^3\frac{h_{fg}'}{c_p\Delta T}} \tag{29}$$

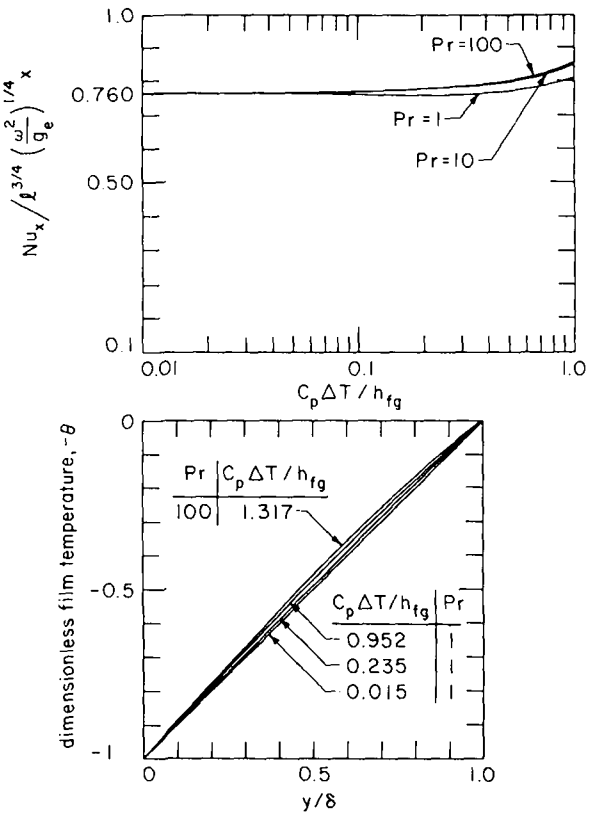

Fig. 3 Heat transfer results and temperature distribution in the condensate layer on a rotating plate

Thus the following constants apply in the Nusselt number expression for the upper half of cylinder:

boundary layer theory, almost-cylinder:[2]	0.856
Nusselt-Rohsenow theory, almost-cylinder:	0.852
boundary layer theory, true cylinder:[2]	obtainable from [7]
Nusselt-Rohsenow theory, true cylinder:[3]	0.866

In this case the Nusselt-Rohsenow theory is less than $^1/_2$ percent low and the almost-cylinder approximation is valid within about $1^1/_2$ percent. Actually the Nusselt-Rohsenow theory is even closer to the boundary layer theory than it appears to be, since it employs a corrected value of the latent heat ($h_{fg}' \equiv h_{fg} + 0.68\, c_p\Delta T$) which is slightly higher than h_{fg}.

The Synchronously Rotating Plate. We shall do this example in somewhat more detail since it has never been solved by boundary layer methods before. Using the previously obtained values of $A = B = 3$ in equation (7), we can integrate it numerically, subject to conditions (9) and (24). The result will be values of $\theta'(0)$ that depend on Pr and $c_p\Delta T/h_{fg}$. The use of these values in equation (25) gives us

$$\mathrm{Nu}_x = -\frac{\theta'(0)}{\sqrt[4]{3}}\left[\frac{c_p\Delta T}{h_{fg}}\right]^{1/4}\left[\frac{\rho_f(\rho_f-\rho_g)h_{fg}\omega^2}{\mu k\Delta T}\right]^{1/4} x \quad (30)$$

In Fig. 3, Nu_x is plotted as a function of $c_p\Delta T/h_{fg}$ for Pr = 1, 10, and 100. For $c_p\Delta T/h_{fg} \simeq 0.01$, Nu_x values closely approach the value given by the Nusselt-Rohsenow theory [4]. In this case δ = constant. The temperature distribution in the condensate is also plotted in Fig. 3 for some of the values of $c_p\Delta T/h_{fg}$ and Pr. The temperature profiles remain nearly linear, even for fairly large values of $c_p\Delta T/h_{fg}$.

For steam at 1 atm, equation (23) indicates that the foregoing results are valid for curved bodies at earth-normal gravity as long as:

$$x/L \gg 0.028/(L\ \mathrm{ft})^{3/8}$$

For plates of any size, this criterion will be unsatisfied only near $x = 0$.

Conclusions

1 It is possible to obtain a similar solution for a two-dimensional laminar film condensation problem if $g(x) \sim x^n$.

2 The shape of these bodies in an earth-normal gravity field is given in Fig. 2. The usual boundary layer solutions should only be used for such bodies where equation (23) is satisfied.

3 If $n = 1/\sqrt{2}$ the body resembles a circular cylinder and heat transfer results are very similar to those for a true cylinder.

4 Complete boundary layer results are presented for the syncronously rotating plate. The improvement over the results given by an appropriate Nusselt-Rohsenow theory is negligible in cases of practical interest since inertia contributions are minimal.

References

1 Sparrow, E. M., and Gregg, J. L., "A Boundary-Layer Treatment of Laminar-Film Condensation," JOURNAL OF HEAT TRANSFER, TRANS. ASME, Series C, Vol. 81, No. 1, Feb. 1959, pp. 13–18.

2 Nusselt, W., "Die Oberflächenkondensation des Wasserdampfes," *Z. Ver. Deutsch. Ing.*, Vol. 60, 1916, pp. 541–546, 569–575.

3 Rohsenow, W. M., "Heat Transfer and Temperature Distribution in Laminar Film Condensation," JOURNAL OF HEAT TRANSFER, TRANS. ASME, Series C, Vol. 87, 1965, pp. 1645–1648.

4 Dhir, V. K., and Lienhard, J. H., "Laminar Film Condensation on Plane and Axisymetric Bodies in Nonuniform Gravity," JOURNAL OF HEAT TRANSFER, TRANS. ASME, Series C, Vol. 91, No. 1, Feb. 1971, pp. 97–100.

5 Lienhard, J. H., and Dhir, V. K., "A Simple Analysis of Laminar Film Condensation With Suction," JOURNAL OF HEAT TRANSFER, TRANS. ASME, Series C, Vol. 92, No. 3, Aug. 1972, pp. 334–336.

6 Braun, N. H., Ostrach, S., and Heighway, J. E., "Free-Convection Similarity Flows About Two Dimensional and Axi-Symmetric Bodies With Closed Lower Ends," *International Journal of Heat and Mass Transfer*, Vol. 2, No. 1/2, 1961, pp. 121–135.

7 Sparrow, E. M., and Gregg, J. L., "Laminar Condensation Heat Transfer on a Horizontal Cylinder," JOURNAL OF HEAT TRANSFER, TRANS. ASME, Series C, Vol. 81, No. 3, Nov. 1959, pp. 291–296.

8 Leppert, G., and Nimmo, B., "Laminar Film Condensation on Surfaces Normal to Body or Inertial Forces," JOURNAL OF HEAT TRANSFER, TRANS. ASME, Series C, Vol. 90, No. 1, 1968, pp. 178–179.

[2] The boundary-layer results given here are for values of $c_p\Delta T/h_{fg}$ that are small enough to insure that the constant is independent of both $c_p\Delta T/h_{fg}$ and Pr.

[3] Without benefit of the digital computer, Nusselt [2] obtained 0.861.

J. D. LOCKWOOD
Components Incorporated,
El Paso, Texas

G. P. MULHOLLAND
Department of Mechanical Engineering,
New Mexico State University,
Las Cruces, N. Mex. Mem. ASME

Diffusion Through Laminated Composite Cylinders Subjected to a Circumferentially Varying External Heat Flux

The diffusion equation for the temperature distribution in each of k sections of a hollow laminated composite cylinder with a circumferentially varying external heat flux is solved. The composite consists of k discrete cylinders each of a different material with perfect thermal contact at each of the k-1 interfaces. The cylinders have an arbitrary initial temperature distribution and the temperature on the inside surface of the composite is an arbitrary function of time. The solution is obtained by using a Fourier integral transformation and a dependent variable substitution. This produces a new partial differential equation with homogeneous boundary conditions. This new equation is then solved by using a type of orthogonality relationship developed by Vodicka.

Introduction

There are many problems of engineering interest which require a detailed knowledge of the transient temperature distribution and heat flux in the interior of cylinders composed of two or more distinct layers. The treatment of the heat transfer in the direction normal to the layers of the composite usually is the major factor in the thermal design of these composites, and hence, there are a number of articles concerned with the solution of the one-dimensional diffusion equation [1, 2, 3].[1] Carslaw and Jaeger [2] use the Laplace transformation method to solve the heat transfer problem in multi-layer solids. However, if the number of layers in the solid is more than two, the inverse transform is very difficult; hence, the technique is limited. Bulavin and Kascheev [1] use a separation of variables technique and employ a unique "Quasi-Orthogonality" condition developed by a Czechoslovakian mathematician V. Vodicka [4, 5].

For actual systems, however, the heat flow inside the composite is seldom one-dimensional in the normal direction. A logical means of extending the one-dimensional theory is to consider each layer of the laminated composite as a continuous, homogeneous media having two-dimensional heat flow, and then to consider each layer as a continuous, homogeneous, but anisotropic media with prescribed normal and lateral thermal conductivities. The problem considered here will be that of treating the layers of the composite as continuous, homogeneous media with two-dimensional heat flow.

There are many areas of application for this type of problem. One area is that of thermal insulation for cryogenic systems [6]. An insulator that is lightweight, compact, and highly efficient is desirable. The current developments involve the use of evacuated multi-layer insulation in the form of numerous thin low-emittance radiation shields separated by low conductivity spacers.

A second area of application is in the field of solar ovens. If a singly curved mirror is used, a composite cylinder placed at the focus will again be subject to a circumferentially varying time dependent heat flux.

Analysis

The temperature distribution in the ith section of k solidly joined cylinders is given by the diffusion equation:

$$r\frac{\partial}{\partial r}\left[r\frac{\partial T_i}{\partial r}(r,\theta,t)\right]+\frac{\partial^2 T_i}{\partial \theta^2}(r,\theta,t)=\frac{r^2}{D_i^2}\frac{\partial T_i}{\partial t}(r,\theta,t) \quad (1)$$

$$r_i \le r \le r_{i+1}, \qquad i = 1, 2, 3, \ldots k, \qquad t \ge 0$$

where

T_i = temperature in the ith section

t = time

r = radial coordinate

θ = angular coordinate

D_i^2 = thermal diffusivity in the ith section $= \dfrac{K_i}{\rho_i C p_i}$

[1] Numbers in brackets designate References at end of paper.

Contributed by the Heat Transfer Division for publication (without presentation) in the JOURNAL OF HEAT TRANSFER. Manuscript received by the Heat Transfer Division, March 23, 1973. Paper No. 73-HT-V.

ρ_i = density in the ith section

C_{pi} = specific heat in the ith section

The cylinders are subject to the following boundary and initial conditions:

$$T_1(r_1, \theta, t) = T_1(t) \tag{2a}$$

$$K_k \frac{\partial T_k}{\partial_r}(r_{k+1}, \theta, t) = F(\theta, t) \tag{2b}$$

$$T_i(r, \theta, t) = T_i(r, \theta + 2\pi, t) \tag{2c}$$

$$\frac{\partial T_i}{\partial \theta}(r, \theta, t) = \frac{\partial T_i}{\partial \theta}(r, \theta + 2\pi, t) \tag{2d}$$

$$T_i(r_{i+1}, \theta, t) = T_{i+1}(r_{i+1}, \theta, t) \tag{2e}$$

$$K_i \frac{\partial T_i}{\partial r}(r_{i+1}, \theta, t) = K_{i+1} \frac{\partial T_{i+1}}{\partial r}(r_{i+1}, \theta, t) \tag{2f}$$

$$T_i(r, \theta, 0) = f_i(r, \theta) \tag{2g}$$

Define a Fourier series expansion of the form,

$$Y(\theta) = \frac{a_0}{2\pi} + \frac{1}{\pi} \sum_{n=1}^{\infty} a_n \cos n\theta + b_n \sin n\theta \tag{3}$$

where

$$a_0 = \int_0^{2\pi} Y(\theta) d\theta = \bar{Y}(0) \tag{4}$$

$$a_n = \int_0^{2\pi} Y(\theta) \cos n\theta d\theta = \bar{Y}_c(n) \tag{5}$$

$$b_n = \int_0^{2\pi} Y(\theta) \sin n\theta d\theta = \bar{Y}_s(n) \tag{6}$$

Equations (4), (5), and (6) define the integral transforms and the inverse transform is given by

$$Y(\theta) = \frac{1}{2\pi} \bar{Y}(0) + \frac{1}{\pi} \sum_{n=1} \bar{Y}_c(n) \cos n\theta + \frac{1}{\pi} \sum_{n=1}^{\infty} \bar{Y}_s(n) \sin n\theta \tag{7}$$

When equation (7) is applied to equation (1), the result for the null space, or the case where $n = 0$, is

$$r \frac{\partial}{\partial r}\left[r \frac{\partial \bar{T}_i}{\partial r}(r, 0, t) \right] = \frac{r^2}{D_i^2} \frac{\partial \bar{T}_i}{\partial t}(r, 0, t) \tag{8}$$

where $\bar{T}_i$ is the singly transformed temperature.

Transformation of the boundary conditions gives

$$\int_0^{2\pi} T_1(r_1, \theta, t) d\theta = \bar{T}_1(r, 0, t) = 2\pi T_1(t) = \bar{T}_1(t) \tag{9a}$$

$$\int_0^{2\pi} K_k \frac{\partial T_k}{\partial r}(r_{k+1}, \theta, t) d\theta = K_k \frac{\partial \bar{T}_k}{\partial r}(r_{k+1}, 0, t) = \int_0^{2\pi} F(0, t) d\theta = \bar{F}(0, t) \tag{9b}$$

$$\bar{T}_i(r_{i+1}, 0, t) = \bar{T}_{i+1}(r_{i+1}, 0, t) \tag{9c}$$

$$K_i \frac{\partial \bar{T}_i}{\partial r}(r_{i+1}, 0, t) = K_{i+1} \frac{\partial \bar{T}_{i+1}}{\partial r}(r_{i+1}, 0, t) \tag{9d}$$

$$\int_0^{2\pi} T_i(r, \theta, 0) = \bar{T}_i(r, 0, 0) = \int_0^{2\pi} f_i(r, \theta) d\theta = \bar{f}_i(r, 0) \tag{9e}$$

The solution technique has been fully explained elsewhere [7] and need not be repeated here. The solution of equation (8) is

$$\bar{T}_i(r, 0, t) = U_i(r, 0, t) + L_{i1}(r)\bar{T}_1(t) + L_{i2}(r)\bar{F}(0, t) \tag{10}$$

where

$$U_i(r, 0, t) = \sum_{m=1}^{\infty} \left\{ g_m e^{-\gamma^2{}_m t} - l_{m1} e^{-\gamma^2{}_m t} * \frac{d\bar{T}_1(t)}{dt} - l_{m2} e^{-\gamma^2{}_m t} * \frac{\partial F}{\partial t}(0, t) X_{im}(r) \right. \tag{11}$$

$$l_{mj} = \frac{1}{N_m} \sum_{i=1}^{k} \rho_i C p_i \int_{r_i}^{r_{i+1}} [r L_{ij}(r) X_{im}(r) dr, \quad j = 1, 2, m = 1, 2 \ldots \tag{12}$$

$$g_m = \frac{1}{N_m} \sum_{i=1}^{k} \rho_i C p_i \int_{r_i}^{r} r G_i(r) X_{im}(r) dr, \qquad m = 1, 2, \ldots \tag{13}$$

$$N_m = \sum_{i=1}^{k} \rho_i C p_i \int_{r_i}^{r_{i+1}} [X_{im}(r)]^2 dr, \qquad m = 1, 2 \ldots \tag{14}$$

$$G_i(r) = \bar{f}_i(r, 0) - L_{i1}(r)\bar{T}_1(t) - L_{i2}(r)\bar{F}(0, 0) \tag{15}$$

and where the symbol * denotes convolution. The L_{ij}, $j = 1, 2$, functions are obtained by solving the differential equation

$$\frac{d}{dr}\left[r \frac{dL_{ij}(r)}{dr} \right] = 0, \qquad i = 1, 2, 3, \ldots, k, j = 1, 2 \tag{16}$$

subject to the following boundary conditions:

$$L_{11}(r_1) = 1 \tag{17a}$$

Nomenclature

$A_{im}, B_{im}, C_{ij}, D_{ij}, E_{ij}$ = constants

C_{pi} = specific heat of the ith section

D_i^2 = thermal diffusivity of the ith section

F = outside heat flux

$\bar{F}$ = transformed heat flux

f_i = initial temperature distribution

$\bar{f}_i$ = transformed initial distribution

G_i = function defined by equations (15) and (27)

g_m = function defined by equations (13) and (24)

H_i = function defined by equation (28)

h_m = function defined by equation (25)

K_i = thermal conductivity of the ith section

k = number of layers in the composite

L_{ij} = function defined by equations (15) and (26)

l_{mj} = function defined by equation (12)

r = radial coordinate

T_i = temperature of the ith section

$\bar{T}_i$ = singly transformed temperature

t = time

X_{im} = eigenfunctions

θ = angular coordinate

ρ_i = density of the ith section

$$\frac{dL_{k1}}{dr}(r_{k+1}) = 0 \tag{17b}$$

$$L_{i1}(r_{i+1}) = L_{i+1}(r_{i+1}), \qquad i = 1, 2, 3, \ldots, k-1 \tag{17c}$$

$$K_i \frac{dL_{i1}}{dr}(r_{i+1}) = K_{i+1} \frac{dL_{i+1,1}}{dr}(r_{i+1}), \qquad i = 1, 2, 3, \ldots, k-1 \tag{17d}$$

and

$$L_{12}(r_1) = 0 \tag{18a}$$

$$K_k \frac{dL_{k2}}{dr}(r_{k+1}) = 1 \tag{18b}$$

$$L_{i2}(r_{i+1}) = L_{i+1,2}(r_{i+1}), \qquad i = 1, 2, 3, \ldots, k-1 \tag{18c}$$

$$K_i \frac{dL_{i2}}{dr}(r_{i+1}) = K_{i+1} \frac{dL_{i+1,2}}{dr}(r_{i+1}), \qquad i = 1, 2, 3, \ldots, k-1 \tag{18d}$$

The eigenfunctions $X_{im}(r)$ are

$$X_{im}(r) = A_{im} J_0\left(\frac{\gamma_m r}{D_i}\right) + B_{im} Y_0\left(\frac{\gamma_m r}{D_i}\right) \tag{19}$$

The constants A_{im}, B_{im}, and the eigenvalues γ_m are obtained by applying the boundary condition and internal conditions

$$X_{1m}(r_1) = 0 \tag{20a}$$

$$\frac{dX_{km}}{dr}(r_{k+1}) = 0 \tag{20b}$$

$$X_{im}(r_{i+1}) = X_{i+1,m}(r_{i+1}), \qquad l = 1, 2, 3, \ldots, k-1 \tag{20c}$$

$$K_i \frac{dX_{im}}{dr}(r_{i+1}) = K_{i+1} \frac{dX_{i+1,m}}{dr}(r_{i+1}), \qquad i = 1, 2, 3, \ldots, k-1 \tag{20d}$$

to the eigenfunctions X_{im} [7, 8].

When the transform defined previously is applied to equation (1) for $n > 0$ the result is

$$\frac{D_i^2}{r}\frac{\partial}{\partial r}\left[r\frac{\partial \bar{T}_{in}}{\partial r}(r, n, t)\right] - \frac{n^2 D_i^2 \bar{T}_{in}}{r^2}(r, n, t) = \frac{\partial \bar{T}_{in}}{\partial t}(r, n, t) \tag{21}$$

where $\bar{T}_{in}$ is the singly transformed temperature. The transformation will differ slightly depending on whether it is a sine or cosine transform, but the method of solution is the same in either case so no distinction will be made here.

Equation (21) has the following boundary and initial conditions:

$$\bar{T}_{1n}(r_1, n, t) = 0 \tag{22a}$$

$$K_k \frac{\partial \bar{T}_{kn}}{\partial r}(r_{k+1}, n, t) = \bar{F}_n(n, t) \tag{22b}$$

$$\bar{T}_{in}(r_{i+1}, n, t) = \bar{T}_{i+1,n}(r_{i+1}, n, t), \qquad i = 1, 2, 3, \ldots, k-1 \tag{22c}$$

$$K_i \frac{\partial \bar{T}_{in}}{\partial r}(r_{i+1}, n, t) = K_{i+1} \frac{\partial \bar{T}_{i+1,n}}{\partial r}(r_{i+1}, n, t), \qquad i = 1, 2, 3, \ldots, k-1 \tag{22d}$$

$$\bar{T}_{in}(r, n, 0) = \bar{f}_{in}(r, n) \tag{22e}$$

The solution of equation (21) subject to the boundary and initial conditions given by equation (22) is [7]

$$\bar{T}_{in}(r, n, t) = \sum_{m=1}^{\infty} [g_m e^{-\gamma_{mn} n^2 t} + h_m * e^{-\gamma^2 t_{mn}}] X_{imn}(r) - L_{i2}(r)\bar{F}(n, t) \tag{23}$$

where

$$g_m = \frac{1}{N_m}\sum_{i=1}^{k} \rho_i C p_i \int_{r_i}^{r_{i+1}} r G_i(r) X_{imn}(r) dr, \qquad m = 1, 2, 3, \ldots \tag{24}$$

$$h_m = \frac{1}{N_m}\sum_{i=1}^{k} \rho_i C p_i \int_{r_i}^{r_{i+1}} r H_i(r) X_{imn}(r) dr, \qquad m = 1, 2, 3, \ldots \tag{25}$$

$$N_m = \sum_{i=1}^{k} \rho_i C p_i \int_{r_i}^{r_{i+1}} r[X_{imn}(r)]^2 dr, \qquad m = 1, 2, 3 \ldots \tag{26}$$

$$G_i(r) = \bar{f}_{in}(r, n) + L_{i2}(r)\bar{F}_n(n, 0) \tag{27}$$

and

$$H_i(r) = \frac{n^2 D_i^2}{r^2} L_{i2}(r)\bar{F}_n(n, t) + L_{i2}(r)\frac{d\bar{F}_n}{dt}(n, t) - \frac{D_i^2}{r} C_{i2}\bar{F}_n(n, t) \tag{28}$$

The $L_{i2}(r)$ functions are

$$L_{i2}(r) = C_{i2} r + E_{i2} \tag{29}$$

$$r_i \le r \le r_{i+1}, \qquad i = 1, 2, 3, \ldots, k$$

subject to the following boundary and internal conditions:

$$L_{12}(r_1) = 0 \tag{30a}$$

$$K_k \frac{dL_{k2}}{dr}(r_{k+1}) = -1 \tag{30b}$$

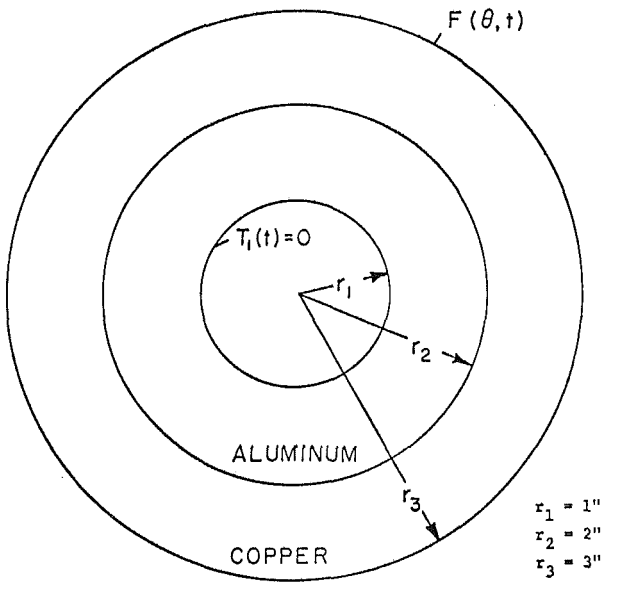

Copper	Aluminum
Density = 556 lb/ft^3	Density = 165 lb/ft^3
Specific Heat = 0.092 Btu/lbm°R	Specific Heat = 0.215 Btu/lbm °R
Thermal Conductivity = 223 Btu/hr ft °R	Thermal Conducitivity = 132 Btu/hr ft °R

Fig. 1 Cross-sectional cylinder

Table 1 Eigenvalues for $n = 0, 1$

$n = 0$	$n = 1$
3.12345409	5.0808430
14.40289511	15.52333932
22.43859863	23.16754150
33.09927368	33.59228516
41.14616394	41.59065247
51.68597412	51.98706055
59.83886719	60.16111755
70.23217773	70.44459543
78.53883362	78.79383850
88.75335683	88.91548157
97.25077466	97.46202087
107.25683594	107.38700867
115.97302246	116.14219116
125.74732971	125.85690308
134.70184326	134.85864258
144.23071289	144.32467651
153.43467712	153.57348633
162.71061707	162.79350281
172.16746521	172.29133606
181.19149780	181.26626587
180.8602661	191.00708878
199.67748023	199.74642068
209.61630249	209.71612549
218.17279053	218.23842676
228.32424927	228.41410828

$$L_{i2}(r_{i+1}) = L_{i+1,2}(r_{i+1}), \qquad i = 1, 2, 3, \ldots, k-1 \tag{30c}$$

$$K_i \frac{dL_{i2}}{dr}(r_{i+1}) = K_{i+1} \frac{dL_{i+1,2}}{dr}(r_{i+1}), \qquad i = 1, 2, 3, \ldots, k-1 \tag{30d}$$

The eigenfunctions $X_{imn}(r)$ are

$$X_{imn}(r) = A_{imn} J_n\left(\frac{\gamma_{mn}}{D_i} r\right) + B_{imn} Y_n\left(\frac{\gamma_{mn}}{D_i} r\right) \tag{31}$$

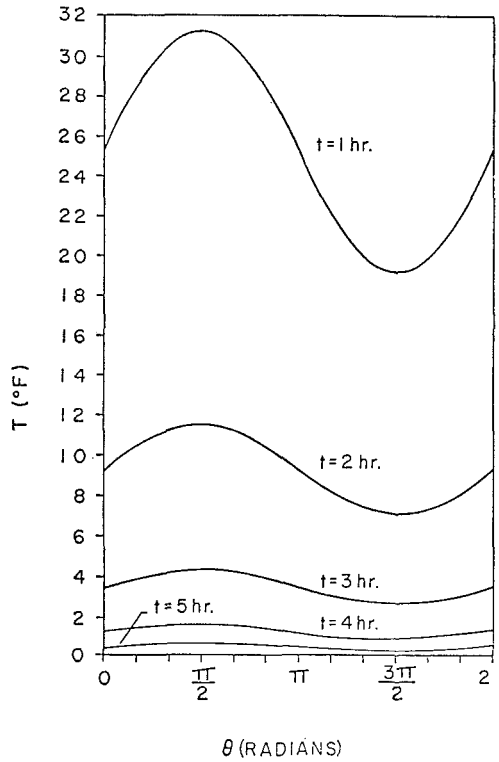

Fig. 2 Temperature versus angular displacement for $r = 0.1750$ ft

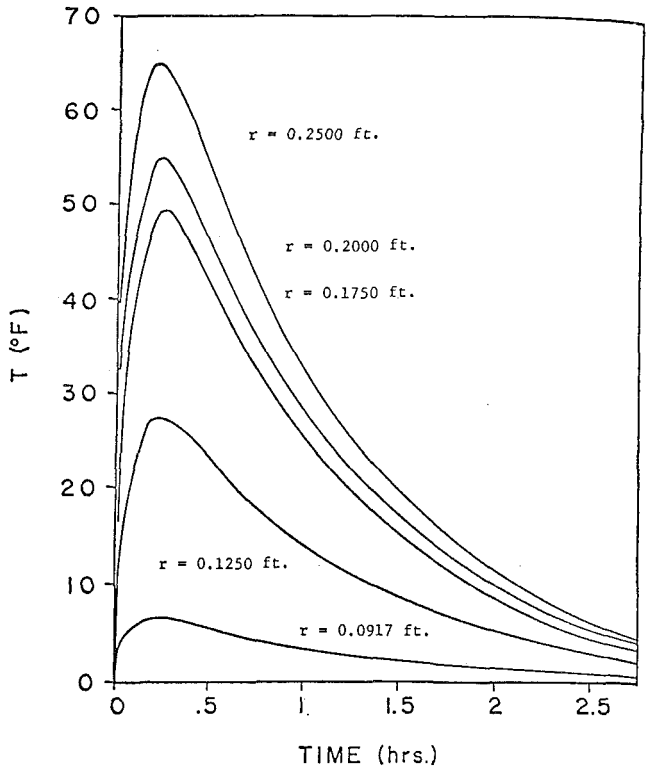

Fig. 3 Temperature versus time for five radii at $\theta = 0$

The constants A_{imn}, B_{imn} and the eigenvalues γ_{mn} are obtained by applying the boundary conditions:

$$X_{1mn}(r_1) = 0 \tag{32a}$$

$$\frac{dX_{kmn}}{dr}(r_{k+1}) = 0 \tag{32b}$$

$$X_{imn}(r_{i+1}) = K_{i+1,mn}(r_{i+1}) \tag{32c}$$

$$K_i \frac{dX_{imn}}{dr}(r_{i+1}) = K_{i+1} \frac{dX_{i+1,mn}}{dr}(r_{i+1}) \tag{32d}$$

to the eigenfunctions X_{imn} [7, 8].

Let $\bar{T}_{in}(r, n_c, t)$ be the solution corresponding to the cosine transform, and $\bar{T}_{in}(r, n_s, t)$ be the solution corresponding to the sine transform. Then the final solution is

$$T_i(r, \theta, t) = \frac{1}{2\pi} \bar{T}_i(r, 0, t) + \frac{1}{\pi} \sum_{n=1}^{\infty} \{\bar{T}_{in}(r, n_c, t) \cos n\theta + \bar{T}_{in}(r, n_s, t) \sin n\theta\} \tag{33}$$

where $\bar{T}_i(r, 0, t)$ is given by equation (10) and where

$$\bar{T}_{in}(r, n_c, t) = \sum_{m=1}^{\infty} [g_{mc} e^{-\gamma_{mn}^2 t} + h_{mc} * e^{-\gamma_{mn}^2 t}] X_{imn}(r) - L_{i2}(r) \bar{F}_{nc}(n, t) \tag{34}$$

and

$$\bar{T}_{in}(r, n_s, t) = \sum_{m=1}^{\infty} [g_{ms} e^{-\gamma_{mn}^2 t} + h_{ms} * e^{-\gamma_{mn}^2 t}] X_{imn}(r) - L_{i2}(r) \bar{F}_{ns}(n, t) \tag{35}$$

Thus the temperature distribution in any of k cylinders subject to a circumferentially varying time dependent heat flux at any position r and θ, and any time t is now known.

Example

Consider the situation where a two-layered composite initially at zero temperature is subjected to a heat flux.

$$F(\theta, t) = [50{,}000 + 25{,}000 \sin \theta]e^{-t} \text{ Btu/hr ft}^2 \quad (36)$$

at the outside wall while the inner wall is held at zero, Fig. 1. In equation (36) the angular displacement in radians is denoted by θ and the time in hours is t.

The eigenvalues of the problem are determined by expanding a four by four determinant and equating it to zero. The first 25 eigenvalues for $n = 0$ and $n = 1$ are shown in Table 1. These are the only values needed since there are only two terms in the expansion for n ($n = 0, 1$); this is due to the form of the heat flux, equation (36).

With the eigenvalues known, the expansions for g_m, h_m, l_{m2}, can be calculated. In addition, the L_{ij} functions are given by

$$L_{12}(r) = (r_3/k_1) \ln (r/r_1) \quad (37)$$

$$L_{22}(r) = (r_3/k) \ln (r_2/r_1) + (r_3/k_2) \ln (r/r_2) \quad (38)$$

for $n = 0$, and

$$L_{12}(r) = (r_1 - r)/k_1 \quad (39)$$

$$L_{22}(r) = (r_1 - r_2)/k_1 + (r_2 - r)/k_2 \quad (40)$$

for $n = 1$.

The resulting temperature distribution is given in Figs. 2 and 3 for various values of position and time.

Conclusions

The problem of determining the transient temperature distribution in a composite cylinder made of k layers with an inside temperature that is an arbitrary function of time, and subject to an external heat flux that is an arbitrary function of both circumferential displacement and time is solved.

References

1 Bulavin, P. E., and Kascheev, V. M., "Solution of the Non-Homogeneous Heat Conduction Equation for Multilayered Bodies," *International Chemical Engineering*, V, Vol. 1, 1965, pp. 112–115.

2 Carslaw, H. S., and Jaeger, J. C., *Conduction of Heat in Solids*, Oxford University Press, London, 1959.

3 Tittle, C. W., "Boundary Value Problems in Composite Media," *Journal of Applied Physics*, XXXVI, Vol. 4, 1965, pp. 1486–1488.

4 Vodicka, V. "Wärmeleitung in geschichteten Kugel-und Zylinderkörpern," *Schweizer Archiv*, Vol. 10, 1950.

5 Vodicka, V. "Eindimensionale Wärmeleitung in geschichteten Körpern," *Mathematische Nachrichten*, Vol. 14, 1955.

6 Tien, C. L., "Heat Transfer in Cryogenic Insulation," *Cryogenic Technology*, VII, Vol. 5, Sept./Oct. 1971, pp. 157–159.

7 Mulholland, G. P., and Cobble, M. N., "Diffusion Through Composite Media," *International Journal of Heat and Mass Transfer*, Vol. 15, 1972, pp. 147–160.

8 Lockwood, J. D., "Heat Transfer Through Composite Cylinders Subjected to a Circumferentially Varying Heat Flux," MS thesis, Mechanical Engineering Department, New Mexico State University, Las Cruces, N. Mex., 1972.

S. A. ANDERSON
Assistant Professor.
Mem. ASME

L. A. HALE
Associate Professor.
Mem. ASME

Department of Mechanical Engineering,
Texas A&M University,
College Station, Texas

H. H. HUNT
Assistant Professor,
Institute of Statistics,
Texas A&M University,
College Station, Texas

P. E. PULLEY
Associate Professor,
Department of Industrial Engineering,
Texas A&M University,
College Station, Texas

A Technique for Determining the Transient Heat Flux at a Solid Interface Using the Measured Transient Interfacial Temperature

A method for determining the transient heat flux across a solid interface, based on experimentally acquired interfacial temperature-time data, is presented. This method results from the application of Duhamel's integral method to a third order natural splined fit of the discrete data. General case closed form equations that result from splined and least-squares modeling of the experimental data are developed, presented and illustrated.

Introduction

THE PROBLEM of accurately measuring a transient interfacial temperature and/or heat flux is common to many technical endeavors. Many specific instances of this problem have, for one reason or another, led to the situation in which the temperature at some point interior to the body has been measured as a function of time in order to predict the temperature or heat flux at the surface of the body. This problem, called the inverse heat conduction problem, has been examined by many authors, among them Mirsepassi [1][1], Stolz [2], Burggraf [3], Sparrow, et al. [4], and Beck [5]. Despite the sophistication of the various techniques which may be used, all inverse techniques suffer from one common fault, namely:

> "In a heat-conduction system the effect of boundary conditions is always damped at interior points, and the inverse problem involves basically the extrapolation of the damped datum to the surface.... [2]."

It seems logical, then, to place the temperature sensing element as close to the surface as possible and, if the physical situation permits, to place the sensor at the surface to avoid this damping of the effect of the boundary conditions associated with the inverse problem. The problem becomes, then, a limiting case of the inverse problem (and the direct problem as well). If the surface temperature is available as a function of time, the evaluation of the heat flux as a function of time becomes a matter of solving the convolution integral equation of Volterra type obtained by the direct application of Duhamel's integral to the temperature-time data. The purpose of this paper is to present a method for simply and accurately evaluating the integral equation for the transient heat flux, given an accurate analog record of the transient surface temperature.

The superposition integral [6] expresses the response of a linear system at time "t," $y(t)$, to a forcing function, $f(t)$, in terms of the response $\chi(t)$ of the system to a unit step increase in the forcing function at time zero,

$$y(t) = \chi(0) \cdot f(t) + \int_0^t \chi'(t - \tau) \cdot f(\tau) d\tau. \qquad (1)$$

In this case let

$y(t) = q(t)$ = the heat flux at the surface of a solid due to a change in surface temperature,

$f(t) = \theta(t)$ = the surface temperature excess where $\theta = T' - T_0$, where T_0 is the surface temperature at time zero and T is the temperature at time t,

[1] Numbers in brackets designate References at end of paper.

Contributed by the Heat Transfer Division of THE AMERICAN SOCIETY OF MECHANICAL ENGINEERS and presented at the AIChE-ASME Heat Transfer Conference, Denver, Colo., August 6-9, 1972. Manuscript received at ASME Headquarters April 10, 1972; revised manuscript received September 22, 1972. Paper No. 72-HT-18.

$\chi(t)$ = the heat flux at the surface at time t due to a unit step increase in θ at time 0.

Then

$$q(t) = \chi(0)\cdot\theta(t) + \int_0^t \chi'(t-\tau)\cdot\theta(\tau)d\tau. \quad (2)$$

If the solid is very thick or if the transient of interest is very short, i.e., if the transient is much shorter than the time constant of the solid, the transient will not "penetrate" very far into the solid and the solid may be treated as if it extended without limit in the direction perpendicular to the interface. Then, neglecting two-dimensional effects and any initial nonuniform temperature distribution in the solid, the temperature distribution in the solid for a unit step change in surface temperature will be

$$T(x, t) = erfc \frac{x}{\sqrt{\pi\alpha_s t}} + T(0). \quad (3)$$

It follows from the definition of $\chi(t)$ that

$$\chi(\tau) = \frac{k_s}{\sqrt{\pi\alpha_s\tau}} \quad (4)$$

and therefore

$$q(t) = \chi(0)\cdot\theta(t) + \int_0^t \left\{-\frac{k_s}{\sqrt{\pi\alpha_s}}(t-\tau)^{-3/2}\right\}\theta(\tau)\cdot d\tau. \quad (5)$$

Integrating by parts and simplifying yields [7]

$$q(t) = \frac{k_s}{\sqrt{\pi\alpha_s}}\left\{\frac{\theta(t)}{\sqrt{t}} + \frac{1}{2}\int_0^t \frac{\theta(t)-\theta(\tau)}{(t-\tau)^{3/2}}\,d\tau\right\}. \quad (6)$$

The evaluation of the integral portion of equation (6) is the central problem of this presentation. The analog data to be used in evaluating equation (6) is ultimately utilized in a digital form consisting of discrete data points of elapsed time and interfacial temperatures. In an attempt to minimize the magnitude of the unknown errors which are inherent in common numerical integration procedures, an effort must be made to reproduce the original analog record, in the best possible analytical form for the evaluation of the integral in closed form.

Data Analysis Technique Based on Polynomial Curve Fitting of the Data

Regression techniques can be applied to the data and a polynomial relationship for the surface temperature-time response can be obtained as

$$T(t) = A_0t^0 + A_1t^1 + \ldots + A_mt^m + \delta,\ 0 \le t \le t_n \quad (7)$$

where δ represents the error between $T(t)$ and the analog record described by the n data points. The A's are coefficients unique to each set of data. In the absence of prior information, determining the degree of an approximating polynomial (equation (7)) is usually subjective and limited only by the number and nature of the data points available. If the experimenter hypothesizes that the error variability is the same and independent of time, then his decision is in part based on the following:

(a) The deviations (observed minus expected value) should be nominally of the same magnitude across the interval of observation.

(b) The signs of the deviations should be uniformly randomly distributed across the interval of observation.

If (a) and (b) are reasonably satisfied, then another criterion comes into play. This criterion may be called economization of parameters. As the degree of an approximating polynomial increases over a given data set, the over-all variance estimate tends to approach a minimum. Eventually a point is reached where increasing the degree of the polynomial has little effect on the variance. This then can determine the minimum degree and hence the minimum parameter set. In the case at hand, an additional constraint was that the approximating polynomial should have no real roots within the interval of observation.

It follows from the definition of $\theta(t)$ that $\theta(t)$ can be defined in terms of the general polynomial of degree m as

$$\theta(t) = T(t) - A_0, \text{ or}$$

$$\theta(t) = A_1t^1 + A_2t^2 + \ldots + A_mt^m + \delta. \quad (8)$$

Substitution of the polynomial relationship for $\theta(t)$ into equation (6) yields

$$q(t) = \frac{k_s}{\sqrt{\pi\alpha_s}}\left[[t^{1/2}(A_1 + A_2t + \ldots + A_mt^{m-1}) + \frac{1}{2}\int_0^t \left\{\frac{(A_1t + A_2t^2 + \ldots + A_mt^m + \delta_1)}{(t-\tau)^{3/2}} - \frac{(A_1\tau + A_2\tau^2 + \ldots + A_m\tau^m + \delta_2)}{(t-\tau)^{3/2}}\right\} d\tau + \frac{\delta_1}{\sqrt{t}}\right] \quad (9)$$

where δ_1 and δ_2 are error terms dependant on t and τ, respectively. The integral portion of equation (9) can be arranged as

$$\frac{1}{2}\int_0^t \frac{\sum_{j=1}^{j=m}(A_jt^j - A_j\tau^j)}{(t-\tau)^{3/2}}\,d\tau + \frac{1}{2}\int_0^t \frac{\delta_1-\delta_2}{(t-\tau)^{3/2}}\,d\tau,$$
$$= \frac{1}{2}\sum_{j=1}^{j=m}\int_0^t \frac{A_j(t^j-\tau^j)}{(t-\tau)^{3/2}}\,d\tau + \frac{1}{2}\int_0^t \frac{\delta_1-\delta_2}{(t-\tau)^{3/2}}\,d\tau. \quad (10)$$

Simplifying each integral on the right side of the equality by

Nomenclature

A = coefficients of temperature-time polynomials
c = specific heat, Btu/lbm deg F
f = a forcing function
h = convective conductance, Btu/hr ft^2 deg F
k = thermal conductivity, Btu/hr ft deg F
P = third order splined fit polynomial
q = heat flux, Btu/hr ft^2 deg F
S = a coefficient of splined data fit
T = temperature, deg F
t = time, hr
x = position coordinate, ft
y = response of a system
α = thermal diffusivity, ft^2/hr
δ = a random error, deg F
θ = the surface temperature excess, deg F
ρ = density, lbm/ft^3
τ = a dummy index having dimension of time
χ = the response of a system to a unit step increase in the forcing function

Subscripts

s = solid
i = summation index
j = summation index
k = summation index
m = order of polynomial data fit
n = number of data points from the analog record
0 = at time zero

Superscripts

(j) = order of derivative with respect to time

partial fractions, and integrating term by term yields, for a single polynomial approximation to a set of n data points,

$$\frac{1}{2}\int_0^t \frac{\theta(t) - \theta(\tau)}{(t - \tau)^{3/2}}\,d\tau$$

$$= \sum_{j=1}^{j=m}\left\{\frac{2^{2j-1}[(j - 1)!]^2}{(2j - 1)!}\,t^{1/2}\sum_{k=j}^{k=m} A_k t^{k-1}\right\}$$

$$+ \frac{1}{2}\int_0^t \frac{\delta_1 - \delta_2}{(t - \tau)^{3/2}}\,d\tau. \qquad (11)$$

Hence

$$q(t) = \frac{k_s}{\sqrt{\pi\alpha_s}}\sum_{k=1}^{k=m} A_k t^{(2k-1)/2}\left[1 + \sum_{j=1}^{j=k}\frac{2^{2j-2}(j - 1)!]^2}{(2j - 1)!}\right]$$

$$+ \frac{1}{2}\int_0^t \frac{\delta_1 - \delta_2}{(t - \tau)^{3/2}}\,d\tau + \delta_1\sqrt{t},\ t_n \geq t \geq t_1,\ t_1 = 0. \qquad (12)$$

The error terms

$$\frac{1}{2}\int_0^t \frac{\delta_1 - \delta_2}{(t - \tau)^{3/2}}\,d\tau \text{ and } \delta_1\sqrt{t},$$

may be of little significance in some cases and may be neglected.

Data Analysis Technique Based on Splined Fitting of the Data

In the event that the error terms associated with the polynomial data fit cannot be neglected, an alternate procedure which is based on third order splined fitting of the data [8][2] may be used. This procedure defines a set of $(n - 1)$ third order polynomials to the $(n - 1)$ intervals which are in turn defined by the n data points over the data interval (t_1, t_n), subject to the following constraints:

1 At each data point, t_i, the polynomials defined for adjacent intervals must be equal; i.e.,

$$P_i(t_i) = P_{i+1}(t_i) = T_i$$

where $P_i(t)$ is defined for the interval $[t_{i-1}, t_i]$ and $P_{i+1}(t)$ is defined for the interval $[t_i, t_{i+1}]$. In addition, the polynomials that span the outermost intervals must pass through the outermost data points.

2 At each data point t_i, (not including the end points t_1 and t_n),

$$P_i^{(j)}(t_i) = P_{i+1}^{(j)}(t_i),\ j = 1, 2.$$

3 The "ripple" (undulation) across the entire interval must be a minimum subject to constraints 1 and 2. This is accomplished by minimizing the integral of $[P^{(2)}(t)]^2$ over the entire data interval, $[t_1, t_n]$, with respect to the coefficients of the polynomials, $P_i(t)$.

With the possible exception of splined data fits that have an order greater than three, under the foregoing criteria, and in the absence of a known analytical function, there is no function or set of functions that can better describe a set of n data points. The least-squares polynomial procedure will not, in general, reproduce the data set. Although the splined procedure does not, in general, reproduce the original analog record, it does reproduce the original data set and it produces a function with minimum ripple between data points. Hence, intuitively, it would produce less error in subsequent manipulations than the results of a polynomial curve fitting procedure across the entire data set.

Table 1 Time-temperature-heat flux, analytical example

Time (sec)	Surface temperature (deg F)	Surface heat flux (Btu/hr-Ft^2)
0.000	100.000	-1.0000×10^5
0.005	94.320	-9.4320×10^4
0.010	92.115	-9.2115×10^4
0.015	90.478	-9.0478×10^4
0.020	89.134	-8.9134×10^4
0.025	87.976	-8.7976×10^4
0.030	86.950	-8.6950×10^4
0.035	86.023	-8.6023×10^4
0.040	85.174	-8.5174×10^4
0.045	84.389	-8.4389×10^4
0.050	83.658	-8.3658×10^4
0.055	82.971	-8.2971×10^4
0.060	82.324	-8.2324×10^4
0.065	81.710	-8.1710×10^4

A natural spline is any spline where the fitting polynomials are of odd order; splines of even order tend to be intractable. While higher than third order splining techniques exist, they become cumbersome mathematically as the order increases and they generally do not yield results that justify the associated additional mathematical complexity of computation. Hence this discussion has been limited to third order splined fits of the data. If a third order splined technique is applied to a set of n data points to yield a set of third order polynomials

$$P_1 = S_{(1,0)} + S_{(1,1)}t + S_{(1,2)}t^2 + S_{(1,3)}t^3,\ t_1 \leq t \leq t_2,\ t_1 = 0,$$

$$P_2 = S_{(2,0)} + S_{(2,1)}t + S_{(2,2)}t^2 + S_{(2,3)}t^3,\ t_2 \leq t \leq t_3,$$

$$P_3 = S_{(3,0)} + S_{(3,1)}t + S_{(3,2)}t^2 + S_{(3,3)}t^3,\ t_3 \leq t \leq t_4,$$

$$P_{n-1} = S_{(n-1,0)} + S_{(n-1,1)}t + S_{(n-1,2)}t^2 + S_{(n-1,3)}t^3,\ t_{n-1} \leq t \leq t_n,$$

then it follows that equation (6) applied to the splined fit of the data points as indicated in the foregoing yields, after considerable algebraic manipulation, the heat flux in segmented form,

$$q(t) = \frac{k_s}{\sqrt{\pi\alpha_s}}\left((2S_{(1,1)}t^{1/2} + \frac{8}{3}\,S_{(1,2)}t^{3/2} + \frac{16}{5}\,S_{(1,3)}t^{5/2}\right.$$

$$\left. + \frac{16}{5}\sum_{i=1}^{i=j}\,[S_{(i,3)} - S_{(i-1,3)}][t - t_i]\right),\ t_n \geq t \geq t_j,\ t_1 = 0. \qquad (13)$$

To illustrate the procedures developed previously, consider the analytical solution for the surface temperature of a semi-infinite homogeneous solid, initially at a uniform temperature T_0 and suddenly exposed to an environmental temperature T_∞ [9],

$$T(t) = [T_0 - T_\infty]\left[e^{(h/k)^2\alpha t}\,erfc\left(\frac{h}{k}\sqrt{\alpha t}\right)\right] + T_\infty. \qquad (14)$$

Table 1 shows the solution for a particular case: $T_0 = 100$ deg F, $T_\infty = 0.0$ deg F, $h = 1000$ BTU/hr ft^2 deg F, $k = 12.249$ BTU/hr ft deg F, $c = 0.094$ BTU/lbm-deg F, $\rho = 556.410$ lbm/ft^3 (the properties of 431 stainless steel).

When a third order splining technique is applied to the temperature-time data of Table 1, subject to the constraints mentioned previously, the set of coefficients in Table 2 is generated. The best polynomial fit to the temperature-time data given in Table 1 yielded the coefficients given in Table 3.

The use of the coefficients from Table 2 in equation (13) and the coefficients from Table 3 in equation (12)[3] produces the heat flux values given in Table 4.

The results of the application of the two techniques for calculating the heat fluxes clearly indicate that the splined technique is superior to the polynomial technique.

While the foregoing example illustrates the techniques developed and presented by equations (12) and (13) for the calculation of heat flux, it can be readily seen that the heat flux

---

[2] While the splined fitting procedure is described in this reference, the computer program from this reference was not used for generating the splined fit coefficients.

[3] The error terms in equation (12) are neglected.

Table 2 Coefficients of the third order splined data fit to the analytical example

k	$S_{(k,0)}$	$S_{(k,1)}$	$S_{(k,2)}$	$S_{(k,3)}$	Time
					0.000
1	1.000×10^{2}	-1.724×10^{3}	1.415×10^{5}	-4.802×10^{6}	
					0.005
2	1.000×10^{2}	-1.724×10^{3}	1.415×10^{5}	-4.802×10^{6}	
					0.010
3	9.445×10^{1}	-5.795×10^{1}	-2.503×10^{4}	7.503×10^{5}	
					0.015
4	9.834×10^{1}	-8.359×10^{2}	2.683×10^{4}	-4.022×10^{5}	
					0.020
5	9.506×10^{1}	-3.451×10^{2}	2.293×10^{3}	6.785×10^{3}	
					0.025
6	9.612×10^{1}	-4.720×10^{2}	7.368×10^{3}	-6.088×10^{4}	
					0.030
7	9.507×10^{1}	-3.663×10^{2}	3.845×10^{3}	-2.174×10^{4}	
					0.035
8	9.500×10^{1}	-3.609×10^{2}	3.691×10^{3}	-2.027×10^{4}	
					0.40
9	9.458×10^{1}	-3.296×10^{2}	2.908×10^{3}	-1.374×10^{4}	
					0.045
10	9.420×10^{1}	-3.037×10^{2}	2.332×10^{3}	-9.474×10^{3}	
					0.050
11	9.454×10^{1}	-3.241×10^{2}	2.740×10^{3}	-1.220×10^{4}	
					0.055
12	9.105×10^{1}	-1.339×10^{2}	-7.172×10^{2}	8.757×10^{3}	
					0.060
13	1.064×10^{2}	-8.996×10^{2}	1.204×10^{4}	-6.214×10^{4}	
					0.065

calculations are dependent on the original temperature record and the predicted temperature record which is obtained from a particular data fitting procedure. Obviously, errors can be introduced into subsequent mathematical procedures when regression polynomials or splined fitting data techniques are used to describe a set of data points and when the mathematical relationship that describes the original temperature record is unknown. In this situation there is no way to bound the errors in the heat flux values. While the splined fit procedure will reproduce the data points precisely and will produce a smooth relation (with minimum ripple) between data points in contrast to a polynomial regression data fitting technique, the values predicted by the splined fit may not correspond to the original data record between data points sampled from the original data record. Intuitively, the use of a splined fit should result in less error and should produce the most accurate results for any given set of data.

If the original data record is in error, i.e., the recorded temperatures are in error, no amount of algebraic manipulation can improve the accuracy of that sequential data set. This second potential source of error in calculation of heat flux arises from errors in the original temperature-time data record. Great caution should be exercised in assuming that the output of a thermocouple accurately represents a particular temperature; aside from recorder errors, thermocouple errors have been shown to be related to depth of the thermocouple junction [10] and to the dissimilarity of thermocouple and base material properties.

Consider as an actual experimental situation, the rapid evaporation of a thin FREON-11 film (<0.001 in. thick) from a 431 stainless steel base material [11]. In this instance a 1/64 in. OD thermocouple was embedded in the base material as illustrated in Fig. 1. The thermocouple junction, Fig. 2, was formed by lightly buffing the surface until electrical continuity existed and was estimated to be less than 10^{-6} in. thick. The sheath

Table 3 Coefficients of the polynomial data fit to the analytical example

(Area for rejection is 0.05)

$$A_0 = 9.995 \times 10^{1} \pm 2.549 \times 10^{-2}$$
$$A_1 = -1.377 \times 10^{3} \pm 1.330 \times 10^{1}$$
$$A_2 = 9.930 \times 10^{4} \pm 2.051 \times 10^{3}$$
$$A_3 = -4.305 \times 10^{6} \pm 1.261 \times 10^{5}$$
$$A_4 = 9.919 \times 10^{7} \pm 3.625 \times 10^{6}$$
$$A_5 = -1.140 \times 10^{9} \pm 4.893 \times 10^{7}$$
$$A_6 = 5.150 \times 10^{9} \pm 2.501 \times 10^{8}$$

Overall variance = 0.130
Degrees of freedom = 7.0

Table 4 Calculated heat fluxes and errors for the analytical example

Time (sec)	Heat fluxes			Heat flux errors			
	Splined fit	Polynomial fit	Actual	Splined fit	Polynomial fit	Splined fit	Polynomial fit
		(Btu/hr-ft²)		Magnitudes		Percent	
0.000	0.000×10^{-1}	0.000×10^{-1}	-1.000×10^{5}	1.000×10^{5}	1.000×10^{5}	−100.00	−100.00
0.005	-1.046×10^{5}	-1.032×10^{5}	-9.488×10^{4}	-9.744×10^{3}	-8.338×10^{3}	10.27	8.79
0.010	-9.232×10^{4}	-9.817×10^{4}	-9.287×10^{4}	5.538×10^{2}	-5.300×10^{3}	−0.60	5.70
0.015	-9.238×10^{4}	-9.027×10^{4}	-9.138×10^{4}	-9.990×10^{2}	1.113×10^{3}	1.09	−1.22
0.020	-9.039×10^{4}	-8.758×10^{4}	-9.015×10^{4}	-2.396×10^{2}	2.570×10^{3}	0.27	−2.85
0.025	-8.938×10^{4}	-8.842×10^{4}	-8.909×10^{4}	-2.834×10^{2}	6.777×10^{2}	0.32	−0.76
0.030	-8.834×10^{4}	-8.956×10^{4}	-8.815×10^{4}	-1.815×10^{2}	-1.411×10^{3}	0.20	1.60
0.035	-8.745×10^{4}	-8.904×10^{4}	-8.730×10^{4}	-1.519×10^{2}	-1.737×10^{3}	0.17	1.99
0.040	-8.664×10^{4}	-8.678×10^{4}	-8.652×10^{4}	-1.211×10^{2}	-2.603×10^{2}	0.14	0.30
0.045	-8.590×10^{4}	-8.428×10^{4}	-8.580×10^{4}	-1.021×10^{2}	1.515×10^{3}	0.12	−1.77
0.050	-8.521×10^{4}	-8.347×10^{4}	-8.512×10^{4}	-8.531×10^{1}	1.650×10^{3}	0.10	−1.94
0.055	-8.457×10^{4}	-8.506×10^{4}	-8.449×10^{4}	-7.898×10^{1}	-5.674×10^{2}	0.09	0.67
0.060	-8.394×10^{4}	-8.639×10^{4}	-8.389×10^{4}	-4.966×10^{1}	-2.497×10^{3}	0.06	2.98
0.065	-8.344×10^{4}	-7.896×10^{4}	-8.332×10^{4}	-1.168×10^{2}	4.356×10^{3}	0.14	−5.23

and wire materials of the thermocouple were chromel and constantan, respectively, because of similiarity in the values of $\sqrt{\rho ck}$ for the various thermocouple elements and the base material. This material selection criterion is suggested by the solution for the transient heat flux from a homogeneous, one-dimensional, semi-infinite solid subject to a step change in surface temperature [12]. In this case the values of $\sqrt{\rho ck}$ for the 431 stainless steel, chromel, and constantan are 24.8, 25.4, and 28.25 BTU/deg F ft^2 hr$^{1/2}$, respectively. To estimate the magnitude of temperature error due to two-dimensional effects caused by the thermocouple, a finite difference, two-dimensional numerical program was developed to determine the temperature distribution in the vicinity of the thermocouple junction. The problem was formulated with a graduated grid system having very small elements in the area of the thermocouple tip. The indicated temperature was taken as the weighed average of the two surface elements at the outer edge of the wire and inner edge of the sheath (see Fig. 2). These annular elements were 0.003125 in. thick and were 0.00125 and 0.001875 in. wide, respectively. The calculated error due to two-dimensional effects was in every case much less than the computational error due to the finite difference technique. This error was less than 0.77 percent in all cases and was less than 0.3 percent after eight iterations (6.5×10^{-4} sec per iteration). The error decreased with increasing iterations to a total time of 0.065 sec at program termination. Hence, for this particular thermocouple arrangement the indicated temperature would be expected to accurately represent the surface temperature-time relationship provided suitable instrumentation is used to monitor and record the thermocouple output.

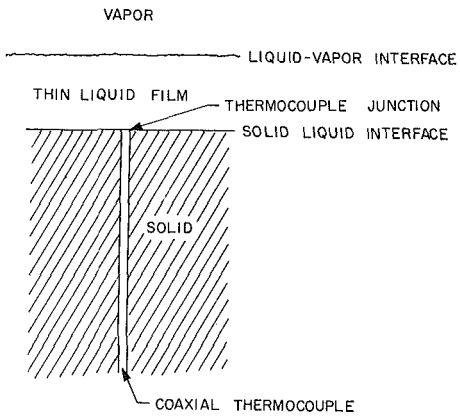

Fig. 1 Thermocouple placement for thin film evaporation test

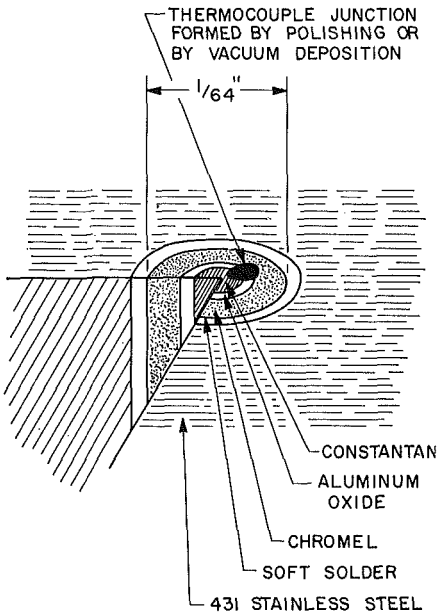

Fig. 2 Placement of a coaxial thermocouple at a solid-surface

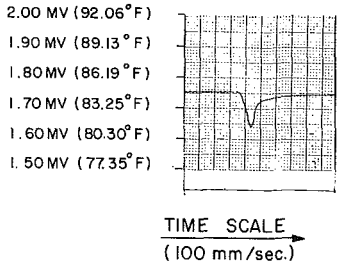

SIGNAL FROM CHROMEL-CONSTANTAN (TYPE "E") THERMOCOUPLE AT SOLID-LIQUID INTERFACE

Fig. 3 Temperature transient due to evaporation of FREON—11 film

Table 5 Time-temperature data from analog record

Time (sec)	Temperature (deg F)
0.000	84.82
0.005	84.78
0.010	84.57
0.015	84.23
0.020	83.82
0.025	83.41
0.030	82.97
0.035	82.36
0.040	81.79
0.045	81.55

Table 6 Coefficients of the polynomial data fit

(Area for rejection is 0.05)

$$A_0 = 8.482 \times 10^{1} \pm 1.611 \times 10^{-1}$$
$$A_1 = -2.028 \times 10^{1} \pm 2.488 \times 10^{0}$$
$$A_2 = 7.827 \times 10^{3} \pm 8.202 \times 10^{2}$$
$$A_3 = -1.567 \times 10^{6} \pm 1.032 \times 10^{5}$$
$$A_4 = 1.004 \times 10^{8} \pm 6.323 \times 10^{6}$$
$$A_5 = -3.049 \times 10^{9} \pm 2.023 \times 10^{8}$$
$$A_6 = 4.376 \times 10^{10} \pm 3.242 \times 10^{9}$$
$$A_7 = -2.352 \times 10^{11} \pm 2.055 \times 10^{10}$$

Overall variance $= 1.936 \times 10^{-2}$
Degrees of freedom $= 2.0$

The interfacial temperature-time response corresponding to the evaporation of the liquid film as determined from the analog record as shown in Fig. 3 is given in Table 5. The best least-squares regression fit to the measured data (Table 5) yielded the coefficients shown in Table 6. A third order splined fit to the same data yielded the coefficients in Table 7. The heat fluxes, as determined from equations (12)[4] and (13), are given in Table 8. An instrumentation recorder[5] was used which should not have produced a significant distortion in the indicated transient.

In the previous analytical example the largest error due to the evaluation of the heat flux integral using the spline fitting technique was 10.3 percent (discounting the heat flux calculation at

[4] The data generated form using equation (12) assumes all δ's are zero; any error term associated with equation (13) is also neglected.

[5] Hewlett-Packard Model 7706B Thermal Recording System with Hewlett-Packard Model 8803A low level Preamplifier.

Table 7 Coefficients of the third order splined data fit

k	$S_{(k,0)}$	$S_{(k,1)}$	$S_{(k,2)}$	$S_{(k,3)}$	Time
					0.000
1	8.482×10^{1}	1.065×10^{1}	-4.161×10^{3}	5.468×10^{4}	
					0.005
2	8.482×10^{1}	1.065×10^{1}	-4.161×10^{3}	5.468×10^{4}	
					0.010
3	8.482×10^{1}	1.013×10^{1}	-4.109×10^{3}	5.295×10^{4}	
					0.015
4	8.448×10^{1}	7.792×10^{1}	-8.628×10^{3}	1.534×10^{5}	
					0.020
5	8.596×10^{1}	-1.466×10^{2}	2.595×10^{3}	-3.375×10^{4}	
					0.025
6	9.090×10^{1}	-7.374×10^{2}	2.623×10^{4}	-3.488×10^{5}	
					0.030
7	7.168×10^{1}	1.184×10^{3}	-3.784×10^{4}	3.631×10^{5}	
					0.035
8	6.290×10^{1}	1.937×10^{3}	-5.934×10^{4}	5.678×10^{5}	
					0.040
9	1.171×10^{2}	-2.132×10^{3}	4.240×10^{4}	-2.800×10^{5}	
					0.045

Table 8 Calculated heat fluxes

Time (sec)	Heat fluxes: Splined data fit (Btu/hr ft)	Polynomial data fit (Btu/hr ft)
0.000	0.000×10^{-1}	0.000×10^{-1}
0.005	-1.806×10^{3}	-1.640×10^{3}
0.010	-6.184×10^{3}	-6.289×10^{3}
0.015	-1.111×10^{4}	-1.119×10^{4}
0.020	-1.539×10^{4}	-1.504×10^{4}
0.025	-1.817×10^{4}	-1.836×10^{4}
0.030	-2.221×10^{4}	-2.255×10^{4}
0.035	-2.870×10^{4}	-2.794×10^{4}
0.040	-3.028×10^{4}	-3.131×10^{4}
0.045	-2.493×10^{4}	-2.269×10^{4}

time zero, an obvious triviality). This large error, at the end of the first time interval, can be ascribed to the discontinuity in the surface temperature at time zero. In real situations this discontinuity never occurs. And, so long as the time interval used in sampling the data record is small compared to the total interval of interest, the error associated with the use of equation (13) will be very small. Considering all sources of error, the total error in instantaneous heat flux measurement in this application, using the splined technique, was considered to be less than ±3 percent.

Summary and Conclusions

The present problem is highly restrictive in that:

(*a*) the thermal properties of the material are assumed constant over the limited range of temperature encountered;

(*b*) the temperature distribution is initially uniform;

(*c*) the solution is developed only for a plane semi-infinite slab;

(*d*) the solid-medium interfacial temperature-time response is the only data available;

(*e*) surface temperature and heat flux, although variable with time, are uniform over the entire surface.

The purpose of the development, also highly restrictive, was to provide a method for accurately and rapidly determining the instantaneous heat flux to a thin liquid film as it rapidly evaporates from a solid surface.

The splined data fitting technique, in conjunction with Duhamel's integral method, (resulting in equation (13)) has been shown to yield results superior to those obtained using the more common polynomial regression data fitting technique. Furthermore, the errors introduced by the mathematical manipulation of the data have been shown to be small.

Acknowledgment

This work was unsponsored and was carried out in the Heat Transfer Laboratory, Department of Mechanical Engineering, Texas A&M University. Support was provided by the Department of Mechanical Engineering, Dr. C. M. Simmang, Head.

References

1 Mirsepassi, T. S., "Heat Transfer Charts for Time-Variable Boundary Conditions," *British Chemical Engineering*, Vol. 1, 1959, pp. 130–136.

2 Stolz, Jr., G., "Numerical Solutions to an Inverse Problem of Heat Conduction for Simple Shapes," JOURNAL OF HEAT TRANSFER, TRANS. ASME, Series C, Vol. 82, No. 2, Feb. 1960, pp. 20–26.

3 Burggraf, O. R., "An Exact Solution of the Inverse Problem in Heat Conduction Theory and Applications," JOURNAL OF HEAT TRANSFER, TRANS. ASME, Series C, Vol. 86, No. 3, Aug. 1964, pp. 373–380.

4 Sparrow, E. M., Hajl-Sheikh, A., and Lundgren, T. S., "The Inverse Problem in Transient Heat Conduction," *Journal of Applied Mechanics*, TRANS. ASME, Vol. 86, Series E, Sept. 1964, pp. 369–375.

5 Beck, James V, "Surface Heat Flux Determination Using an Integral Method," *Nuclear Engineering Design*, Vol. 7, 1968, pp. 170–178.

6 Wylie, C. R., *Advanced Engineering Mathematics*, McGraw-Hill, New York, second ed., 1960, pp. 336–340.

7 Hale, L. A., "An Investigation of the Transition Region of Pool Boiling by Direct Measurement of the Surface Temperature Variations," Dissertation presented to the Faculty of the Graduate School of the University of Texas, Austin, Texas, Aug. 1964.

8 Greville, T. N. E., "Spline Functions, Interpolation, and Numerical Quadrature," in *Mathematical Methods for Digital Computers*, Vol. 2, Ralston, Anthony and Wilf, H. S., eds., Wiley, New York, 1967, pp. 156–168.

9 Carslaw, H. S., and Jaeger, J. C., *Conduction of Heat in Solids*, Second ed., Oxford University Press, London, England, 1959, pp. 70–71.

10 Kovacs, A., and Mesler, R. B., "Making and Testing Small Surface Thermocouples for Fast Response," *The Review of Scientific Instruments*, Vol. 35, No. 4, Apr. 1964, pp. 485–488.

11 Anderson, S. A., "The Evaporation of a Thin Liquid Film From a Solid Surface," Dissertation presented to the Faculty of the Graduate School of Texas A&M University, College Station, Texas.

12 Kreith, F., *Principles of Heat Transfer*, International Textbook Company, Scranton, Pa., 1958, pp. 146–147.

J. L. S. CHEN
Assistant Professor,
Department of Mechanical Engineering,
University of Pittsburgh,
Pittsburgh, Pa. Assoc. Mem. ASME

P. T. RADULOVIC[1]
Graduate Student,
Department of Mechanical Engineering,
University of Michigan,
Ann Arbor, Mich.

Heat Transfer in Non-Newtonian Flow Past a Wedge With Nonisothermal Surfaces

The steady heat transfer in the incompressible laminar boundary layer flow of power law fluids past a wedge having a step discontinuity in surface temperature is studied analytically. The solution method recently introduced by Chao and Cheema is extended to the present problem. The solution is obtained in terms of an infinite set of similar solutions which are expressible as universal functions. Tabulations of such functions are given. For most of the non-Newtonian fluids commonly encountered having large Prandtl numbers, only a very few terms of the functions are needed to yield accurate results.

Introduction

Recently there has been considerable interest in non-Newtonian fluid dynamics and heat transfer due to the growing use of such fluids in various manufacturing and processing industries such as those dealing with plastics, polymers, foods, etc. In the 1950s, research efforts on non-Newtonian fluid flow were concentrated on internal pipe channel flow problems; a review of the subject was given by Metzner [1].[2] Acrivos, et al. [2], Shah [3], and Shah, et al. [4] were probably the first to study in the early 1960's laminar boundary layer flows of non-Newtonian fluids past external surfaces. In their analyses of the thermal boundary layers, a linear velocity distribution similar to Lighthill's approximation [5] was used and hence the solutions were valid only for asymptotically large Prandtl number fluids. Using the Blasius series approach, Wolf and Szewczyk [6] studied the heat transfer to an incompressible, laminar flow of power-law non-Newtonian fluids from an arbitrary symmetrical cylinder, and results were presented only for isothermal circular cylinders. The work offered an improvement over the Lighthill type of approximations used in [2-4] by retaining more terms of the velocity series.

Lee and Ames [7] have established that similarity solutions for forced-convection heat transfer to power-law fluids are possible only for the flow past a right-angle wedge with an isothermal surface. The same conclusion has been independently reported by Luikov, et al. [8].

There appear to be no solutions available in the literature for the heat convection of non-Newtonian fluid flow past a body having a nonisothermal surface except for the special case of Newtonian fluids. Reviews of the general problem of heat transfer to Newtonian fluid flow from nonisothermal surfaces were given by Tribus and Klein [9] in 1952, and by Cheema [10] in 1970. Thus they will not be repeated here.

In a recent paper, Chao and Cheema [11] analyzed theoretically the problem of laminar forced convection heat transfer to Newtonian flow from wedges having nonisothermal surfaces. They developed an ingenious technique of finding temperature profile in the boundary layer and heat flux at the wedge wall when the wall temperature variation was arbitrarily prescribed. The essential features of the solution method are: (i) An appropriate transformation of the energy boundary layer equation leads to an infinite set of ordinary differential equations; this means that the nonsimilar solution of the problem can be decomposed into an infinite sequence of similar solutions; (ii) the solutions of the resulting ordinary differential equations are expressible as universal functions and thus can be tabulated once and for all; (iii) for large Prandtl number fluids, only a very few terms of the functions are needed to give highly accurate results.

In the present work, an analysis is presented of the steady-forced-convection heat transfer in the incompressible, laminar boundary layer flow of power-law fluids past wedges of an arbitrary opening angle having a step change in wall temperatures. The solution method used is an extension of that introduced by Chao and Cheema [11].

Analysis

Consider a steady, two-dimensional, incompressible, laminar boundary-layer flow of non-Newtonian fluids which obey the power-law model past a wedge of included angle $\pi\beta$. The leading portion of the wedge surface of length x_0 measured from the forward stagnation is at the same temperature T_∞ of the incoming free stream fluid; and the remaining portion of the wedge surface, $x > x_0$, is maintained at a uniform temperature T_w which differs from T_∞. Under the assumptions of constant fluid properties and negligible viscous dissipation, the governing boundary

[1] Formerly graduate assistant at the University of Pittsburgh.
[2] Numbers in brackets designate References at end of paper.

Contributed by the Heat Transfer Division and presented at the Winter Annual Meeting, Detroit, Mich., November 11–15, 1973, of The American Society of Mechanical Engineers. Manuscript received by the Heat Transfer Division March 28, 1973. Paper No. 73-WA/HT-29.

layer equations of continuity, momentum, and energy are, respectively,

$$\frac{\partial u}{\partial x} + \frac{\partial v}{\partial y} = 0 \tag{1}$$

$$u\frac{\partial u}{\partial x} + v\frac{\partial u}{\partial y} = U\frac{dU}{dx} + \frac{1}{\rho}\frac{\partial \tau_{xy}}{\partial y} \tag{2}$$

$$u\frac{\partial T}{\partial x} + v\frac{\partial T}{\partial y} = \kappa\frac{\partial^2 T}{\partial y^2} \tag{3}$$

where $U = Cx^m$ and is the velocity outside the boundary layer, C being a constant and $m = \beta/(2 - \beta)$. For power-law fluids, the equation of state is [12]

$$\tau_{xy} = K\left(\frac{\partial u}{\partial y}\right)^n \tag{4}$$

The boundary conditions to be satisfied are:

$$u(x, 0) = v(x, 0) = 0; u(x, \infty) = U \tag{5}$$

$$T(x_0, y > 0) = T_\infty \tag{6}$$

$$T(x > x_0, 0) = T_w; T(x > x_0, \infty) = T_\infty \tag{7}$$

The solution of (1) and (2) with (4) under the boundary conditions (5) is

$$u = Uf', v = -\frac{m - \alpha_2}{\alpha_1} Ux^{-(1+\alpha_2)}\left(\frac{\alpha_2}{m - \alpha_2}\eta f' + f\right) \tag{8}$$

where the similarity variable η is defined as

$$\eta = \alpha_1 y x^{\alpha_2} \tag{9}$$

with

$$\alpha_1 = \left[\frac{\rho C^{2-n}}{K}\cdot\frac{m(2n-1)+1}{n(n+1)}\right]^{\frac{1}{n+1}}, \alpha_2 = \frac{m(2-n)-1}{n+1} \tag{10}$$

and the dimensionless stream function $f(\eta)$ satisfies

$$f''' + f(f'')^{2-n} + \alpha_0[1 - (f')^2](f'')^{1-n} = 0 \tag{11}$$

with

$$f(0) = f'(0) = 0; f'(\infty) = 1. \tag{12}$$

The primes in the foregoing equations denote the differentiation with respect to η, and

$$\alpha_0 = \frac{m(n+1)}{m(2n-1)+1}. \tag{13}$$

Equation (11) with (12) has been recently solved by Hsu and Cothern [13], using Meksyn's method [14]. The series solution is of the form

$$f = \sum_{j=2}^{\infty}\frac{a_j}{j!}\eta^j \tag{14}$$

with

$$a_2 = a, a_3 = -\alpha_0 a^t, a_4 = \alpha_0{}^2 t a^{2t-1},$$
$$a_5 = -\alpha_0{}^3 t(2t-1)a^{3t-2} + (2\alpha_0 - 1)a^{t+2}, \text{ etc.}, \tag{15}$$

where $t = 1 - n$.

Values of a, which is equal to $f''(0)$, for various values of β and n are tabulated in [13]. In order to check the accuracy of those results, we have numerically integrated (11) with the boundary conditions (12), using the data of $f''(0)$ reported in [13] as our starting values. It is found that for $0.6 \leqq n \leqq 2.0$ the discrepancy is 1.67 percent or less, and that for $0.2 \leqq n < 0.6$ it is up to 6.56 percent. To minimize the errors in the present calculation of thermal boundary layers, values of $f''(0)$ numerically recomputed by us will be used. They are plotted in Fig. 1 for β = 0, 0.5, 1.0 (which correspond to a flat plate, a right angle wedge, and the stagnation flow condition, respectively) and for n ranging from 0.2 to 2.0.

Although similarity solutions exist for the velocity boundary layers, the temperature profiles are, in general, nonsimilar due to the presence of the reference length x_0.

To transform the energy equation to an appropriate dimensionless form, we introduce the temperature function

$$\theta = \frac{T - T_\infty}{T_w - T_\infty} \tag{16}$$

and the coordinate transformation

Nomenclature

$a = f''(0)$
a_j = coefficients in series, equation (14)
$b = (a\alpha_3 \mathrm{Pr}/6)^{1/3}$
C = coefficient in Falkner-Skan free stream velocity expression
C_{mn} = parameter defined by (42b)
$c = 3/2\,(m+1)/(n+1)$
f = dimensionless stream function of Falkner-Skan flow
K = parameter in power law model defined by (4)
k = thermal conductivity
M_0, M_1, M_2 = parameters defined by (35)
m = exponent in Falkner-Skan free stream velocity expression
Nu = local Nusselt number
n = flow behavior index defined by (4)
Pr = generalized Prandtl number defined by (19)
q_w = heat flux at wall
Re = generalized Reynolds number defined by (42c)
T = temperature
U = velocity at edge of boundary layer
u = velocity component in x-direction
v = velocity component in y-direction
X = transformed dimensionless coordinate defined by (17a)
x = coordinate along wedge surface
x_0 = length of the wedge surface, measured from the front stagnation, at temperature T_∞
y = coordinate normal to wedge surface
α_0 = parameter defined by (13)
α_1, α_2 = parameters defined by (10)
α_3 = parameter defined by (18)
α_4, α_5 = parameters defined by (22)
β = wedge angle divided by π
$\Gamma(r)$ = gamma function, $= \int_0^\infty z^{r-1}e^{-z}dz$
$\Gamma(r, x)$ = incomplete gamma function, $= \int_0^x z^{r-1}e^{-z}dz$
η = dimensionless coordinate defined by (9)
θ = dimensionless temperature defined by (16)
κ = thermal diffusivity
ξ = transformed dimensionless coordinate defined by (17b)
ρ = density
τ_{xy} = shear stress defined by (4)

Subscripts

w = wedge surface
∞ = free stream

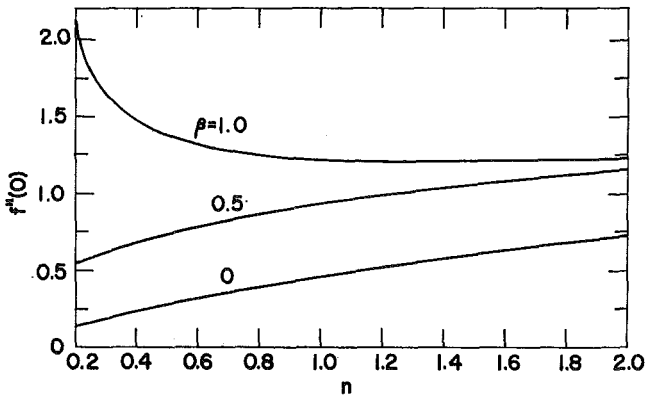

Fig. 1 Values of $f''(0)$ for $\beta = 0$, 0.5, and 1.0

$$X = \left[1 - \left(\frac{x_0}{x}\right)^c\right]^{1/3}, \tag{17a}$$

$$\xi = b\,\frac{\eta}{X} \tag{17b}$$

with $b = (a\alpha_3 \mathrm{Pr}/6)^{1/3}$ and $c = 3/2\,(m+1)/(n+1)$, where

$$\alpha_3 = \left(\frac{1+m}{1+n}\right)\left[\frac{n(n+1)}{m(2n-1)+1}\right]^{\frac{2}{n+1}} \tag{18}$$

and

$$\mathrm{Pr} = \frac{1}{\kappa}\left(\frac{K}{\rho}\right)^{\frac{2}{n+1}} (C^3 x_0^{3m-1})^{\frac{n-1}{n+1}} \tag{19}$$

is the generalized Prandtl number. Using (16) and (17a) and (17b), (3) becomes

$$\frac{\partial^2\theta}{\partial\xi^2} + \frac{\alpha_3}{b}\,\mathrm{Pr}(1-X^3)^{\alpha_4}\left[\alpha_5 X f + \frac{1-X^3}{2X^2}\,\xi\,\frac{df}{d\xi}\right]\frac{\partial\theta}{\partial\xi} - \frac{\alpha_3}{2b}\,\mathrm{Pr}\,\frac{(1-X^3)^{\alpha_4+1}}{X}\,\frac{df}{d\xi}\,\frac{\partial\theta}{\partial X} = 0 \tag{20}$$

with

$$\theta(X > 0, 0) = 1, \tag{21a}$$

$$\theta(X, \infty) = 0 \tag{21b}$$

where

$$\alpha_4 = \frac{2(1-n)(3m-1)}{3(m+1)},\quad \alpha_5 = \frac{m(2n-1)+1}{m+1} \tag{22}$$

It is noted that the argument of the stream function f in (20) is now ξ and that the entrance condition (6) has merged into (21b) because of (17b).

We now seek a series solution for (20) of the form

$$\theta = \sum_{s=0}^{\infty} F_s(\xi) X^s \tag{23}$$

in which X is bounded between 0 and 1 because of (17a), and set

$$F_0(0) = 1,\ F_1(0) = F_2(0) = \ldots = 0; \tag{24a}$$

$$F_0(\infty) = F_1(\infty) = \ldots = 0 \tag{24b}$$

so that the boundary conditions (21a) and (21b) are satisfied. Substituting (23) into (20) and equating the coefficients of like powers of X result

$$F_0'' + 3\xi^2 F_0' = 0 \tag{25}$$

$$F_1'' + 3\xi^2 F_1' - 3\xi F_1 = g_1 F_0' \tag{26}$$

$$F_2'' + 3\xi^2 F_2' - 6\xi F_2 = g_1 F_1' + g_2 F_0' - h_1 F_1 \tag{27}$$

$$F_3'' + 3\xi^2 F_3' - 9\xi F_3 = g_1 F_2' + g_2 F_1' + g_3 F_0' - 2h_1 F_2 - h_2 F_1 \tag{28}$$

etc. In general, for $s \geqq 1$

$$F_s'' + 3\xi^2 F_s' - 3s\xi F_s = g_1 F_{s-1}' + g_2 F_{s-2}' + \ldots + g_s F_0' - (s-1)h_1 F_{s-1} - (s-2)h_2 F_{s-2} - \ldots - h_{s-1} F_1 \tag{29}$$

with

$$g_1 = -\frac{a_3\alpha_3\mathrm{Pr}}{4b^4}\,\xi^3,\ g_2 = -\frac{a_4\alpha_3\mathrm{Pr}}{12b^5}\,\xi^4,$$

$$g_3 = -3(\alpha_5 - \alpha_4 - 1)\xi^2 - \frac{a_5\alpha_3\mathrm{Pr}}{48b^6}\,\xi^5, \text{ etc., and} \tag{30}$$

$$h_1 = \frac{g_1}{\xi},\ h_2 = \frac{g_2}{\xi},\ h_3 = 3\alpha_5\xi + \frac{g_3}{\xi}, \text{ etc.}$$

Equation (25) under the boundary conditions $F_0(0) = 1$ and $F_0(\infty) = 0$ can be solved in closed form and the solution is [11]

$$F_0 = 1 - \frac{\Gamma(1/3,\ \xi^3)}{\Gamma(1/3)} \tag{31}$$

An examination of the general equation (29) reveals that it is always possible to express the functions F_s as linear combinations of universal functions which depend only on ξ and thus they can be tabulated once and for all. Let us define

$$F_1 = M_0 \mathrm{Pr}^{-1/3}\bar{F}_1 \tag{32}$$

$$F_2 = M_0^2 \mathrm{Pr}^{-2/3}(\bar{F}_{2,1} + t\bar{F}_{2,2}) \tag{33}$$

$$F_3 = \mathrm{Pr}^{-1}(M_0^3\bar{F}_{3,1} + M_1\bar{F}_{3,2} + tM_0^3\bar{F}_{3,3}) + M_2\bar{F}_{3,4} \tag{34}$$

with

$$M_0 = -3a_3\left(\frac{3}{4a^4\alpha_3}\right)^{1/3},\ M_1 = -\frac{a_5}{a^2\alpha_3},\ M_2 = \alpha_5 - \alpha_4 - 1 \tag{35}$$

so that (26), (27), and (28) become, respectively,

$$\bar{F}_1'' + 3\xi^2\bar{F}_1' - 3\xi\bar{F}_1 = -3\lambda\xi^3 \tag{36}$$

$$\bar{F}_{2,1}'' + 3\xi^2\bar{F}_{2,1}' - 6\xi\bar{F}_{2,1} = -3/5\lambda\xi^7 \tag{37a}$$

$$\bar{F}_{2,2}'' + 3\xi^2\bar{F}_{2,2}' - 6\xi\bar{F}_{2,2} = 2/3\lambda\xi^4 \tag{37b}$$

$$\bar{F}_{3,1}'' + 3\xi^2\bar{F}_{3,1}' - 9\xi\bar{F}_{3,1} = \xi^3\bar{F}_{2,1}' - 2\xi^2\bar{F}_{2,1} \tag{38a}$$

$$\bar{F}_{3,2}'' + 3\xi^2\bar{F}_{3,2}' - 9\xi\bar{F}_{3,2} = -9/4\lambda\xi^5 \tag{38b}$$

$$\bar{F}_{3,3}'' + 3\xi^2\bar{F}_{3,3}' - 9\xi\bar{F}_{3,3} = 2/15\lambda\xi^8 + \xi^3\bar{F}_{2,2}' - 2\xi^2\bar{F}_{2,2} \tag{38c}$$

$$\bar{F}_{3,4}'' + 3\xi^2\bar{F}_{3,4}' - 9\xi\bar{F}_{3,4} = 9\lambda\xi^2 \tag{38d}$$

where $\lambda = \exp(-\xi^3)/\Gamma(1/3)$. Equations (36) and (38$d$) with the respective boundary conditions $\bar{F}_1(0) = \bar{F}_1(\infty) = 0$ and $\bar{F}_{3,4}(0) = \bar{F}_{3,4}(\infty) = 0$ can be integrated twice to yield the closed form solutions

$$\bar{F}_1 = \frac{1}{5\Gamma(1/3)}\,\xi[\Gamma(4/3) - \Gamma(4/3,\ \xi^3)], \tag{39}$$

$$\bar{F}_{3,4} = -1/2\lambda\xi. \tag{40}$$

It seems that solutions to the remaining universal function equations, (37a) to (38c), could not be obtained in closed forms. Numerical integrations of these equations with the associated homogeneous boundary conditions at $\xi = 0$ and $\xi \to \infty$ have been carried out on an IBM 360 digital computer using a Runge-Kutta iterative procedure with a step size of $\Delta\xi = 0.05$. Since the universal functions F_0, $\bar{F}_1$, $\bar{F}_{2,1}$ (= $\bar{F}_2$ in Chao and Cheema's notation), $\bar{F}_{3,1}$, and $\bar{F}_{3,2}$ are precisely the same as those for the special case of Newtonian fluids given by Chao and Cheema [11], the comparison of our results with their tabulated data shows that

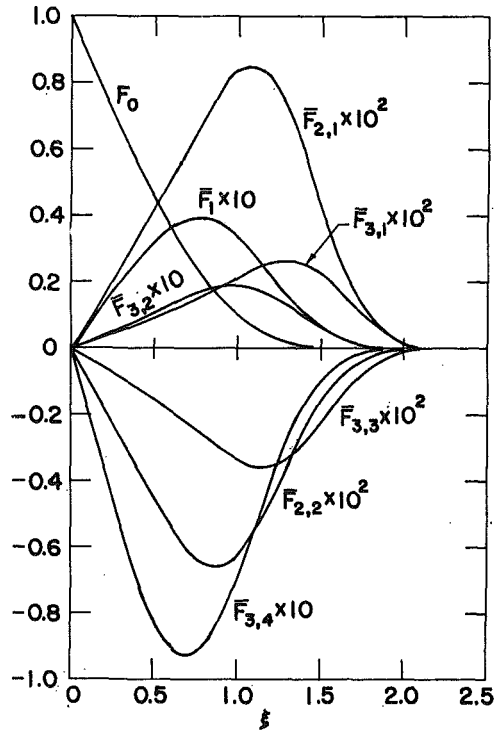

Fig. 2(a) Universal functions for wedges with arbitrary opening angle

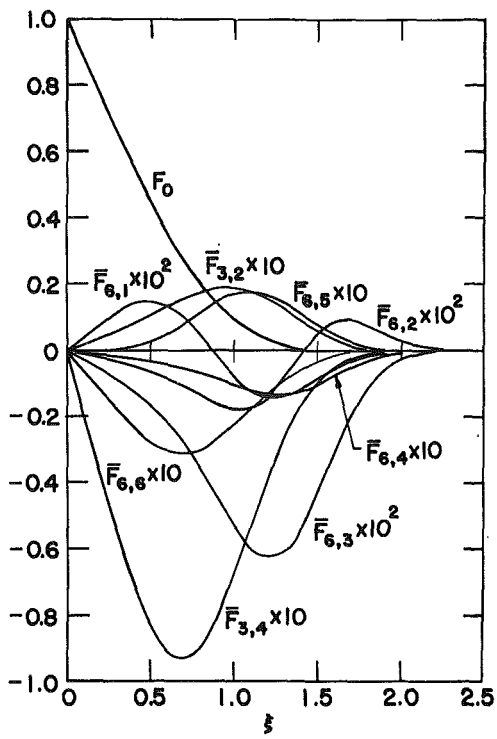

Fig. 2(b) Universal functions for a semi-infinite flat plate

these universal functions for the entire range of ξ and their wall derivatives are in agreement up to the fifth significant digit except for a few cases where the agreement is up to the fourth significant figure. Thus it is only necessary to tabulate the results of the remaining universal functions and their derivatives. They are given in Tables 1 and 2, respectively. Data for all the computed universal functions are also graphically displayed in Figs. 2(*a*) and 2(*b*).

In view of the fact that most of the non-Newtonian fluids commonly encountered are highly viscous and have relatively large Prandtl numbers, highly accurate results are obtainable by retaining only the first several terms of the series solution (23). We shall return to this point later. With those universal functions and their derivatives at the wall already evaluated, the temperature distribution in the boundary layer is:

$$\theta = \sum_{s=0}^{\infty} F_s(\xi)X^s = F_0 + M_0\mathrm{Pr}^{-1/3}\bar{F}_1X + M_0^2\mathrm{Pr}^{-2/3}(\bar{F}_{2,1} + t\bar{F}_{2,2})X^2 + [\mathrm{Pr}^{-1}(M_0^3\bar{F}_{3,1} + M_1\bar{F}_{3,2} + tM_0^3\bar{F}_{3,3}) + M_2\bar{F}_{3,4}]X^3 + \ldots \quad (41)$$

and the heat flux at the wall is

$$q_w = -k\frac{\partial T}{\partial y}(x, 0) = -k(T_w - T_\infty)\alpha_1 b x^{\alpha_2}X^{-1}\frac{\partial\theta}{\partial\xi}(X, 0) \quad (42)$$

so that the corresponding Nusselt number is given by

$$\mathrm{Nu} = \frac{q_w x}{k(T_w - T_\infty)} = -C_{mn}\mathrm{Re}^{\frac{1}{n+1}}\mathrm{Pr}^{1/3}X^{-1}\frac{\partial\theta}{\partial\xi}(X, 0) \quad (42a)$$

where

$$C_{mn} = \left\{\frac{a}{6}\left(\frac{m+1}{n+1}\right)\left[\frac{m(2n-1)+1}{n(n+1)}\right]^{\frac{1}{n+1}}\right\}^{1/3},$$

$$\mathrm{Re} = \frac{\rho}{K}C^{2-n}x^{m(2-n)+n} \quad (42b, c)$$

and

$$-\frac{\partial\theta}{\partial\xi}(X, 0) = -\sum_{s=0}^{\infty}F_s'(0)X^s = 1.1198 - {}^1/_{15}M_0\mathrm{Pr}^{-1/3}X - (0.81748 - 0.90831t)10^{-2}M_0^2\mathrm{Pr}^{-2/3}X^2 - [\mathrm{Pr}^{-1} \times (0.17204 \times 10^{-2}M_0^3 + 0.20737 \times 10^{-1}M_1 - 0.28675 \times 10^{-2}tM_0^3) - 0.18664M_2]X^3 + \ldots \quad (42d)$$

In passing, we note that (41) and (42) with (42*d*) reduce to precisely Chao and Cheema's [11] results for the Newtonian fluid case when $n = 1$.

For asymptotically large Prandtl number ($\mathrm{Pr} \to \infty$) fluids, the Lighthill's method [5] of using a linear velocity distribution is valid. This corresponds to retaining only the first term of the series (14) for f; i.e., $f = {}^1/_2a\eta^2$. Under this condition and in the case of Newtonian fluids, both Bond [15] and Chao and Cheema [11] have shown that the temperature fields are self-similar. If a linear velocity distribution is used for the present problem, all a_j's vanish except a_2 in (14), and (35) gives $M_0 = M_1 = 0$ and $M_2 = \alpha_5 - \alpha_4 - 1$ so that (41) becomes

$$\theta_L = \sum_{s=0}^{\infty}F_s(\xi)X^s = F_0 + M_2\bar{F}_{3,4}X^3 + \ldots, \quad \mathrm{Pr} \to \infty \quad (43)$$

where the subscript L refers to the use of linear velocity distribution. Therefore the temperature field for the problem of power-law non-Newtonian fluids under consideration is in general non-similar even when $\mathrm{Pr} \to \infty$, except for the Newtonian fluid case ($n = 1$) for which all F_s's other than F_0 would vanish [11]. By comparing (41) and (43), the additional terms in (41), which are denoted by θ_c, may be regarded as corrections for the actual velocity profile in departure from the linear distribution so that we have

$$\theta_c = M_0\mathrm{Pr}^{-1/3}\bar{F}_1X + M_0^2\mathrm{Pr}^{-2/3}(\bar{F}_{2,1} + t\bar{F}_{2,2})X^2 + \mathrm{Pr}^{-1}(M_0^3\bar{F}_{3,1} + M_1\bar{F}_{3,2} + tM_0^3\bar{F}_{3,3})X^3 + \ldots \quad (44)$$

It is interesting to note that the series solution, $\theta = \theta_L + \theta_c$, is in ascending powers of $1/\mathrm{Pr}$, and that X is bounded between 0 and 1 as seen from (17*a*). As has been pointed out earlier, most of

Table 1 Universal functions[a]

ξ	$\bar{F}_{2,2} \times 10^2$	$\bar{F}_{3,3} \times 10^2$	$\bar{F}_{3,4} \times 10$	$\bar{F}_{6,3}\dagger \times 10^2$	$\bar{F}_{6,4}\dagger \times 10$	$\bar{F}_{6,5}\dagger \times 10$	$\bar{F}_{6,6}\dagger \times 10$
0.00	0.00000	0.00000	0.00000	0.00000	0.00000	0.00000	0.00000
0.10	−0.09085	−0.02869	−0.18645	−0.02769	−0.00691	0.00005	−0.06215
0.20	−0.18197	−0.05756	−0.37031	−0.05585	−0.01380	0.00074	−0.12344
0.30	−0.27373	−0.08707	−0.54501	−0.08576	−0.02063	0.00368	−0.18167
0.40	−0.36581	−0.11789	−0.70028	−0.11950	−0.02742	0.01120	−0.23343
0.50	−0.45604	−0.15080	−0.82355	−0.16000	−0.03443	0.02574	−0.27452
0.60	−0.53936	−0.18655	−0.90230	−0.21067	−0.04234	0.04872	−0.30077
0.70	−0.60757	−0.22535	−0.92713	−0.27452	−0.05226	0.07950	−0.30904
0.80	−0.65053	−0.26626	−0.89483	−0.35230	−0.06542	0.11454	−0.29828
0.90	−0.65881	−0.30625	−0.81031	−0.43999	−0.08231	0.14768	−0.27010
1.00	−0.62727	−0.33984	−0.68661	−0.52677	−0.10172	0.17165	−0.22887
1.10	−0.55795	−0.35962	−0.54244	−0.59559	−0.12023	0.18050	−0.18081
1.20	−0.46071	−0.35847	−0.39786	−0.62754	−0.13283	0.17187	−0.13262
1.30	−0.35100	−0.33265	−0.26965	−0.60930	−0.13491	0.14811	−0.08988
1.40	−0.24526	−0.28433	−0.16805	−0.54012	−0.12448	0.11528	−0.05602
1.50	−0.15627	−0.22177	−0.09580	−0.43373	−0.10346	0.08083	−0.03193
1.60	−0.09028	−0.15654	−0.04969	−0.31338	−0.07696	0.05088	−0.01656
1.70	−0.04702	−0.09927	−0.02332	−0.20249	−0.05096	0.02865	−0.00777
1.80	−0.02196	−0.05618	−0.00985	−0.11634	−0.02988	0.01436	−0.00328
1.90	−0.00914	−0.02820	−0.00372	−0.05911	−0.01544	0.00638	−0.00124
2.00	−0.00338	−0.01248	−0.00125	−0.02642	−0.00700	0.00250	−0.00042
2.10	−0.00110	−0.00484	−0.00037	−0.01034	−0.00277	0.00086	−0.00012
2.20	−0.00031	−0.00164	−0.00010	−0.00352	−0.00095	0.00026	−0.00003
2.30	−0.00008	−0.00048	−0.00002	−0.00104	−0.00028	0.00007	−0.00001
2.40	−0.00002	−0.00012	0.00000	−0.00026	−0.00007	0.00002	0.00000

[a] The universal functions F_0, $\bar{F}_1$, $\bar{F}_{2,1}$, $\bar{F}_{3,1}$, $\bar{F}_{3,2}$, $\bar{F}_{6,1}\dagger$ and $\bar{F}_{6,2}\dagger$ are identical to those given by Chao and Cheema [11] and the tabulated results of these functions may be found in [11].
† $\bar{F}_{6,1}$, $\bar{F}_{6,2}$, $\bar{F}_{6,3}$, $\bar{F}_{6,4}$, $\bar{F}_{6,5}$, $\bar{F}_{6,6}$ are valid for $\beta=0$ only.

Table 2 Wall derivatives of the universal functions[a]

$\bar{F}_{2,2}'(0)$	-0.90831×10^{-2}	$\bar{F}_{6,4}'(0)$	-0.69126×10^{-2}
$\bar{F}_{3,3}'(0)$	-0.28675×10^{-2}	$\bar{F}_{6,5}'(0)$	-0.56684×10^{-10}
$\bar{F}_{3,4}'(0)$	-0.18664	$\bar{F}_{6,6}'(0)$	-0.62214×10^{-1}
$\bar{F}_{6,3}'(0)$	-0.27651×10^{-2}		

[a] Values of $F_0'(0)$, $\bar{F}_1'(0)$, $\bar{F}_{2,1}'(0)$, $\bar{F}_{3,1}'(0)$, $\bar{F}_{3,2}'(0)$, $\bar{F}_{6,1}'(0)$, and $\bar{F}_{6,2}'(0)$ can be found in [11].

the non-Newtonian fluids commonly encountered have large Pr. For these fluids, the series would appear to be convergent, and its "apparent" convergence becomes very rapid near the leading edge of a thermal boundary layer (near $x = x_0$), even for small Pr. It is of further interest to point out that the correction (44) vanishes at the surface temperature discontinuity ($x = x_0$) so that the asymptotic solution of (43) would mathematically become exact. However, at $x = x_0$, the rate of heat transfer at the wall becomes infinite as shown by (42). This result which can hardly be realized physically is due to the usual defect of boundary layer approximations arising from the omission of diffusion terms involving $\partial^2/\partial x^2$. Thus we should not expect (42) to remain valid in the immediate neighborhood of $x = x_0$. As a last remark, we note that when $\Pr \leq 1$, $\beta = 1$ and $n = 0.2$ the solution series does not converge. One might assume that, in general, it is semidivergent and Euler's transformation may be used to evaluate its sum [14, 16].

In the case of longitudinal flow past a semi-infinite flat plate ($\beta = 0$), $M_0 = 0$ so that $F_1 = F_2 = 0$ and $F_3 = M_1\Pr^{-1}\bar{F}_{3,2} + M_2\bar{F}_{3,4}$. It can also be shown that $F_4 = F_5 = 0$ when $\beta = 0$. In order to provide one more nonvanishing term in the series solution for this case, F_6 can be expressed as a combination of six universal functions as follows:

$$F_6 = M_1\Pr^{-1}\bar{F}_{6,1} + M_1^2\Pr^{-2}\bar{F}_{6,2} + tM_1^2\Pr^{-2}\bar{F}_{6,3} + M_1M_2\Pr^{-1}\bar{F}_{6,4} + M_2^2\bar{F}_{6,5} + 2M_2\bar{F}_{6,6} \quad (45)$$

In (45), the first two universal functions $\bar{F}_{6,1}$ and $\bar{F}_{6,2}$ are identical to those given in [11] and the tabulated data for these two functions can be found therein; numerical results for the remaining universal functions $\bar{F}_{6,3}$, $\bar{F}_{6,4}$, $\bar{F}_{6,5}$, $\bar{F}_{6,6}$ and their wall derivatives are included in Tables 1 and 2, respectively. Thus, for the case of flow past a flat plate, the temperature distribution in the boundary layer is

$$\theta = \sum_{s=0}^{\infty} F_s(\xi)X^s = F_0 + (M_1\Pr^{-1}\bar{F}_{3,2} + M_2\bar{F}_{3,4})X^3 + (M_1\Pr^{-1}\bar{F}_{6,1} + M_1^2\Pr^{-2}\bar{F}_{6,2} + tM_1^2\Pr^{-2}\bar{F}_{6,3} + M_1M_2\Pr^{-1}\bar{F}_{6,4} + M_2^2\bar{F}_{6,5} + 2M_2\bar{F}_{6,6})X^6 + \ldots \quad (46)$$

and the wall heat flux can be calculated from (42) by putting $m = 0$ and with

$$-\frac{\partial\theta}{\partial\xi}(X, 0) = 1.1198 - (0.20737 \times 10^{-1}M_1\Pr^{-1} - 0.18664M_2)X^3 - (0.41502M_1\Pr^{-1} - 0.10445M_1^2\Pr^{-2} - 0.27651tM_1^2\Pr^{-2} - 0.69126M_1M_2\Pr^{-1} - 0.56684 \times 10^{-8}M_2^2 - 12.4428M_2)10^{-2}X^6 + \ldots \quad (47)$$

in which M_1 and M_2 are given by (35). It is noted that for asymptotically large Prandtl number ($\Pr \to \infty$) fluids, $M_1 = 0$.

The local Nusselt number at the wedge surface can be readily calculated by using (42a) together with (42d) or (47). The heat transfer rates as a function of x_0/x are illustrated in Figs. 3(a) and 3(b) for, respectively, one pseudoplastic fluid having flow behavior index $n = 0.5$ and one dilatant fluid having $n = 1.5$. In these figures, Pr equal to 1, 10 and 100 and β equal to 0, 0.5 and 1.0 have been chosen. The results for large Pr follow the general trend, like the case of Newtonian fluid flow past an isothermal wedge [16], that $\mathrm{Nu}\cdot\mathrm{Re}^{-1/(1+n)}$ varies as $\Pr^{1/3}$ for all values of β and n considered. The influence of β is clearly revealed. Data for the accelerated flow ($\beta = 0.5$ and 1.0) lie above that for the flat plate ($\beta = 0$) since higher flow acceleration results in a larger temperature gradient at the wall. This effect is most pronounced for Pr = 100 and gradually decreases with decreasing Pr. Fig. 4 shows the effect of the flow behavior index on the local Nusselt number of an isothermal surface when Pr = 10 for various values of β and Re. As expected, Nu decreases with increasing n.

Comparison of Results

The accuracy of the results for the case of Newtonian fluid flow ($n = 1.0$) past a wedge by using a finite number of terms of the

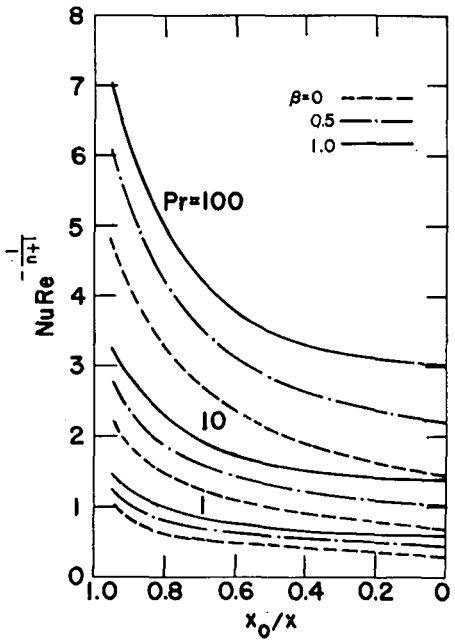

Fig. 3(a) Local heat transfer for $n = 0.5$

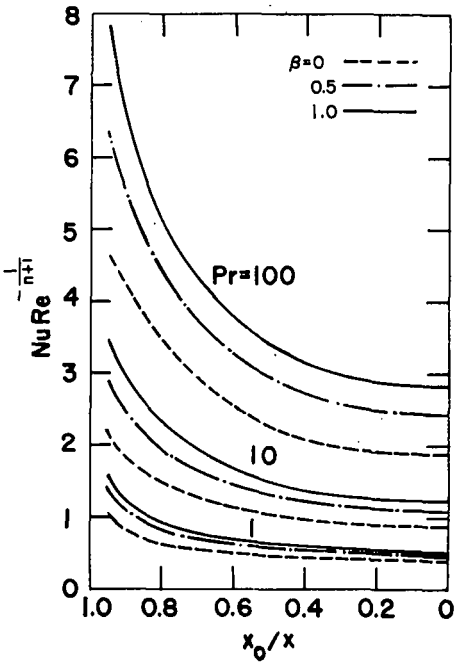

Fig. 3(b) Local heat transfer for $n = 1.5$

series solution (23) was examined by Chao and Cheema [11]. They showed that for Newtonian fluids having Pr of the order of unity or larger, only a very few terms were needed to yield highly *accurate results. To the authors' knowledge, the only exact* solution available for the present problem under investigation is the similar solution for the special case of non-Newtonian fluid flow past a wedge with 90 deg included angle ($\beta = 0.5$) having an isothermal surface ($X = 1$) reported by Lee and Ames [7]. Comparison of our results with theirs for the local heat transfer rate at the isothermal wedge surface for $\beta = 0.5$ and Pr = 0.8, 1, 5, 10, 100, and 300 is presented in Fig. 5. Four terms in the series (42*d*) are used to calculate $\mathrm{NuRe}^{-1/(1+n)}$ given by (42*a*). It is found that the errors resulting from using the limited number of terms in the series are within 2 percent when $0.6 \leqq n \leqq 2.0$ and within 4.5 percent when $0.2 \leqq n < 0.6$. It appears that the

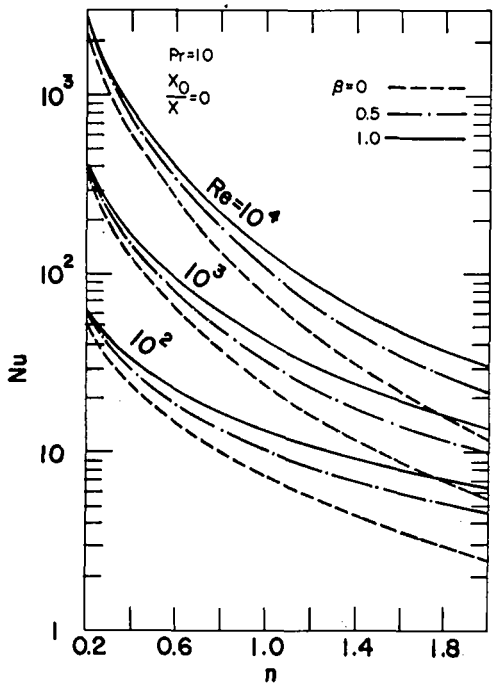

Fig. 4 Local Nusselt number versus n

errors are insensitive to Pr. This is due to the fact that the corrections for the linear velocity distribution are still small in the range of Pr shown in Fig. 5. The significance of the corrections for a given flow behavior index n increases with increasing longitudinal flow pressure gradient (or β) as well as with decreasing Pr.

Eckert [17] reported results of the exact solution for the heat transfer in the stagnation region of cylindrical bodies ($\beta = 1.0$) having isothermal surfaces ($X = 1.0$) in a Newtonian flow ($n = 1$) normal to their axes. Recently, Elzy and Sisson [18] tabulated data of a numerical computation for wall temperature gradients in laminar boundary layer Newtonian flow past an isothermal wedge for wide ranges of Pr and β. Table 3 compares the results of our calculation by using four terms in the series (42*d*) with those reported in [17] and [18]. Eckert's results are identical to those numerical data tabulated in [18] except for Pr = 10 for which Eckert's result is slightly higher. This might be due to a computational error in [17]. It is seen that the agreement of our results with those in [18] is very good, particularly for higher Pr fluids.

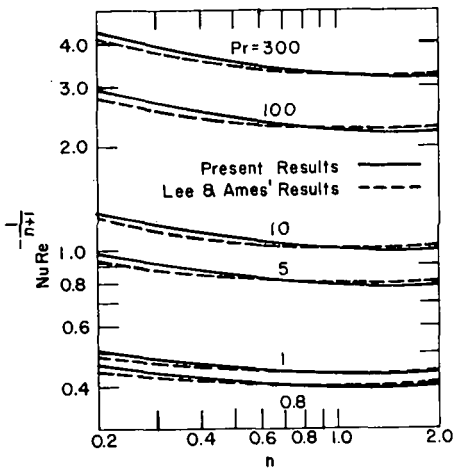

Fig. 5 Comparison of heat transfer results for an isothermal wedge surface with 90 deg included angle ($\beta = 0.5$)

Table 3 Comparison of results of $Nu \cdot Re^{-1/2}$ for $\beta = 1.0$, $n = 1.0$, and $X = 1.0$. Values in parentheses are percentage errors

Pr	0.7	0.8	1.0	5.0	10.0	100	1000
Elzy and Sisson [18]	0.496	0.523	0.570	1.043	1.339	2.986	6.529
Eckert [17]	0.496 (0.0)	0.523 (0.0)	0.570 (0.0)	1.043 (0.0)	1.344 (+0.37)		
Present, (42*a*)	0.486 (−1.94)	0.514 (−1.72)	0.562 (−1.35)	1.038 (−0.48)	1.333 (−0.45)	2.981 (−0.17)	6.523 (−0.09)

Concluding Remarks

The present analysis presents solutions for heat transfer in the boundary layer flow of power law fluids past a wedge having a step discontinuity in surface temperature. Since the energy equation (3) is linear, solutions for problems with an arbitrary surface-temperature variation can be obtained through either Duhamel's integral or numerical superposition. (A detailed discussion of the superposition method may be found elsewhere, for example, in [17].) The analytical procedure provides a relatively simple and rapid means of computing surface heat flux and temperature field. For power-law non-Newtonian fluids frequently encountered having large Pr, only a very few terms of the solution series are needed to yield accurate results. There appear to be no general solutions available to the present problem for comparison except those for a few special cases mentioned in the text. Finally, it can be concluded that the present theory offers a significant improvement over Lighthill's approximation for $Pr \rightarrow \infty$ used by Acrivos, et al. [2], Shah [3], and Shah, et al. [4].

References

1 Metzner, A. B., "Heat Transfer in Non-Newtonian Fluids," *Advances in Heat Transfer*, Vol. 2, 1965, pp. 357–397.

2 Acrivos, A., Shah, M. J., and Petersen, E. E., "Momentum and Heat Transfer in Laminar Boundary-Layer Flows of Non-Newtonian Fluids Past External Surfaces," *AIChE Journal*, Vol. 6, No. 2, 1960, pp. 312–317.

3 Shah, M. J., "On the Rate of Heat Transfer in Laminar Boundary-Layer Flows of Non-Newtonian Fluids Past a Horizontal Cylinder," PhD thesis, University of California, Berkeley, 1961.

4 Shah, M. J., Petersen, E. E., and Acrivos, A., "Heat Transfer From a Cylinder to a Power-Law Non-Newtonian Fluid," *AIChE Journal*, Vol. 8, No. 4, 1962, pp. 542–549.

5 Lighthill, M. J., "Contributions to the Theory of Heat Transfer Through a Laminar Boundary-Layer," *Proc. Roy. Soc. London*, Vol. A202, 1950, pp. 359–377.

6 Wolf, C. J., and Szewczyk, A. A., "Laminar Heat Transfer to Power-Model Non-Newtonian Fluids From Arbitrary Cylinders," *Proc. 3rd Int'l Heat Transfer Conf.*, Chicago, Ill., Vol. I, 1966, pp. 388–397.

7 Lee, S. Y., and Ames, W. F., "Similarity Solutions for Non-Newtonian Fluids," *AIChE Journal*, Vol. 12, No. 4, 1966, pp. 700–708.

8 Luikov, A. V., Shulman, Z. P., and Berkovsky, B. M., "Heat and Mass Transfer in a Boundary Layer of Non-Newtonian Fluids," *Proc. 3rd Int'l. Heat Transfer Conf.*, Chicago, Ill., Vol. I, 1966, pp. 377–387.

9 Tribus, M., and Klein, J., "Forced Convection From Non-Isothermal Surfaces," Heat Transfer Symposium, Engineering Research Institute, University of Michigan, Aug. 1952.

10 Cheema, L. S., "Forced Convection in Laminar Boundary Layer Over Wedges of Arbitrary Temperature and Flux Distribution," PhD thesis, University of Illinois at Urbana-Champaign, 1970.

11 Chao, B. T., and Cheema, L. S., "Forced Convection in Wedge Flow With Non-Isothermal Surfaces," *International Journal of Heat and Mass Transfer*, Vol. 14, 1971, pp. 1363–1375.

12 Schowalter, W. R., "The Application of Boundary-Layer Theory to Power-Law Pseudoplastic Fluids: Similar Solutions," *AIChE Journal*, Vol. 6, No. 1, 1960, pp. 24–28.

13 Hsu, C. C., and Cothern, J. H., "Falkner-Skan Flows of Power-Law Fluids," ASME Paper No. 71-FE-35.

14 Meksyn, D., *New Methods in Laminar Boundary-Layer Theory*, Pergamon Press, New York, 1961.

15 Bond, R., "Heat Transfer to a Laminar Boundary Layer With Non-Uniform Free Stream Velocity and Non-Uniform Wall Temperature," Institute of Eng. Research Ser. 2, No. 10, University of California, Berkeley, 1950.

16 Chen, J. L. S., and Chao, B. T., "Thermal Response Behavior of Laminar Boundary Layers in Wedge Flow," *International Journal of Heat and Mass Transfer*, Vol. 13, 1970, pp. 1101–1114.

17 Eckert, E. R. G., and Drake, R. M., Jr., *Heat and Mass Transfer*, 2nd ed., McGraw-Hill, New York, 1959, pp. 178–184.

18 Elzy, E., and Sisson, R. M., *Tables of Similar Solutions to the Equations of Momentum, Heat and Mass Transfer in Laminar Boundary Layer Flow*, Engineering Experiment Station Bulletin No. 40, Oregon State University, Corvallis, 1967.

D. J. WILSON
Associate Professor,
Department of Mechanical Engineering,
University of Alberta,
Edmonton, Canada

R. J. GOLDSTEIN
Professor,
Department of Mechanical Engineering,
University of Minnesota,
Minneapolis, Minn.

Effect of Film Cooling Injection on Downstream Heat Transfer Coefficients in High Speed Flow

An experimental and theoretical investigation was performed to examine the effect of film cooling injection from a two-dimensional slot on the downstream surface heat transfer. The coolant gas was ejected normal to the wall from a porous section on a flat plate under a supersonic Mach 3 mainstream. The mass velocity of injection was 1 percent to 2 percent of the mainstream value and resulted in decreases of 10 percent to 20 percent in the heat transfer coefficients near the slot. A simple theoretical model was formulated which accounted for the effect of the injection on thickening the boundary layer, and which accurately predicted the moderate decreases in heat transfer coefficients observed in the experiments.

Introduction

Most previous analytical and experimental investigations of film cooling have focused their attention on the temperature along an adiabatic wall downstream from a slot or row of holes from which the coolant gas was ejected. A recent review of the extensive literature concerning film cooling is available [1].[1]

In general real surfaces are not adiabatic. Eckert [2] suggested in 1953 that if the heat transfer coefficient was defined as

$$h = \frac{q_w}{(T_w - T_{aw})} \tag{1}$$

with the adiabatic wall temperature T_{aw} evaluated in the presence of film cooling, then the heat transfer coefficient h_0 for a surface without film cooling could be employed. Scesa [3], and Seban, Chan, and Scesa [4], investigating both normal and tangential slots verified that using $(T_w - T_{aw})$ to define h allows the use of $h \cong h_0$ at large distances from the slot. Near the slot they found that injection increased h above h_0 for normal injection with $M = 0.52$ to 0.70. Seban [5], using a step tangential slot confirmed that for x greater than about 50 to 70 slots heights $h = h_0$ is a good approximation.

Hartnett, Birkebak, and Eckert [6] measured the heat transfer and effectiveness downstream from a flush tangential slot in both favorable and adverse pressure gradients as well as in a zero pressure gradient. Although the pressure gradient changed h_0 by up to a factor of 2, the ratio h/h_0 was altered only slightly by acceleration or deceleration. Later experiments by Seban and Back [7] with a step slot confirmed this behavior. For the zero pressure gradient case Hartnett, Birkebak, and Eckert [6, 8] found that for low M, $h/h_0 < 1$ was observed, and increases in M caused further slight decreases in h/h_0. At higher M values the reverse was true with $h/h_0 > 1$, and increasing M causing substantial increases in h/h_0. Metzger, Carper, and Swank [9], and Metzger and Fletcher [10], measured heat transfer coefficients averaged in the streamwise direction behind an angled slot, finding no apparent systematic dependence on the injection parameter M, which ranged from 0.24 to 1.00. Parthasarthy and Zakkay [12] performed heat transfer and skin friction measurements in supersonic flow at a Mach number of 6 behind an axisymmetric tangential step slot. A decrease in skin friction of about 40 percent at $M = 0.75$ was observed, implying a similar decrease in the heat transfer coefficient.

Analytical Model for Heat Transfer With Film Cooling

A review of the existing data indicates that as the rate of film cooling injection is increased, the heat transfer coefficient h undergoes first a decrease and then at higher rates of injection, a substantial increase over its zero injection value h_0. This observation lends support to the hypothesis that there are two opposing effects caused by the injection, one of which dominates at small M and the other at large M. A likely choice for these two opposing effects are boundary layer thickening and increased turbulence. In the present analysis we consider only the situation where the rate of injection is small enough so that boundary layer thickening is the dominant effect.

[1] Numbers in brackets designate References at end of paper.

Contributed by the Heat Transfer Division for publication (without presentation) in the Journal of Heat Transfer. Manuscript received by the Heat Transfer Division, August 8, 1972. Paper No. 73-HT-T.

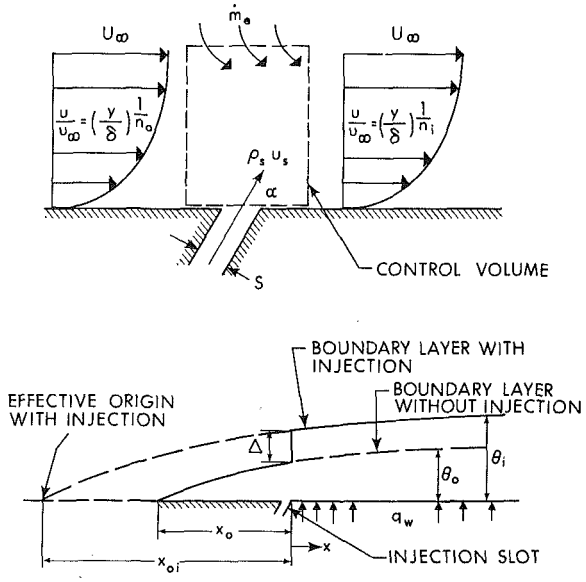

Fig. 1 Model for effect of film cooling

The model used to account for the effect of injection on downstream heat transfer is shown schematically in Fig. 1. The net effect of the film cooling injection on the heat transfer downstream from the slot is to shift the effective origin of the boundary layer from a distance x_0 upstream of the slot to a new location x_{0i}, and to change the velocity profile from a $1/n_0$ to a $1/n_i$ power law. It is assumed that the injected fluid remains within the boundary layer. It is not physically realistic to assume that the distorted velocity profile will retain its $1/n_i$ power law at distances far from the slot. At large values of x the boundary layer will again assume its equilibrium $1/n_0$ power law shape with n_0 only a weak function of Re_x. However, the present investigation will focus its attention on the region close to the slot where n_i will be taken as constant in order to allow a qualitative examination of the effects of velocity profile distortion.

The effect of an adiabatic hydrodynamic starting length has been determined by Reynolds, Kays, and Kline [13], whose analysis yields, for temperature and velocity profiles obeying a $1/n$ power law,

$$\mathrm{St}_* = \overline{\mathrm{St}_*}\left[1 - \left(\frac{\theta(0)}{\theta(x)}\right)^{\frac{n+2}{n+1}}\right]^{-\frac{1}{n+2}} \tag{2}$$

for a constant wall temperature on the heated surface. Reynolds, Kays, and Kline [14] also verified the existence of a modified Colburn analogy,

$$\overline{\mathrm{St}_*} = \frac{C_{f*}}{2}\mathrm{Pr}_*^{-0.4} \tag{3}$$

The preceding equations were developed for incompressible flows and have been extended to compressible flows by evaluating the fluid properties at a reference state, defined by a reference temperature, T_*. To permit a closed form solution, this reference temperature will be taken as independant of x, and of injection temperature.

The empirical skin friction relation developed by Ludwig and Tillman [16] is,

$$\frac{C_{f*}}{2} = \frac{0.123}{(10)^{0.678\left(\frac{n+2}{n}\right)}}\left(\frac{\rho_* u_\infty \theta}{\mu_*}\right)^{-0.268} \tag{4}$$

Using (4) in the integral momentum equation for a compressible boundary layer with a uniform mainstream, [22]

$$\frac{\theta}{\bar{x}} = \frac{0.230}{(10)^{0.535\left(\frac{n+2}{n}\right)}}\left(\frac{\rho_* u_\infty \bar{x}}{\mu_*}\right)^{-0.21}\left(\frac{\rho_*}{\rho_\infty}\right) \tag{5}$$

Substituting (5) in (4) to find C_{f*} in terms of x and then combining this with (2) and (3) yields

Nomenclature

A_1, A_2, A_3 = constants defined in equations (6), (7), and (11)
C_{f*} = $2\tau_w/\rho_* u_\infty^2$, skin friction coefficient
h = heat transfer coefficient, defined in (1)
h/h_0 = ratio of heat transfer coefficients with and without film cooling at the same location and mainstream conditions
M = $\rho_s u_s/\rho_\infty u_\infty$, injection parameter, ratio of mass velocity of injection to that of mainstream
$\dot{m}_e$ = mass flow entrained from mainstream at the slot due to injection effects
$\dot{m}_s$ = $\rho_s u_s S$, film cooling injection rate
n = velocity power coefficient, $u/u_\infty = (y/\delta)^{1/n}$
n_0 = velocity power coefficient without film cooling injection
n_i = velocity power coefficient with film cooling injection
Pr_* = Prandtl number with fluid properties evaluated at the reference state
q_w = wall heat flux per unit area
S = film cooling slot dimension normal to the injection flow
St_* = $h/\rho_* u_\infty C_{p*}$, Stanton number with fluid properties at the reference state
$\overline{\mathrm{St}_*}$ = Stanton number at reference state for heating starting at the leading edge $x_0 = 0$, or $x_{0i} = 0$
T = absolute temperature
u = velocity
x = distance from the downstream edge of the film cooling slot measured in the mainstream direction, see Fig. 1
x_0 = distance upstream from slot to leading edge, see Fig. 1
x_{0i} = distance upstream from slot to apparent origin of boundary layer with injection, see Fig. 1
$\bar{x}$ = distance from boundary layer origin, either $x + x_0$ or $x + x_{0i}$
y = distance normal to surface
α = angle of injection, see Fig. 1
Δ = $\theta_2 - \theta_1$, change in momentum thickness at the slot due to injection
θ = $\int_0^\delta \frac{\rho u}{\rho_\infty u_\infty}\left(1 - \frac{u}{u_\infty}\right) dy$, momentum thickness
ρ = density
τ_w = wall shear stress
μ = dynamic viscosity

Subscripts

aw = on an adiabatic wall with film cooling
r = recovery condition, adiabatic wall without film cooling injection
s = of the injection fluid
w = on the surface
0 = without film cooling injection
$*$ = at the reference state (P_∞, T_*)
∞ = of the mainstream
1 = at upstream edge of slot
2 = at downstream edge of slot
i = with injection

$$St_{*_0} = A_1 \left(\frac{\rho_* u_\infty (x + x_0)}{\mu_*}\right)^{-0.21} \times \left[1 - \left(\frac{x_0}{x + x_0}\right)^{0.79\left(\frac{n_0+2}{n_0+1}\right)}\right]^{\frac{-1}{n_0+2}} \quad (6)$$

where

$$A_1 = \frac{0.182}{Pr_*^{0.4}(10)^{0.535\left(\frac{n_0+2}{n_0}\right)}}$$

A similar equation involving x_{0i} and n_i can be written for the boundary layer with film cooling. Because the reference state was assumed to be independent of the presence or absence of film cooling, the ratio of heat transfer coefficients with and without injection is,

$$\frac{h}{h_0} = A_2 \left[\frac{(x + x_0)}{(x + x_{0i})}\right]^{0.21} \left[\frac{\left(1 - \left(\frac{x_0}{x + x_0}\right)^{0.79\left(\frac{n_0+2}{n_0+1}\right)}\right)^{\frac{1}{n_0+2}}}{\left(1 - \left(\frac{x_{0i}}{x + x_{0i}}\right)^{0.79\left(\frac{n_i+2}{n_i+1}\right)}\right)^{\frac{1}{n_i+2}}}\right] \quad (7)$$

where

$$A_2 = (10)^{0.535\left(\left(\frac{n_0+2}{n_0}\right) - \left(\frac{n_i+2}{n_i}\right)\right)}$$

In order to determine x_{0i}, the virtual origin of the boundary layer with injection, consider a mass and momentum balance on the boundary layer at the slot. The measurements of Goldstein, Shavitt, and Chen [17] downstream from normal injection demonstrated that the injected fluid induces a considerable extra entrainment, $\dot{m}_e$, into the boundary layer in the region close to the slot. Using the definition for θ, and referring to the control volume in Fig. 1,

$$\Delta = \frac{1}{\rho_\infty u_\infty}(\dot{m}_s + \dot{m}_e) - \frac{1}{\rho_\infty u_\infty^2}(\dot{m}_s u_s \cos\alpha + \dot{m}_e u_\infty) \quad (8)$$

Assuming that the injected fluid is an ideal gas of the same composition as the mainstream, and noting that the terms involving $\dot{m}_e$ will cancel, (8) can be reduced to

$$\Delta = MS\left[1 - M\left(\frac{T_s}{T_\infty}\right)\cos\alpha\right] \quad (9)$$

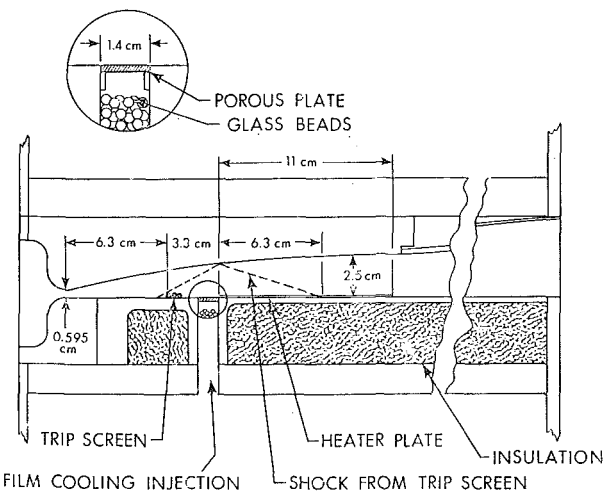

Fig. 2 Test section and Mach 3 nozzle

Using (5) to determine the momentum thicknesses before and after the slot,

$$\frac{\Delta}{0.23}\left(\frac{\rho_\infty}{\rho_*}\right)\left[\frac{\rho_* u_\infty}{\mu_*}\right]^{0.21} = \frac{x_{0i}^{0.79}}{10^{0.535\left(\frac{n_i+2}{n_i}\right)}} - \frac{x_0^{0.79}}{10^{0.535\left(\frac{n_0+2}{n_0}\right)}} \quad (10)$$

Combining (9) and (10) and solving for x_{0i},

$$\left(\frac{x_{0i}}{S}\right)^{0.79} = \frac{1}{A_2}\left(\frac{x_0}{S}\right)^{0.79} + A_3\left[M - M^2\left(\frac{T_s}{T_\infty}\right)\cos\alpha\right] \quad (11)$$

where

$$A_3 = 4.35(10)^{0.535\left(\frac{n_i+2}{n_i}\right)}\left(\frac{\rho_* u_\infty S}{\mu_*}\right)^{0.21}\left(\frac{\rho_\infty}{\rho_*}\right)$$

Once the rate of injection, characterized by M, is established, (11) can be employed to determine the displacement of the virtual origin of the boundary layer from x_0 to x_{0i}. Subsequently, using (7), the change in heat transfer coefficient can be computed at any downstream location.

Test Section Configuration and Operating Conditions

The test section, shown in Fig. 2, consisted of a two-dimensional supersonic half nozzle in which the flat plate section on which film cooling studies were performed formed the bottom. This system is described in detail in [21].

The surface downstream of the slot was insulated on its lower surface and covered with a stainless steel heater plate. The heater was supplied with power from a d-c source to generate a constant wall heat flux on the film cooled surface. Wall temperatures were measured by calibrated iron-constantan thermocouples embedded in the test plate.

The operating Mach number of 2.90 and the fixed stagnation condition of 2.76 bar and 24 deg C resulted in a free stream Reynolds number of 5.39×10^4/cm.

Experimental Results

A series of measurements were performed in the absence of film cooling injection. The heat transfer coefficients were compared with the zero-injection prediction of equation (6), using a value of $n_0 = 6$, which is consistent with the flat plate data of Reynolds, Kays, and Kline [14] and Klebanoff and Diehl [18]. The influence of the boundary layer trip made it difficult to assign a location to the origin of the boundary layer, and the value $x_0 = 5$ cm was chosen as a reasonable estimate, placing the origin about 2 cm upstream from the trip.

The reference temperature proposed by Eckert [15] in the form

$$T_* = T_\infty + 0.72(T_r - T_\infty) \quad (12)$$

did as well or better than more sophisticated forms for T_* in accounting for variable property effects.

Using these values for n_0, x_0, and T_*, the measured values of h_0 showed a maximum deviation of about 20 percent from the predictions of equation (6). Both the influence of the boundary layer trip with its oblique shock system, and the surface roughness at the slot may have been responsible for these variations. However, the measurements of Hartnett, Birkebak and Eckert [6] demonstrate that the shape of the curve for St_0 has relatively little effect on the shape of the relative curves for h/h_0.

The theory presented in this paper was developed for a constant wall temperature, while the experiments were performed for the constant wall heat flux case. By means of a Duhamel integral in the form suggested by Tribus and Klein [19], the heat transfer coefficients for the constant heat flux boundary condition were computed from the constant temperature case given by

equation (6). These Stanton numbers were slightly greater at all x locations than their constant temperature counterparts but because this increase did not exceed 5 percent for h_0 and was less than 1 percent for h/h_0, it was concluded that the present analysis could be used to determine the relative effect of injection for both boundary conditions.

Heat Transfer With Film Cooling

The heat transfer coefficients with upstream film cooling injection were determined by first measuring the adiabatic wall temperatures on the film cooled surface, and then applying electric power to the heater plate without disturbing the film cooling injection rate. The ratio h/h_0 was computed, and is presented as a function of downstream location in Fig. 3. The theoretical predictions for h/h_0, determined from (7) and (11) are also shown.

In order to examine the effect on h/h_0 of changes in the velocity profile shape, two limiting cases were computed. In the first case the injection was assumed to have no effect on the profile shape, that is, $n_0 = n_i = 6$, resulting in the solid curves in Fig. 3. This assumption will be valid far downstream from the slot, after the initially distorted velocity profile has decayed back to its equilibrium form. For the other extreme, the series of dashed curves were generated by estimating the value of n_i that would exist immediately downstream from the slot. These values of n_i were estimated by examining the velocity profiles measured by McRee, Peterson, and Braslow [20] whose data for the range of MS values in the present investigation indicate that n_i decreases from 7 to 5 as MS increased from zero to 0.0325 cm, corresponding to $M = 0.0258$ in the present study.

The theory did not account for changes in the velocity profile shape with position, and because of this, the use of different values for n_0 and n_i implies that the distorted velocity profile never recovered its original shape. This is an unrealistic situation and resulted in asymptotic values of h/h_0 less than unity. For this reason the dashed curves must be regarded as valid only at positions close to the slot. With this in mind, the data show a good agreement with the predictions, indicating that a simple power law velocity profile can be used to estimate the effects of injection on h/h_0 in the region near the slot. Particularly at the higher blowing rates, the effect of a change in profile shape, which caused a minimum to appear on the h/h_0 curves, is evident in both the theory and the experimental data.

Conclusions

Considering its simplicity the theory does remarkably well in predicting the effect of film cooling on heat transfer coefficients at small rates of injection. The theory is attractive not only because of its simplicity but also because of the absence of empirically determined constants. It must be emphasized, how-

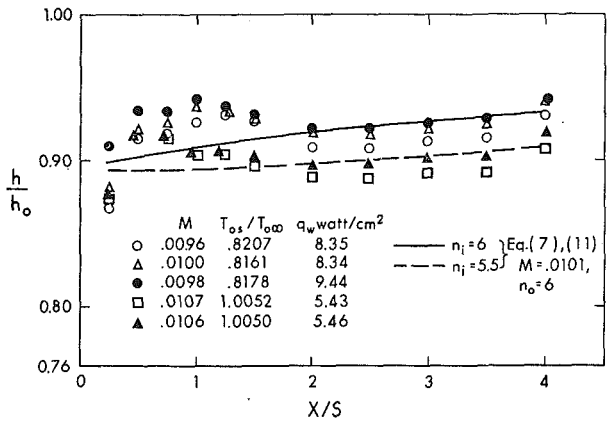

Fig. 3(a)

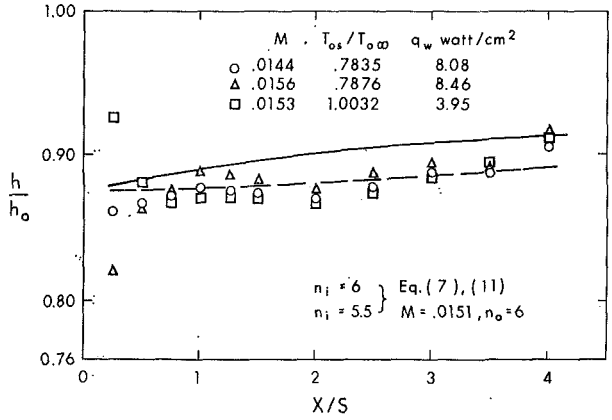

Fig. 3(b)

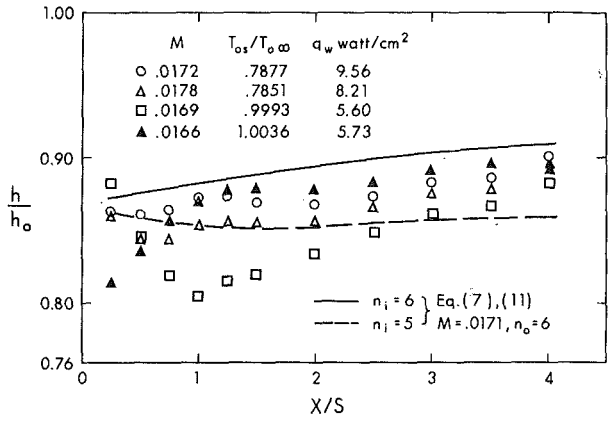

Fig. 3(c)

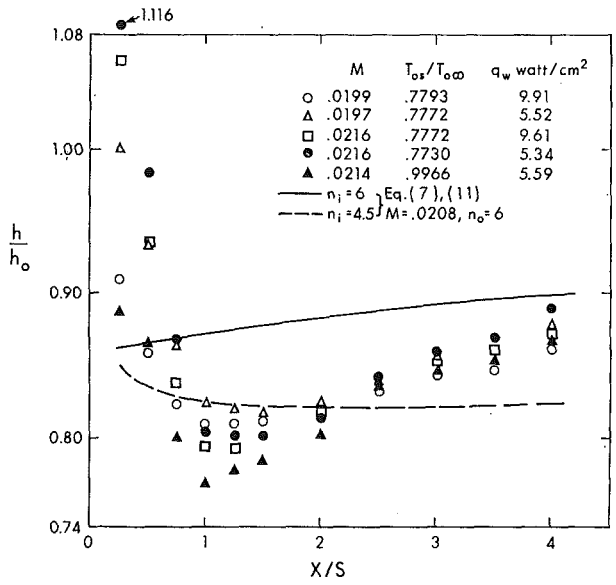

Fig. 3(d)

Fig. 3 Effect of film cooling on downstream heat transfer coefficients

ever, that even though the distance x_0 is a physically determined parameter, the absence of sharp leading edges makes its specification difficult in practical situations.

The measurements of h/h_0 by other investigators suggest that for a given geometry the heat transfer coefficient will show the moderate decreases observed in this study only when M is small. As M increases the trend reverses and substantial increases in h might be observed. Because this critical M value at which the reversal occurs will probably depend strongly on injection geometry, the prediction procedure outlined in this paper must be used with caution until an upper limit of M at which it remains valid can be determined from further investigations.

Acknowledgment

The support of the Power Branch of the Office of Naval Research through NONR 710(57), as well as the support provided by the National Research Council of Canada is gratefully acknowledged.

References

1 Goldstein, R. J., "Film Cooling," in *Advances in Heat Transfer*, Vol. 7, Academic Press, New York, 1971, pp. 321–379.

2 Eckert, E. R. G., "Transpiration and Film Cooling," *Heat Transfer Symposium*, Univ. Michigan Press, Ann Arbor, 1953, pp. 195–210.

3 Scesa, S., "Effect of Local Normal Injection on Flat Plate Heat Transfer," PhD thesis, University of California, Berkeley, 1954.

4 Seban, R. A., Chan, H. W., and Scesa, S., "Heat Transfer to a Turbulent Boundary Layer Downstream of an Injection Slot," ASME Paper No. 57-A-36, 1957.

5 Seban, R. A., "Heat Transfer and Effectiveness for a Turbulent Boundary Layer With Tangential Fluid Injection," JOURNAL OF HEAT TRANSFER, TRANS. ASME, Series C, Vol. 82, 1960, pp. 303–312.

6 Hartnett, J. P., Birkebak, R. C., and Eckert, E. R. G., "Velocity Distributions, Temperature Distributions, Effectiveness and Heat Transfer in Cooling of a Surface with a Pressure Gradient," *International Developments in Heat Transfer*, Part IV, ASME, New York, 1961, pp. 682–689.

7 Seban, R. A., and Back, L. H., "Effectiveness and Heat Transfer for a Turbulent Boundary Layer With Tangential Injection and Variable Free Stream Velocity," JOURNAL OF HEAT TRANSFER, TRANS. ASME, Series C, Vol. 84, 1962, pp. 235–244.

8 Hartnett, J. P., Birkebak, R. C., and Eckert, E. R. G., "Velocity Distributions Temperature Distributions Effectiveness and Heat Transfer for Air Injected Through a Tangential Slot Into a Turbulent Boundary Layer," JOURNAL OF HEAT TRANSFER, TRANS. ASME, Series C, Vol. 83, 1961, pp. 293–306.

9 Metzger, D. E., Carper, H. J., and Swank, L. R., "Heat Transfer With Film Cooling Near Nontangential Injection Slots," *Journal of Engineering for Power*, TRANS. ASME, Series A, Vol. 90, 1968, pp. 157–163.

10 Metzger, D. E., and Fletcher, D. D., "Evaluation of Heat Transfer for Film-Cooled Turbine Components," *Journal of Aircraft*, Vol. 8, 1971, pp. 33–38.

11 Eckert, E. R. G., Goldstein, R. J., and Pedersen, D. R., "Comment on Evaluation of Heat Transfer for Film Cooled Turbine Blades," *Journal of Aircraft*, Vol. 8, 1971, pp. 63–64.

12 Parthasarthy, K., and Zakkay, V., "An Experimental Investigation of Turbulent Slot Injection at Mach 6," *AIAA Journal*, Vol. 8, 1970, pp. 1302–1307.

13 Reynolds, W. C., Kays, W. M., and Kline, S. J., "Heat Transfer in the Turbulent Incompressible Boundary Layer," Part II Step Wall-Temperature Distribution NASA Memorandum 12-2-58W, 1958.

14 Reynolds, W. C., Kays, W. M., and Kline, S. J., "Heat Transfer in the Turbulent Incompressible Boundary Layer," Part I Constant Wall Temperature, NASA Memorandum 12-1-58W, 1958.

15 Eckert, E. R. G., "Survey of Heat Transfer at High Speeds," Wright Aero. Development Center Tech. Rept. 54-70, 1954, also see Eckert, E. R. G. and Drake, R. M., *Heat and Mass Transfer*, McGraw-Hill, 1959, p. 270.

16 Ludwig, H., and Tillman, W., "Untersuchungen über die Wandschubspannung in turbulenten Riebungsschichten," *Ing.-Arch.*, Vol. 17, 1949, pp. 288–399, English translation as NACA TM 1285, 1950.

17 Goldstein, R. J., Shavit, G., and Chen, T. S., "Film Cooling Effectiveness With Injection Through a Porous Section," JOURNAL OF HEAT TRANSFER, TRANS. ASME, Series C, Vol. 87, 1965, pp. 353–361.

18 Klebanoff, P. S., and Diehl, Z. W., "Some Features of Artificially Thickened Fully Developed Turbulent Boundary Layers With Zero Pressure Gradient," NACA Rept. 1110, 1952.

19 Tribus, M., and Klein, J., "Forced Convection From Non-Isothermal Surfaces," *Heat Transfer Symposium*, 1952, Univ. Michigan Press, Ann Arbor, 1953, pp. 211–236.

20 McRee, D. I., Peterson, J. B., and Braslow, A. L., "Effect of Air Injection Through a Porous Surface and Through Slots on Turbulent Skin Friction at Mach 3," NASA TN-D-2427, 1964.

21 Goldstein, R. J., Eckert, E. R. G., and Wilson, D. J., "Film Cooling With Normal Injection Into a Supersonic Flow," *Journal of Engineering for Industry*, TRANS. ASME, Series B, Vol. 90, 1968, pp. 584–588.

22 Schlichting, H., *Boundary Layer Theory*, McGraw-Hill, Fourth ed., 1960, p. 358.

Controlled Transpiration Cooling of the Anode in a High Intensity Arc

C. V. BOFFA[1]
E. PFENDER

Heat Transfer Division,
Department of Mechanical Engineers,
University of Minnesota,
Minneapolis, Minn.

A high intensity arc plasma torch with controlled transpiration cooling of the anode has been developed. The plenum chamber surrounding the porous anode is subdivided into several independent compartments which allow for individual control of the pressure and of the ensuing mass flow rates through the corresponding anode segments. In this way, the inherent instabilities of transpiration cooling may be alleviated. Arc performance characteristics are determined utilizing a porous carbon anode and argon at atmospheric pressure as working fluid. It is shown that the temperature distribution of the porous anode segments depends only on the transpiring mass flow rate and on the pressure drop through the porous material. Theoretical predictions compare favorably with experimental results. By using a two-step temperature model, the arc attachment size on a particular anode segment may be estimated. The torch efficiency which is a measure of the effectiveness of transpiration cooling on net anode losses and the mean enthalpy of the emanating plasma jet are measured as a function of mass flow rate and power input.

Introduction

In this paper a high intensity arc plasma torch with controlled transpiration cooling of the anode is described, and its characteristic parameters and performances are evaluated.

The increasing interest in transpiration cooling arises from its recent engineering applications in space vehicle thermal protection, cooling of gas turbine blades, combustion chambers, rocket nozzles, etc. Such interest is reflected in the extensive research work which has been carried out on heat and mass transfer in the interior of porous matrices. Many papers on the subject can be found in the literature. In recent years, the application of transpiration cooling has been extended to high intensity arc plasma generators [1–9].[2]

There is, however, a major drawback in the application of transpiration cooling to high-intensity arc plasma torches: the required pressure drop for a given mass flow rate of the cooling gas flowing through the porous material is an increasing function of its temperature. Therefore, a local temperature rise in the porous matrix causes a reduction of the cooling gas flow rate in this area resulting in a further temperature increase; i.e., transpiration cooling is inherently an unstable cooling process.

A solution to this problem is proposed in this work since the flow of cooling gas may be controlled by the pressure. The plenum chamber surrounding the porous anode is subdivided into several independent plenum chambers which allows individual control of the pressure in each of these chambers. If the temperature increases in one zone of the anode, the pressure can be increased in the corresponding plenum chamber; and the cooling gas flow rate can, therefore, be increased in the area where it is most needed. In this way a sensitive control of the anode temperature can be obtained and the arc can be safely operated under predetermined conditions.

For a basic understanding of the performance of a transpiration cooled plasma torch, it is indispensable to know the characteristics of the gas flow through high temperature porous carbon. These characteristics were previously determined and a theoretical model was derived for correlating the experimental results [10]. Reference to this work will be made without discussing details.

In the first part of this paper, the high intensity arc apparatus, with the multiple-plenum-chambers-transpiration-cooled porous anode, and the auxiliary equipment are briefly described. In the second part, the experimental results obtained with this apparatus are presented and the parameters evaluated which determine the performances of the arc itself and of the porous anode; the advantages of the multiple plenum chamber system are demonstrated.

---

[1] Now with the Istituto di Fisica Tecnica, Politecnico di Torino, Italy.

[2] Numbers in brackets designate References at end of paper.

Contributed by the Heat Transfer Division and presented at the Winter Annual Meeting, Detroit, Mich., November 11–15, 1973, of The American Society of Mechanical Engineers. Manuscript received by the Heat Transfer Division February 20, 1973. Paper No. 73-WA/HT-31.

Experimental Apparatus

Plasma Torch. The plasma torch consists essentially of a water-cooled thoriated tungsten cathode with a conical tip and a nozzle-shaped porous carbon anode supported by a copper and brass structure. In this supporting structure, five plenum chambers are located which regulate the argon mass flow rate transpiring through five different sectors of the porous anode.

A schematic drawing of the plasma torch is shown in Fig. 1 and the major components are labeled. Further details of the arrangement may be found in references [9, 10].

Since every plenum chamber is perfectly sealed from its neighbor, the pressure can be varied independently. Consequently, the argon mass flow rate transpiring through the corresponding sector of the anode may be varied without altering the mass flow through the other sectors.

It should be pointed out that the porous anode is not subdivided into five sectors; it consists of one single piece of porous carbon and, therefore, does not present on the inner surface any nonuniformities which would result in preferred attachment spots for the arc.

Control Panel and Auxiliary Equipment. The instruments mounted on the control panel allow for controlling and measuring the argon mass flow rate and the pressure in each of the six plenum chambers independently, as well as the cathode and anode holder cooling water mass flow rate.

The distilled water closed circuit, which provides the cooling for the anode holder and the cathode, consists of a commercial water pump with an incorporated heat exchanger, pressure gauges, calibrated Fisher and Porter flow rators, and needle valves for flow rate control.

A sufficient cooling water flow rate is provided by a pressure of 10^6 kg/msec^2 at the pump outlet. An analogous circuit provides the cathode cooling water.

The electrical power for the arc is supplied by a Miller 40 kW rectifier. Its associated current regulating rheostat, on-off switch, and high frequency starter are incorporated into a commercial control console, separated from the main control panel described in the foregoing.

Stability during arc operation and extension of the current range is provided by placing an adjustable water-cooled resistor of approximately 1.2 Ω maximum resistance in series with the electrical circuit.

Transpiration Cooled Anode

Cold Flow Tests and Preliminary Observations. In cold flow tests, the total pressure drop across each of the four main anode sectors is measured as a function of the transpiring argon mass flow rate. Using the equation of motion of fluids through porous media [10] with the measured values of the mass flow rate, the pressure drop may be calculated. These calculated values are in excellent agreement with the experimental data for all four anode sectors which behave identically as far as the transpiring flow is concerned.

The previously mentioned cold flow tests are repeated after each arc run to check for possible damages of the porous anode or of the seals of the plenum chambers. The data proved to be consistent and reproducible.

Trial arc runs demonstrated that the arc can be operated steadily and reproducibly in a current range from 60 to 120 amp over a wide range of argon mass flow rates without any tendencies to form preferred attachment spots on the anode surface. The size of the arc attachment derived from anode surface temperature distributions is of the same order of magnitude as the area of one anode sector. The arc will always attach to that sector through which the transpiring argon flow rate is a minimum; however, once the arc attaches to this particular segment, it tends to remain there and moves to a new segment only when the difference in the transpiring gas flow rates becomes relatively large.

For an effective cooling of the anode surface, it is mandatory to keep the mass flow distribution of the transpiring gas as uniform as possible over the entire porous surface. Measurements of the mass flow distribution downstream of porous matrices [10] indicate a sufficient level of uniformity for porous carbon samples similar to those used for the present work.

Segmented Porous Anode: Transpiring Flow Characteristics During Arc Operation. The desired control of the operating conditions and performance of this type of plasma torch is possible only when the functional relationships between porous matrix temperature and transpiring gas flow rate and pressure are known inside of the main four sectors of the porous anode. Therefore, an extensive experimental investigation is required on the transpiring flow characteristics through each sector of the porous anode during arc operation.

The total pressure drop across each anode sector is measured as a function of the mass flow rate passing through the sector for arc currents ranging from 60 to 120 amp. For each current, the measurements are subsequently performed with the arc attaching to each of the four anode sectors. An example of the results is shown in Fig. 2, which indicates that the pressure drop across the segment with the arc attaching is consistently higher than without arc attachment. This fact suggests that the temperature of this segment is considerably higher than that of the other segments as it should be because of the high heat flux from the arc attachment [11]. The pressure drop for the segments on which the arc does not attach are very close to each other, indicating that the same temperatures can be attributed to each of these segments. It is obvious that the arc attachment is restricted to a single segment and the size of the attachment area is less than the surface area of the segment. There is, however, a minor deviation of the pressure drop across the segment opposite from the arc attachment which tends to be slightly lower than that pertaining to the two adjacent segments. This is due to increased radiation and convection heat transfer from the arc to the two segments adjacent to the attaching arc and due to heat conduction to these segments from the high temperature arc attachment.

The pressure drop as a function of the arc current is also determined for transpiring mass flow rates per unit area varying from 2.5 to 5.8 kg/m^2 sec. An example of the results is shown in Fig. 3 which are in agreement with the previous data and which allow a similar interpretation.

Nomenclature

A = area
A^* = flow coefficient
B^* = flow coefficient
c_p = specific heat
I = arc current
K_w = porous matrix thermal conductivity
$\dot{m}$ = mass flow rate
p = pressure
$\dot{Q}_{El}$ = electrode losses
$\dot{Q}_p$ = enthalpy flux
$\dot{Q}_{\mathrm{Rad}}$ = radiative heat flux
$\dot{q}_R$ = radiative heat flux per unit area
R^* = gas constant
T = temperature
T_g = gas temperature
T_w = uniform temperature of porous segment outside surface
T_∞ = temperature far away from wall
V = arc voltage
x = space coordinate
x_w = space coordinate of porous segment outside surface
ϵ = total emissivity
η = viscosity
σ_B = Stephan Boltzmann constant

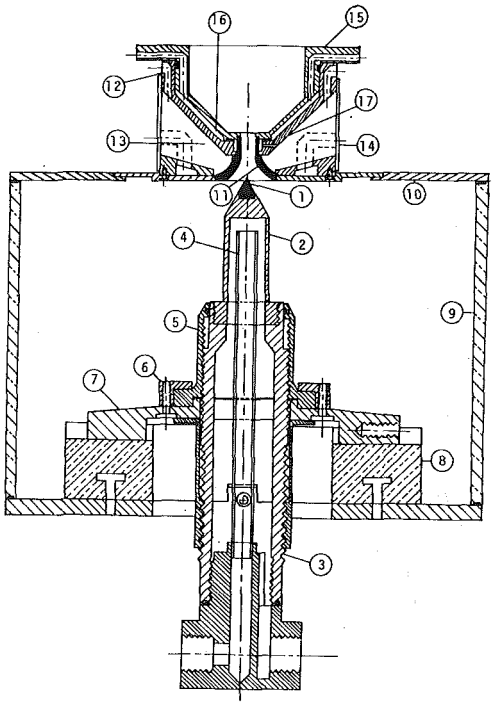

Fig. 1 Schematic of the plasma torch: 1 thoriated tungsten tip (cathode), 2 copper holder, 3 brass support, 4 cooling water duct (stainless steel), 5 vertical cathode adjustment (brass), 6 ring for adjustment, 7 supporting brass plate, 8 teflon ring, 9 plexiglas cylinder, 10 copper plate, 11 porous carbon anode, 12 anode support (copper), 13 plenum chamber, 14 plexiglas window, 15 supporting structure (brass), 16 water passage, 17 small cylindrical plenum chamber

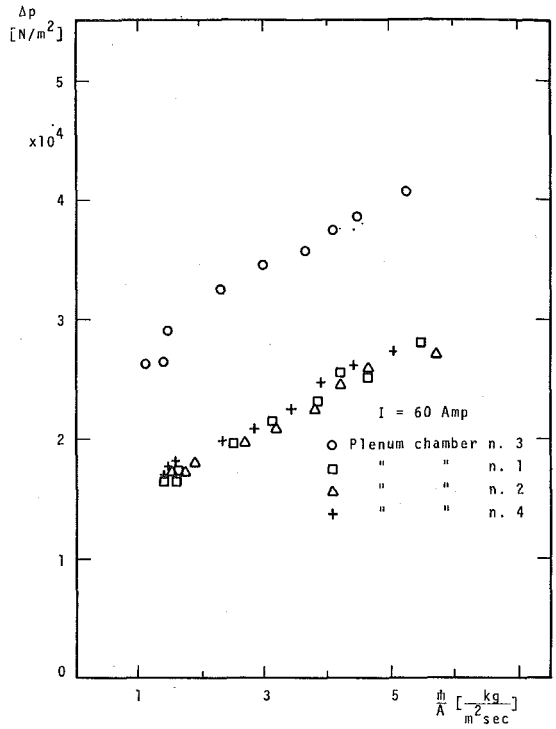

Fig. 2 Flow characteristics of porous anode segments during arc operation

Temperature Distribution in the Porous Anode Sectors

Theoretical Analysis. For the sake of this analysis, each sector of the porous anode, due to its small thickness and large radius of curvature compared to the other dimensions, is considered in a first approximation as a plane slab; and the steady flow of the gas transpiring through it is assumed to be one-dimensional. An energy balance within the porous material, per unit area in flow direction (minus x-direction), yields:

$$\frac{d}{dx}\left(K_w \frac{dT}{dx}\right) + \frac{\dot{m}}{A}\frac{d}{dx}(c_p T_g) = 0 \tag{3a}$$

Over the temperature range of interest, c_p may be considered constant and an average value may be taken for K_w.

The large specific surface of the porous matrix is reflected in a high value of the volumetric heat transfer coefficient for the heat transfer process between the porous wall and the transpiring gas. Hence, local values of gas and wall temperatures may be considered as equal. Equation (3a), therefore, can be written:

$$\frac{d^2T}{dx^2} + \frac{\dot{m}}{A}\frac{c_p}{K_w}\frac{dT}{dx} = 0 \tag{3b}$$

with the two boundary conditions

$$T = T_w \text{ at } x = x_w \tag{3c}$$

and

$$-K_w\left(\frac{dT}{dx}\right)_{x=x_w} = \frac{\dot{m}}{A} c_p (T_w - T_\infty) + \dot{q}_R \tag{3d}$$

the solution of equation (3b) becomes

$$T = \left[(T_w - T_\infty) + \frac{A}{\dot{m}}\frac{\dot{q}_R}{c_p}\right] e^{\frac{\dot{m}}{A}\frac{c_p}{K_w}(x_w - x)} + T_\infty - \frac{\dot{q}_R}{c_p}\frac{A}{\dot{m}} \tag{3e}$$

where

$$\dot{q}_R = \epsilon\sigma_B(T_w^4 - T_\infty^4) \tag{3f}$$

In the foregoing derivation, it has been assumed that the energy conducted to the outer surface of the porous segment is either intercepted by the transpiring gas or lost by radiation. Equation (3e) represents the temperature distribution inside the porous wall as a function of the mass flow rate per unit area and of the temperature of the outside surface. However, if the outer surface of the porous sector is not glowing, an accurate measurement of this temperature is rather difficult. Therefore, a method is proposed which does not require the knowledge of the temperature of the outside wall, provided that this temperature is uniform over the sector surface.

If the continuity equation and the perfect gas law are introduced into the equation of motion of the gas flow through porous media as described in [10], one obtains

$$\frac{dp}{dx} = A^*\eta\frac{\dot{m}}{A}\frac{R^*T}{p} + B^*\left(\frac{\dot{m}}{A}\right)^2\frac{R^*T}{p} \tag{3g}$$

The pressure in the plenum chamber can be measured easily and accurately (within 1 percent) and then serves as boundary condition in equation (3g). Assuming various temperature values for the outside surface of the porous sector, the temperature distribution within the porous matrix can be determined. Correspondingly, a numerical solution of equation (3g) provides the pressure distribution across the porous matrix; and the total pressure drop may then be compared with experimental values. Finally, by iteration, the correct outside surface temperature may be found.

After the iteration process converges, the particular temperature distribution is directly correlated with the total pressure drop across the porous wall for the chosen mass flow rate transpiring through it. In this way, temperature distributions can be derived only from pressure and mass flow rate measurements which are much easier and more accurate than temperature measurements in this situation.

Results. Temperature profiles are numerically calculated as indicated in the foregoing for pressure drops ranging from 1 ×

10^4 to 6×10^4 [N/m^2] and transpiring mass flow rates per unit area ranging from 0.5 to 5 kg/m² sec. The values of the flow parameters A^* and B^*, which must be known with precision for the method to be accurate, have been experimentally determined as described in [10]. The temperatures of the outside and inside surface of the porous sector are represented in Fig. 4 as a function of pressure drop and transpiring mass flow rate. This figure permits a quick and relatively accurate graphical determination of the inside and outside surface temperature of the porous anode, when the values of the pressure drop and the transpiring mass flow rate per unit area are known. For this reason, frequent reference to Fig. 4 will be required in the following calculations.

In order to compare the theoretical predictions with experimental results, the mass flow rate passing through each sector, to which the arc does not attach, is decreased until the outside surface reaches glowing temperature. In this case, the temperature distribution appears uniform over the surface throughout the entire arc current range. The value of this temperature is then determined utilizing a calibrated optical pyrometer and compared with predictions derived from Fig. 4. Table 1 illustrates this type of comparison for currents of 60, 100, and 120 amp. The results show that for the sector to which the arc does not attach, a good agreement exists between theoretical and experimental values.

Table 1

Current I [Amp]	Mass flow rate $\dot{m}/A$ [kg/m²sec]	$T_{w_{exp.}}$ [deg K]	$T_{w_{theor.}}$ [deg K]
60	1.0	1440	1410
60	1.2	1350	1310
60	1.4	1205	1290
100	2.0	1320	1400
100	2.1	1270	1310
120	2.0	1440	1490
120	2.3	1340	1310
120	2.5	1305	1260

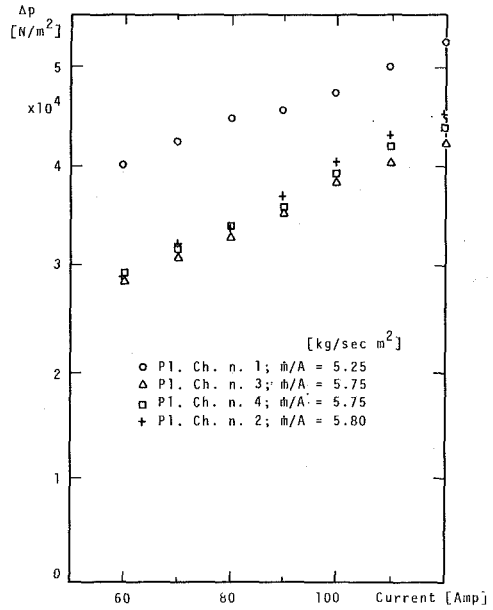

Fig. 3 Pressure drop across porous anode sectors versus arc current

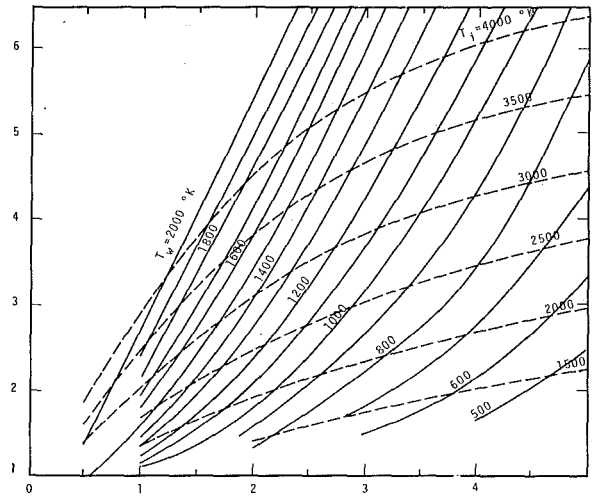

Fig. 4 Pressure drop through porous matrix as a function of mass flow rate for various inside (T_i) and outside (T_w) surface temperatures

In Fig. 5, theoretical and experimental temperature values of the outer surface of the porous sectors to which the arc attaches are represented as a function of the transpiring mass flow rate per unit area for currents of 60, 100, and 120 amp. The solid lines refer to the calculated temperatures. The experimentally determined temperatures, referring to the central portion of the segment, are higher than the theoretical predictions derived from Fig. 4; and this difference increases with increasing mass flow rate, but as shown in Fig. 5, decreases with increasing current. The discrepancies between experimental and theoretical values and their trends with increasing mass flow rate and increasing arc current will be explained in the following.

At low arc currents, the arc attachment area covers only a certain portion of the inside surface of a porous sector, leaving the outer regions relatively cold. The temperature, therefore, is nonuniform over the surface and this nonuniformity persists throughout the porous material to the outer surface of the sector, due to its small thickness. Since the plenum chamber pressure, which forces the gas through the porous sector, is uniform over the entire surface, a higher mass flow rate per unit area will flow through the outer region of the surface according to equation (3g). The predicted temperatures, however, are based on the assumption of uniform temperature distribution; and, therefore, they represent the uniform temperature which would pertain to the sector in order for the mass flow and the pressure drop to assume the experimentally measured values. By means of the optical pyrometer, the temperature of the hotter glowing portion of the porous segment is measured, which is obviously higher than the average temperature. When a higher transpiring argon mass flow rate is forced through the porous matrix by increasing the pressure in the corresponding plenum chamber, most of the added

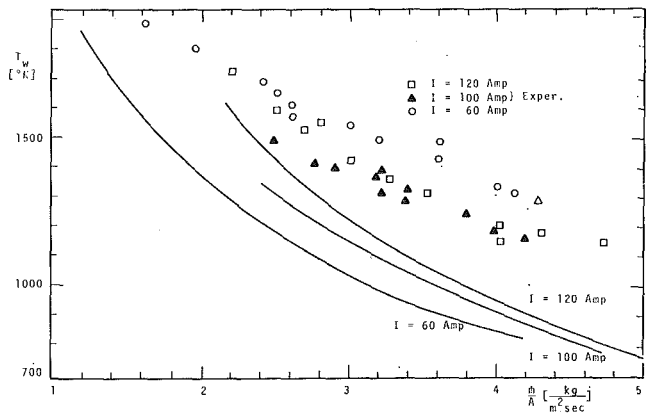

Fig. 5 Comparison of theoretical and experimental temperature values of porous anode sectors outside surface

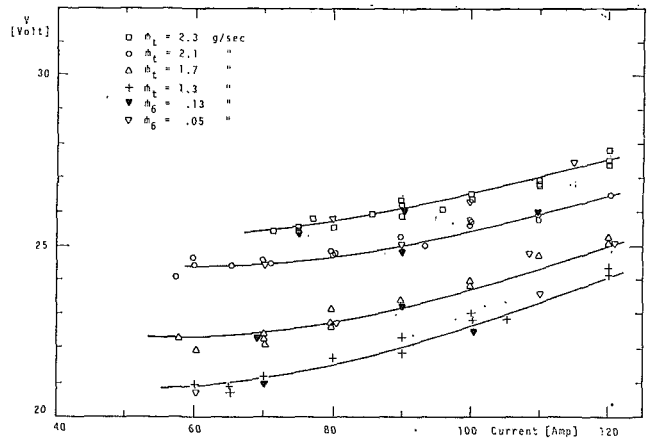

Fig. 6 Arc characteristics

transpiring mass will flow through the outer cooler regions of the segment, thus enhancing the temperature difference between the central part of the segment surface and the surrounding part. On the other hand, when the current increases, the arc attachment size increases. Therefore, the high temperature region comprises a larger portion of the segment surface and the value of its "average" temperature approaches the temperature which is recorded by the pyrometer.

Arc Characteristics. Arc voltage-current characteristics are measured as a function of the argon mass flow rate passing through the five anode sectors and of the flow rate providing the cathode swirl.

Preliminary tests showed that the mass flow rate transpiring through the fifth cylindrical sector in the downstream portion of the anode has no detectable influence on the arc characteristics. The same is true for the small mass flow producing the cathode swirl. The experimental results show that the arc characteristics are only a function of the total mass flow rate, $\dot{m}_t$, passing through the four main anode sectors regardless of the mass flow through individual sectors. This result seems to indicate that convective heat losses from the arc are essentially independent of the flow distribution for the parameter range covered by these experiments.

In Fig. 6, the measured arc voltages are plotted versus the arc current for four different total mass flow rates. The cathode swirl mass flow rate is an order of magnitude smaller than that through the four main sectors. Therefore, its variation has a negligible effect on the arc characteristics as shown in Fig. 6 ($\dot{m}_6$).

For currents below 55 amp, the arc becomes unstable and its attachment spot moves erratically along the lower edge of the anode nozzle. This instability increases with increasing transpiring mass flow rate, probably because the relatively "weak" arc is strongly affected by fluidynamic affects. At currents beyond 120 amp, the required transpiration mass flow rate seems to force the attachment downstream toward the end of the anode nozzle. Therefore, a current of 120 amp is considered as the upper limit for these runs.

The reasons for rising characteristics and their dependence on mass flow rate have been discussed in the literature [12] for the case of an arc with axial flow and a plane, water-cooled anode. In principle, the same arguments hold for the case of the transpiration cooled, nozzle-shaped anode used in the present work.

It is interesting to notice that the influence of the mass flow rate on the arc voltage decreases with increasing current. This is due to the fact that the Lorentz forces balancing the convective forces, exerted on the arc by the cold argon mass flow, increase with increasing current [13].

Estimate of the Arc Attachment Size. The temperature at the location of the anode arc attachment shows, in general, pronounced nonuniformities. From the difference in temperature between the central glowing portion on the outside porous surface and its average temperature pertaining to each arc run, the size of the arc attachment can be estimated.

A two-step model is adopted to represent the temperature distribution on the surface. The corresponding set of equations is solved by an iteration procedure and results obtained for arc currents of 60, 100, and 120 amp indicate arc attachment sizes between 0.15 and 0.25 cm². The arc attachment size decreases with increasing mass flow rate and increases with increasing current.

The decrease of the arc attachment size with increasing mass flow rate is a consequence of the increase of convective heat losses from the arc. Since the arc current is kept constant, the arc shrinks according to the higher energy losses. The increase in arc attachment size with increasing arc current reflects a corresponding increase of the arc diameter.

Torch Efficiency. The torch efficiency may be considered as a measure of the effectiveness of the transpiring mass flow on net anode losses. An overall energy balance for the plasma torch yields

$$\dot{Q}_p = VI - \dot{Q}_{El} - \dot{Q}_{Rad} \tag{3h}$$

$\dot{Q}_p$ represents the enthalpy flux through the cross section of the plasma jet emerging from the anode nozzle; VI represents the power input to the arc, and $\dot{Q}_{El}$ the power losses to the electrodes removed by the cooling water; $\dot{Q}_{Rad}$ indicates the power radiated from the outer surface of the porous anode segments through the plexiglas windows which seal the four plenum chambers.

The power input to the plasma jet $\dot{Q}_p$ is measured by a calorimeter which fits on top of the plasma torch [14]. The measured values of $\dot{Q}_p$ are consistent with those obtained from equation (3h) using measured values of VI and $\dot{Q}_{El}$ and estimates of $\dot{Q}_R$.

VI and $\dot{Q}_{El}$ are determined with conventional methods. $\dot{Q}_R$ is estimated from the measured values of the outside temperature of the transpiration cooled anode sectors. Torch efficiencies and mean enthalpies are shown in Fig. 7.

For high mass flow rates, the torch efficiency is essentially independent of the power input, whereas for low transpiring mass flow rates it displays a maximum. The rising portion of the efficiency curve is associated with the increasing arc length with increasing current in this arc current range.

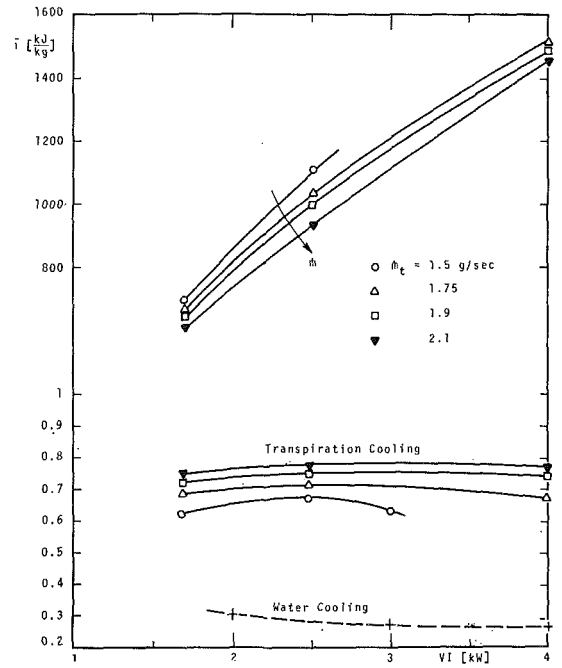

Fig. 7 Mean enthalpies and efficiencies

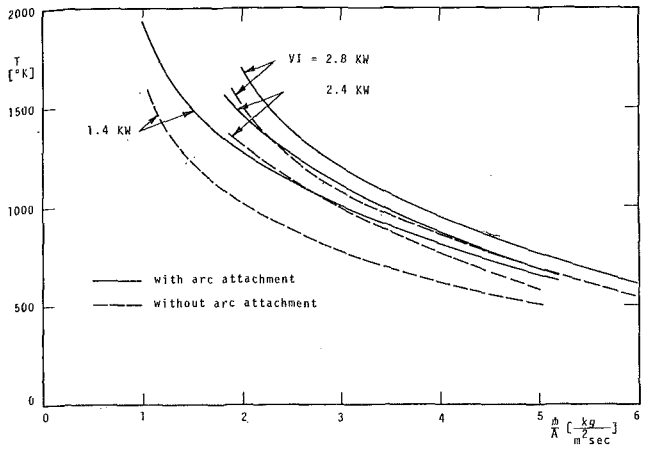

Fig. 8 Anode outside surface temperatures

As the arc power level increases, the anode temperature which reflects anode losses shows little increase as long as the transpiring flow is sufficiently strong (see Fig. 8). This implies that a large percentage of the increasing power input to the arc is transferred back to the plasma. In the falling portion of the efficiency curve, this trend is reversed and correspondingly the anode temperature now shows a substantial increase (Fig. 8). The transpiring flow is no longer able to return sufficient energy from the anode to the plasma flow. This finding also agrees with the increasing trend of the efficiency with increasing mass flow rate as shown in Fig. 7. The peak of the efficiency curves is shifted to higher power levels (current levels) as the mass flow rate increases and for mass fluxes $\geq$ 1.9 g/sec the peak occurs beyond the power levels covered by these experiments.

The behavior of the anode fall (which may influence anode losses [14]) as a function of the transpiring mass flow rate is still unclarified although it appears that there is no strong effect.

For comparison, the efficiency of a water-cooled plasma torch which is geometrically similar to the previously described torch [15] is also included in Fig. 7. It should be pointed out that the efficiencies of water-cooled plasma torches are, in general, appreciably higher than those reported in Fig. 7. Under similar conditions, however, they always remain below those of plasma torches with transpiration-cooled anodes.

Summary

Controlled transpiration cooling of the anode of a high intensity arc may be accomplished by segmenting the plenum chamber which surrounds the anode. In this way, the inherent instabilities of transpiration cooling are substantially alleviated or entirely eliminated.

The governing parameters which characterize the operation of a plasma torch with such an anode are evaluated. The arc characteristics are measured, and the experimental results indicate a strong similarity with those pertaining to the traditional plasma torch with a water-cooled anode although the current range for which stable and reproducible operation can be achieved is restricted from 60 to 120 amp.

Since the anode temperature is an important parameter for the arc performance, a method for calculation of the temperature distribution in the porous anode wall is derived which only requires transpiring flow rate per unit area and pressure drop through the porous matrix. These parameters can be easily measured with high accuracy.

The experiments provide information about temperature distribution of the porous anode as a function of the arc current, the transpiring mass flux, and the pressure drop across the porous matrix. This distribution can be reproduced from run to run. The temperature of the porous anode at the location of arc attachment is substantially higher than on neighboring segments and the temperature distribution is related to the arc attachment size. The arc attachment area increases with arc current and decreases with the transpiring mass flux increases.

The efficiency of the torch increases with transpiring mass flow rate for a given power input to the arc. The dependence of the efficiency on the power input to the arc is less pronounced and shows a maximum for a given mass flow rate.

References

1 Sheer, C., Cooney, J. A., Rothacker, D. L., "Fluid Transpiration Through Anodic Boundary of an Electric Arc," *AIAA Journal*, Vol. 2, 1964, p. 483.

2 Cremers, C. J., Eckert, E. R. G., "Temperature Field in an Arc With a Transpiration Cooled Anode," *AIAA Journal*, Vol. 3, 1965, p. 1876.

3 Cremers, C. J., Birkebak, R. C., "The Prediction of the Mode Transition in an Arc With a Transpiration-Cooled Anode," *AIAA Journal*, Vol. 4, 1966, p. 167.

4 Druxes, H., Schmitz, G., Patt, H. J., "Der Einfluss einer radialen Masseneinströmung auf elektrische Lichtbogen," *Zs. f. Physik*, Vol. 203, 1967, p. 192.

5 Pfender, E., Eckert, E. R. G., Raithby, G. D., "Energy Transfer Studies in a Wall Stabilized, Cascaded Arc," *Proceedings of the Seventh International Conference on Phenomena in Ionized Gases*, Vol. I, Beograd, 1966.

6 Pfender, E., Gruber, G., Eckert, E. R. G., "Experimental Investigation of a Transpiration-Cooled Constricted Arc," *Proceedings of the Eighth International Conference on Phenomena in Ionized Gases*, Vienna, 1967.

7 Anderson, J. E., Eckert, E. R. G., "Transpiration Cooling of a Constricted Electric Arc Heater," *AIAA Journal*, Vol. 5, No. 4, 1967.

8 Heberlein, J., Pfender, E., "Transpiration Cooling of the Constrictor Walls of an Electric High Intensity Arc," JOURNAL OF HEAT TRANSFER, TRANS. ASME, Series C, Vol. 93, No. 2, 1971.

9 Boffa, C., Pfender, E., "Controlled Generation of Monodisperse Aerosols in the Submicron Range," *Aerosol Science*, Vol. 4, 1973, p. 103.

10 Boffa, C., Pfender, E., "Utilization of a High Intensity Arc for the Controlled Generation of Ultrafine Monodisperse Aerosols," E.P.A. Final Report, HTL TR No. 106, 1972.

11 Shih, K. T., Pfender E., "Electrode Energy Transfer Mechanisms in an MPD Arc," *AIAA Journal*, Vol. 8, No. 2, 1970.

12 Eckert, E. R. G., Pfender, E., "Advances in Plasma Heat Transfer," *Advances in Heat Transfer*, Vol. 4, Academic Press, New York, 1967.

13 Wutzke, S. A., Pfender, E., Eckert, E. R. G., "Symptomatic Behavior of an Electric Arc With a Superimposed Flow," *AIAA Journal*, Vol. 6, No. 8, 1968.

14 Pfender, E., Raithby, G. D., Eckert, E. R. G., "An Anode Comparison Study in a Wall Stabilized Argon Arc," ARL 65-232, 1965.

15 Boffa, C., Pfender, E., "Enthalpy Probe and Spectrometric Studies in an Argon Plasma Jet," HTL TR No. 90, 1967.

L. L. HARDIN
D. F. DYER
Department of Mechanical Engineering,
Auburn University,
Auburn, Ala.

Heat and Mass Transfer in Beds of Particles Undergoing Sublimation Dehydration

A theoretical analysis as well as an experimental study of sublimation freeze-drying is reported. The theoretical and experimental results compare within 10 percent for a test case. In addition, the theoretical work confirms that drying rates increase linearly with bed thickness for particle bed drying, as reported in earlier experiments. Drying times for a slab and particle beds with the same mass and dryer surface area are compared. It is shown that the drying time for the particle bed can be reduced by more than a factor of two compared to the equivalent slab. It is also shown that the optimum way to increase the drying rate of particle beds is to increase the number of layers rather than the size of particles.

Introduction

One objective of studying the process of sublimation dehydration is to find ways of accelerating the process so that it can be used commercially to remove water from a wide variety of materials, whether it be for preservation (e.g., food products) or for other purposes. Another objective is to better understand the mechanism of sublimation dehydration (more commonly, freeze-drying) process so that it may be extended to a much broader spectrum of applications than those presently being used.

The most common geometry of materials to be freeze-dried is in the slab form, which in many cases is the most desirable configuration considering the fact that the bulk of materials to be freeze-dried are in that form. However, the dried layer which builds up as the material freeze dries has such a low thermal conductivity that it has an insulating effect on the transmission of heat to the sublimating interface. Since the supply of heat to the water undergoing phase change is usually the critical factor in the freeze-drying rate, the slab geometry proves to be undesirable from this standpoint. Reference [1][1] predicts a reduction on the order of 40 percent in total drying time by placing a vapor seal on one of the slab surfaces and heating both surfaces with radiant heat. The frozen region has a much higher thermal conductivity than the dried material, allowing much more heat to be conducted to the sublimating interface and, subsequently, the total drying time is reduced. But the primary difficulty with the method described is maintaining a vapor seal that will permit passage of a relatively large quantity of heat and yet prevent that surface from experiencing any drying.

Drying rates for materials of other geometries such as spheres and cylinders have been predicted and verified experimentally, but the problem of the buildup of the dried layer is still present.

Another configuration is that of the particle bed, the particles having much smaller diameters than the overall dimensions of the bed. The problem of heat and mass transmission through the particle bed is not so readily defined as with the other geometries mentioned previously.

According to reference [2], most of the work done on sublimating packed beds is directed toward processing. Some limited experimental studies of sublimating beds of biological materials exist. Although much work has been done with heat and mass transfer through packed beds of particles, the present work is important because it represents the first theoretical analysis of heat and mass transfer in sublimating particle beds. Thus, the problem is to analyze energy and mass transfer through a bed of particles undergoing sublimation dehydration and to predict drying rates in terms of the geometry of the bed, the properties of the material composing the bed, and the environmental conditions surrounding the bed.

The problem is solved as follows. A physical model of a sublimating bed is established, and mathematical equations for this model are developed and solved numerically. A limited experimental investigation of the same problem is performed, and the results of the experimental and theoretical work are compared to assess the validity of the theoretical work.

Analytical Investigation

Mathematical Model. The model is assumed to be a bed composed of spherical particles each having the same radius R_0 as illustrated in Fig. 1. Radiant heat is supplied to each surface

[1] Numbers in brackets designate References at end of paper.

Contributed by the Heat Transfer Division for publication (without presentation) in the Journal of Heat Transfer. Manuscript received by the Heat Transfer Division, April 24, 1972. Paper No. 73-HT-U.

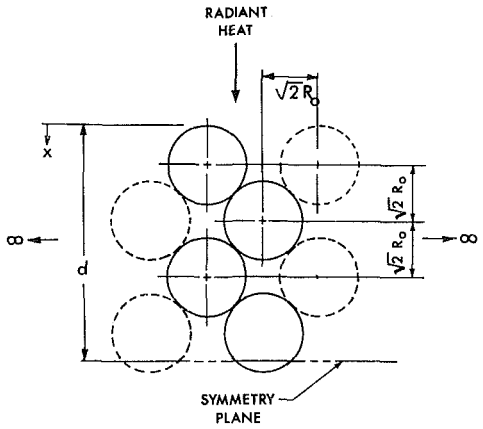

Fig. 1 Model of particle bed

at the same rate so that a plane of symmetry exists a distance d from either surface. The dimensions of the bed in directions transverse to the radiant heat flux are much greater than d, making the end effects insignificant. As a result, the problem involves the flow of heat and mass in a direction perpendicular to the bed surface, and all dimensions are measured in that direction.

Until it is dried, each particle is assumed to consist of a dried outer shell and a frozen core. Since the problem is one-dimensional, it can be reduced to analyzing a single "stack" of particles from the surface to the center line of the bed as shown in Fig. 1. In order to predict the heat transfer at a given depth in the bed, it is necessary that an equivalent value of thermal conductivity and area be known. This value is determined by the method discussed in the following.

An analytical solution [3] for a single sphere with a uniform surface temperature shows that no heat is transferred through the frozen core of the particles. Even though the present problem involves a slightly nonuniform temperature distribution over the surface of each sphere, the assumption of no heat flux through the frozen region is made. Thus, it is assumed that the heat is conducted through the dried layer and the interstitial gas. The equivalent thermal conductivity is assumed constant for any given layer of particles parallel to the symmetry plane and is based on the relative area of gas and dry material for that layer, namely,

$$k_{EQ} = \frac{k_{DM}A_{DM} + k_G A_G}{A_G + A_{DM}} \tag{1}$$

By a geometrical analysis it can be shown that for a given layer the equivalent areas for gas and dry material, respectively, are:

$$A_G = \frac{(4\sqrt{2} - \frac{4}{3}\pi)\,R_0^2}{\sqrt{2}R_0}$$

and (2)

$$A_{DM} = \frac{\frac{4}{3}\pi\,(R_0^3 - R_i^3)}{\sqrt{2}R_0}$$

Papers by Chen and Churchill [4], Yagi and Kunii [5], and Schotte [6] show that radiation effects on the thermal conductivity of packed beds for temperatures less than 100 deg C are insignificant. Yagi and Kunii state that the size of the particles composing the bed significantly affects the total thermal conductivity only at very high temperatures. Consequently, the equivalent thermal conductivity used does not include the insignificant effect of radiation. Additionally, convection of energy is negligible (see reference [2]).

Two boundary conditions are assumed in the model. One is the condition of constant surface temperature, that is, $T = T_0$ at $x = 0$. The other condition comes from symmetry, $\frac{dT}{dx} = 0$ at $x = d$.

Finite Difference Analysis. Dyer and Sunderland [3] predict the drying rate of spherical particles as a function of the particle properties and outside radius. Their solution assumes that the spherical particle has a uniform surface temperature and a uniform frozen core temperature. This latter assumption is equivalent to assuming that the process is heat transfer limited. Recently, Fox, et al. [7], have shown that for the sublimation dehydration process this is a good assumption. It is assumed that each particle layer parallel to the symmetry plane has a uniform surface temperature. As a result, the analysis given in reference [3] is applicable.

The solution of the particle bed drying problem must satisfy conservation of energy. Energy conservation requires that the energy to sublimate the mass loss from a layer equal the net energy transfer into a given layer by conduction. This energy balance is achieved indirectly by comparing the time required to sublimate a given amount of mass and the time required to conduct the necessary energy into the layer for sublimating this amount of mass. The solution is accomplished by adjusting the temperature distribution within the bed by trial and error until the two times discussed previously are the same. To analyze the total drying period the procedure described in the foregoing is carried out for small time increments, beginning with an undried bed and continuing until the bed is completely dried.

The steps of the analysis for a given time period are as follows:

1 The temperature decreases as shown in Fig. 2 for each successive layer. The temperature for the surface at $x = 0$ is T_0, and at the symmetry plane the temperature is T_F. Values at intermediate points between the two foregoing surfaces are assumed.

(Steps 2 through 5 are for the outermost drying layer.)

2 To initiate the calculation the first sphere is allowed to dry a small amount. This is done by decreasing R_1 by a small amount (e.g., $R_0/100$) from its previous value, R_{P1}. For the first time period $R_{P1} = R_0$ where R_0 is the particle radius. The amount of heat absorbed by the phase change of the small volume of ice which sublimates from the sphere is calculated by a simple energy balance:

Nomenclature

A = area, ft²
c_p = specific heat, BTU/lbm deg F
d = half-thickness, ft
h_{ig} = enthalpy of sublimation, BTU/lbm
k = thermal conductivity, BTU/hr-ft-deg F
Q = heat, BTU
$\dot{Q}$ = heat rate, BTU/hr
R = radial interface position, ft
R_0 = outside particle radius, ft
t = time, hr
T = temperature, deg F
x = position variable, ft
ρ = mass density, lbm/ft³
σ = porosity, $\frac{\text{void volume}}{\text{total volume}}$

Subscripts

DM = dry material
E = entering
EQ = equivalent property
F = frozen region
G = gas
i = denotes ith particle
L = leaving
N = net quantity
P^1 = previous value for layer 1
P^2 = previous value for layer 2
P^3 = previous value for layer 3
P = previous general value
PH = denotes phase change
S = current general value
SL = denotes slab geometry
0 = bed surface value
1 = layer 1
2 = layer 2
3 = layer 3

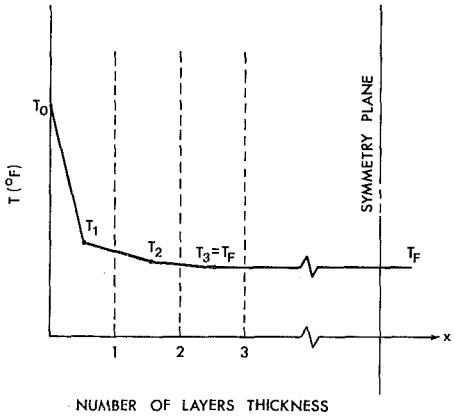

Fig. 2 Assumed initial temperature profile

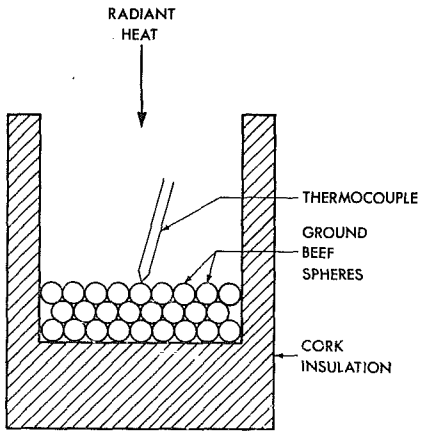

Fig. 3 Experimental test section

$$Q_{PH} = \tfrac{4}{3}\pi\rho\sigma h_{ig}(R_{P1}^3 - R_1^3) \tag{3}$$

3 Assuming a temperature profile as shown in Fig. 3 gives the amount of heat conducted into the layer, from the Fourier-Biot law:

$$\dot{Q}_E = k_{EQ}\frac{(T_0 - T_1)}{\frac{\sqrt{2}}{2}R_0}(A_{DM} + A_G) \tag{4}$$

Similarly, the heat conducted out is given by

$$\dot{Q}_L = k_{EQ}\,A_{EQ}\frac{(T_1 - T_2)}{\sqrt{2}R_0} \tag{5}$$

Thus the net rate of heat conduction into the first layer is

$$\dot{Q}_N = \dot{Q}_E - \dot{Q}_L \tag{6}$$

The time to conduct into the first layer an amount of heat sufficient to dry from R_{P1} to R_1 is obtained by dividing Q_{PH} by the net heat conduction rate into the first layer:

$$\Delta t_A = \frac{Q_{PH}}{\dot{Q}_N} \tag{7}$$

The problem becomes one of "double trial-and-error" because the value of $\dot{Q}_L$ is not known at this stage. To continue the procedure $\dot{Q}_L$ is set equal to zero, and Δt_A is calculated from equation (7).

4 From the solution by Dyer and Sunderland [3], the time required for the first sphere to dry to any interface position R_1 is given by

$$t_S = \frac{c_p\sigma\rho}{k_{DM}G}\left(\frac{R_1^3}{3R_0} + \frac{R_0^2}{6} - \frac{R_1^2}{2}\right) \tag{8}$$

where

$$G = \ln\left(1 - \frac{1}{a}\right)$$

and

$$a = \frac{h_{ig}}{c_p(T_F - T_1)}$$

The time required for the sphere to dry to the previous interface position R_{P1}, using the same value of T_1, is

$$t_P = \frac{c_p\sigma\rho}{k_{DM}G}\left(\frac{R_{P1}^3}{3R_0} + \frac{R_0^2}{6} - \frac{R_{P1}^2}{2}\right) \tag{9}$$

Then the net time required to dry each incremental volume of each sphere in the first layer is

$$\Delta t_B = t_S - t_P \tag{10}$$

For the first time period, $t_P = 0$ since $R_{P1} = R_0$.

5 The value of Δt_A and Δt_B is compared. If $\Delta t_A > \Delta t_B$, then T_1 should be decreased slightly. On the other hand, if $\Delta t_A > \Delta t_B$, then T_1 should be increased slightly. Steps 3 through 5 should be repeated until Δt_A and Δt_B approach each other within reasonable tolerance (e.g., one percent).

(Steps 6 through 9 are for the second layer.)

6 The analysis is continued to the second layer and a temperature profile between the first and second layers is assumed, as shown in Fig. 3. An energy balance on the second stage gives the heat absorbed by that layer during the interval Δt:

$$Q_N = \Delta t\left[k_{EQ}A_{EQ}\frac{(T_1 - T_2)}{\sqrt{2}R_0} - \dot{Q}_L\right] \tag{11}$$

where Δt is the time found in steps 2 through 5 to dry the first layer from R_{P1} to R_1. Again $\dot{Q}_L$ is set equal to zero. A new quantity t_T is defined as the total elapsed time at any point during the particle bed drying analysis and which is given by

$$t_T = t_{PT} + \Delta t \tag{12}$$

where t_{PT} is the previous total elapsed drying time. For the calculation of the first drying period, $t_{PT} = 0$.

7 The amount of heat absorbed by the phase change of each particle in the second layer is given by

$$Q_{PH} = \tfrac{4}{3}\pi\rho\sigma h_{ig}(R_{P2}^3 - R_2^3) \tag{13}$$

and Q_{PH} must be equal to Q_N which is given by equation (11). The foregoing expression is used to solve for R_2, the interface radius of each sphere in the second layer:

$$R_2 = \left(R_{P2}^3 - \frac{Q_N}{\frac{4}{3}\pi\rho\sigma h_{ig}}\right)^{1/3} \tag{14}$$

In equation (14) Q_{PH} has been set equal to Q_N.

8 The assumed value of T_2 and R_2 from step 7 is used to calculate the time required for the sphere to dry to the interface position R_2.

$$t_S = \frac{c_p\sigma\rho}{k_{DM}G}\left(\frac{R_2^3}{3R_0} + \frac{R_0^2}{6} - \frac{R_2^2}{2}\right) \tag{15}$$

where

$$G = \ln\left(1 - \frac{1}{a}\right)$$

and

$$a = \frac{h_{ig}}{c_p(T_F - T_2)}$$

Equation (15) in the foregoing is from reference [3]. The time which would be required for the sphere to dry to the previous interface position under the influence of the same T_2 as previously, is calculated using

$$t_P = \frac{c_p \sigma \rho}{k_{DM} G} \left(\frac{R_{P2}^3}{3R_0} + \frac{R_0^2}{6} - \frac{R_{P2}^2}{2} \right) \tag{16}$$

A quantity t_2, the trial total elapsed drying time of the second layer of the particle bed, is calculated using

$$t_2 = t_{PT} + (t_S - t_P) \tag{17}$$

9 The times t_T from the first layer and t_2 are compared. Since t_T is fixed, t_2 must be adjusted until it approaches t_T satisfactorily. Equations (15) through (17) show that increasing T_2 decreases t_2. Likewise, decreasing T_2 increases t_2. Then, if $t_2 < t_T$, T_2 should be decreased slightly. If $t_2 > t_T$, T_2 should be increased slightly. After each adjustment of T_2, steps 6 through 9 should be repeated until t_2 sufficiently approaches t_T, and the energy balance is satisfied.

The analysis used on the second layer could be used on the third layer also. However, the third layer is temporarily excluded from the analysis for reasons explained in the following. When the present analysis is applied to a particle bed freeze-drying problem, the results show that the difference between the frozen core temperature T_F and T_2 is very small. Since T_3 must have a value between T_2 and T_F, the temperature gradient between the second and third layers is negligible, and, for this reason, $\dot{Q}_L$ for the second layer (step 6) is assumed to be zero. The negligible temperature gradient allows the third and all successive layers to be excluded from the analysis of the first and second layers of particles. After the first layer is completely dried (and the second layer is partially dried), the second and third layers become the subject of the analysis, with the fourth and all successive layers being excluded. The pattern of a two-layer analysis progresses through the bed until the entire bed is dried.

To complete this "two-layer analysis," attention is returned to step 3 where it is recalled that $\dot{Q}_L$, the heat conducted out of the first layer and into the second, was taken to be zero. Since the temperatures T_1 and T_2 have been determined, $\dot{Q}_L$ for the first layer is determined from equation (5). A new value of Δt_A is calculated from step 3 by inserting the nonzero value of $\dot{Q}_L$ into equation (6). The iteration in steps 3 through 5 results in a new value of T_1. The old and new values of T_1 are compared and, if they are within a fixed tolerance (e.g., one percent), then the set of calculations is complete. If they are not within the tolerance, the iteration of steps 6 through 9 is repeated, and then steps 3 through 5 again until the old and new values of T_1 converge satisfactorily.[2]

At this point another time increment is taken in the quasi-steady analysis of the particle bed drying problem. This is done by returning to step 2 and decreasing R_1 by another small increment. Steps 2 through 9 are repeated until the first layer is dried. The initial trial temperatures T_1 and T_2 for each new set of calculations are simply the last values of T_1 and T_2 from the previous set of calculations.

After the first layer is dried it is assumed that the entire layer instantaneously reaches a uniform temperature T_0. This assumption is valid because the latent heat required in drying a given layer is much larger than the sensible energy required to raise the temperature of the dried layer. Therefore, for analytical purposes, the first layer is discarded, and the previous second layer becomes the new first layer, and so forth, through the particle bed. The previous values T_2, R_2, and R_{P2} become the new values T_1, R_1, and R_{P1}, respectively. Likewise, the previous values T_3, R_3, and R_{P3} become the new values T_2, R_2, and R_{P2}, respectively. As each layer of the bed dries, the remaining layers advance one layer in this manner until the particle bed is completely dried.

[2] No more than three iterations are required for convergence.

Experimental Test

One experiment was designed and performed in an effort to verify the model and finite difference analysis presented in the previous section. The experimental test was devised so that it conformed to the mathematical model as nearly as possible. The material selected to undergo sublimation was ground beef. Fig. 3 shows a cross section of the arrangement of the experimental test section. The tests were conducted with the same equipment and procedure as described in reference [8].

One experimental run was made at 2-mm total pressure. The heated surface was maintained at 100 deg F during most of the run. During the process of drying, the weight of the bed was recorded at various time (15 min) intervals. The average particle diameter for the bed tested was 0.01 ft and the bed was three layers thick.

The experimental results are given and discussed in the following section.

Results

Comparison of Analytical and Experimental Results. The method chosen to compare the experimental and analytical results is to compare the quantity of meat dried experimentally as a function of time to the analytically predicted quantity of meat dried as a function of time. A dimensionless quantity b is defined as the ratio of the mass of material dried at any time t to the final total mass of material dried. If it is assumed that the material has a uniform density, b can be expressed by the ratio of volume of material dried to the total volume of material.

The properties used in the analytical calculation are as follows: $k_{DM} = 0.09$ BTU/hr-ft-deg F, $\sigma = 0.57$, $T_F = 28$ deg F, $c_p = 0.46$ BTU/lbm deg R, $\rho = 57.4$ lbm/ft^3, $h_{ig} = 1220$ BTU/lbm, $k_G = 0.014$ BTU/hr-ft-deg F. The first three values are taken from reference [8], the next three from reference [9], and the remaining one from reference [10].

Fig. 4 shows a curve of "b" versus time for the analytical and experimental results. The figure shows a satisfactory correspondence, the total drying times being within ten percent of each other. It is believed that the longer experimental drying time can be attributed to the fact that it takes more than an hour for the particle bed surface to reach a temperature of 100 deg F, whereas in the analytical case it is assumed to reach a temperature of 100 deg F instantaneously. It is believed that the faster drying rates at intermediate points on the experimental curve can be attributed to end effects on the particle bed. The thermal conductivity of cork is 0.025 BTU/hr-ft-deg F [11], while that of water vapor and freeze-dried ground beef are 0.014 and 0.09 BTU/hr-ft-deg F, respectively. Although one of the best available insulating materials was used, the heat transfer through the cork could significantly affect the results.

Comparison With Earlier Published Work. A research finding on an experimental basis which has provoked considerable controversy

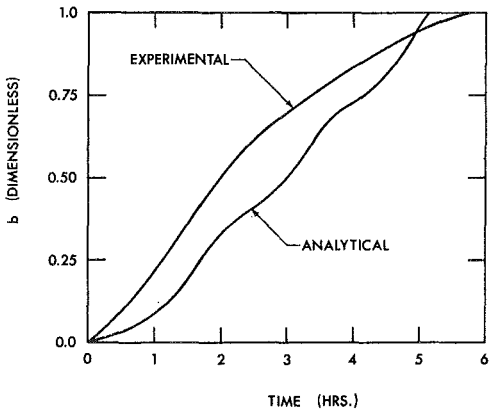

Fig. 4 Fraction of material dried versus time

Table 1 Drying time for various numbers of layers of particles

Number of layers of particles	Radius of particles (ft)	Total drying time (hr)
1	0.024	12.3
2	0.024	22.4
3	0.024	32.4
4	0.024	42.5
5	0.024	52.5

Table 2 Comparison of drying times for slabs and particle beds

	d_{SL} = 0.1 ft, t_{SL} = 40.0 hr		d_{SL} = 0.2 ft, t_{SL} = 160 hr	
M	R_0 (ft)	t (hr)	R_0 (ft)	t (hr)
1	0.0955	195.	0.191	782.
2	0.0477	88.7	0.0955	354.
3	0.0318	56.9	0.0637	228.
4	0.0239	42.5	0.0477	168.
5	0.0191	33.2	0.0382	133.
6	0.0159	27.5	0.0318	110.
7	0.0136	23.3	0.0273	93.9
8	0.0119	20.3	0.0239	82.0
9	0.0106	18.1	0.0212	72.4
10	0.00955	16.3	0.0191	65.1

among the research workers in the area is that of Seltzer [12]. His work in freeze-drying of peas demonstrated a linear relationship between the number of layers and the required total drying time, which is contradictory to the results for drying of slabs in which the drying increases roughly with the square of the slab thickness.

In order to see if this trend would also apply for packed beds of ground beef spheres, analytical results were calculated as described earlier for beds of particles of radius 0.024 ft. Beds of one through five layers were considered, and the property values and thermal conditions were taken as those used in the analytical calculation described above except that the porosity, σ, was taken as 0.72. The results of these calculations are presented in Table 1 and very strikingly demonstrate the linear relationship reported by Seltzer.

Optimization. For a given unit of freeze dryer equipment, where dryer surface area is the limiting factor in freeze-drying capacity, it is interesting to know the optimum depth of material which should be dried and to know whether the material should be in slab or particle form. For this consideration a one-sq-ft slab of ground beef freeze, dried with each of the larger surfaces being held at 100 deg F, is first analyzed using the results of reference [1]. Slabs of 0.1 and 0.2-ft thickness were analyzed.

For comparison, a one-sq-ft particle bed having the same mass as the slab is considered. Calculations were made for particle beds of 1 to 10 layers with a total mass equivalent to the two slabs of different thicknesses which were analyzed. In the calculations the same thermal conditions and property values, except σ = 0.72, were used as given in the foregoing.

Table 2 gives the drying times for the calculations described above. It is seen that, in either case, the total drying time for a particle bed having four layers or less is greater than the drying time of the equivalent mass slab. As seen in Table 2, particle beds having at least nine or ten layers have a total drying time which is less than half the total time for a slab of equal mass, indicating the advantage of the particle bed over the slab from the standpoint of drying rate when surface area in the dryer is considered the controlling factor.

For a given mass of material to be freeze-dried, the results indicate that the smaller the size of the particles composing the particle bed, the shorter the total drying time. However, in realistic circumstances the smallness of the particles likely would be limited to a point where making them smaller would not be economically feasible. Also, the drying time appears to be approaching an asymptotic value with increasing number of layers so that little would be gained using more than ten layers.

If it is desired to increase the amount of mass in a given dryer, the results in Table 2 indicate how this should be done to optimize drying time. For example, the mass could be doubled by: (*a*) doubling the number of layers with the same size particles, or (*b*) doubling the particle diameter with the same number of layers.

Table 2 shows that for two layers of particles and a radius of 0.0477 ft the drying time is 88.7 hr. For the same radius and twice the number of layers the drying time is 168 hr; thus, doubling the mass resulted in doubling the drying time. On the other hand, for a radius with a value twice 0.0477 ft (0.0955 ft) but with two layers the drying time shown in Table 2 is 354 hr. For this method, doubling the mass caused the drying time to increase by a factor of four. This example illustrates that for optimum conditions (when it is desired to increase the mass dried) the number of layers should be increased rather than the size of particles.

References

1 Dyer, D. F., Hardin, T. C., and Sunderland, J. E., "A Quasi-Steady Solution for Unidirectional Freeze-Drying," unpublished report, Georgia Institute of Technology, Atlanta, Ga., 1965.

2 Cox, C. C., "Freeze-Drying of Spheres and Cylinders," MS thesis, Auburn University, Auburn, Ala., 1969.

3 Dyer, D. F., and Sunderland, J. E., "Sublimation Dehydration of Particles," *Transactions of Sixth Southeastern Seminar on Thermal Sciences*, North Carolina State University, Raleigh, N. C., 1970, pp. 33-42.

4 Chen, J. C., and Churchill, S. W., "Radiant Heat Transfer in Packed Beds," *American Institute of Chemical Engineers' Journal*, Vol. 9, No. 1, 1963, pp. 35–41.

5 Yagi, S., and Kunii, D., "Studies on Effective Thermal Conductivities in Packed Beds," *American Institute of Chemical Engineers' Journal*, Vol. 3, No. 3, 1957, pp. 373–381.

6 Schotte, W., "Thermal Conductivity of Packed Beds," *American Institute of Chemical Engineers' Journal*, Vol. 6, No. 1, 1960, pp. 63–67.

7 Fox, E. C., and Thomson, W. J., "Coupled Heat and Mass Transport in Unsteady Sublimation Drying," *AIChE Journal*, Vol. 18, 1972, pp. 792–797.

8 Hardin, L. L., and Dyer, D. F., "An Experimental Study of Particle Freeze-Drying," presented at the Eighth International Congress of Refrigeration, Washington, D. C., 1971.

9 Keenan, J. H., and Keyes, F. G., *Thermodynamic Properties of Steam*, Wiley, New York, 1967.

10 Bird, B. R., Stewart, W. E., and Lightfoot, E. N., "Thermal Conductivity and the Mechanism of Energy Transport," *Transport Phenomena*, Wiley, New York, 1960, pp. 243-264.

11 Kreith, F., *Principles of Heat Transfer*, International, Scranton, Pa., 1965, p. 594.

12 Seltzer, E., "Accelerating Freeze-Dehydration," *Freeze-Dehydration of Foods*, Research and Development Associates, Food and Container Institute, Chicago, 1960.

L. C. WITTE
Professor and Chairman.
Mem. ASME

T. J. VYAS[1]
A. A. GELABERT[1]

Department of Mechanical Engineering,
University of Houston,
Houston, Texas

Heat Transfer and Fragmentation During Molten-Metal/Water Interactions

Molten metals, (mercury, lead, zinc, bismuth, tin, and aluminum) were quenched in water and liquid nitrogen. High-speed photographs provide insight into the fragmentation phenomenon. The key to the vapor explosion is the very rapid transfer of heat which requires substantial surface area: fragmentation provides this necessary surface area. Prior fragmentation theories are examined in light of these experiments and are found to be inadequate. This study indicates strongly that fragmentation occurs when a sample is molten and fragmentation is a response to an external stimulus. Alternate causes of fragmentation are proposed and are predicated upon the initial collapse of a vapor film around the molten metal. The data also show that energy required to form new surface area and to displace water during the fragmentation phenomenon is not significant when compared to the energy available in a molten sample.

Introduction

A PHENOMENON of considerable industrial importance under investigation in recent years is the so-called "vapor" explosion; it involves extremely rapid heat transfer from molten material introduced into a liquid. An understanding of the phenomenon is complicated since heat transfer is accompanied by a very rapid dispersal of the molten material into the liquid.

For years, industry has been plagued by sporadic explosions responsible for the loss of life and property (see [1][2]). Explosions have occurred in the metal industry when molten metal was spilled into water [2]; in the paper industry, where quenching of smelt in green liquor is part of the process [3]; and apparently in nuclear reactors, when molten core material was dispersed in the coolant [4].

The problem has been studied using molten metals, but data are scarce and further experimentation is merited; especially for the case of fragmentation (i.e., the breakup of molten metal into small globules, perhaps down to a few microns). The key to the occurrence of a vapor explosion is the very rapid transfer of heat which requires substantial surface area; fragmentation provides this necessary surface area. In the studies reported here, the following areas were pursued:

(*a*) Investigations consisting of dropping small quantities of molten aluminum, tin, bismuth, lead, zinc, and mercury into water and liquid nitrogen.

(*b*) Evaluation of the proposed theories for fragmentation in light of the experiments.

Item (*a*) consisted of two separate programs. The first [5] involved dropping of relatively large amounts of molten metals (aluminum, bismuth, tin, lead, zinc, and mercury) into water and liquid nitrogen (LN_2) contained in a rather shallow container. The rectangular container was located in an explosion chamber. A gas-fired crucible was used as the heating/dropping container. A shaft rotated 180 deg to invert the crucible and to permit the molten metal to fall. High-speed films showed that a nearly spheroidal particle was produced if the turning was performed rapidly. A Chromel Alumel thermocouple in a stainless-steel thermowell measured the temperature of molten specimens. The temperatures ranged from 903 C for bismuth to 20 C for mercury, and were estimated to be accurate to within ±5 percent. Sample sizes ranged from 10 to 65 gs.

More extensive experimentation [6] was performed with an apparatus shown in Fig. 1 originally developed by Henningson [7, 8]. Basically, the apparatus was a 7/8-in. ID quartz tube, 8-in. long; the tube was situated below a gas-heated crucible containing the metal. This apparatus yielded information concerning the time sequence of events as molten metal fragmented in water by high-speed photography. In contrast, the work using the shallow container yielded information generally only about the aftermath of the interaction, i.e., the configuration of the solidified metal.

The heating/dropping mechanism was a 10-ml porcelain crucible, 30 mm in diameter and 20 mm in height. The tempera-

[1] Presently with Brown and Root, Houston, Texas.

[2] Numbers in brackets designate References at end of paper.

Contributed by the Heat Transfer Division and presented at the Winter Annual Meeting, Detroit, Mich., November 11–15, 1973, of THE AMERICAN SOCIETY OF MECHANICAL ENGINEERS. Manuscript received by the Heat Transfer Division, July 17, 1973. Paper No. 73-WA/HT-28.

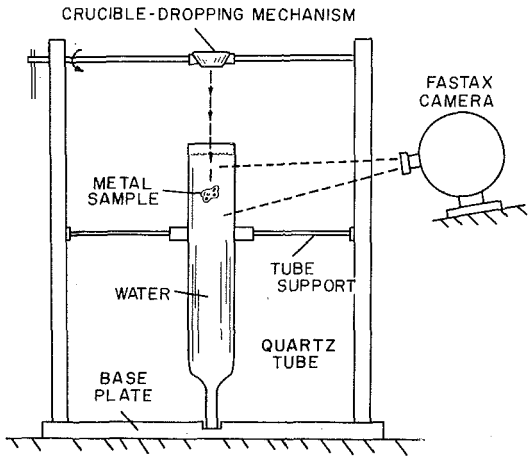

Fig. 1 Schematic drawing of quartz-tube apparatus

ture of the metal was measured with a sheathed Chromel Alumel thermocouple. The water temperature was measured by an Iron Constantan thermocouple. Sample size ranged up to 8.93 gms of lead and the metal temperature went up to 826 C for tin. Lead, tin and bismuth were used. A 16-mm Fastax Model WF-3 camera was used to photograph the interaction.

Experimental Results

Shallow Container. Forty-eight experiments with water and eight with LN_2 were analyzed. The major result was a demonstration of the effects of system variables (sample and coolant temperature, primarily) upon the extent of fragmentation as evidenced by the configuration of the solidified debris.

Fig. 2 shows the effect of increasing the initial temperature of the metal; it shows bismuth after interacting with highly subcooled water (20 C). However, if the coolant temperature approaches the saturation temperature, essentially no fragmentation occurs. This is demonstrated in Fig. 3 which shows the results of high temperature bismuth dropped into saturated LN_2 and nearly saturated water.

Experiments with lead and tin also demonstrated that the extent of fragmentation increases with increasing sample temperature. Lead dropped into saturated LN_2 exhibited no fragmentation. Seven experiments with aluminum were performed—two in LN_2, the remainder in water. Fragmentation did not occur with water or LN_2; the absence of fragmentation may be because the maximum temperature was about 830 C, less than 200 C above the melting point. Fig. 4 shows the solidified samples; they are rather flat on the bottom with protuberant bulges on the top. Fig. 4(*c*) shows that the samples seem to have bonded to the container near their outer edge and to have "puffed-up" in the center. On the top "blow-holes" appear, suggesting that vapor had been pushed up from below through the sample (while still partially molten).

Table 1 Summary of quartz-tube tests

Test number	Metal	T_i (deg C)	T_w (deg C)	M (g)	Type of interaction
1	Pb	589	26.7	8.93	rupture
2	Pb	550	29.4	7.88	shape changes
3	Pb	456	43.3	3.11	rupture
4	Pb	427	35.0	1.99	no change
5	Bi	740	33.9	6.10	violent fragmentation
6	Bi	639	48.9	3.19	no movie results
7	Bi	578	28.9	3.24	mild fragmentation
8	Bi	503	26.6	0.83	mild fragmentation
9	Bi	478	30.6	2.12	rupture
10	Bi	456	26.7	1.22	rupture
11	Bi	503	23.9	5.31	no movie results
12	Sn	526	35.0	0.40	no movie results
13	Sn	700	37.8	5.65	no movie results
14	Sn	690	37.8	2.81	no movie results
15	Sn	643	42.2	2.60	violent fragmentation
16	Sn	572	36.7	2.40	violent fragmentation
17	Sn	571	29.4	3.05	no movie results
18	Sn	543	32.2	3.95	no movie results
19	Sn	503	37.8	2.18	mild fragmentation
20	Sn	477	33.9	2.98	violent fragmentation
21	Sn	484	28.3	3.85	violent fragmentation
22	Sn	394	28.3	2.26	violent fragmentation
23	Sn	368	29.4	2.12	violent fragmentation
24	Sn	337	29.4	2.50	rupture
25	Sn	325	51.6	3.74	no change

Experiments with mercury in water carry the inherent disadvantage that even if fragmentation does occur, the mercury will coalesce afterwards, making a record of the interaction impossible. However, mercury solidifies in LN_2 and for the case of 65 gm dropped in saturated LN_2, no fragmentation occurred.

Tube Results. The quartz tube provides a deep, narrow container compared to the shallow container used previously. Since the high-speed photographs showed the interaction in progress, more insight into the mechanism of fragmentation was provided. Generally, fragmentation proceeds as illustrated in Fig. 5. The sample penetrates the water (time = 0), penetrates deeper into the water, fragmentation is initiated (time = $\Delta\theta_1$), and finally fragmentation is completed as the metal solidifies (time = $\Delta\theta_1 + \Delta\theta_2$).

Four experiments used molten lead; none of the samples up to 590 C fragmented. Some minor ruptures of the samples were noted (probably caused by stresses in the shell as the sample solidified). Many bismuth samples fragmented extensively, becoming more extensive as the temperature was increased. At relatively low temperature only mild ruptures were observed. Experiments with tin covered a range of temperatures from 325 C to 826 C. Above about 370 C, the fragmentation was very violent with significant amounts of water ejected from the tube. Sometimes the phenomenon was so violent that tin fragments were ejected. Table 1 summarizes the tube results.

In addition to the basic observations described in the foregoing,

Nomenclature

A_0 = initial area
A_f = final area
c_p = specific heat capacity
D = diameter of molten metal sphere
P_0 = initial pressure in liquid
P_i = internal sample pressure
P_e = pressure external to sample
h_L = latent heat of metal
ΔH = height of ejected water
M = mass of molten sample
M_w = mass of water
$\dot{Q}$ = average heat transfer rate
q'' = heat flux
R = sphere radius
R_0 = initial cavity radius
T_i = initial metal temperature
T_w = initial water temperature
T_f = final water temperature
w = work
$\dot{w}$ = work rate to form new area
$\dot{w}_{ej}$ = work rate to eject water
$\Delta\theta$ = time interval from sample entry to solidification
$\Delta\theta_1$ = time interval from sample entry to fragmentation initiation
$\Delta\theta_2$ = time interval from fragmentation initiation to solidification
β = liquid compressibility
σ = surface tension
σ_{12} = liquid-liquid interfacial tension
$\sigma_{1,2}$ = surface tension of individual liquid against its vapor
σ_i^d = dispersion force in ith liquid

the initial metal temperature, the water temperature (before and after a test), the sample weight, and the amount of water ejected from the tube were obtained. These data were used to determine (*a*) the average heat transfer rates from the metal, (*b*) the increase of heat transfer area due to fragmentation, and (*c*) the energy required to effect fragmentation.

Heat Transfer Rates. The average heat transfer rate $\dot{Q}$ between a sample and water was computed according to

$$\dot{Q} = \frac{M[c_p(T_i - T_w) + h_L]}{\Delta\theta} \tag{1}$$

It is assumed in equation (1) that the c_p of molten and solid metal is not greatly different. The $\Delta\theta$ is the time interval between entry and completion of fragmentation and solidification. In some cases several metal drops (rather than a single drop) fell into the water and for those cases the $\Delta\theta$ includes the completion of fragmentation for all drops. Therefore, some average heat transfer rates may appear to be lower than actual. Table 2 contains the results of this calculation.

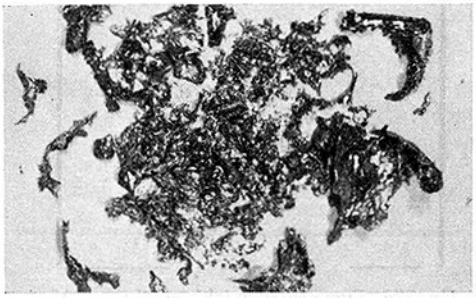

Fig. 2(*a*) 324 C Bismuth, 20 C water, 40 g

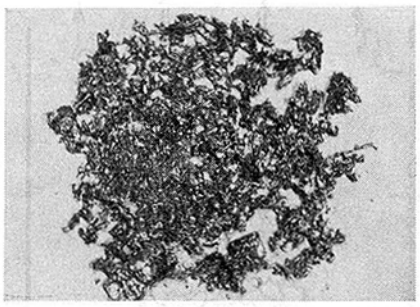

Fig. 2(*b*) 601 C Bismuth, 20 C water, 40 g

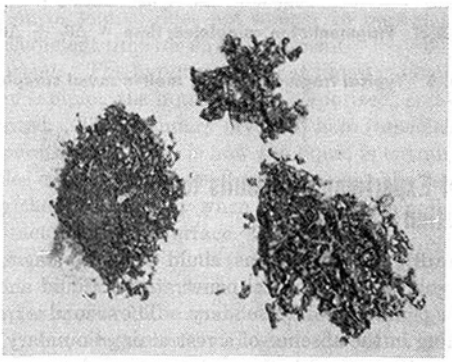

Fig. 2(*c*) 871 C Bismuth 20 C water, 40 g

Fig. 2 The effect of initial temperature upon fragmentation of Bismuth

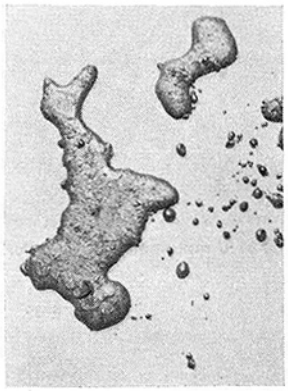

Fig. 3(*a*) 829 C Bismuth, −210 C nitrogen, 30 g

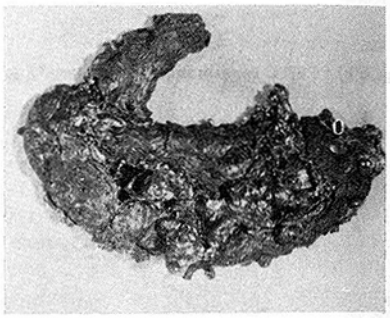

Fig. 3(*b*) 820 C Bismuth, 95 C water, 28 g

Fig. 3 Residue of Bismuth samples dropped into nitrogen and water

Surface Area Increase. When molten metal contacts water and fragments, an increase in surface area occurs. The extent of the heat transfer area increase along with the *rate* of increase controls the intensity of the interaction. It is difficult to estimate the increase because of the wide distribution of particle sizes and shapes. However, an estimate was obtained from the metal samples retrieved in this investigation.

In this work, all particles, including the original drop, were assumed to be spherical. The residue were screened through sieves and the weight of metal collected by each sieve was obtained with a precision balance. By relating area to weight and assuming that the particles were distributed uniformly according to sieve size, the final surface area was estimated. Table 2 contains data for (*a*) the initial sample area, (*b*) the final area, and (*c*) the fractional area increase for the samples to which the foregoing procedure could be applied. This procedure underestimates the area increase since a sphere has the minimum area for a given mass.

Energy Consideration. Once molten metal begins to fragment, only a few msec are required for completion, and in that period a large increase in heat transfer area occurs. The work required to form new area must come from conversion of the internal energy of the sample, and is the energy required to overcome the surface tension of the molten metal. A question is: Is this work a significant part of the internal energy of a molten sample? If so, the energy available to be converted into pressure forces would be reduced. The work done to form new area is

$$w = \sigma(\Delta A) \tag{2}$$

where σ applies to the metal/water interface. The results of this calculation are given in Table 2 as work rate $\dot{w}$, found by dividing the work by $\Delta\theta_2$. Clearly, the energy required to form new area is *not* a significant portion of energy being transferred.

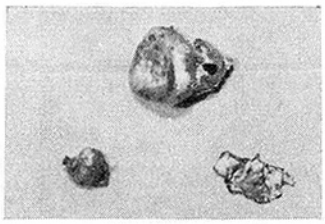

Fig. 4(a) 731 C aluminum, 20 C water, 12 g

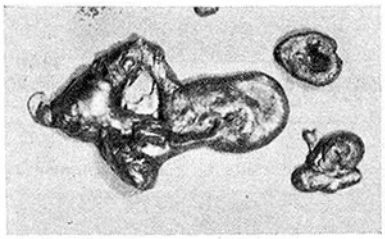

Fig. 4(b) 787 C aluminum, 20 C water, 17 g

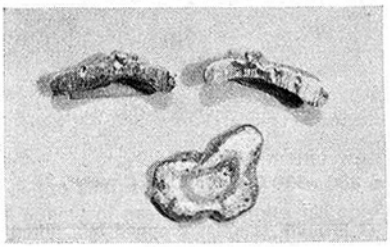

Fig. 4(c) 727 C aluminum, 20 C water, 12 g

Fig. 4 Aluminum samples showing blowholes and bottom cavities

When a sample fragmented, the violence generally resulted in water being ejected from the tube. The kinetic energy of ejected water could not be obtained; however, the potential energy could be approximated since the amount of water ejected and the height to which it was ejected could be obtained.
The work required then is

$$w_{ej} = \Delta M_w \Delta H \tag{3}$$

Table 2 shows the work rate for ejection, found by dividing w_{ej} by $\Delta\theta_2$. Although $\dot{w}_{ej}$ is higher than $\dot{w}$, it is still small compared to the total energy transfer rate.

Physical Nature of Fragmentation

In addition to the quantitative data, there was valuable information from the high-speed photographs of a strictly visual nature, mostly from the quartz-tube work.

It was repeatedly observed in the films that bismuth dispersed immediately as it penetrated the water. This apparently was the result of the Weber number effect (i.e., the inertial effects of the water on the sample broke it into smaller, more stable drops). However, after the initially dispersed drop had dropped further into the tube, these same droplets fragmented massively.

In some cases, the metal entered the water as several droplets, rather than a single drop. In some of these cases, fragmentation of a single droplet was followed immediately by fragmentation of the other drops, as depicted in Fig. 6. In this case, there were three drops involved—one fragmented and set off the other two. There is little doubt that the first event initiated the other. The implication of this observation is discussed later.

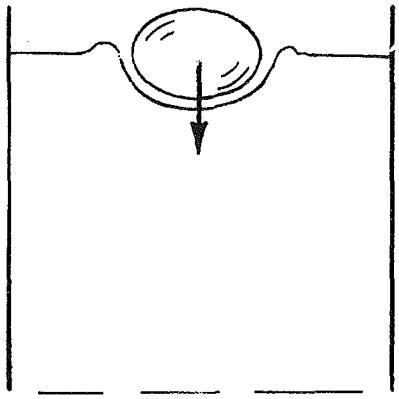

Fig. 5(a) Sample penetrating surface; time = 0

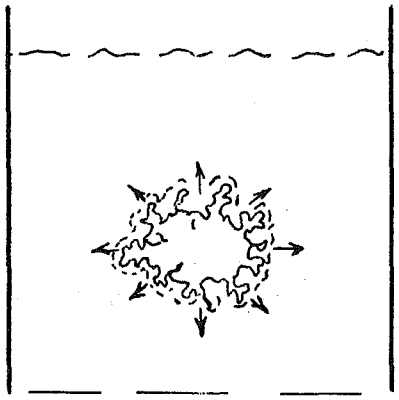

Fig. 5(b) Fragmentation initiated; time = $\Delta\theta_1$

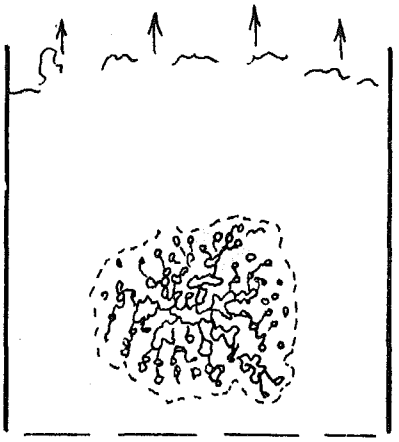

Fig. 5(c) Fragmentation completed; time = $\Delta\theta_1 + \Delta\theta_2$

Fig. 5 Typical fragmentation of molten metal sample

Relation of Experimental Results to Fragmentation Theories

Theoretically, two situations could lead to fragmentation; the first involves molten metal penetrating a liquid and entrapping liquid against the solid boundary. The second is fragmentation occurring in the absence of a restraining boundary (i.e., the fragmentation occurs with the metal surrounded only by bulk liquid). The result may be the same, but the cases are clearly different and should be considered individually. Both situations

Table 2 Quartz tube research data

T/N	$\Delta\theta_1$ (sec)	$\Delta\theta_2$ (sec)	$\dot{Q}$ (kwatts)	(T_f) (deg C)	A_0 (cm²)	A_f (cm²)	$\frac{A_f - A_0}{A_0}$	$\dot{w}$ (kwatts × 10^{-5})	$\dot{w}_{ej}$ (kwatts × 10^{-5})
1	...	...	...	37	...	...	...	...	...
2	...	...	...	36	...	...	...	...	...
3	...	...	...	47	...	...	...	...	...
4	...	...	...	38	...	...	...	...	...
5	0.01	...	8.65	43	5.1	35.0	5.90	...	...
6	...	...	...	54	2.3	6.8	1.90	...	...
7	...	...	...	36	2.9	6.8	1.35	...	...
8	0.003	0.001	2.45	30	0.9	2.6	1.80	6.33	442.0
9	0.042	...	7.53	33	2.7	4.3	0.56	...	...
10	0.050	...	2.54	31	1.2	1.9	0.55	...	...
11	...	...	...	29	...	...	...	...	...
12	...	...	...	39	...	...	...	...	...
13	...	...	...	49	4.1	38.0	8.30	...	...
14	...	...	...	46	2.6	23.4	8.12	...	...
15	0.0075	0.00133	32.90	45	2.4	9.7	2.98	28.5	1000.0
16	0.0080	0.00133	24.50	42	3.3	13.1	2.90	38.0	661.0
17	...	...	...	34	...	...	...	...	...
18	...	...	...	37	...	...	...	...	...
19	0.009	0.0030	20.10	40	3.1	4.4	0.42	2.11	...
20	0.0094	0.0025	28.40	40	2.7	14.6	4.50	24.90	177.2
21	0.006	0.00227	37.60	38	3.9	15.5	2.93	26.50	672.0
22	0.050	0.00228	5.96	34	2.2	16.1	6.27	31.90	584.0
23	0.070	0.00220	3.71	32	2.1	15.3	6.20	31.20	807.0
24	0.25	...	1.31	32	3.4	10.1	1.96	...	...
25	...	...	...	34	...	...	...	...	...

were experienced in this study; however, entrapment is well-known and will not be discussed further. Fragmentation in the bulk occurs when metal is dropped into a relatively deep container and does not contact a container surface. High-speed films showed that fragmentation in this situation occurs only when the sample is still molten.

In the past, three theories have been proposed for fragmentation of this type. They are (*a*) the violent boiling theory, (*b*) the entrainment theory, and (*c*) the Weber number effect.

Violent Boiling. When a sample is quenched in a liquid, the cooling is characterized by a boiling curve traced in reverse (i.e., from high to low temperatures as in Fig. 7). Film boiling is hydrodynamically "quiet;" i.e., little turbulence is attributed to film boiling. However, the transition and nucleate regimes are relatively violent. The collapse and re-formation of vapor creates a rapidly varying pressure field near the hot surface. The violent boiling hypothesis states that, if the sample enters the transition-nucleate regime in the molten state, the hydrodynamic violence tears the particle apart.

Results of this study indicate that the violent boiling hypothesis (as stated) is not valid because of the time scales involved. Transition boiling around solid particles has been studied by Stevens [9]; the oscillation time for vapor collapse and re-formation around small spheres was found to be on-the-order-of a few msec. Our results indicate that the entire fragmentation occurs in a slightly longer period. Therefore, if transition has any effect upon fragmentation initiation, it must occur in the *initial* collapse of the vapor film. The violence (caused by collapse and re-formation of vapor) does not appear to be significant since there is insufficient time for its development.

Entrainment. The hypothesis is that liquid is introduced into the molten sample; the liquid is then vaporized, and the sample is fragmented. The quandary involved here (especially for very high temperature samples) is how the liquid is entrained. Very hot samples enter water enveloped by vapor; the sample is not wetted by the liquid. Only when the vapor film collapses could liquid contact the sample surface.

Photographs obtained in this study show no evidence of entrainment. In fact, just prior to initiation of fragmentation, most samples appear to be completely surrounded by vapor; in the next frame, fragmentation began. It seems unlikely that liquid could have penetrated into the sample in the intervening period. Another observation tends to discredit entrainment. As mentioned before, fragmentation of a droplet in one part of the tube "set-off" the fragmentation of other droplets, indicating that triggering is caused by an external source (i.e., something outside the sample). If fragmentation were caused by the vaporization of entrained liquid, the fragmentation of one droplet should have no effect upon the fragmentation of other droplets.

Weber Number Effect. Fragmentation may result when the inertial forces acting upon a sample overcome the surface tension forces holding the sample together. The ratio of these two forces is called the Weber number.

The Weber number effect does cause dispersal of the sample; however, the Weber number effect is *not* the major cause of fragmentation. This was apparent in several photographic sequences where the sample dispersed somewhat upon entering, but fragmented violently at a greater depth. Consequently, the Weber number effect can be discounted as the prime mechanism for fragmentation. This observation agrees with the results of Ivins [10] for gallium and water.

The foregoing discussion discounts the three most accepted hypotheses for fragmentation; therefore, the mechanism is still unknown. However, the results of the investigations indicate strongly that (1) fragmentation is a response to an external stimulus, (2) fragmentation occurs only when the sample is still molten. Further discussion of fragmentation should include these two observations as inherent to the phenomenon.

If a spherical sample is molten and in *static* equilibrium, the pressure forces are balanced by the surface tension forces.

$$P_i - P_e = \frac{4\sigma}{D} \tag{4}$$

If the diameter remains unchanged, an increase in ΔP will overcome the σ-forces and the sample may subdivide into smaller, more stable drops. The criterion for fragmentation is then established; but the mechanism by which the equilibrium equation (4), is violated remains unknown at present. From energy considerations it is apparent the fragmentation energy required must come from the sample's internal energy. Some of the possible mechanisms are now discussed.

Fragmentation Caused by Vapor Film Collapse. Extremely hot drops are blanketed by vapor when they penetrate the liquid (i.e., they are in the film boiling regime). As the body cools, eventually the film collapses and transition from film to nucleate boiling ensues. For small spheres, the initial collapse of the vapor film is very rapid; Stevens [11], for example, observed that the

collapse around silver spheres occurs in less than 0.25 msec.

The vapor film collapse leads to a number of possible mechanisms that could cause fragmentation:

Impact Pressures. If the film collapses completely, the liquid strikes the sample surface, causing the water to be decelerated very rapidly, giving rise to the so-called impact pressure. If this pressure is transmitted into the sample, an imbalance of pressures could occur.

Lord Rayleigh [12] solved the problem of the impact pressure of a liquid impacting a solid sphere if the cavity between the sphere and the liquid is a vacuum. Rayleigh's result is

$$P_{\text{impact}} = \left[\frac{2}{3}\beta P_0 \left(\frac{R_0^3}{R^3} - 1\right)\right]^{1/2} \tag{5}$$

The application of equation (5) to a situation typical of our experiments yields an impact pressure of ~100 atmospheres. This shows that the impact pressure on a molten-metal surface may be a significant factor in the fragmentation process. The phenomenon of vapor film collapse is clearly more complicated than Rayleigh's problem; the mechanics of vapor film collapse are not well understood at this point. Consequently, the calculation above must be viewed as a first approximation to the actual impact pressures that might occur.

Reduction in Surface Tension. In equation (4), the surface tension is a property of the molten metal *and* the environment surrounding the sample. For example, σ of molten materials against a gas may be considerably greater than the σ against a liquid. As the vapor collapses, the sample may undergo almost a step change in surface tension. Since the environment suddenly changes from a gas (water vapor) to a liquid, the surface tension may be drastically reduced as the liquid touches the surface.

Calculation of the surface tension change as the vapor film collapses is indeed a difficult problem. According to Fowkes [13], liquid-liquid interfacial tension can be expressed as

$$\sigma_{12} = \sigma_1 + \sigma_2 - 2[\sigma_1^d \sigma_2^d]^{1/2} \tag{6}$$

The application of equation (6) to metal-water systems will give the approximation

$$\Delta\sigma = -\sigma_{H_2O} + 2[\sigma_m^d \sigma_{H_2O}^d]^{1/2} \tag{7}$$

The literature yields practically no data for σ_m^d for the metals of interest. By using data for mercury [13] for estimation, we find that

$$\sigma_{Hg}^d/\sigma_{Hg} \approx 0.40$$

and also for water,

$$\frac{\sigma_{H_2O}^d}{\sigma_{H_2O}} \approx 0.30$$

and then equation (7) reduces to

$$\Delta\sigma \simeq -\sigma_{H_2O} + 0.7[\sigma_m \sigma_{H_2O}]^{1/2} \tag{8}$$

Again, from Fowkes [13], we find that for the metals of interest here that $\sigma_m \approx 6\sigma_{H_2O}$. Then, equation (8) further reduces to

$$\Delta\sigma \approx 0.7\sigma_{H_2O} \tag{9}$$

From equation (9), we can conjecture that the magnitude of change in the surface tension of the molten metal is at most on the order of the magnitude of the surface tension of the water which

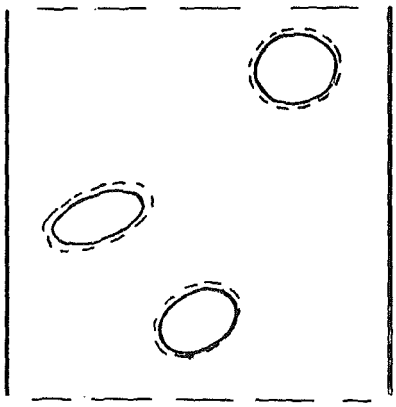

Fig. 6(a) Three unfragmented droplets

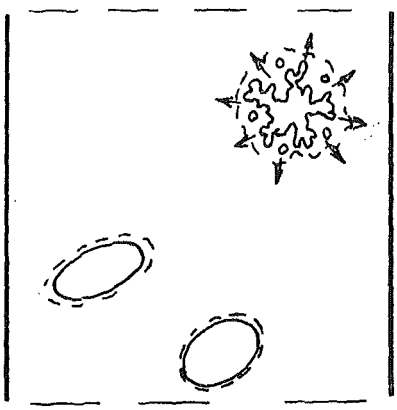

Fig. 6(b) Fragmentation initiated; other droplets unfragmented

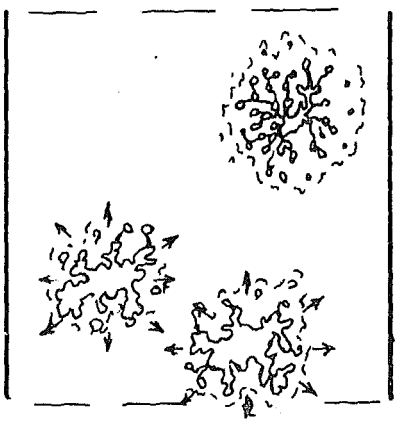

Fig. 6(c) Initiation of fragmentation of other droplets

Fig. 6 Illustration of the effect of fragmentation upon nearby droplets

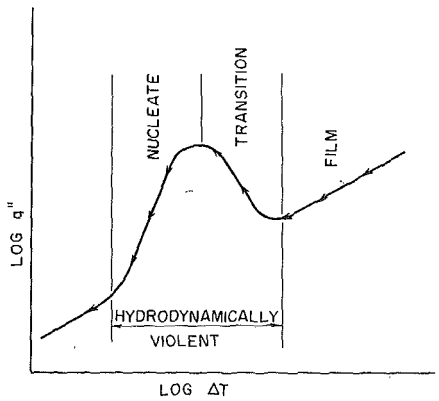

Fig. 7 Boiling regimes for molten metal quenching

contacts it as the vapor film collapses. Still, the order of magnitude of the surface tension decrease is considerably less than the magnitude of the surface tension of the molten metal itself. Therefore, contingent upon the limitations of the approximations made above, it appears that surface tension reduction is not significant enough to account for fragmentation initiation. However, if fragmentation is induced during liquid-liquid contact, it will be considerably enhanced by the reduced interfacial tension.

Thermally Controlled Phenomenon. If, as the vapor film collapses, liquid-liquid contact is achieved, rapid superheating of the liquid adjacent to the metal surface will occur. Katz and Sliepcevich [14] and Nakanishi and Reid [15] in work relating to physical explosions of liquified hydrocarbons attribute the explosion to flashing of superheated liquid as the limit-of-superheat is reached. The limit-of-superheat is the temperature at which vapor nucleation in the bulk of the liquid occurs because of molecular fluctuations. Apfel [16] recently showed that the limit-of-superheat for many liquids is from 0.84 to 0.90 of the critical temperature.

For water at atmospheric pressure the limit-of-superheat is approximately 320 C. Apparently, the data in this paper do not violate the concept of limit-of-superheat, since for all samples experiencing fragmentation, the initial temperature is considerably above the limit-of-superheat. The temperature of the metal surface when the vapor film collapses is unknown, so a direct application of the limit-of-superheat concept to our data is impossible. However, the data of Swift and Baker [17] show exceptions to a direct link between fragmentation and the limit-of-superheat. Notably, for the case of aluminum at 1500 C dropped into 250 C sodium, the aluminum experienced considerable fragmentation even though the limit-of-superheat for sodium at atmospheric pressure is approximately 2100 C, based on the critical point measurements of Dillon [18]. Additionally, the data of Bradley and Witte [19] show that extensive fragmentation of molten jets in water can occur even though the metal is considerably below the limit-of-superheat temperature. Both tin and lead-tin alloy fragmented violently when injected at 260 C into 24 C water.

Therefore, it appears safe to deduce that fragmentation can occur even though the limit-of-superheat is not achieved. This deduction does not preclude the flashing of superheated liquid that might induce fragmentation. However, the nucleation process may occur at the liquid-liquid interface rather than in the bulk of the liquid.

If the vapor film collapses extremely rapidly, another thermal phenomenon might arise. The outer layers of the metal sample could experience cooling so rapidly that the temperature change would take on the character of a "wave" moving into the sample. Then, even though we generally think of a liquid as being incapable of being stressed as a solid might be, the density change of cooler outer layers actually could lead to large pressure increases. This thermal stress mechanism can be valid only if the relaxation time for the sample is longer than the time required for the temperature change to be effected. That is, if the wave can travel into the sample, reflect, and travel back to the free surface quicker than the phenomenon inducing the wave can occur. Anderson [20] reports high speed photographic data of a water-molten salt explosion where the explosion triggering mechanism occurs between two frames at 13,000 frames per sec. So, it is conceivable that a molten sample could be thermally stressed, although presently there is no way to prove or disprove this theory.

Summary

The proposed mechanisms for fragmentation (violent boiling, entrainment, and Weber number effect) were reviewed in light of experiments reported here. The theories are inadequate to account for fragmentation. It is likely that the indirect cause of the breakup is the *initial* collapse of the vapor film (as film boiling around a sample becomes unstable). Alternate mechanisms are presented, predicated upon the collapse of the vapor film upon the metal surface. The direct cause of fragmentation could be (either individually or collectively) pressure differences, surface tension changes, or a thermal phenomenon. Insufficient evidence is available to pin-point the exact cause. Photographs provided the time interval required for fragmentation. These intervals are very short, corresponding to the rapidity of the phenomenon. The entire phenomenon occurs so rapidly that it will be exceedingly difficult to capture photographically the sequence of events that initiate the fragmentation.

Acknowledgment

The authors are indebted to the USAEC for support of Explosive Vapor Formation Research under contract AT-(40-1)-3936.

References

1 Witte, L. C., Cox, J. E., and Bouvier, J. E., "The Vapor Explosion," *Journal of Metals*, Vol. 22, No. 2, 1970, pp. 39–44.

2 Lipsett, S. G., "Explosions From Molten Materials and Water," *Fire Technology*, May 1966, pp. 118–226.

3 Sallack, J. A., "On Investigations of Explosions in the Soda Smelt Dissolving Operation," Canadian Pulp and Paper Association Meeting, Quebec, Canada, June 6–8, 1955.

4 Miller, R. W., Spano, A. H., Dugone, J., Wieland, D. D., and Houghtaling, J. E., "Experimental Results and Damage Effects of Destructive Tests," *Trans. Am. Nuclear Soc.*, Vol. 6, 1963, p. 138.

5 Gelabert, A. A., "An Investigation of the Fast Quenching of Molten Materials," unpublished MS thesis, University of Houston, May 1970.

6 Vyas, T. J., "High-Speed Photographic Study of Molten Metal/Water Interaction," unpublished MS thesis, University of Houston, May 1971.

7 Henningson, P. J., "Identification of Boiling Regimes by Force Measurements," unpublished MS thesis, University of Houston, May 1969.

8 Witte, L. C., and Henningson, P. J., "Identification of Boiling Regimes With a Reaction-Force Apparatus," *Journal of Scientific Instruments*, Series 2, Vol. 2, Nov. 1969, p. 306.

9 Stevens, J. W., and Witte, L. C., "Transient Film and Transition Boiling Around Spheres," *Int. Journal of Heat and Mass Transfer*, Vol. 14, 1971, pp. 443–450.

10 Argonne National Laboratory, Chemical Engineering Division Semi-Annual Report, ANL-7399, Nov. 1967, pp. 162–167.

11 Stevens, J. W., "Transient Film and Transition Boiling From a Sphere," unpublished PhD dissertation, University of Houston, May 1972.

12 Lord Rayleigh, "On the Pressure Developed in a Liquid During the Collapse of a Vapor Cavity," *Philosophical Magazine*, Vol. 34, 1917, pp. 44–98.

13 Fowkes, F. M., "Attractive Forces at Interfaces," *Ind. and Eng. Chem.*, Vol. 5b, No. 12, Dec. 1964, pp. 40–52.

14 Katz, D. L., and Sliepcevich, C. M., "LNG/Water Explosions: Cause and Effect," *Hydrocarbon Processing*, Vol. 50, Nov. 1971, pp. 240–244.

15 Nakanishi, E., and Reid, R. C., "Liquid Natural Gas-Water Reactions," *Chemical Engineering Progress*, Vol. 69, No. 12, Dec. 1971, pp. 36–41.

16 Apfel, R. E., "A Novel Technique for Measuring the Strength of Liquids," *Journal of the Acoustical Society of America*, Vol. 49, Part 2, No. 1, Jan. 1971, pp. 145–155.

17 Swift, D. L., and Baker, L., Jr., "Experimental Studies of High-Temperature Interaction of Fuel and Cladding Materials With Liquid Sodium," Argonne National Laboratory Report ANL-7120, 1965, pp. 839–847.

18 Dillon, I. G., Nelson, P. A., and Swanson, B. S., "Critical Temperatures and Densities of the Alkali Metals," Argonne National Laboratory Report ANL-7025, Aug. 1965.

19 Bradley, R. H., and Witte, L. C., "Explosive Interaction of Molten Metals Injected Into Water," *Nuclear Science and Engineering*, Vol. 48, No. 4, Aug. 1972, pp. 387–396.

20 Anderson, R. P., Data reported at Superheat Explosion Conference, Univ. of Michigan, Ann Arbor, Mich., Nov. 20–21, 1972.

B. S. SHIRALKAR

R. T. LAHEY, JR.

General Electric Company,
Atomic Power Equipment Department,
San Jose, Calif.

The Effect of Obstacles on a Liquid Film

It has been observed in simulated nuclear reactor critical heat flux (CHF) experiments that CHF tends to occur upstream of flow obstructions, such as grid type spacers. An experimental program was conducted to quantify the effect of various obstacles on a liquid film. Although this was an adiabatic (air-water) study, a phenomenological mechanism causing dryout was observed. A simplified analysis of the observed phenomena has indicated that, above a critical Weber number, the ratio of the momenta of the liquid and vapor streams is the important parameter in determining when an upstream dry patch will form.

Introduction

It has been noted in multirod bundles [1][1] that critical heat flux (CHF) tends to occur upstream of flow obstructions such as grid type spacers. In both adiabatic and diabatic annular two-phase flow a liquid film covers the conduit walls, while the vapor phase and entrained droplets flow primarily in the central core region. Although this is a highly idealized description of the flow regime which exists in a rod bundle, it does suggest that the mechanism causing upstream CHF may be related to the disruption of the cooling liquid film.

The present study addresses itself to establishing the basic mechanism of liquid film disruption and the quantification of this effect. It has been carried out under adiabatic conditions in a low pressure air-water test table. Obstructions of various shape and size were used and their effect on liquid film disruption was noted. Although these obstacles were of relatively simple geometry, they do simulate various spacer components and thus provide design guidance in optimizing the thermal performance of a typical grid type spacer.

The conditions under which a thin liquid film, flowing concurrently with a higher velocity air stream, will tend to completely wet the surface were first investigated by Hartley and Murgatroyd [2]. They suggested a criterion based on a force balance at the upstream stagnation point of a dry patch and considered the stability of such a dry patch. Fig. 1 is taken from their paper and shows the major forces acting on the dry patch; viz., the dynamic pressure of the liquid and the surface tension force. Numerous other investigators [3–8], have extended this original analysis to account for diabatic effects such as thermocapillarity and vapor thrust.

Applying a similar type of analysis to the case where obstacles are present, it is found that one must include the effect of the pressure rise in front of the obstacle due to stagnation of the vapor stream. Thus the resultant force balance becomes,

$$\delta(\Delta p_{Stag}) + \sigma(1 - \cos\theta) + \frac{\rho_V}{g_c}\left[\frac{q''}{\rho_V h_{fg}}\right]^2 \frac{(\rho_L - \rho_V)}{\rho_L}\delta\cos^2\theta + \frac{d\sigma}{dT}\frac{q''}{K}\delta\cos\theta = \frac{\rho_L}{2g_c}\int_0^\delta V_L(y)^2 dy + (K_1 + K_2)\tau_i\delta + \frac{\rho_L g}{2g_c}\delta^2 \quad (1)$$

In the present case of adiabatic, horizontal, two-component, two-phase flow this generalized force balance on the liquid film reduces to,

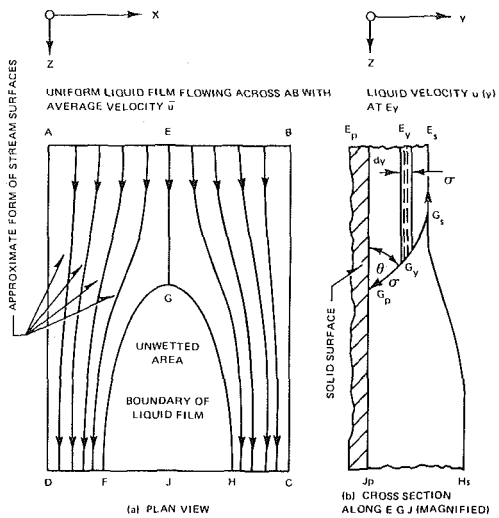

Fig. 1 Dry patch formation in a liquid film

[1] Numbers in brackets designate References at end of paper.

Contributed by the Heat Transfer Division of The Amebican Society of Mechanical Engineers and presented at the AIChE-ASME Heat Transfer Conference, Denver Colo., August 6–9, 1972. Manuscript received at ASME Headquarters, April 20, 1973; revised manuscript received October 20, 1972. Paper No. 72-HT-31.

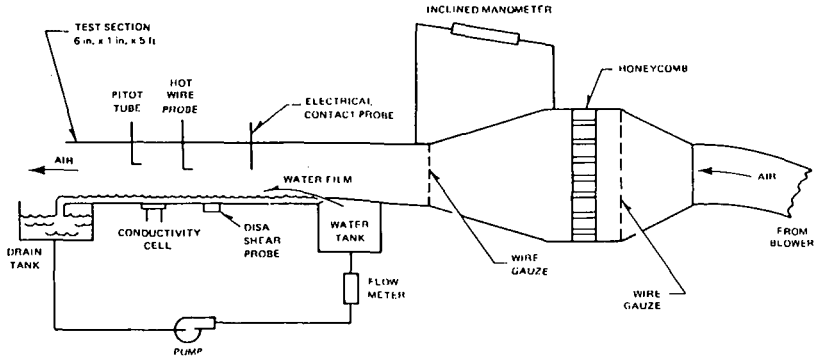

Fig. 2 Schematic of air-water test table

$$\delta(\Delta p_{air}) + \sigma(1 - \text{Cos } \theta) = \frac{\rho_L}{2g_c}\int_0^\delta V_L(y)^2 dy + (K_1 + K_2)\tau_i\delta + 0(\delta^2) \quad (2)$$

Equation (2) will be used in the subsequent analysis of the data in order to quantify the observed mechanism causing adiabatic upstream dryout.

Experimental Apparatus and Measurements

Based on the discussion in the previous section it appears that the following parameters need to be measured in order to predict the dryout in the liquid film.

1 Mean air velocity
2 Mean liquid film flow rate
3 Film thickness
4 Shear stress.

For this purpose, an experimental study was conducted in a plexiglass air-water channel shown schematically in Fig. 2.

Air was supplied from a blower (3 hp, 1120 cu ft/min at 10 in. SP) and passed through an entrance section, which included several wire mesh screens and a honeycomb for flow straightening, and a venturi. Average air velocities of up to 120 ft/sec could be obtained with the blower. A two-dimensional air velocity profile was obtained in the test section, which was a rectangular channel 6 in. wide × 1 in. high (the height is hereinafter referred to as the gap) and 5 ft long. The bottom surface of the channel consists of a ground-glass plate to ensure uniform wetting, and the other three sides were made of clear plexiglass to allow visual observation. The channel gap could be reduced to 1/2 in. over a 20-in. length by attaching a piece with a streamlined leading edge to the underside of the top plate.

Water was introduced as a film between a projecting lip and the ground-glass bottom place, the nominal entry gap being 1/16 in.

In addition to the water flow rate, which was measured by a rotameter, the air flow rate was monitored with the venturi in conjunction with a 4-in. inclined manometer. Other instrumentation included a pitot tube and hot wire probe which could be traversed to measure air and water velocity profiles. The pressure drop across 3-1/2 ft of the test section was measured with the inclined manometer.

The film thickness was measured by using a conductivity cell and an electrical contact probe. These instruments are described in detail in reference [9], where it is also shown that the agreement between the two measurement techniques is quite good.

The flush shear probe used was made by DISA Electronics (Model No. 55-A93). The sensor was a nickel film deposited by sputtering on the end of a quartz rod. A protective quartz coating of 0.00008 in. was applied to the sensor and conductor pads for use in a conductive medium like water. The length of the film was 0.018 in. and the width 0.006 in. The temperature coefficient of resistance was 0.14 percent per deg F.

The probe was mounted in the bottom glass plate so that it was flush with the top surface of the plate, and was oriented so that the length of the film was normal to the direction of the flow. The probe was connected to a DISA model 55-D01 constant-temperature anemometer and was operated at a constant temperature of about 30 deg F higher than the water temperature.

The bridge voltage of the anemometer, E, required to maintain the sensor at a temperature T'_0, in a flowing fluid at a temperature of T'_∞, can be expressed as [9],

$$E^2 = A_1 + B_1\tau_w^{1/3}$$

where τ_w is the wall shear stress and A_1 and B_1 are constants for given values of T'_0 and T'_∞.

To calibrate the probe, a plexiglass block with a gap of 0.030 in. was used. Water was pumped through the gap, and the pressure drop along 9 in. of the length was measured.

The calibration was then used for two-phase flow shear stress measurements. This is valid when the thermal boundary layer thickness at the downstream end of the probe film is small compared with both the liquid film thickness and the half gap (0.015

Nomenclature

A = area
A_1, B_1 = constants relating shear stress to probe voltage
E = bridge voltage of anemometer
g_c = constant, $\frac{\text{lb}_m}{\text{lb}_f}\frac{\text{ft}}{\text{sec}^2}$
h_{fg} = latent heat of evaporation
k = thermal conductivity of liquid
K_1, K_2 = empirical constants in Hartley's formulation
M = ratio of momenta of air and liquid
q'' = heat flux at heater wall
R = radius of cylindrical obstacle
T_0 = temperature of probe
T_∞ = temperature at a remote point in the air stream
$\bar{V}_a$ = mean air velocity
$\bar{V}_L$ = mean liquid velocity
V_∞ = freestream air velocity far upstream of obstacle
We = Weber number
z = distance along heater
Γ = film flow rate/unit width of channel
δ = liquid film thickness
Δp_{air} = pressure rise due to stagnation of air stream upstream of obstacle
θ = contact angle
τ_i = interfacial shear stress
τ_w = wall shear stress
ρ_a = air density
ρ_L = liquid density
ρ_V = vapor density (diabatic case)
σ = surface tension

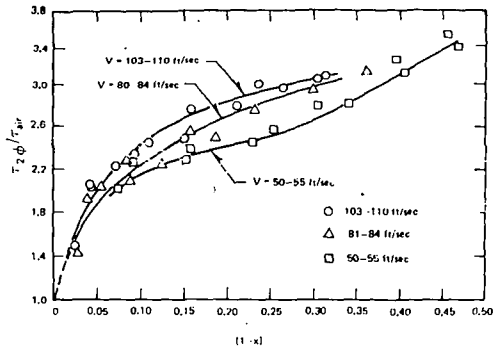

Fig. 3 Measured two-phase shear stress

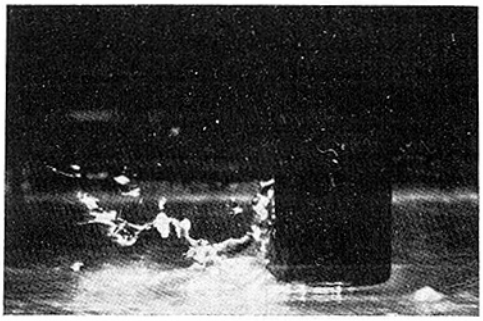

Fig. 5 Long cylinder: V_a = 78 ft/sec, Γ = 270 lb/ft-h

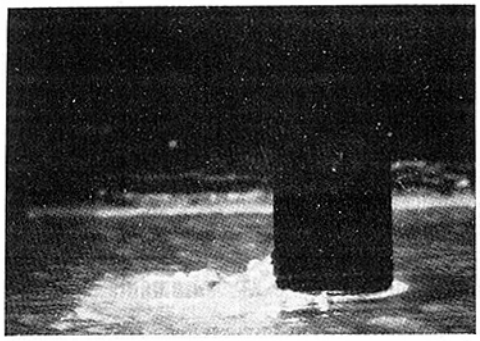

Fig. 6 Long cylinder: V_a = 78 ft/sec, Γ = 170 lb/ft-h

in.) of the calibration piece. Since the nickel film was 0.006 in. wide, the thermal boundary layer thickness is of the order of 0.0001 in. at the downstream end of the element, and the assumption of an "infinite" fluid stream is valid.

The shear stress was measured for a variety of two-phase flow conditions, and some of the data are plotted in Fig. 3. These measurements are in good agreement with the analytical method proposed by Wallis [10], particularly at the lower velocities.

Flow Visualization

During the preliminary calibration runs without obstacles it was observed that as the liquid flow rate was reduced, dry patches appeared in the film, starting near the entrance where the shearing action was the greatest, and propagating downstream. The critical flow rate of water was of the order of 0.05 gpm, corresponding to 50 lb/h-ft at high air velocities, and was lower at low air velocities. This was considered satisfactory and compares favorably with the values of film flow rate at breakup calculated by Hartley and Murgatroyd [2].

At low air and liquid flow rates, ripples appeared on the surface which rapidly formed two-dimensional waves. On increasing the air or liquid flow rates, the water surface became "pebbled." At still higher air flow rates, roll waves formed on the liquid surface. These observations are in agreement with those of Hanratty and Engen [11].

The major emphasis of this experimental program was on the effect of obstacles on the liquid film. Cylindrical and rectangular obstacles were used in this study.

The air and liquid flow rates were first set so that the liquid film covered the floor of the channel. Then, as the liquid film flow was reduced, dry patches were observed near the obstacles. Typically, these patches occurred in front of the 1-in.-high cylinder and the rectangular pieces, as shown in Fig. 4(*a*) (TYPE I). Sometimes the dry patch occurred behind the object, particularly for the short cylinder as shown in Fig. 4(*b*) (TYPE II).

Typical photographs of the flow in the vicinity of various obstacles are shown in Figs. 5 through 13. These photographs were taken with strobe light illumination and an exposure time of 1/1000 sec. In all these photographs, the flow direction is from right to left.

Figs. 5 through 7 show the effect of lowering the water flow rate at an air velocity of 78 ft/sec. At a water flow rate of 170 lb/ft-h, a small dry patch appeared in front of the cylinder. Dry patches appear bright due to light reflecting from the exposed ground-glass surface. When the film flow rate was reduced to 100 lb/ft-h, the dry patch became larger and extended for an appreciable distance in front of the cylinder. It was possible to see a thinning of the liquid film in front of the cylinder, followed by the appearance and enlargement of the dry patches. The interface was generally wavy and substantial entrainment occurred downstream at the higher air velocities. This type of dry patch, which will be discussed in more detail later, appears to be related to the occurrence of diabatic film dryout (CHF), observed upstream of grid-type spacers.

As mentioned earlier, a dry patch appeared preferentially behind short cylinders. This has the shape of a long, narrow strip, which cannot be easily rewetted by increasing the water flow. Figs. 8 and 9 exhibit the thinning of the liquid film and formation of the dry strip as the liquid film flow rate was reduced. This type of behavior is sometimes noted in out-of-pile CHF tests resulting in long blackened areas on the heater rods, typically a few inches behind a grid type spacer, although CHF normally occurs upstream of the spacer prior to observing downstream overheating.

Two rectangular objects (shapes *A* and *B*) were tested with the channel gap reduced to 1/2 in. Dry patches were found to occur

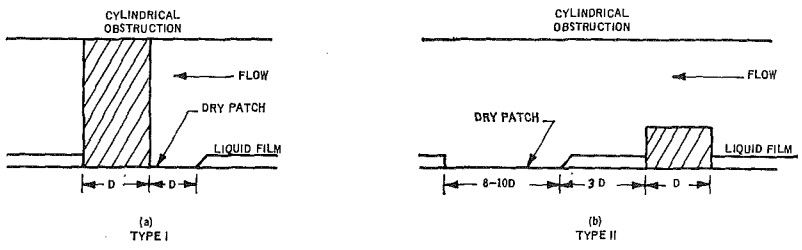

Fig. 4 Location of dry patch

both behind and in front of these obstacles. However, except at the highest air velocities tested, the dry patches appeared ahead of the objects first, as the film flow rate was reduced. As shown in Figs. 10 through 12, for an air velocity of 105 ft/sec, shape *A* was found to cause less thinning of the liquid film immediately in front of it, and dryout occurred at fairly low water flow rates. Fig. 13 shows the relatively large unwetted region in front of shape *B*, at larger film flow rates and a lower air velocity. It can be easily seen that some shapes are definitely more detrimental to the liquid film than others.

Discussion

In annular flow, the critical heat flux is hypothesized to occur when the film flow rate on the heated surface approaches zero. In the presence of the obstacles examined in the previous section, it is obvious that dryout can occur because of the hydrodynamics of the flow at finite values of the film flow rate. To examine quantitatively the influence of these different objects, it was decided to plot the critical film flow rate at which dry patches first occur versus the air velocity for each object. Naturally, the higher the film flow rate is at dryout the poorer the performance of the component from the point of view of CHF. It was very difficult to determine exactly when a dry spot first forms in front of an object, since the film successively passes through the stages of thinning, partial dewetting, and rewetting, leading to formation of a small dry spot which further enlarges as the film flow rate is reduced.

As a basis for comparison, the critical flow rate was *defined* to be that which causes a dry spot 1/8-in. long in front of the object. It should be noted that this arbitrarily defined dry spot does not necessarily correspond to CHF under diabatic conditions. In contrast, when dryout occurred behind an object, the phenomenon was quite sudden and a sizeable patch appeared with a small decrease in film flow rate.

Cylindrical and rectangular objects were evaluated in terms of the critical film flow rate. Fig. 14 is a plot of the critical film flow rate for two 1/2-in.-dia cylinders, one spanning a 1-in. gap and the second one spanning a 1/2-in. gap. The region above the line represents a completely wetted region, whereas at liquid flow rates below the line, dry patches exist. Two plots have been made for each object. One is where, starting from the completely wetted condition, the film flow rate was continuously decreased at a set value of air velocity until a dry patch appeared. The other plot is where, starting from the existence of a dry patch, the film flow rate was continuously increased until the dry patch disappeared. At low air flow rates there is a wide difference in these plots due to the relative importance of surface tension. At higher air velocities, the curves approach each other. This phenomenon was seen for all the objects tested.

A critical Weber number can be defined as,

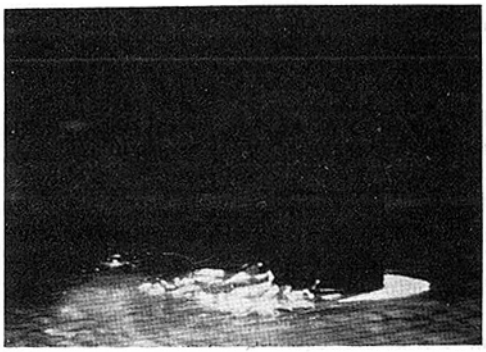

Fig. 7 Long cylinder: $V_a = 78$ ft/sec, $\Gamma = 100$ lb/ft-h

Fig. 8 Short cylinder: $V_a = 47$ ft/sec, $\Gamma = 185$ lb/ft-h

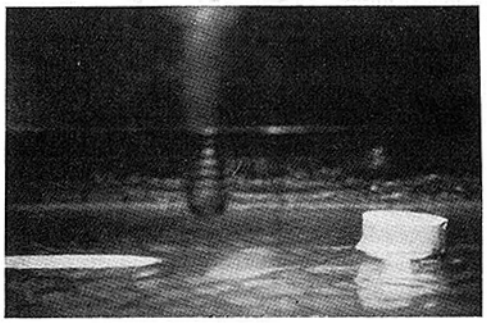

Fig. 9 Short cylinder: $V_a = 47$ ft/sec, $\Gamma = 80$ lb/ft-h

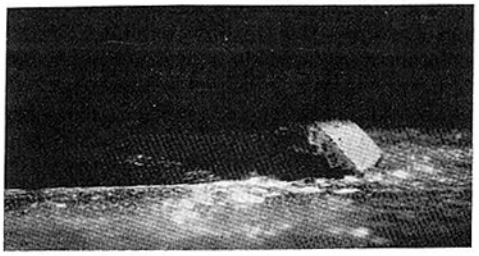

Fig. 10 Rectangular object (shape *A*): $V_a = 105$ ft/sec, $\Gamma = 200$ lb/ft-h

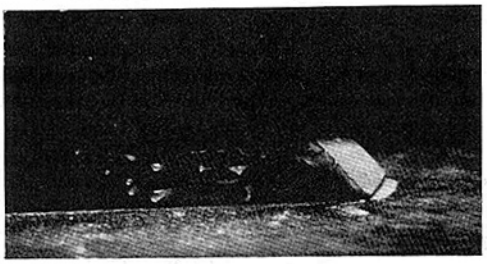

Fig. 11 Rectangular object (shape *A*): $V_a = 105$ ft/sec, $\Gamma = 100$ lb/ft-h

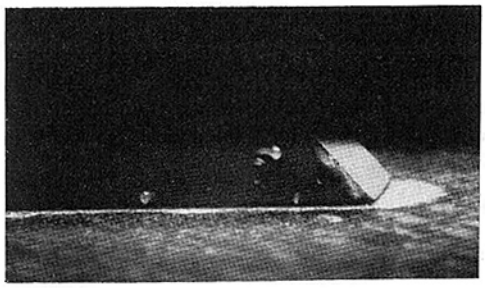

Fig. 12 Rectangular object (shape *A*): $V_a = 105$ ft/sec, $\Gamma = 70$ lb/ft-h

Fig. 13 Rectangular object (shape B): $V_a = 32$ ft/sec, $\Gamma = 150$ lb/ft-h

$$\mathrm{We}_{\mathrm{crit}} \triangleq \frac{(\rho V^2)_{\mathrm{air}}\delta}{g_c\sigma}$$

above which the surface tension effects are no longer important. This has been found to be of the order of 2 to 3. Note that the performance of the two cylinders is very similar, and also that at higher air velocities the critical film flow rate is independent of the air velocity.

Fig. 15 is a composite of some of the results obtained for the various obstacles, showing only the curves made for decreasing film flow rate since this is normally the situation of interest. Some of the conclusions that can be drawn from this study are:

(*a*) Certain shapes are noticeably worse than others with respect to film disruption.

(*b*) Performance of the obstructions appears to be a function of the ratio of the height of the object to the gap size; when dryout occurs in front of the obstacle, the situation was improved by reducing the height of the obstacle with respect to the gap. For dryout behind the object, this trend is not clear. From the evidence available, there appears to be a particular height where the film disruption was a maximum behind an object.

(*c*) When the width of the obstacle was reduced (e.g., 1/4-in.-dia cylinder compared with the 1/2-in.-dia cylinder) the severity of dry patch was reduced. The ratio of the size of the dry spot to the width of the object was found to be about the same for equivalent flow conditions.

Analysis

The flow visualization experiments have shown that upstream dryout can occur due to stagnation of the vapor stream causing a horse-shoe vortex which "scrubs out" the liquid film in front of the obstruction. In order to be able to extend these results to practical cases of interest (i.e., high pressure, diabatic two-phase flow), the force balance on the liquid film will be evaluated to examine the relative importance of the various terms.

Assuming a linear velocity profile in the liquid film, equation (2) can be expressed as:

$$\delta(\Delta p_{\mathrm{air}}) + \sigma(1 - \mathrm{Cos}\ \theta) = \frac{2}{3}\frac{\Gamma^2}{\rho_L\delta g_c} + (K_1 + K_2)\tau_i\delta \qquad (3)$$

The increase in air pressure in front of simple objects can be approximated from potential theory; e.g., for an infinite cylinder,

$$|\Delta p_{\mathrm{air}}|_s = \frac{\rho_a V_\infty^2}{2g_c}\left[\frac{2R^3}{z^3} - \frac{R^6}{z^6}\right]$$

As an example, consider the experimental dryout in front of the long cylinder (1/2-in. dia) which was defined as a dry patch of length 1/8 in. Here,

$V_\infty = 100$ fps

$\Gamma = 150$ lb/h-ft

$\delta = 8.5 \times 10^{-3}$ in. (reference [9])

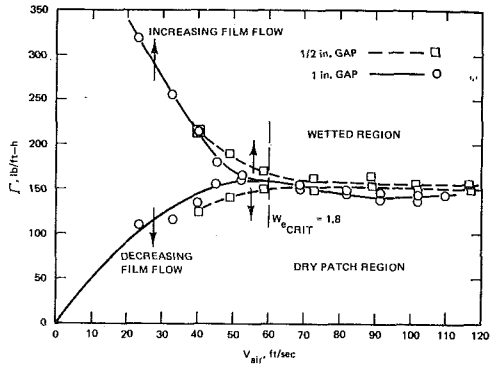

Fig. 14 Critical film flow rate versus air velocity: long circular cylinder (1/2 in. dia)

$z = 3/8$ in.

The force due to stagnation pressure rise is thus,

$$\delta(\Delta p_{\mathrm{air}}) = 5.39 \times 10^{-3}\ \mathrm{lb/ft}$$

Surface tension force ($\theta = 64$ deg),

$$\sigma(1 - \mathrm{Cos}\ \theta) = 2.0 \times 10^{-3}\ \mathrm{lb/ft}$$

Liquid kinetic energy,

$$\frac{2}{3}\frac{\Gamma^2}{\rho_L\delta g_c} = 8.08 \times 10^{-4}\ \mathrm{lb/ft}$$

Form force,

$$(K_1 + K_2)\tau_i\delta = 1.50 \times 10^{-3}\ \mathrm{lb/ft}$$

(using the value of $K_1 + K_2 = 50$ as suggested by Murgatroyd [4]).

Substitution into equation (3) shows that the liquid kinetic energy is an order of magnitude too small to prevent stagnation of the film. For neutral equilibrium, $\Gamma = 500$ lb/h-ft, which is three times the measured value. This corresponds to the incipience of the dry patch in the absence of surface waves. Thus, in order to achieve an accurate force balance, the kinetic energy term in equation (3) must be modified to account for the kinetic energy of the observed surface waves.

It appears that the kinetic energies of the air stream and the liquid waves are the governing factors. Since the wave velocity and the kinetic energy depend on the air and water densities and velocities, the ratio of the average momenta of the air and water is a likely parameter for correlating critical film flow values, particularly at high air flow rates:

$$M \triangleq \frac{\rho_a \bar{V}_a^2}{\rho_L \bar{V}_L^2} = \frac{\rho_L\rho_a \bar{V}_a^2\delta^2}{\Gamma^2} \qquad (4)$$

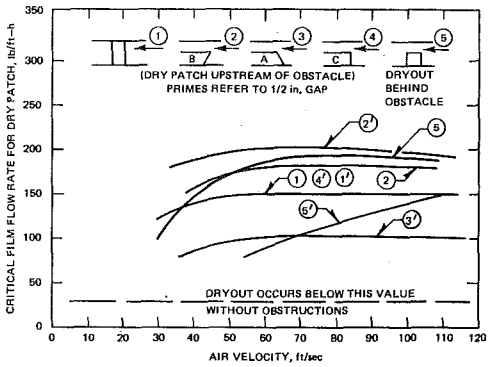

Fig. 15 Comparison of critical film flow rates for various obstacles

Fig. 16 shows the values of M for dryout in front of three of the objects. For the long cylinder, M increases at low air velocities but remains constant in the neighborhood of 14 at higher air velocities. Similar behavior is seen in front of other obstacles with different critical values of M. The corresponding values of M were 32 and 9 for the rectangular objects (shapes A and B, respectively).

With heat addition, the other forces in equation (1) come into play, but none of these is estimated to be very significant [6].

It is expected that the relative performances of various obstacles will be similar in air/water and diabatic steam/water flows. Thus the critical momentum ratio M could be used for steam/water flow (if the liquid-vapor interface characteristics are similar) to get an order-of-magnitude estimate of the critical film flow rate.

Another possible effect is upstream propatation of the dry patch due to thermal conduction. However, a simplified analysis has shown [9] that this will not lead to large upstream enlargement of the dry patch. This implies that significant damage could occur to the heater surface if temperature detectors are not located in the immediate vicinity of the dryout region, an observation known all too well to the experimentalist.

The observed dryout behind the obstacles is a more complex phenomenon involving the interaction between the slow-moving wake flow in the film and the air flow. This occurs generally when there is less blockage to the air stream and less of an increase in air pressure upstream of the object. Some work has been done by researchers [12], on the phenomenon of air flow over bluff obstacles. The pressure field increases in the axial direction starting at a point near the center of the trailing vortex. This slight adverse pressure is sufficient to cause stagnation of the film in this region. The drag coefficient for complex bluff bodies is a function of the Reynold's number, the surface roughness and the amount of boundary layer immersion. Here also the liquid and air momenta appear to be the important parameters. The larger the drag coefficient C_D of the object, the worse its performance is likely to be, since this implies a greater reduction in the liquid momentum.

Summary and Conclusions

In the presence of obstacles, two main types of dry patch formation were obtained. The first type, involving upstream dryout, can be satisfactorily explained in terms of stagnation of the liquid film. The kinetic energy of the waves in the liquid and the pressure rise in the air stream are the dominating factors in the phenomenon. The ratio of the momenta of the air and liquid appears to be a promising parameter for correlating the incipience of dry patches.

Dry patches of the second type, which occur due to stagnation of the wake flow behind obstacles, are dependent on the strength of the downstream air vortex (a function of the air velocity) and the liquid momentum in that region.

The general trends in the behavior of the obstacles are expected to be similar in diabatic flow. It is apparent that some geometric shapes are more conducive to liquid film disruption than others. It appears that an a priori estimate of the effect of a given obstacle shape can be made by calculating the upstream pressure rise from potential theory. The greater the pressure rise, the larger the critical film flow rate and thus the worse the thermal performance of that obstacle if it is used in a nuclear reactor grid spacer.

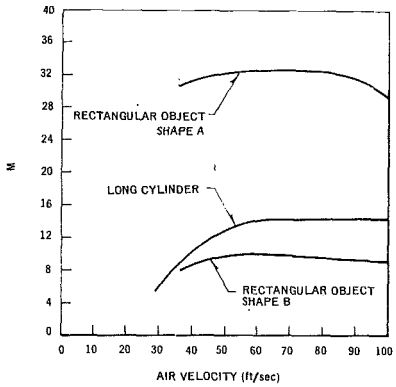

Fig. 16 Critical momentum ratio versus critical air velocity

Acknowledgments

The authors wish to acknowledge the support given this work under AEC Contract AT(04-3)-189, PA-44, and the advice and assistance of Mr. Y. H. Kong.

References

1 Janssen, E., "Two-Phase Flow and Heat Transfer in Multirod Geometries—Final Report," GEAP-10347, Mar. 1971.

2 Hartley, D. E., and Murgatroyd, W., "Criteria for the Breakup of Thin Liquid Layers Flowing Isothermally Over Solid Surfaces," *Int. J. of Heat and Mass Transfer*, Vol. 7, 1964.

3 Hewitt, G. F., and Lacey, P. M. C., "The Breakdown of the Liquid Film in Annular Two-Phase Flow," AERE-R4303, 1963.

4 Murgatroyd, W., "The Role of Shear and Form Forces in the Stability of a Dry Patch in Two-Phase Film Flow," *Int. J. of Heat and Mass Transfer*, Vol. 8, 1965.

5 Zuber, N., and Staub, F. W., "Stability of Dry Patches Forming in Liquid Film Flowing Over Heated Surfaces," *Int. J. of Heat and Mass Transfer*, Vol. 9, 1966.

6 Thompson, T. S., and Murgatroyd, W., "Stability and Breakdown of Liquid Films in Steam Flow With Heat Transfer," Preprint B5.2, presented at the International Heat Transfer Conference, Paris, Aug. 1970.

7 McPherson, G. D., "Axial Stability of the Dry Patch Formed in Dryout of a Two-Phase Annular Flow," *Int. J. Heat and Mass Transfer*, Vol. 13, 1970.

8 Ruckenstein, E., "On the Breakup of Thin Liquid Layers Flowing Along a Surface," *Int. J. of Heat and Mass Transfer*, Vol. 14, 1971.

9 Shiralkar, B. S., "Two-Phase Flow and Heat Transfer in Multirod Geometries: A Study of the Liquid Film in Adiabatic Air-Water Flow With and Without Obstacles," GEAP-10248, Oct. 1970.

10 Wallis, G. B., "One-Dimensional Two-Phase Flow," Chapter 11; equations (11.22) and (11.34), McGraw-Hill, New York, 1969.

11 Hanratty and Engen, "Interaction between a Turbulent Air Stream and a Moving Water Surface," *A.I.ChE.*, Vol. 3, No. 3, 1957.

12 Good, M. C., and Joubert, P. N., "The Form Drag of Two-Dimensional Bluff-Plates Immersed in Turbulent Boundary Layers," *J. Fluid Mechanics*, Vol. 31, No. 3, 1968.

journal of heat transfer

technical briefs

This section consists of contributions of 1500 words or less (about 5 double-spaced typewritten pages, including figures). Technical briefs will be reviewed and approved by the specific division's reviewing committee prior to publication. After approval such contributions will be published as soon as possible, normally in the next issue of the journal.

Effect of Film Thickness on the Infrared Reflectance of Very Thin Metallic Films

E. M. SPARROW,[1] R. P. HEINISCH,[2] and K. K. TIEN[2]

Introduction

When a very thin metallic film is deposited on a substrate, the reflectance of the film-substrate system will vary as the thickness of the film is increased. Beyond a certain thickness, however, further thickening of the film has essentially no effect on the reflectance. The film thus becomes optically opaque and the presence of the substrate no longer affects the reflectance.

In engineering applications involving thin metallic films, it may be relevant to know the thickness at which the film becomes effectively opaque. Furthermore, for film thicknesses smaller than that for opacity, a knowledge of the reflectance versus thickness variation may be needed, as might the minimum thickness at which the reflectance first becomes significantly different from that of the uncoated substrate.

In principle, this information can be obtained by evaluating algebraic equations deduced from electromagnetic theory on the basis of a model in which the media are assumed to be homogeneous and isotropic and the interfaces are optically smooth. As input for such calculations, it is necessary to provide the optical constants (index of refraction n, extinction coefficient k) of the participating media. It has been found that the optical constants of thin films can differ markedly from those of thick specimens of the same material, e.g., [1].[3] For instance, for gold at a wavelength of 10.6 μ, the authoritative *American Institute of Physics Handbook* [2] gives $n = 12.6$, $k = 72$ (interpolated values) for the bulk material, whereas Heavens's survey article [3] gives $n = 0.2$, $k = 50$ for films having thicknesses of at least 1000 Å. The films that were employed in the present investigation had thicknesses on the order of 100 Å (a factor of 10 thinner than those cited by Heavens), thereby adding to the uncertainty of using handbook values of the optical constants.

The just-discussed uncertain nature of analytical predictions for very thin metallic films served to motivate the present investigation. Measurements of monochromatic, specular reflectance were made for metallic films of controlled thickness on a fused-silica substrate. The radiation incident on the test specimens was provided by a CO_2 laser operating at 10.6 μ, a wavelength in the intermediate infrared. Two film materials were investigated—gold and silver. The films were vacuum-deposited with a thickness range from 40 to 150 Å. Measurements were made at angles of incidence between 15 and 65 deg at intervals of 5 deg. The experiments were performed for both perpendicular polarized incident radiation and parallel polarized incident radiation. Direct measurements were made of both the specularly reflected radiation and the incident radiation, and their quotient gave the absolute specular reflectance.

Experimental Apparatus

A single fused-silica substrate 2.38 cm in diameter and 0.635 cm thick, with a highly polished surface was used as the basis for all the test specimens. Subsequent to the completion of a data run, the film was stripped off and a new film deposited, all operations being performed to a high standard of cleanliness. Deposition of the films was performed in a bell jar at a pressure level of 2 to 3×10^{-6} torr, the deposition rates being 0.9 Å/sec and 1.1 Å/sec for gold and silver, respectively. The film thicknesses were measured by noting the frequency changes of a vibrating gold-covered quartz crystal mounted near the test specimen in the deposition chamber.

The apparatus for performing the reflectance measurements is described in Fig. 1. The main components of the apparatus are a 10.6-μ CO_2 laser A, chopper B, test specimen C, specimen holder D, turntable E for positioning of specimen, detector F, turntable G for positioning of detector, and swing arm H to facilitate alignment. Other units, not shown, included a preamplifier, a lock-in amplifier, and a chopper speed control. The laser provides linearly polarized radiation. By mounting the laser in either of two orientations, either perpendicular polarized or parallel polarized incident radiation was obtained.

For any given test specimen, the first step in the measurement sequence was to determine the incident radiation. Then, after measurements were made of the reflected radiation at three consecutive angular positions, the incident radiation was re-

[1] Department of Mechanical Engineering, University of Minnesota, Minneapolis, Minn. Mem. ASME.

[2] Honeywell, Inc., St. Paul, Minn.

[3] Numbers in brackets designate References at end of technical brief.

Contributed by the Heat Transfer Division of The American Society of Mechanical Engineers. Manuscript received by the Heat Transfer Division, September 21, 1972.

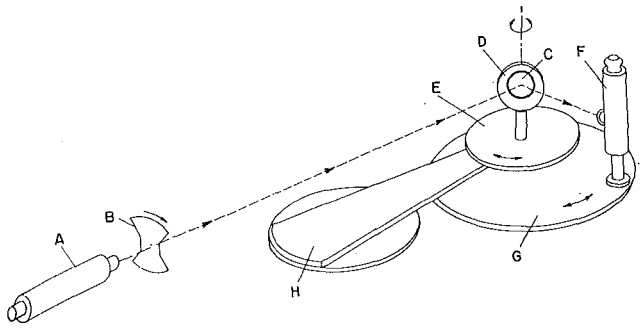

Fig. 1 Apparatus for reflectance measurements

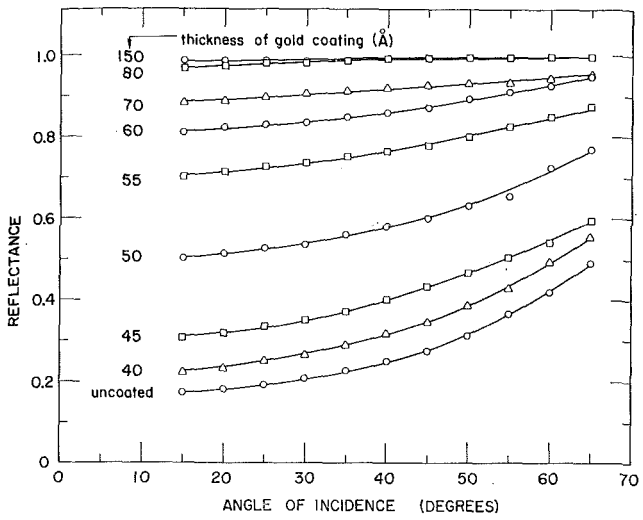

Fig. 2 Effect of gold-film thickness on monochromatic specular reflectance, perpendicular polarized radiation

measured. This pattern was continued until all of the angular measurements had been completed. Further details of experimental apparatus and procedure are available in [4].

Results and Discussion

The measured monochromatic specular reflectance results are presented in Figs. 2 and 3 for perpendicular polarized radiation, respectively for gold films and for silver films. In each figure, the reflectance is plotted as a function of the angle of incidence, with the film thickness as a parameter. Curves have been faired through the data to provide continuity. For all cases indicated in the figures, the reflectance increases monotonically with increasing film thickness.

For the gold films, Fig. 2, it is seen that the presence of a 40-Å film gives rise to a substantial increase in reflectance relative to the uncoated substrate, so that the threshold film thickness is somewhat below 40 Å. The effect of increasing film thickness on the reflectance is most marked in the range from 45 Å to 60 Å. It appears that a film with a thickness of about 150 Å may be regarded as an infinitely thick film. For silver films, Fig. 3, the effect of a 40-Å film is somewhat less marked than was in evidence for a gold film. The film thickness that brings about opacity is slightly greater for a silver film than for a gold film.

The results for parallel polarized radiation have been omitted owing to space limitations, but are available in [4]. A comparison indicates that the first manifestation of the presence of the film occurs at a somewhat smaller thickness for perpendicular polarized radiation than for parallel polarized radiation. Furthermore, the opaque film condition is attained at a smaller thickness for the perpendicular polarized case.

The results given here should not be extrapolated to wavelengths that are very different from the wavelength of the measurements. In this connection, it should be noted that the 150-Å gold and silver films were at least partially transparent when viewed with the naked eye, that is, in the visible range.

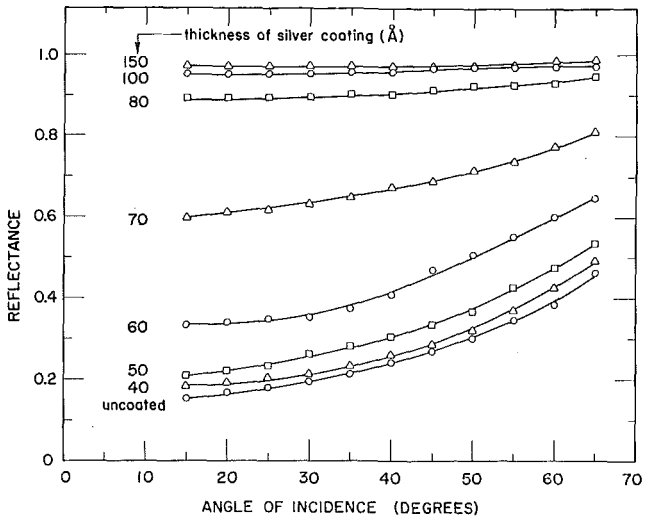

Fig. 3 Effect of silver-film thickness on monochromatic specular reflectance, perpendicular polarized radiation

References

1 Bennett, J. M., Stanford, J. L., and Ashley, E. J., "Optical Constants of Silver Sulfide Tarnish Films," *Journal of the Optical Society of America*, Vol. 60, 1970, pp. 224–232.

2 Gray, D. E., coord. ed., *American Institute of Physics Handbook*, 3rd ed., McGraw-Hill, New York, 1972, p. 6–138.

3 Heavens, O. S., "Optical Properties of Thin Films," in: *Reports on Progress in Physics*, Stickland, A. C., ed., Vol. 23, 1960, p. 34.

4 Tien, K. K., "Effect of Thickness on the Monochromatic Specular Reflectance of Metallic Films," MS thesis, Department of Mechanical Engineering, University of Minnesota, Minneapolis, Minn., 1972.

Theoretical Determination of Absorption With an Emphasis on High Temperatures and a Specific Application to Carbon Monoxide

J. C. LIN[1] **and R. GREIF**[1]

The absorption of a vibrational-rotational band has been studied and the contribution from the first hot band has been included. A specific application has been made to carbon monoxide and good agreement with experimental results has been obtained.

Introduction

In a previous study the absorption of a radiating gas was determined from the basic spectroscopic variables. To test the results a specific application was made to the 4.7 micron band of carbon monoxide and the resulting comparison between the theoretical and experimental results showed excellent agreement at 300 deg K over a broad range of pressures and pathlengths [1].[2] However, at elevated temperatures the agreement was not very good. In the previous study we had only considered the

[1] Mechanical Engineering, University of California, Berkeley, Calif.

[2] Numbers in brackets designate References at end of technical brief.

Contributed by the Heat Transfer Division of The American Society of Mechanical Engineers. Manuscript received by the Heat Transfer Division, August 1, 1972.

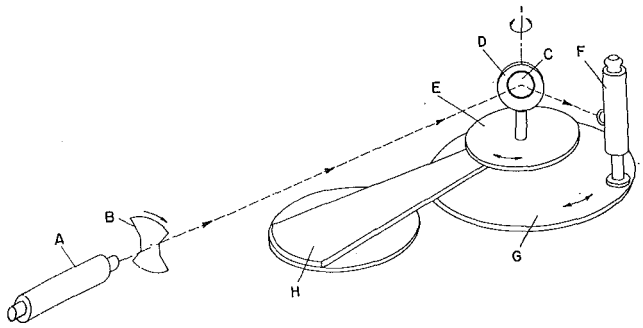

Fig. 1 Apparatus for reflectance measurements

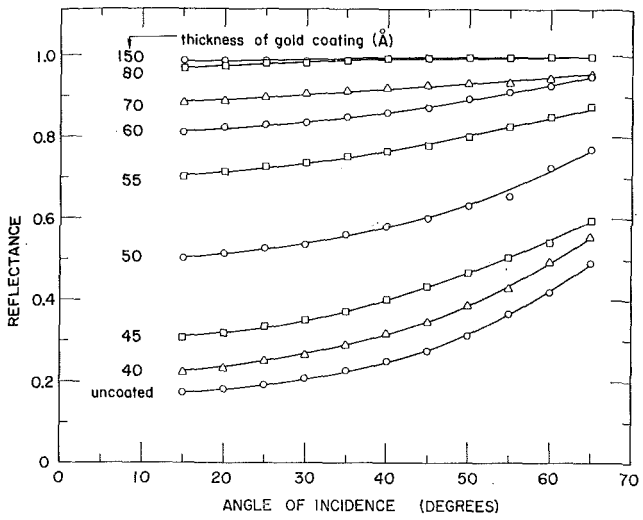

Fig. 2 Effect of gold-film thickness on monochromatic specular reflectance, perpendicular polarized radiation

measured. This pattern was continued until all of the angular measurements had been completed. Further details of experimental apparatus and procedure are available in [4].

Results and Discussion

The measured monochromatic specular reflectance results are presented in Figs. 2 and 3 for perpendicular polarized radiation, respectively for gold films and for silver films. In each figure, the reflectance is plotted as a function of the angle of incidence, with the film thickness as a parameter. Curves have been faired through the data to provide continuity. For all cases indicated in the figures, the reflectance increases monotonically with increasing film thickness.

For the gold films, Fig. 2, it is seen that the presence of a 40-Å film gives rise to a substantial increase in reflectance relative to the uncoated substrate, so that the threshold film thickness is somewhat below 40 Å. The effect of increasing film thickness on the reflectance is most marked in the range from 45 Å to 60 Å. It appears that a film with a thickness of about 150 Å may be regarded as an infinitely thick film. For silver films, Fig. 3, the effect of a 40-Å film is somewhat less marked than was in evidence for a gold film. The film thickness that brings about opacity is slightly greater for a silver film than for a gold film.

The results for parallel polarized radiation have been omitted owing to space limitations, but are available in [4]. A comparison indicates that the first manifestation of the presence of the film occurs at a somewhat smaller thickness for perpendicular polarized radiation than for parallel polarized radiation. Furthermore, the opaque film condition is attained at a smaller thickness for the perpendicular polarized case.

The results given here should not be extrapolated to wavelengths that are very different from the wavelength of the measurements. In this connection, it should be noted that the 150-Å gold and silver films were at least partially transparent when viewed with the naked eye, that is, in the visible range.

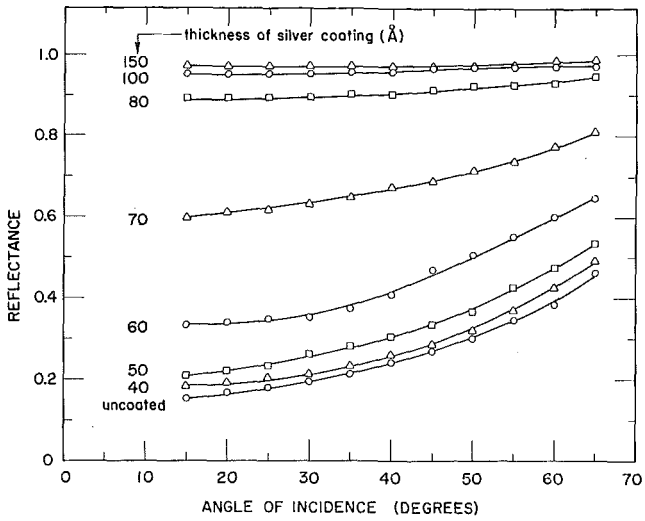

Fig. 3 Effect of silver-film thickness on monochromatic specular reflectance, perpendicular polarized radiation

References

1 Bennett, J. M., Stanford, J. L., and Ashley, E. J., "Optical Constants of Silver Sulfide Tarnish Films," *Journal of the Optical Society of America*, Vol. 60, 1970, pp. 224–232.

2 Gray, D. E., coord. ed., *American Institute of Physics Handbook*, 3rd ed., McGraw-Hill, New York, 1972, p. 6–138.

3 Heavens, O. S., "Optical Properties of Thin Films," in: *Reports on Progress in Physics*, Stickland, A. C., ed., Vol. 23, 1960, p. 34.

4 Tien, K. K., "Effect of Thickness on the Monochromatic Specular Reflectance of Metallic Films," MS thesis, Department of Mechanical Engineering, University of Minnesota, Minneapolis, Minn., 1972.

Theoretical Determination of Absorption With an Emphasis on High Temperatures and a Specific Application to Carbon Monoxide

J. C. LIN[1] and R. GREIF[1]

The absorption of a vibrational-rotational band has been studied and the contribution from the first hot band has been included. A specific application has been made to carbon monoxide and good agreement with experimental results has been obtained.

Introduction

In a previous study the absorption of a radiating gas was determined from the basic spectroscopic variables. To test the results a specific application was made to the 4.7 micron band of carbon monoxide and the resulting comparison between the theoretical and experimental results showed excellent agreement at 300 deg K over a broad range of pressures and pathlengths [1].[2] However, at elevated temperatures the agreement was not very good. In the previous study we had only considered the

[1] Mechanical Engineering, University of California, Berkeley, Calif.

[2] Numbers in brackets designate References at end of technical brief.

Contributed by the Heat Transfer Division of The American Society of Mechanical Engineers. Manuscript received by the Heat Transfer Division, August 1, 1972.

fundamental vibration-rotation band corresponding to the transition between the vibrational levels $v = 0$ and $v = 1$ to account for the absorption. This is an excellent assumption at low temperatures but for increasing temperatures the population of the molecules in the higher energy levels increases until finally the contribution resulting from the transitions between higher levels, e.g., between $v = 1$ and $v = 2$, and $v = 2$ and $v = 3$, etc., that is, the "hot bands," also becomes significant over the pertinent spectral range. We note that the effects of anharmonicity cause the band centers to be different [2].

Analysis

The theoretical expression for the absorption coefficient may be obtained by using the exponential variation of the mean line intensity [3, 1] in conjunction with the dispersion line profile. Following [1] the series may be summed by using the residue theorem [4] which yields the following expression

$$k_\tau = \frac{S_{0,\mathrm{I}}}{d}\left\{\exp\left(\frac{-|\tau|d}{2\pi F}\right) \times \left[\frac{\cos\left(\frac{\beta d}{2\pi F}\sinh\beta + \sin\left(\frac{\beta d}{2\pi F}\right)\sin|\tau|\right]}{\cosh\beta - \cos\tau}\right] - \frac{2\beta}{\beta^2+\tau^2} + I_{\mathrm{I}}\right\} + \frac{S_{0,\mathrm{II}}}{d}\left\{\exp\left(\frac{-|\tau+\delta|d}{2\pi F}\right) \times \left[\frac{\cos\left(\frac{\beta d}{2\pi F}\right)\sinh\beta + \sin\left(\frac{\beta d}{2\pi F}\right)\sin|\tau+\delta|}{\cosh\beta - \cos|\tau+\delta|}\right] - \frac{2\beta}{\beta^2+(\tau+\delta)^2} + I_{\mathrm{II}}\right\} \quad (1)$$

where $\tau = 2\pi(\nu - \nu_{0,\mathrm{I}})/d$, $\delta = 2\pi(\nu_{0,\mathrm{I}} - \nu_{0,\mathrm{II}})/d$, and $\beta = 2\pi b/d$, with $F = F_R$ for $\tau > 0$ and $F = F_P$ for $\tau < 0$. The subscripts R, P, I, and II refer to the R and P branches, and the 0–1 and 1–2 bands, respectively. The quantities I_{I} and I_{II} are the contour integrals that result from the evaluation of k_τ from the residue theorem.

We shall restrict our discussion to small values of the line width to band width ratio b/F_R or b/F_P.[3] It is not necessary to make this restriction but it is valid over a broad range. The following two important limiting cases immediately result. For small values of β and $\frac{d}{2\pi F}$, equations (1) yield

$$k_\tau = \frac{S_{0,\mathrm{I}}}{d}\left\{\frac{\beta}{1+(\beta^2/2)-\cos\tau}\exp\left(\frac{-|\tau|d}{2\pi F}\right) - \frac{2\beta}{\tau^2+\beta^2}\right\} + \frac{S_{0,\mathrm{II}}}{d}\left\{\frac{\beta}{1+(\beta^2/2)-\cos|\tau+\delta|}\exp\left(\frac{-|\tau+\delta|d}{2\pi F}\right) - \frac{2\beta}{\beta^2+(\tau+\delta)^2}\right\} \quad (2)$$

while for the moderately large values of β the absorption coefficient decays exponentially from the band center according to[4]

$$k_\tau = \frac{S_{0,\mathrm{I}}}{d}\exp(-|\tau|d/2\pi F) + \frac{S_{0,\mathrm{II}}}{d}\exp(-|\tau+\delta|d/2\pi F) \quad (3)$$

These relations are particularly useful in obtaining analytic expressions for the total band absorptance A, which is defined by $A = \int_{-\infty}^{\infty}[1 - e^{-k_\nu w}]d(\nu - \nu_{0,\mathrm{I}})$ where w is the pressure pathlength.

Previously, for the single band problem, generalized relationships were obtained for the total band absorptance by substituting relations corresponding to equations (2) and (3) with no further restriction. This does not, however, appear to be the case for the present problem. Thus, for the large β condition *and* for small pathlengths,[5] one obtains

$$A = F_R\left\{\sum_{n=1}^{\infty}\frac{(-1)^{n+1}}{nn!}[v_R{}^n - 2v_A{}^n\sinh(nd/2F_R)] + \frac{S_{0,\mathrm{II}}w}{d}[\exp(-d/2F_R) - \exp([\nu_{0,\mathrm{II}} - \nu_{0,\mathrm{I}} - d/2]/F_R)]\right\} + F_P\left\{\sum_{n=1}^{\infty}\frac{(-1)^{n+1}}{nn!}[v_p{}^n + 2v_B{}^n \times \sinh(nd/2F_P)] + \frac{S_{0,\mathrm{I}}w}{d}[\exp(-d/2F_P) - \exp([\nu_{0,\mathrm{II}} - \nu_{0,\mathrm{I}} - d/2]/F_P)]\right\} \quad (4)$$

where

$$v_A = \frac{S_{0,\mathrm{II}}w}{d}\exp(-[\nu_{0,\mathrm{I}} - \nu_{0,\mathrm{II}}]/F_R),$$

$$v_B = \frac{S_{0,\mathrm{I}}w}{d}\exp(-[\nu_{0,\mathrm{I}} - \nu_{0,\mathrm{II}}]/F_P),$$

$$v_R = \frac{S_{0,\mathrm{I}}w}{d} + v_A \quad \text{and} \quad v_P = \frac{S_{0,\mathrm{II}}w}{d} + v_B$$

For large β *and* large pathlengths there results

$$A = F_R[E_1(v_R) + \ln(v_R) + \gamma + E_1(v_Ae^{-d/2F_R}) - E_1(v_Ae^{d/2F_R})] + F_P[E_1(v_P) + \ln(v_P) + \gamma + E_1(v_Be^{d/2F_P}) - E_1(v_Be^{-d/2F_P})] + (\nu_{0,\mathrm{I}} - \nu_{0,\mathrm{II}}) - d \quad (5)$$

where γ is Euler's constant (0.577 . . .) and E_1 is the exponential integral [6]. For large values of the argument the asymptotic expansion for E_1 may be used [1, 6].

For small values of β the lines are effectively isolated and the following form proves to be particularly suitable for the evaluation of the total band absorptance:

$$A = \sum_{n=-\infty}^{\infty}\int_{(n-1/2)d}^{(n+1/2)d}(1 - e^{-k_\nu x})d(\nu - \nu_{0,\mathrm{I}}) = (d/2\pi)\sum_{n=-\infty}^{\infty}\int_{(2n-1)\pi}^{(2n+1)\pi}(1 - e^{-k_\tau x})d\tau = \sum_{n=-\infty}^{\infty}A_n \quad (6)$$

The evaluation of A_n follows, fairly closely, the analysis of reference [1]. We shall therefore omit the details and present the results for $A = \Sigma A_n$ corresponding to various limiting conditions.

One important consideration is whether the lines from band I overlap with the lines from band II. If there is no overlapping, then the results from the single band analysis can be directly applied to the two band problem. These results will not be repeated here. On the other hand if there is overlapping the single band analysis must be altered. For this condition *and* with the restriction $v_n/2 \ll \beta/2 \ll 1/v_n$, the following linear dependence on pathlength is obtained:

$$A = (F_Re^{-d/F_R} + F_pe^{-d/F_P})u \quad (7)$$

where

[3] To simplify the notation, we have dropped the I, II designations on F. We will also drop the P, R designations but will recover them in the final results.

[4] In this range alternative approximations are available [5].

[5] A sufficient condition is that $(S_{0,\mathrm{I}} + S_{0,\mathrm{II}})w/d$ be small.

Table 1 Total band absorptance of the 4.7 micron band of carbon monoxide

Temperature deg K	Effective pressure Pe(atm)	Pressure pathlength Pw(atm-cm)	Experimental data (Tien and Giedt [11], Abu-Romia and Tien [15]) (cm^{-1})	Present results, two bands (cm^{-1})	One band result [1] (cm^{-1})	Correlation result [3, 14] (cm^{-1})
300	0.51	0.5	22.0	27.5	27.5	31.7
	1.02	1.0	48.5	53.9	53.9	61.6
	2.04	2	90.0	93.2	93.2	100.5
	3.06	3	127.2	122	122	126.3
	0.255	1.25	30.2	31.2	31.2	34.3
	0.51	2.5	58.2	60.0	60.0	69.5
	1.02	5	112.0	99.6	99.6	113.5
	2.04	10	159.2	152	152	160.5
	3.06	15	193.5	187.	187	187.5
	0.255	2.5	45.0	43.3	43.3	44.9
	0.51	5	89.0	78.6	78.6	91.4
	1.02	10	148.0	126	126	138.9
	2.04	20	184	188	188	186.2
	3.06	30	205	219	219	209.7
	0.255	5	66.0	60	60	69.5
	0.51	10	122.0	99.6	99.6	115.6
	1.02	20	169.0	152	152	164.2
	2.04	40	210.0	212	212	212.0
	3.06	60	226.0	250	250	239.0
900	1.02	1.0	27.7	30	30.9	36.9
	2.04	2.0	57.6	60.3	62.7	66.5
	3.06	3.0	90.5	89.5	93.4	102.4
	0.51	2.5	38.0	39.7	34.2	41.1
	1.02	5.0	82.0	82.3	69.7	86.2
	2.04	10	134.3	124.5	133.6	149.4
	3.06	15.0	191.0	168	167	196.0
	0.255	2.5	26.3	29.4	24.2	25.0
	0.51	5.0	55.0	69.7	49.5	59.5
	1.02	10.0	106.2	114	94	118.5
	2.04	20.0	176.2	160.5	163.0	191.3
	3.06	30.0	234	210.2	212.5	240.0
	0.255	5.0	37.8	39.7	34.8	37.5
	0.51	10.0	66.0	67.5	70.5	90.0
	1.02	20.0	134.0	124.5	128.0	153.0
	2.04	40.0	226.0	202.3	206.0	237.0
	3.06	60.0	273.0	258.0	261.0	285.5
1800	1.02	10.0	129	97.7	71	131
	1.53	15.0	172	145.5	106.5	173
	2.04	20.0	195	192.3	137	208
	2.55	25.0	247	238.5	165	238
	3.06	30.0	278	278	191.5	262
	1.02	20.0	159	139.8	99.5	179
	1.53	30.0	221	202	143	228
	2.04	40.0	268	264	181.5	268
	2.55	50.0	317	316	177.4	300
	3.06	60.0	347	368.5	246.5	325

$$u = (S_{0,\mathrm{I}} + S_{0,\mathrm{II}})w/d,$$

$$v_n = \frac{S_{0,\mathrm{I}}w}{d}\, e^{-nd/F_P} + \frac{S_{0,\mathrm{II}}w}{d}\, e^{-(\nu_{0,\mathrm{I}} - \nu_{0,\mathrm{II}} - nd)/F_R} \quad (8)$$

For the limiting case given by $v_A \gg 1$ and $v_n\beta/2 \ll 1$ we obtain

$$\frac{A}{d} = \left(\frac{2v_R\beta}{\pi}\right)^{1/2} \frac{1}{e^{d/2F_R} - 1} + \left(\frac{2v_P\beta}{\pi}\right)^{1/2} \frac{1}{e^{d/2F_P} - 1} + \left(\frac{2v_A\beta}{\pi}\right)^{1/2} + \left(\frac{2v_B\beta}{\pi}\right)^{1/2} + \sum_{n=1}^{N-1} \left(\frac{2v_n\beta}{\pi}\right)^{1/2}. \quad (9)$$

Additional limiting relations may also be obtained.

Results and Discussion

We now wish to make a direct comparison with experimental data but before this can be accomplished F, S_0, etc., must be specified. Referring to reference [1], these quantities may be related to the fundamental spectroscopic variables as follows:

$$F(\mathrm{cm}^{-1}) = \frac{1}{D_1}\left(\frac{kTB_e}{hc}\right)^{1/2} = \frac{19.2}{D_1}\left[\frac{T(\mathrm{deg\ K})}{273}\right]^{1/2} \quad (10)$$

$$S_{0\mathrm{I,II}}(\mathrm{atm}^{-1}\ \mathrm{cm}^{-2}) = D_1\alpha_{\mathrm{I,II}}(T)\left(\frac{hcB_e}{kT}\right)^{1/2} = 0.1D_1\alpha_{\mathrm{I,II}}(T)\left[\frac{273}{T(\mathrm{deg\ K})}\right] \quad (11)$$

Note that the line spacing, $d = 2B_e = 3.863\ \mathrm{cm}^{-1}$ has been used. This is the value for the fundamental vibration rotation band of carbon monoxide which has the band center at 2143 cm^{-1} (4.7 microns). For simplicity we also take $F_P = F_R = F$ for bands I and II; however, this can easily be altered if necessary. D_1 is an arbitrary constant and is a consequence of the approximate intensity variation used (cf. equation (1)). The value chosen for D_1 is unity [1]. The relation for the integrated band intensity, $\alpha_{\mathrm{I\ or\ II}} = \int_{\mathrm{I\ or\ II}} S_J dJ$, is given by Penner [7, p. 158]. Note that the value of 260 $(\mathrm{atm\ cm})^{-1}\ \mathrm{cm}^{-1}$ reported by Burch and Williams [8] at a temperature 273 deg K is for α (the total integrated band intensity equal to $\alpha_{\mathrm{I}} + \alpha_{\mathrm{II}} + \alpha_{\mathrm{III}} + \ldots$). However, at this temperature the primary contribution is from α_{I}.

The remaining quantity required for the determination of the total band absorptance is the broadening parameter $\beta = 2\pi b/d$. The line half width b is given by Penner [7, p. 305] and the line spacing d is given in the foregoing so that $\beta = 0.126[T(\mathrm{deg\ K})/$

$300]^{-1/2}P_e$. For pure carbon monoxide $P_e = 1.02P$ where P is the gas pressure in atmospheres.

The total band absorptance A may now be directly calculated and results are presented in Table 1 for the 4.7 micron band of carbon monoxide. A comparison of the present results using two bands with the previous calculations using only one band shows a large increase in absorption resulting from the hot band $1 - 2$ for the 1800 deg K condition.[6] This confirms the conclusion reached by Weiner and Edwards [9] (also see Balakrishnan and Edwards [10]).

A comparison of the present results with the experimental data of Tien and Giedt [11] at 1800 deg K shows good agreement. The agreement would be improved if more accurate relations were used for the broadening parameter as well as for the mean line intensity. Furthermore, considering additional bands, for example, 2–3, 3–4, etc., should also yield improved results. This effect becomes more pronounced at high temperatures (see, for example, Giedt and Travis [12] and Edwards [13]). For completeness, the correlation of Edwards and Menard [3] and Tien and Lowder [14] is also presented in Table 1 along with the experimental data of Abu-Romia and Tien [15].

In summary, the absorption of a radiating gas has been studied with particular attention given to high temperatures. A specific application to the 4.7 micron bands of carbon monoxide results in good agreement with experimental data and the importance of hot bands at high temperatures has been demonstrated in a fundamental way. Furthermore, the analysis presented may be extended to gas mixtures.

Acknowledgments

The authors acknowledge with appreciation the partial support of this research by the National Science Foundation.

References

1 Hsieh, T. C., and Greif, R., "Theoretical Determination of the Absorption Coefficient and the Total Band Absorptance Including a Specific Application to Carbon Monoxide," *International Journal of Heat and Mass Transfer*, Vol. 15, 1972, pp. 1477–1487.

2 Herzberg, G., *Spectra of Diatomic Molecules*, Van Nostrand, New York, 1961.

3 Edwards, D. K., and Menard, W. A., "Comparison of Models for Correlation of Band Absorption," *Applied Optics*, Vol. 3, 1964, pp. 621–625.

4 Copson, E. T., *An Introduction to the Theory of Functions of a Complex Variable*, Oxford University Press, 1955.

5 Penner, S. S., Sepucha, R. C., and Lowder, J. E., "Approximate Calculations of Spectral Absorption Coefficients in Infrared Vibration-Rotation Spectra," *J. Quant. Spectrosc. Radiat. Transfer*, Vol. 10, 1001–1010, 1970.

6 Abramowitz, M., and Stegun, I. A., "Handbook of Mathematical Functions," U. S. Dept. of Commerce, N.B.S., A.M.S. 55, 1964.

7 Penner, S. S., *Quantitative Molecular Spectroscopy and Gas Emissivities*, Addison-Wesley, Reading, Mass., 1959.

8 Burch, D. E., and Williams, D., "Total Absorptance of Carbon Monoxide and Methane in the Infrared," *Applied Optics*, Vol. 1, 1962, pp. 587–594.

9 Weiner, M. M., and Edwards, D. K., "Theoretical Expression of Water Vapor Spectral Emissivity with Allowance for Line Structure," *International Journal of Heat and Mass Transfer*, Vol. 11, 1968, pp. 55–65.

10 Balakrishnan, A. and Edwards, D. K., Discussion of the paper by Chan, S. H., and Tien, C. L., "Infrared Radiation Properties of Sulfur Dioxide," JOURNAL OF HEAT TRANSFER, Vol. 93, 1971, pp. 177–178.

11 Tien, C. L., and Giedt, W. H., "Experimental Determination of Infrared Absorption of High Temperature Gases," in *Advances in Thermophysical Properties at Extreme Pressures and Temperatures*, S. Gratch, ed., ASME, New York, 1965, pp. 167–173.

12 Giedt, W. H., and Travis, L. P., "Infrared Absorption of Carbon Monoxide at High Temperatures," Fourth International Heat Transfer Conference, Paris-Versailles, Verein Deutscher Ingenieure, Dusseldorf, Vol. III, R 1.3, 1970.

13 Edwards, D. K., Report on Paper R 1.3: "Infrared Absorption of Carbon Monoxide at High Temperatures," Fourth International Heat Transfer Conference, Paris-Versailles, Verein Deutscher Ingenieure, Dusseldorf, Vol. VI, 1970.

14 Tien, C. L., and Lowder, J. E., "A Correlation for Total Band Absorptance of Radiating Gases," *International Journal of Heat and Mass Transfer*, Vol. 9, 1966, pp. 968–701.

15 Abu-Romia, M. M., and Tien, C. L., "Measurements and Correlations of Infrared Radiation of Carbon Monoxide at Elevated Temperatures," *J. Quant. Spectrosc. Radiat. Transfer*, Vol. 6, 1966, pp. 143–167.

[6] We note that the single band results employed the simplification $e^{-d/F} \approx 1$. This is not necessary and has not been used in the present study. Indeed, this causes the two band results to be slightly less than some of the single band results for the 900 deg K condition as given in Table 1.

Heat Transfer in an Absorbing, Emitting and Scattering Slug Flow Between Parallel Plates

C. C. LII[1] and M. N. ÖZIŞIK[2]

Most of the investigations of interaction of radiation with forced convection inside a channel are restricted to an absorbing and emitting fluid [1–4];[3] when scattering is included, an approximate technique is used [5]. The purpose of this work is to investigate the effects of radiation on heat transfer and temperature distribution in the thermally developing region of an absorbing, emitting, isotropically scattering slug flow inside a parallel plate channel with reflecting boundaries. The results show that when radiation effects are strong, fully thermally developed state does not exist.

Analysis

Consider thermally developing slug flow between two infinite parallel plates at a distance $2L$ apart. The flow enters the heated section of the channel with a uniform temperature T_0 at the origin $x = 0$ of the axial coordinate while the walls are kept at a constant temperature T_w for $x \geq 0$. The energy equation in the nondimensional form is taken as

$$\frac{\partial^2}{\partial\tau^2}\theta(\tau,\xi) - \frac{1}{4\pi N}\frac{\partial}{\partial\tau}Q^r(\tau,\xi) = \frac{\partial}{\partial\xi}\theta(\tau,\xi) \quad \text{in} \quad 0 \leq \tau \leq \tau_0, \quad \xi > 0 \tag{1}$$

with the boundary conditions

$$\theta(\tau,\xi) = 1 \quad \text{at} \quad \tau = 0, \qquad \xi > 0 \tag{2a}$$

$$\frac{\partial}{\partial\tau}\theta(\tau,\xi) = 0 \quad \text{at} \quad \tau = \tau = \tau_0, \qquad \xi > 0 \tag{2b}$$

$$\theta(\tau,\xi) = \theta_0 \quad \text{at} \quad \xi = 0, \qquad 0 \leq \tau \leq \tau_0 \tag{2c}$$

where symmetry is assumed about the central axis at $\tau = \tau_0$ and various nondimensional quantities are defined as:

$$N = k\beta/4n^2\sigma T_w^3, \qquad Q^r(\tau,\xi) = q^r(\tau,\xi)/(n^2\sigma T_w^4/\pi),$$
$$\theta(\tau,\xi) = T(\tau,\xi)/T_w, \qquad \theta_0 = T_0/T_w, \qquad \tau = \beta y,$$
$$\tau_0 = \beta L, \qquad \xi = k\beta^2 x/\rho u c_p = 16\tau_0^2\frac{x/D_e}{\mathrm{Re\,Pr}}, \qquad D_e = 4L$$

c_p is the specific heat, k is the thermal conductivity, n is the re-

[1] Visiting Assistant Professor, Department of Mechanical and Aerospace Engineering, North Carolina State University, Raleigh, N. C.

[2] Professor, Department of Mechanical and Aerospace Engineering North Carolina State University, Raleigh, N. C.

[3] Numbers in brackets designate References at end of technical brief.

Contributed by the Heat Transfer Division of THE AMERICAN SOCIETY OF MECHANICAL ENGINEERS. Manuscript received by the Heat Transfer Division, April 3, 1973.

$300]^{-1/2}P_e$. For pure carbon monoxide $P_e = 1.02P$ where P is the gas pressure in atmospheres.

The total band absorptance A may now be directly calculated and results are presented in Table 1 for the 4.7 micron band of carbon monoxide. A comparison of the present results using two bands with the previous calculations using only one band shows a large increase in absorption resulting from the hot band $1 - 2$ for the 1800 deg K condition.[6] This confirms the conclusion reached by Weiner and Edwards [9] (also see Balakrishnan and Edwards [10]).

A comparison of the present results with the experimental data of Tien and Giedt [11] at 1800 deg K shows good agreement. The agreement would be improved if more accurate relations were used for the broadening parameter as well as for the mean line intensity. Furthermore, considering additional bands, for example, 2–3, 3–4, etc., should also yield improved results. This effect becomes more pronounced at high temperatures (see, for example, Giedt and Travis [12] and Edwards [13]). For completeness, the correlation of Edwards and Menard [3] and Tien and Lowder [14] is also presented in Table 1 along with the experimental data of Abu-Romia and Tien [15].

In summary, the absorption of a radiating gas has been studied with particular attention given to high temperatures. A specific application to the 4.7 micron bands of carbon monoxide results in good agreement with experimental data and the importance of hot bands at high temperatures has been demonstrated in a fundamental way. Furthermore, the analysis presented may be extended to gas mixtures.

Acknowledgments

The authors acknowledge with appreciation the partial support of this research by the National Science Foundation.

References

1 Hsieh, T. C., and Greif, R., "Theoretical Determination of the Absorption Coefficient and the Total Band Absorptance Including a Specific Application to Carbon Monoxide," *International Journal of Heat and Mass Transfer*, Vol. 15, 1972, pp. 1477–1487.

2 Herzberg, G., *Spectra of Diatomic Molecules*, Van Nostrand, New York, 1961.

3 Edwards, D. K., and Menard, W. A., "Comparison of Models for Correlation of Band Absorption," *Applied Optics*, Vol. 3, 1964, pp. 621–625.

4 Copson, E. T., *An Introduction to the Theory of Functions of a Complex Variable*, Oxford University Press, 1955.

5 Penner, S. S., Sepucha, R. C., and Lowder, J. E., "Approximate Calculations of Spectral Absorption Coefficients in Infrared Vibration-Rotation Spectra," *J. Quant. Spectrosc. Radiat. Transfer*, Vol. 10, 1001–1010, 1970.

6 Abramowitz, M., and Stegun, I. A., "Handbook of Mathematical Functions," U. S. Dept. of Commerce, N.B.S., A.M.S. 55, 1964.

7 Penner, S. S., *Quantitative Molecular Spectroscopy and Gas Emissivities*, Addison-Wesley, Reading, Mass., 1959.

8 Burch, D. E., and Williams, D., "Total Absorptance of Carbon Monoxide and Methane in the Infrared," *Applied Optics*, Vol. 1, 1962, pp. 587–594.

9 Weiner, M. M., and Edwards, D. K., "Theoretical Expression of Water Vapor Spectral Emissivity with Allowance for Line Structure," *International Journal of Heat and Mass Transfer*, Vol. 11, 1968, pp. 55–65.

10 Balakrishnan, A. and Edwards, D. K., Discussion of the paper by Chan, S. H., and Tien, C. L., "Infrared Radiation Properties of Sulfur Dioxide," JOURNAL OF HEAT TRANSFER, Vol. 93, 1971, pp. 177–178.

11 Tien, C. L., and Giedt, W. H., "Experimental Determination of Infrared Absorption of High Temperature Gases," in *Advances in Thermophysical Properties at Extreme Pressures and Temperatures*, S. Gratch, ed., ASME, New York, 1965, pp. 167–173.

12 Giedt, W. H., and Travis, L. P., "Infrared Absorption of Carbon Monoxide at High Temperatures," Fourth International Heat Transfer Conference, Paris-Versailles, Verein Deutscher Ingenieure, Dusseldorf, Vol. III, R 1.3, 1970.

13 Edwards, D. K., Report on Paper R 1.3: "Infrared Absorption of Carbon Monoxide at High Temperatures," Fourth International Heat Transfer Conference, Paris-Versailles, Verein Deutscher Ingenieure, Dusseldorf, Vol. VI, 1970.

14 Tien, C. L., and Lowder, J. E., "A Correlation for Total Band Absorptance of Radiating Gases," *International Journal of Heat and Mass Transfer*, Vol. 9, 1966, pp. 968–701.

15 Abu-Romia, M. M., and Tien, C. L., "Measurements and Correlations of Infrared Radiation of Carbon Monoxide at Elevated Temperatures," *J. Quant. Spectrosc. Radiat. Transfer*, Vol. 6, 1966, pp. 143–167.

[6] We note that the single band results employed the simplification $e^{-d/F} \approx 1$. This is not necessary and has not been used in the present study. Indeed, this causes the two band results to be slightly less than some of the single band results for the 900 deg K condition as given in Table 1.

Heat Transfer in an Absorbing, Emitting and Scattering Slug Flow Between Parallel Plates

C. C. LII[1] and M. N. ÖZIŞIK[2]

Most of the investigations of interaction of radiation with forced convection inside a channel are restricted to an absorbing and emitting fluid [1–4];[3] when scattering is included, an approximate technique is used [5]. The purpose of this work is to investigate the effects of radiation on heat transfer and temperature distribution in the thermally developing region of an absorbing, emitting, isotropically scattering slug flow inside a parallel plate channel with reflecting boundaries. The results show that when radiation effects are strong, fully thermally developed state does not exist.

Analysis

Consider thermally developing slug flow between two infinite parallel plates at a distance $2L$ apart. The flow enters the heated section of the channel with a uniform temperature T_0 at the origin $x = 0$ of the axial coordinate while the walls are kept at a constant temperature T_w for $x \geq 0$. The energy equation in the nondimensional form is taken as

$$\frac{\partial^2}{\partial\tau^2}\theta(\tau,\xi) - \frac{1}{4\pi N}\frac{\partial}{\partial\tau}Q^r(\tau,\xi) = \frac{\partial}{\partial\xi}\theta(\tau,\xi) \quad \text{in} \quad 0 \leq \tau \leq \tau_0, \quad \xi > 0 \tag{1}$$

with the boundary conditions

$$\theta(\tau,\xi) = 1 \quad \text{at} \quad \tau = 0, \qquad \xi > 0 \tag{2a}$$

$$\frac{\partial}{\partial\tau}\theta(\tau,\xi) = 0 \quad \text{at} \quad \tau = \tau = \tau_0, \qquad \xi > 0 \tag{2b}$$

$$\theta(\tau,\xi) = \theta_0 \quad \text{at} \quad \xi = 0, \qquad 0 \leq \tau \leq \tau_0 \tag{2c}$$

where symmetry is assumed about the central axis at $\tau = \tau_0$ and various nondimensional quantities are defined as:

$$N = k\beta/4n^2\sigma T_w^3, \qquad Q^r(\tau,\xi) = q^r(\tau,\xi)/(n^2\sigma T_w^4/\pi),$$

$$\theta(\tau,\xi) = T(\tau,\xi)/T_w, \qquad \theta_0 = T_0/T_w, \qquad \tau = \beta y,$$

$$\tau_0 = \beta L, \qquad \xi = k\beta^2 x/\rho u c_p = 16\tau_0^2\frac{x/D_e}{\mathrm{Re\,Pr}}, \qquad D_e = 4L$$

c_p is the specific heat, k is the thermal conductivity, n is the re-

[1] Visiting Assistant Professor, Department of Mechanical and Aerospace Engineering, North Carolina State University, Raleigh, N. C.

[2] Professor, Department of Mechanical and Aerospace Engineering North Carolina State University, Raleigh, N. C.

[3] Numbers in brackets designate References at end of technical brief.

Contributed by the Heat Transfer Division of THE AMERICAN SOCIETY OF MECHANICAL ENGINEERS. Manuscript received by the Heat Transfer Division, April 3, 1973.

fractive index, β is the extention coefficient, σ is the Stefan-Boltzmann constant, and ρ is the density of the fluid. For slug flow the velocity u is constant everywhere. The dimensionless net radiative heat flux $Q^r(\tau, \xi)$ is related to $\psi(\tau, \mu, \xi)$ by

$$Q^r(\tau, \xi) = 2\pi \int_{-1}^{1} \psi(\tau, \mu, \xi)\mu d\mu \tag{3}$$

where $\psi(\tau, \mu, \xi)$ satisfies the equation of radiative transfer

$$\mu \frac{\partial}{\partial \tau} \psi(\tau, \mu, \xi) + \psi(\tau, \mu, \xi) = (1 - \omega)\theta^4(\tau, \xi) + \frac{\omega}{2} \int_{-1}^{1} \psi(\tau, \mu', \xi)d\mu', \qquad -1 \leq \mu \leq 1 \tag{4}$$

Here ω is the single scattering albedo and μ is the cosine of the angle between the direction of the radiation intensity and the positive τ axis.

The boundaries at $\tau = 0$ and $\tau = 2\tau_0$ are assumed to be gray, opaque, diffuse emitters and have reflectivity which can be expressed as a sum of a specular ρ^s and diffuse ρ^d reflectivity components. Then the boundary conditions at $\tau = 0$ and $\tau = \tau_0$ are given as

$$\psi(0, \mu, \xi) = \epsilon + \rho^s\psi(0, -\mu, \xi) + 2\rho^d \int_0^1 \psi(0, -\mu' \cdot \xi)\mu' d\mu', \qquad \mu > 0 \tag{5}$$

$$\psi(\tau_0, -\mu, \xi) = \psi(\tau_0, \mu, \xi) \tag{6}$$

The normal-mode expansion technique [6] is applied to solve the radiation part of the problem. The solution of the equation of radiative transfer equation (4) is written as a linear combination of the normal modes satisfying the homogeneous version of this equation and a particular solution in the form [6, 7]

$$\psi(\tau, \mu, \xi) = A(\eta_0, \xi)\phi(\eta_0, \mu)e^{-\tau/\eta_0} + A(-\eta_0, \xi)\phi(-\eta_0, \mu)e^{\tau/\eta_0} + \int_0^1 A(\eta, \xi)\phi(\eta, \mu)e^{-\tau/\eta}\, d\eta + \int_0^1 A(-\eta, \xi)\phi(-\eta, \mu)e^{\tau/\eta}\, d\eta + \psi_p(\tau, \mu, \xi) \tag{7}$$

where $A(\pm\eta_0, \xi)$ and $A(\pm\eta, \xi)$, $\eta\epsilon(0, 1)$ are the expansion coefficients, and $\psi_p(\tau, \mu, \xi)$ is a particular solution of the equation (4). Here, the particular solution $\psi_p(\tau, \mu, \xi)$ depends on the inhomogeneous term $(1 - \omega)\theta^4(\tau, \xi)$; for the purpose of determining a particular solution, it is assumed that an initial guess is available for the temperature distribution $\theta_0(\tau, \xi)$ and the inhomogeneous term is represented as a polynomial in the optical variable τ in the form

$$(1 - \omega)[\theta^0(\tau, \xi)]^4 = (1 - \omega) \sum_{n=0}^{N} B_n(\xi)\tau^n, \qquad 0 < \tau < \tau_0 \tag{8}$$

and that the coefficients $B_n(\xi)$ are determined. A particular solution $\psi_{p,n}(\tau, \xi)$ for an inhomogeneous term of the form $(1 - \omega)\tau^n$ is obtained [8], and the total particular solution $\psi_p(\tau, \mu, \xi)$ for an inhomogeneous term the form $(1 - \omega) \sum_{n=0}^{N} B_n(\xi)\tau^n$ is determined from

$$\psi_p(\tau, \mu, \xi) = \sum_{n=0}^{N} B_n(\xi)\psi_{p,n}(\tau, \mu) \tag{9}$$

By treating $\frac{\partial}{\partial \tau} Q^r(\tau, \xi)$ as a prescribed function, equation (1) is integrated with the boundary condition equation (2) by the application of a finite integral transform technique [9] to yield

$$\theta(\tau, \xi) = 1 + \frac{2}{\tau_0} \sum_{m=1}^{\infty} \sin \nu_m\tau \left[\frac{\theta_0 - 1}{\nu_m} e^{-\nu_m^2\xi} - \frac{1}{4\pi N} \times \int_{\xi'=0}^{\xi} e^{-\nu_m^2(\xi - \xi')} \int_{\tau'=0}^{\tau_0} \sin \nu_m\tau' \frac{\partial Q^r(\tau', \xi')}{\partial \tau'} d\tau' d\xi' \right] \tag{10}$$

where the eigenvalues ν_m are given as

$$\nu_m = \frac{(2m - 1)\pi}{2\tau_0}, \qquad m = 1, 2, 3, \ldots$$

The total heat flux at the wall $q^t(0, \xi)$ is determined from

$$\frac{q^t(0, \xi)}{k\beta T_w} = -\frac{\partial}{\partial \tau} \theta(\tau, \xi)_o \Big|_{\tau=0} + \frac{1}{4\pi N} Q^r(\tau, \xi)_o \Big|_{\tau=0} \tag{11}$$

and the local Nusselt from

$$\mathrm{Nu} = \frac{4\tau_0}{1 - \theta_m(\xi)} \left[-\frac{\partial}{\partial \tau} \theta(\tau, \xi) + \frac{1}{4\pi N} Q^r(\tau, \xi)_o \right]_{\tau=0} \tag{12}$$

where $\theta_m(\xi)$ is the dimensionless mean temperature.

Numerical Calculations and Results

All computations are performed in double-precision on the IBM 360/75 computer. The expansion coefficients $A(\pm\eta_0, \xi)$ and $A(\pm\eta, \xi)$ are determined as described in reference [10] and equation (10) is evaluated by iteration. The problem considered in the foregoing for the heating of a fluid (i.e., $0 \leq \theta_0 < 1$ and $\theta_w = 1$) contains several parameters: N, θ_0, τ_0, ξ, ω, ϵ, ρ^s, and ρ^d. The temperature distribution, radiative, conductive, and total heat fluxes and local Nusselt number are determined at several different axial locations along the channel. In the present analysis the axis radiation is neglected; it may be important at the entrance region for large values of θ_0.

Fig. 1 shows the effect of single scattering albedo ω on the local Nusselt number. The curve for $\omega = 1$ characterizes the case with no radiation, since radiation does not interact with conduction and convection in a purely scattering medium. The local Nusselt number increases as ω decreases and reaches a maximum when $\omega = 0$ (i.e., purely absorbing and emitting medium). In contrast to the case with no radiation, the local Nusselt number does not seem to reach a constant value; that is thermally fully developed state does not occur with radiating flow when radiation effects are strong. At distances far from the inlet the fully developed temperature profile is not established because radiation effects continue to flatten the temperature profile, which in turn increases θ_m and the Nusselt number.

Fig. 2 shows the effect of the conduction-to-radiation parameter N on the local Nusselt number for the cases $\omega = 0.9$, $\omega = 0$.

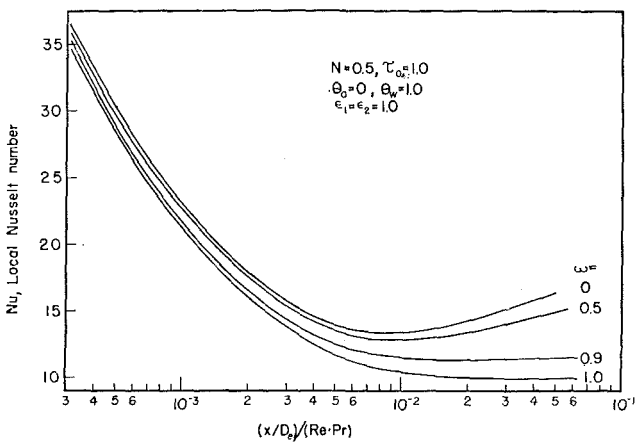

Fig. 1 Effect of ω on the local Nusselt number

The curve $N = 10$ is for weak radiation interaction; in this case it is not possible to distinguish the curves for $\omega = 0.9$ and 0, and in fact the curve coincides with that for no radiation. The local Nusselt number increases with decreasing N (i.e., increasing radiation) and when radiation effects are strong thermally fully developed state does not seem to occur.

References

1 Timofeyev, V. N., Shklyar, F. R., Malkin, V. M., and Berland, A. K. H., "Combined Heat Transfer in an Absorbing Stream Moving in a Flat Channel," *Heat Transfer—Soviet Research*, Parts I, II, III, Vol. 1, No. 6, 1969, pp. 57–93.

2 Kurosaki, Yasuo, "Heat Transfer by Simultaneous Radiation and Convection in an Absorbing and Emitting Medium in a Flow Between Parallel Plates," *Fourth International Heat Transfer Conference*, Section R 2.5, 1970, pp. 1–11.

3 Habib, I. S., and Greif, R., "Heat Transfer to a Flowing Non-Gray Radiating Gas: An Experimental and Theoretical Study," *International Journal of Heat and Mass Transfer*, Vol. 13, 1970, pp. 1571–1582.

4 Thorsen, R. S., "Combined Conduction, Convection, and Radiation Effects in Optically Thin Tube Flow," ASME Paper, No. 71-HT-17, 1971.

5 Chen, J. C., "Simultaneous Radiative and Convective Heat Transfer in an Absorbing, Emitting and Scattering Medium in Slug Flow Between Parallel Plates," *AIChE Journal*, Vol. 2, 1964, pp. 253–259.

6 Case, K. M., and Zweifel, P. F., *Linear Transport Theory*, Addison-Wesley, Reading, Mass., 1967.

7 Özişik, M. N., and Siewert, C. E., "On the Normal-Mode-Expansion Technique for Radiative Transfer in a Scattering, Absorbing and Emitting Slab With Specularly Reflecting Boundaries," *International Journal of Heat and Mass Transfer*, Vol. 121, 1952, pp. 175–182.

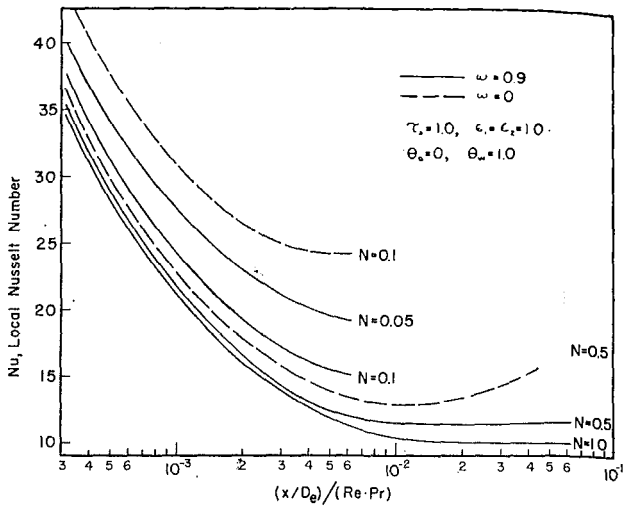

Fig. 2 Effect of N on the local Nusselt number

8 Lundquist, C. A., and Horak, H. G., "The Transfer of Radiation by an Emitting Atmosphere IV," *The Astrophysical Journal*, Vol. 121, 1952, pp. 175–182.

9 Özişik, M. N., *Boundary Value Problems of Heat Conduction*, International Textbook Company, Scranton, Pa., 1968.

10 Beach, H. L., Özişik, M. N., and Siewert, C. E., "Radiative Transfer in Linearly Anisotropic-Scattering, Conservative and Non-Conservative Slabs With Reflective Boundaries," *International Journal of Heat and Mass Transfer*, Vol. 14, 1971, pp. 1551–1565.

A Correlation for Laminar Free Convection From a Vertical Plate

S. W. CHURCHILL[1] and H. OZOE[2]

Nomenclature

A = coefficient in equations (2) and (10), dimensionless
B = coefficient in equations (1) and (9), dimensionless
g = gravitational acceleration, ft/sec^2
j = local heat-flux density, Btu/hr-ft^2
k = thermal conductivity, Btu/hr-ft-deg F
n = exponent in equation (11), dimensionless
Nu_x = $jx/k(T_w - T_\infty)$, local Nusselt number, dimensionless
Pr = ν/α, Prandtl number, dimensionless
Ra_x = $g\beta(T_w - T_\infty)x^3/\nu\alpha$, local Rayleigh number, dimensionless
T = temperature, deg F
T_w = wall temperature, deg F
T_∞ = ambient temperature, deg F
u = velocity component in x direction, ft/sec
v = velocity component in y direction, ft/sec
x = distance upward from bottom of plate, ft
y = distance from plate, ft
α = thermal diffusivity, ft^2/sec
β = volumetric coefficient of thermal expansion, deg F^{-1}
Δ_T = distance from plate for which $(T - T_\infty)/(T_w - T_\infty) = 0.01$
ν = kinematic viscosity, ft^2/sec

THE EXPRESSION proposed by Churchill and Usagi [1][3] has been used to construct a correlation for laminar free convection from a vertical plate. The correlation applies to both uniform heating and uniform wall temperature.

Uniform Wall Temperature

The limiting solutions derived by LeFevre [2] for an isothermal plate are

$$\mathrm{Nu}_x = 0.6004(\mathrm{Ra}_x\mathrm{Pr})^{1/4} \quad \text{for} \quad \mathrm{Pr} \to 0 \tag{1}$$

$$\mathrm{Nu}_x = 0.5027\ \mathrm{Ra}_x^{1/4} \quad \text{for} \quad \mathrm{Pr} \to \infty \tag{2}$$

These equations and the available numerically computed solutions for intermediate Pr were used by Churchill and Usagi to construct the empirical correlation

$$\mathrm{Nu}_x = 0.503\ \mathrm{Ra}_x^{1/4}/[1 + (0.492/\mathrm{Pr})^{9/16}]^{4/9} \tag{3}$$

which represents all of the computed values within 1 percent.

Uniform Heat-Flux Density

The solutions for uniform heat-flux density are less complete. Sparrow and Gregg [3] obtained numerical solutions for Pr = 0.1, 1, 10, and 100 and Chang, et al. [4] for Pr = 0.03 and 0.1.

[1] Carl V. S. Patterson Professor of Chemical Engineering, University of Pennsylvania, Philadelphia, Pa.

[2] Assistant Professor, Department of Industrial and Mechanical Engineering, Okayama University, Okayama, Japan.

Contributed by the Heat Transfer Division of THE AMERICAN SOCIETY OF MECHANICAL ENGINEERS. Manuscript received by the Heat Transfer Division, November 22, 1972.

[3] Numbers in brackets designate References at end of technical brief.

The curve $N = 10$ is for weak radiation interaction; in this case it is not possible to distinguish the curves for $\omega = 0.9$ and 0, and in fact the curve coincides with that for no radiation. The local Nusselt number increases with decreasing N (i.e., increasing radiation) and when radiation effects are strong thermally fully developed state does not seem to occur.

References

1 Timofeyev, V. N., Shklyar, F. R., Malkin, V. M., and Berland, A. K. H., "Combined Heat Transfer in an Absorbing Stream Moving in a Flat Channel," *Heat Transfer—Soviet Research*, Parts I, II, III, Vol. 1, No. 6, 1969, pp. 57–93.

2 Kurosaki, Yasuo, "Heat Transfer by Simultaneous Radiation and Convection in an Absorbing and Emitting Medium in a Flow Between Parallel Plates," *Fourth International Heat Transfer Conference*, Section R 2.5, 1970, pp. 1–11.

3 Habib, I. S., and Greif, R., "Heat Transfer to a Flowing Non-Gray Radiating Gas: An Experimental and Theoretical Study," *International Journal of Heat and Mass Transfer*, Vol. 13, 1970, pp. 1571–1582.

4 Thorsen, R. S., "Combined Conduction, Convection, and Radiation Effects in Optically Thin Tube Flow," ASME Paper, No. 71-HT-17, 1971.

5 Chen, J. C., "Simultaneous Radiative and Convective Heat Transfer in an Absorbing, Emitting and Scattering Medium in Slug Flow Between Parallel Plates," *AIChE Journal*, Vol. 2, 1964, pp. 253–259.

6 Case, K. M., and Zweifel, P. F., *Linear Transport Theory*, Addison-Wesley, Reading, Mass., 1967.

7 Özişik, M. N., and Siewert, C. E., "On the Normal-Mode-Expansion Technique for Radiative Transfer in a Scattering, Absorbing and Emitting Slab With Specularly Reflecting Boundaries," *International Journal of Heat and Mass Transfer*, Vol. 121, 1952, pp. 175–182.

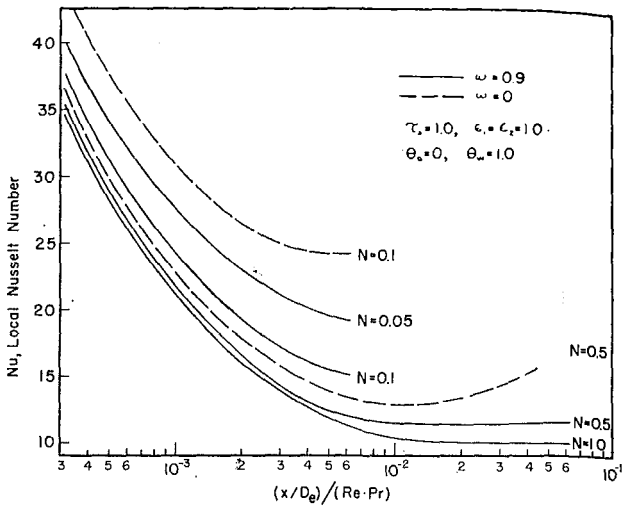

Fig. 2 Effect of N on the local Nusselt number

8 Lundquist, C. A., and Horak, H. G., "The Transfer of Radiation by an Emitting Atmosphere IV," *The Astrophysical Journal*, Vol. 121, 1952, pp. 175–182.

9 Özişik, M. N., *Boundary Value Problems of Heat Conduction*, International Textbook Company, Scranton, Pa., 1968.

10 Beach, H. L., Özişik, M. N., and Siewert, C. E., "Radiative Transfer in Linearly Anisotropic-Scattering, Conservative and Non-Conservative Slabs With Reflective Boundaries," *International Journal of Heat and Mass Transfer*, Vol. 14, 1971, pp. 1551–1565.

A Correlation for Laminar Free Convection From a Vertical Plate

S. W. CHURCHILL[1] and H. OZOE[2]

Nomenclature

A = coefficient in equations (2) and (10), dimensionless
B = coefficient in equations (1) and (9), dimensionless
g = gravitational acceleration, ft/sec^2
j = local heat-flux density, Btu/hr-ft^2
k = thermal conductivity, Btu/hr-ft-deg F
n = exponent in equation (11), dimensionless
Nu_x = $jx/k(T_w - T_\infty)$, local Nusselt number, dimensionless
Pr = ν/α, Prandtl number, dimensionless
Ra_x = $g\beta(T_w - T_\infty)x^3/\nu\alpha$, local Rayleigh number, dimensionless
T = temperature, deg F
T_w = wall temperature, deg F
T_∞ = ambient temperature, deg F
u = velocity component in x direction, ft/sec
v = velocity component in y direction, ft/sec
x = distance upward from bottom of plate, ft
y = distance from plate, ft
α = thermal diffusivity, ft^2/sec
β = volumetric coefficient of thermal expansion, deg F^{-1}
Δ_T = distance from plate for which $(T - T_\infty)/(T_w - T_\infty) = 0.01$
ν = kinematic viscosity, ft^2/sec

THE EXPRESSION proposed by Churchill and Usagi [1][3] has been used to construct a correlation for laminar free convection from a vertical plate. The correlation applies to both uniform heating and uniform wall temperature.

Uniform Wall Temperature

The limiting solutions derived by LeFevre [2] for an isothermal plate are

$$\mathrm{Nu}_x = 0.6004(\mathrm{Ra}_x\mathrm{Pr})^{1/4} \quad \text{for} \quad \mathrm{Pr} \to 0 \tag{1}$$

$$\mathrm{Nu}_x = 0.5027\ \mathrm{Ra}_x^{1/4} \quad \text{for} \quad \mathrm{Pr} \to \infty \tag{2}$$

These equations and the available numerically computed solutions for intermediate Pr were used by Churchill and Usagi to construct the empirical correlation

$$\mathrm{Nu}_x = 0.503\ \mathrm{Ra}_x^{1/4}/[1 + (0.492/\mathrm{Pr})^{9/16}]^{4/9} \tag{3}$$

which represents all of the computed values within 1 percent.

Uniform Heat-Flux Density

The solutions for uniform heat-flux density are less complete. Sparrow and Gregg [3] obtained numerical solutions for Pr = 0.1, 1, 10, and 100 and Chang, et al. [4] for Pr = 0.03 and 0.1.

[1] Carl V. S. Patterson Professor of Chemical Engineering, University of Pennsylvania, Philadelphia, Pa.

[2] Assistant Professor, Department of Industrial and Mechanical Engineering, Okayama University, Okayama, Japan.

Contributed by the Heat Transfer Division of THE AMERICAN SOCIETY OF MECHANICAL ENGINEERS. Manuscript received by the Heat Transfer Division, November 22, 1972.

[3] Numbers in brackets designate References at end of technical brief.

Table 1 Computed coefficients for uniform heat-flux density

Pr	0	0.001	0.01	0.10	1.0	10	100	1000	∞
$\frac{Nu_x}{Ra_x^{1/4}}$				0.336	0.456	0.524	0.550	0.559	0.5627
$\frac{Nu_x}{(Ra_xPr)^{1/4}}$	0.6922	0.688	0.670	0.597	0.456				

Selman and Newman [5] derived by a perturbation expansion an asymptotic solution for free convection due to a uniform component flux density for $Sc \to \infty$ which is equivalent to that for a uniform heat flux.

In order to supplement these values, asymptotic solutions have been derived for $Pr \to 0$ as well as for $Pr \to \infty$, and numerical results have been obtained for $Pr = 0, 0.001, 0.01, 0.1, 1, 10, 100, 1000$, and ∞. The solutions are for the following model which incorporates the boundary-layer and Boussinesq approximations:

$$\frac{\partial u}{\partial x} + \frac{\partial v}{\partial y} = 0 \tag{4}$$

$$u\frac{\partial u}{\partial x} + v\frac{\partial u}{\partial y} = g\beta(T - T_\infty) + \nu\frac{\partial^2 u}{\partial y^2} \tag{5}$$

$$u\frac{\partial T}{\partial x} + v\frac{\partial T}{\partial y} = \alpha\frac{\partial^2 T}{\partial y^2} \tag{6}$$

with

$$u = v = 0 \quad \text{and} \quad j = -k\frac{\partial T}{\partial y} \quad \text{at} \quad y = 0 \tag{7}$$

$$u = v = 0 \quad \text{and} \quad T = T_\infty \quad \text{at} \quad y \to \infty \quad \text{and at} \quad x = 0 \tag{8}$$

The partial differential equations were reduced to ordinary differential equations by the method of Hellums and Churchill [6], and the optimal forms for large and small Pr were solved numerically. The resulting asymptotic solutions are

$$Nu_x = 0.692(Ra_xPr)^{1/4} \quad \text{for} \quad Pr \to 0 \tag{9}$$

$$Nu_x = 0.563\ Ra_x^{1/4} \quad \text{for} \quad Pr \to \infty \tag{10}$$

The coefficient obtained by Selman and Newman agrees with that in equation (10) to four significant figures, although their procedure does not appear to give quite so accurate values for the velocity field as the procedure used herein, perhaps because of their choice of a boundary condition. Values for intermediate Pr are given in Table 1. These values and those computed by Sparrow and Gregg and by Chang, et al. are plotted in Fig. 1 in the form suggested by Churchill and Usagi. The values are well represented by the expression

$$Nu_x = 0.563\ Ra_x^{1/4}/[1 + (0.437/Pr)^{n/4}]^{1/n} \tag{11}$$

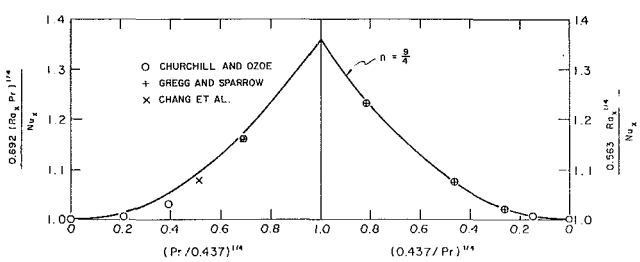

Fig. 1 Correlation for laminar free convection from a vertical plate with a uniform heat-flux density

with $n = 9/4$. The term $(0.437/Pr)^{1/4}$ represents the ratio of the asymptotic solution for $Pr \to \infty$ to that for $Pr \to 0$, and 0.437 is thus the central value of Pr for a uniform heat-flux density corresponding to 0.492 for uniform wall temperature.

General Correlation for Both Uniform Heating and Uniform Wall Temperature

Since the correlations are identical except for the coefficients, the single general expression

$$Nu_x = A\ Ra_x^{1/4}/[1 + (A/B)^{9/4}/Pr^{9/16}]^{4/9} \tag{12}$$

can be used to represent the computed values within 1 percent for all Pr and either uniform heating or uniform wall temperature.

Experimental Confirmation

The experimental data for uniform wall temperature as summarized by Ede [7] appear to scatter about equation (3). The experimental results of Rajan and Picot [8] for uniform heating of liquids were correlated with a coefficient equivalent to 0.66 rather than 0.563 in equations (10) and (11). However, the value of β is quite uncertain for these liquids.

Thermal Boundary-Layer Thickness for Uniform Heating

The thermal boundary-layer thickness such that $(T - T_\infty)/(T_w - T_\infty) = 0.01$ was determined in the course of the calculations. The following equation, which was constructed by the same procedure used for the Nusselt number, represents the computed values within 2 percent over the entire range.

$$\Delta_T(g\beta j/k\alpha^2 x)^{1/5} = 4.50[1 + (Pr/7.22)^{9/10}]^{2/9} \tag{13}$$

Thus the dimensionless thermal boundary-layer thickness is essentially constant for small Pr and increases as $Pr^{1/5}$ for very large Pr.

References

1 Churchill, S. W., and Usagi, R., "A General Expression for the Correlation of Rates of Transfer and Other Phenomena," *AIChE Journal*, Vol. 18, 1972, p. 1121–1128.

2 LeFevre, E. J., "Laminar Free Convection from a Vertical Plane Surface," *Proc. 9th Intern. Congr. Appl. Mech.*, Vol. 4, Brussels, Belgium, 1957, pp. 168–174.

3 Sparrow, E. M., and Gregg, J. L., "Laminar Free Convection From a Vertical Plate With Uniform Surface Heat Flux," TRANS. ASME, Vol. 78, 1956, pp. 435–440.

4 Chang, K. S., Akins, R. G., Burris, L., Jr., and Bankoff, S. G., "Free Convection of a Low Prandtl Number Fluid in Contact With a Uniformly Heated Vertical Plate," Argonne National Laboratory Report ANL-6835, Argonne, Ill., Jan. 1964.

5 Selman, J. R., and Newman, J., "High Sc Limit of Free Convection at a Vertical Plate With Uniform Flux Condition," JOURNAL OF HEAT TRANSFER, TRANS. ASME, Series C, Vol. 93, No. 4, Nov. 1971, pp. 465–466.

6 Hellums, J. D., and Churchill, S. W., "Mathematical Simplification of Boundary and Initial Value Problems," *AIChE Journal*, Vol. 10, 1964, pp. 110–114.

7 Ede, A. J., "Advances in Free Convection," in: *Advances in Heat Transfer*, Vol. 4, Hartnett, J. P., and Irvine, T. F., Jr., eds., Academic, New York, N. Y., 1967, pp. 1–64.

8 Rajan, V. S. V., and Picot, J. J. C., "Experimental Study of the Laminar Free Convection From a Vertical Plate," *Ind. Eng. Chem. Funda.*, Vol. 10, 1971, pp. 132–134.

Free Convection Nusselt Number for Vertical U-Shaped Channels

D. W. VAN DE POL[1] **and J. K. TIERNEY**[1]

Nomenclature

a = channel aspect ratio = S/L
C_p = specific heat at constant pressure
g = acceleration due to gravity
Gr_H = Grashof number = $g\beta(T_w - T_\infty)H^3/\nu^2$
Gr_r = Grashof number = $g\beta(T_w - T_\infty)r^3/\nu^2$
$\bar{h}$ = average heat transfer coefficient
H = height of channel
k = thermal conductivity
L = channel depth
Nu_H = Nusselt number = $\bar{h}H/k$
Nu_r = Nusselt number = $\bar{h}r/k$
Pr = Prandtl number = $\mu C_p/k$
r = characteristic length = $2LS/(2L + S)$
Ra^* = modified Rayleigh number = $(r/H)\mathrm{Gr}_r\mathrm{Pr}$
S = channel width
T = temperature
V = constant in equation (2) = -11.8 (1/in.)
β = volumetric coefficient of expansion
μ = dynamic viscosity
ν = kinematic viscosity
ψ = channel configuration factor

Subscripts

∞ = ambient condition
w = wall condition

Introduction

In electronic equipment, finned surfaces are frequently used as an efficient method of rejecting waste heat. Colloquially known as heat sinks, these finned surfaces are economical and highly reliable when cooling is by natural convection and radiation.

Elenbaas [1][2] has developed thermal relationships for closed channels and parallel plates, but not for U-shaped channels, shown in Fig. 1, which characterize heat sinks. Siegel and Norris [2] have also studied local heat transfer from large vertical parallel plates, while Bodoia and Osterle [3] have presented a theoretical analysis for natural convection which gave results closely agreeing with Elenbaas' correlations of actual test data.

Aibara [4] has shown that U-shaped channels may be approximated by parallel flat plates within an error of 5 percent in the heat transfer rate only if the ratio of channel depth to channel width (L/S) is greater than 5. However, many practical heat sink designs may consist of a series of relatively short fins attached to a heated base plate and the ratio L/S is often less than 5. In these cases the base plate creates additional surface area and a corner geometry having a significant effect on heat transfer rates. Fin arrays of this type have been investigated experimentally by Starner and McManus [5] and Welling and Wooldridge [6]. Additional experimental investigations have been conducted by Izume and Nakamura [7] who have also developed a mathematical relationship describing heat transfer from fin arrays. Their relationship, however, does not hold in the limiting cases of very large or very small channel depth to channel width ratios (L/S).

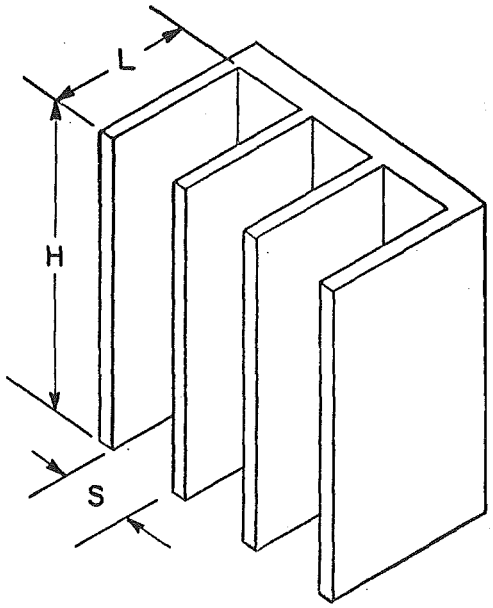

Fig. 1 U-shaped channel and heat sink configuration

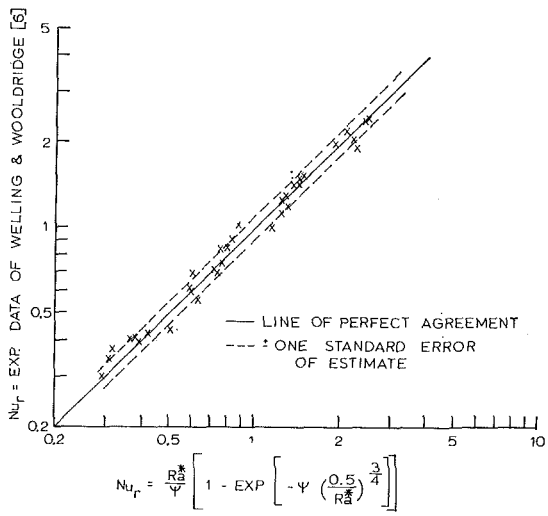

Fig. 2 Standard error of estimate of the Nusselt number

Nusselt Number for U-Shaped Geometry

The authors have developed a mathematical relationship for laminar flow heat transfer from constant temperature U-shaped channels which exhibits the proper behavior for both very deep and very shallow channels. Therefore, channel depth to channel width ratios (L/S) ranging from zero to infinity may be considered.

This relationship, expressed as a Nusselt number, has a form identical to that used by Elenbaas [1] for laminar flow in constant temperature ducts:

$$\mathrm{Nu}_r = \frac{\mathrm{Ra}^*}{\psi}\left\{1 - \exp\left[-\psi\left(\frac{0.5}{\mathrm{Ra}^*}\right)^{3/4}\right]\right\} \qquad (1)$$

For U-shaped channels, the authors have developed a relationship for ψ which fits the experimental data of Welling and Wooldridge [6] with a standard error of estimate based on the log of the Nusselt number of 0.039 (see Fig. 2). This relationship is:

$$\psi = \frac{24(1 - 0.483e^{-0.17/a})}{\left\{\left[1 + \frac{a}{2}\right][1 + (1 - e^{-0.83a})(9.14a^{1/2}e^{VS} - 0.61)]\right\}^3} \qquad (2)$$

---

[1] Member of the Technical Staff, Bell Laboratories, Whippany, N. J.

[2] Numbers in brackets designate References at end of technical brief.

Contributed by the Heat Transfer Division of The American Society of Mechanical Engineers. Manuscript received by the Heat Transfer Division, March 22, 1973.

The Nusselt number relationship with this ψ results in a heat transfer coefficient which approaches the Elenbaas [1] parallel flat plate solution as the ratio L/S approaches infinity, that is,

$$\mathrm{Nu}_r = \frac{\mathrm{Ra}^*}{24}\left\{1 - \exp\left[-24\left(\frac{0.5}{\mathrm{Ra}^*}\right)^{3/4}\right]\right\} \quad (3)$$

where $r \to S$ as $L/S \to \infty$

As the ratio L/S approaches zero, the resulting heat transfer coefficient is given by

$$\mathrm{Nu}_H = 0.595(\mathrm{Gr}_H\mathrm{Pr})^{1/4} \quad (4)$$

which is within 1 percent of the constant temperature flat plate solution given by McAdams. All physical properties are evaluated at the wall temperature, with the exception of β, which is evaluated at the fluid temperature. The wall temperature was used instead of the mean fluid temperature since the data of Welling and Wooldridge were presented in this form.

Closure

The Nusselt number described in the foregoing may be used to calculate natural convection heat transfer from vertical fin arrays. Combined with radiation calculations, this frequently used geometry may be characterized in a free convection environment.

References

1 Elenbaas, W., "Dissipation of Heat by Free Convection," Parts I and II, Philips Research Report, 3, N. V. Philips, Gloeilampenfabrieken, Eindhoven, Netherlands, 1948.

2 Siegel, R., and Norris, R. H., "Tests of Free Convection in a Partially Enclosed Space Between Two Heated Vertical Plates," JOURNAL OF HEAT TRANSFER, TRANS. ASME, Series C, Vol. 79, 1957, pp. 663–72.

3 Bodoia, J. R., and Osterle, J. F., "The Development of Free Convection Between Heated Vertical Plates," JOURNAL OF HEAT TRANSFER, TRANS. ASME, Series C, Vol. 84, 1962, pp. 40–44.

4 Aibara, T., "Natural Convective Heat Transfer in Vertical Parallel Fins of Rectangular Profile," *Jap. Soc. Mech. Eng.* Vol. 34, 1968, pp. 915–926.

5 Starner, K. E., and McManus, H. N., "An Experimental Investigation of Free Convection Heat Transfer From Rectangular Fin Arrays," JOURNAL OF HEAT TRANSFER, TRANS. ASME, Series C, Vol. 85, 1963, pp. 273–278.

6 Welling, J. R., and Wooldridge, C. B., "Free Convection Heat Transfer Coefficients From Rectangular Vertical Fins," JOURNAL OF HEAT TRANSFER, TRANS. ASME, Series C, Vol. 87, 1965, pp. 439–444.

7 Izume, K., and Nakamura, H., "Heat Transfer by Convection on the Heated Surface With Parallel Fins," *Jap. Soc. Mech. Eng.*, Vol. 34, (261), 1968, pp. 909–914.

8 McAdams, W. H., *Heat Transmission*, McGraw-Hill, New York, p. 172.

The Boundary-Layer Regime for Natural Convection in a Differentially Heated, Tilted Rectangular Cavity

PORTONOVO AYYASWAMY[1] and IVAN CATTON[2]

Nomenclature

A = aspect ratio = (H/L)
Pr = Prandtl number = (ν/κ)
R_H = Rayleigh number = $\alpha g \Delta T H^3/\kappa\nu$
R_L = Rayleigh number = $\alpha g \Delta T L^3/\kappa\nu$
α = coefficient of thermal expansion
δ = boundary layer thickness
κ = thermal diffusivity
ν = kinematic viscosity
ξ = vorticity
ψ = stream function
Ψ = order of magnitude of stream function

Subscripts

$*$ = dimensional variables

Superscripts

$**$ = scaled solution

Introduction

IN A CAVITY with differentially heated side walls, the prevalent motion corresponds to the boundary layer regime when the Rayleigh number is large. Gill [1][3] has studied this regime of convective motion in a vertical cavity. Gill's contribution has been critically examined by Quon [2]. In this note, it is demonstrated that under certain restrictions, Gill's results can be reinterpreted for a titled cavity problem.

Equations and Boundary Conditions

The geometry and boundary conditions of the problem are summarized in Fig. 1. The extreme case of L/H being very large is excluded in the following discussion. The steady-state vorticity equation of a Boussinesq fluid is

$$u^*\frac{\partial \xi_*}{\partial x_*} + w_*\frac{\partial \xi_*}{\partial z_*} = \nu\left(\frac{\partial^2 \xi_*}{\partial {x_*}^2} + \frac{\partial^2 \xi_*}{\partial {z_*}^2}\right) + \alpha g\left(\frac{\partial T_*}{\partial x_*}\cos\theta + \frac{\partial T_*}{\partial z_*}\sin\theta\right) \quad (1)$$

The heat equation is

$$(\mathbf{V}_* \cdot \nabla)T_* = \kappa\nabla^2 T_* \quad (2)$$

Boundary conditions are

$$\psi_* = \frac{\partial \psi_*}{\partial x_*} = 0 \text{ at } x = 0, L \qquad T_* = \pm T_H \text{ at } x = 0, L \quad (3)$$

$$\psi_* = \frac{\partial \psi_*}{\partial z_*} = \frac{\partial T_*}{\partial z_*} = 0 \text{ at } z = \pm H/2 \quad (4)$$

Boundary-Layer Regime Equations and Order of Magnitude Analysis

Consider $\delta \ll H$ and $\delta \ll L$, so that the boundary layers on the two walls are distinct and separated by a core region. The usual boundary layer assumptions are

$$\frac{\partial T_*}{\partial x_*} \gg \frac{\partial T_*}{\partial z_*}\tan\theta, \qquad \frac{\partial^2 \xi_*}{\partial {x_*}^2} \gg \frac{\partial^2 \xi_*}{\partial {z_*}^2} \quad (5)$$

Following Gill [1], orders of magnitude of ψ and δ can be deduced from the governing equations to be $\Psi = \kappa H/\delta$ and $\delta^4 = (\nu\kappa H/\alpha g \Delta T)/\cos\theta$ for fluids of Prandtl number very high or of order unity.

The variables in the governing equations are scaled as follows:

---

[1] Postdoctoral Scholar, Institute of Geophysics and Planetary Physics, UCLA, Calif.

[2] Assistant Professor, Energy and Kinetics Department, UCLA, Calif.

[3] Numbers in brackets designate References at end of technical brief.

Contributed by the Heat Transfer Division of THE AMERICAN SOCIETY OF MECHANICAL ENGINEERS. Manuscript received by the Heat Transfer Division, December 13, 1972.

The Nusselt number relationship with this ψ results in a heat transfer coefficient which approaches the Elenbaas [1] parallel flat plate solution as the ratio L/S approaches infinity, that is,

$$\mathrm{Nu}_r = \frac{\mathrm{Ra}^*}{24}\left\{1 - \exp\left[-24\left(\frac{0.5}{\mathrm{Ra}^*}\right)^{3/4}\right]\right\} \tag{3}$$

where $r \to S$ as $L/S \to \infty$

As the ratio L/S approaches zero, the resulting heat transfer coefficient is given by

$$\mathrm{Nu}_H = 0.595(\mathrm{Gr}_H\mathrm{Pr})^{1/4} \tag{4}$$

which is within 1 percent of the constant temperature flat plate solution given by McAdams. All physical properties are evaluated at the wall temperature, with the exception of β, which is evaluated at the fluid temperature. The wall temperature was used instead of the mean fluid temperature since the data of Welling and Wooldridge were presented in this form.

Closure

The Nusselt number described in the foregoing may be used to calculate natural convection heat transfer from vertical fin arrays. Combined with radiation calculations, this frequently used geometry may be characterized in a free convection environment.

References

1 Elenbaas, W., "Dissipation of Heat by Free Convection," Parts I and II, Philips Research Report, 3, N. V. Philips, Gloeilampenfabrieken, Eindhoven, Netherlands, 1948.

2 Siegel, R., and Norris, R. H., "Tests of Free Convection in a Partially Enclosed Space Between Two Heated Vertical Plates," JOURNAL OF HEAT TRANSFER, TRANS. ASME, Series C, Vol. 79, 1957, pp. 663–72.

3 Bodoia, J. R., and Osterle, J. F., "The Development of Free Convection Between Heated Vertical Plates," JOURNAL OF HEAT TRANSFER, TRANS. ASME, Series C, Vol. 84, 1962, pp. 40–44.

4 Aibara, T., "Natural Convective Heat Transfer in Vertical Parallel Fins of Rectangular Profile," *Jap. Soc. Mech. Eng.* Vol. 34, 1968, pp. 915–926.

5 Starner, K. E., and McManus, H. N., "An Experimental Investigation of Free Convection Heat Transfer From Rectangular Fin Arrays," JOURNAL OF HEAT TRANSFER, TRANS. ASME, Series C, Vol. 85, 1963, pp. 273–278.

6 Welling, J. R., and Wooldridge, C. B., "Free Convection Heat Transfer Coefficients From Rectangular Vertical Fins," JOURNAL OF HEAT TRANSFER, TRANS. ASME, Series C, Vol. 87, 1965, pp. 439–444.

7 Izume, K., and Nakamura, H., "Heat Transfer by Convection on the Heated Surface With Parallel Fins," *Jap. Soc. Mech. Eng.*, Vol. 34, (261), 1968, pp. 909–914.

8 McAdams, W. H., *Heat Transmission*, McGraw-Hill, New York, p. 172.

The Boundary-Layer Regime for Natural Convection in a Differentially Heated, Tilted Rectangular Cavity

PORTONOVO AYYASWAMY[1] and IVAN CATTON[2]

Nomenclature

A = aspect ratio = (H/L)
Pr = Prandtl number = (ν/κ)
R_H = Rayleigh number = $\alpha g \Delta T H^3/\kappa\nu$
R_L = Rayleigh number = $\alpha g \Delta T L^3/\kappa\nu$
α = coefficient of thermal expansion
δ = boundary layer thickness
κ = thermal diffusivity
ν = kinematic viscosity
ξ = vorticity
ψ = stream function
Ψ = order of magnitude of stream function

Subscripts

$*$ = dimensional variables

Superscripts

$**$ = scaled solution

Introduction

IN A CAVITY with differentially heated side walls, the prevalent motion corresponds to the boundary layer regime when the Rayleigh number is large. Gill [1][3] has studied this regime of convective motion in a vertical cavity. Gill's contribution has been critically examined by Quon [2]. In this note, it is demonstrated that under certain restrictions, Gill's results can be reinterpreted for a titled cavity problem.

Equations and Boundary Conditions

The geometry and boundary conditions of the problem are summarized in Fig. 1. The extreme case of L/H being very large is excluded in the following discussion. The steady-state vorticity equation of a Boussinesq fluid is

$$u^*\frac{\partial \xi_*}{\partial x_*} + w_*\frac{\partial \xi_*}{\partial z_*} = \nu\left(\frac{\partial^2 \xi_*}{\partial {x_*}^2} + \frac{\partial^2 \xi_*}{\partial {z_*}^2}\right) + \alpha g\left(\frac{\partial T_*}{\partial x_*}\cos\theta + \frac{\partial T_*}{\partial z_*}\sin\theta\right) \tag{1}$$

The heat equation is

$$(\mathbf{V}_* \cdot \nabla)T_* = \kappa\nabla^2 T_* \tag{2}$$

Boundary conditions are

$$\psi_* = \frac{\partial \psi_*}{\partial x_*} = 0 \text{ at } x = 0, L \qquad T_* = \pm T_H \text{ at } x = 0, L \tag{3}$$

$$\psi_* = \frac{\partial \psi_*}{\partial z_*} = \frac{\partial T_*}{\partial z_*} = 0 \text{ at } z = \pm H/2 \tag{4}$$

Boundary-Layer Regime Equations and Order of Magnitude Analysis

Consider $\delta \ll H$ and $\delta \ll L$, so that the boundary layers on the two walls are distinct and separated by a core region. The usual boundary layer assumptions are

$$\frac{\partial T_*}{\partial x_*} \gg \frac{\partial T_*}{\partial z_*}\tan\theta, \qquad \frac{\partial^2 \xi_*}{\partial {x_*}^2} \gg \frac{\partial^2 \xi_*}{\partial {z_*}^2} \tag{5}$$

Following Gill [1], orders of magnitude of ψ and δ can be deduced from the governing equations to be $\Psi = \kappa H/\delta$ and $\delta^4 = (\nu\kappa H/\alpha g \Delta T)/\cos\theta$ for fluids of Prandtl number very high or of order unity.

The variables in the governing equations are scaled as follows:

---

[1] Postdoctoral Scholar, Institute of Geophysics and Planetary Physics, UCLA, Calif.

[2] Assistant Professor, Energy and Kinetics Department, UCLA, Calif.

[3] Numbers in brackets designate References at end of technical brief.

Contributed by the Heat Transfer Division of THE AMERICAN SOCIETY OF MECHANICAL ENGINEERS. Manuscript received by the Heat Transfer Division, December 13, 1972.

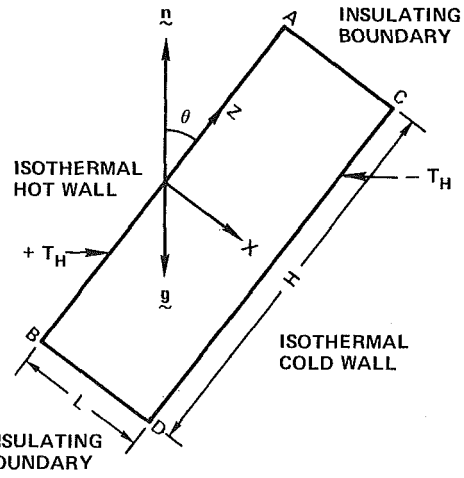

Fig. 1 Geometry and coordinate system of the tilted cavity

$$x = x_*/\delta, \quad z = z_*/H, \quad T = T_*/2T_H, \quad \psi = \psi_*/\Psi,$$
$$u = (H/\Psi)u_*, \quad w = (\delta/\Psi)w_* \quad \text{and} \quad \xi = (\delta^2/\Psi)\xi_*$$

With this scheme, the first of (5) requires that

$$\frac{\partial T}{\partial x} \gg (\delta/H)\frac{\partial T}{\partial z}\tan\theta \tag{6}$$

If $(\delta/H) \sim 10^{-1}$ and $\tan\theta \sim 1$, (6) is satisfied and, from (2),

$$u\frac{\partial T}{\partial x} + w\frac{\partial T}{\partial z} = \frac{\partial^2 T}{\partial x^2} + (\delta/H)^2\frac{\partial^2 T}{\partial z^2} \tag{7}$$

With $(\delta/H)^2 \sim 10^{-2}$, the foregoing equation reduces to

$$u\frac{\partial T}{\partial x} + w\frac{\partial T}{\partial z} = \frac{\partial^2 T}{\partial x^2} \tag{8}$$

An immediate consequence of $(\delta/H)^2 \sim 10^{-2}$ is that

$$\cos\theta \geq 10^4/\mathrm{R}_H \tag{9}$$

The vorticity equation (1) in nondimensional form becomes

$$\frac{1}{\mathrm{Pr}}\left(u\frac{\partial \xi}{\partial x} + w\frac{\partial \xi}{\partial z}\right) = \frac{\partial^2 \xi}{\partial x^2} + (\delta/H)^2\frac{\partial^2 \xi}{\partial z^2} + \frac{\partial T}{\partial x} + (\delta/H)\tan\theta\frac{\partial T}{\partial z} \tag{10}$$

For $\mathrm{Pr} \sim 0(1)$ or higher, and $(\delta/H)\tan\theta \sim 10^{-1}$, the foregoing equation reduces to

$$\frac{1}{\mathrm{Pr}}\left(u\frac{\partial \xi}{\partial x} + w\frac{\partial \xi}{\partial z}\right) = \frac{\partial^2 \xi}{\partial x^2} + \frac{\partial T}{\partial x} \tag{11}$$

The order of $(\delta/H)\tan\theta$ gives us the additional constraint

$$\frac{\tan^4\theta}{\mathrm{R}_H\cos\theta} \leq 10^{-4} \tag{12}$$

An order of magnitude analysis on the core equations gives still more conditions to be satisfied for proper rescaling. In order that the conduction terms relative to the convection terms in the core are small, we can deduce that, for $L/H \sim 0(1)$ or less,

$$\delta/H \ll L/H \ll H/L \tag{13}$$

The convection, diffusion, and the sin θ dependent buoyancy term in (1) are, respectively, of order $\delta^2/\mathrm{Pr}L^2$, δ^3/L^3, and $L\tan\theta/H$ compared with the cos θ dependent buoyancy term. With (13), the only condition arising would be

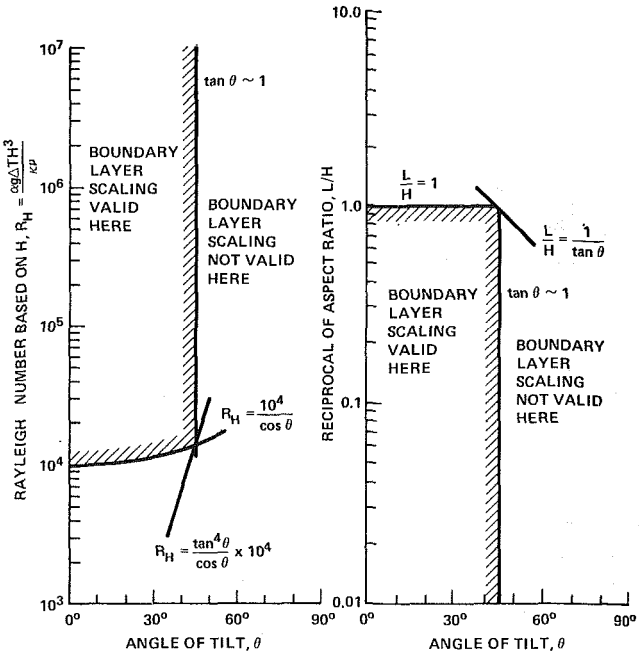

a. Limiting Rayleigh Number Based on Height b. Limiting Aspect Ratio

Fig. 2 Scaling restrictions on Rayleigh number and aspect ratio

$$H/L \gg \tan\theta \tag{14}$$

Gill [1] has solved approximately the convection problem posed by (8) and (11) for consistent core and boundary layer solutions for the case of a vertical slot and a high Prandtl number fluid. For a range of tilt angles such that $\tan\theta \sim 1$, Rayleigh numbers and aspect ratios constrained by (9)–(14), it is possible to rescale his results.

Results and Discussion

Fig. 2(*a*) shows a plot of R_H against θ restricted by (9) and (12), while the allowable inclination for rescaling is such that $\tan\theta \sim 1$. The condition imposed by (9) limits the rescaling region to $\theta \leq 45$ deg. At this limiting angle, (9) and (12) coincide and $\tan\theta = 1$ becomes the controlling characteristic. Fig. 2(*b*) is a plot of (L/H) against θ as restricted by (13) and (14). The controlling parameters here are $(L/H) = 1$ and $\tan\theta \sim 1$.

The rescaling presents no difficulty for positive angles of tilt (heated from above). For negative angles, Hart's observations [3] suggest restricting the region that permits rescaling to within $\theta > -10$ deg.

By defining $x^{**} = (x/\cos^{1/4}\theta)$ and $w^{**} = (w/\cos^{1/2}\theta)$, it is possible to represent the rescaled solutions (Figs. 3 and 4). The proper rescaling for δ and ψ, would be $\delta^{**} = (\delta/\cos^{1/2}\theta)$ and $\psi^{**} = (\psi/\cos^{1/4}\theta)$. Comparisons of the rescaled solutions with the preliminary Galerkin solutions obtained by Catton, Ayyaswamy, and Clever [4] were made. Figs. 3(*b*) and 4(*a*) for the temperature and the Nusselt number show fair comparison while Figs. 3(*a*) and 4(*d*) do not do so. Also note that Fig. 3(*b*) shows better comparison for (L/H) smaller and R_H larger values, while in Fig. 4(*a*) the scaled results predict the heat transport better with increasing Rayleigh numbers. It has been pointed out by Quon [2] that the vertical velocity field calculated by Gill, does not agree with the experimental results as well as first appears in Gill's paper. This was due to an incorrect scaling of Elder's [5] experimental measurements, and Quon shows that the predicted maximum for Gill's theory is ~25 percent higher than that observed in experiments. The temperature in the core, Fig. 4(*d*), reflects the same features as in Gill's Fig. 3, for which

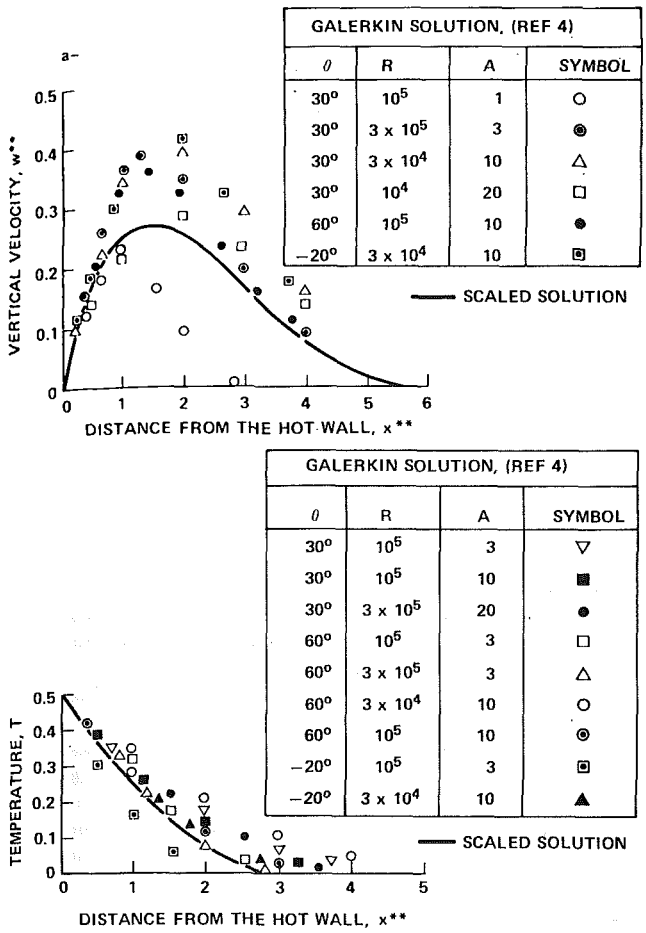

Fig. 3 Variation of w^{**} and T with x^{**} at the cavity midheight

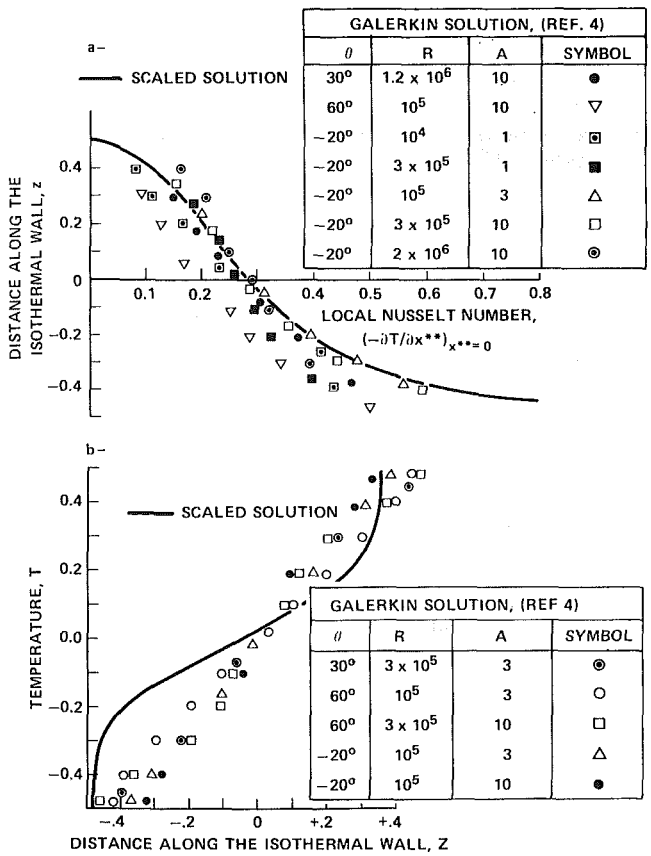

Fig. 4 Local Nusselt number $(-\partial T/\partial x^{**})_{x^{**}=0}$ and core temperature as a function of z

he has chosen the constant C in his equation (6.19) differently from his other Figs. 4–7. The choice of this constant and its effect upon the predictions are discussed in detail by Quon.

From Fig. 4(a), it is seen that for a given aspect ratio and a boundary-layer regime flow, the averaged Nusselt number, $\mathrm{Nu}(\theta)$ is related to the averaged Nusselt number, $\mathrm{Nu}(\theta = 0)$, corresponding to the vertical configuration by the relation

$$\mathrm{Nu}(\theta) = \mathrm{Nu}(\theta = 0)\cos^{1/4}\theta \qquad (15)$$

A comparison in Table 1 of the scaled results with the numerical solutions of [4] indicates a favorable level of agreement for the averaged Nusselt numbers. In conclusion, the most valuable contribution of this effort lies in its engineering value inasmuch as results applicable to a tilted cavity flow may quickly be obtained by properly reinterpreting the results for the well-understood vertical cavity problem.

Table 1

R	θ	A	$\mathrm{Nu}_{\theta=0}$ (reference [4])	$\mathrm{Nu}_{\theta=\theta} = \mathrm{Nu}_{\theta=0} \times \cos^{1/4}\theta$ (Scaled result prediction)	$\mathrm{Nu}_{\theta=\theta}$ (reference [4])
3×10^5	−20 deg	5	5.2	5.12	5.2
10^6	−20 deg	10	5.8	5.72	5.8
3×10^5	+30 deg	5	5.2	5.00	4.6
10^6	+30 deg	10	5.8	5.58	5.2
3×10^5	+60 deg	10	4.4	3.70	3.4
10^6	+60 deg	10	5.8	4.87	4.58

Acknowledgments

The authors are thankful to Prof. R. E. Kelly for many useful consultations. One of the referees who made helpful suggestions, and sponsorship of this work by the National Science Foundation Grant GK35892, are gratefully acknowledged.

References

1 Gill, A. E., "The Boundary-Layer Regime for Convection in a Rectangular Cavity," *Journal of Fluid Mechanics*, Vol. 26, 1966, pp. 515–526.

2 Quon, Charles, "High Rayleigh Number Convection in an Enclosure—A Numerical Study," *Phys. Fl.*, Vol. 15, 1972, pp. 12–19.

3 Hart, John E., "Stability of the Flow in a Differentially Heated Inclined Box," *Journal of Fluid Mechanics*, Vol. 47, 1971, pp. 547–576.

4 Catton, I., Ayyaswamy, P. S., and Clever, R. M., "Natural Convection Flow in a Finite Rectangular Slot Arbitrarily Oriented With Respect to the Gravity Vector," to appear in the *International Journal of Heat and Mass Transfer*.

5 Elder, J. W., "Laminar Free Convection in a Vertical Slot," *Journal of Fluid Mechanics*, Vol. 23, 1965, pp. 77–98.

Convective Heat Transfer From a Rotating Inner Sphere to a Stationary Outer Sphere

GLENNON MAPLES,[1] DAVID F. DYER,[1] KERIM ASKIN,[2] and DUPREE MAPLES[3]

The convection heat transfer rate between a rotating, isothermal sphere and a concentrically located, isothermal outer sphere is experimentally determined for various Grashof and Reynolds numbers. A comparison of data with that for a single sphere rotating in an infinite media is given. The heat transfer rate for the single sphere is higher than for the concentric spheres at the same Reynolds number. The present experiment is shown to involve both free and forced convection heat transfer.

Nomenclature

A = surface area of inner sphere
D = inner sphere diameter
f = functional relation
$\bar{h}$ = average convective heat transfer coefficient
k = thermal conductivity
N_{GR} = Grashof number
N_{NU} = Nusselt number
N_{RE} = rotational Reynolds number
q = heat transfer rate
T = temperature
$\Delta T = T_i - T_o$
ω = angular velocity

Subscripts

c = heat transfer by convection
i = inner sphere outer surface
L = combined heat transfer by radiation and conduction
m = arithmetric mean
o = outer sphere inner surface
T = total heat transfer by radiation, conduction, and convection

Introduction

THIS PAPER reports experimental data for convective heat transfer rates between concentric spheres where the inner sphere rotates. Such data are of general theoretical interest and of practical importance in the design of rotating machinery.

Many experimental investigations have been performed to determine convective heat transfer rates between stationary concentric cylinders and between stationary concentric spheres, e.g., Bishop, et al. [1],[4] Mack and Hardee [2], and Powe, et al. [3]. Kreith, et al. [4], gives important experimental data for a single sphere rotating in an infinite media. Similar results are given for rotating cylinders, e.g., Holloway [5], Kramer [6], and Kays and Bjorklund [7]. The latter authors include the effect of crossflow. Erdogan [8] has solved analytically the fundamental equations for the heat transfer rate to a viscous fluid confined between two rotating spheres.

Experimental Apparatus

The basic apparatus consists, as shown in Fig. 1, of two concentric spheres placed in a cylindrical water tank. The apparatus, briefly described in the following, was designed and built with extreme care (see reference [9] for details). The hollow inner sphere is made of two 5-in. OD aluminum hemispheres (with $^5/_8$-in. wall) which are threaded together. The outer sphere is constructed similarly and has a 10-in. ID. The heat transfer surfaces of the two spheres are polished and carefully machined to be concentric. The inner sphere is supported and rotated by teflon tubes of 0.625-in. OD by 0.187-in. wall thickness. These tubes extend through the outer sphere. Bishop [10] has shown that this geometry has negligible effect on the flow phenomena. The rate of heat transfer through the spheres via radiation and conduction through the support tubes is accounted for by a calibration procedure in which the space between the spheres is evacuated and the heat transfer rate measured for the outer sphere temperature used and for different inner sphere temperatures.

The outer surface of the outer sphere is maintained for all experiments at 40 $\pm$ $^1/_2$ deg F by a thermally controlled water bath. A simple calculation for the maximum heat transfer rate occurring during the experiments shows that there is less than 0.02 deg F maximum temperature drop through the walls of the sphere so that the inside and outside walls of a sphere are practically at the same temperature.

Thermal control of the surface of the inner sphere is achieved by admitting freon into the inside cavity in an amount sufficient to cause saturated liquid to exist in the bottom portion of the sphere with vapor above it. An electrical resistance heater is used to maintain the freon at constant temperature. During the experiments reported in this paper, the wall temperature of this cavity was measured at the equator and near the upper pole of the sphere. Since these two temperatures did not ever differ by more than $^1/_2$ deg F, it is reasonable to conclude that the inner sphere was practically isothermal during each of the experiments.

Experimental Procedure

The essence of the experimental procedure is described in this section. The outer and inner sphere temperatures are regulated at the desired condition by the apparatus described in the foregoing. Dry air is introduced between the spheres and the inner sphere is rotated at the desired angular velocity. The temperatures of the inner and outer spheres are monitored and, after equilibrium is achieved in roughly 17 hr, the energy input to the heater is measured. This energy input minus the radiation and conduction losses, obtained from the calibration tests, equals the net convective heat transfer.

Presentation of Results

The Nusselt number can be expressed in terms of measured quantities as

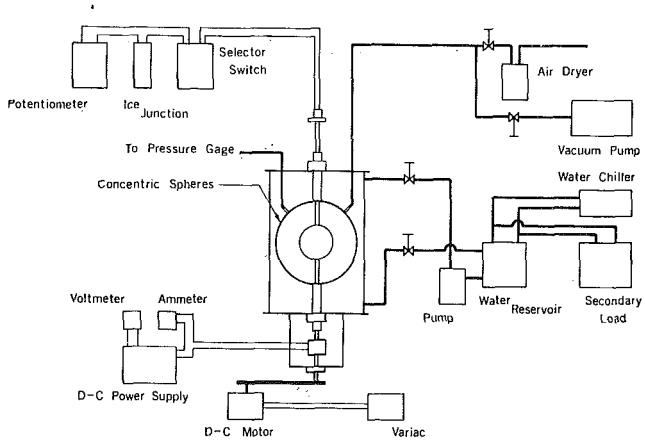

Fig. 1 Schematic of apparatus

[1] Associate Professor, Department of Mechanical Engineering, Auburn University, Auburn, Ala.
[2] Engineer, Southwire Company, Carrollton, Ga.
[3] Associate Professor, Department of Mechanical Engineering, Louisiana State University, Baton Rouge, La.
[4] Numbers in brackets designate References at end of technical brief.

Contributed by the Heat Transfer Division of THE AMERICAN SOCIETY OF MECHANICAL ENGINEERS. Manuscript received by the Heat Transfer Division, April 9, 1973.

Table 1 Heat transfer from a rotating inner sphere to a stationary outer sphere

ω (rpm)	Run No.	T_o (F)	T_i (F)	$N_{GR} \times 10^{-4}$	N_{NU}	N_{RE}
55	1	39.66	69.74	606.9320	17.762	3212
	2	40.03	90.52	963.9776	19.680	3151
	3	39.93	130.79	1550.7536	21.222	3018
	4	40.33	153.80	1797.1448	21.276	2946
85	1	40.00	69.82	601.6800	19.990	4993
	2	40.13	92.43	994.7520	20.914	4867
	3	39.83	133.96	1592.9488	20.772	4660
	4	40.10	155.58	1828.9728	22.394	4550
115	1	39.87	69.56	599.0624	21.726	6769
	2	39.64	92.61	1007.4896	22.350	6588
	3	39.70	136.08	1624.0176	22.462	6271
	4	39.74	158.20	1858.9856	23.134	6159
165	1	39.80	68.22	575.4936	23.422	9675
	2	39.73	94.08	1029.7640	23.270	9430
	3	39.87	135.46	1610.7104	23.728	8975
	4	40.01	156.04	1837.7232	24.968	8816

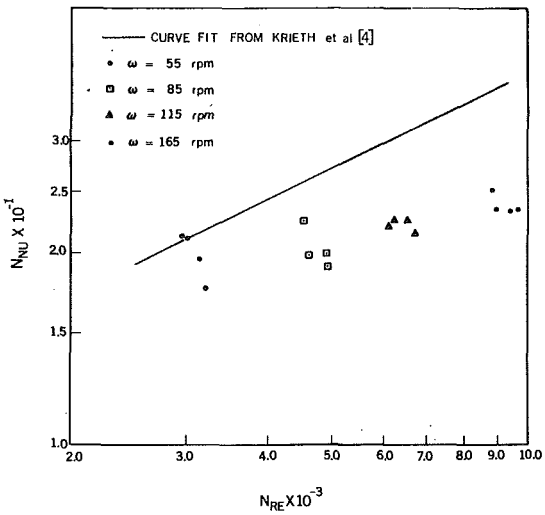

Fig. 2 Heat transfer as a function of Reynolds number

$$N_{NU} \equiv \frac{\bar{h}D}{k} = \frac{q_c D}{A(T_i - T_o)k}.$$

In this equation the thermal conductivity is evaluated at a mean temperature calculated according to an equation from reference [1], namely

$$T_m = \left(\frac{D_m^3 - D_i^3}{D_o^3 - D_i^3}\right) T_i + \left(\frac{D_o^3 - D_m^3}{D_o^3 - D_i^3}\right) T_o.$$

The Grashof and Reynolds numbers are calculated directly from their definitions with the viscosity and density evaluated at T_m. For all cases the Prandtl number is approximately 0.72.

Based on earlier work by Bishop [10] and Kreith, et al. [4], it is concluded that the Nusselt number can be correlated as follows:

$$N_{NU} = f(N_{GR}, N_{PR}, N_{RE})$$

where the reference length in these dimensionless numbers is taken as the inner sphere diameter since the gap width between the spheres is much greater than the boundary layer thickness.

Results

Table 1 summarizes the sixteen experiments considered in this investigation. Essentially two parameters were varied, namely, the inner sphere rotational rate (Reynolds number) and the inner sphere temperature (Grashof number). Since (to the authors' knowledge) these data are unique, it will be of interest to those requiring an understanding of heat transfer in such a configuration and to those doing research in the same or related areas. In the following discussion, two basic observations are made regarding these data.

Fig. 2 shows the data from Table 1 (see reference [9] for a complete tabulation of the data) plotted as the Nusselt number versus the Reynolds number. The spread in data at a given Reynolds number is attributed to free convection effects. For a single sphere rotating in an infinite media, Nordlie, et al. [11], concludes that the significance of free convection is determined by the ratio, N_{GR}/N_{RE}^2. For N_{GR}/N_{RE}^2 less than 0.1, they find that free convection is negligible. For the present experiments, N_{GR}/N_{RE}^2 is much greater than 0.1 so that some free convection is to be expected. This observation is further substantiated by the fact that the spread in data is greatest at the lowest Reynolds number. At the low Reynolds number N_{GR}/N_{RE}^2 varies from 0.6 to 2.0 while at the highest Reynolds number N_{GR}/N_{RE}^2 varies roughly from 0.06 to 0.2.

The second observation to be made regarding Fig. 2 is the comparison of the present experimental data with the data of Kreith, et al. [4], which are shown as a solid line in the plot. The data of Kreith, et al., were taken, where free convection is negligible, for a single sphere rotating in an infinite media. The heat transfer rate for the present case is much lower with a closer correlation to Kreith's data at low Reynolds numbers. This effect is probably due to the fact that free convection effects relative to forced convection are more important at low rotational speeds. The authors feel that the apparent increase in heat transfer rates for the single sphere can be explained as follows: With no outer shell the free stream temperature "penetrates" more closely to the inner sphere so that the thermal gradient and heat transfer rates are larger.

References

1 Bishop, E. H., Mack, L. R., and Scanlan, J. A., "Heat Transfer by Natural Convection Between Concentric Spheres," *International Journal of Heat and Mass Transfer*, Vol. 9, 1966, pp. 649–662.

2 Mack, L. R., and Hardee, H. R., "Natural Convection Between Concentric Spheres at Low Rayleigh Numbers," *International Journal of Heat and Mass Transfer*, Vol. 11, 1968, pp. 387–396.

3 Powe, R. E., Carley, C. T., and Bishop, E. H., "Free Convection Flow Patterns in Cylindrical Annuli," TRANS. ASME, Aug. 1969, pp. 310–314.

4 Kreith, F., Roberts, L. G., Sullivan, J. A., and Sinha, S. N., "Convection Heat Transfer and Flow Phenomena of Rotating Spheres," *International Journal of Heat and Mass Transfer*, Vol. 6, 1963, pp. 881–895.

5 Holloway, J. T., Jr., "A Study of Convective Heat Transfer From a Cylinder Rotating in Air at Sub-Atmospheric Pressures," MS thesis, Louisiana State University, Baton Rouge, La., 1966.

6 Kramer, F. R., "Heated Rotating Cylinders," *Chemical Engineering*, July, 1966, pp. 173–175.

7 Kays, W. M., and Bjorklund, I. S., "Heat Transfer From a Rotating Cylinder With and Without Crossflow," TRANS. ASME, Vol. 78, 1956, pp. 70–78.

8 Erdogan, M. E., "Transmission de la Chaleur a un Fluide Visqueux se Mouvant entre Deux Spheres Concentriques Tournantes," *International Brief Reports*, Vol. 15, 1964, pp. 66–67.

9 Askin, Kerim, "Convective Heat Transfer From a Rotating Inner Sphere to a Stationary Outer Sphere," MS thesis, Auburn University, Auburn, Ala., 1971.

10 Bishop, E. H., "Heat Transfer by Natural Convection Between Isothermal Concentric Spheres," PhD thesis, University of Texas, Austin, Texas, 1964.

11 Nordlie, R., and Kreith, F., "Convection Heat Transfer From a Rotating Sphere," *International Development in Heat Transfer*, ASME, 1961, pp. 461–467.

The Use of a Hot Film Anemometer to Measure Velocities Below 5 cm/sec in Mercury

JOHN C. HURT[1] and JAMES R. WELTY[2]

Introduction

THIS PAPER discusses velocity measurements in mercury with a constant temperature hot film anemometer. The study was motivated by a desire to further the investigation of natural convection velocities in mercury [6, 7].[3] Experimental difficulties have been reported in the literature by those researchers using insulated hot wires or hot films to measure velocities in mercury [1 through 9]. The major problems have been calibration drift with time, calibration change with reimmersion, and erratic voltage output. Hoff [4] reported that the presence of a gold film, vapor deposited onto the quartz insulation, significantly reduced the randomness of the output signal; White [6] did not find such a gold film particularly helpful.

The Experiment

A constant temperature anemometer[4] with standard quartz coated hot film probes[5] was used for these experiments. The method of calibration and an apparatus description is reported by Hurt [10]. Essentially, the probe was moved vertically down through a container of mercury at a known velocity, and the bridge voltage output corresponding to that velocity was measured. The stationary mercury was kept at a constant temperature during calibration. Although provision was made to calibrate at different temperatures, all data presented here was obtained at 24 deg C, with a sensor overheat ratio of 1.10.

The purpose of the experimental program was to determine the limitations on the use of the hot film anemometer for low velocity measurements in mercury, and to eliminate them if possible. The results are presented in three parts: step changes with probe reimmersion; calibration drift with time; and effects of metallic films plated onto the sensor.

Step Changes With Probe Reimmersion

The procedure for these tests was to immerse the probe into the mercury, calibrate it, pull it out, clean it, and reimmerse it for calibration once more. This procedure was carried out a total of nine times, with reimmersion through the following surfaces:

1 clean-dry mercury,
2 distilled water over clean[6] mercury,
3 distilled water over mercury covered with a base metal oxide film, and
4 clean mercury with a film of mineral oil applied to the sensor.

Each calibration consisted of 40 velocity settings ranging from 0.25 cm/sec to 5 cm/sec. The raw data were reduced to velocity versus ΔE, where ΔE is the voltage output at the given velocity minus the voltage output at zero velocity. Each set of data was fitted to a second order equation by the least squares method. Each combination of two calibrations was then combined into a restricted model. A second order equation was fitted to this restricted model, giving the required data to calculated the F statistic by the extra sum of squares method. This F statistic was then compared to the 90 percent confidence interval for the appropriate degrees of freedom.

It was found that the calibration curve for the probe did not change significantly when the probe was immersed either through a clean-dry surface or through a distilled water over clean mercury surface. Calibration after immersion through a base metal oxide film reduced ΔE for any given velocity by 18 percent. The mineral oil applied to the sensor caused the greatest reduction in heat transfer, reducing ΔE by about 53 percent.

It is thus apparent that the probe calibration can be significantly changed by the introduction of foreign materials to the mercury surface. The reduction in ΔE is believed to be caused by the additional thermal resistance to heat transfer created by an impurity layer around the probe. If this impurity layer changes in thickness with each immersion into the mercury, then the probe calibration will also change. The authors believe that the cleanliness of the mercury surface reduced this thermal contact resistance to a minimum, thus causing the least calibration change with reimmersion. Previous difficulties [1 through 6] are presumed to have been caused by mercury surfaces not as free of contaminants as used for this experiment. The fact that a water covering did not influence the calibration is contrary to the results of Malcolm [5] (who concluded the air-mercury interface to be best) and Dunn [8] (who concluded the water-mercury interface to be best). The authors know of no reason for this conflict in results.

Calibration Drift With Time

To investigate the time dependency of a calibration, a probe was immersed through a clean-dry mercury surface and calibrated eight times over a period of 20 days. The total run time for this sensor during these tests was 200 hr. The first and last calibration are shown in Fig. 1. The F statistic was calculated for each calibration pair and the result was that the calibration of the sensor showed no significant change over the 20-day period considered.

Effect of Metallic Sensor Coatings

The rest voltage variation during the tests was of an intermittent nature with a standard deviation usually between 10 and 25 mv. In an attempt to reduce the voltage variation, metallic sensor coatings (suggested by Hoff [4]) were examined. The three coatings tried were gold, silver, and nickel.

Two probes coated with vapor-deposited gold[7] were examined. The first probe developed a short circuit to the mercury soon

[7] These probes were coated by Mr. Marc Hoff, Grumman Aircraft Engineering Corporation, Bethpage, N. Y.

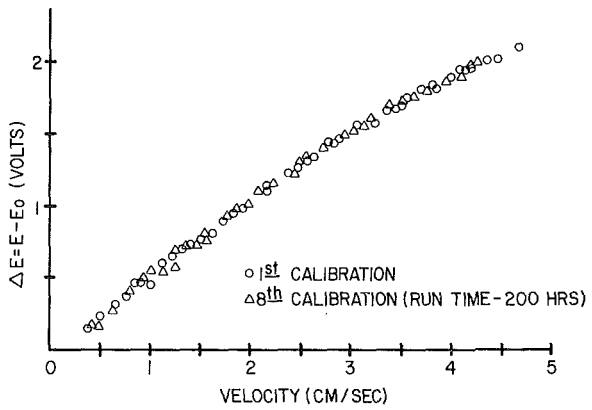

Fig. 1 Drift test calibrations

[1] Member of the Technical Staff, Bell Telephone Laboratories, Naperville, Ill.
[2] Professor and Head, Department of Mechanical and Metallurgical Engineering, Oregon State University, Corvallis, Ore.
[3] Numbers in brackets designate References at end of technical brief.
[4] Series 1050 anemometer, Thermo-Systems, Inc., St. Paul, Minn.
[5] Thermo-Systems Series 1212 probes, 53 μ diam.
[6] Clean mercury is defined here as having no visual trace of surface contaminants.

Contributed by the Heat Transfer Division of THE AMERICAN SOCIETY OF MECHANICAL ENGINEERS. Manuscript received by the Heat Transfer Division, March 6, 1973.

Table 1 Summary of calibration data for the two nickel probes

Probe	Sensor coating	Time immersed	Sample size	Std. dev. rest volt.	Res. sum of sqs.
1	Quartz	0.5 hr.	29	0.0214	0.384
1	Nickel	0.5 hr.	26	0.0045	0.116
1	Nickel	8 hr.	25	0.0259	0.363
2	Quartz	0.5 hr.	21	0.0243	0.366
2	Nickel	0.5 hr.	23	0.0052	0.140
2	Nickel	5 hr.	20	0.0334	0.481

after immersion, rendering it useless. The second probe was examined each day for 7 days and showed no improvement over standard quartz-coated probes. Several probes were coated with silver by chemical plating, but the silver was lost by amalgamation within seconds after immersion.

Two standard probes were calibrated and then coated with about 5 μ of nickel by catalytic deposition. Table 1 summarizes the statistics of the calibration data. Both the standard deviation of the rest voltage and the residual sum of squares about the regression line were significantly reduced after application of the nickel film, but this advantage was gone after 5 to 8 hr of immersion. The nickel remained on the sensors after several weeks of immersion in the mercury and reimmersion of a nickel probe did not reproduce the initial behavior.

A gold cyanide solution was used to plate a gold film over a nickel plated probe, but like the silver, it quickly amalgamated away after immersion.

Conclusion

A probe was operated for 200 hr over a period of 20 days, without drift in calibration. It was found that when the mercury surface was kept clean, probe calibration remained unchanged after several immersions into the mercury. This will allow an investigator to calibrate probes in one vessel and perform experiments in a separate apparatus. The authors believe that the standard quartz-coated cylindrical hot film probe is a satisfactory sensor for velocity measurement in mercury. Although a thin nickel coating over the quartz insulation did reduce the voltage fluctuations for a few hours, it is felt that coating the sensor with metallic films is not necessary for successful velocity measurement in mercury.

References

1 Sajben, M., "Hot Wire Anemometer in Liquid Mercury," *Review of Scientific Instruments*, Vol. 36, No. 7, 1965. pp. 945–949.

2 Easley, D. C., "Characteristics of a Hot Film Anemometer in a Liquid Mercury System," MS thesis, Purdue University, Lafayette, Ind., 1966, 110 pp.

3 Hill, J. C., and Sleicher, C. A., "Convective Heat Transfer From Small Cylinders to Mercury," *International Journal of Heat and Mass Transfer*, Vol. 12, 1969, pp. 1595–1604.

4 Hoff, M., "Hot-Film Anemometry in Liquid Mercury," *Instrument and Control Systems*, Vol. 42, 1969, pp. 83–86.

5 Malcolm, D. G., "Some Aspects of Turbulence Measurement in Liquid Mercury Using Cylindrical Quartz-Insulated Hot-Film Sensors," *Journal of Fluid Mechanics*, Vol. 37, No. 4, 1969, pp. 701–713.

6 White, D. H., "An Experimental Investigation of Natural Convection Heat Transfer From Vertical Flat Plates in Mercury," PhD thesis, Oregon State University, Corvallis, Ore., 1971, 200 pp.

7 White, D. H., Welty, J. R., and Hurt, J. C., "Experimental Study of Natural Convection Heat Transfer From Vertical Flat Plates in Mercury," *Heat Transfer in Liquid Metals Conference*, Trogir, Yugoslavia, 1971; to be published in Progress in Heat and Mass Transfer, Vol. 7.

8 Dunn, P. F., "Magneto-Fluid-Mechanic Natural and Forced Heat Transfer From Horizontal Hot-Film Probes," MS thesis, Purdue University, Lafayette, Ind., 1971, 54 pp.

9 Gardner, R. A., and Lykoudis, P. S., "Magneto-Fluid-Mechanic Pipe Flow in a Transverse Magnetic Field," Part 1, Isothermal Flow, *Journal of Fluid Mechanics*, Vol. 47, Part 4, 1971, pp. 737–764.

10 Hurt, J. C., "The Use of a Hot Film Anemometer to Measure Velocities Below 5 cm/sec in Mercury," MS thesis, Oregon State University, Corvallis, Ore., 1972, 86 pp.

Errors in One-Dimensional Heat Transfer Analysis in Straight and Annular Fins

WAH LAU[1] AND C. W. TAN[2]

Introduction

THE ONE-DIMENSIONAL approximation for the analysis of fin problems is widely used in current texts and industrial practice. Unfortunately, justification of this approximation has been based only on the criterion of large fin length to thickness ratio. This does not take into consideration the ratio of interior (conductive) to exterior (convective) resistances, the Biot number. Irey [1][3] has shown by means of an analysis of a circular pin fin that only for small Biot numbers is the one-dimensional solution a satisfactory approximation. Two-dimensional analyses have also been carried out for both the straight [2] and the annular [3] fin: the latter, unfortunately, did not use the Biot number explicitly as an independent parameter and reached conclusions which are valid only for small Biot numbers. Other works [4, 5] have also shown analytically that the sole requirement for reducing the exact solution to the one-dimensional approximation is the existence of a transverse Biot number which is much less than unity. This note treats the straight and the annular fin and attempts to provide the basis of establishing quantitative limits of applicability of the one-dimensional approximation to a larger group of fin problems.

Two-Dimensional Solutions

The steady-state two-dimensional heat conduction equation describing temperature distribution in a fin, with x designating the distance along the fin length and y that along the fin thickness, can be written as [6, 7]

$$\frac{1}{x^c}\frac{\partial}{\partial x}\left(x^c\frac{\partial\theta}{\partial x}\right)+\frac{\partial^2\theta}{\partial y^2}=0 \tag{1}$$

where $\theta=(t-t_\infty)/(t_b-t_\infty)$, t_b is the temperature at the fin base and t_∞ is the ambient fluid temperature. For a straight fin, $c=0$; and for a pin or annular fin, $c=1$ and x is the radial distance r along the fin length.

The pertinent boundary conditions are [6, 7]:

for straight fin

$$\theta(x=0,y)=1,\ \frac{\partial\theta}{\partial y}(x,w/2)+\frac{h}{k}\theta(x,w/2)=0$$
$$\frac{\partial\theta}{\partial y}(x,0)=0,\ \frac{\partial\theta}{\partial x}(L,y)+\frac{h_e}{k}\theta(L,y)=0 \tag{2a}$$

for annular fin

$$\theta(r_b,y)=1,\ \frac{\partial\theta}{\partial y}(r,w/2)+\frac{h}{k}\theta(r,w/2)=0$$
$$\frac{\partial\theta}{\partial y}(r,0)=0,\ \frac{\partial\theta}{\partial r}(r_e,y)+\frac{h_e}{k}\theta(r_e,y)=0 \tag{2b}$$

where h is the circumferential surface heat-transfer coefficient; h_e, the heat-transfer coefficient at the free end of the fin; k, the fin thermal conductivity; r_b and r_e, the radial distance along the

[1] Project Engineer, Economides & Goldberg, Consulting Engineers, New York, N. Y.

[2] Professor of Mechanical Engineering, The Cooper Union, Cooper Square, New York, N. Y.

[3] Numbers in brackets designate References at end of technical brief.

Contributed by the Heat Transfer Division of THE AMERICAN SOCIETY OF MECHANICAL ENGINEERS. Manuscript received by the Heat Transfer Division, April 16, 1973.

Table 1 Summary of calibration data for the two nickel probes

Probe	Sensor coating	Time immersed	Sample size	Std. dev. rest volt.	Res. sum of sqs.
1	Quartz	0.5 hr.	29	0.0214	0.384
1	Nickel	0.5 hr.	26	0.0045	0.116
1	Nickel	8 hr.	25	0.0259	0.363
2	Quartz	0.5 hr.	21	0.0243	0.366
2	Nickel	0.5 hr.	23	0.0052	0.140
2	Nickel	5 hr.	20	0.0334	0.481

after immersion, rendering it useless. The second probe was examined each day for 7 days and showed no improvement over standard quartz-coated probes. Several probes were coated with silver by chemical plating, but the silver was lost by amalgamation within seconds after immersion.

Two standard probes were calibrated and then coated with about 5 μ of nickel by catalytic deposition. Table 1 summarizes the statistics of the calibration data. Both the standard deviation of the rest voltage and the residual sum of squares about the regression line were significantly reduced after application of the nickel film, but this advantage was gone after 5 to 8 hr of immersion. The nickel remained on the sensors after several weeks of immersion in the mercury and reimmersion of a nickel probe did not reproduce the initial behavior.

A gold cyanide solution was used to plate a gold film over a nickel plated probe, but like the silver, it quickly amalgamated away after immersion.

Conclusion

A probe was operated for 200 hr over a period of 20 days, without drift in calibration. It was found that when the mercury surface was kept clean, probe calibration remained unchanged after several immersions into the mercury. This will allow an investigator to calibrate probes in one vessel and perform experiments in a separate apparatus. The authors believe that the standard quartz-coated cylindrical hot film probe is a satisfactory sensor for velocity measurement in mercury. Although a thin nickel coating over the quartz insulation did reduce the voltage fluctuations for a few hours, it is felt that coating the sensor with metallic films is not necessary for successful velocity measurement in mercury.

References

1 Sajben, M., "Hot Wire Anemometer in Liquid Mercury," *Review of Scientific Instruments*, Vol. 36, No. 7, 1965. pp. 945–949.

2 Easley, D. C., "Characteristics of a Hot Film Anemometer in a Liquid Mercury System," MS thesis, Purdue University, Lafayette, Ind., 1966, 110 pp.

3 Hill, J. C., and Sleicher, C. A., "Convective Heat Transfer From Small Cylinders to Mercury," *International Journal of Heat and Mass Transfer*, Vol. 12, 1969, pp. 1595–1604.

4 Hoff, M., "Hot-Film Anemometry in Liquid Mercury," *Instrument and Control Systems*, Vol. 42, 1969, pp. 83–86.

5 Malcolm, D. G., "Some Aspects of Turbulence Measurement in Liquid Mercury Using Cylindrical Quartz-Insulated Hot-Film Sensors," *Journal of Fluid Mechanics*, Vol. 37, No. 4, 1969, pp. 701–713.

6 White, D. H., "An Experimental Investigation of Natural Convection Heat Transfer From Vertical Flat Plates in Mercury," PhD thesis, Oregon State University, Corvallis, Ore., 1971, 200 pp.

7 White, D. H., Welty, J. R., and Hurt, J. C., "Experimental Study of Natural Convection Heat Transfer From Vertical Flat Plates in Mercury," *Heat Transfer in Liquid Metals Conference*, Trogir, Yugoslavia, 1971; to be published in Progress in Heat and Mass Transfer, Vol. 7.

8 Dunn, P. F., "Magneto-Fluid-Mechanic Natural and Forced Heat Transfer From Horizontal Hot-Film Probes," MS thesis, Purdue University, Lafayette, Ind., 1971, 54 pp.

9 Gardner, R. A., and Lykoudis, P. S., "Magneto-Fluid-Mechanic Pipe Flow in a Transverse Magnetic Field," Part 1, Isothermal Flow, *Journal of Fluid Mechanics*, Vol. 47, Part 4, 1971, pp. 737–764.

10 Hurt, J. C., "The Use of a Hot Film Anemometer to Measure Velocities Below 5 cm/sec in Mercury," MS thesis, Oregon State University, Corvallis, Ore., 1972, 86 pp.

Errors in One-Dimensional Heat Transfer Analysis in Straight and Annular Fins

WAH LAU[1] AND C. W. TAN[2]

Introduction

THE ONE-DIMENSIONAL approximation for the analysis of fin problems is widely used in current texts and industrial practice. Unfortunately, justification of this approximation has been based only on the criterion of large fin length to thickness ratio. This does not take into consideration the ratio of interior (conductive) to exterior (convective) resistances, the Biot number. Irey [1][3] has shown by means of an analysis of a circular pin fin that only for small Biot numbers is the one-dimensional solution a satisfactory approximation. Two-dimensional analyses have also been carried out for both the straight [2] and the annular [3] fin: the latter, unfortunately, did not use the Biot number explicitly as an independent parameter and reached conclusions which are valid only for small Biot numbers. Other works [4, 5] have also shown analytically that the sole requirement for reducing the exact solution to the one-dimensional approximation is the existence of a transverse Biot number which is much less than unity. This note treats the straight and the annular fin and attempts to provide the basis of establishing quantitative limits of applicability of the one-dimensional approximation to a larger group of fin problems.

Two-Dimensional Solutions

The steady-state two-dimensional heat conduction equation describing temperature distribution in a fin, with x designating the distance along the fin length and y that along the fin thickness, can be written as [6, 7]

$$\frac{1}{x^c}\frac{\partial}{\partial x}\left(x^c\frac{\partial\theta}{\partial x}\right)+\frac{\partial^2\theta}{\partial y^2}=0 \tag{1}$$

where $\theta=(t-t_\infty)/(t_b-t_\infty)$, t_b is the temperature at the fin base and t_∞ is the ambient fluid temperature. For a straight fin, $c=0$; and for a pin or annular fin, $c=1$ and x is the radial distance r along the fin length.

The pertinent boundary conditions are [6, 7]:

for straight fin

$$\theta(x=0,y)=1,\ \frac{\partial\theta}{\partial y}(x,w/2)+\frac{h}{k}\theta(x,w/2)=0$$
$$\frac{\partial\theta}{\partial y}(x,0)=0,\ \frac{\partial\theta}{\partial x}(L,y)+\frac{h_e}{k}\theta(L,y)=0 \tag{2a}$$

for annular fin

$$\theta(r_b,y)=1,\ \frac{\partial\theta}{\partial y}(r,w/2)+\frac{h}{k}\theta(r,w/2)=0$$
$$\frac{\partial\theta}{\partial y}(r,0)=0,\ \frac{\partial\theta}{\partial r}(r_e,y)+\frac{h_e}{k}\theta(r_e,y)=0 \tag{2b}$$

where h is the circumferential surface heat-transfer coefficient; h_e, the heat-transfer coefficient at the free end of the fin; k, the fin thermal conductivity; r_b and r_e, the radial distance along the

[1] Project Engineer, Economides & Goldberg, Consulting Engineers, New York, N. Y.

[2] Professor of Mechanical Engineering, The Cooper Union, Cooper Square, New York, N. Y.

[3] Numbers in brackets designate References at end of technical brief.

Contributed by the Heat Transfer Division of THE AMERICAN SOCIETY OF MECHANICAL ENGINEERS. Manuscript received by the Heat Transfer Division, April 16, 1973.

fin length to the fin base and to the end face of the fin, respectively; L, the fin length; and w, the fin thickness.

In the following analysis, however, $h_e = h$ is assumed throughout. This condition may not necessarily hold in all cases. Because of symmetry or other considerations, the heat-transfer coefficient at the "end" may be different from that of the fin surfaces, and can in fact be zero. Under those circumstances, the variation of the error with the length to thickness ratio may differ significantly from that given in this analysis.

Utilizing the usual method of separation of variables, the temperature distributions in a straight and an annular fin are, respectively, found to be

$$\theta(X, Y) = 2 \sum_{n=1}^{\infty} \left\{ \frac{\sin \alpha_n \cos \alpha_n Y}{\alpha_n + \sin \alpha_n \cos \alpha_n} \right\} \cdot \left\{ \frac{B_i \sinh \alpha_n K(1 - X) + \alpha_n \cosh \alpha_n K(1 - X)}{B_i \sinh \alpha_n K + \alpha_n \cosh \alpha_n K} \right\} \quad (3)$$

and

$$\theta(R, Y) = 2 \sum_{n=1}^{\infty} \left\{ \frac{\sin \alpha_n \cos \alpha_n Y}{\alpha_n + \sin \alpha_n \cos \alpha_n} \right\} \cdot \left\{ \frac{K_0(\alpha_n \gamma R)[B_i I_0(\alpha_n \gamma) + \alpha_n I_1(\alpha_n \gamma)] - I_0(\alpha_n \gamma R)[B_i K_0(\alpha_n \gamma) - \alpha_n K_1(\alpha_n \gamma)]}{K_0(\alpha_n \gamma R_b)[B_i I_0(\alpha_n \gamma) + \alpha_n I_1(\alpha_n \gamma)] - I_0(\alpha_n \gamma R_b)[B_i K_0(\alpha_n \gamma) - \alpha_n K_1(\alpha_n \gamma)]} \right\} \quad (4)$$

Here, $B_i = hw/2k$ is the Biot number; (I_0, I_1) and (K_0, K_1) are the modified Bessel functions of the first and second kind, respectively; $X = x/L$; $Y = y/(w/2)$; $R = r/r_e$; $R_b = r_b/r_e$; $K = L/(w/2)$; $\gamma = r_e/(w/2)$; and α_n are the eigenvalues given by

$$\alpha_n \tan \alpha_n = B_i \quad (5)$$

The temperature solution for the straight fin, equation (3), is similar to that obtained in [2] though different in form.

The total fin heat transfer, q, per unit depth in a straight fin can be found to be

$$Q_2 = \frac{q}{k(t_b - t_\infty)} = 4 \sum_{n=1}^{\infty} \left\{ \frac{\sin^2 \alpha_n}{\alpha_n + \sin \alpha_n \cos \alpha_n} \right\} \cdot \left\{ \frac{B_i \cosh \alpha_n K + \alpha_n \sinh \alpha_n K}{B_i \sinh \alpha_n K + \alpha_n \cosh \alpha_n K} \right\} \quad (6)$$

and for an annular fin,

$$Q_2 = \frac{q}{2k\pi r_b(t_b - t_\infty)} = 4 \sum_{n=1}^{\infty} \left\{ \frac{\sin^2 \alpha_n}{\alpha_n + \sin \alpha_n \cos \alpha_n} \right\} \cdot \left\{ \frac{K_1(\alpha_n \gamma R_b)[B_i I_0(\alpha_n \gamma) + \alpha_n I_1(\alpha_n \gamma)] + I_1(\alpha_n \gamma R_b)[B_i K_0(\alpha_n \gamma) - \alpha_n K_1(\alpha_n \gamma)]}{K_0(\alpha_n \gamma R_b)[B_i I_0(\alpha_n \gamma) + \alpha_n I_1(\alpha_n \gamma)] - I_0(\alpha_n \gamma R_b)[B_i K_0(\alpha_n \gamma) - \alpha_n K_1(\alpha_n \gamma)]} \right\} \quad (7)$$

The corresponding one-dimensional solutions for the temperature distributions and the total fin heat transfer in the straight and the annular fins can be found in [6, 7] and will not be repeated here.

Results

The total fin heat transfer, depicted by equations (6) and (7), is shown in Fig. 1 for both the annular and the straight fin as a function of K for the straight fin or $\gamma(1 - R_b)$ for the annular fin. For K or $\gamma(1 - R_b) < 10^2$, the total heat removal, Q_2, is higher for the annular fin with the smaller R_b than for the straight fin, and is strongly dependent on the Biot number. For K or $\gamma(1 - R_b) > 10^2$, however, Q_2 for the annular fin converges for all values of R_b, which in turn merges asymptotically with the Q_2 for the straight fin. Furthermore, Q_2 seems to remain fairly constant for K or $\gamma(1 - R_b) > 10^2$, increasing only with increasing Biot numbers.

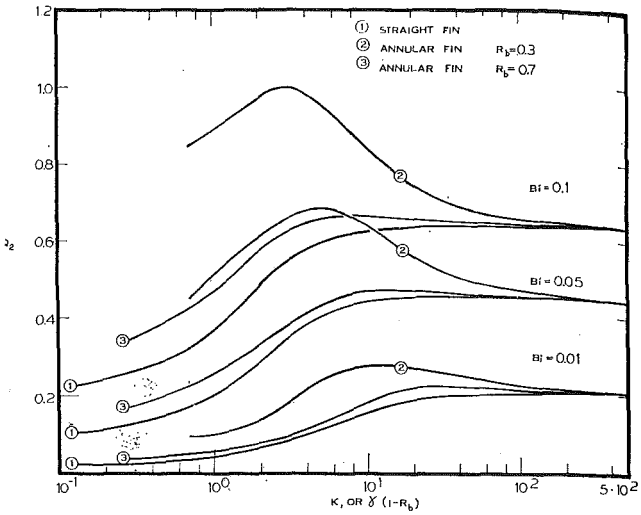

Fig. 1 Total heat transfer in straight and annular fins

A comparison is made between the straight fin and the annular fin with the pin fin studied by Irey [1], Fig. 2, where $(Q_1 - Q_2)/Q_2$ is plotted against K for the straight and the pin fins and $\gamma(1 - R_b)$ for the annular fin. Q_1 is the corresponding fin heat transfer based on one-dimensional analysis. For this comparison, Bi = 0.01, 0.1, 1.0, and 10 and $R_b = 0.3$ and 0.7 are used. The percent error of the one-dimensional from the two-dimensional analysis decreases with decreasing values of K or $\gamma(1 - R_b)$. This is to be expected because as the fin length to thickness ratio becomes smaller, the heat transfer through the end face of the fin becomes a significant fraction of the total heat flow through the base and ultimately swamps the heat flow through the fin surfaces as the fin length goes to zero. In the limit, therefore, as the fin length goes to zero, the physical heat flow becomes one-dimensional, and the percent error becomes negligible. It is observed that $(Q_1 - Q_2)/Q_2$ is dependent on Bi and K or $\gamma(1 - R_b)$ when K or $\gamma(1 - R_b) < 1$. However, for K or $\gamma(1 - R_b) > 1$, $(Q_1 - Q_2)/Q_2$ seems to vary only with Bi and is relatively insensitive

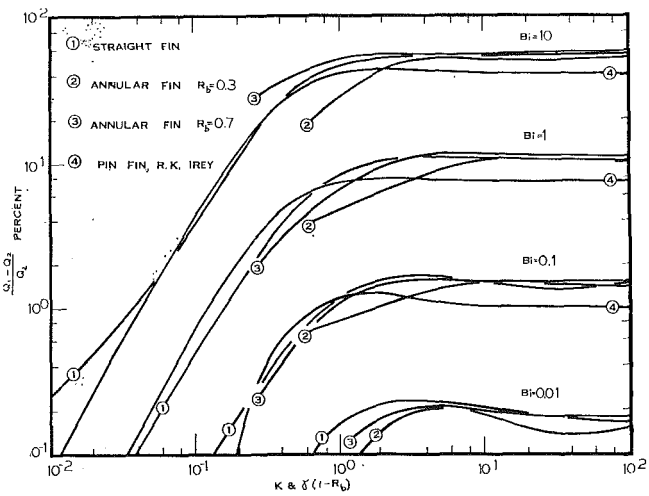

Fig. 2 Errors in total fin heat transfer

to changes in K or $\gamma(1 - R_b)$, consistent with the findings of [1, 4, 5]. It is also interesting to note that with this plot all four curves (1 for straight fin, 1 for pin fin, and 2 for the annular fin), for each Biot number, exhibit a similar trend and assume values essentially of the same order of magnitude for a wide range of fin length to thickness ratios.

References

1 Irey, R. K., "Errors in the One-Dimensional Fin Solution," JOURNAL OF HEAT TRANSFER, TRANS. ASME, Series C, Vol. 90, No. 1, Feb. 1968, pp. 175–176.

2 Avrami, M., and Little, J. B., "Diffusion of Heat Through a Rectangular Bar and the Cooling and Insulating Effect of Fins," *Journal of Applied Physics*, Vol. 13, Apr. 1942, pp. 255–264.

3 Keller, H. H., and Somers, E. V., "Heat Transfer From an Annular Fin of Constant Thickness," JOURNAL OF HEAT TRANSFER, TRANS. ASME, Series C, Vol. 81, No. 2, May 1959, pp. 151–156.

4 Crank, J., and Parker, I. B., "Approximate Methods for Two Dimensional Problems in Heat Flow," *Q. J. Mech. Appl. Math.*, Vol. XIX, Part 2, 1966, pp. 167–181.

5 Levitsky, M., "The Criterion for Validity of the Fin Approximation," *Int. Journal of Heat and Mass Transfer*, Vol. 15, Oct. 1972, pp. 1960–1963.

6 Kreith, F., *Principles of Heat Transfer*, International, Scranton, Pa., 1965.

7 Chapman, A., *Heat Transfer*, MacMillan, New York, 1967.

Thermal Spike Model With Temperature-Dependent Specific Heat

KALIMULLAH[1] and J. N. ANNO[1]

The thermal spike model is examined with a linear temperature-dependent specific heat. The predicted microvolume of melted material in this case is not significantly different from that predicted with constant specific heat. This result indicates that the thermal spike calculation, as presented here, is not strongly dependent on the variation of physical properties with temperature.

Nomenclature

A = cross-sectional area of melted microvolume
c = specific heat
c_0 = specific heat at $T = 0$
$\left(\frac{dE}{dx}\right)$ = stopping power; energy loss per unit path in material
E = total kinetic energy of particle being stopped in material
k = thermal conductivity
Q = heat content per unit volume
r = radial coordinate in cylindrical coordinate system
R_P = range of charged particle
t = time
T = temperature
T_m = melting temperature of material
T' = translated temperature coordinate
V = volume of melted material in thermal spike
x = axial coordinate in cylindrical coordinate system
α = thermal diffusivity
γ = temperature coefficient of specific heat
ρ = density of material
θ = dimensionless time variable

[1] Department of Chemical and Nuclear Engineering, University of Cincinnati, Cincinnati, Ohio.

Contributed by the Heat Transfer Division of THE AMERICAN SOCIETY OF MECHANICAL ENGINEERS. Manuscript received by the Heat Transfer Division, May 1, 1973.

Introduction

WHEN A CHARGED-PARTICLE interacts with a material, its kinetic energy is converted ultimately into thermal energy in a very short distance. This local deposition of energy in a small volume, or microvolume, with the resulting elevation of local temperature is referred to as a "thermal spike." The thermal spike has long been recognized as a possible mechanism in radiation damage studies, particularly with energetic heavy charged particles such as alpha particles and, especially, fission fragments. For example, a fission fragment with an energy of about 85 Mev at birth is stopped in fuel materials in a distance of only 10 microns (10^{-3} cm) [1].[2] On a microscopic scale, this is an enormous local energy deposition, and must certainly affect the local properties of the material.

In the thermal spike model, it is imagined that the stopping of the charged particle produces essentially an instantaneous line source of thermal energy at infinite temperature. The heat diffuses radially from the line source, elevating the temperature of the surrounding material above the melting point within a certain microvolume. The mathematical problem is to calculate the size of the microvolume. The gross, and perhaps unrealistic, assumption is made that macroscopic concepts and physical properties are applicable on a very short time scale and in a volume containing relatively few atoms. Nevertheless, such assumptions are necessary to render the problem tractable for a thermal calculation.

Early treatments of the thermal spike problem, such as that presented by Seitz and Koehler [2], assumed constant physical properties (density, thermal conductivity, and specific heat). Granted that the thermodynamic assumptions probably do not justify a more accurate treatment for estimates of radiation damage for use in various developments, it is nevertheless of interest to examine the *magnitude* of the effect of including a temperature dependency of the physical properties in the calculation of the melted microvolume. This article presents the analysis of the thermal spike model with a specific heat varying linearly with temperature. The magnitude of the effect will be shown to be small, lending confidence to the use of the constant-property thermal spike model.

Thermal Spike With Constant Physical Properties

As background for comparison with the analysis to be presented later in this article, the "standard" thermal spike model will be briefly presented in this section. Fourier's heat conduction equation in general form is

$$\rho c \frac{\partial T}{\partial t} = \nabla \cdot (k \nabla T) \tag{1}$$

(see Nomenclature for definition of symbols).

Using cylindrical coordinates along the straight-line path of the charged particles (x-axis), assuming all heat to be conducted radially and with constant physical properties, equation (1) reduces to

$$\frac{\partial T}{\partial t} = \frac{\alpha}{r} \frac{\partial}{\partial r} \left(r \frac{\partial T}{\partial r} \right) \tag{2}$$

Assuming initial conditions at time $t = 0$ of

$$T = 0 \quad \text{for} \quad r \neq 0, \qquad T = \infty \quad \text{for} \quad r = 0 \tag{3}$$

Equation (2) has as its solution (neglecting latent heats[3])

$$T(r, t) = \frac{C_1}{t} e^{-r^2/0.4\alpha t} \tag{4}$$

[2] Numbers in brackets designate References at end of technical brief.

[3] For a material such as UO_2 this assumption is not a severe limitation to the theoretical development. For example, the specific enthalpy of UO_2 at the melting point is more than four times the latent heat of fusion [3].

to changes in K or $\gamma(1 - R_b)$, consistent with the findings of [1, 4, 5]. It is also interesting to note that with this plot all four curves (1 for straight fin, 1 for pin fin, and 2 for the annular fin), for each Biot number, exhibit a similar trend and assume values essentially of the same order of magnitude for a wide range of fin length to thickness ratios.

References

1 Irey, R. K., "Errors in the One-Dimensional Fin Solution," JOURNAL OF HEAT TRANSFER, TRANS. ASME, Series C, Vol. 90, No. 1, Feb. 1968, pp. 175–176.

2 Avrami, M., and Little, J. B., "Diffusion of Heat Through a Rectangular Bar and the Cooling and Insulating Effect of Fins," *Journal of Applied Physics*, Vol. 13, Apr. 1942, pp. 255–264.

3 Keller, H. H., and Somers, E. V., "Heat Transfer From an Annular Fin of Constant Thickness," JOURNAL OF HEAT TRANSFER, TRANS. ASME, Series C, Vol. 81, No. 2, May 1959, pp. 151–156.

4 Crank, J., and Parker, I. B., "Approximate Methods for Two Dimensional Problems in Heat Flow," *Q. J. Mech. Appl. Math.*, Vol. XIX, Part 2, 1966, pp. 167–181.

5 Levitsky, M., "The Criterion for Validity of the Fin Approximation," *Int. Journal of Heat and Mass Transfer*, Vol. 15, Oct. 1972, pp. 1960–1963.

6 Kreith, F., *Principles of Heat Transfer*, International, Scranton, Pa., 1965.

7 Chapman, A., *Heat Transfer*, MacMillan, New York, 1967.

Thermal Spike Model With Temperature-Dependent Specific Heat

KALIMULLAH[1] and J. N. ANNO[1]

The thermal spike model is examined with a linear temperature-dependent specific heat. The predicted microvolume of melted material in this case is not significantly different from that predicted with constant specific heat. This result indicates that the thermal spike calculation, as presented here, is not strongly dependent on the variation of physical properties with temperature.

Nomenclature

A = cross-sectional area of melted microvolume
c = specific heat
c_0 = specific heat at $T = 0$
$\left(\frac{dE}{dx}\right)$ = stopping power; energy loss per unit path in material
E = total kinetic energy of particle being stopped in material
k = thermal conductivity
Q = heat content per unit volume
r = radial coordinate in cylindrical coordinate system
R_P = range of charged particle
t = time
T = temperature
T_m = melting temperature of material
T' = translated temperature coordinate
V = volume of melted material in thermal spike
x = axial coordinate in cylindrical coordinate system
α = thermal diffusivity
γ = temperature coefficient of specific heat
ρ = density of material
θ = dimensionless time variable

[1] Department of Chemical and Nuclear Engineering, University of Cincinnati, Cincinnati, Ohio.

Contributed by the Heat Transfer Division of THE AMERICAN SOCIETY OF MECHANICAL ENGINEERS. Manuscript received by the Heat Transfer Division, May 1, 1973.

Introduction

WHEN A CHARGED-PARTICLE interacts with a material, its kinetic energy is converted ultimately into thermal energy in a very short distance. This local deposition of energy in a small volume, or microvolume, with the resulting elevation of local temperature is referred to as a "thermal spike." The thermal spike has long been recognized as a possible mechanism in radiation damage studies, particularly with energetic heavy charged particles such as alpha particles and, especially, fission fragments. For example, a fission fragment with an energy of about 85 Mev at birth is stopped in fuel materials in a distance of only 10 microns (10^{-3} cm) [1].[2] On a microscopic scale, this is an enormous local energy deposition, and must certainly affect the local properties of the material.

In the thermal spike model, it is imagined that the stopping of the charged particle produces essentially an instantaneous line source of thermal energy at infinite temperature. The heat diffuses radially from the line source, elevating the temperature of the surrounding material above the melting point within a certain microvolume. The mathematical problem is to calculate the size of the microvolume. The gross, and perhaps unrealistic, assumption is made that macroscopic concepts and physical properties are applicable on a very short time scale and in a volume containing relatively few atoms. Nevertheless, such assumptions are necessary to render the problem tractable for a thermal calculation.

Early treatments of the thermal spike problem, such as that presented by Seitz and Koehler [2], assumed constant physical properties (density, thermal conductivity, and specific heat). Granted that the thermodynamic assumptions probably do not justify a more accurate treatment for estimates of radiation damage for use in various developments, it is nevertheless of interest to examine the *magnitude* of the effect of including a temperature dependency of the physical properties in the calculation of the melted microvolume. This article presents the analysis of the thermal spike model with a specific heat varying linearly with temperature. The magnitude of the effect will be shown to be small, lending confidence to the use of the constant-property thermal spike model.

Thermal Spike With Constant Physical Properties

As background for comparison with the analysis to be presented later in this article, the "standard" thermal spike model will be briefly presented in this section. Fourier's heat conduction equation in general form is

$$\rho c \frac{\partial T}{\partial t} = \nabla \cdot (k \nabla T) \tag{1}$$

(see Nomenclature for definition of symbols).

Using cylindrical coordinates along the straight-line path of the charged particles (x-axis), assuming all heat to be conducted radially and with constant physical properties, equation (1) reduces to

$$\frac{\partial T}{\partial t} = \frac{\alpha}{r} \frac{\partial}{\partial r} \left(r \frac{\partial T}{\partial r} \right) \tag{2}$$

Assuming initial conditions at time $t = 0$ of

$$T = 0 \quad \text{for} \quad r \neq 0, \qquad T = \infty \quad \text{for} \quad r = 0 \tag{3}$$

Equation (2) has as its solution (neglecting latent heats[3])

$$T(r, t) = \frac{C_1}{t} e^{-r^2/0.4\alpha t} \tag{4}$$

[2] Numbers in brackets designate References at end of technical brief.

[3] For a material such as UO_2 this assumption is not a severe limitation to the theoretical development. For example, the specific enthalpy of UO_2 at the melting point is more than four times the latent heat of fusion [3].

where C_1 is a constant with respect to r and t evaluated from the assumption that all heat is conducted radially, i.e.,

$$\frac{dE}{dx} = -2\pi k \int_0^\infty r \frac{\partial T}{\partial r}\, dt \tag{5}$$

which gives $C_1 = \left(\frac{dE}{dx}\right) \Big/ 4\pi k$ which, in general, could be a weak function of x, so long as the axial heat conduction is negligible with respect to the radial conduction. Now, at any given radius ($r \neq 0$), the temperature first increases to some maximum temperature and then decreases with time. The maximum temperature is found from

$$\frac{\partial T}{\partial t} = \frac{T}{t}\left[\frac{r^2}{4\alpha t} - 1\right] = 0 \tag{6}$$

to be

$$T_{\max} = \frac{\left(\frac{dE}{dx}\right)\alpha}{\pi k e r^2} \tag{7}$$

where e is the base of the Naperian logarithm. At radii at which the temperature reaches T_m, the cross-sectional area which is heated above the melting point (again neglecting the latent heat of fusion) is

$$A = \pi r^2 = \left(\frac{dE}{dx}\right) \Big/ (ec\rho T_m) \tag{8}$$

The microvolume thus melted is then simply

$$V = \int_0^{R_P} A dx = \frac{E}{ec\rho T_m} \tag{9}$$

Note that the microvolume size is independent of the thermal conductivity (although the time required for melting is dependent on k). It would seem logical, then, in investigating the effect of temperature dependency of the physical properties, to first study the effect of a temperature dependency of the product ($c\rho$).

Thermal Spike With Temperature-Dependent Specific Heat

Assume, for the purposes of illustration, a linear dependency of the specific heat on temperature,[4]

$$c = c_0(1 + \gamma T) \tag{10}$$

With a specific heat dependency of this form, the reference temperature can be shifted to a lower reference temperature, with respect to which equation (10) can be written

$$c = \beta T' \tag{11}$$

where T' and T are related by

$$T' = T + \frac{c_0}{\beta} = T + \frac{1}{\gamma} \tag{12}$$

Let $Q = {}^1/_2 \rho c T'$, the heat per unit volume,[5] then from equation (11),

$$T' = \left(\frac{2Q}{\rho\beta}\right)^{1/2} \tag{13}$$

and Fourier's heat conduction equation [equation (1)] becomes

$$\frac{\partial Q}{\partial \theta} = \nabla^2 Q^{1/2} \tag{14}$$

where $\theta = \left(\frac{kt}{\sqrt{\frac{\rho\beta}{2}}}\right)$. To solve equation (14), first assume a solution of the form

$$Q(r, \theta) = U(\theta)Y(X) \tag{15}$$

where $X = \frac{r}{R(\theta)}$. Then, in cylindrical coordinates, equation (14) becomes

$$\frac{U^{1/2}}{XR^2}\left[X(Y^{1/2})'\right]' = \frac{1}{R}\left[RYU' - XUR'Y'\right] \tag{16}$$

where primes denote total differentiation with respect to X or to θ. Following Ames [4], equation (16) is separable if $R = U^{-a}$ is chosen.

$$\frac{\left[X(Y^{1/2})'\right]'}{X(Y + aXY')} = \frac{R^2U'}{U^{1/2}} = -B \tag{17}$$

The energy per unit length in the spike gives the integral condition[6]

$$\frac{dE}{dx} = \int_0^\infty Q 2\pi r dr \tag{18}$$

which, on using equation (15), reduces to

$$\frac{dE}{dx} = 2\pi R^2 U \int_0^\infty XY dX \tag{19}$$

Hence R^2U = constant = U^{1-2a}, so that $a = {}^1/_2$ and $R = U^{-1/2}$. With these conditions equation (19) becomes

$$\frac{dE}{dx} = 2\pi \int_0^\infty XY dX \tag{20}$$

Further, from equation (17), $U' = -BU^{3/2}$, which upon integration yields

$$U = \left(\frac{B\theta}{2}\right)^{-2} \tag{21}$$

where the constant of integration has been set equal to zero with the initial condition that, at $\theta = 0$, $R = 0$ (wave-front radius) and hence $U \to \infty$. Similarly, integrating the left-hand member of equation (17),

$$Y(X) = \frac{16}{(BX^2 + D)^2} \tag{22}$$

where D is a constant of integration and the condition $\lim_{X\to 0} X(Y^{1/2})' = 0$ has been used. Substituting equation (22) into equation (20) and integrating gives

$$BD = 16\pi \Big/ \left(\frac{dE}{dx}\right) \tag{23}$$

Combining equations (21), (22), and (23),

$$Q(r, \theta) = UY = \left(\frac{dE/dx}{2\pi\theta}\right)^2 \left(1 + \frac{\frac{dE}{dx} r^2}{4\pi\theta^2}\right)^{-2} \tag{24}$$

so that[7]

[4] It will be recognized that this assumption can readily be generalized to a linear variation of the product (ρc) with temperature.

[5] The factor of ${}^1/_2$ enters because of the assumed temperature dependency, i.e., $Q = \int_0^{T'} \rho c dT'' = \int_0^{T'} \rho\beta T'' dT'' = {}^1/_2 \rho c T'$.

[6] This relation assumes a strong temperature dependency so that the T and T' reference frames are sufficiently close to ignore the energy required to heat the material from $T' = 0$ to $T = 0$.

[7] It will be recognized that this solution is valid only in the limit of infinite γ. It should be a good approximation, however, for a strongly temperature-dependent specific heat.

$$T'(r, t) = \left(\frac{2Q}{\rho\beta}\right)^{1/2} = \frac{\left(\frac{dE}{dx}\right)}{2\pi kt}\left[1 + \frac{r^2\rho\beta\left(\frac{dE}{dx}\right)}{8\pi k^2t^2}\right]^{-1} \quad (25)$$

Again, at any given radius ($r \neq 0$), the temperature first increases to some maximum temperature and then decreases with time. The maximum temperature is found from $\frac{\partial T'}{\partial t} = 0$ to be

$$T_{max}' = \left[\frac{\left(\frac{dE}{dx}\right)}{2\pi r^2\rho\beta}\right]^{1/2} \quad (26)$$

and the melted microvolume is

$$V = \frac{E}{2\rho\beta T_m'^2} = \frac{E}{2\rho c_m T_m'} \quad (27)$$

where $T_m' = T_m + \frac{c_0}{\beta} = T_m + \frac{1}{\gamma}$ and $c_m = \beta T_m'$ = the specific heat at the melting temperature.

Discussion of Results

Comparison of the microvolume expression for the case of a temperature-dependent specific heat (equation (27)) with that for constant physical properties (equation (9)) shows very equivalent forms. As would probably be expected, for the assumed strong temperature dependency the microvolume would appear to be smaller for the temperature-dependent case, but not severely so (depending, of course, on the magnitude of β). For a strong temperature dependency, the only essential difference in the two solutions is the replacement of the specific heat in equation (9) with that at the melting temperature (and, of course, the replacement of e by 2). Again, in the temperature-dependent case, the microvolume is independent of the thermal conductivity. One is thus led to believe that, despite its drawbacks, the thermal spike calculation as presented here is not strongly dependent on the variation of physical properties with temperature.

References

1 Holden, A. N., *Physical Metallurgy of Uranium*, Addison-Wesley, Reading, Mass., 1958, p. 206.

2 Seitz, Frederick, and Koehler, J. S., *Solid State Physics*, Volume 2, Academic Press, New York, 1956, pp. 351–355.

3 Kerrick, J. F., and Clifton, D. G., *Nuclear Technology*, Vol. 16, December, 1972, pp. 534–536.

4 Ames, W. F., *Nonlinear Partial Differential Equations in Engineering*, Academic Press, New York, 1965, p. 150.

Technical Note on Planar Solidification With Fixed Wall Temperature and Variable Thermal Properties[1]

R. I. PEDROSO[2] and G. A. DOMOTO[3]

Nomenclature

- $c(T)$ = specific heat of the solidified material as a function of the temperature
- $k(T)$ = thermal conductivity of the solidified material as a function of the temperature
- L = latent heat of fusion
- T = temperature in the solidified material
- T_f = freezing temperature
- T_w = temperature at the fixed wall in contact with the solidified material
- t = time
- x = position
- x_f = freezing-front position
- ρ = density of the solidified material
- θ_1^*, θ_2^* = the temperature distribution θ after application, respectively, of the first and second transformations of Shanks [2] (see equations (9)) to the terms in equations (8)

Introduction

THE PROBLEM of planar solidification with fixed wall temperature and variable thermal properties is solved with a perturbation technique steming from the work of reference [1].[4] This paper is restricted to the case of thermal properties of the solidified material which vary as functions of the temperature and density assumed constant. The liquid is assumed to remain at the freezing temperature. Both the freezing temperature and the latent heat of fusion are taken as constants. For an arbitrary variation of thermal properties with temperature, the solution is presented in terms of integrals. A particular example is then considered and analytical solutions are presented for the first four terms of the perturbation solution. The first-order nonlinear transformations of Shanks [2] are applied to increase the range and rate of convergence of the series solution.

Analysis

For planar solidification with variable thermal properties, the boundary-value problem is

$$\rho c(T)\frac{\partial T}{\partial t} = \frac{\partial}{\partial x}\left[k(T)\frac{\partial T}{\partial x}\right], \qquad T(x = 0, t) = T_w$$

$$T(x = x_f, t) = T_f, \qquad \rho L\frac{dx_f}{dt} = k(T)\frac{\partial T}{\partial x}\bigg|_{x=x_f} \quad (1)$$

Define the average value of the thermal conductivity $\bar{k}$, the average specific heat $\bar{c}$, a new time variable τ, the temperature distribution after Kirchhoff's transformation is applied θ, the averaged parameter ϵ, and the function $f(\theta)$ as

$$\bar{k} = \frac{\int_{T_w}^{T_f} k(y)dy}{T_f - T_w}, \qquad \bar{c} = \frac{\int_{T_w}^{T_f} c(y)dy}{T_f - T_w},$$

$$\tau = \frac{\bar{k}(T_f - T_w)t}{\rho L} \quad (2)$$

$$\theta = \frac{\int_{T_w}^{T} k(y)dy}{\bar{k}(T_f - T_w)}, \qquad \epsilon = \frac{\bar{c}(T_f - T_w)}{L}, \qquad f(\theta) = \frac{c(\theta)/\bar{c}}{k(\theta)/\bar{k}}$$

[1] Portion of Doctoral dissertation, Department of Mechanical Engineering, Columbia University, New York, N. Y.

[2] Professional Staff Member, Philips Laboratories, Briarcliff Manor, N. Y. Assoc. Mem. ASME.

[3] Associate Professor, Department of Mechanical Engineering, Columbia University, New York, N. Y. Assoc. Mem. ASME.

Contributed by the Heat Transfer Division of THE AMERICAN SOCIETY OF MECHANICAL ENGINEERS. Manuscript received by the Heat Transfer Division, March 9, 1973.

[4] Numbers in brackets designate References at end of technical brief.

$$T'(r, t) = \left(\frac{2Q}{\rho\beta}\right)^{1/2} = \frac{\left(\frac{dE}{dx}\right)}{2\pi kt}\left[1 + \frac{r^2\rho\beta\left(\frac{dE}{dx}\right)}{8\pi k^2t^2}\right]^{-1} \quad (25)$$

Again, at any given radius ($r \neq 0$), the temperature first increases to some maximum temperature and then decreases with time. The maximum temperature is found from $\frac{\partial T'}{\partial t} = 0$ to be

$$T_{max}' = \left[\frac{\left(\frac{dE}{dx}\right)}{2\pi r^2\rho\beta}\right]^{1/2} \quad (26)$$

and the melted microvolume is

$$V = \frac{E}{2\rho\beta T_m'^2} = \frac{E}{2\rho c_m T_m'} \quad (27)$$

where $T_m' = T_m + \frac{c_0}{\beta} = T_m + \frac{1}{\gamma}$ and $c_m = \beta T_m'$ = the specific heat at the melting temperature.

Discussion of Results

Comparison of the microvolume expression for the case of a temperature-dependent specific heat (equation (27)) with that for constant physical properties (equation (9)) shows very equivalent forms. As would probably be expected, for the assumed strong temperature dependency the microvolume would appear to be smaller for the temperature-dependent case, but not severely so (depending, of course, on the magnitude of β). For a strong temperature dependency, the only essential difference in the two solutions is the replacement of the specific heat in equation (9) with that at the melting temperature (and, of course, the replacement of e by 2). Again, in the temperature-dependent case, the microvolume is independent of the thermal conductivity. One is thus led to believe that, despite its drawbacks, the thermal spike calculation as presented here is not strongly dependent on the variation of physical properties with temperature.

References

1 Holden, A. N., *Physical Metallurgy of Uranium*, Addison-Wesley, Reading, Mass., 1958, p. 206.

2 Seitz, Frederick, and Koehler, J. S., *Solid State Physics*, Volume 2, Academic Press, New York, 1956, pp. 351–355.

3 Kerrick, J. F., and Clifton, D. G., *Nuclear Technology*, Vol. 16, December, 1972, pp. 534–536.

4 Ames, W. F., *Nonlinear Partial Differential Equations in Engineering*, Academic Press, New York, 1965, p. 150.

Technical Note on Planar Solidification With Fixed Wall Temperature and Variable Thermal Properties[1]

R. I. PEDROSO[2] and G. A. DOMOTO[3]

Nomenclature

- $c(T)$ = specific heat of the solidified material as a function of the temperature
- $k(T)$ = thermal conductivity of the solidified material as a function of the temperature
- L = latent heat of fusion
- T = temperature in the solidified material
- T_f = freezing temperature
- T_w = temperature at the fixed wall in contact with the solidified material
- t = time
- x = position
- x_f = freezing-front position
- ρ = density of the solidified material
- θ_1^*, θ_2^* = the temperature distribution θ after application, respectively, of the first and second transformations of Shanks [2] (see equations (9)) to the terms in equations (8)

Introduction

THE PROBLEM of planar solidification with fixed wall temperature and variable thermal properties is solved with a perturbation technique steming from the work of reference [1].[4] This paper is restricted to the case of thermal properties of the solidified material which vary as functions of the temperature and density assumed constant. The liquid is assumed to remain at the freezing temperature. Both the freezing temperature and the latent heat of fusion are taken as constants. For an arbitrary variation of thermal properties with temperature, the solution is presented in terms of integrals. A particular example is then considered and analytical solutions are presented for the first four terms of the perturbation solution. The first-order nonlinear transformations of Shanks [2] are applied to increase the range and rate of convergence of the series solution.

Analysis

For planar solidification with variable thermal properties, the boundary-value problem is

$$\rho c(T)\frac{\partial T}{\partial t} = \frac{\partial}{\partial x}\left[k(T)\frac{\partial T}{\partial x}\right], \qquad T(x = 0, t) = T_w$$

$$T(x = x_f, t) = T_f, \qquad \rho L\frac{dx_f}{dt} = k(T)\frac{\partial T}{\partial x}\bigg|_{x=x_f} \quad (1)$$

Define the average value of the thermal conductivity $\bar{k}$, the average specific heat $\bar{c}$, a new time variable τ, the temperature distribution after Kirchhoff's transformation is applied θ, the averaged parameter ϵ, and the function $f(\theta)$ as

$$\bar{k} = \frac{\int_{T_w}^{T_f} k(y)dy}{T_f - T_w}, \qquad \bar{c} = \frac{\int_{T_w}^{T_f} c(y)dy}{T_f - T_w},$$

$$\tau = \frac{\bar{k}(T_f - T_w)t}{\rho L} \quad (2)$$

$$\theta = \frac{\int_{T_w}^{T} k(y)dy}{\bar{k}(T_f - T_w)}, \qquad \epsilon = \frac{\bar{c}(T_f - T_w)}{L}, \qquad f(\theta) = \frac{c(\theta)/\bar{c}}{k(\theta)/\bar{k}}$$

[1] Portion of Doctoral dissertation, Department of Mechanical Engineering, Columbia University, New York, N. Y.

[2] Professional Staff Member, Philips Laboratories, Briarcliff Manor, N. Y. Assoc. Mem. ASME.

[3] Associate Professor, Department of Mechanical Engineering, Columbia University, New York, N. Y. Assoc. Mem. ASME.

Contributed by the Heat Transfer Division of THE AMERICAN SOCIETY OF MECHANICAL ENGINEERS. Manuscript received by the Heat Transfer Division, March 9, 1973.

[4] Numbers in brackets designate References at end of technical brief.

Substitute equations (2) into (1), define the similarity variable $\eta = \dfrac{x}{x_f}$ and change variables $(x, \tau) \rightarrow \eta$ to obtain

$$\theta'' + \epsilon f(\theta)\theta'(1)\eta\theta' = 0$$
$$\theta(0) = 0, \qquad \theta(1) = 1, \qquad \frac{{x_f}^2}{2\tau} = \theta'(1) \tag{3}$$

Expand the temperature distribution θ and the function $f(\theta)$ in power series in ϵ:

$$\theta(\eta;\epsilon) = \theta_0(\eta) + \epsilon\theta_1(\eta) + \epsilon^2\theta_2(\eta) + \epsilon^3\theta_3(\eta) + \ldots$$
$$f[\theta(\eta;\epsilon)] = f(\theta_0) + \epsilon f'(\theta_0)\theta_1 + \frac{\epsilon^2}{2}[f''(\theta_0)\theta_1^2 + 2f'(\theta_0)\theta_2] \ldots \tag{4}$$

The zeroth-order temperature distribution, $\theta_0(\eta)$, in the perturbation expansion corresponds to the case of complete absence of specific heat in the solidified material, $c(T) = 0$.

Introduce the integral operators p and q applied to an arbitrary function $g(\eta)$ as

$$p\{g(\eta)\} = \left\{\eta\int_0^1\int_0^\beta - \int_0^\eta\int_0^\beta\right\}g(\xi)d\xi d\beta$$
$$q\{g(\eta)\} = \int_0^1\int_0^\beta g(\xi)d\xi d\beta - \int_0^1 g(\xi)d\xi \tag{5}$$

Substitute equations (4) into (3) and equate coefficients of equal power of ϵ to obtain a linear system of equations with solutions for the first four terms as

$$\theta_0 = \eta, \qquad \theta_1 = p\{\eta f(\eta)\}$$
$$\theta_2 = \theta_1'(1)\theta_1 + p\{\eta[f(\eta)\theta_1' + f'(\eta)\theta_1]\}$$
$$\theta_3 = \{\theta_2'(1) - [\theta_1'(1)]^2\}\theta_1 + \theta_1'(1)\theta_2 + p\left\{\eta\left[f(\eta)\theta_2' + f'(\eta)(\theta_2 + \theta_1\theta_1') + \frac{f''(\eta)}{2}\theta_1^2\right]\right\}$$
$$\theta_1'(1) = q\{\eta f(\eta)\}$$
$$\theta_2'(1) = [\theta_1'(1)]^2 + q\{\eta[f(\eta)\theta_1' + f'(\eta)\theta_1]\}$$
$$\theta_3'(1) = 2\theta_1'(1)\theta_2'(1) - [\theta_1'(1)]^3 + q\left\{\eta\left[f(\eta)\theta_2' + f'(\eta)(\theta_2 + \theta_1\theta_1') + \frac{f''(\eta)}{2}\theta_1^2\right]\right\} \tag{6}$$

Equations (6) are general solutions in terms of integrals for any variations in thermal properties given by the function $f(\theta)$.

The solution up to and including the fourth term can be written for the linear function $f(\theta) = a + b\theta$ as

$$\theta_1 = \frac{\eta}{6}\left[a(1-\eta^2) + \frac{b}{2}(1-\eta^3)\right]$$
$$\theta_2 = -\frac{\eta}{2}\left[a\frac{a+b}{18}(1-\eta^2) + \frac{b^2}{72}(1-\eta^3) + \frac{a^2}{20}(1-\eta^4) + \frac{ab}{15}(1-\eta^5) + \frac{5}{252}b^2(1-\eta^6)\right]$$
$$\theta_3 = \frac{\eta}{2}\left[\left(\frac{17}{15}a^3 + \frac{11}{5}a^2b + \frac{43}{42}ab^2\right)\frac{1-\eta^2}{72} + \left(\frac{b^3}{14} - \frac{a^2b}{5} - \frac{ab^2}{15}\right)\frac{1-\eta^3}{36} + \left(a^3 + \frac{5}{6}a^2b\right)\frac{1-\eta^4}{40} + (a^2b + ab^2)\frac{1-\eta^5}{45} + \left(a^3 + \frac{5}{9}ab^2 + \frac{5}{6}b^3\right)\times\frac{1-\eta^6}{168} + \frac{13}{840}a^2b(1-\eta^7) + \frac{7}{630}ab^2(1-\eta^8) + \frac{b^3}{420}(1-\eta^9)\right] \tag{7}$$
$$\theta_1'(1) = -\left(\frac{a}{3} + \frac{b}{4}\right), \qquad \theta_2'(1) = \frac{7}{45}a^2 + \frac{2}{9}ab + \frac{9}{112}b^2$$
$$\theta_3'(1) = -\left(\frac{79}{945}a^3 + \frac{25}{144}a^2b + \frac{367}{3024}ab^2 + \frac{b^3}{35}\right)$$

The series for the freezing-front position can be inverted to yield:

$$\frac{2\tau}{{x_f}^2} = \tau_0 + \epsilon\tau_1 + \epsilon^2\tau_2 + \epsilon^3\tau_3 + \ldots$$
$$\tau_0 = 1, \qquad \tau_1 = \frac{a}{3} + \frac{b}{4}, \qquad \tau_2 = -\left(\frac{2}{45}a^2 + \frac{ab}{18} + \frac{b^2}{56}\right) \tag{8}$$
$$\tau_3 = \frac{16}{945}a^3 + \frac{67}{2160}a^2b + \frac{29}{1512}ab^2 + \frac{63}{15680}b^3$$

For instance $a = 0.60$, $b = 0.83$ and $\epsilon = 0.522$ can be shown, from the data in reference [3] to be a good approximation for solidification of water at atmospheric pressure with the wall temperature maintained at -100 deg C.

The following two nonlinear transformations of Shanks [2] can be applied to the four terms in equations (7):

$$\tau_1^* = \frac{\tau_0\tau_1 - \epsilon(\tau_0\tau_2 - \tau_1^2)}{\tau_1 - \epsilon\tau_2}$$
$$\tau_2^* = \frac{\tau_0\tau_2 + \epsilon(\tau_1\tau_2 - \tau_0\tau_3) + \epsilon^2(\tau_2^2 - \tau_1\tau_3)}{\tau_2 - \epsilon\tau_3} \tag{9}$$

The boundary-value problem in equations (3) was solved numerically with a Runge Kutta fourth-order method with increments $\Delta\eta = -0.01$. Starting at the freezing front with an estimated value of $\theta'(1)$, iteration was performed until $|\theta(0)| < 10^{-6}$.

Table 1 Perturbation and numerical solutions for freezing time

$$f(\theta) = a + b\theta, \qquad \tau_i{}^t = \sum_{j=0}^{i}\epsilon^j\tau_j$$

Top row: $a = 1.5$ and $b = -1$; middle row: $a = 1$ and $b = 0$; bottom row: $a = 0.5$ and $b = 1$.

ϵ	τ_n	$\tau_1{}^t$	$\tau_2{}^t$	$\tau_3{}^t$	$\tau_1{}^*$	$\tau_2{}^*$
	1.118	1.125	1.116	1.118	1.117	1.118
0.5	1.157	1.167	1.156	1.158	1.156	1.157
	1.196	1.208	1.194	1.197	1.195	1.197
	1.224	1.250	1.215	1.228	1.220	1.224
1	1.300	1.333	1.289	1.306	1.294	1.301
	1.376	1.417	1.360	1.383	1.367	1.377
	1.415	1.500	1.362	1.459	1.392	1.419
2	1.560	1.667	1.489	1.624	1.526	1.566
	1.701	1.833	1.606	1.794	1.655	1.709
	1.745	2.00	1.448	2.222	1.644	1.770
4	2.017	2.33	1.622	2.706	1.870	2.052
	2.278	2.6	1.759	3.261	2.079	2.325

Results and Discussion

It is found in general that the series solution for the freezing time, equation (8) yields better agreement with the numerical solution of equations (3) than the series for freezing front position formed directly from equations (7) and the last of equations (3). However, the nonlinear transformations in equations (9) will yield the same result when applied to either series.

Table 1 shows the sequence of partial sums in the perturbation solution for the freezing time for several values of the perturbation parameter, ϵ. Two linear functions $f(\theta)$ are considered

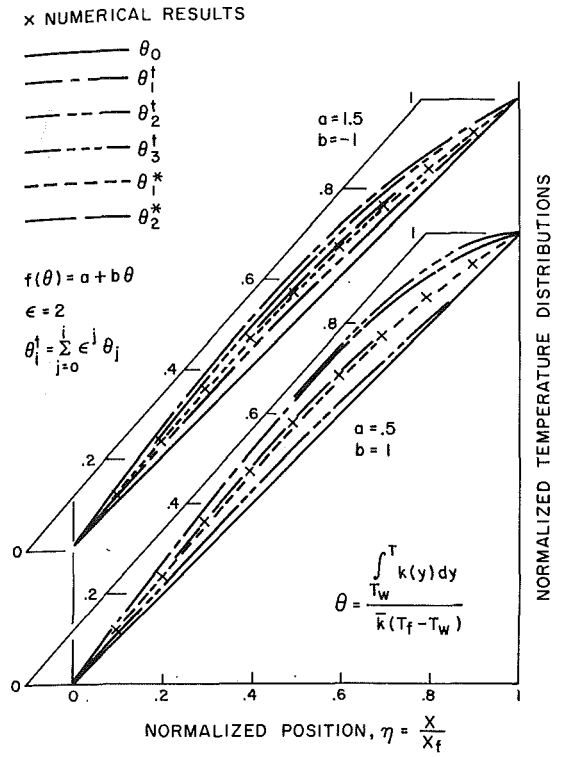

Fig. 1 Temperature distributions for planar solidification with variable thermal properties, constant wall temperature, and liquid at the freezing temperature

with slopes of plus and minus one and average value of one. The constant property case, $f(\theta) = 1$, is also shown for the sake of comparison. The perturbation solutions converge faster when $f(\theta)$ has a slope of minus one. Next follows the constant property case. Lastly, the case of $f(\theta)$ with a slope of plus one shows the slowest rate of convergence. Good agreement is found, in all three cases, with the numerical solutions, τ_n. This is especially true of the nonlinear transformed solutions τ_1^* and τ_2^*. For the same linear functions $f(\theta)$ and $\epsilon = 2$, the perturbation solutions for the temperature distribution are shown in Fig. 1. The nonlinear transformations θ_1^* and θ_2^*, and the numerical results, θ_n, are also shown. The rapid decrease in magnitude of the first few coefficients in the perturbation solutions makes possible its application even for moderate values of the perturbation parameter ϵ.

The solutions presented in the foregoing assume the liquid to be always at the freezing temperature. Alternatively, a convective heat transfer coefficient can be assumed on the liquid side of the freezing front. A similarity solution will no longer exist. However, a perturbation solution similar to the one considered previously should still be applicable, but in terms of independent variables x, x_f. The perturbation technique presented in this paper will not apply in solidification problems where thermal conduction is assumed in both the liquid and solid. In the latter type of problems, difficulties will be encountered in obtaining the zeroth-order solution or in obtaining a uniformly convergent perturbation solution.

References

1 Pedroso, R. I., and Domoto, G. A., "Perturbation Solutions for Spherical Solidification of Saturated Liquids," JOURNAL OF HEAT TRANSFER, TRANS. ASME, Series C, Vol. 95, No. 1, Feb. 1973.

2 Shanks, D., "Non-Linear Transformations of Divergent and Slowly Convergent Sequences," *Journ. of Math. and Phys.*, Vol. 34, No. 1, 1955.

3 Dorsey, N. E., "Properties of Ordinary Water Substance," American Chemical Society Monograph Series No. 81, Reinhold Publishing Co., New York, 1940.

An Exact Solution for the Flow of Temperature-Dependent Viscous Fluids in Heated Rectangular Ducts

H. W. BUTLER[1] and D. E. McKEE[2]

An exact solution has been developed for the fully-developed flow of fluids having temperature-dependent viscosity and thermal conductivity in rectangular ducts with transverse heat conduction. The problem is uniquely defined in terms of four parameters: the height-to-width ratio, E, the product of the friction factor and the Reynold's number, $f \cdot Re$, the temperature ratio across the duct, T_2/T_1, and the exponent of the viscosity dependence on temperature. The results indicate that significant departures from the isothermal case may obtain for heated flows.

Nomenclature

a, b = duct width and height, respectively
E = duct aspect ratio, b/a
f = friction factor, $2\tau/\rho\bar{v}^2$
Re = Reynold's number, $\bar{v}D\rho/\mu_0$
D_h = hydraulic diameter
k = thermal conductivity
T = absolute temperature
n = temperature exponent in viscosity relation, μT^n = constant
q = heat flux
p = pressure
v = axial velocity
$\bar{v}$ = average axial velocity
u = dimensionless velocity, $v/\bar{v}$
x, y, z = duct coordinates
α = temperature parameter, $n \ln \gamma$
β = dimensionless parameter = $\frac{(1+E)^2 f \cdot \mathrm{Re}}{2(T_0/T_1)^n}$
γ = temperature ratio across duct, T_2/T_1
θ = temperature ratio, T/T_1
ρ = density
μ = absolute viscosity
τ_{ij} = viscous stress tensor
ξ, η = dimensionless coordinates, x/a, y/b

Introduction

FOR A NUMBER of fluids, the dependence of the thermal conductivity and viscosity on temperature may be considered to vary according to the relations

$$k = \frac{k_0 T_0}{T} \quad \text{and} \quad \mu = \frac{\mu_0 T_0^n}{T^n} \tag{1}$$

The reference state indicated by the zero-subscripts may be taken at any convenient point, so that a wide range of liquids may be represented quite well by these relations. For light oils, a value of $n = 12$ agrees very closely with experimental data.

The particular problem selected to investigate the effects of such temperature-sensitive fluids is that of a steady, fully-developed flow along a rectangular duct. The velocity field is two-dimensional, but the temperature field is limited to one direction by considering a transverse heat flux only, with sidewalls insulated. Fig. 1 shows the coordinate system and the physical arrangement.

[1] Professor of Mechanical Engineering, West Virginia University, Morgantown, W. Va.

[2] Assistant Professor of Mechanical Engineering, West Virginia University, Morgantown, W. Va.

Contributed by the Heat Transfer Division of THE AMERICAN SOCIETY OF MECHANICAL ENGINEERS. Manuscript received by the Heat Transfer Division, April 18, 1973.

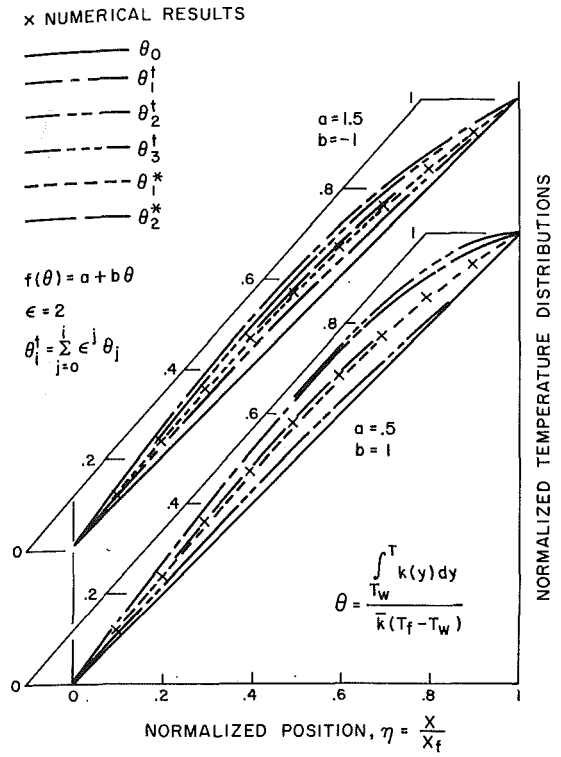

Fig. 1 Temperature distributions for planar solidification with variable thermal properties, constant wall temperature, and liquid at the freezing temperature

with slopes of plus and minus one and average value of one. The constant property case, $f(\theta) = 1$, is also shown for the sake of comparison. The perturbation solutions converge faster when $f(\theta)$ has a slope of minus one. Next follows the constant property case. Lastly, the case of $f(\theta)$ with a slope of plus one shows the slowest rate of convergence. Good agreement is found, in all three cases, with the numerical solutions, τ_n. This is especially true of the nonlinear transformed solutions τ_1^* and τ_2^*. For the same linear functions $f(\theta)$ and $\epsilon = 2$, the perturbation solutions for the temperature distribution are shown in Fig. 1. The nonlinear transformations θ_1^* and θ_2^*, and the numerical results, θ_n, are also shown. The rapid decrease in magnitude of the first few coefficients in the perturbation solutions makes possible its application even for moderate values of the perturbation parameter ϵ.

The solutions presented in the foregoing assume the liquid to be always at the freezing temperature. Alternatively, a convective heat transfer coefficient can be assumed on the liquid side of the freezing front. A similarity solution will no longer exist. However, a perturbation solution similar to the one considered previously should still be applicable, but in terms of independent variables x, x_f. The perturbation technique presented in this paper will not apply in solidification problems where thermal conduction is assumed in both the liquid and solid. In the latter type of problems, difficulties will be encountered in obtaining the zeroth-order solution or in obtaining a uniformly convergent perturbation solution.

References

1 Pedroso, R. I., and Domoto, G. A., "Perturbation Solutions for Spherical Solidification of Saturated Liquids," JOURNAL OF HEAT TRANSFER, TRANS. ASME, Series C, Vol. 95, No. 1, Feb. 1973.

2 Shanks, D., "Non-Linear Transformations of Divergent and Slowly Convergent Sequences," *Journ. of Math. and Phys.*, Vol. 34, No. 1, 1955.

3 Dorsey, N. E., "Properties of Ordinary Water Substance," American Chemical Society Monograph Series No. 81, Reinhold Publishing Co., New York, 1940.

An Exact Solution for the Flow of Temperature-Dependent Viscous Fluids in Heated Rectangular Ducts

H. W. BUTLER[1] and D. E. McKEE[2]

An exact solution has been developed for the fully-developed flow of fluids having temperature-dependent viscosity and thermal conductivity in rectangular ducts with transverse heat conduction. The problem is uniquely defined in terms of four parameters: the height-to-width ratio, E, the product of the friction factor and the Reynold's number, $f \cdot Re$, the temperature ratio across the duct, T_2/T_1, and the exponent of the viscosity dependence on temperature. The results indicate that significant departures from the isothermal case may obtain for heated flows.

Nomenclature

a, b = duct width and height, respectively
E = duct aspect ratio, b/a
f = friction factor, $2\tau/\rho\bar{v}^2$
Re = Reynold's number, $\bar{v}D\rho/\mu_0$
D_h = hydraulic diameter
k = thermal conductivity
T = absolute temperature
n = temperature exponent in viscosity relation, μT^n = constant
q = heat flux
p = pressure
v = axial velocity
$\bar{v}$ = average axial velocity
u = dimensionless velocity, $v/\bar{v}$
x, y, z = duct coordinates
α = temperature parameter, $n \ln \gamma$
β = dimensionless parameter = $\frac{(1+E)^2 f \cdot \mathrm{Re}}{2(T_0/T_1)^n}$
γ = temperature ratio across duct, T_2/T_1
θ = temperature ratio, T/T_1
ρ = density
μ = absolute viscosity
τ_{ij} = viscous stress tensor
ξ, η = dimensionless coordinates, x/a, y/b

Introduction

FOR A NUMBER of fluids, the dependence of the thermal conductivity and viscosity on temperature may be considered to vary according to the relations

$$k = \frac{k_0 T_0}{T} \quad \text{and} \quad \mu = \frac{\mu_0 T_0^n}{T^n} \tag{1}$$

The reference state indicated by the zero-subscripts may be taken at any convenient point, so that a wide range of liquids may be represented quite well by these relations. For light oils, a value of $n = 12$ agrees very closely with experimental data.

The particular problem selected to investigate the effects of such temperature-sensitive fluids is that of a steady, fully-developed flow along a rectangular duct. The velocity field is two-dimensional, but the temperature field is limited to one direction by considering a transverse heat flux only, with sidewalls insulated. Fig. 1 shows the coordinate system and the physical arrangement.

[1] Professor of Mechanical Engineering, West Virginia University, Morgantown, W. Va.

[2] Assistant Professor of Mechanical Engineering, West Virginia University, Morgantown, W. Va.

Contributed by the Heat Transfer Division of THE AMERICAN SOCIETY OF MECHANICAL ENGINEERS. Manuscript received by the Heat Transfer Division, April 18, 1973.

An isothermal solution for this problem was obtained by Kays and Clark [1][3] and a constant property solution to a similar problem by Sparrow and Siegel [2]. Rosenberg and Hellums [3] considered variable properties in a circular tube, and Lyutikas and Zhykauskas [4] studied a flat duct. Test [5] compared a numerical solution for a circular duct with experimental results, and Hwang and Hong [6] considered variable viscosity in a rectangular duct.

We assume that the viscous dissipation will have a negligible effect on the temperature distribution in comparison with the transverse heat flux, and that the velocity distribution over the duct will thus be governed by transversely varying but laterally constant viscosity. Since steady, transverse heat conduction is considered, the energy balance reduces to $\frac{dq}{dy} = 0$, where

$$q = -\left(\frac{k_0 T_0}{T}\right)\frac{dT}{dy} \tag{2}$$

The temperature across the duct is thus given by

$$\frac{T}{T_1} = \theta = e^{(\ln T_2/T_1)y/b} = \gamma^n \tag{3}$$

The velocity distribution is governed by the form of Newton's law which simply balances the viscous forces with pressure drop force which for the fully-developed flow is constant. Thus,

$$\frac{\partial \tau_{xz}}{\partial x} + \frac{\partial \tau_{yz}}{\partial y} = \frac{\partial p}{\partial z} \tag{4}$$

or, in terms explicit to this problem,

$$\frac{\partial}{\partial x}\left(\mu_{(T)}\frac{\partial v}{\partial x}\right) + \frac{\partial}{\partial y}\left(\mu_{(T)}\frac{\partial v}{\partial y}\right) = \frac{dp}{dz} \tag{5}$$

where $v = v_{(x,y)}$ is the axial velocity and the viscosity, μ, is given by equation (1). When nondimensional coordinates and velocity are introduced, the result is given by

$$E^2\frac{\partial^2 u}{\partial \xi^2} + \frac{\partial^2 u}{\partial \eta^2} - \alpha\frac{\partial u}{\partial \eta} + \beta e^{\alpha\eta} = 0. \tag{6}$$

Asymptotic Solutions

Before proceeding with the solution of equation (6) we will develop the asymptotic solutions for the two cases where the aspect ratio, E, takes on extreme values. For the case where $E \gg 1.0$, equation (6) reduces to

$$E^2\frac{d^2 u}{d\xi^2} = -\beta e^{\alpha\eta} \tag{7}$$

with the solution

$$u = \frac{\beta e^{\alpha\eta}}{2E^2}(\xi - \xi^2) \tag{8}$$

which is valid except near $\eta = 0, 1$. This is the case of a thin duct with the temperature constant across the thin dimension but varying along the wide dimension.

For $E \ll 1$, equation (6) reduces to

$$\frac{d^2 u}{d\eta^2} - \alpha\frac{du}{d\eta} + \beta e^{\alpha\eta} = 0 \tag{9}$$

which has the solution

$$u = \frac{\beta}{\alpha}\left[\frac{1 - e^{-\alpha\eta}}{1 - e^{-\alpha}} - \eta\right]e^{\alpha\eta} \tag{10}$$

which is valid except near $\xi = 0, 1$ and is the case where the thin duct has a transverse temperature gradient.

General Solution

The exponential term in equation (6) may be eliminated by the substitution

[3] Numbers in brackets designate References at end of technical brief.

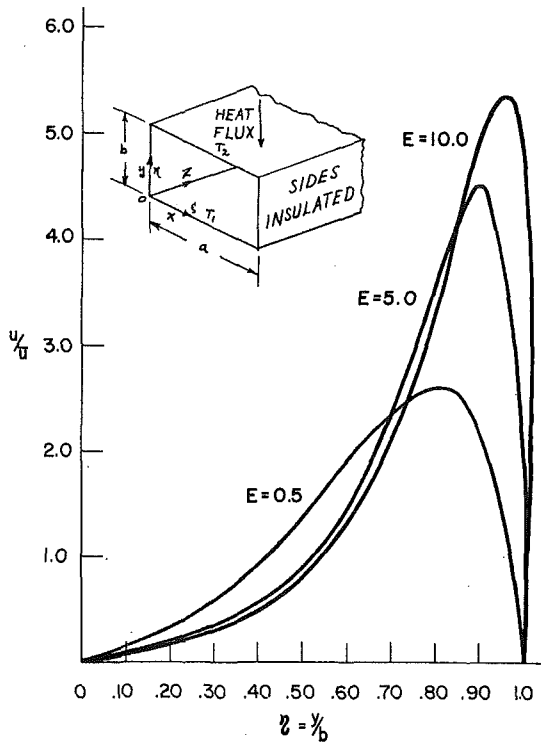

Fig. 1 Velocity distribution along thermal gradient axis, for $\gamma = 1.5$, $n = 12$, $\xi = 0.5$

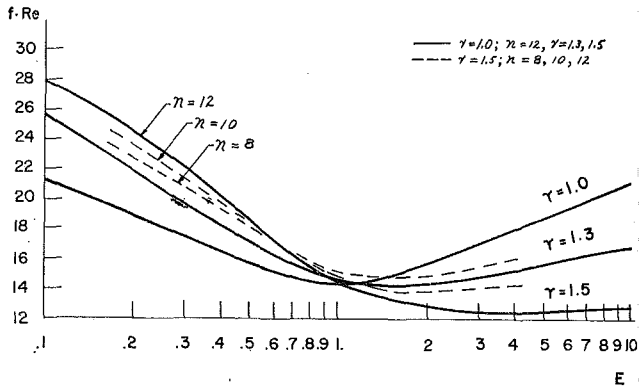

Fig. 2 $F \cdot Re$ versus E

$$w = ue^{-\alpha\eta} + \frac{\beta}{\alpha}\eta \tag{11}$$

giving

$$E^2\frac{\partial^2 w}{\partial \xi^2} + \frac{\partial^2 w}{\partial \eta^2} + \alpha\frac{\partial w}{\partial \eta} = 0 \tag{12}$$

with the boundary conditions

$$w_{(\xi,0)} = 0 \qquad w_{(0,\eta)} = \frac{\beta}{\alpha}\eta$$

$$w_{(\xi,1)} = \frac{\beta}{\alpha} \qquad w_{(1,\eta)} = \frac{\beta}{\alpha}\eta \tag{13}$$

The pseudo-velocity, w, in equation (12) is clearly separable into the conventional product form

$$w_{(\xi,\eta)} = X_{(\xi)} \cdot Y_{(\eta)} \tag{14}$$

leading to the usual type of second order ordinary differential equations. When the boundary conditions are satisfied the general solution is found to be

$$u = \frac{\beta}{\alpha}\left\{-\eta e^{\alpha\eta} + \frac{4}{\pi}e^{\alpha/2(1+\eta)}\sum_{i=1}^{\infty}\left[\frac{\sinh\sqrt{\left(\frac{\alpha}{2}\right)^2 + (2i-1)^2\pi^2E^2\eta}}{\sinh\sqrt{\left(\frac{\alpha}{2}\right)^2 + (2i-1)^2\pi^2E^2}}\cdot\frac{\sin(2i-1)\pi\xi}{(2i-1)}\right] + 2e^{\alpha/2\eta}\sum_{j=1}^{\infty}\left[(-1)^{j-1}\frac{4j\pi e^{\alpha/2}}{(4j^2\pi^2+\alpha^2)}\right.\right.$$

$$\left.\left.\times\left(1 - \frac{4\alpha}{(4j^2\pi^2+\alpha^2)}\right) - \frac{16\alpha j\pi}{(4j^2\pi^2+\alpha^2)}\right]\cdot\left[\frac{\sinh\left(\frac{1}{2E}\sqrt{4j^2\pi^2+\alpha^2\xi}\right) + \sinh\left(\frac{1}{2E}\sqrt{4j^2\pi^2+\alpha^2(1-\xi)}\right)}{\sinh\left(\frac{1}{2E}\sqrt{4j^2\pi^2+\alpha^2}\right)}\right]\sin j\,\pi\eta\right\} \quad (15)$$

Results

Fig. 1 shows the velocity profile distortion that results from temperature dependent viscosity, with the maximum velocity shifted well off center toward the hotter wall. Such distortions might be expected to trigger instability at lower Reynold's numbers. The average wall stress will have a different value for the hot, cold and side walls, which will tend to produce internal rotation in the flow. Fig. 2 shows how the $f \cdot \mathrm{Re}$ product varies with the aspect ratio for several values of the temperature ratio. The isothermal case, ($\gamma = 1$) corresponds to the solution obtained by Kays and Clark based on the torsion of rectangular bars. The effect of the viscosity temperature exponent, n, is also indicated on the figure.

References

1 Kays, W. M., and Clark, S. N., Stanford Tech. Report No. 17, 1953.

2 Sparrow, E. M., and Siegel, R., "A Variational Method for Fully-Developed Laminar Heat Transfer in Ducts," TRANS. ASME Series C, Vol. 81, 1959, p. 157.

3 Rosenberg, D. E., and Hellums, J. D., "Flow Development and Heat Transfer in Variable Viscosity Fluids," *Industrial Engineering Chemical Fundamentals*, Vol. 4, 1965, p. 417.

4 Lyutikas, N. S., and Zhukauskas, A. A., "An Investigation of the Influence of Variable Viscosity on Laminar Heat Transfer in a Flat Duct," *International Chemical Engineering*, Vol. 8, 1968, p. 301.

5 Test, F. L., "Laminar Flow Heat Transfer and Fluid Flow for Liquids With Temperature-Dependent Viscosity," ASME Paper No. 67-WA/HT-8, 1967.

6 Hwang, S. T., and Hong, S. W., AICHE, Preprint 8, 11th Heat Transfer Conference, 1969.

Heat Transfer in Tubes With Spiral and Helical Turbulators

ADAM KLACZAK[1]

Nomenclature

Import symbols

c = specific heat of the fluid, $\frac{\mathrm{J}}{\mathrm{kg\,deg}}$

d = inner diameter of the tube and the outer diameter of the turbulator, mm

F = heat exchange surface of the exchanger with the turbulators, m^2

F_0 = heat exchange surface of the exchanger without the turbulators, m^2

L = length of the heated part of the tube, mm

s = turns lead of the turbulator, mm

$\bar{v}$ = mean axial speed of the water in the tubes with the turbulators, $\frac{\mathrm{m}}{\mathrm{s}}$

α_w = coefficient of the heat transfer between the tube with the turbulator and the flowing medium, $\frac{W}{\mathrm{m^2\,deg}}$

λ = coefficient of thermal conductivity of the fluid, $\frac{W}{\mathrm{m\,deg}}$

ν = kinematic coefficient of viscosity of the fluid, $\frac{\mathrm{m}^2}{\mathrm{s}}$

ρ = density of fluid, $\frac{\mathrm{kg}}{\mathrm{m}^3}$

ϕ = diameter of the wire used for the spiral turbulators, mm

Dimensionless

$(\mathrm{Nu})_L$ = Nusselt number for the experimental exchanger of the proportion $L/d = 30$

$\mathrm{Nu} = \frac{d\alpha_w}{\lambda}$ = Nusselt number in the tubes with the turbulators

$\mathrm{Pr} = \frac{c\nu\rho}{\lambda}$ = Prandtl's number for the mean temperature of fluid

$\mathrm{Re} = \frac{\bar{v}d}{\nu}$ = Reynold's number in the tubes with the turbulators

THE INCREASE of the intensity of the heat transfer in various kinds of heat exchangers is a constant aim of designers. This problem is of great importance for industry because it will bring about some savings in the overall dimensions and weight of the machines. Generally speaking, this problem is reduced to the investigation of the usefulness in a technical and economic way of various kinds of turbulators and, in particular, spiral and helical turbulators which cause the increase of flow turbulence.

Many scientists, especially the authors of the papers [1, 3, 4],[2] have investigated in the last years the influence of turbulence promoters in the form of twisted tapes on heat transfer. The heat transfer in spirally corrugated tubes was also investigated [2, 6]. In such tubes the medium had also a steady rotation relatively to the flow axis. In all cases a rise of the heat transfer intensity was recorded. This note presents the results of investigations on the influence of helical and spiral turbulators on the heat transfer for turbulent flows in the range $1700 \leqslant \mathrm{Re} \leqslant 20000$. Correlation equations in terms of the similarity numbers

[1] Cracow University of Technology, Cracow, Poland.

Contributed by the Heat Transfer Division of THE AMERICAN SOCIETY OF MECHANICAL ENGINEERS. Manuscript received by the Heat Transfer Division, April 18, 1972.

[2] Numbers in brackets designate References at end of technical brief.

$$u = \frac{\beta}{\alpha}\left\{-\eta e^{\alpha\eta} + \frac{4}{\pi}e^{\alpha/2(1+\eta)}\sum_{i=1}^{\infty}\left[\frac{\sinh\sqrt{\left(\frac{\alpha}{2}\right)^2 + (2i-1)^2\pi^2E^2\eta}}{\sinh\sqrt{\left(\frac{\alpha}{2}\right)^2 + (2i-1)^2\pi^2E^2}}\cdot\frac{\sin(2i-1)\pi\xi}{(2i-1)}\right] + 2e^{\alpha/2\eta}\sum_{j=1}^{\infty}\left[(-1)^{j-1}\frac{4j\pi e^{\alpha/2}}{(4j^2\pi^2+\alpha^2)}\right.\right.$$

$$\left.\left.\times\left(1 - \frac{4\alpha}{(4j^2\pi^2+\alpha^2)}\right) - \frac{16\alpha j\pi}{(4j^2\pi^2+\alpha^2)}\right]\cdot\left[\frac{\sinh\left(\frac{1}{2E}\sqrt{4j^2\pi^2+\alpha^2\xi}\right) + \sinh\left(\frac{1}{2E}\sqrt{4j^2\pi^2+\alpha^2(1-\xi)}\right)}{\sinh\left(\frac{1}{2E}\sqrt{4j^2\pi^2+\alpha^2}\right)}\right]\sin j\,\pi\eta\right\} \quad (15)$$

Results

Fig. 1 shows the velocity profile distortion that results from temperature dependent viscosity, with the maximum velocity shifted well off center toward the hotter wall. Such distortions might be expected to trigger instability at lower Reynold's numbers. The average wall stress will have a different value for the hot, cold and side walls, which will tend to produce internal rotation in the flow. Fig. 2 shows how the $f \cdot \mathrm{Re}$ product varies with the aspect ratio for several values of the temperature ratio. The isothermal case, ($\gamma = 1$) corresponds to the solution obtained by Kays and Clark based on the torsion of rectangular bars. The effect of the viscosity temperature exponent, n, is also indicated on the figure.

References

1 Kays, W. M., and Clark, S. N., Stanford Tech. Report No. 17, 1953.

2 Sparrow, E. M., and Siegel, R., "A Variational Method for Fully-Developed Laminar Heat Transfer in Ducts," TRANS. ASME Series C, Vol. 81, 1959, p. 157.

3 Rosenberg, D. E., and Hellums, J. D., "Flow Development and Heat Transfer in Variable Viscosity Fluids," *Industrial Engineering Chemical Fundamentals*, Vol. 4, 1965, p. 417.

4 Lyutikas, N. S., and Zhukauskas, A. A., "An Investigation of the Influence of Variable Viscosity on Laminar Heat Transfer in a Flat Duct," *International Chemical Engineering*, Vol. 8, 1968, p. 301.

5 Test, F. L., "Laminar Flow Heat Transfer and Fluid Flow for Liquids With Temperature-Dependent Viscosity," ASME Paper No. 67-WA/HT-8, 1967.

6 Hwang, S. T., and Hong, S. W., AICHE, Preprint 8, 11th Heat Transfer Conference, 1969.

Heat Transfer in Tubes With Spiral and Helical Turbulators

ADAM KLACZAK[1]

Nomenclature

Import symbols

c = specific heat of the fluid, $\frac{\mathrm{J}}{\mathrm{kg\,deg}}$

d = inner diameter of the tube and the outer diameter of the turbulator, mm

F = heat exchange surface of the exchanger with the turbulators, m^2

F_0 = heat exchange surface of the exchanger without the turbulators, m^2

L = length of the heated part of the tube, mm

s = turns lead of the turbulator, mm

$\bar{v}$ = mean axial speed of the water in the tubes with the turbulators, $\frac{\mathrm{m}}{\mathrm{s}}$

α_w = coefficient of the heat transfer between the tube with the turbulator and the flowing medium, $\frac{W}{\mathrm{m^2\,deg}}$

λ = coefficient of thermal conductivity of the fluid, $\frac{W}{\mathrm{m\,deg}}$

ν = kinematic coefficient of viscosity of the fluid, $\frac{\mathrm{m}^2}{\mathrm{s}}$

ρ = density of fluid, $\frac{\mathrm{kg}}{\mathrm{m}^3}$

ϕ = diameter of the wire used for the spiral turbulators, mm

Dimensionless

$(\mathrm{Nu})_L$ = Nusselt number for the experimental exchanger of the proportion $L/d = 30$

$\mathrm{Nu} = \frac{d\alpha_w}{\lambda}$ = Nusselt number in the tubes with the turbulators

$\mathrm{Pr} = \frac{c\nu\rho}{\lambda}$ = Prandtl's number for the mean temperature of fluid

$\mathrm{Re} = \frac{\bar{v}d}{\nu}$ = Reynold's number in the tubes with the turbulators

THE INCREASE of the intensity of the heat transfer in various kinds of heat exchangers is a constant aim of designers. This problem is of great importance for industry because it will bring about some savings in the overall dimensions and weight of the machines. Generally speaking, this problem is reduced to the investigation of the usefulness in a technical and economic way of various kinds of turbulators and, in particular, spiral and helical turbulators which cause the increase of flow turbulence.

Many scientists, especially the authors of the papers [1, 3, 4],[2] have investigated in the last years the influence of turbulence promoters in the form of twisted tapes on heat transfer. The heat transfer in spirally corrugated tubes was also investigated [2, 6]. In such tubes the medium had also a steady rotation relatively to the flow axis. In all cases a rise of the heat transfer intensity was recorded. This note presents the results of investigations on the influence of helical and spiral turbulators on the heat transfer for turbulent flows in the range $1700 \leqslant \mathrm{Re} \leqslant 20000$. Correlation equations in terms of the similarity numbers

[1] Cracow University of Technology, Cracow, Poland.

Contributed by the Heat Transfer Division of THE AMERICAN SOCIETY OF MECHANICAL ENGINEERS. Manuscript received by the Heat Transfer Division, April 18, 1972.

[2] Numbers in brackets designate References at end of technical brief.

Table 1 Dimension of spiral turbulatar

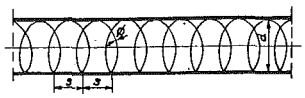

d=6.8 mm for all tests
4.65 mm $\leqslant s \leqslant$ 19.60 mm
0.7 mm $\leqslant \phi \leqslant$ 1.5 mm
Thirteen separate test sections
$0.6837 \leqslant \frac{s}{d} \leqslant 2.882$
$0.1029 \leqslant \frac{\phi}{d} \leqslant 0.2206$

Table 2 Dimension of helical turbulators

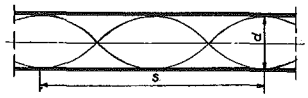

d=6.8 mm for all tests
22.2 mm $\leqslant s \leqslant$ 51.6 mm
Three separate test sections
s/d=3.26 , 5.28 and 7.59

are presented. These equations describe the heat exchange effects.

The Apparatus and the Method of Making Measurements

Measurements were made in two Reynolds number ranges, $800 \leqslant \mathrm{Re} \leqslant 8000$ and $5000 \leqslant \mathrm{Re} \leqslant 20000$. In the experimental heat exchanger the water was heated with various initial temperatures with the use of saturated steam. The experimental exchanger was made up of a small copper tube of inside diameter 6.8 mm with wall thickness of 0.5 mm and the surrounding jacket was made of steel sheet. The other conductors were made of plastic.

The saturated steam was led from the generator where the overpressure was in order 2.0 m H_2O through the outdropper to the exchanger.

It was tried to keep the pressure of the steam in the exchanger always on the same level ~150 mm H_2O varying it with the help of the U-tube which was placed behind the exchanger.

The experiments were made at various speeds of the water flow through the exchanger at first for the tube without the turbulators and then for the tube with the turbulators. The length of all the turbulators was about 35 d = 240 mm. The turbulator was placed in the whole heated part of the experimental exchanger. All the turns of the turbulator adhered to the inside surface of the tube.

Results

Spiral turbulators made of copper and steel wire, and helical turbulators made of copper sheet having the thickness 0.5 mm were used for the experiments.

The dimensions of the turbulators used in the experiments are given in Tables 1 and 2.

Studying these results and the investigations which have been performed previously, it is possible to say that the coefficient (α_w) is functionally connected with the following quantities

$$\alpha_w = f(\bar{v};\ \rho;\ d;\ \nu;\ c;\ \lambda;\ s;\ \phi) \tag{1}$$

The dimensional analysis of the foregoing function gives the dependence of five dimensionless criterion numbers

$$\frac{\alpha_w d}{\lambda} = C\left(\frac{\bar{v}d}{\nu}\right)^a \cdot \left(\frac{c\rho\nu}{\lambda}\right)^b \cdot \left(\frac{s}{d}\right)^g \cdot \left(\frac{\phi}{d}\right)^h \tag{2}$$

It is possible to write equation (2) for the spiral turbulators also in the form

$$(\mathrm{Nu})_L = C\,\mathrm{Re}^a \cdot \mathrm{Pr}^b \cdot \left(\frac{s}{d}\right)^g \cdot \left(\frac{\phi}{d}\right)^h \tag{3}$$

and for the helical turbulators

$$(\mathrm{Nu})_L = C\,\mathrm{Re}^a \cdot \mathrm{Pr}^b \cdot \left(\frac{s}{d}\right)^g \tag{4}$$

The linear equations with five and four unknowns were obtained after taking logarithms of (3) and (4)

$$\lg C + a \lg \mathrm{Re} + b \lg \mathrm{Pr} + g \lg \frac{s}{d} + h \lg \frac{\phi}{d} - \lg (\mathrm{Nu})_L = 0 \tag{5}$$

$$\lg C + a \lg \mathrm{Re} + b \lg \mathrm{Pr} + g \lg \frac{s}{d} - \lg (\mathrm{Nu})_L = 0 \tag{6}$$

Equations (5) and (6) were used to calculate the general correlation equations for the turbulent flow. Here the method of least squares was used, giving

$$(\mathrm{Nu})_L = 1.1355\ \mathrm{Re}^{0.52} \cdot \mathrm{Pr}^{0.54} \cdot \left(\frac{s}{d}\right)^{-0.29} \cdot \left(\frac{\phi}{d}\right)^{0.35} \pm 8.3 \text{ percent} \tag{7}$$

$$(\mathrm{Nu})_L = 2.0040\ \mathrm{Re}^{0.44} \cdot \mathrm{Pr}^{0.36} \cdot \left(\frac{s}{d}\right)^{-0.33} \pm 10 \text{ percent} \tag{8}$$

The precision of the equations was counted for the probability 95 percent. All the results obtained in the investigations are shown in Figs. 1 and 2 with the help of the auxiliary function

$$\beta_1 = f(\mathrm{Re});\quad \beta_2 = f(\mathrm{Re})$$

transforming the correlation equations (7) and (8) to the form

$$\beta_1 = \frac{(\mathrm{Nu})_L}{\mathrm{Pr}^{0.54} \cdot \left(\frac{s}{d}\right)^{-0.29} \cdot \left(\frac{\phi}{d}\right)^{0.35}} = \left(\frac{s}{d}\right)^{0.29} \cdot \left(\frac{\phi}{d}\right)^{-0.35} \cdot \frac{(\mathrm{Nu})_L}{\mathrm{Pr}^{0.54}} = 1.1355\mathrm{Re}^{0.52} \tag{9}$$

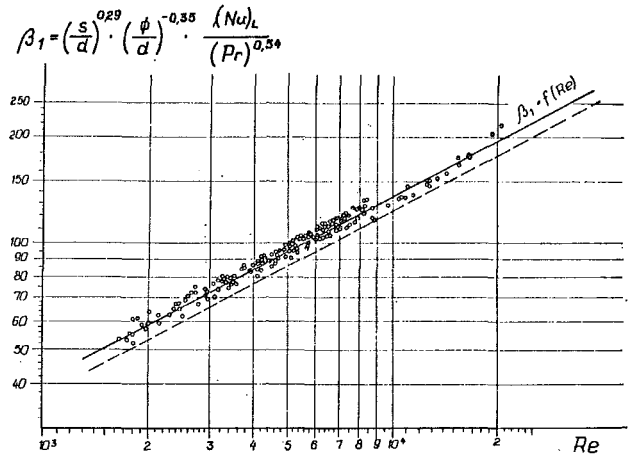

Fig. 1 The dependence $\beta_1 = f(\mathrm{Re})$ for the spiral turbulators: ——— the recommended values in the practical calculations

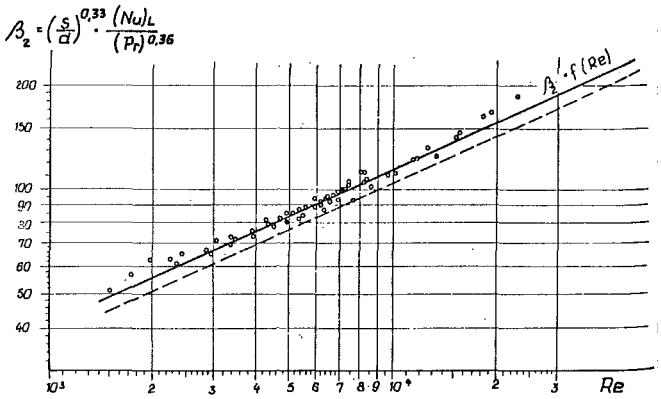

Fig. 2 The dependence $\beta_2 = f(\mathrm{Re})$ for the helical turbulators: ——— the recommended values in the practical calculations

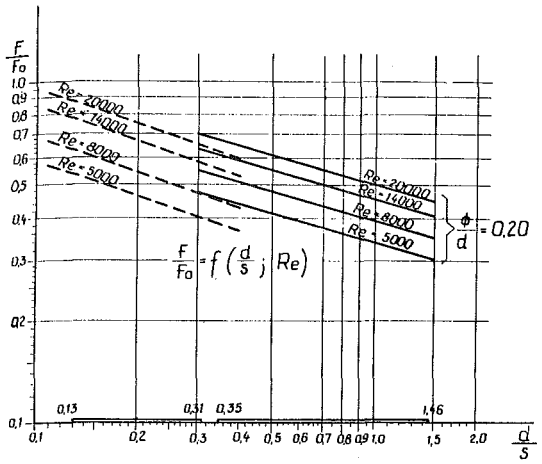

Fig. 3 Saving of the exchange surface because of using the turbulators: ——— spiral turbulators, ——— helical turbulators, ═══ insertigated range

$$\beta_2 = \left(\frac{s}{d}\right)^{0.33} \cdot \frac{(\mathrm{Nu})_L}{\mathrm{Pr}^{0.36}} = 2.0040\mathrm{Re}^{0.44} \tag{10}$$

For usability of the equations (7) and (8) also for determination of the heat exchange in the long heated conductors of $L \geq 60d$ the influence of the intake disturbances using the correction proposed by Kroll was considered, which is

$$\epsilon = 1 + \left(\frac{d}{L}\right)^{0.7} \tag{11}$$

For the experimental exchanger

$$\epsilon = 1 + \left(\frac{6.8}{204}\right)^{0.7} = 1.09 \tag{12}$$

After putting in Kroll's coefficient, the value of the constant (C) in the equations (7) and (8) will be changed as follows

$$C' = \frac{C}{\epsilon} = \frac{1.1355}{1.09} = 1.04 \tag{13}$$

$$C'' = \frac{C}{\epsilon} = \frac{2.0040}{1.09} = 1.84 \tag{14}$$

The general correlations for the long conductors of $L \geq 60d$ and turbulent flow will have the form (For the spiral turbulators)

$$\mathrm{Nu} = 1.04\ \mathrm{Re}^{0.52} \cdot \mathrm{Pr}^{0.54} \cdot \left(\frac{d}{s}\right)^{0.29} \cdot \left(\frac{\phi}{d}\right)^{0.35} \tag{15}$$

The equation (15) holds true in the investigated range

$$1700 \leqslant \mathrm{Re} \leqslant 20000$$

$$2.5 \leqslant \mathrm{Pr} \leqslant 9.0$$

$$0.35 \leqslant \frac{d}{s} \leqslant 1.46$$

$$0.10 \leqslant \frac{\phi}{d} \leqslant 0.22$$

For the helical turbulators:

$$\mathrm{Nu} = 1.84\ \mathrm{Re}^{0.44} \cdot \mathrm{Pr}^{0.36} \cdot \left(\frac{d}{s}\right)^{0.33} \tag{16}$$

The equation (16) holds true in the range:

$$1700 \leqslant \mathrm{Re} \leqslant 20000$$

$$2.5 \leqslant \mathrm{Pr} \leqslant 9.0$$

$$0.13 \leqslant \frac{d}{s} \leqslant 0.31$$

For calculations the physical properties should be based on the arithmetic mean temperature of the fluid at the inlet and exit of the exchanger.

The Saving of the Heat Exchange Surface

A comparison was made between the heat exchange surface of tubes generally used in the construction of heat exchangers. This comparison is usually made for the same quantity of heat exchanged in the tubes, for the same temperature conditions, for the same medium and for identical diameters of the tubes. The dependence

$$\frac{F}{F_0} = f\left(\frac{d}{s}; \mathrm{Re}\right)$$

for the spiral and helical turbulators is shown on Fig. 3. The great saving of the heat exchange surface is visible.

References

1 Gambill, W. R., "Subcooled Swirl—Flow Boiling and Burnout With Electrically Heated Twisted Tapes and Zero Wall Flux," JOURNAL OF HEAT TRANSFER, TRANS. ASME, Series C, Vol. 87, No. 3, Aug. 1965, pp. 342–348.

2 Ridd, G. J., Jr., "The Heat Transfer and Pressure—Drop Characteristics of Gas Flow Inside Spirally Corrugated Tubes," JOURNAL OF HEAT TRANSFER, TRANS. ASME, Series C, Vol. 92, No. 3, Aug. 1970, pp. 513–519.

3 Smithberg, E., and Landis, F., "Friction and Forced Convection Heat-Transfer Characteristics in Tubes With Twisted Tape Swirl Generators," JOURNAL OF HEAT TRANSFER, TRANS. ASME, Series C, Vol. 86, No. 1, Feb. 1964, pp. 39–49.

4 Thorsen, R., and Landis, F., "Friction and Heat Transfer Characteristics in Turbulent Swirl Flow Subjected to Large Transverse Temperature Gradients," JOURNAL OF HEAT TRANSFER TRANS. ASME, Series C, Vol. 90, No. 1, Feb. 1968, pp. 87–97.

5 Klaczak, A., "Heat Absorption in Pipes With Spiral and Helical Turbulators," *Archiwum Budowy Maszyn.*, Vol. XIX, No. 1, 1972, pp. 75–99.

6 Klaczak, A., "Turbulence Pipes in Construction of Heat Exchangers," *Cieptownictwo, Ogrzewnictwo, Wentylacja.*, No. 10, Oct. 1972, pp. 289–294.

Numerical Model of Heat Transfer in a Rod Bundle With Helical Wire Wrap Spacers

A. W. GRAVES[1] and I. CATTON[2]

Nomenclature

A = cross-sectional area of a flow channel
C_p = heat capacity
h = specific enthalpy
k = thermal conductivity
Q_N = nuclear heat generation
T = temperature
$\bar{W}$ = average bundle flow velocity
W_A, W_B, W_C = velocity components in A, B, and C directions

[1] Member of Technical Staff, Atomics International, A Division of North American Rockwell Corp.

[2] Assistant Professor, Consultant to Atomics International, University of California, Los Angeles, Calif. Mem. ASME.

Contributed by the Heat Transfer Division of THE AMERICAN SOCIETY OF MECHANICAL ENGINEERS. Manuscript received by the Heat Transfer Division, September 26, 1972.

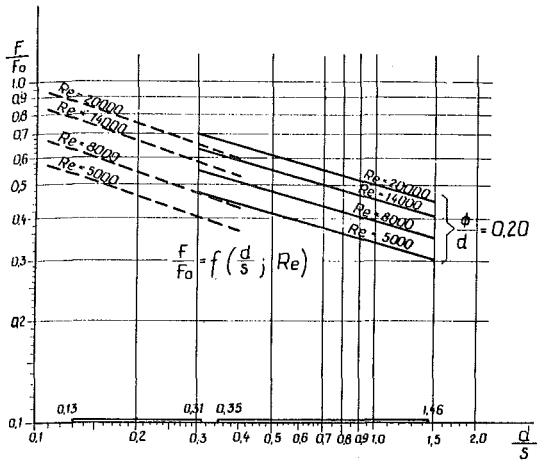

Fig. 3 Saving of the exchange surface because of using the turbulators: ——— spiral turbulators, ——— helical turbulators, ═══ insertigated range

$$\beta_2 = \left(\frac{s}{d}\right)^{0.33} \cdot \frac{(\mathrm{Nu})_L}{\mathrm{Pr}^{0.36}} = 2.0040\mathrm{Re}^{0.44} \tag{10}$$

For usability of the equations (7) and (8) also for determination of the heat exchange in the long heated conductors of $L \geq 60d$ the influence of the intake disturbances using the correction proposed by Kroll was considered, which is

$$\epsilon = 1 + \left(\frac{d}{L}\right)^{0.7} \tag{11}$$

For the experimental exchanger

$$\epsilon = 1 + \left(\frac{6.8}{204}\right)^{0.7} = 1.09 \tag{12}$$

After putting in Kroll's coefficient, the value of the constant (C) in the equations (7) and (8) will be changed as follows

$$C' = \frac{C}{\epsilon} = \frac{1.1355}{1.09} = 1.04 \tag{13}$$

$$C'' = \frac{C}{\epsilon} = \frac{2.0040}{1.09} = 1.84 \tag{14}$$

The general correlations for the long conductors of $L \geq 60d$ and turbulent flow will have the form (For the spiral turbulators)

$$\mathrm{Nu} = 1.04\ \mathrm{Re}^{0.52} \cdot \mathrm{Pr}^{0.54} \cdot \left(\frac{d}{s}\right)^{0.29} \cdot \left(\frac{\phi}{d}\right)^{0.35} \tag{15}$$

The equation (15) holds true in the investigated range

$$1700 \leqslant \mathrm{Re} \leqslant 20000$$

$$2.5 \leqslant \mathrm{Pr} \leqslant 9.0$$

$$0.35 \leqslant \frac{d}{s} \leqslant 1.46$$

$$0.10 \leqslant \frac{\phi}{d} \leqslant 0.22$$

For the helical turbulators:

$$\mathrm{Nu} = 1.84\ \mathrm{Re}^{0.44} \cdot \mathrm{Pr}^{0.36} \cdot \left(\frac{d}{s}\right)^{0.33} \tag{16}$$

The equation (16) holds true in the range:

$$1700 \leqslant \mathrm{Re} \leqslant 20000$$

$$2.5 \leqslant \mathrm{Pr} \leqslant 9.0$$

$$0.13 \leqslant \frac{d}{s} \leqslant 0.31$$

For calculations the physical properties should be based on the arithmetic mean temperature of the fluid at the inlet and exit of the exchanger.

The Saving of the Heat Exchange Surface

A comparison was made between the heat exchange surface of tubes generally used in the construction of heat exchangers. This comparison is usually made for the same quantity of heat exchanged in the tubes, for the same temperature conditions, for the same medium and for identical diameters of the tubes. The dependence

$$\frac{F}{F_0} = f\left(\frac{d}{s}; \mathrm{Re}\right)$$

for the spiral and helical turbulators is shown on Fig. 3. The great saving of the heat exchange surface is visible.

References

1 Gambill, W. R., "Subcooled Swirl—Flow Boiling and Burnout With Electrically Heated Twisted Tapes and Zero Wall Flux," JOURNAL OF HEAT TRANSFER, TRANS. ASME, Series C, Vol. 87, No. 3, Aug. 1965, pp. 342–348.

2 Ridd, G. J., Jr., "The Heat Transfer and Pressure—Drop Characteristics of Gas Flow Inside Spirally Corrugated Tubes," JOURNAL OF HEAT TRANSFER, TRANS. ASME, Series C, Vol. 92, No. 3, Aug. 1970, pp. 513–519.

3 Smithberg, E., and Landis, F., "Friction and Forced Convection Heat-Transfer Characteristics in Tubes With Twisted Tape Swirl Generators," JOURNAL OF HEAT TRANSFER, TRANS. ASME, Series C, Vol. 86, No. 1, Feb. 1964, pp. 39–49.

4 Thorsen, R., and Landis, F., "Friction and Heat Transfer Characteristics in Turbulent Swirl Flow Subjected to Large Transverse Temperature Gradients," JOURNAL OF HEAT TRANSFER TRANS. ASME, Series C, Vol. 90, No. 1, Feb. 1968, pp. 87–97.

5 Klaczak, A., "Heat Absorption in Pipes With Spiral and Helical Turbulators," *Archiwum Budowy Maszyn.*, Vol. XIX, No. 1, 1972, pp. 75–99.

6 Klaczak, A., "Turbulence Pipes in Construction of Heat Exchangers," *Cieptownictwo, Ogrzewnictwo, Wentylacja.*, No. 10, Oct. 1972, pp. 289–294.

Numerical Model of Heat Transfer in a Rod Bundle With Helical Wire Wrap Spacers

A. W. GRAVES[1] and I. CATTON[2]

Nomenclature

A = cross-sectional area of a flow channel
C_p = heat capacity
h = specific enthalpy
k = thermal conductivity
Q_N = nuclear heat generation
T = temperature
$\bar{W}$ = average bundle flow velocity
W_A, W_B, W_C = velocity components in A, B, and C directions

[1] Member of Technical Staff, Atomics International, A Division of North American Rockwell Corp.

[2] Assistant Professor, Consultant to Atomics International, University of California, Los Angeles, Calif. Mem. ASME.

Contributed by the Heat Transfer Division of THE AMERICAN SOCIETY OF MECHANICAL ENGINEERS. Manuscript received by the Heat Transfer Division, September 26, 1972.

W_P = peripheral velocity in wall channels
X, Y, Z = coordinate directions
α = adjustable constant, equation (1)
γ = phase angle, equation (1)
ρ = density
ϵ_h = turbulent eddy transport coefficient
η = channel-to-channel centroid distance
Γ = thermal diffusivity

Introduction

THERE ARE a number of computer programs which treat cross-flow mixing in terms of the separate mixing effects. Several such codes are discussed by Todreas and Rogers [1][3] and their Table 4 lists the mixing considerations of each. Of the codes mentioned, none consider the flow sweeping in more than a gross way. A number of recently developed codes [2–4] attempt to relate the channel-to-channel directed flow to the wire wrap configuration.

Much of the subchannel physical behavior is speculative, and to consider the various modes of mixing separately and additively is probably incorrect. The accuracy of empirical correlations which attribute all the cross-flow mixing to turbulence is questionable. Sweep velocities on the order of 1 to 3 ft/sec exist in present LMFBR designs, and pure turbulent mixing in the flow direction can probably be neglected if the forced flow diversion is computed correctly. Salt mixing tests by Collingham, Thorne, and McCormack [5] substantiate that a very regular flow pattern is set up and that the lateral flow between any two rods alternates in direction as the coolant traverses axially through the pin bundle. The nature of an alternating flow is depicted in Fig. 1. Attempts to simulate this regular swirl motion by adjusting the turbulent eddy coefficient to achieve an equivalent degree of mixing does not allow for preferential transport in the direction of the sweep. It was decided that a simple model was needed which focused on computing the forced flow created by the wires.

Computer Model

Flow Field. The cross-flow mixing rates induced by a wire wrap are frequently expressed in terms of the pin and wire diameter, the axial pitch of the wire, and a coefficient to account for slip over the wire. Each flow channel is influenced by the wires wrapped around the defining pins (Fig. 1). Each of the three openings feeding a single flow channel will alternately have flow swept in and out, and the flow magnitude will be a maximum when the wire is near the gap between two pins. This alternating nature suggests that the lateral component of the flow could be related to the cosine of the angular displacement of the wire from each side of the gap. Further, the wires on each of the three pins interact to cause a continuous sweeping effect. Therefore, it is postulated that the cross-flow sweeping rate can be represented by

$$W = \alpha\pi \frac{P}{l} \bar{W} \cos\left(\frac{2\pi}{l} z + \gamma\right) \quad (1)$$

Near the housing wall, the amount of fluid swept laterally by the wires will be affected by the presence of the walls. The flow field for the wall channels (C_1 types in Fig. 1) is composed of three major varying components. The first component is the peripheral lateral flow that circumscribes the entire bundle and is denoted as W_{PK}. The second is the lateral cross-flow from the C_2-type channels, and is either a W_A, W_B, or W_C vector depending on which of the six housing sides is being considered. The third component is the local axial velocity. Fuel assembly model water tests at Atomics International [6] have shown that the average lateral peripheral velocity is equal to the sweep velocity of the wire wrap, and that the average axial velocity in the wall channels equals the bulk average axial velocity for the assembly. Both test results represent the integrated values of the flow components over multiples of full wire pitch lengths.

Both the local axial and local lateral peripheral velocity components are expected to vary periodically and are thus each computed on relative wire position and coupled by continuity considerations. The peripheral lateral velocity at any elevation is then expressed as

$$W_{PK} = \sum_{N=1}^{k} W_N + C \quad (2)$$

where C is an experimental constant used to set the value of the minimum local peripheral velocity.

Energy Equation. The energy transport must consider all possible modes of transport, including a diffusive and convective mechanism for this problem. The diffusive mode includes thermal conduction, as well as turbulence. Thermal conduction in the flow direction can be neglected and the flow field can be specified (based on the model described in the foregoing). The energy equation may be written

$$\frac{\partial W_Z \rho h}{\partial Z} = \frac{\partial}{\partial X}(k + \rho C_p \epsilon_h)\frac{\partial T}{\partial X} + \frac{\partial}{\partial Y}(k + \rho C_p \epsilon_h)\frac{\partial T'}{\partial Y} - \frac{\partial}{\partial X}(\rho W_X h) - \frac{\partial}{\partial Y}(\rho W_Y h) + Q_N \quad (3)$$

It is assumed that the physical properties do not vary with location in the bundle at a given elevation (i.e., no variation in the cross-stream direction). The boundary condition for the bundle walls is either a prescribed temperature field outside the bundle housing wall, or an adiabatic housing wall. The inlet temperature to the assembly is known.

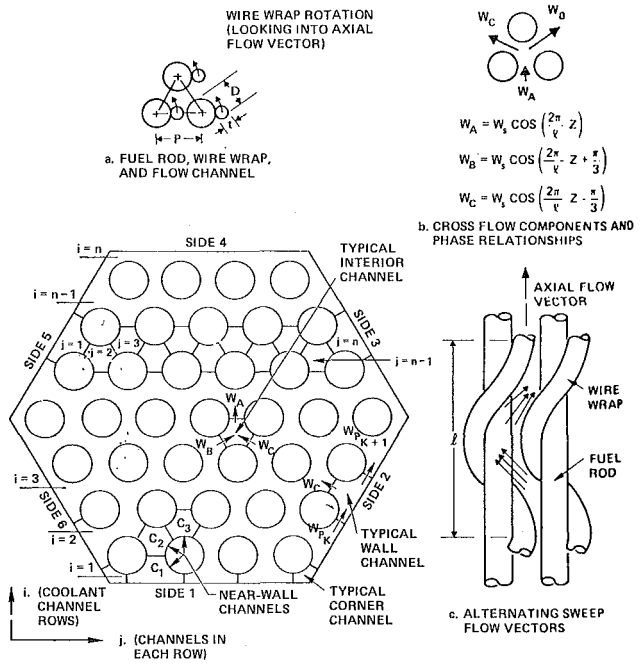

Fig. 1 Geometric arrangement of rod-bundle sweep velocity phase relationships and fuel-assembly model schematic

[3] Numbers in brackets designate References at end of technical brief.

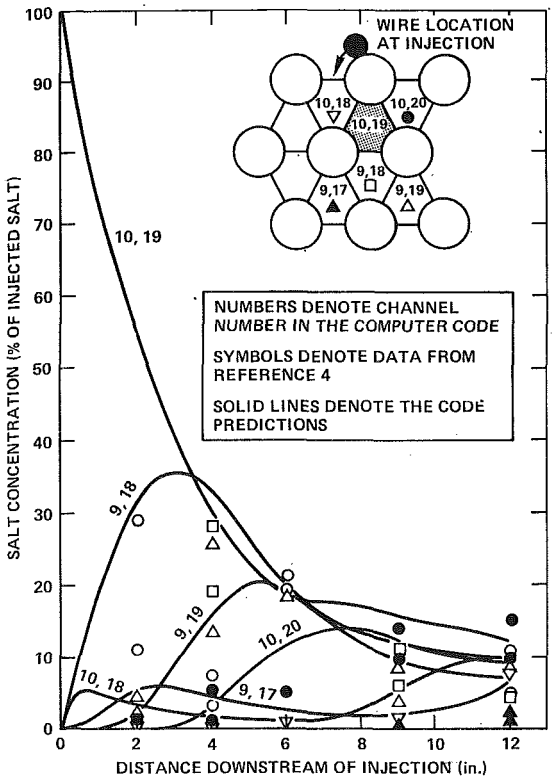

Fig. 2 Axial concentration gradients for interior channel injection

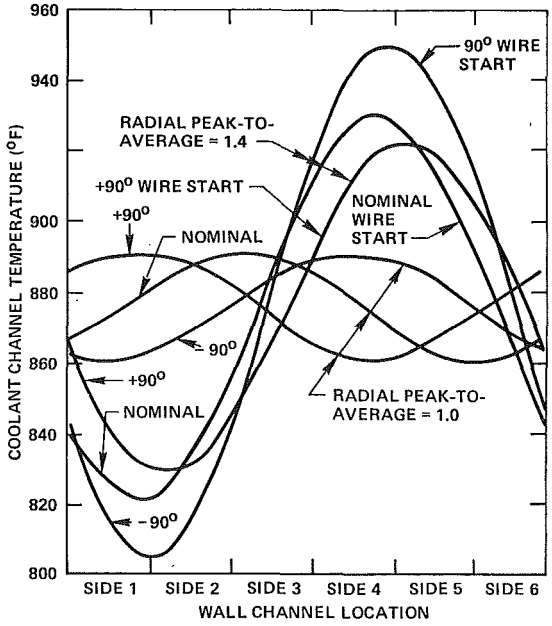

Fig. 3 Circumferential temperature profiles for a typical FFTF fuel assembly

Method of Solution

Equation (3) is a parabolic equation in Z and can be solved by any of a number of numerical techniques. In this work, a lumped parameter model and a simple forward marching scheme are used. In developing the difference form of equation (3), conservation of mass, $dh = C_P dT$, and the assumption that the sweep velocities are locally constant are used. The resulting equation for the axial temperature gradient in each flow channel using the sign convention shown in Fig. 1 is

$$T_{ij}(z + \delta z) = T_{ij}(z) + \frac{\delta z}{\bar{W}_{ij}A_{ij}}\left[\frac{\Gamma + \epsilon_h}{n}(T_1 + T_2 + T_3 + 3T_{ij}) + f(W_{Aij})(T_1 - T_{ij}) + f(-W_{Bij})(T_2 - T_{ij}) + f(-W_{Cij})(T_3 - T_{ij})\right](P - D) + Q_{Nij}\delta z \quad (4)$$

Subscripts 1, 2, and 3 are used to designate the three channels surrounding channel ij in the A, B, and C vector directions, respectively. The term f represents a function that is set equal to its argument if the argument is positive and zero if the argument is negative. The negative sign is associated with W_B and W_C so that the function is positive when the flow is into the ij channel. Similar equations are easily obtained for the wall and corner channels.

The initial conditions are that all $T_{ij} = T_0$ at $Z = Z_0$ and $\bar{W}_{ij}$ for the near-wall channels are selected such that their local variations fluctuate about the bundle average (integrated) velocity.

A typical code for the largest pin bundle presently under consideration (271 pins), requires less than 6000 storage locations for the variables needed. Typical running time on an IBM 360/85 for a 271-pin bundle that is 10 ft long using $^1/_4$-in. axial increments is 60 sec, with complete CRT output.

Results and Discussion

Comparison With Test Data. Equivalent salt concentration profiles were calculated for comparison with the experiments conducted by Collingham, Thorne, and McCormack [5]. These salt concentration profiles are shown in Fig. 2 for six flow channels near the injection zone. The data presented by reference [5], and reproduced here in Fig. 2, indicate an abnormally low salt concentration value for the injection flow channel near the injection point. Davidson [6] has indicated that these low concentration measurements in a region of obviously high concentration are associated with a boundary layer phenomenon which exists for up to 6 in. downstream of the injection. The inaccuracy of the measurements in the initial region support the contention that the predictions satisfactorily represent the flow process. The predicted phase relationships of all six flow channels are identical to those measured by Collingham, et al. [5]. In general, the comparisons with experiment are favorable and fall within the data scatter of two similar runs presented in reference [5]. Beyond 12 in., the effect of local flow sweeping has been substantially homogenized and therefore comparisons are expected to be good for all analytical models.

The analysis of a typical FFTF fuel assembly indicates the presence of a lateral coolant temperature gradient in the flow channels adjacent to the assembly housing walls for an assembly without a radial power gradient. This temperature profile shifts with wire wrap start orientation relative to the fuel pin and housing walls, i.e., the resultant wall-channel coolant temperature profile rotates relative to the pin bundle as the wire start position on the pins is rotated. This temperature component is thus seen to be independent of the radial power profile, but dependent on the flow field. The effect of a circumferential temperature profile that is independent of a radial power gradient will be an additive factor to the temperature profile resulting solely from the radial power gradient. This effect is illustrated in Fig. 3, where the radial power profile is assigned across sides 1 and 4 (as denoted in Fig. 1), with side 4 having the higher powers (nearest the reactor core center line). Three wire start orientations are included for illustration. The flow dependent results are indicated by the flat radial power profile curves (radial peak-to-average = 1.0). The combined effect of the wire start orientation and a radial peak-to-average power skew of 1.4 is also shown in the figure. The cause of the circumferential ΔT for the flat power profile is the oscillating character of the wire-driven flow field in the wall flow channels. There are three flow components contributing to the oscillating field. One com-

ponent is the lateral flow increasing the energy exchange between the interior channels and the wall channels in a periodic way. Another contributor to the circumferential ΔT is the changing vertical velocity component of the flow (increasing when the lateral flow is directed toward the wall and decreasing when it is away from the wall) and its effect on the thermal capacitance ($\rho C_p W_Z$) at a given axial elevation. The changing thermal capacitance causes a change in the temperature response of the wall channels for any specified local nuclear fuel addition. The third component is the lateral flow parallel to the housing wall that circumscribes the rod bundle.

Conclusion

A practical solution to the problem of predicting operating temperatures for nuclear fuel assemblies containing wire-wrapped fuel pins spaced in a triangular array has been presented. It has been shown that the flow field predictions for the subpitch length (below 12 in. for these data) agree with experimental data obtained from prototypic LMFBR model fuel assembly tests. The existence of a circumferential temperature gradient in wire-wrapped fuel assemblies independent of a radial nuclear power skew has been demonstrated and verified by Fontana, et al. [7].

References

1 Todreas, N. E., and Rogers J. T., "Coolant Interchannel Mixing in Reactor Fuel Rod Bundles," *Heat Transfer in Rod Bundles*, ASME, New York, 1968.

2 Wantland, J. L., "ØRRIBLE—A Computer Program for Flow and Temperature Distribution in LMFBR Fuel Rod Bundles," ORNL-TM-3516, Oak Ridge National Laboratory, Oak Ridge, Tenn., 1971.

3 Rowe, D. S., "COBRA-III: A Digital Computer Program for Steady State and Transient Thermal-Hydraulic Analysis of Rod Bundle Nuclear Fuel Elements," BNWL-B-82, 1971.

4 Todreas, N. E., and Turi, J. A., "Interchannel Mixing in Wire Wrapped Liquid Metal Fast Reactor Fuel Assemblies," *Nuclear Technology*, Vol. 13, 1972.

5 Collingham, R. E., Thorne, W. L., and McCormack, J. D., "217-Pin Wire-Wrapped Bundle Coolant Mixing Test," HEDL-TME-71-146, Hanford Engineering Development Laboratory, Richland, Wash., 1971.

6 Davidson, R. L., Personal Communication, Atomics International, 1972.

7 Fontana, M. H., MacPherson, R. E., Gnadt, P. A., Wantland, J. L., and Parsley, L. F., "Temperature Distribution in the Duct Wall of a 19-Rod Simulated LMFBR Fuel Assembly," *Trans. American Nuclear Society*, Vol. 15, No. 1, 1972, p. 409–410.

Effect of Viscous Dissipation on Turbulent Forced Convective Heat Transfer

BENJAMIN T. F. CHUNG[1] and LINDON C. THOMAS[1]

DUE TO THE COMPLEXITY of turbulent convective heat transfer processes, the effects of viscous dissipation have generally been ignored or handled by dimensional analysis. There are, however, many engineering applications where the viscous dissipation may become important, such as high speed flow through small conduits, capillary flow, and extrusion processes. Although considerable attention has been given to the dissipation effect on laminar flow [1–4, etc.],[2] little success has been achieved in the analysis of the more complex turbulent flow problem. Recently, a theoretical analysis for the recovery factor of high-speed turbulent flow has been presented by these authors [5] using a basic surface renewal and penetration model. The computed recovery factor from the analysis can be well correlated by a simple expression of the form, $R = \mathrm{Pr}^{0.363}$, which agrees well with the previous experimental data [6, 7]. In this work, the same basic concept is employed to determine the effects of viscous dissipation on the heat transfer coefficient and temperature profile within the wall region; furthermore, a closed form solution for the recovery factor of high speed flow is presented.

Analysis

Consideration is given to the case of heat transfer from a conduit or a flat plate to a turbulent flow. Based on the surface renewal and penetration principle, the following energy equations can be written for a single eddy in contact with the wall when the viscous dissipation is taken into account and the thermal properties of the fluid are assumed constant [5]:

$$\frac{\partial t}{\partial \theta} = \alpha \frac{\partial^2 t}{\partial y^2} + \frac{\nu}{c_p}\left(\frac{\partial u}{\partial y}\right)^2 \quad 0 \le y < \infty$$

The associated initial and boundary conditions are

$$t = T_b \text{ for } \theta = 0,\ y > 0 \tag{2}$$

$$t = T_0 \text{ for } \theta > 0,\ y = 0 \tag{3}$$

$$t = T_b \text{ for } \theta > 0,\ y \to \infty \tag{4}$$

where the subscripts 0 and b indicate the conditions at wall and at bulk or free stream, respectively.

Equation (1) cannot be solved without knowledge of the velocity profile. This, as suggested by Hanratty [8] and Einstein and Li [9], may be achieved by the adaption of the surface renewal principle to momentum transfer, and is given by

$$\frac{u}{U_i} = \mathrm{erf}\,\frac{y}{2\sqrt{\nu\theta}} \tag{5}$$

where U_i is the axial velocity of eddies just prior to contact with the surface and θ represents the instantaneous contact time of eddies. The value of U_i may be reasonably assumed to be equal to the bulk or free stream velocity [10]. Note that equation (5) is derived on the basis of the assumption that $dp/dx = 0$, which is reasonable for tube flow with $\mathrm{Re} > 10^4$ [11].

The mean temperature profile, T, may be obtained from the sum of the individual contributions of eddies of all ages:

$$T = \int_0^\infty t\phi(\theta)d\theta \tag{6}$$

In the present analysis, the random age distribution [12] is employed:

$$\phi(\theta) = \frac{1}{\tau}\exp\left(-\frac{\theta}{\tau}\right) \tag{7}$$

Based on the adaptation of the surface renewal principle to momentum transfer, the mean residence time, τ, associated with turbulent flow for solid-fluid interfaces for $dp/dx \simeq 0$, may be written as

$$\tau = \frac{\nu}{U^{*2} f/2} \tag{8}$$

[1] Department of Mechanical Engineering, University of Akron, Akron, Ohio.

[2] Numbers in brackets designate References at end of technical brief.

Contributed by the Heat Transfer Division of THE AMERICAN SOCIETY OF MECHANICAL ENGINEERS. Manuscript received by the Heat Transfer Division, May 21, 1973.

ponent is the lateral flow increasing the energy exchange between the interior channels and the wall channels in a periodic way. Another contributor to the circumferential ΔT is the changing vertical velocity component of the flow (increasing when the lateral flow is directed toward the wall and decreasing when it is away from the wall) and its effect on the thermal capacitance ($\rho C_p W_Z$) at a given axial elevation. The changing thermal capacitance causes a change in the temperature response of the wall channels for any specified local nuclear fuel addition. The third component is the lateral flow parallel to the housing wall that circumscribes the rod bundle.

Conclusion

A practical solution to the problem of predicting operating temperatures for nuclear fuel assemblies containing wire-wrapped fuel pins spaced in a triangular array has been presented. It has been shown that the flow field predictions for the subpitch length (below 12 in. for these data) agree with experimental data obtained from prototypic LMFBR model fuel assembly tests. The existence of a circumferential temperature gradient in wire-wrapped fuel assemblies independent of a radial nuclear power skew has been demonstrated and verified by Fontana, et al. [7].

References

1 Todreas, N. E., and Rogers J. T., "Coolant Interchannel Mixing in Reactor Fuel Rod Bundles," *Heat Transfer in Rod Bundles*, ASME, New York, 1968.

2 Wantland, J. L., "ØRRIBLE—A Computer Program for Flow and Temperature Distribution in LMFBR Fuel Rod Bundles," ORNL-TM-3516, Oak Ridge National Laboratory, Oak Ridge, Tenn., 1971.

3 Rowe, D. S., "COBRA-III: A Digital Computer Program for Steady State and Transient Thermal-Hydraulic Analysis of Rod Bundle Nuclear Fuel Elements," BNWL-B-82, 1971.

4 Todreas, N. E., and Turi, J. A., "Interchannel Mixing in Wire Wrapped Liquid Metal Fast Reactor Fuel Assemblies," *Nuclear Technology*, Vol. 13, 1972.

5 Collingham, R. E., Thorne, W. L., and McCormack, J. D., "217-Pin Wire-Wrapped Bundle Coolant Mixing Test," HEDL-TME-71-146, Hanford Engineering Development Laboratory, Richland, Wash., 1971.

6 Davidson, R. L., Personal Communication, Atomics International, 1972.

7 Fontana, M. H., MacPherson, R. E., Gnadt, P. A., Wantland, J. L., and Parsley, L. F., "Temperature Distribution in the Duct Wall of a 19-Rod Simulated LMFBR Fuel Assembly," *Trans. American Nuclear Society*, Vol. 15, No. 1, 1972, p. 409–410.

Effect of Viscous Dissipation on Turbulent Forced Convective Heat Transfer

BENJAMIN T. F. CHUNG[1] and LINDON C. THOMAS[1]

DUE TO THE COMPLEXITY of turbulent convective heat transfer processes, the effects of viscous dissipation have generally been ignored or handled by dimensional analysis. There are, however, many engineering applications where the viscous dissipation may become important, such as high speed flow through small conduits, capillary flow, and extrusion processes. Although considerable attention has been given to the dissipation effect on laminar flow [1–4, etc.],[2] little success has been achieved in the analysis of the more complex turbulent flow problem. Recently, a theoretical analysis for the recovery factor of high-speed turbulent flow has been presented by these authors [5] using a basic surface renewal and penetration model. The computed recovery factor from the analysis can be well correlated by a simple expression of the form, $R = \mathrm{Pr}^{0.363}$, which agrees well with the previous experimental data [6, 7]. In this work, the same basic concept is employed to determine the effects of viscous dissipation on the heat transfer coefficient and temperature profile within the wall region; furthermore, a closed form solution for the recovery factor of high speed flow is presented.

Analysis

Consideration is given to the case of heat transfer from a conduit or a flat plate to a turbulent flow. Based on the surface renewal and penetration principle, the following energy equations can be written for a single eddy in contact with the wall when the viscous dissipation is taken into account and the thermal properties of the fluid are assumed constant [5]:

$$\frac{\partial t}{\partial \theta} = \alpha \frac{\partial^2 t}{\partial y^2} + \frac{\nu}{c_p}\left(\frac{\partial u}{\partial y}\right)^2 \quad 0 \leq y < \infty$$

The associated initial and boundary conditions are

$$t = T_b \text{ for } \theta = 0,\ y > 0 \tag{2}$$

$$t = T_0 \text{ for } \theta > 0,\ y = 0 \tag{3}$$

$$t = T_b \text{ for } \theta > 0,\ y \to \infty \tag{4}$$

where the subscripts 0 and b indicate the conditions at wall and at bulk or free stream, respectively.

Equation (1) cannot be solved without knowledge of the velocity profile. This, as suggested by Hanratty [8] and Einstein and Li [9], may be achieved by the adaption of the surface renewal principle to momentum transfer, and is given by

$$\frac{u}{U_i} = \mathrm{erf}\,\frac{y}{2\sqrt{\nu\theta}} \tag{5}$$

where U_i is the axial velocity of eddies just prior to contact with the surface and θ represents the instantaneous contact time of eddies. The value of U_i may be reasonably assumed to be equal to the bulk or free stream velocity [10]. Note that equation (5) is derived on the basis of the assumption that $dp/dx = 0$, which is reasonable for tube flow with $\mathrm{Re} > 10^4$ [11].

The mean temperature profile, T, may be obtained from the sum of the individual contributions of eddies of all ages:

$$T = \int_0^\infty t\phi(\theta)d\theta \tag{6}$$

In the present analysis, the random age distribution [12] is employed:

$$\phi(\theta) = \frac{1}{\tau}\exp\left(-\frac{\theta}{\tau}\right) \tag{7}$$

Based on the adaptation of the surface renewal principle to momentum transfer, the mean residence time, τ, associated with turbulent flow for solid-fluid interfaces for $dp/dx \simeq 0$, may be written as

$$\tau = \frac{\nu}{U^{*2}f/2} \tag{8}$$

[1] Department of Mechanical Engineering, University of Akron, Akron, Ohio.

[2] Numbers in brackets designate References at end of technical brief.

Contributed by the Heat Transfer Division of THE AMERICAN SOCIETY OF MECHANICAL ENGINEERS. Manuscript received by the Heat Transfer Division, May 21, 1973.

where U^* is the friction velocity and f is the Fanning friction factor.

The local mean heat-transfer coefficient, h, is defined by

$$h = \frac{-k}{T_0 - T_b} \left.\frac{\partial T}{\partial y}\right|_{y=0} \tag{9}$$

Solving equations (1) through (9) by using either the Fourier integral transform or the Boltzmann transform, one obtains expressions for mean Nusselt number, Nu, and dimensionless temperature profile, T^+, of the forms [13]

$$\mathrm{Nu} = \frac{f}{2} \mathrm{Re}\sqrt{\mathrm{Pr}}\,(1 - G) \tag{10}$$

$$T^+ = \frac{(T_0 - T)\rho C_p U^*}{g_0} = \frac{\sqrt{2 \cdot \mathrm{Pr}/f}}{1 - G} \times \left\{1 - \exp\left[-y^+\sqrt{\mathrm{Pr} \cdot f/2}\right] - \frac{A}{\sqrt{\mathrm{Pr}}} \times \int_{\eta=0}^{\infty} e^{-\eta} \int_0^{\eta} \frac{\exp\left\{-y^{+2} \frac{f}{2} \mathrm{Pr}/2[(\mathrm{Pr} - 2)\xi + 2\eta]\right\}}{\sqrt{[(\mathrm{Pr} - 2)\xi + 2\eta]\xi}} \times \mathrm{erf}\left[\frac{y^+\mathrm{Pr}}{2}\sqrt{\frac{\xi f/2}{[(\mathrm{Pr} - 2)\xi + 2\eta](\eta - \xi)}}\right] d\xi d\eta\right\} \tag{11}$$

where $y^+ = \dfrac{yU^*}{\nu}$; the parameters G and A are defined as

$$G = \begin{cases} \dfrac{2A \tan^{-1}\sqrt{\dfrac{2 - \mathrm{Pr}}{\mathrm{Pr}}}}{\sqrt{\mathrm{Pr}(2 - \mathrm{Pr})}} & \text{for } \mathrm{Pr} < 2 \\ \dfrac{A \log\left|\dfrac{1 + \sqrt{1 - 2/\mathrm{Pr}}}{1 - \sqrt{1 - 2/\mathrm{Pr}}}\right|}{\sqrt{\mathrm{Pr}(\mathrm{Pr} - 2)}} & \text{for } \mathrm{Pr} > 2 \\ A & \text{for } \mathrm{Pr} = 2 \end{cases} \tag{12}$$

$$A = \frac{\mu U_b^2}{(T_0 - T_b)\pi k} = \frac{\mathrm{Br}}{\pi} \tag{13}$$

and Br is the Brinkman number. For a high speed flow, it is customary to replace the T_b in equation (9) by T_{a0}, the adiabatic wall temperature, i.e.,

$$\mathcal{K} = -k \left.\frac{\partial T}{\partial y}\right|_{y=0} \Big/ (T_0 - T_{a0}), \quad \text{or} \quad \mathfrak{N}\mathrm{u} = \frac{\mathcal{K}D}{k} \tag{14}$$

T_{a0} may be expressed in terms of recovery factor as

$$T_{a0} = T_b + R \frac{U_b^2}{2c_p} \tag{15}$$

The conventional Nusselt number for high speed flow, $\mathfrak{N}\mathrm{u}$, is solved from equations (1) through (8), and equations (14), to give [13]

$$\mathfrak{N}\mathrm{u} = \frac{f}{2} \mathrm{Re}\sqrt{\mathrm{Pr}} \tag{16}$$

Combining equations (10), (12), (15), and (16) yields a closed form solution for the recovery factor in terms of Prandtl number as

$$R = \begin{cases} \dfrac{4}{\pi}\sqrt{\dfrac{\mathrm{Pr}}{2 - \mathrm{Pr}}} \tan^{-1}\sqrt{\dfrac{2 - \mathrm{Pr}}{\mathrm{Pr}}} & \text{for } \mathrm{Pr} < 2 \\ \dfrac{2}{\pi}\sqrt{\dfrac{\mathrm{Pr}}{\mathrm{Pr} - 2}} \log_e\left|\dfrac{1 + \sqrt{1 - 2/\mathrm{Pr}}}{1 - \sqrt{1 - 2/\mathrm{Pr}}}\right| & \text{for } \mathrm{Pr} > 2 \\ \dfrac{4}{\pi} & \text{for } \mathrm{Pr} = 2 \end{cases} \tag{17}$$

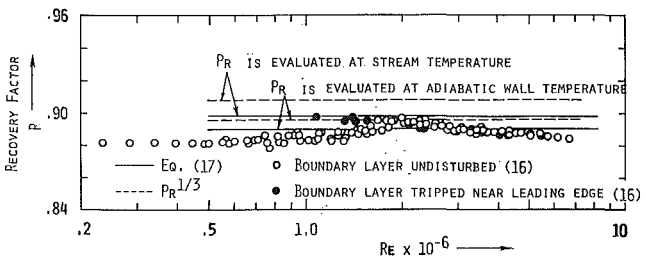

Fig. 1 Dissipation effects on temperature profile for tube flow

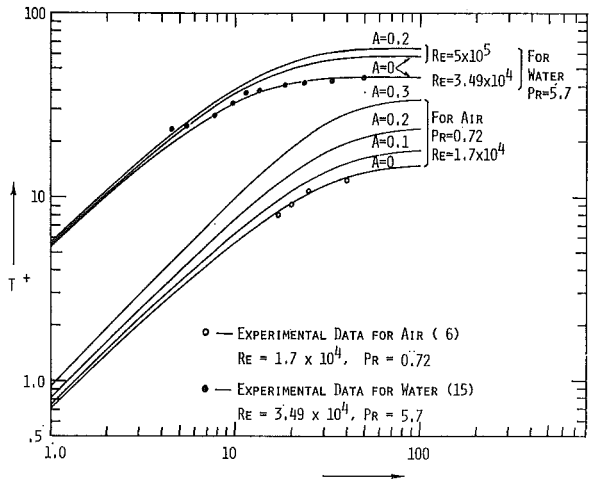

Fig. 2 Comparison of present analysis with experimental data and other correlations

Discussion

As in the case for heat transfer associated with laminar flow, the Brinkman number, Br, characterizes the effect of viscous dissipation in turbulent pipe flow. This effect may be represented by Nu/Nu′, the ratio of predicted Nusselt number to the Nusselt number without heat dissipation. Numerical computations reveal that Nu/Nu′ decreases as A increases; Nu/Nu′ is more sensitive to Brinkman number for low Prandtl numbers than for high Prandtl numbers. Fig. 1 illustrates the dimensionless temperature profile for water and air at different values of the Reynolds number and the parameter A. It is seen that the temperature profile of the air raises appreciably when A increases from 0 to 0.3. The experimental results by Deissler and Eian [13], and Gowen and Smith [14] are also included in Fig. 1. The values of A in these experimental studies are insignificantly small.

The proposed expression for recovery factor given by equation (17) is found to be in excellent agreement with the earlier prediction [5]. The results from equation (17) are compared in Fig. 2 with the experimental data for flow of air over a flat plate [16] and with the semiempirical relationship $R = \mathrm{Pr}^{1/3}$. The Prandtl number is evaluated at both adiabatic wall temperature and free stream temperature. As can be seen, this analysis agrees well with various experimental findings [6, 7, 16].

Lelchuk [18] has presented experimental heat transfer and friction factor results for the high speed flow of air in tubes. The data fit a Reynolds analogy of the form

$$\mathfrak{N}\mathrm{u} = 0.0364\,(\mathrm{RePr})^{0.76} \tag{18}$$

in which the friction coefficient given by $f = 0.079\,\mathrm{Re}^{-0.25}$ is employed. Applying the same expression for the friction coeffi-

cient and setting Pr = 0.72 for air, equation (16) can be approximately written as $\mathfrak{N}u = 0.0428\ (\mathrm{RePr})^{0.75}$, which is 17.5 percent higher in comparison with equation (18). The overprediction of the Nusselt number in the present analysis is partially due to the assumption that the instantaneous temperature of eddies just prior to contact with the wall is set equal to T_b. This assumption is reasonable for all liquids (except liquid metals) but may introduce a slight error for gases. Note that part of the temperature drop of gases is beyond the wall region (see Fig. 1).

The experimental study by Popovich and Hummel [18] has indicated that the turbulent eddies generally do not move into direct contact with the wall. Consequently, the basic surface renewal model becomes inappropriate for fluids with high Prandtl number [19]. Although the application of the present model is restricted to fluids with moderate Prandtl numbers ($0.5 \lesssim \mathrm{Pr} \lesssim 5$), this analysis provides a foundation for modeling turbulent heat transfer to high Prandtl number fluids.

Acknowledgment

This study was supported in part by the National Science Foundation under grant GK-35883. The authors wish to acknowledge Mr. Y. Pang for his assistance in numerical computations.

References

1 Brinkman, H. C., "Heat Effects in Capillary Flow—I," *Appl. Sci. Res. Sec. A*, Vol. 2, 1951, p. 120.

2 Bird, R. B., and Turian, R. M., "Viscous Heating Effects in a Cone and Plate Viscometer—I," *Chem. Eng. Sci.*, Vol. 17, 1962, p. 331.

3 Iqbal, M., Aggarwala, B. D., and Rokerya, M. S., "Viscous Dissipation Effects on Combined Free and Forced Convection Through Vertical Circular Tubes," *Journal of Applied Mechanics*, Vol. 37, TRANS. ASME, Vol. 92, Series E, 1970, p. 931.

4 Huang, C. L., Knieper, P. J., and Fan, L. T., "Effects of Viscous Dissipation on Heat Transfer Parameters for Flow Between Parallel Plates," *ZAMP*, Vol. 16, 1965, p. 599.

5 Thomas, L. C., and Chung, B. T. F., "A Theoretical Analysis of the Recovery Factor for High Speed Turbulent Flow," JOURNAL OF HEAT TRANSFER, TRANS. ASME, Series C, Vol. 95, 1973, p. 272.

6 Deissler R. G. Weiland, W. F., and Lowdermilk, W. H., "Analytical and Experimental Investigation of Temperature Recovery Factors for Fully Developed Flow of Air in Tube," NACA TN 4376, 1958.

7 Schilichting, H., *Boundary Layer Theory*, McGraw-Hill, New York, 1968.

8 Hanratty, T. J., "Turbulent Exchange of Mass and Momentum With Boundary," *AIChE Journal*, Vol. 2, 1956, p. 359.

9 Einstein, H. A., and Li, H., "The Viscous Sublayer Along a Smooth Boundary," *Proc. ASCE J. Eng. Mech. Div.*, Vol. 82, EM2, No. 1 1956.

10 Thomas, L. C., "Temperature Profiles for Liquid Metals and Moderate Prandtl-Number Fluid," JOURNAL OF HEAT TRANSFER, TRANS. ASME, Series C, Vol. 92, 1970, p. 565.

11 Gross, R. J., and Thomas, L. C., "Significance of the Pressure Gradient on Fully Developed Turbulent Flow in a Pipe," JOURNAL OF HEAT TRANSFER, TRANS. ASME, Series C, Vol. 94, 1972, p. 494.

12 Danckwerts, P. V., "Significance of Liquid-Film Coefficients in Gas Absorption," *I.&E.C.*, Vol. 43, 1951, p. 1460.

13 Chung, B. T. F., and Thomas, L. C., "Effect of Viscous Dissipation on Turbulent Forced Convection Heat Transfer," Research Report, University of Akron, Akron, Ohio, 1973.

14 Deissler, R. G., and Eian, C. S., "Analytical and Experimental Investigation of Fully Developed Turbulent Flow of Air in a Smooth Tube With Heat Transfer With Variable Fluid Properties," NACA TN 2629, 1952.

15 Gowen, R. A. and Smith, J. W., "The Effect of Prandtl Number on Temperature Profiles for Heat Transfer in Turbulent Pipe Flow," *Chem. Eng. Sci.*, Vol. 22, 1967, p. 1701.

16 Stalder, J. R., Rubesin, M. W., and Tendeland, T., "A Determination of the Laminar, Transitional and Turbulent-Boundary-Layer Temperature Recovery Factors on a Flat Plate in Supersonic Flow," NACA TN 2077, 1950.

17 Lelchuk, V. L., "Heat Transfer and Hydraulic Flow Resistance for Streams of High Velocity," NACA TM 1054, 1943.

18 Popovich, A. T., and Hummel, R. L., "Experimental Study of the Viscous Sublayer in Turbulent Pipe Flow," *AIChE Journal*, Vol. 13, 1967, p. 854.

19 Thomas, L. C., Chung, B. T. F., and Mahaldar, S. K., "Temperature Profiles for Turbulent Flow of High Prandtl Number Fluids," *International Journal of Heat and Mass Transfer*, Vol. 14, 1971, p. 1665.

A Simplified Model for Stagnation Heat Transfer and Ignition of a Gaseous Mixture

A. ALKIDAS[1] and P. DURBETAKI[2]

Nomenclature

a = coefficient of the potential flow velocity
B = overall frequency factor
c_p = specific heat at constant pressure
D = mass diffusivity
$\bar{D}_{\mathrm{I}}$ = $(1/2)\nu_0 Y_{F,e}(B\rho_e/a)$, Damköhler's first dimensionless group
$\bar{D}_{\mathrm{I},i}$ = ignition first Damköhler number
$\bar{D}_{\mathrm{II}}$ = $q^0 Y_{F,e}/c_{p,e}T_e\nu_F W_F$, Damköhler's second dimensionless group
E = activation energy
E^* = dimensionless activation energy, E/RT_e
k = thermal conductivity
Le = Lewis number, $\rho_e D c_{p,e}/k_e$
$\mathbf{n}$ = unit surface vector
n_e = dimensionless "stoichiometry" $(Y_{0,e}\nu_F W_F/Y_{F,e}\nu_0 W_0) - 1$
Nu = Nusselt number, $q_w x/k(T_e - T_w)$
Pr = Prandtl number, $c_{p,e}\mu_e/k_e$
q^0 = standard heat of reaction
R = universal gas constant
Re = Reynolds number, $\rho_e u_e x/\mu_e$
T = temperature
u = component of velocity in x-direction
W_i = molecular weight of species i
x = distance along surface
y = distance normal to surface
Y_i = mass fraction of species i
α_i = $Y_i/Y_{i,e}$
δ = boundary layer thickness
θ = dimensionless temperature, T/T_e
μ = viscosity
ν_i = stoichiometric coefficient of species i
ρ = density

Subscripts

e = free stream
F = fuel
i = species i
O = oxidant
w = at the wall surface

THE HEAT INTERACTION between a combustible mixture and a constant temperature surface, as well as the ignition of the premixed gases by the hot surface, have been investigated and results calculated with extensive numerical computations [1–3].[3] This note presents a simplified analytical model analogous to the present thermal theories and it is applied to three types of boundary layer flows: (i) planar stagnation flow, (ii) axisymmetric stagnation flow, and (iii) flow over a flat plate.

In order to obtain a simple expression describing the ignition process of a premixed gas by a hot surface the following two primary assumptions were made: (*a*) the chemical reaction occurs in a stagnant film near the wall of the heated body, and (*b*)

[1] Guggenheim Laboratories, Princeton University, Princeton, N. J.

[2] Associate Professor, School of Mechanical Engineering, Georgia Institute of Technology, Atlanta, Ga. Mem. ASME.

[3] Numbers in brackets designate References at end of technical brief.

Contributed by the Heat Transfer Division of THE AMERICAN SOCIETY OF MECHANICAL ENGINEERS. Manuscript received by the Heat Transfer Division, May 22, 1973.

cient and setting Pr = 0.72 for air, equation (16) can be approximately written as $\mathfrak{Nu} = 0.0428\ (\mathrm{RePr})^{0.75}$, which is 17.5 percent higher in comparison with equation (18). The overprediction of the Nusselt number in the present analysis is partially due to the assumption that the instantaneous temperature of eddies just prior to contact with the wall is set equal to T_b. This assumption is reasonable for all liquids (except liquid metals) but may introduce a slight error for gases. Note that part of the temperature drop of gases is beyond the wall region (see Fig. 1).

The experimental study by Popovich and Hummel [18] has indicated that the turbulent eddies generally do not move into direct contact with the wall. Consequently, the basic surface renewal model becomes inappropriate for fluids with high Prandtl number [19]. Although the application of the present model is restricted to fluids with moderate Prandtl numbers ($0.5 \lesssim \mathrm{Pr} \lesssim 5$), this analysis provides a foundation for modeling turbulent heat transfer to high Prandtl number fluids.

Acknowledgment

This study was supported in part by the National Science Foundation under grant GK-35883. The authors wish to acknowledge Mr. Y. Pang for his assistance in numerical computations.

References

1 Brinkman, H. C., "Heat Effects in Capillary Flow—I," *Appl. Sci. Res. Sec. A*, Vol. 2, 1951, p. 120.

2 Bird, R. B., and Turian, R. M., "Viscous Heating Effects in a Cone and Plate Viscometer—I," *Chem. Eng. Sci.*, Vol. 17, 1962, p. 331.

3 Iqbal, M., Aggarwala, B. D., and Rokerya, M. S., "Viscous Dissipation Effects on Combined Free and Forced Convection Through Vertical Circular Tubes," *Journal of Applied Mechanics*, Vol. 37, TRANS. ASME, Vol. 92, Series E, 1970, p. 931.

4 Huang, C. L., Knieper, P. J., and Fan, L. T., "Effects of Viscous Dissipation on Heat Transfer Parameters for Flow Between Parallel Plates," *ZAMP*, Vol. 16, 1965, p. 599.

5 Thomas, L. C., and Chung, B. T. F., "A Theoretical Analysis of the Recovery Factor for High Speed Turbulent Flow," JOURNAL OF HEAT TRANSFER, TRANS. ASME, Series C, Vol. 95, 1973, p. 272.

6 Deissler R. G. Weiland, W. F., and Lowdermilk, W. H., "Analytical and Experimental Investigation of Temperature Recovery Factors for Fully Developed Flow of Air in Tube," NACA TN 4376, 1958.

7 Schilichting, H., *Boundary Layer Theory*, McGraw-Hill, New York, 1968.

8 Hanratty, T. J., "Turbulent Exchange of Mass and Momentum With Boundary," *AIChE Journal*, Vol. 2, 1956, p. 359.

9 Einstein, H. A., and Li, H., "The Viscous Sublayer Along a Smooth Boundary," *Proc. ASCE J. Eng. Mech. Div.*, Vol. 82, EM2, No. 1 1956.

10 Thomas, L. C., "Temperature Profiles for Liquid Metals and Moderate Prandtl-Number Fluid," JOURNAL OF HEAT TRANSFER, TRANS. ASME, Series C, Vol. 92, 1970, p. 565.

11 Gross, R. J., and Thomas, L. C., "Significance of the Pressure Gradient on Fully Developed Turbulent Flow in a Pipe," JOURNAL OF HEAT TRANSFER, TRANS. ASME, Series C, Vol. 94, 1972, p. 494.

12 Danckwerts, P. V., "Significance of Liquid-Film Coefficients in Gas Absorption," *I.&E.C.*, Vol. 43, 1951, p. 1460.

13 Chung, B. T. F., and Thomas, L. C., "Effect of Viscous Dissipation on Turbulent Forced Convection Heat Transfer," Research Report, University of Akron, Akron, Ohio, 1973.

14 Deissler, R. G., and Eian, C. S., "Analytical and Experimental Investigation of Fully Developed Turbulent Flow of Air in a Smooth Tube With Heat Transfer With Variable Fluid Properties," NACA TN 2629, 1952.

15 Gowen, R. A. and Smith, J. W., "The Effect of Prandtl Number on Temperature Profiles for Heat Transfer in Turbulent Pipe Flow," *Chem. Eng. Sci.*, Vol. 22, 1967, p. 1701.

16 Stalder, J. R., Rubesin, M. W., and Tendeland, T., "A Determination of the Laminar, Transitional and Turbulent-Boundary-Layer Temperature Recovery Factors on a Flat Plate in Supersonic Flow," NACA TN 2077, 1950.

17 Lelchuk, V. L., "Heat Transfer and Hydraulic Flow Resistance for Streams of High Velocity," NACA TM 1054, 1943.

18 Popovich, A. T., and Hummel, R. L., "Experimental Study of the Viscous Sublayer in Turbulent Pipe Flow," *AIChE Journal*, Vol. 13, 1967, p. 854.

19 Thomas, L. C., Chung, B. T. F., and Mahaldar, S. K., "Temperature Profiles for Turbulent Flow of High Prandtl Number Fluids," *International Journal of Heat and Mass Transfer*, Vol. 14, 1971, p. 1665.

A Simplified Model for Stagnation Heat Transfer and Ignition of a Gaseous Mixture

A. ALKIDAS[1] and P. DURBETAKI[2]

Nomenclature

a = coefficient of the potential flow velocity
B = overall frequency factor
c_p = specific heat at constant pressure
D = mass diffusivity
$\bar{D}_{\mathrm{I}}$ = $(1/2)\nu_0 Y_{F,e}(B\rho_e/a)$, Damköhler's first dimensionless group
$\bar{D}_{\mathrm{I},i}$ = ignition first Damköhler number
$\bar{D}_{\mathrm{II}}$ = $q^0 Y_{F,e}/c_{p,e}T_e\nu_F W_F$, Damköhler's second dimensionless group
E = activation energy
E^* = dimensionless activation energy, E/RT_e
k = thermal conductivity
Le = Lewis number, $\rho_e D c_{p,e}/k_e$
$\mathbf{n}$ = unit surface vector
n_e = dimensionless "stoichiometry" $(Y_{0,e}\nu_F W_F/Y_{F,e}\nu_0 W_0) - 1$
Nu = Nusselt number, $q_w x/k(T_e - T_w)$
Pr = Prandtl number, $c_{p,e}\mu_e/k_e$
q^0 = standard heat of reaction
R = universal gas constant
Re = Reynolds number, $\rho_e u_e x/\mu_e$
T = temperature
u = component of velocity in x-direction
W_i = molecular weight of species i
x = distance along surface
y = distance normal to surface
Y_i = mass fraction of species i
α_i = $Y_i/Y_{i,e}$
δ = boundary layer thickness
θ = dimensionless temperature, T/T_e
μ = viscosity
ν_i = stoichiometric coefficient of species i
ρ = density

Subscripts

e = free stream
F = fuel
i = species i
O = oxidant
w = at the wall surface

THE HEAT INTERACTION between a combustible mixture and a constant temperature surface, as well as the ignition of the premixed gases by the hot surface, have been investigated and results calculated with extensive numerical computations [1–3].[3] This note presents a simplified analytical model analogous to the present thermal theories and it is applied to three types of boundary layer flows: (i) planar stagnation flow, (ii) axisymmetric stagnation flow, and (iii) flow over a flat plate.

In order to obtain a simple expression describing the ignition process of a premixed gas by a hot surface the following two primary assumptions were made: (*a*) the chemical reaction occurs in a stagnant film near the wall of the heated body, and (*b*)

[1] Guggenheim Laboratories, Princeton University, Princeton, N. J.

[2] Associate Professor, School of Mechanical Engineering, Georgia Institute of Technology, Atlanta, Ga. Mem. ASME.

[3] Numbers in brackets designate References at end of technical brief.

Contributed by the Heat Transfer Division of THE AMERICAN SOCIETY OF MECHANICAL ENGINEERS. Manuscript received by the Heat Transfer Division, May 22, 1973.

the heat transfer by convection is independent of the chemical reaction. Both assumptions were originally used by Khitrin and Goldenberg [4] to develop the thermal theory of ignition of flowing combustible mixtures.

First, we consider the heat transfer due to the chemical reaction alone. The energy conservation equation of the stagnant film is

$$\frac{d}{dy}\left(k\frac{d\theta}{dy}\right) = -q^0\left(\frac{1}{T_e}\right)B\rho^2 Y_{O,e}Y_{F,e}\alpha_O\alpha_F e^{-E^*/\theta} \quad (1a)$$

The boundary conditions are

$$\text{at } y = 0: \quad \theta = \theta_w, \text{ and at } y = \delta: \quad \theta = 1 \quad (1b)$$

Equation (1) can be integrated with respect to the temperature θ to give the surface heat transfer due to chemical reaction. Assuming that the biggest contribution of the reaction is near the wall where the temperature is the highest, from equation (1) the temperature gradient at the surface can be approximated as

$$\left(\frac{d\theta}{dy}\right)_w = \left[\frac{2q^0B\rho w^2 Y_{O,e}Y_{F,e}(\alpha_O\alpha_F)_w}{k_wT_e}\int_1^{\theta_w} e^{-E^*/\theta}d\theta\right]^{1/2} \quad (2a)$$

In the first approximation the integral of equation (2a) can be evaluated as

$$\int_1^{\theta_w} e^{-E^*/\theta}d\theta \approx \frac{\theta_w^2}{E^*}e^{-E^*/\theta_w} \quad (2b)$$

From the foregoing two equations the surface heat transfer due to chemical reaction in dimensionless form becomes

$$\mathrm{Nu}_{ch} = 2[(1+n_e)\,\mathrm{Pr}\,\bar{D}_I\bar{D}_{II}(\alpha_O\alpha_F)_w\theta_w/E^*]^{1/2} \times \frac{e^{-E^*/2\theta_w}}{\theta_w - 1}(\mathrm{Re})^{1/2} \quad (2c)$$

Utilizing the second of the primary assumptions, the convective heat transfer can be expressed in the following general form

$$\mathrm{Nu}_{con} = \beta\mathrm{Pr}^n\mathrm{Re}^m \quad (3)$$

where the values of β, n, and m depend on the geometry of the boundary layer considered and whether the flow is laminar or turbulent.

In this simplified approach, the Van't Hoff ignition criterion, $\partial\theta/\partial n = 0$ can be written as

$$\mathrm{Nu}_{con} = \mathrm{Nu}_{ch} \quad (4)$$

The unknown quantities $\alpha_{O,w}$ and $\alpha_{F,w}$ are expressed in terms of known properties of the system. From the species conservation equations subject to the boundary conditions, the oxidizer and fuel mass fractions are linearly related by the equation

$$\alpha_O = 1 - (1+\alpha_F)/(n_e+1) \quad (5)$$

and in the case of $\mathrm{Le} = 1$ the fuel mass fraction and the temperature are related by [5]

$$\alpha_F = \bar{D}_{II}(1 + \bar{D}_{II} - \theta) \quad (6)$$

The Van't Hoff criterion with equations (5) and (6) give

$$\bar{D}_{I,i} = \frac{(\beta/2)^2\,(\mathrm{Pr})^{2n-1}\,(\mathrm{Re})^{2m-1}\,(\theta_w - 1)^2\bar{D}_{II}E^*e^{E^*/\theta_w}}{\theta_w(\bar{D}_{II} + 1 - \theta_w)(\bar{D}_{II}(n_e+1) + 1 - \theta_w)} \quad (7)$$

This equation relates the ignition Damköhler number to the ignition temperature, the combustible mixture properties, and the flow geometry. The values of β, n, and m for three geometries are given in Table 1.

Table 1 Values of β, m, and n in equation (3) of three geometries

Flow	β	m	n
Flat plate	0.332	0.5	1/3
Planar stagnation	0.57	0.5	0.4
Axisymmetric stagnation	0.763	0.5	0.4

Flat Plate

The ignition of a combustible mixture in the laminar boundary layer of a constant-temperature flat plate has been treated by several investigators [2, 6, 7]. Their aim was to obtain the distance downstream of the leading edge where ignition occurs. The ignition point was identified by the condition that the temperature gradient normal to the wall is zero. Along the characteristic length the plate acts as a heat source and in the remaining part as a heat sink. Toong [7] obtained analytically the characteristic length for two values of the dimensionless wall temperature 3.9 and 4.1. His results are compared with our simplified method in Table 2.

Table 2 Comparison of ignition distance

$\mathrm{Pr} = 0.65 \quad E^* = 5.75 \quad \bar{D}_{II} = 6.64 \quad n_e = 0$

θ_w	$\bar{D}_{I,i}$ Toong [7]	$\bar{D}_{I,i}$ Present method
3.9	0.387×10^7	0.474×10^7
4.1	0.217×10^7	0.280×10^7

An approximate method was derived, also, by Sharma and Sirignano [2]. In our notation their expression for the ignition distance becomes

$$\bar{D}_{I,i} = \gamma(\theta_w - 1)\theta_w e^{E^*/\theta_w} \quad (8)$$

The coefficient γ should be derived from a direct comparison with the exact numerical method or experimental results.

The results from the present method are shown to be fairly accurate compared to Toong's results. Furthermore, since the quantity $\bar{D}_I$ is directly proportional to the distance from the leading edge x, then $\bar{D}_{I,i}$ establishes the length x_i where ignition will occur. This ignition length is overestimated by the present method which is in favor of this approach in view of the fact that in practice ignition will occur further downstream than the theoretically defined ignition point.

Planar Stagnation Flow

Sharma and Sirignano [8], using a second-order Arrhenius law, have numerically solved the plane and axisymmetric reactive stagnation point flows by the method of quasilinearization. For a first order approximation $\bar{D}_{I,i}$ is given by

$$\bar{D}_{I,i} = \frac{0.09\bar{D}_{II}E^*e^{E^*/\theta_w}}{\theta_w(\bar{D}_{II} + 1 - \theta_w)^2} \quad (9)$$

A comparison of Sharma and Sirignano's exact and approximate methods (first and second order approximations) with our method is shown in Table 3.

Table 3 Comparison of ignition temperatures

$\mathrm{Pr} = 0.75 \quad E^* = 28.55 \quad \bar{D}_{II} = 8.84 \quad n_e = 0 \quad \bar{D}_I = 0.5 \times 10^4$

	θ_w
Exact method	3.75
First-order approximation	2.76
Second-order approximation	2.82
Present method	3.26

The present method gives better results than the other approximate equations used. A possible reason for the large deviation from the exact solution is that these approximate methods are valid when E^*/θ_w is much greater than unity. The relative value of this assumption can be seen from a comparison of the first and second approximations. It will be expected that at higher values of the activation energy the present method should give much closer results.

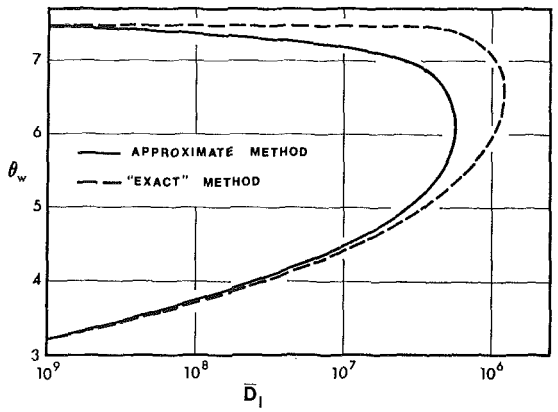

Fig. 1 Ignition temperature versus $\bar{D}_I$, comparison of the approximate and "exact" method

Axisymmetric Stagnation Flow

Fig. 1 shows a plot of the first Damköhler number $\bar{D}_I$ versus the ignition temperature θ_w, obtained from equation (7). For comparison, the corresponding curve obtained by numerically integrating the governing equations was superimposed [5]. It is evident that the approximate method gives excellent results for ignition temperature upto $\theta_w = 5.0$. At higher wall temperatures the correlation breaks down. A possible explanation for the large differences obtained at higher temperatures is that the convective heat transfer correlation used, was obtained for the frozen flow case. As the state of the mixture departs from the frozen limit, equation (7) becomes a crude approximation.

Conclusion

The agreement of the results obtained by the previously described simplified method is of considerable importance in obtaining the ignition temperature of systems with complex patterns. In such systems a complete solution of the governing equations is not practical. In order to obtain a relation similar to equation (7) for such flows, an expression of the frozen convective heat-transfer coefficient is required. Such an expression can be obtained from past literature or through experimentation.

References

1 Alkidas, A., and Durbetaki, P., "Stagnation-Point Heat Transfer: The Effect of the First Damköhler Similarity Parameter," JOURNAL OF HEAT TRANSFER, TRANS. ASME, Series C, Vol. 94, 1972, p. 410.

2 Sharma, O. P., and Sirignano, W. A., "On the Ignition of a Premixed Fuel by a Hot Projectile," *Combustion Science and Technology*, Vol. 1, 1970, p. 481.

3 Smith, H. W., Schmitz, R. A., and Ladd, R. G., "Combustion of a Premixed System in Stagnation Flow—1," *Combustion Science and Technology*, Vol. 4, 1971, p. 131.

4 Khirtin, L. N., and Goldenberg, S. A., "Thermal Theory of Ignition of Gas Mixtures: Limiting Conditions," *Sixth International Symposium on Combustion*, Reinhold Publishing Corp., New York, 1957, p. 545.

5 Alkidas, A., and Durbetaki, P., "Ignition Characteristics of a Stagnation Point Combustible Mixture," *Combustion Science and Technology*, Vol. 3, 1971, p. 187.

6 Dooley, D. A., "Ignition in the Laminar Boundary Layer of a Heated Plate," *Proceedings of the 1957 Heat Transfer and Fluid Mechanics Institute*, Stanford University Press, Stanford, 1957.

7 Toong, T. Y., "Ignition and Combustion in a Laminar Boundary Layer Over a Hot Surface," *Sixth International Symposium on Combustion*, Reinhold Publishing Corp., New York, 1957, p. 532.

8 Sharma, O. P., and Sirignano, W. A., "Ignition of Stagnation Point Flow by a Hot Body," *Combustion Science and Technology*, Vol. 1, 1969, p. 95.

Transport to a Rotating Disk in Turbulent Flow at High Prandtl or Schmidt Number

J. A. PATERSON[1] and R. GREIF[1]

The eddy viscosity distribution near the surface of a rotating disk is determined from an analysis of the basic conservation equations. The results are applied to the high Schmidt number problem and good agreement is obtained with experimental data for the mass flux.

Introduction

THE PROBLEM of interest to us is the determination of the heat or mass transport to a rotating disk in turbulent flow at high Prandtl or Schmidt numbers. In a previous study at high Schmidt numbers, Ellison and Cornet [1][2] applied the eddy diffusivity results from fully developed pipe flow to the rotating disc problem and obtained good agreement with their experimental data for the mass transfer. (Also refer to Kreith [2].) In the present study the basic conservation equations, that is, the equations of continuity, momentum and energy (or diffusion), are applied to a disk that is rotating in a quiescent fluid.

[1] Department of Mechanical Engineering, University of California, Berkeley, Calif.

[2] Numbers in brackets designate References at end of technical brief.

Contributed by the Heat Transfer Division of THE AMERICAN SOCIETY OF MECHANICAL ENGINEERS. Manuscript received by the Heat Transfer Division, May 3, 1973.

Eddy Transport of Momentum

The boundary layer equations for steady, incompressible, three-dimensional, axisymmetric turbulent flow near a rotating disk in the absence of a radial pressure gradient can be written in cylindrical coordinates as follows:

$$\frac{V_r \partial V_r}{\partial r} - \frac{V_\phi^2}{r} + \frac{V_z \partial V_r}{\partial z} = \frac{\nu \partial^2 V_r}{\partial z^2} - \frac{\partial}{\partial z}\overline{v_r' v_z'} \tag{1}$$

$$\frac{V_r \partial V_\phi}{\partial r} + \frac{V_r V_\phi}{r} + \frac{V_z \partial V_\phi}{\partial z} = \frac{\nu \partial^2 V_\phi}{\partial z^2} - \frac{\partial}{\partial z}\overline{v_z' v_\phi'} \tag{2}$$

$$\frac{1}{r}\frac{\partial (r V_r)}{\partial r} + \frac{\partial V_z}{\partial z} = 0 \tag{3}$$

$$\frac{1}{r}\frac{\partial (r v_r')}{\partial r} + \frac{\partial v_z'}{\partial z} + \frac{1}{r}\frac{\partial v_\phi'}{\partial \phi} = 0 \tag{4}$$

with boundary conditions $V_r = V_z = v_r' = v_z' = v\phi' = 0$, and $V\phi = r\omega$, at $z = 0$; $V_r = V\phi = 0$ at $z = \infty$. The complete equations are presented in Dorfman [8] and an order of magnitude analysis yields the foregoing results (cf. Margolis and Lumley [14]).

Following Tien, Wasan, and Wilke [3, 4, 5] the mean and fluctuating velocities near the surface are expanded in a Taylor series:

$$V_r(r, z) = R_0 + R_1 z + \ldots; \quad V\phi(r, z) = \Phi_0 + \Phi_1 z + \ldots;$$
$$V_z(r, z) = Z_0 + Z_1 z + \ldots; \quad v_r'(r, z, \phi, t) = r_0 + r_1 z + \ldots;$$
$$v\phi'(r, z, \phi, t) = \phi_0 + \phi_1 z + \ldots;$$
$$v_z'(r, z, \phi, t) = z_0 + z_1 z + \ldots \tag{5}$$

From the boundary conditions we have $R_0 = Z_0 = r_0 = \phi_0 =$

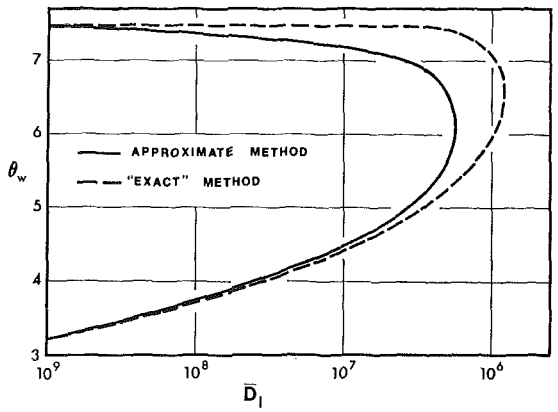

Fig. 1 Ignition temperature versus $\bar{D}_I$, comparison of the approximate and "exact" method

Axisymmetric Stagnation Flow

Fig. 1 shows a plot of the first Damköhler number $\bar{D}_I$ versus the ignition temperature θ_w, obtained from equation (7). For comparison, the corresponding curve obtained by numerically integrating the governing equations was superimposed [5]. It is evident that the approximate method gives excellent results for ignition temperature upto $\theta_w = 5.0$. At higher wall temperatures the correlation breaks down. A possible explanation for the large differences obtained at higher temperatures is that the convective heat transfer correlation used, was obtained for the frozen flow case. As the state of the mixture departs from the frozen limit, equation (7) becomes a crude approximation.

Conclusion

The agreement of the results obtained by the previously described simplified method is of considerable importance in obtaining the ignition temperature of systems with complex patterns. In such systems a complete solution of the governing equations is not practical. In order to obtain a relation similar to equation (7) for such flows, an expression of the frozen convective heat-transfer coefficient is required. Such an expression can be obtained from past literature or through experimentation.

References

1 Alkidas, A., and Durbetaki, P., "Stagnation-Point Heat Transfer: The Effect of the First Damköhler Similarity Parameter," JOURNAL OF HEAT TRANSFER, TRANS. ASME, Series C, Vol. 94, 1972, p. 410.

2 Sharma, O. P., and Sirignano, W. A., "On the Ignition of a Premixed Fuel by a Hot Projectile," *Combustion Science and Technology*, Vol. 1, 1970, p. 481.

3 Smith, H. W., Schmitz, R. A., and Ladd, R. G., "Combustion of a Premixed System in Stagnation Flow—1," *Combustion Science and Technology*, Vol. 4, 1971, p. 131.

4 Khirtin, L. N., and Goldenberg, S. A., "Thermal Theory of Ignition of Gas Mixtures: Limiting Conditions," *Sixth International Symposium on Combustion*, Reinhold Publishing Corp., New York, 1957, p. 545.

5 Alkidas, A., and Durbetaki, P., "Ignition Characteristics of a Stagnation Point Combustible Mixture," *Combustion Science and Technology*, Vol. 3, 1971, p. 187.

6 Dooley, D. A., "Ignition in the Laminar Boundary Layer of a Heated Plate," *Proceedings of the 1957 Heat Transfer and Fluid Mechanics Institute*, Stanford University Press, Stanford, 1957.

7 Toong, T. Y., "Ignition and Combustion in a Laminar Boundary Layer Over a Hot Surface," *Sixth International Symposium on Combustion*, Reinhold Publishing Corp., New York, 1957, p. 532.

8 Sharma, O. P., and Sirignano, W. A., "Ignition of Stagnation Point Flow by a Hot Body," *Combustion Science and Technology*, Vol. 1, 1969, p. 95.

Transport to a Rotating Disk in Turbulent Flow at High Prandtl or Schmidt Number

J. A. PATERSON[1] and R. GREIF[1]

The eddy viscosity distribution near the surface of a rotating disk is determined from an analysis of the basic conservation equations. The results are applied to the high Schmidt number problem and good agreement is obtained with experimental data for the mass flux.

Introduction

THE PROBLEM of interest to us is the determination of the heat or mass transport to a rotating disk in turbulent flow at high Prandtl or Schmidt numbers. In a previous study at high Schmidt numbers, Ellison and Cornet [1][2] applied the eddy diffusivity results from fully developed pipe flow to the rotating disc problem and obtained good agreement with their experimental data for the mass transfer. (Also refer to Kreith [2].) In the present study the basic conservation equations, that is, the equations of continuity, momentum and energy (or diffusion), are applied to a disk that is rotating in a quiescent fluid.

[1] Department of Mechanical Engineering, University of California, Berkeley, Calif.

[2] Numbers in brackets designate References at end of technical brief.

Contributed by the Heat Transfer Division of THE AMERICAN SOCIETY OF MECHANICAL ENGINEERS. Manuscript received by the Heat Transfer Division, May 3, 1973.

Eddy Transport of Momentum

The boundary layer equations for steady, incompressible, three-dimensional, axisymmetric turbulent flow near a rotating disk in the absence of a radial pressure gradient can be written in cylindrical coordinates as follows:

$$\frac{V_r \partial V_r}{\partial r} - \frac{V_\phi^2}{r} + \frac{V_z \partial V_r}{\partial z} = \frac{\nu \partial^2 V_r}{\partial z^2} - \frac{\partial}{\partial z}\overline{v_r' v_z'} \tag{1}$$

$$\frac{V_r \partial V_\phi}{\partial r} + \frac{V_r V_\phi}{r} + \frac{V_z \partial V_\phi}{\partial z} = \frac{\nu \partial^2 V_\phi}{\partial z^2} - \frac{\partial}{\partial z}\overline{v_z' v_\phi'} \tag{2}$$

$$\frac{1}{r}\frac{\partial (r V_r)}{\partial r} + \frac{\partial V_z}{\partial z} = 0 \tag{3}$$

$$\frac{1}{r}\frac{\partial (r v_r')}{\partial r} + \frac{\partial v_z'}{\partial z} + \frac{1}{r}\frac{\partial v_\phi'}{\partial \phi} = 0 \tag{4}$$

with boundary conditions $V_r = V_z = v_r' = v_z' = v\phi' = 0$, and $V\phi = r\omega$, at $z = 0$; $V_r = V\phi = 0$ at $z = \infty$. The complete equations are presented in Dorfman [8] and an order of magnitude analysis yields the foregoing results (cf. Margolis and Lumley [14]).

Following Tien, Wasan, and Wilke [3, 4, 5] the mean and fluctuating velocities near the surface are expanded in a Taylor series:

$$V_r(r, z) = R_0 + R_1 z + \ldots; \quad V\phi(r, z) = \Phi_0 + \Phi_1 z + \ldots;$$
$$V_z(r, z) = Z_0 + Z_1 z + \ldots; \quad v_r'(r, z, \phi, t) = r_0 + r_1 z + \ldots;$$
$$v\phi'(r, z, \phi, t) = \phi_0 + \phi_1 z + \ldots;$$
$$v_z'(r, z, \phi, t) = z_0 + z_1 z + \ldots \tag{5}$$

From the boundary conditions we have $R_0 = Z_0 = r_0 = \phi_0 =$

$z_0 = 0$ and $\Phi_0 = r\omega$. From the conservation equations and expansions we obtain[3] $Z_1 = z_1 = 0$ and

$$\frac{\partial R_n}{\partial r} + \frac{R_n}{r} + (n+1)Z_{n+1} = 0, \tag{6}$$

as well as a corresponding expression for the fluctuating terms. From equation (5) the Reynolds stress components may be obtained; for example,

$$\overline{v_\phi' v_z'} = (\overline{\phi_1 z_2})z^3 + (\overline{\phi_1 z_3} + \overline{\phi_2 z_2})z^4 + \ldots \tag{7}$$

The coefficients may then be determined by integrating the momentum equations with respect to z which yields

$$\overline{v_\phi' v_z'} = \nu(\Phi_1 + 2\Phi_2 z + 3\Phi_3 z^2 + 4\Phi_4 z^3 + \ldots) - \left(\frac{R_1\omega z^2}{2} + \left(\frac{R_1\partial\Phi_1}{\partial r} + R_2\omega\right)\frac{z^3}{3} + \ldots\right) - \frac{1}{r}\left(\frac{R_1 r\omega z^2}{2} + (R_2 r\omega + R_1\Phi_1)\frac{z^3}{3} + \ldots\right) - \left(\frac{Z_2\Phi_1 z^3}{3} + \ldots\right) + f(r) \tag{8}$$

as well as a similar expression for the radial contribution $\overline{v_r' v_z'}$ which has an $F(r)$ term. At the wall, $z = 0$, we require the Reynolds stress components to vanish so that $f(r) = -\nu\Phi_1$, along with the similar result $F(r) = -\nu R_1$. From equations (6), (7), and (8) and the corresponding relations for $\overline{v_r' v_z'}$ we obtain

$$\Phi_2 = 0,\ \Phi_3 = \frac{R_1\omega}{3\nu},\ R_2 = \frac{-r\omega^2}{2\nu},\ R_3 = \frac{-\omega\Phi_1}{3\nu}, \tag{9}$$

$$\overline{\phi_1 z_2} = 4\nu\Phi_4 - \frac{R_1}{3}\frac{\partial\Phi_1}{\partial r} - \frac{2R_2\omega}{3} - \frac{R_1\Phi_1}{6r} + \frac{\Phi_1}{6}\frac{\partial R_1}{\partial r} \tag{10}$$

as well as comparable result for $\overline{r_1 z_2}$.

It is now possible to determine the eddy viscosity for tangential momentum:

$$\frac{\epsilon_{M_1\phi}}{\nu} = -\frac{\overline{v_z' v_\phi'}}{\nu\dfrac{\partial V_\phi}{\partial z}} = \left[\frac{4\nu^4\Phi_4}{u_\tau^5} - \frac{R_1\nu^3}{3u_\tau^5}\frac{\partial\Phi_1}{\partial r} + \frac{r\omega^3\nu^2}{3u_\tau^5} + \frac{R_1\nu^2}{6ru_\tau^3} - \frac{\nu^2}{6u_\tau^3}\frac{\partial R_1}{\partial r}\right] z^{+3} + \ldots \tag{11}$$

where $u_\tau^2 \equiv -\nu(\partial V_\phi/\partial z)_0$ and $z^+ \equiv zu_\tau/\nu$. The functions Φ_1 and R_1 are directly related to the tangential and radial shear stress components on the disk surface according to (cf. equations (5)):

$$\Phi_1 = \left(\frac{\partial V_\phi}{\partial z}\right)_0 = -\frac{\tau_{z\phi}}{\mu},\ R_1 = \left(\frac{\partial V_r}{\partial z}\right)_0 = -\frac{\tau_{zr}}{\mu} \tag{12}$$

Substituting the results for the shear stress components [7, 8] yields

$$\Phi_1 = -0.0267\,\omega\mathrm{Re}_r^{0.8} = -u_\tau^2/\nu,\ R_1 = 0.00433\,\omega\mathrm{Re}_r^{0.8} \tag{13}$$

where the Reynolds number $\mathrm{Re}_r = r^2\omega/\nu$. Using the foregoing results, the tangential eddy viscosity becomes

$$\frac{\epsilon_{M_1\phi}}{\nu} = (4\Phi_4^+ + 0.43\,\mathrm{Re}_r^{-0.9} + 2800\,\mathrm{Re}_r^{-1.5})z^{+3} + \ldots = Gz^{+3} + \ldots \tag{14}$$

where $\Phi_4^+ = \nu^4\Phi_4/u_\tau^5$ and G is the term in parentheses.

Eddy Transport of Heat

We shall now restrict our attention to the high Prandtl number problem for turbulent flow about an isothermal rotating disk. For this condition the essential temperature change takes place in the region very close to the surface and the equation for the conservation of energy is given by

$$\frac{\partial}{\partial z}\left(\frac{\alpha\partial T}{\partial z} - \overline{v_z' t'}\right) = 0 \tag{15}$$

Following the previous analysis we expand the mean and fluctuating temperatures near the surface in a Taylor series

$$T(r, z) = T_0 + T_1 z + \ldots,\ t'(r, z, \phi, t) = t_0 + t_1 z + \ldots \tag{16}$$

and note that $t_0 = 0$. Then, from equations (15), (16) and equation (5) for v_z' we obtain

$$T_2 = T_3 = 0,\quad \overline{z_2 t_1} = 4\alpha T_4, \text{ etc.}, \tag{17}$$

so that the eddy flux term becomes

$$\overline{v_z' t'} = (\overline{t_1 z_2})z^3 + (\overline{t_1 z_3} + \overline{t_2 z_2})z^4 + \ldots \tag{18}$$

The mean temperature, T, and the dimensionless temperature, T^+, are given by

$$T = T_0 + T_1 z + T_4 z^4 + \ldots,$$

$$T^+ = \frac{T\rho c u_\tau}{q_0} = T_0^+ - \mathrm{Pr}z^+ + T_4^+ z^{+4} + \ldots, \tag{19}$$

with

$$T_1 = (\partial T/\partial z)_0 = -q_0/k,\ T_4^+ = T_4\rho c\nu^4/q_0 u_\tau^3 \tag{20}$$

Thus, the eddy diffusivity for heat transport, ϵ_H, is given by

$$\frac{\epsilon_H}{\nu} = \frac{\overline{-v_z' t'}}{\nu\dfrac{\partial T}{\partial z}} = \left(\frac{4T_4^+}{\mathrm{Pr}^2}\right)z^{+3} + \cdots = \mathrm{H}z^{+3} + \cdots \tag{21}$$

Nusselt Number

Integrating the energy equation and using the boundary condition $q_0(r) = -k(\partial T/\partial z)_0$ yields

$$\frac{T_0 - T_\infty}{q_0/\rho c u_\tau} = \int_0^\infty \frac{dz^+}{\dfrac{1}{\mathrm{Pr}} + \dfrac{\epsilon_H}{\nu}} \tag{22}$$

Once the integral has been evaluated the local Nusselt number, Nu_r, is known where $\mathrm{Nu}_r = q_0 r/k(T_0 - T_\infty)$. The average Nusselt number is given by

$$\overline{\mathrm{Nu}} \equiv \overline{q_0}R/k(T_0 - T_\infty) = 2\int_0^R \mathrm{Nu}_r dr/R \tag{23}$$

with R the radius of the disk, and $\overline{q_0} \equiv 2\int_0^R rq_0 dr/R^2$.

Discussion of Results and Conclusions

The remaining consideration for the determination of the heat transfer is the specification of the eddy diffusivity. Using equation (21) with H a function of the Prandtl number we obtain

$$\overline{\mathrm{Nu}} = 0.0965\,H^{1/3}\,\mathrm{Pr}^{1/3}\,\mathrm{Re}^{0.9} \tag{24}$$

where $\mathrm{Re} = R^2\omega/\nu$. Note that this relation for $\overline{\mathrm{Nu}}$ was obtained by using equation (21) as the eddy diffusivity throughout the fluid. Recall that we are considering the high Prandtl number problem so that the region very close to the surface dominates. We therefore expect the result for $\overline{\mathrm{Nu}}$ given by equation (24) to be valid for this condition.

Now, an approximation that is frequently made is to set the eddy diffusivity for heat transport equal to that for momentum transport. For example, Hartnett, et al. [9] made this assumption in their study of the rotating disk problem by setting $\epsilon_{M_1\phi} = \epsilon_H$, and obtained good agreement with experimental data. Proceeding in this manner, we obtain

[3] The details are available (Paterson [15]).

$$H \equiv 4T_4^+/\mathrm{Pr}^2 = G \equiv 4\Phi_4^+ + 0.43\ \mathrm{Re}_r^{-0.9} + 2800\ \mathrm{Re}_r^{-1.5} \quad (25)$$

To evaluate Φ_4^+ we use the results for V_ϕ, Φ_3, and R_1 to obtain

$$\frac{r\omega - V_\phi}{u_\tau} = z^+ - 2\ \mathrm{Re}_r^{-0.8}\ z^{+3} - \Phi_4^+ z^{+4} + \ldots \quad (26)$$

Now, our primary interest is in the overall heat transfer so that we omit that small portion of the disk which is in laminar flow. A detailed calculation justifies this (Ellison [10]). Note that the Reynolds number at transition is approximately equal to 3×10^5. As a consequence, we omit the second term in equation (26). (Also refer to Fig. 9 of Cooper [11]).

Following Tien, Wasan, and Wilke [3, 4, 5] we determine Φ_4^+ by matching the velocity and the velocity gradient from equation (26) with the velocity distribution reported by Goldstein [12]. This yields a value for Φ_4^+ of 0.741×10^{-4}. Thus, the terms which are dependent on the Reynolds number may be omitted in equation (25) so that the resulting eddy viscosity distribution proves to be compatible with that obtained from fully developed pipe flow. (Recall that for the turbulent flow regime $\mathrm{Re}_r > 3 \times 10^5$.) We therefore have $H = 4\Phi_4^+ = 2.96 \cdot 10^{-4}$ and from equation (24) obtain

$$\overline{\mathrm{Nu}} = 0.00643\ \mathrm{Re}^{0.9}\ \mathrm{Pr}^{1/3} \quad (27)$$

It is appropriate to compare this result with high Schmidt (Prandtl) number experiments. Daguenet's experiments [6] were carried out over a Schmidt number range from 345 to 6450 and were correlated by

$$\overline{\mathrm{Sh}} = 0.00707\ \mathrm{Re}^{0.9}\ \mathrm{Sc}^{1/3} \quad (28)$$

This result is plotted in Fig. 1 and is obviously in excellent agreement with the present result, equation (27). The data of Ellison and Cornet [1] over the Schmidt number range from 34 to 1300 is presented in Fig. 1 along with the equation they recommend:

$$\overline{\mathrm{Sh}} = 0.0117\ \mathrm{Re}^{0.896}\ \mathrm{Sc}^{0.249} \quad (29)$$

It is apparent that for large Schmidt numbers there is excellent agreement between the present results and the experimental data. For moderate values of the Schmidt number the theoretical relation, equation (27), differs from the experimental data of Ellison and Cornet. We attribute this difference to the increasing importance of the region away from the wall in determining the heat or mass transport. For this condition, equations (24) and (27) should not be valid. For completeness, it should be noted that an eddy diffusivity dependence of z^{+4} gives a $\mathrm{Sc}^{1/4}$ power (cf. Deissler [13]) which is in agreement with equation (29) but is not in agreement with equation (28).

In summary, the eddy diffusivity distribution near the surface of a rotating disk may be obtained from an analysis of the basic conservation equations and the results prove to be successful in predicting the transport at high Schmidt numbers. Furthermore, the results are compatible with those obtained from fully developed pipe flow and thus provides an explanation for the success of pipe flow equations when applied to the rotating disk problem.

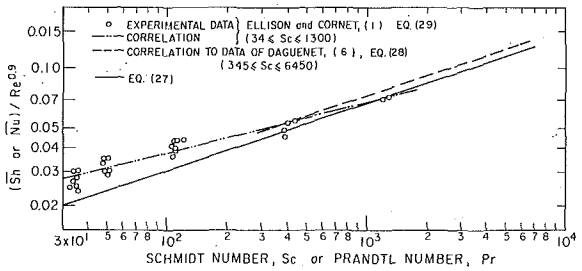

Fig. 1 Comparison of experimental and theoretical results

Acknowledgment

The authors acknowledge with appreciation the support of this research by the Office of Saline Water, U.S. Department of the Interior, Grant No. 14-30-2545 and the Sea Water Conversion Laboratory of the University of California, Berkeley.

References

1 Ellison, B. T., and Cornet, I., "Mass Transfer to a Rotating Disc," *Electrochemical Science*, Vol. 118, 1971, pp. 68–72.

2 Kreith, F., "Convection Heat Transfer in Rotating Systems," *Advances in Heat Transfer*, Academic Press, Vol. 5, New York, 1968.

3 Tien, C. L., and Wasan, D. T., "Law of the Wall in Turbulent Channel Flow," *Physics of Fluids*, Vol. 6, 1963, pp. 144–145.

4 Wasan, D. T., Tien, C. L., and Wilke, C. R., "Theoretical Correlation of Velocity and Eddy Viscosity for Flow Close to a Pipe Wall," *A.I.Ch.E. Journal*, Vol. 9, 1963, 567–68.

5 Tien, C. L., "A Note on Distribution of Temperature and Eddy Diffusivity for Heat in Turbulent Flow Near and Wall," *Z.A.M.P.*, Vol. 15, 1964, pp. 63–66.

6 Daguenet, M., "Etude du transport de matière en solution, a l'aide des électrodes à disque et à anneau tournants," *International Journal of Heat and Mass Transfer*, Vol. 11, 1968, pp. 1581-1596.

7 Kármán, Th. Von., "Über laminare und turbulente Reibung," *Z. angew. Math. Mech.*, Vol. 1, 1921, pp. 233–252.

8 Dorfman, L. A., *Hydrodynamic Resistance and the Heat Loss of Rotating Solids*, Oliver and Boyd, Ltd., Edinburgh and London, (1963), p. 56.

9 Hartnett, J. P., Tsai, S. H., and Jantscher, H. N., "Heat Transfer to a Nonisothermal Rotating Disc With a Turbulent Boundary Layer," JOURNAL OF HEAT TRANSFER, TRANS. ASME, Series C, Vol. 87, 1965, pp. 362–368.

10 Ellison, B. T., "Mass Transfer to a Rotating Disc," PhD dissertation, University of California, Berkeley, 1969.

11 Cooper, P., "Turbulent Boundary Layer on a Rotating Disc Calculated With an Effective Viscosity," *A.I.A.A. Journal*, Vol. 9, 1971, pp. 255–263.

12 Goldstein, S., "On the Resistance to the Rotation of a Disc Immersed in a Fluid," *Proceedings Cam. Phil. Soc.*, Vol. 31, 1935, pp. 232–241.

13 Deissler, R. G., "Analysis of Turbulent Heat Transfer, Mass Transfer, and Friction in Smooth Tubes at High Prandtl and Schmidt Numbers," N.A.C.A. Report 1210, 1955, pp. 69–82.

14 Margolis, D. P., and Lumley, J. L., "Curved Turbulent Mixing Layer," *Physics of Fluids*, Vol. 8, 1965, pp. 1775–1784.

15 Paterson, J. A., "Heat, Mass and Momentum Transport in Rotating Flows," PhD dissertation, University of California, Berkeley, 1973.

Temperature Distribution in Free Axisymmetric Liquid Sheets

J. H. LIENHARD[1] and S. N. SINGH[2]

Introduction and Formulation

THE PROBLEM of specifying the temperature distribution in jets and sheets is one that has relevance to a variety of industrial processes. Our specific interest in this problem is motivated by the spray forming capabilities of highly superheated liquids passing through orifices. The present study is made in the hope of anticipating the behavior of flashing in spreading sheets. Fig. 1 shows the configuration to be treated here. Two cases will be considered: *A, There is a heat transfer coefficient, h, between the sheet and the surroundings;* and *B, the liquid enters superheated so that the surface of the sheet takes on the saturation temperature.*

[1] Professor, University of Kentucky, Lexington, Ky. Mem. ASME.

[2] Associate Professor, University of Kentucky, Lexington, Ky. Mem. ASME.

Contributed by the Heat Transfer division of THE AMERICAN SOCIETY OF MECHANICAL ENGINEERS. Manuscript received by the Heat Transfer Division, March 8, 1973.

$$H \equiv 4T_4^+/\mathrm{Pr}^2 = G \equiv 4\Phi_4^+ + 0.43\ \mathrm{Re}_r^{-0.9} + 2800\ \mathrm{Re}_r^{-1.5} \quad (25)$$

To evaluate Φ_4^+ we use the results for V_ϕ, Φ_3, and R_1 to obtain

$$\frac{r\omega - V_\phi}{u_\tau} = z^+ - 2\ \mathrm{Re}_r^{-0.8}\ z^{+3} - \Phi_4^+ z^{+4} + \ldots \quad (26)$$

Now, our primary interest is in the overall heat transfer so that we omit that small portion of the disk which is in laminar flow. A detailed calculation justifies this (Ellison [10]). Note that the Reynolds number at transition is approximately equal to 3×10^5. As a consequence, we omit the second term in equation (26). (Also refer to Fig. 9 of Cooper [11]).

Following Tien, Wasan, and Wilke [3, 4, 5] we determine Φ_4^+ by matching the velocity and the velocity gradient from equation (26) with the velocity distribution reported by Goldstein [12]. This yields a value for Φ_4^+ of 0.741×10^{-4}. Thus, the terms which are dependent on the Reynolds number may be omitted in equation (25) so that the resulting eddy viscosity distribution proves to be compatible with that obtained from fully developed pipe flow. (Recall that for the turbulent flow regime $\mathrm{Re}_r > 3 \times 10^5$.) We therefore have $H = 4\Phi_4^+ = 2.96 \cdot 10^{-4}$ and from equation (24) obtain

$$\overline{\mathrm{Nu}} = 0.00643\ \mathrm{Re}^{0.9}\ \mathrm{Pr}^{1/3} \quad (27)$$

It is appropriate to compare this result with high Schmidt (Prandtl) number experiments. Daguenet's experiments [6] were carried out over a Schmidt number range from 345 to 6450 and were correlated by

$$\overline{\mathrm{Sh}} = 0.00707\ \mathrm{Re}^{0.9}\ \mathrm{Sc}^{1/3} \quad (28)$$

This result is plotted in Fig. 1 and is obviously in excellent agreement with the present result, equation (27). The data of Ellison and Cornet [1] over the Schmidt number range from 34 to 1300 is presented in Fig. 1 along with the equation they recommend:

$$\overline{\mathrm{Sh}} = 0.0117\ \mathrm{Re}^{0.896}\ \mathrm{Sc}^{0.249} \quad (29)$$

It is apparent that for large Schmidt numbers there is excellent agreement between the present results and the experimental data. For moderate values of the Schmidt number the theoretical relation, equation (27), differs from the experimental data of Ellison and Cornet. We attribute this difference to the increasing importance of the region away from the wall in determining the heat or mass transport. For this condition, equations (24) and (27) should not be valid. For completeness, it should be noted that an eddy diffusivity dependence of z^{+4} gives a $\mathrm{Sc}^{1/4}$ power (cf. Deissler [13]) which is in agreement with equation (29) but is not in agreement with equation (28).

In summary, the eddy diffusivity distribution near the surface of a rotating disk may be obtained from an analysis of the basic conservation equations and the results prove to be successful in predicting the transport at high Schmidt numbers. Furthermore, the results are compatible with those obtained from fully developed pipe flow and thus provides an explanation for the success of pipe flow equations when applied to the rotating disk problem.

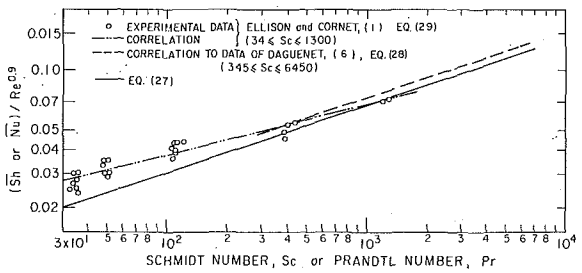

Fig. 1 Comparison of experimental and theoretical results

Acknowledgment

The authors acknowledge with appreciation the support of this research by the Office of Saline Water, U.S. Department of the Interior, Grant No. 14-30-2545 and the Sea Water Conversion Laboratory of the University of California, Berkeley.

References

1 Ellison, B. T., and Cornet, I., "Mass Transfer to a Rotating Disc," *Electrochemical Science*, Vol. 118, 1971, pp. 68–72.

2 Kreith, F., "Convection Heat Transfer in Rotating Systems," *Advances in Heat Transfer*, Academic Press, Vol. 5, New York, 1968.

3 Tien, C. L., and Wasan, D. T., "Law of the Wall in Turbulent Channel Flow," *Physics of Fluids*, Vol. 6, 1963, pp. 144–145.

4 Wasan, D. T., Tien, C. L., and Wilke, C. R., "Theoretical Correlation of Velocity and Eddy Viscosity for Flow Close to a Pipe Wall," *A.I.Ch.E. Journal*, Vol. 9, 1963, 567–68.

5 Tien, C. L., "A Note on Distribution of Temperature and Eddy Diffusivity for Heat in Turbulent Flow Near and Wall," *Z.A.M.P.*, Vol. 15, 1964, pp. 63–66.

6 Daguenet, M., "Etude du transport de matière en solution, a l'aide des électrodes à disque et à anneau tournants," *International Journal of Heat and Mass Transfer*, Vol. 11, 1968, pp. 1581-1596.

7 Kármán, Th. Von., "Über laminare und turbulente Reibung," *Z. angew. Math. Mech.*, Vol. 1, 1921, pp. 233–252.

8 Dorfman, L. A., *Hydrodynamic Resistance and the Heal Loss of Rotating Solids*, Oliver and Boyd, Ltd., Edinburgh and London, (1963), p. 56.

9 Hartnett, J. P., Tsai, S. H., and Jantscher, H. N., "Heat Transfer to a Nonisothermal Rotating Disc With a Turbulent Boundary Layer," JOURNAL OF HEAT TRANSFER, TRANS. ASME, Series C, Vol. 87, 1965, pp. 362–368.

10 Ellison, B. T., "Mass Transfer to a Rotating Disc," PhD dissertation, University of California, Berkeley, 1969.

11 Cooper, P., "Turbulent Boundary Layer on a Rotating Disc Calculated With an Effective Viscosity," *A.I.A.A. Journal*, Vol. 9, 1971, pp. 255–263.

12 Goldstein, S., "On the Resistance to the Rotation of a Disc Immersed in a Fluid," *Proceedings Cam. Phil. Soc.*, Vol. 31, 1935, pp. 232–241.

13 Deissler, R. G., "Analysis of Turbulent Heat Transfer, Mass Transfer, and Friction in Smooth Tubes at High Prandtl and Schmidt Numbers," N.A.C.A. Report 1210, 1955, pp. 69–82.

14 Margolis, D. P., and Lumley, J. L., "Curved Turbulent Mixing Layer," *Physics of Fluids*, Vol. 8, 1965, pp. 1775–1784.

15 Paterson, J. A., "Heat, Mass and Momentum Transport in Rotating Flows," PhD dissertation, University of California, Berkeley, 1973.

Temperature Distribution in Free Axisymmetric Liquid Sheets

J. H. LIENHARD[1] and S. N. SINGH[2]

Introduction and Formulation

THE PROBLEM of specifying the temperature distribution in jets and sheets is one that has relevance to a variety of industrial processes. Our specific interest in this problem is motivated by the spray forming capabilities of highly superheated liquids passing through orifices. The present study is made in the hope of anticipating the behavior of flashing in spreading sheets. Fig. 1 shows the configuration to be treated here. Two cases will be considered: *A, There is a heat transfer coefficient, h, between the sheet and the surroundings;* and *B, the liquid enters superheated so that the surface of the sheet takes on the saturation temperature.*

[1] Professor, University of Kentucky, Lexington, Ky. Mem. ASME.

[2] Associate Professor, University of Kentucky, Lexington, Ky. Mem. ASME.

Contributed by the Heat Transfer division of THE AMERICAN SOCIETY OF MECHANICAL ENGINEERS. Manuscript received by the Heat Transfer Division, March 8, 1973.

Nomenclature

Bi = Biot number, r_0 (heat transfer coefficient/thermal conductivity)
Pe = the Peclet number, ur_0/(thermal diffusivity)
r, r_0 = radial coordinate; subscript denotes radius of impinging jet
T, T_{amb}, T_{sat}, T_0 = temperature; subscripts denote ambient, saturation, and impinging jet temperatures, respectively
T_{ref} = reference temperature, equal to either T_{amb} in Case A or T_{sat} in Case B
u = constant radial velocity in the axisymmetric sheet
v = axial velocity component in the axisymmetric sheet
z = axial coordinate
δ = thickness of the sheet, r_0^2/r
ζ = z/r_0
η, η' = r/r_0; prime denotes transformed radial coordinate, equal to η
η_k = r/r_0 evaluated where equation (18) gives θ = 1
θ, θ_c = $(T - T_{ref})/(T_0 - T_{ref})$; $\theta_c = \theta(\zeta = 0)$
θ_n = outward-drawn normal derivative of θ at liquid surface
ξ = $\zeta\eta$ or z/δ

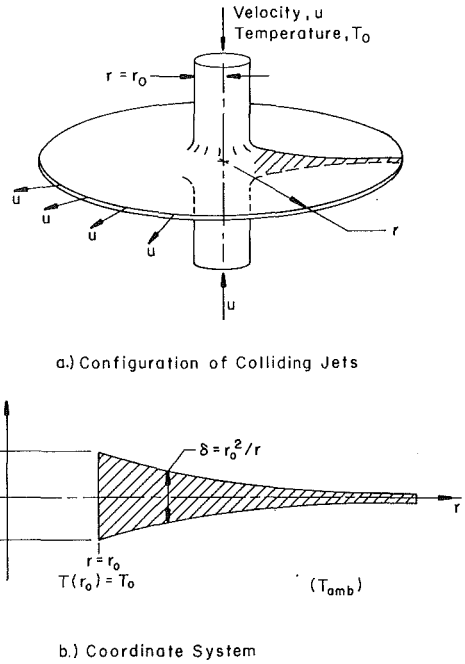

Fig. 1 Configuration and coordinate system for axisymmetric sheets

Under the following nondimensionalizations:

$$\theta(\eta, \zeta) \equiv \frac{T - T_{ref}}{T_0 - T_{ref}}; \quad \eta \equiv \frac{r}{r_0}; \quad \zeta \equiv \frac{z}{r_0} \tag{1}$$

the energy equation for this flow can be expressed as

$$\mathrm{Pe}\left[\frac{\partial\theta}{\partial\eta} + \frac{v}{u}\frac{\partial\theta}{\partial\zeta}\right] = \frac{\partial^2\theta}{\partial\zeta^2} + \frac{1}{\eta}\frac{\partial}{\partial\eta}\left(\eta\frac{\partial\theta}{\partial\eta}\right) \tag{2}$$

The radial velocity of the sheet, u, will be assumed constant. Howarth[3] and Lienhard and Newton[4] have treated skin drag and internal viscous drag, respectively, for liquid sheets. Their results show that the constant velocity assumption is almost always accurate within a few percent. The axial velocity, v, is significant only for r close to r_0.

The boundary conditions for Case A are:

$$\theta(1, \zeta) = 1; \quad \theta_\zeta(\eta, 0) = 0; \quad \theta_n\left(\eta, \frac{1}{2\eta}\right) = -\mathrm{Bi}\theta\left(\eta, \frac{1}{2\eta}\right) \tag{3}$$

where $T_{ref} = T_{amb}$ and θ_n is a derivative normal to the interface ($\theta_n \simeq \theta_\zeta$ except very near $\eta = 1$). For Case B, $T_{ref} = T_{sat}$ and the boundary conditions are:

$$\theta(1, \zeta) = 1; \quad \theta_\zeta(\eta, 0) = 0; \quad \theta\left(\eta, \frac{1}{2\eta}\right) = 0 \tag{4}$$

In the last of conditions (3) we wish to include the possibility of a variable heat transfer coefficient so that, in general, Bi = Bi(η). We also assume that evaporation does not consume the surface significantly.

The latter condition will be true as long as the ratio of sensible to latent heat (or Jakob number) is not large. In a typical case in which water, superheated 50 deg F, is injected in a 1-atm environment, this ratio would be only about 0.02, so we would experience less than 2 percent loss of the sheet by evaporation at any point.

Solutions for Case A

The unsimplified form of Case A is a formidable problem. However, we can learn a great deal by considering the far simpler case in which we average θ over the axial coordinate. This can be done when the Biot number, Bi, is small. Such an averaging of equation (2) over ζ yields

$$\theta'' - \mathrm{Pe}\,\theta' - [2\eta\ \mathrm{Bi}(\eta)]\theta = 0 \tag{5}$$

where θ is here an average over ζ which depends only on η. The boundary conditions (3) are replaced by

$$\theta(1) = 1 \text{ and } \theta(\infty) = 0 \tag{6}$$

In the limit of large Peclét numbers, radial conduction as characterized by θ'' is negligible. Omitting θ'' from equation (5) and solving it subject to $\theta(1) = 1$, we obtain

$$\theta = \exp\left(-2\int_1^\eta \frac{\mathrm{Bi}(\eta)}{\mathrm{Pe}}\,\eta d\eta\right); \quad \mathrm{Pe} \text{ and } (1/\mathrm{Bi}) \gg 1 \tag{7}$$

If Bi (η) can be approximated as a constant, equation (7) becomes

$$\theta = \exp\left[-(\mathrm{Bi}/\mathrm{Pe})(\eta^2 - 1)\right]; \quad \mathrm{Pe} \text{ and } (1/\mathrm{Bi}) \gg 1 \tag{8}$$

These expressions become more accurate with increasing η since both radial conduction and axial temperature variations decrease with η.

A better approximate solution of equation (5) for small η can be formed if we note that neither Bi nor Pe^{-1} can ever exceed unity. To predict $\theta(\eta)$ under these circumstances we use a kind of singular perturbation in Bi about $\eta = 1$.

$$\theta = \theta_0 + \mathrm{Bi}\,\theta_1 + \mathrm{Bi}^2\theta_2 + \ldots \tag{9}$$

Substitution of this in equation (5) and solution of the resulting differential equations for θ_0 and θ_1 lead to

$$\theta = 1 - \frac{\mathrm{Bi}}{\mathrm{Pe}}\left[(\eta^2 - 1) + \frac{2}{\mathrm{Pe}}(\eta - 1)\right] \tag{10}$$

Equation (10) is accurate at least up to $\eta^2 = \mathrm{Pe}/10\mathrm{Bi}$. Beyond this value, equation (7) or (8) should be used after rede-

[3] Howarth, L., Appendix for "The Dynamics of Thin Sheets of Liquid," by G. I. Taylor, *Proceedings Royal Society*, London, England, Vol. 253, Series A, 1959, pp. 294–295.

[4] Lienhard, J. H., and Newton, T. A., "Effect of Viscosity Upon Liquid Velocity in Axi-Symmetric Sheets, *Zeit. für Ang. Math. und Phys.* (*ZAMP*), Vol. 17, 1966, pp. 348–353.

fining the initial conditions such that equation (10) applies at the point $\eta = \sqrt{\mathrm{Pe}/10\mathrm{Bi}}$,

$$\theta = \left[0.9 + \frac{\mathrm{Bi}}{\mathrm{Pe}} - \frac{2\mathrm{Bi}}{\mathrm{Pe}^2}\left(\sqrt{\frac{\mathrm{Bi}}{10\mathrm{Pe}}} - 1\right)\right] \times \exp\left[-\frac{\mathrm{Bi}}{\mathrm{Pe}}\left(\eta^2 - \frac{\mathrm{Pe}}{10\mathrm{Bi}}\right)\right] \quad (11)$$

To test equations (10) and (11) we compare their solutions against two fairly severe cases in Fig. 2. Here we plot these expressions for (Bi = 0.1, Pe = 5) and (Bi = 0.4, Pe = 10) against the numerical integration of equations (5) and (6). The comparison shows that equations (10) and (11) give a very good prediction of θ, even in a severe test, although there is a discontinuity in the derivatives of θ.

When Bi $\geq$ 1, equation (5) no longer applies, but another difficulty also enters: A heat transfer coefficient arising from a boundary layer in the ambient gas will require that there is traction on the liquid surface. While Howarth showed that such traction does not generally slow the gross velocity of the sheet, it can cause a velocity profile to evolve in the sheet. Any significant axial temperature variation would interact with the velocity profile. To treat the influence of the resulting internal convection would mean solving the coupled boundary layer problems in the gas and liquid—a really difficult problem. However, the spreading sheet has been shown by Huang[5] to break up when $20 \geq \eta \geq 100$ in all cases. Thus complete evolution of the velocity profile is usually prevented.

Fortunately, high Biot numbers will not generally occur in any but liquid metal flows. The use of equation (5) with Biot numbers on the order of unity is probably admissible since the *local* Biot number decreases as $1/\eta$ from its initial value based on $r = r_0$.

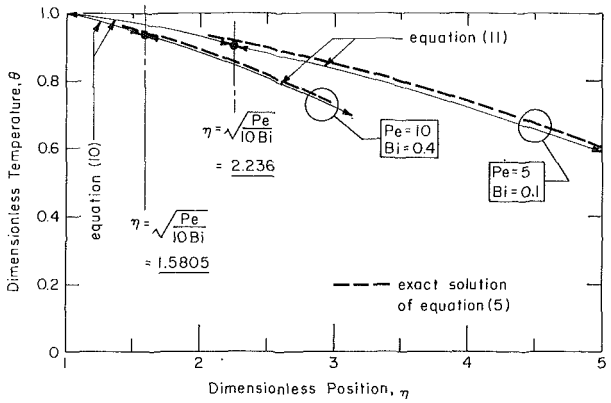

Fig. 2 Comparison of approximate and exact $\theta(\eta)$ for Case A with low Bi

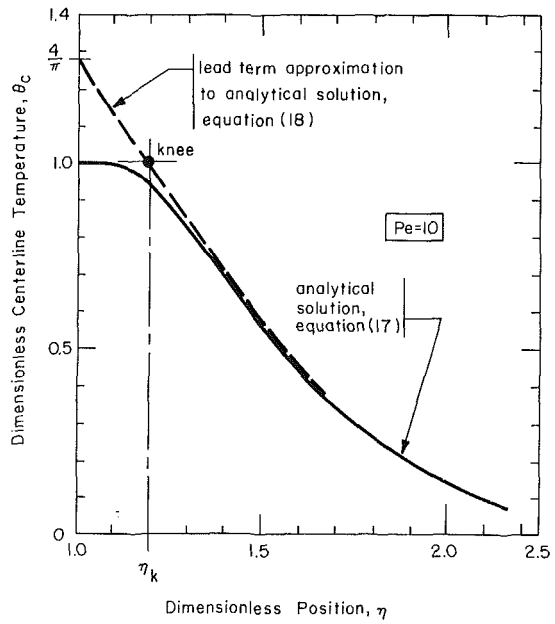

Fig. 3 Comparison of an actual center-line temperature variation with the asymptotic limits, Case B

Simplification of the Governing Equation for High Pe

Equation (2), even after the elimination of the radial conduction term, might appear to present serious difficulties in combination with either boundary conditions (3) or (4). However, the convective derivative can be greatly simplified using a form of the von Mises transformation:

We begin by taking u to be constant and solving the resulting continuity equation for v, noting that a constant of integration vanishes because $v(z = 0) = 0$. The result is

$$\frac{v}{u} = -\frac{\zeta}{\eta} \quad (12)$$

Substituting equation (12) in (2) gives the following governing equation for negligible radial conduction (as would be the case for Pe $\gg$ 1):

$$\mathrm{Pe}\left[\frac{\partial\theta}{\partial\eta} - \frac{\zeta}{\eta}\frac{\partial\theta}{\partial\zeta}\right] = \frac{\partial^2\theta}{\partial\zeta^2} \quad (13)$$

The transformation $\xi = \zeta\eta$ and $\eta' = \eta$ then reduces equation (13) to

$$\frac{\mathrm{Pe}}{\eta'^2}\frac{\partial\theta}{\partial\eta'} = \frac{\partial^2\theta}{\partial\xi^2} \quad (14)$$

with greatly simplified boundary conditions. For Case A they are:

$$\theta(1, \xi) = 1; \quad \theta_\xi(\eta', 0) = 0; \quad \theta_\xi(\eta', 1/2) \simeq -\frac{\mathrm{Bi}}{\eta'}\theta(\eta', 1/2) \quad (15)$$

and for Case B

$$\theta(1, \xi) = 1; \quad \theta_\xi(\eta', 0) = 0; \quad \theta(\eta', 1/2) = 0 \quad (16)$$

Analytical Solution for Case B With High Pe

Equation (14) with boundary conditions (16) can be solved by the method of separation of variables with the result:

$$\theta(\eta, \zeta) = \frac{4}{\pi}\sum_{n=0}^{\infty}\frac{(-1)^n}{(2n+1)}\exp\left[-\frac{(2n+1)^2\pi^2}{3\,\mathrm{Pe}}(\eta^3 - 1)\right] \times \cos(2n+1)\pi\eta\zeta \quad (17)$$

The simple asymptotic result applicable away from the point of collision of the jets follows from equation (17) as

$$\theta(\eta, \zeta) \simeq \frac{4}{\pi}\exp\left[-\frac{\pi^2}{3\mathrm{Pe}}(\eta^3 - 1)\right]\cos\pi\eta\zeta; \quad \frac{\eta^3 - 1}{\mathrm{Pe}} > 0.1 \quad (18)$$

The Knee of the Cooling Curve. We have now seen that the temperature of a sheet falls off roughly as $\exp(1 - \eta^3)$ in Case B and as $\exp(1 - \eta^2)$ in the lumped capacity limit of Case A. In either case, the temperature will drop off very little up to some characteristic value of η; then it will plunge rapidly. In any process application of heated liquid sheets, it would be of great practical value to know the location of this "knee" in the curve.

Fig. 3 shows the center-line temperature, θ_c, for a sheet sub-

[5] Huang, J. C. P., "The Breakup of Axisymmetric Liquid Sheets," *Journal of Fluid Mechanics*, Vol. 43, Part 2, 1970, pp. 305–319.

jected to a constant surface temperature and for which Pe = 10. The temperature was computed with equation (17) at $\zeta = 0$. The initial and final asymptotic behavior has been included in this figure. As η approaches unity from above, the asymptotic value of θ_c is given by equation (18) with $\zeta = 0$.

An effective knee of the curve, $\eta = \eta_k$, can be identified by equating these asymptotes (see Fig. 3).

Summary

The cooling of an axisymmetric liquid sheet can be predicted as follows:

A When the liquid enters below its saturation temperature:

1 Low Bi; low Pe: integrate equation (5) numerically.

2 Low Bi; Pe > 1: use equation (10) to η = Pe/10Bi and equation (11) beyond it. For large Pe and low Bi (probably the commonest case) equation (8) may be used over the entire range.

B When the liquid enters superheated:

1 Pe < 10: no solution is offered. The situation probably has very limited importance.

2 Pe $\geq$ 10: use equation (11). If $(\eta^3 - 1)/\text{Pe} > 0.1$, use equation (18).

3 The temperature will begin to decrease sharply when η reaches η_k.

A Two-Dimensional Theory of Temperature and Pressure Effects on Ice Melting Rates with a Heated Plate

J. F. LEA[1] AND R. D. STEGALL[2]

Nomenclature

C_p = specific heat
h = heat of fusion
I = variable in equation (9*a*)
K = dimensionless grouping defined in equation (9*b*)
k = thermal conductivity of melted solid
L = dimensionless grouping defined in equation (10*c*)
l = length of plate
M = dimensionless grouping defined in equation (10*d*)
p = local pressure
P = average pressure
T = temperature
u = velocity in the x direction
V = melt velocity of the solid
x, y = Cartesian coordinate system defined in Fig. 1
Pe = Peclet number, $\frac{\rho V \delta}{\mu} \cdot \frac{\mu c_p}{k}$
Pr = Prandtl number, $\frac{\mu c_p}{k}$
Re = Reynolds number, $\frac{\rho V \delta}{\mu}$
δ = gap thickness
μ = dynamic viscosity
η = thermal efficiency
ρ = density

Superscripts

m = melt, also condition at $(l, \delta/2)$
o = ambient conditions

Subscripts

$'$ = indicates dimensional quantities

[1] Senior Research Engineer, Sun Oil Production Research Laboratory, 503 N. Central Expressway, Richardson, Texas. Assoc. Mem. ASME.

[2] Research Engineer, Sun Oil Production Research Laboratory, 503 N. Central Expressway, Richardson, Texas. Assoc. Mem. ASME.

Contributed by the Heat Transfer Division of THE AMERICAN SOCIETY OF MECHANICAL ENGINEERS. Manuscript received by the Heat Transfer Division, March 2, 1973.

Introduction

ONE OF THE MAIN problems to be solved before commercial production of oil and gas can begin in the Arctic is that of maintaining position of a platform while working on the moving ice sheet. There appear to be instances where a heated hull may be used to melt away ice, especially when waste heat is available. This study predicts the relationship between a heated plate size, contact pressure, plate temperature, and melting rate.

Earlier work in the area of this investigation was done by Rosenthal [5].[3] Landau [4] considered a melting solid when the melt liquid was removed as soon as it was formed. Carslaw and Jaeger [1] investigated melting for a variety of conditions. Goodman and Shea [2] used the heat balance integral to obtain approximate solutions for a finite slab with a moving melt line and a fixed heated surface. Yen and Tien [6] determined analytically the temperature profiles in a fluid flowing over a flat plate using the assumption of flow of the modified Leveque type. Hahne and Grigull [3] studied the regelation of ice with the inclusion of temperature effect.

Analysis

The geometry of the problem and coordinate system are illustrated in Fig. 1. A plate melting ice at velocity V is shown separated from the ice surface by a distance δ. The melted ice water is shown escaping through the gap δ with a velocity profile u'. The temperature of the plate drops to the ice temperature with a profile T'. The plate is forced toward the ice with a contact pressure p'.

The first step in the analysis is to describe the dynamics of the escaping water. The assumptions used to reduce the governing Navier-Stokes equation for the x' direction are: 1 Inertia forces $\ll$ than viscous forces; 2 $\delta \ll l$; 3 no body forces present; 4 steady state flow; 5 constant physical properties. Utilizing the following transformations to nondimensionalize the resulting equation:

$$u = u'/V \tag{1a}$$

$$x = x'/l \tag{1b}$$

$$y = y'/\delta \tag{1c}$$

$$p = p'/\rho V^2. \tag{1d}$$

The resultant equation is:

$$\frac{\partial p}{\partial x} = \frac{l/\delta}{\text{Re}} \frac{\partial^2 u}{\partial y^2}. \tag{2}$$

To solve for the velocity distribution of the melted ice water, the following conditions must be satisfied for one-half of the plate:

$$u = 0 \quad \text{at} \quad y = 0, \tag{3a}$$

$$u = 0 \quad \text{at} \quad y = 1, \tag{3b}$$

$$p = p_0 \quad \text{at} \quad x = 1, \tag{3c}$$

$$\partial p/\partial x = 0 \quad \text{at} \quad x = 1/2. \tag{3d}$$

[3] Numbers in brackets designate References at end of technical brief.

jected to a constant surface temperature and for which Pe = 10. The temperature was computed with equation (17) at $\zeta = 0$. The initial and final asymptotic behavior has been included in this figure. As η approaches unity from above, the asymptotic value of θ_c is given by equation (18) with $\zeta = 0$.

An effective knee of the curve, $\eta = \eta_k$, can be identified by equating these asymptotes (see Fig. 3).

Summary

The cooling of an axisymmetric liquid sheet can be predicted as follows:

A When the liquid enters below its saturation temperature:

1 Low Bi; low Pe: integrate equation (5) numerically.

2 Low Bi; Pe > 1: use equation (10) to $\eta = \text{Pe}/10\text{Bi}$ and equation (11) beyond it. For large Pe and low Bi (probably the commonest case) equation (8) may be used over the entire range.

B When the liquid enters superheated:

1 Pe < 10: no solution is offered. The situation probably has very limited importance.

2 Pe $\geq$ 10: use equation (11). If $(\eta^3 - 1)/\text{Pe} > 0.1$, use equation (18).

3 The temperature will begin to decrease sharply when η reaches η_k.

A Two-Dimensional Theory of Temperature and Pressure Effects on Ice Melting Rates with a Heated Plate

J. F. LEA[1] AND R. D. STEGALL[2]

Nomenclature

C_p = specific heat
h = heat of fusion
I = variable in equation (9*a*)
K = dimensionless grouping defined in equation (9*b*)
k = thermal conductivity of melted solid
L = dimensionless grouping defined in equation (10*c*)
l = length of plate
M = dimensionless grouping defined in equation (10*d*)
p = local pressure
P = average pressure
T = temperature
u = velocity in the x direction
V = melt velocity of the solid
x, y = Cartesian coordinate system defined in Fig. 1
Pe = Peclet number, $\frac{\rho V \delta}{\mu} \cdot \frac{\mu c_p}{k}$
Pr = Prandtl number, $\frac{\mu c_p}{k}$
Re = Reynolds number, $\frac{\rho V \delta}{\mu}$
δ = gap thickness
μ = dynamic viscosity
η = thermal efficiency
ρ = density

Superscripts

m = melt, also condition at $(l, \delta/2)$
o = ambient conditions

Subscripts

$'$ = indicates dimensional quantities

[1] Senior Research Engineer, Sun Oil Production Research Laboratory, 503 N. Central Expressway, Richardson, Texas. Assoc. Mem. ASME.

[2] Research Engineer, Sun Oil Production Research Laboratory, 503 N. Central Expressway, Richardson, Texas. Assoc. Mem. ASME.

Contributed by the Heat Transfer Division of THE AMERICAN SOCIETY OF MECHANICAL ENGINEERS. Manuscript received by the Heat Transfer Division, March 2, 1973.

Introduction

ONE OF THE MAIN problems to be solved before commercial production of oil and gas can begin in the Arctic is that of maintaining position of a platform while working on the moving ice sheet. There appear to be instances where a heated hull may be used to melt away ice, especially when waste heat is available. This study predicts the relationship between a heated plate size, contact pressure, plate temperature, and melting rate.

Earlier work in the area of this investigation was done by Rosenthal [5].[3] Landau [4] considered a melting solid when the melt liquid was removed as soon as it was formed. Carslaw and Jaeger [1] investigated melting for a variety of conditions. Goodman and Shea [2] used the heat balance integral to obtain approximate solutions for a finite slab with a moving melt line and a fixed heated surface. Yen and Tien [6] determined analytically the temperature profiles in a fluid flowing over a flat plate using the assumption of flow of the modified Leveque type. Hahne and Grigull [3] studied the regelation of ice with the inclusion of temperature effect.

Analysis

The geometry of the problem and coordinate system are illustrated in Fig. 1. A plate melting ice at velocity V is shown separated from the ice surface by a distance δ. The melted ice water is shown escaping through the gap δ with a velocity profile u'. The temperature of the plate drops to the ice temperature with a profile T'. The plate is forced toward the ice with a contact pressure p'.

The first step in the analysis is to describe the dynamics of the escaping water. The assumptions used to reduce the governing Navier-Stokes equation for the x' direction are: 1 Inertia forces $\ll$ than viscous forces; 2 $\delta \ll l$; 3 no body forces present; 4 steady state flow; 5 constant physical properties. Utilizing the following transformations to nondimensionalize the resulting equation:

$$u = u'/V \tag{1a}$$

$$x = x'/l \tag{1b}$$

$$y = y'/\delta \tag{1c}$$

$$p = p'/\rho V^2. \tag{1d}$$

The resultant equation is:

$$\frac{\partial p}{\partial x} = \frac{l/\delta}{\text{Re}} \frac{\partial^2 u}{\partial y^2}. \tag{2}$$

To solve for the velocity distribution of the melted ice water, the following conditions must be satisfied for one-half of the plate:

$$u = 0 \quad \text{at} \quad y = 0, \tag{3a}$$

$$u = 0 \quad \text{at} \quad y = 1, \tag{3b}$$

$$p = p_0 \quad \text{at} \quad x = 1, \tag{3c}$$

$$\partial p/\partial x = 0 \quad \text{at} \quad x = 1/2. \tag{3d}$$

[3] Numbers in brackets designate References at end of technical brief.

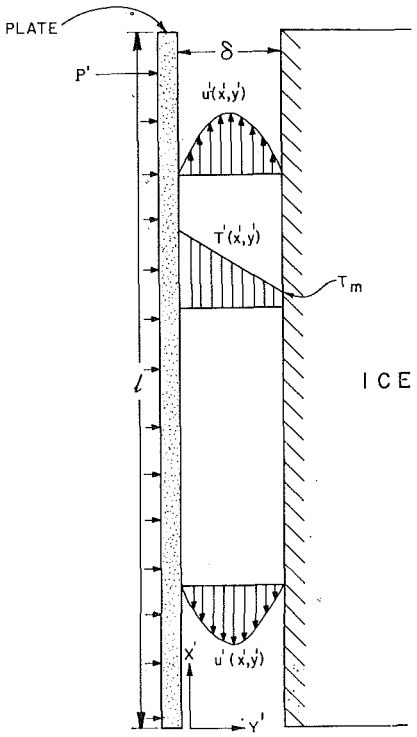

Fig. 1 Diagram of the plate-melting solid considered

Through the use of equation (2) and a mass balance of the flowing liquid, the following expressions for the pressure distribution and liquid velocity profiles may be obtained.

$$p = p_0 - \frac{6}{\mathrm{Re}}\left(\frac{l}{\delta}\right)^2 (x^2 - x) \tag{4}$$

$$u = \frac{3l}{\delta}(2x - 1)(y - y^2) \tag{5}$$

The gap thickness, δ, can be found by integrating equation (4) over the plate length.

Solving for δ yields

$$\delta = \left[\frac{V\mu l^2}{P' - p_0'}\right]^{1/3} \tag{6}$$

which is the result for melted water film thickness in terms of melting rate V, plate length l, and average contact pressure P'.

The thermal analysis consists of making an energy balance across a small section of length dx' for the water film of thickness δ. Conduction in the x' direction is neglected. Balancing the heat transport terms yields equation (7), where $T = T'/T_m$,

$$\frac{\delta}{l}\frac{\partial}{\partial x}\int_0^1 uT\,dy = 1 + \frac{1}{\mathrm{Pe}}\left[\left.\frac{\partial T}{\partial y}\right|_{y=1} - \left.\frac{\partial T}{\partial y}\right|_{y=0}\right] \tag{7}$$

The dimensionless boundary conditions for the temperature profile across the melted ice water film are:

$$T = 1 \qquad \text{at} \qquad y = 1 \tag{8a}$$

$$\partial T/\partial y = -h\rho V\delta/T_m k \qquad \text{at} \qquad y = 1 \tag{8b}$$

Assuming $T = G(x) + H(x)y + I(x)y^2$, equation (9$a$) for the temperature profile in the liquid may be obtained from equations (8a) and (8b).

$$T = 1 + (I - K) + (K - 2I)y + Iy^2 \tag{9a}$$

where

$$K = -\mathrm{Pe}\, h/T_m C_p \tag{9b}$$

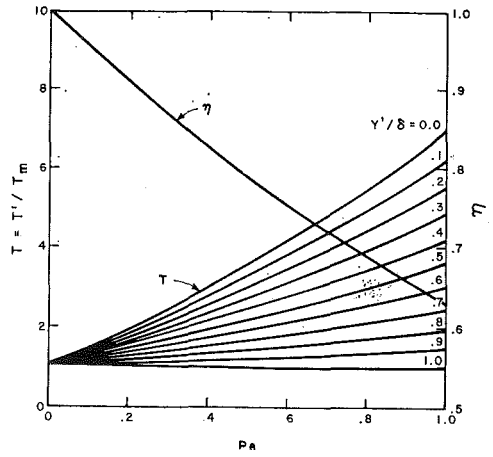

Fig. 2 Dimensionless temperature profiles and thermal efficiency as a function of Peclet number

After substituting equation (9a) into equation (7), a differential equation in $I(x)$ is obtained.

$$z\frac{dI}{dz} - LI = M \tag{10a}$$

$$z = 3(2x - 1)/20 \tag{10b}$$

$$L = 20/3\ \mathrm{Pe} - 1 \tag{10c}$$

$$M = 10K/6 \tag{10d}$$

A solution of equation (10a) was found to be:

$$I(x) = S[3(2x - 1)/20]^L - M/L \tag{11}$$

This completes the solution for the temperature profile throughout the film of melted ice water in terms of a constant S. For ice properties and temperatures constant with x, the condition

$$\partial T/\partial y|_{y=0^{x=0}} = \partial T|\partial y_{y=0^{x=1}} \quad \text{indicates } S = 0.$$

A final formulation of the thermal efficiency of plate melting was made. The efficiency η was defined as the amount of heat that actually reaches and melts the ice, divided by the total amount of heat which leaves the plate, with the remainder lost through the melt water.

$$\eta = \frac{\displaystyle\int_{\frac{1}{2}}^{1} \left.\frac{\partial T}{\partial y}\right|_{y=1} dx}{\displaystyle\int_{\frac{1}{2}}^{1} \left.\frac{\partial T}{\partial y}\right|_{y=0} dx} = \frac{K}{[2M/L + K]} \tag{12}$$

Results and Discussion

The temperature profiles between the plate and ice may be represented on a dimensionless plot for all conditions of melting up to the boiling point at the plate. The results are presented in Fig. 2 with dimensionless temperature plotted against Peclet number. To use Fig. 2, a Peclet number must be calculated using fluid properties at the plate-ice mean temperature. This procedure requires iteration for the correct Peclet number which then may be used to find the plate temperature at $y'/\delta = 0$ and also the melt efficiency, η.

Inertia forces in the melted ice water are assumed much less than viscous forces. The largest inertia force is $\rho u'\partial u'/\partial x'$ and the largest viscous force is $\mu\partial^2 u'/\partial y'^2$. From the analysis the maximum liquid velocity, u_m, occurs at $\delta/2$ and at the plate ends. The following should approximate the largest ratio of inertia to viscous forces:

$$\mathrm{Re}^* = \frac{\text{Inertia forces}}{\text{Viscous forces}} = \frac{\rho u' \partial u'/\partial x'}{\mu \partial^2 u'/\partial y'^2} = \frac{\rho u_m \delta}{2\mu} \cdot \frac{\delta}{l} \qquad (13)$$

Calculations indicate that Re* begins to exceed 0.1 around a Peclet number of about 1.0.

The thermal balance excludes conduction in the x' direction. This assumption is valid if the ratio of convection to conduction in the x' direction is large. This normally is indicated by a Peclet number in excess of about 100. A reduced Peclet number may be defined as follows:

$$\mathrm{Pe}^* = \frac{\text{Convection effects}}{\text{Conduction effects}} = \frac{\rho V C_p |2x' - l| l}{4\delta k} \qquad (14)$$

Sample calculations indicate that $\mathrm{Pe}^* \gg 100$ for about 99 percent of the plate with low values only at or near the plate center where the velocity is zero.

Acknowledgments

The authors would like to thank the management of Sun Oil Company Production Research Laboratory for permission to publish these calculations.

References

1 Carslaw, H. S., and Jaeger, J. C., *Conduction of Heat in Solids*, Oxford at the Clarendon Press, 1959.

2 Goodman, T. R., and Shea, J. J., "The Melting of Finite Slabs," *Journal of Applied Mechanics*, Mar. 1960, pp. 16–24.

3 Hahne, E. W. P., and Grigull, U., "The Regelation of Ice—A Problem of Heat Conduction," *International Journal of Heat and Mass Transfer*, Vol. 15, No. 5, May, 1962, pp. 1057–1066.

4 Landau, H. G., "Heat Conduction in a Melting Solid," *Quarterly of Applied Mathematics*, Vol. VIII, No. 1, 1950, pp. 81–94.

5 Rosenthal, D., "The Theory of Moving Sources of Heat and Its Application to Metal Treatments," TRANS. ASME, Nov. 1946, pp. 849–866.

6 Yen, Y. C. and Tien, C., "Laminar Heat Transfer Over a Melting Plate, The Modified Leveque Problem," *Journal of Geophysical Research*, Vol. 68, No. 12, June 15, 1963, pp. 3673–3678.

ERRATA

Churchill, S. W., and Ozoe, H., "Correlations for Laminar Forced Convection in Flow Over an Isothermal Flat Plate and in Developing and Fully Developed Flow in an Isothermal Tube," published in the Aug., 1973, issue of JOURNAL OF HEAT TRANSFER, pp. 416–419.

Third line below equation (1) should be $y(x)$ not $y(z)$.
Third line below equation (1) should read arbitrary.
Reference [16] should be p. 281 not pp. 281.
Reference [23] should be Heat and Mass Transfer.

journal of heat transfer

discussion

The Effect of Curvature on Heat or Mass Transfer From an Isothermal Sphere[1]

Tsutomu Hirose.[2] The discusser is much interested in this valuable article on curvature effect, since he is studying the particle–fluid heat/mass transfer processes.

The author derived the following equation

$$\overline{\mathrm{Nu}} = 1.156\sqrt{\mathrm{Pe}} + 4.73 + \mathrm{o}(\mathrm{Pe}^{-1/2}) \tag{1}$$

for a sphere in the potential flow region and concluded that the curvature effect becomes quite important at moderate Peclet number ($\mathrm{Pe} < 10^3$). However, the details of numerical evaluation, i.e., manipulation from (22) to (23), were not given there.

The discusser evaluated the integral (22) as shown in the Appendix to reach a different result, as

$$\overline{\mathrm{Nu}} = 1.128\sqrt{\mathrm{Pe}} + 0.821 + \mathrm{o}(\mathrm{Pe}^{-1/2}) \tag{2}$$

with a smaller curvature effect than that given by (1). Thus the curvature effect is not significant (less than 10 percent) for $\mathrm{Pe} > 10^2$, in contrast to the author's conclusion. The curvature effect consists of two contributions: (*a*) increase of the diffusion area and (*b*) decrease of tangential velocity with increasing normal distance from the surface of a sphere. The former enhances the transfer rate while the latter lowers it. Because of such conflicting contributions, a large effect of curvature would not be expected in the case of potential flow.

Appendix. Substituting (21) into (22) gives, after some manipulation using (14*a*), (14*b*), and (17*a*),

$$\overline{\mathrm{Nu}} = \frac{\sqrt{3}\sqrt{\mathrm{Pe}}}{2}\int_0^{\frac{4}{3}}\left\{\frac{1}{\sqrt{\pi\zeta}} - \frac{2/\sqrt{\mathrm{Pe}}}{\sqrt{3\pi}\,\Gamma(3/2)} \times \int_0^1 \frac{\sqrt{\tau}(1-2\tau)}{\sqrt{1-\tau}\,\sin^2\theta(\zeta\tau)}\,d\tau\right\}d\zeta = \frac{\sqrt{3}\sqrt{\mathrm{Pe}}}{2}\int_0^{\frac{4}{3}}\frac{1}{\sqrt{\pi\zeta}}\,d\zeta$$

$$- \frac{1/\sqrt{\mathrm{Pe}}}{\sqrt{\pi}\Gamma(3/2)}\int_0^1 \frac{1-2\tau}{\sqrt{\tau}\sqrt{1-\tau}}\,d\tau \int_0^{\frac{4}{3}\tau}\frac{1}{\sin^2\theta(\zeta)}\,d\zeta$$

$$= \frac{2}{\sqrt{\pi}}\sqrt{\mathrm{Pe}} + \frac{1}{\sqrt{\pi}\Gamma(3/2)}\int_0^1 \frac{1}{\sqrt{\tau}\sqrt{1-\tau}} \times \left\{1 - \cos\theta\left(\frac{4}{3}\tau\right)\right\}d\tau - \frac{2}{\sqrt{\pi}\Gamma(3/2)}\int_0^1 \frac{\sqrt{1-\tau}}{\sqrt{\tau}} \times \left\{1 - \cos\theta\left(\frac{4}{3}\tau\right)\right\}d\tau$$

in which θ is a function of ζ as expressed by (14*b*). Since $\cos\theta(\frac{4}{3}\tau) + \cos\theta\{\frac{4}{3}(1-\tau)\} = 0$, the first integral of the last equation equals $\int_0^1 \frac{1}{\sqrt{\tau}\sqrt{1-\tau}}\,d\tau = \Gamma(\frac{1}{2})\Gamma(\frac{1}{2})$. Numerical integration of the second integral gives 0.926. Thus one gets

$$\overline{\mathrm{Nu}} = \frac{2}{\sqrt{\pi}}\sqrt{\mathrm{Pe}} + \frac{1}{\sqrt{\pi}\Gamma(3/2)}\left\{\Gamma\left(\frac{1}{2}\right)\Gamma\left(\frac{1}{2}\right) - (2)(0.926)\right\}$$

which is identical to (2).

Author's Closure

I thank Mr. Hirose for his very careful review of my paper and for his clever reduction of the integral expression for $\overline{\mathrm{Nu}}$ to a simple form. Unfortunately it appears that the value he obtained by numerical integration of the final integral expression in his Appendix is not correct. The value should be

$$\int_0^1 \frac{\sqrt{\tau}}{\sqrt{1-\tau}}\left[1 - \cos\left(\frac{4\tau}{3}\right)\right]d\tau = 2.217$$

instead of 0.926.

In checking my paper I have discovered a sign mistake in equation (21). This equation should read as follows:

$$\mathrm{Nu}(\theta) = \sqrt{3}\sqrt{\mathrm{Pe}}\sin^2\theta\left\{\frac{1}{\sqrt{\pi\zeta}} - \frac{1/\sqrt{\mathrm{Pe}}}{\sqrt{\pi}\,\Gamma\left(\frac{3}{2}\right)} \times \int_0^1 \frac{\sqrt{\zeta}(1-\tau)}{\sqrt{\tau}}(2\tau-1)f[\zeta(1-\tau)]\,d\tau\right\} \tag{21d}$$

When these corrections are made and the value of $\overline{\mathrm{Nu}}$ is evaluated using Mr. Hirose's integrals but with the corrected numerical integral, we find

$$\overline{\mathrm{Nu}} = \frac{2}{\sqrt{\pi}}\mathrm{Pe}^{1/2} + 0.88 \tag{23d}$$

Incidentally, the value reported for Nu(0) is also incorrect. The correct value is

$$\mathrm{Nu}(0) = 2\sqrt{\frac{3}{\pi}}\mathrm{Pe}^{1/2} + \frac{8}{3\pi} \tag{24d}$$

As Mr. Hirose has pointed out, these corrections substantially alter the conclusions regarding the value of Pe at which curvature first becomes significant. More important, the value of C_2 apparently does not change very much with Prandtl number. Most experimental investigators have found this to be the case.

The correct shape of the envelope that bounds the large and small-Prandtl-number results is apparently quite different from that reported earlier at small Peclet numbers. This is the most important point of all. The envelope is shown in Fig. 5 along with the data previously reported and some additional data.

It was the peculiar nature of the data of Kinzer and Gunn that kindled my interest in this problem. In the 20 years since these data were reported, a fair number of papers appeared in the meteorology literature attempting to explain the abnormally large Sherwood numbers reported for Peclet numbers between 1 and 20 or so. The shape of the envelope at small Prandtl numbers as reported in my paper seemed to lend credence to this data, rather than that of Froessling [14].[3] It happens that while my paper was in press Beard and Pruppacher [15] reported some low-Reynolds-number data and Woo and Hamielec [16] reported a numerical study of low-Reynolds-number mass transfer from a sphere that support the Froessling data. These new results and the corrected version of my own results cast some doubt

[1] By R. G. Watts, published in the Feb. 1972 issue of the JOURNAL OF HEAT TRANSFER, TRANS. ASME, Series C, Vol. 94, No. 1, pp. 1–6.

[2] Research Assistant, Department of Chemical Engineering, Kyushu University, Fukuoka, Japan.

[3] Numbers in brackets designate Additional References at end of discussion.

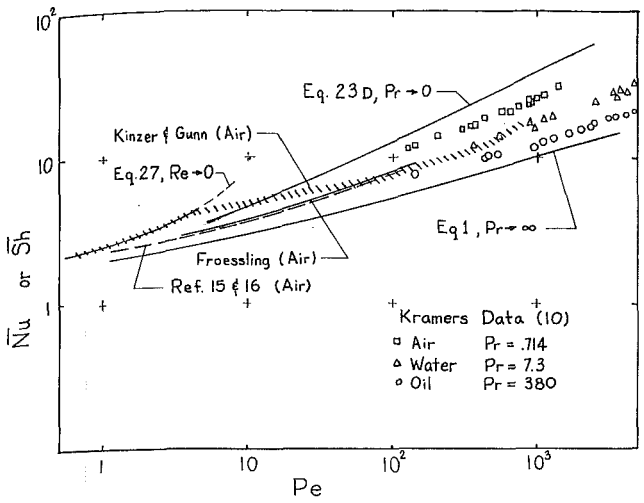

Fig. 5

on the accuracy of the Kinzer–Gunn data. Of course one cannot with great assurance extrapolate the large-Peclet-number part of the envelope to very small Peclet numbers. Nevertheless, the trend seems to support the data of Froessling and that of Beard and Pruppacher rather than the data of Kinzer and Gunn.

It is worth pointing out that the data of Beard and Pruppacher and the theory of Woo and Hamielec fall consistently lower than that of Kramers in the same Peclet-number range.

Hsu [17] has noted that the empirical formula derived by Kramers gives Nusselt numbers that are higher than those computed by other formulae by as much as 50 percent. Data for heat transfer from spheres to air compiled by William [18] agree much better with Beard–Pruppacher and with Woo–Hamielec.

It appears that more work needs to be done, particularly in the low and intermediate-Peclet-number range, in order to obtain an accurate expression of Nusselt number as a function of Reynolds and Prandtl numbers for submerged spheres.

Once again, I would like to express my gratitude to Mr. Hirose for reading my paper so carefully and for pointing out the error in the evaluation of the constants C_1 and C_2. I apologize for this unfortunate error.

Additional References

14 Froessling, N., "Ueber die Verdunstung fallender Tropfen," *Beitr. Geophys.*, Vol. 52, 1938, pp. 170–216.

15 Beard, K. V., and Pruppacher, H. R., "A Wind Tunnel Investigation of the Rate of Evaporation of Small Water Drops Falling at Terminal Velocity in Air," *J. of the Atmos. Sci.*, Vol. 28, 1971, pp. 1455–1464.

16 Woo, S. E., and Hamielec, A. E., "A Numerical Method of Determining the Rate of Evaporation of Small Water Drops Falling at Terminal Velocity in Air," *J. of the Atmos. Sci.*, Vol. 28, 1971, pp. 1448–1454.

17 Hsu, S. T., *Engineering Heat Transfer*, D. Van Nostrand, New York, p. 334.

18 William, G. C., personal communication to W. H. McAdams in W. H. McAdams, *Heat Transmission*, McGraw-Hill, New York, p. 237.